

STUDIES ON GRAVITATIONAL SPREADING CURRENTS

Thesis by

Jing-Chang Chen

In Partial Fulfillment of the Requirements
for the Degree of
Doctor of Philosophy

California Institute of Technology
Pasadena, California

1980

(Submitted March 17, 1980)

© 1980

Jing-Chang Chen

All Rights Reserved

ACKNOWLEDGMENTS

The writer wishes to express his deepest gratitude to his thesis advisor, Professor E. J. List, who offered much guidance, encouragement, and valuable criticism throughout this investigation.

Several talks with Professors Vito A. Vanoni and Norman H. Brooks always gave a long lasting comfortable feeling, which is especially needed in the life of a graduate student at Caltech. His officemate, Dr. Greg Gartrell, Jr., helped in many phases in accomplishing this research and shared many ups and downs of the research life.

The writer would also like to thank Mr. Elton F. Daly, supervisor of the Shop and Laboratory, and Mr. Joe Fontana for their assistance in designing and constructing the experimental set up and their patience in teaching him how to play cribbage during lunch time. Appreciation is also due Mr. David Byrum, who helped in setting up equipment and taking photographs; Mrs. Adelaide R. Massengale, who typed the manuscript; and Mrs. Joan Mathews, who typed some parts of the earlier draft.

For financial aid of his graduate studies at Caltech, the writer is grateful to The Li Foundation Inc., New York for a two-year (1974-76) Fellowship and to the California Institute of Technology for Graduate Laboratory Assistantship (1974-75), and Graduate Research Assistantship (1975-present). The financial support for this research work from the National

Science Foundation through Grant Nos. GK-35774X, ENG75-02985, and ENG77-27398 is greatly appreciated.

Finally, the author wishes to thank his parents and every member of his family for their continuous encouragement for a higher education over the past years, and his wife, Yuan-Lin, for her sacrifice in putting up with most of her time alone, days and nights. Without the strong spiritual support from each member of the family, completing this research work would have been impossible. This thesis is dedicated to his beloved Grandfather.

ABSTRACT

The objective of this investigation is to examine the buoyancy-driven gravitational spreading currents, especially as applied to ocean disposal of wastewater and the accidental release of hazardous fluids.

A series of asymptotic solutions are used to describe the displacement of a gravitationally driven spreading front during an inertial phase of motion and the subsequent viscous phase. Solutions are derived by a force scale analysis and a self-similar technique for flows in stagnant, homogeneous, or linearly density-stratified environments. The self-similar solutions for inertial-buoyancy currents are found using an analogy to the well-known shallow-water wave propagation equations and also to those applicable to a blast wave in gasdynamics. For the viscous-buoyancy currents the analogy is to the viscous long wave approximation to a nonlinear diffusive wave, or thermal wave propagation. Other similarity solutions describing the initial stage of motion of the flow formed by the collapse of a finite volume fluid are developed by analogy to the expansion of a gas cloud into a vacuum. For the case of a continuous discharge there is initially a starting jet flow followed by the buoyancy-driven spreading flow. The jet mixing zone in such flows is described using Prandtl's mixing length theory. Dimensional analysis is used to derive the relevant scaling factors describing these flows.

TABLE OF CONTENTS

	<u>Page</u>
ACKNOWLEDGMENTS	ii
ABSTRACT	iv
TABLE OF CONTENTS	v
LIST OF FIGURES	x
LIST OF TABLES	xxvii
NOMENCLATURE	xxx
CHAPTER 1 INTRODUCTION	1
CHAPTER 2 REVIEW OF PREVIOUS STUDIES	8
2.1 Wastewater Field from Submarine Outfall Discharges	8
2.1.1 Maximum Height or Rise and Spreading Level	8
2.1.2 Observations of Spreading Flows	8
2.1.3 Unsteady Density Spread in a Stagnant Environment	16
2.2 Surface Wastewater Discharge in a Cross Current	26
2.2.1 Non-Buoyant Models	26
2.2.2 Surface Density Spread Models	31
2.3 Gravity-Driven Starting Flows	38
2.3.1 Formation of Gravity-Driven Flows	38
2.3.2 Lock Exchange Flows	39
2.3.3 Plane Surface Starting Buoyant Jets	47
2.3.4 Von Kármán, Prandtl, and Benjamin Theories	56
2.4 Previous Analysis of Density Front Propagation	69
2.4.1 Spreading in a Homogeneous Environment	69
2.4.2 Spreading in a Linearly-Stratified Environment	72
2.5 Further Mixing of Surface Spreading Flow	74
2.5.1 Description of Spreading Flow	74
2.5.2 Surface Buoyant Jet Models	74

	<u>Page</u>
CHAPTER 3 THEORETICAL ANALYSIS	78
3.0 Introductory Note	78
3.1 Force Scale Analysis for Density Currents	78
3.1.1 Free Surface Spreading Currents	78
3.1.2 Bottom Spreading Currents	88
3.1.3 Internal Density Currents	90
3.2 Similarity Solutions for Inertial-Buoyancy Density Currents	94
3.2.1 Longitudinal Internal Shallow-Water Wave Equations	95
3.2.2 Gas Dynamics Analogy	98
3.2.3 Derivation of Self-Similar Formulae	101
3.2.3.1 Method of Separation of Variables	101
3.2.3.2 Taylor's Method	105
3.2.4 Evaluation of Self-Similar Solutions	107
3.2.4.1 General Derivation	107
3.2.4.2 Shock Conditions at Front	112
3.2.5 Asymptotic Solutions for Surface Density Spreading	115
3.2.5.1 Plane and Radial Surface Density Spread from a Finite Volume Release	116
3.2.5.2 Starting Two-Dimensional Stratified Flow	120
3.2.5.3 Surface Radial Starting Plume	122
3.2.6 Asymptotic Solutions for Internal Density Spreading	124
3.2.6.1 Plane and Radial Submerged Density Spread from a Finite Volume Release	125
3.2.6.2 Internal Plane Starting Layer (Continuous Flow)	129
3.2.6.3 Internal Radial Starting Layer (Continuous Flow)	131
3.2.7 Initial Stage of Density Spread	133

	<u>Page</u>
3.3 Similarity Solutions of Viscous-Buoyancy Density Currents	143
3.3.1 Nonlinear Long Wave Equations	144
3.3.2 Derivation of Self-Similar Formula by the Method of Separation of Variables	145
3.3.3 Derivation of General Self-Similar Solutions	147
3.3.4 Solutions for Spreading from a Finite Volume Release	150
3.3.5 Plane Viscous Spreading Layer from a Continuous Discharge	157
3.3.6 Radial Viscous Spreading Layer from a Continuous Discharge	165
3.4 Further Mixing of Surface Spreading Flow	167
3.4.0 Introductory Note	167
3.4.1 Turbulent Surface Jet Mixing	172
3.5 Dimensional Analysis	185
3.5.1 Radial Surface Buoyant Jet	185
3.5.2 Surface and Submerged Horizontal Buoyant Jets	194
3.5.3 Dynamic Collapse	196
3.5.4 Radial Surface Buoyant Jet in a Cross Current	199
CHAPTER 4 EXPERIMENTAL STUDIES AND APPARATUS	203
4.0 Introduction	203
4.1 Surface Buoyant Jet	203
4.1.1 Experimental Set-Up	203
4.1.2 Density and Dilution Measurements	204
4.1.3 Photographic Equipment	206
4.2 Radial Surface Heated and Buoyant Jets	208
4.2.1 General Experimental Set-Up	208
4.2.2 Temperature Measurements	209
4.2.3 Overhead Photographs	216

	<u>Page</u>	
CHAPTER 5	EXPERIMENTAL RESULTS	217
5.1	Half-Radial Surface Buoyant Jet	217
5.1.1	Starting Half-Radial Surface Buoyant Jet	220
5.1.2	Density Measurements	231
5.1.3	Periodic Feature	242
5.2	Radial Heated Surface Jet	242
5.3	Radial Surface Buoyant Jet in a Cross Current	250
CHAPTER 6	COMPARISONS WITH PREVIOUS STUDIES	264
6.1	Spreading Currents in Homogeneous Environment	264
6.1.1	Plane Current from a Finite Volume Release	264
6.1.2	Radial Current from a Finite Volume Release	277
6.1.3	Plane Current from Continuous Steady Discharge	284
6.1.4	Radial Current from Continuous Steady Discharge	295
6.1.5	Initial Stage of Finite Volume Release	308
6.2	Spreading Currents in Linearly Stratified Environment	314
6.2.1	Plane Submerged Current from a Finite Volume Release	314
6.2.2	Plane Submerged Current from Continuous Steady Discharge	337
6.2.3	Radial Submerged Current	357
CHAPTER 7	ENGINEERING APPLICATIONS	360
7.1	Ocean Outfall Discharge	360
7.2	Surface Buoyant Discharge	366
7.3	Barge Disposal of Dredged Spoil and Sludge	372
7.4	Base Surge Flow	374
CHAPTER 8	DISCUSSION AND CONCLUSIONS	377
8.1	On the Similarity Solutions for Buoyant Spreading Currents	377

	<u>Page</u>
8.2 On the Initial Stage of Flows	380
8.3 On the Memory of Spreading Currents	381
8.4 On the Thickness Profile of Spreading Currents	382
8.5 On Dimensional Analysis and Spreading Currents	383
APPENDIX A DERIVATION OF LONGITUDINAL INTERNAL SHALLOW-WATER WAVE EQUATIONS	384
A.0 Basic Equations and Assumptions	384
A.1 Free Surface Density Spreading Flows	386
A.2 Bottom Surface Density Spreading Flows	389
A.3 Submerged Density Spreading Flows	392
APPENDIX B DERIVATION OF SIMILARITY SOLUTIONS FOR INERTIAL- BUOYANCY SPREAD	397
B.1 Surface Density Spreading Flows	397
B.2 Submerged Density Spreading Flows	399
APPENDIX C DERIVATION OF BOUNDARY CONDITIONS AT THE FRONT	402
C.0 Introduction	402
C.1 Surface Density Spread	403
C.2 Submerged Density Spread	405
APPENDIX D SEDOV'S (1957) LINEAR SIMILARITY VELOCITY FUNCTION	408
APPENDIX E DERIVATION OF VISCOUS LONG WAVE EQUATIONS FOR DENSITY SPREAD FLOWS	411
E.0 Basic Equations and Assumptions	411
E.1 Viscous Surface Density Spread	413
E.2 Viscous Submerged Density Spread	417
LIST OF REFERENCES	421

LIST OF FIGURES

<u>Figure</u>		<u>Page</u>
1.1(a)	Surface density spread field from a horizontal single-port outfall discharge into a uniform environment.	3
1.1(b)	Submerged density spread field from a horizontal single-port outfall discharge into a density-stratified environment.	3
1.2(a)	Surface density spreading field due to a multi-port diffuser discharge into a uniform environment.	3
1.2(b)	Submerged density spreading field due to a multi-port diffuser discharge into a density-stratified environment.	3
1.3	Submerged density field from a single-port outfall discharge spreading between two homogeneous layers of densities ρ_u and ρ_a (e.g. epilimnion and hypolimnion).	4
1.4(a)	Bottom turbidity current from a barged sludge disposal.	4
1.4(b)	Spreading turbidity current at the stably stratified interface from barged sludge disposal.	4
1.4(c)	Spreading turbidity current at an intermediate level of density stratified ocean from barged sludge disposal.	4
1.5	Dense bottom currents from a negatively buoyant discharge.	4
1.6	A wide surface density spreading field persisting for a long distance before oceanic turbulent diffusion takes over, aerial photograph taken by Foxworthy and Kneeling (1969) at Ventural Outfall on November 11, 1966.	6

<u>Figure</u>	<u>Page</u>	
2.1.1	A series of radial oceanic fronts in a fjord observed by McClimans (1978). The photograph from which this reproduction was made was taken by T. A. McClimans, who graciously supplied a copy to the author.	12
2.1.2(a)	Radially horizontal spreading cooling tower plume in a stably stratified environment. (Courtesy of Kramer and Seymour, 1976)	15
2.1.2(b)	A series of discontinuous radially spreading fronts. (Courtesy of Kramer and Seymour, 1976)	15
2.1.3(a)	Flow regions resulting from a positive submerged buoyant round or plane jet discharging vertically upwards into a homogeneous environment.	17
2.1.3(b)	Flow regions resulting from a negative buoyant round or plane jet discharging vertically downwards into a homogeneous environment.	17
2.1.4(a)	Free surface spreading front due to a submerged horizontal buoyant round jet discharge.	18
2.1.4(b)	Bottom surface spreading front due to a horizontal buoyant round jet discharge.	18
2.1.5	Unsteady spreading tip position at time t due to a buoyant pipe flow discharge, after Sharp (1971).	18
2.1.6	Simulation of submerged density spreading by a horizontal jet discharging at its own density level in a linearly density-stratified environment, after Maxworthy (1972).	22
2.1.7	Growth history of the interflowing wedge front due to a horizontal slot jet discharging at a neutral buoyant level into a linearly density-stratified ambient, data from Zuluaga-Angel <i>et al.</i> (1972).	23
2.1.8(a)	Three stages of plane submerged density front spread due to a finite volume of homogeneous fluid collapsing at a neutral level in a linearly density-stratified environment, after Wu (1965).	25

<u>Figure</u>	<u>Page</u>
2.1.8(b) Sequential cross sections of plane submerged density front spread at various times, after Wu (1965).	25
2.2.1 A non-buoyant and non-diffusive source in a uniform cross current.	28
2.2.2 Schematic diagram for diffusive field from line-like diffuser in an ocean current, after Brooks (1960).	28
2.2.3(a) Superposition of a series of circular diffusion patches in a horizontal turbulent current.	30
2.2.3(b) Superposition of a series of slices of diffusion elements in a horizontal turbulent current.	30
2.2.4(a) Top view of surface density spread field in a horizontal current.	34
2.2.4(b) Central cross section along x direction of surface density spread field in a horizontal current.	34
2.2.5 Side-spread model for the plume boundary of a surface wastewater field.	35
2.2.6 Radial spread model for the plume boundary of surface wastewater field.	37
2.3.1 Lock exchange flow.	40
2.3.2(a) Lock and channel before removing gate.	43
2.3.2(b) Advancing lock exchange flow.	43
2.3.2(c) Finite-length exchange flow.	43
2.3.3 Idealized shape of saline front from finite-length lock exchange flow, after Keulegan (1957).	43
2.3.4(a) Forced free surface density currents.	49
2.3.4(b) Forced bottom surface density currents.	49
2.3.5 Surface density currents and discharging box used by Barr (1959).	51

<u>Figure</u>		<u>Page</u>
2.3.6	Growth history of starting free surface gravity currents, reproduced from Chen (1975). Experimental data from Almquist (1973).	53
2.3.7	Advancing wedge on the bottom of a channel, after Keulegan (1946).	55
2.3.8(a)	Configuration of a forced plane gravity current as viewed in a fixed reference frame to the ground.	57
2.3.8(b)	Configuration of a forced plane density wedge as viewed in a moving reference frame with the front, after von Kármán (1940).	57
2.3.9	Internally spreading currents between a stably stratified interface.	59
2.3.10(a)	Advancing mass of cold air; actual flow relative to the ground, after Prandtl (1952).	61
2.3.10(b)	Advancing mass of cold air; idealized flow relative to the front, after Prandtl (1952).	61
2.3.11(a)	Cavity front moving at a constant velocity along a two-dimensional box.	64
2.3.11(b)	Arrested cavity front as viewed in a moving frame with the same velocity of front.	64
2.3.12	Comparison of theoretical solution (solid line) of Benjamin (1968) with the experimental results (open circles) of emptying cavity flow in an expansion gallery of surge tank by Ellis and Al-Khairulla (1974).	67
3.1.1	Idealized sketch of free surface spreading density currents.	79
3.1.2	Idealized sketch of bottom spreading density currents.	89
3.1.3	A homogeneous layer intruding at a neutral buoyant level into the linearly density-stratified ambient fluid.	89

<u>Figure</u>	<u>Page</u>
3.2.1(a) Coordinate system for free surface spreading flows.	96
3.2.1(b) Coordinate systems for bottom spreading flows.	96
3.2.1(c) Coordinate system for submerged density flows.	96
3.2.2 Self-similar velocity and thickness distributions of the plane and the radial inertial density wave front propagation due to a finite volume release of buoyant fluid.	119
3.2.3 Velocity and thickness distributions of a starting internal radial ring.	123
3.2.4 Similarity profiles of the half-thickness for a plane ($n=0$) and radial ($n=1$) interflowing layer resulting from a collapsing homogeneous mixed region at a neutral density level in a linearly stratified environment.	128
3.2.5 Similarity profiles of the average velocity and the half-thickness of interflowing radial ring due to a continuous release.	132
3.2.6 Similarity profiles for the mean horizontal velocity and the spreading layer thickness for the initial stage of surface density spreading in a homogeneous environment ($i=0$).	140
3.2.7 Similarity profiles for the average velocity and the half-thickness of interflowing submerged density spreading layer due to a finite volume release in a linearly density-stratified environment ($i=1$).	140
3.3.1 Self-similar thickness distribution of plane and radial viscous surface spread layer due to a finite volume release ($i=0$, $m=0$, $n=0$, and 1).	152
3.3.2 Self-similar thickness distribution of plane and radial viscous submerged density spread layer due to a finite volume release ($i=1$, $m=0$, $n=0$, and 1).	153

<u>Figure</u>		<u>Page</u>
3.3.3	Self-similar distribution of plane and radial viscous surface ($i = 0$) or submerged ($i = 1$) spreading fluid velocity due to a finite volume release ($n = 0, 1$, and $m = 0$).	158
3.3.4	Self-similar thickness distribution of plane viscous surface spread layer due to a constant rate of discharge into a homogeneous environment ($i = 0$, $m = 1$, $n = 0$). Solid line denotes the first approximation, and open circles denote the third approximation.	161
3.3.5	Self-similar half-thickness distribution of plane viscous submerged density spread layer due to a constant rate of discharge into a linearly density-stratified environment ($i = 1$, $m = 1$, $n = 0$). Solid line denotes the first approximation and open circles denote the third approximation.	162
3.3.6	Self-similar thickness distribution of radial viscous surface spread layer due to a constant rate of discharge into a homogeneous environment ($i = 0$, $m = 1$, $n = 1$). Solid line denotes the third term approximation, open circles, the first term approximation, and triangles, the second term approximation.	168
3.3.7	Self-similar half-thickness distribution of radial viscous submerged density spread layer due to a constant rate of discharge into a linearly density-stratified environment ($i = 1$, $m = 1$, $n = 1$). Solid line denotes the third term approximation, open circles, the first term approximation, and triangles, the second term approximation.	169
3.4.1(a)	Flow regimes of an outfall discharge (soon after startup): I: Submerged buoyant jet flow, II: Surface transition, III: Surface buoyant jet flow.	173
3.4.1(b)	A surface buoyant jet flow model with finite dimension of discharge (soon after startup).	173

<u>Figure</u>	<u>Page</u>	
3.4.2	Point source surface jet nomenclature.	174
3.4.3	Two self-similar profiles of mean horizontal velocity, $F'(\xi) = u(r,z)/u_m(r)$, and mean tracer when $K_u = K_c$, $\theta(\xi) = c(r,z)/c_m(r)$. Dash line indicates the solution derived from the Prandtl-Tollmien assumption and solid line from Prandtl-Görtler assumption.	186
3.5.1	Sketch of a radial surface buoyant jet.	187
3.5.2	Three regimes of starting surface or submerged buoyant jet flow.	197
3.5.3	Three stages of dynamic collapse flows.	198
4.1.1	Cross section of the half-radial discharging box.	205
4.1.2	Overall experimental set-up for the half-radial surface buoyant jet.	205
4.1.3	Photograph of a conductivity probe.	207
4.1.4	Typical calibration curve of conductivity probe.	207
4.2.1	Overall experimental set-up for radial surface heated jet.	210
4.2.2	Photograph of a rake of five fast-response thermistors.	212
4.2.3	Fast-response thermistor circuit designed by Gartrell (1979).	212
4.2.4	Buffer circuit for A/D converter from Gartrell (1979).	214
4.2.5	Typical calibration curve for fast-response thermistor.	215
5.1.1(a)	Cross sections of half-circular front at various time t after initiation of discharge. (a) Run No. 10/5/77, $Fr = 5.25$, $Re = 7100$.	221
5.1.1(b)	Run No. 11/16/77, $Fr = 10.0$, $Re = 8840$.	222

<u>Figure</u>	<u>Page</u>
5.1.1(c) Run No. 11/4/77. Fr = 15.0, Re = 8840.	223
5.1.2 Growth history of starting radial surface turbulent buoyant jet flow. Closed symbols indicate the photographs are shown in Figure 5.1.1.	224
5.1.3 Normalized growth history of starting radial surface turbulent buoyant jet flow. Closed symbols indicate the photographs are shown in Figure 5.1.1.	224
5.1.4(a) Relation of starting jet coefficient to jet Reynolds number.	226
5.1.4(b) Relation of starting jet coefficient to radial jet Froude number.	226
5.1.5 Relation of radial starting plume coefficient to (a) jet Reynolds number, (b) Froude number, (c) R_1/ℓ_{QM} .	228
5.1.6 Similarity profiles of viscous radial surface spreading currents at time t (71.4 seconds for No. 9/21/77, 101.7 for 9/28/77, and 96.6 for 10/5/77) after discharge.	230
5.1.7 Radial stratified flow due to a half-radial surface buoyant jet discharge	
(a) Run No. 10/5/77	232
(b) Run No. 11/16/77	233
(c) Run No. 11/4/77.	234
5.1.8 Density measurements of a half-radial surface buoyant jet (Run No. 10/27/77) with Fr = 10.00 at a radial distance r = 32.39 cm (or $r/\ell_{MB} = 0.726$).	235
5.1.9 Distribution of relative density difference respectively at a distance r = 17.15, 32.39, and 67.95 cm (or $r/\ell_{MB} = 0.384, 0.726, \text{ and } 1.523$) for a radial surface flow field (Run No. 10/27/77).	237
5.1.10 Self-similar distribution of relative density deficiency. Dotted line denotes Prandtl-Tollmien's solution.	238

<u>Figure</u>		<u>Page</u>
5.1.11	Relation of the maximum value of relative density deficiency to the radial distance. Symbols are defined in Figure 5.1.10.	239
5.1.12	Relation of the half-thickness to the radial distance. Symbols are defined in Figure 5.1.10.	239
5.1.13	Self-similar distribution of relative density deficiency (Run No. 10/10/77, Fr = 5.26).	240
5.1.14	Relation of the maximum value of relative density deficiency to the radial distance. Symbols are defined in Figure 5.1.13.	241
5.1.15	Relation of the half-thickness to the radial distance. Symbols are defined in Figure 5.1.13.	241
5.1.16	Comparison of the observed period with the predicted value T given by Eq. (3.2.87).	243
5.2.1	Thermal expansion coefficient of water as a function of temperature after Kotsovinos (1975).	247
5.2.2	Kinematic viscosity of water as a function of temperature.	247
5.2.3	Relation of the maximum value of relative mean temperature excess to the relative radial distance r/r_j .	248
5.2.4	Relation of the maximum value of relative mean temperature excess to the normalized radial distance r/ℓ_{MB} .	249
5.2.5	Relation of the normalized half-thickness to the normalized radial distance. Symbols are defined in Figure 5.2.4.	249
5.2.6	Self-similar relative mean temperature excess above the ambient temperature. Solid line denotes the Prandtl-Tollmien solution given in Chapter 3.	
	(a) Run No. 10/19/78, Fr = 6.36.	251
	(b) Run No. 10/20/78, Fr = 6.28.	251
	(c) Run No. 10/18/78, Fr = 10.10.	252
	(d) Run No. 10/17/78, Fr = 9.28.	252

<u>Figure</u>	<u>Page</u>
5.2.7	Profiles of the intensity of turbulent temperature fluctuations for radial surface heated jet (Run No. 10/17/78) versus depth and relative radial distance. 253
5.3.1(a,b)	Photographs of the development of a surface flow due to a radial surface buoyant jet in a cross current (Run No. 4/10/77). (a) t = 35, (b) t = 80 seconds after initiation of discharge. 256
5.3.1(c,d)	Photographs of the development of a surface flow due to a radial surface buoyant jet in a cross current (Run No. 4/10/77). (c) t = 110, (d) t = 485 seconds after initiation of discharge. 257
5.3.2	Growth histories of the downstream edge of an initiating surface field. 258
5.3.3	Upstream edge position of surface buoyant field. Symbols are defined in Table 5.3.2. 261
5.3.4	Growth of a surface buoyant field measured from upstream edge. 263
6.1.1	Growth histories for plane surface spreading currents due to a finite volume release. Experimental data are from Almquist (1973). Symbols are defined in Table 6.1.1. 267
6.1.2	Normalized growth histories of plane surface spreading currents due to a finite volume release. Symbols are defined in Table 6.1.1.
	$R_1 = \left(\frac{g\Delta V^5}{\nu} \right)^{1/7} \quad \text{and} \quad t_1 = \left(\frac{V^4}{(g\Delta)^2 \nu^3} \right)^{1/7} .$ 268
6.1.3	Coefficients of inertial-buoyancy spreading currents expressed as a function of Reynolds number $\sqrt{g\Delta h_0} h_0/\nu$. 270
6.1.4	Coefficients of viscous-buoyancy spreading currents expressed as a function of Reynolds number $\sqrt{g\Delta h_0} h_0/\nu$. 270

<u>Figure</u>		<u>Page</u>
6.1.5	Frontal velocity decay of density currents from a finite-length lock exchange flow, experimental data from Figure 3 of Keulegan (1957). $H = 5.8$ cm, $L_0 = 41.7$ cm, and width of channel = 2.54 cm.	273
6.1.6	Frontal velocity decay of turbidity currents from a finite-length lock exchange flow, experimental data from Figure 10 of Middleton (1966). $H = 20.3$ cm, $L_0 = 28.3$ cm, width of channel = 13.83 cm, and average settling velocity of suspension = 0.9 cm/sec.	274
6.1.7(a)	Frontal trajectory for an inertial-buoyancy oil slick spreading in a channel, data from Run No. 1 of Liang (1971). $V = 131.2$ cm ² , $\Delta = 0.136$.	276
6.1.7(b)	"Wave gage" measurements (in solid curve) of inertial oil slick spreading thickness by photo-cell equipment located at three locations (60, 85, 110 cm from end wall of channel for Station no. 1,2,3). Dotted curves indicate prediction by similarity solutions, data from Liang (1971).	278
6.1.8	Dynamic collapse of a homogeneous region at a stably stratified interface. Numerical calculation data from Figure 7 of Meng and Thomson (1978).	279
6.1.9(a)	Oil spreading sections at four times after release of 1500 cubic meters of oil (1200 tons). Data from Abbott (1961).	281
6.1.9(b)	Growth history of inertial-buoyancy radial oil spreading front. Data from Figure 6.1.9(a).	282
6.1.9(c)	Comparison of oil spreading layer thickness given in Figure 6.1.9(a) with similarity profiles ($n = 0$ denotes plane case, Eq. (6.1.10) and $n = 1$ denotes radial case, Eq. (6.1.11)).	282
6.1.10(a)	Radial gravity currents produced from circular lock exchange flow. The aspect ratio $Ar = 2$ and the initial radius $R_0 = 3.45$ cm, data from Table 1 of Martin and Moyce (1952, Part V).	285

<u>Figure</u>	<u>Page</u>
6.1.10(b) Radial gravity currents produced from circular lock exchange flow. The initial relative density difference $\Delta = 0.428$, data from Table 2 of Martin and Moyce (1952, Part V).	286
6.1.11 Growth history of a volume of syrup spreading on the shining face of aluminum foil.	287
6.1.12(a) Plane surface spreading currents from a continuous steady discharge, data from Barr (1959).	289
6.1.12(b) Plane surface spreading currents from a continuous steady discharge, data from Almquist (1973).	290
6.1.13 Plane bottom spreading currents from a steady continuous discharge.	291
6.1.14 Unsteady surface spreading currents in a channel due to a buoyant pipe flow discharge, data from Sharp (1971).	293
6.1.15(a) Radial surface stratified flow formed after the diluted effluent reached the free surface (77.9 and 155.5 seconds later). Due to a submerged buoyant round jet ($d_j = 0.586$ cm, $\Delta = 0.0170$, $Q_j = 40.8$ cm ³ /sec) discharged vertically into a uniform stagnant environment ($H = 11.72$ cm).	297
6.1.15(b) A band of radial surface stratified flow formed after the diluted effluent reached the free surface (70.5 and 166.5 seconds later). Due to a submerged buoyant round jet ($d_j = 0.586$ cm, $\Delta = 0.0142$, $Q_j = 18.9$ cm ³ /sec) discharged vertically into a uniform stagnant environment ($H = 6.19$ cm).	298
6.1.15(c) A series of outward travelling circular internal waves formed after the diluted effluent reached the free surface (79.1 and 121.6 seconds later). Due to a submerged buoyant round jet ($d_j = 0.586$ cm, $\Delta = 0.1092$, $Q_j = 4.5$ cm ³ /sec) discharged vertically into a uniform stagnant environment ($H = 23.41$ cm).	299
6.1.16 Growth histories of radial surface spreading fronts shown in Figures 6.1.15(a), (b), and (c).	301
6.1.17 Growth histories of bottom radial gravity currents, data from Britter (1979).	302

<u>Figure</u>		<u>Page</u>
6.1.18	Growth history of radial surface spreading fronts due to a submerged buoyant round jet discharging horizontally into a uniform stagnant environment, data from Sharp (1969a).	304
6.1.19	Growth history of radial bottom gravity currents due to a submerged buoyant round jet discharge horizontally into a uniform stagnant environment, data from Sharp (1969b).	305
6.1.20	Radial spreading rate of crude oil on ice. The kinematic viscosity ν of crude oil is assumed as $60 \text{ cm}^2/\text{sec}$ for open symbols and as $23.1 \text{ cm}^2/\text{sec}$ for solid symbols. Data are from McMinn and Golden (1973).	306
6.1.21	Growth history of surface spreading front at centerline of boundary buoyant surface discharge, data from Barr (1959) and Hayashi and Shuto (1967).	307
6.1.22(a)	Initial collapse of a rectangular shape column, line sketch of photograph from Martin and Moyce (1952, part IV).	310
6.1.22(b)	Calculated self-similar profiles of initial collapse shown in Figure 6.1.22(a).	310
6.1.23	Growth history of plane front during initial collapse of a liquid column with rectangular section ($h_1 = 3h_0/2$ in Eq. (6.1.39)). Data from Tables 1, 2, and 3 of Martin and Moyce (1952, part IV).	311
6.1.24	Growth history of plane front during initial collapse of a liquid column with semi-circular section ($h_1 = \frac{3\pi}{8} h_0$ in Eq. (6.1.39)) ($R_0 = 2$ inches), data from Table 4 of Martin and Moyce (1952, part IV).	312
6.1.25	Growth history of radial front during initial collapse of a liquid column with vertical circular cylinder ($h_1 = 2h_0$ in Eq. (6.1.40)), data from Table 5 of Martin and Moyce (1952, part IV).	313
6.1.26	Comparison of self-similar profile with numerical calculation results by Harlow and Welch (1965) and Fox and Goodwin (1952) for the collapse of a plane symmetrical column in vacuo, initially rectangular at rest, at various relative distance $\eta = R(t)/R_0$.	315

<u>Figure</u>	<u>Page</u>
6.1.27	Comparison of self-similar profile with numerical calculation results by the method of characteristics by Penney and Thornhill (1952) for the collapse of an initially semi-cylindrical section column at rest at specific time $t \sqrt{\frac{g}{h_0}} = 0.8$ or $\eta = R(t)/R_0 = 1.78$. 316
6.1.28	Comparison of self-similar profile with numerical calculation results by the method of characteristics by Penney and Thornhill (1952) for the collapse of an initially semi-elliptic column at rest at various time $t\sqrt{gh_0}/R_0 = 0.5, 1.0, 1.5,$ and 2.0 or various relative distance $\eta = R(t)/R_0 = 1.44, 2.08, 2.75,$ and 3.50 . 317
6.2.1	Three spreading stages of a plane mixed region collapsing in a linearly density-stratified environment. 320
6.2.2	Comparison of theoretical solutions (the initial and the final collapse stages) for submerged density spreading front with experimental results by van de Watering (1966) on a plane mixed region collapsing in a linearly density-stratified environment. 324
6.2.3	Eleven cases of growth history for submerged density spread front due to a plane mixed region collapsing in a linearly density-stratified environment. Data are taken from Figures 10, 11, and 12 of Wu (1965). Details of experimental parameters for each case are shown in Table 6.2.1. 325
6.2.4	A plane mixed region collapsing in a linearly density-stratified environment. Comparison of theoretical solutions (the principal and the final collapse stages) for submerged density spreading front with experimental results by Wu (1965). 328
6.2.5	A plane mixed region collapsing in a linearly density-stratified environment. Comparison of theoretical solutions for submerged density spreading front (the inertial-buoyancy and the viscous-buoyancy regions) with experimental results by Wu (1965). 329

<u>Figure</u>		<u>Page</u>
6.2.6	Coefficient of the principal collapse stage (the inertial-buoyancy submerged spread) as a function of Reynolds number Re_N and the initial radius of semi-circular mixed region.	330
6.2.7	Coefficient of the final collapse stage (the viscous-buoyancy submerged spread) as a function of Reynolds number Re_N and the initial size of semi-circular or circular mixed region.	331
6.2.8	Plane mixed region in a linearly density-stratified environment: comparison of theoretical solution with experimental results by Wu (1965), for an interflowing front in the final collapse stage. Detail of recalculation is shown in Figure 6.2.2.	333
6.2.9	Comparison of theoretical solutions with previous numerical calculations by several investigators as shown in Table 6.2.3.	336
6.2.10	Growth history of an inertial starting plume observed by Manins (1976a). Details of experimental parameters are given in Table 6.2.6.	342
6.2.11	Growth history of viscous plume observed by Maxworthy (1972). Details of experimental parameters are given in Table 6.2.6.	344
6.2.12	Growth history for submerged plane horizontal starting buoyant jets observed by Zuluaga-Angel <i>et al.</i> (1972). Details of experimental parameters are given in Table 6.2.6.	347
6.2.13	Intrusion front velocity as a function of buoyancy flux $B_1 = NQ$. Experimental data are taken from Manins (1976a), \bigcirc , $N^2 = 3.5$; \square , $N^2 = 7.0$; Δ , $N^2 = 14.0$.	348
6.2.14	Self-similar distribution of intrusion layer half-thickness near the source. Experimental data are taken from Manins (1976a), \bigcirc , $N^2 = 3.5$; \square , $N^2 = 7.0$; Δ , $N^2 = 14.0$.	348
6.2.15	The plane submerged front velocity due to a starting horizontal slot buoyant jet discharge at its neutral level in a linearly density-stratified environment. The relevant experimental parameters are given in Tables 6.2.5 and 6.2.6.	350

<u>Figure</u>		<u>Page</u>
6.2.16	The coefficient of submerged plane viscous starting plume (or submerged viscous-buoyancy spread) expressed as a function of discharged Richardson number Ri_j and viscous plume Reynolds number Re_v . Experimental parameters given in Table 6.2.6.	351
6.2.17	The coefficient for a submerged plane viscous starting plume expressed as a function of R_1/λ_{QM} . Symbols are defined in Table 6.2.7.	353
6.2.18	The coefficient of spreading for a submerged plane starting jet expressed as a function of discharge Richardson number Ri_j , data from Table 6.2.7.	355
6.2.19(a)	Viscous intrusion layer profiles at each time t . Data are taken from experiment No. R-11 in Table 4 of Zuluaga-Angel <i>et al.</i> (1972).	356
6.2.19(b)	Self-similar thickness distribution of viscous intrusion layer. Solid curve is the viscous long wave solution (3rd order) derived in Subsection 3.3.5.	356
6.2.20	Line sketch for a series of radial ring discontinuities in a horizontal spreading cooling tower plume in atmosphere.	359
7.1.1(a)	Buoyant surface spreading wastewater field from submerged single port (diameter 78 inches) discharge, average discharge rate $Q = 120$ mgd (185.6 cfs), submerged depth $H = 55$ ft, $\Delta = 0.025$. Photograph from Figure 21 of Allan Hancock Foundation (1964).	361
7.1.1(b)	Photograph from Figure 22 of Allan Hancock Foundation (1964).	362
7.1.1(c)	Photograph from Figure 20 of Allan Hancock Foundation (1964).	363
7.1.1(d)	Buoyant surface spreading wastewater field from submerged single port (diameter 36 inches) discharge. Average discharge rate $Q = 2.20$ mgd (3.40 cfs), submerged depth $H = 35$ feet. Photograph from Figure 4 of Foxworthy and Kneeling (1969).	364
7.1.2(a)	Growth of buoyant surface wastewater field shown in Figures 7.1.1(a), (b), (c), and (d).	365

<u>Figure</u>		<u>Page</u>
7.1.2(b)	Dimensionless plotting of growth of buoyant surface wastewater field shown in Figure 7.1.2(a).	365
7.1.3	Growth of heated (a,b,c) and nonheated (d,e) surface plume field due to a submerged outfall discharge. Data from Table 1 of Sonnichsen (1971). (a) $Q = 75,000$ cfs, (b) 110,000 cfs, (c) 145,000 cfs, (d) 50,000 cfs, and (e) 100,000 cfs.	367
7.2.1(a)	Line sketch of the thermal image of a discontinuous radial thermal plume field at Sheboygan Power Station, Wisconsin, on September 15, 1971; aerial photograph taken at a flying height 5000 feet. Photograph was shown in Figure 19 of Scarpace and Green (1973).	368
7.2.1(b)	Line sketch of thermal image of a discontinuous radial thermal plume at Sheboygan Edgewater Plant. Photograph was shown in Figure 8a of Green <i>et al.</i> (1972).	369
7.2.1(c)	Line sketch of thermal image of a discontinuous radial thermal plume at Port Washington harbor on September 1971. Photograph was shown in Figure 8b of Green <i>et al.</i> (1972).	370
7.2.2	Comparison of oscillating period of inertial radial surface thermal plume with theoretical value given by Eq. (3.2.87).	371
7.3.1	The time an axially symmetric bottom turbidity current arrived at four fixed locations at a radial distance r_s from the dump site of dredge spoil; data from Figure 2 of Gordon (1974).	373
7.3.2	"Wave-gage type" record of the spreading layer thickness of the bottom turbid cloud from three different dump operations measured at a radial distance $r_s = 30$ meters from the dump site; data from Figure 5 of Gordon (1974).	375
7.4.1	Propagating mist-laden air forming the base surge following an underwater atomic bomb explosion at Bikini Atoll.	376
A.3.1	Coordinate system of submerged density spread flows.	393

LIST OF TABLES

<u>Table</u>	<u>Page</u>	
2.1.1	Review of previous experiments on the buoyant round ($n=1$) or plane ($n=0$) jet rise into a stagnant linearly density-stratified environment.	9
2.3.1	Experimental studies on lock exchange flows.	41
2.3.2	Experimental studies on plane gravity currents due to a constant rate of discharge at one end of channel.	48
2.4.1	Summary of previous theoretical studies of a plane ($n=0$) or a radial ($n=1$) submerged density front spreading in a linearly density-stratified environment due to a finite volume release ($m=0$) or a continuous discharge ($m=1$) at a neutral level.	73
3.1.1	Asymptotic formulae for starting surface plumes (Chen, 1975).	84
3.1.2	Length and time scales for surface density spreading.	86
3.1.3	Asymptotic formulae for surface density spreading front velocity as a function of frontal distance.	87
3.1.4	Asymptotic formulae for submerged density spreading of an intrusion layer in a linearly density-stratified environment.	92
3.1.5	Length and time scales of submerged density spread for normalization.	93
3.2.1	The original characteristic thickness scale h_1 for the initial stage of surface density spread in a homogeneous environment ($i=0$) expressed as a function of the initial shape of liquid volume before spreading.	138
3.2.2	The original characteristic thickness scale h_1 expressed as a function of initial cross sections for the initial submerged density spread in a linearly density-stratified environment ($i=1$).	139

<u>Table</u>	<u>Page</u>
3.3.1	The value of the integration constant I_{ion} for surface and submerged spreading from a finite volume release ($m = 0$). 155
3.3.2	The frontal trajectory functions for the viscous-buoyant surface or submerged spreading due to a finite volume release ($m = 0$). 156
3.3.3	Integration values I_{i10} for plane viscous-buoyancy spreading currents due to a continuous steady discharge plume. 163
3.3.4	Coefficients b_{i10} for the plane viscous-buoyancy spreading currents to a continuous steady discharge plume. 164
3.3.5	Integration values I_{i11} for the radial viscous-buoyancy spreading currents due to a continuous steady discharge plume. 170
3.3.6	Coefficients b_{i11} for the radial viscous-buoyancy spreading currents due to a continuous steady discharge plume. 171
3.4.1	Prandtl-Tollmien similarity solutions of turbulent surface jet flows. 181
3.5.1	Length, time, and velocity scales of a radial surface buoyant jet. 190
3.5.2	Definitions of volume, momentum, and buoyancy fluxes for a horizontal surface or submerged buoyant plane or radial jet. 195
3.5.3	The ratio of R_{Bv} to R_1 and t_{Bv} to t_1 when $i = 0$. 200
3.5.4	The ratio of R_{Bv} to R_1 and t_{Bv} to t_1 when $i = 1$. 201
4.2.1	Fast-response thermistor characteristics. 209
5.1.1	Summary of data for starting half-radial surface buoyant jet experiments, $r_j = 9.962$ cm, $h_j = 0.3175$ cm, and $h = 75.0$ cm. 218
5.1.2	Summary of calculated data for starting half-radial surface buoyant jet experiments. 219

<u>Table</u>	<u>Page</u>	
5.1.3	Summary of observed and predicted periods.	244
5.2.1	Summary of experiments on radial surface heated jet in a stagnant environment.	245
5.3.1	Summary of experimental data for a radial surface buoyant jet in a cross current.	255
5.3.2	Calculation of upstream edge position.	258
6.1.1	Summary of experiments performed by Almquist (1973) on the plane surface currents due to a finite volume release.	265
6.2.1	Experimental parameters related to Figures 6.2.3, 6.2.4, 6.2.5, 6.2.6, and 6.2.7.	327
6.2.2	Re-calculation of experimental data for the final collapse stage of a plane mixed region in a linearly density-stratified environment. Data are taken from the upper tangent points of principal collapse stage in Tables 1 and 2 of Wu (1965).	334
6.2.3	Parameters of numerical calculations related to Figure 6.2.9.	335
6.2.4	Four flow patterns for a plane intrusion layer due to different combinations of three dimensionless numbers.	339
6.2.5	Summary of experimental parameters for submerged plane intrusion layer propagation in a linearly density-stratified environment due to a horizontal slot buoyant jet discharge at its neutral level	341
6.2.6	Experimental data for plane intrusive layer spreading related to Figures 6.2.10, 6.2.11, 6.2.12, 6.2.15, 6.2.16, and 6.2.17.	343
6.2.7	Calculation of the coefficient of displacement for a submerged plane viscous starting plume as shown in Figure 6.2.17.	354
8.1	Summary of asymptotic formulae of frontal trajectory functions derived by inertial (shallow-water wave) and viscous long wave theories.	379

NOMENCLATURE

A	dimensional constant
$Ar = \frac{h_o}{R_o}$	aspect ratio of a fluid volume
a	dimensionless constant
$a_j, j = 1, 2, \dots$	calibration constants for thermistor probe or coefficients in polynomial expansion series
B	kinematic buoyant flux or channel width
B(x)	half-width of surface spreading field
B_i	kinematic buoyancy flux, $B_o = g\Delta Q$ for $i = 0$ and $B_1 = NQ$ for $i = 1$
B_o	initial half-width of surface spreading field
b	initial width of diffusive wastewater field
b_{imn}	coefficient in asymptotic time function
$b_u(r)$	jet width based on velocity u distribution
$b_c(r)$	jet width based on tracer c distribution
C(x,y)	concentration distribution at (x,y)
C_o	initial concentration
c	sound speed or relative density or temperature difference or inertial starting plume coefficient
c_c	coefficient related mixing length scale λ_c to r
c_u	coefficient related mixing length λ_u to r
$c_m(r)$	maximum tracer concentration at $z = 0$
c_{imn}	coefficient in asymptotic time functions of inertial starting plume
c_j	initial tracer value of jet fluid
D	channel depth

D_j	diameter of pipe
d	thickness of box or starting turbulent jet coefficient
d_j	diameter of submerged round jet or width of plane jet
d_n	elevated height of density head
d_1	trough height near density head
d_2	crest height of density head
E	total energy released during explosion
F	initial Froude number of lock exchange flow, $U/\sqrt{2g(\rho_2 - \rho_1)H}/(\rho_2 + \rho_1)$
F_A	inwards horizontal pressure force at front
F_S	outwards horizontal pressure force at front
F_P	unbalanced total pressure force for surface or submerged spreading, $F_S - F_A$
F_I	inertial force retarding spreading
F_{VA}	viscous force due to boundary layer shear in the ambient fluid
F_{VS}	viscous force due to boundary layer shear in spreading fluid
F_A'	inwards horizontal pressure force at front for bottom gravity currents
F_S'	outward horizontal pressure force at front for bottom gravity currents
F_P'	unbalanced total pressure force for bottom gravity currents, $F_S' - F_A'$
F_D	hydrodynamic drag force resisting spreading
F_{IS}	interfacial shear force resisting spreading
F_i	initial densimetric Froude number of horizontal spreading flow

Fr	discharge Froude number of buoyant jet, l_{MB}/l_{QM}
Fr _j	inlet Froude number, $u_j/\sqrt{g\Delta h_j}$
Fr ₁	Froude number of emptying cavity flow based on cavity depth h_2 , $U/\sqrt{gh_2}$
Fr ₂	Froude number of emptying cavity flow based on total depth d , U/\sqrt{gd}
Fr ₃	Froude number of emptying cavity flow based on flow depth $d-h_2$, $U/\sqrt{g(d-h_2)}$
F _ℓ	local densimetric Froude number $u/\sqrt{g\Delta h}$
F _∞	Froude number at far downstream of plane forced gravity currents, $U/\sqrt{g(\rho_s - \rho_a)h_\infty/\rho_a}$
F ₁	Froude number at far field of finite length lock exchange flow, $U/\sqrt{2g\Delta\rho_f d_1/(\rho_1 + \rho_2)}$
F ₂	Froude number at far field of lock exchange flow, $U/\sqrt{2g\Delta\rho_f d_2/(\rho_1 + \rho_2)}$
f	self-similar fluid velocity distribution function of $(i+4)$ th power function of $H(\xi)$ for viscous spreading flow
g	gravitational acceleration, 980 cm/sec ²
g'	effective gravitational acceleration, $g(\rho_a - \rho_i)/\rho_a$
H	ambient water depth
H(ξ)	similarity thickness distribution
H _B	length scale associated with buoyant plume height of rise
H _M	length scale associated with momentum jet height of rise
H _A (ξ)	approximation function of H(ξ)
H _L (ξ)	lower bound of H(ξ)
H _u (ξ)	upper bound of H(ξ)
H ₁ (ξ)	dimensional self-similar thickness scale

$h(r,t)$	spreading layer thickness at position r and time t
$h,h(t)$	average thickness of spreading field or spreading layer
h_i	initial surface spreading layer thickness due to a submerged buoyant jet discharge
h_j	thickness ($i=0$) or half-thickness ($i=1$) of buoyant jet discharge
h_ℓ	head loss in emptying cavity flow
h_n	height of density nose
h_o	initial thickness of a spreading volume at symmetric point
h_1	thickness scale for initial spreading stage listed in Tables 3.2.1 and 3.2.2
h_2	thickness of cavity in emptying cavity flow in a channel
h_∞	plane gravity current thickness at far downstream from head
I_{imn}	integration constant for the case of i, m, n
i	environment parameter denotes uniform environment with $i=0$ and linearly density-stratified environment with $i=1$
J	dimensional number involving momentum flux integration
j	index integer number 0,1,2,---
K_u	unknown coefficient related to eddy viscosity ϵ_u
K_c	unknown coefficient related to eddy diffusivity ϵ_c
k	unknown integer
k_{in}	shape factor for the case of i and n
$L(t)$	frontal position at time t
L_o	length of finite length lock exchange flow
ℓ	lobe length of three-dimensional feature of density current or unknown integer

l_{MB}	length scale defined by M and B
l_{QM}	length scale defined by Q and M
l_{QB}	length scale defined by Q and B
l_u	mixing length scale of velocity u
l_c	mixing length scale of tracer c
M	kinematic momentum flux of buoyant jet
m	source parameter denotes continuous steady discharge with $m=1$, the finite volume release with $m=0$
N	Brunt-Väisälä frequency of ambient stratification
n	geometric parameter, denotes plane symmetric flow with $n=0$, and radially symmetric flow with $n=1$
P_d	total flow force at downstream of emptying cavity flow
Pr	Prandtl number
P_s	pressure at the nose observed from a coordinate system travelling with front
P_u	total flow force at upstream of emptying cavity flow
P_∞	pressure force at far downstream observed from a coordinate system travelling with front
p	gas pressure
Q	volume flux of buoyant jet
Q_c	computed flow rate of a plane spreading current in a linearly stratified environment
Q_i	calculated volume flux rate at the source of spreading
Q_j	discharge flow rate of submerged buoyant jet
R(t)	frontal distance or radius at time t
Re	general symbol for Reynolds number
Re_j	buoyant jet Reynolds number, $u_{MB} l_{MB} / \nu_j$ or Q / ν_s
Re_N	initial Reynolds number of internal spreading in a linearly stratified environment due to finite volume release, Nh_o^2 / ν_s or NR_o^2 / ν_s

Re_p	plume Reynolds number
$Re_V = \frac{(NQ)^{1/2} h_j}{\nu_s}$	Reynolds number of plane jet discharging into a linearly stratified environment
$Re_1 = \frac{U d_1}{\nu_m}$	Reynolds number of density head based on trough height d_1 and average viscosity ν_m
$Re_2 = \frac{U d_2}{\nu_m}$	Reynolds number of density head based on crest height d_2 and average viscosity ν_m
$Re_3 = \frac{U d_2}{\nu_s}$	Reynolds number of density head based on crest height and spreading fluid viscosity ν_s
$Ri = \frac{\sqrt{g \epsilon} h_\infty}{U}$	frontal Richardson number of plane current in stratified ambient
$Ri(r, t) = \left(\frac{g \Delta_i}{R^2} \right)^{\frac{1}{i+1}} h(r, t)$	local Richardson number
$Ri_f(t) = \left(\frac{g \Delta_i}{R^2} \right)^{\frac{1}{i+1}} h(R, t)$	frontal Richardson number
$Ri_j = \frac{N h_j}{u_j}$	initial plane Richardson number of slot jet discharging into a linearly stratified environment
R_{MB}	length scale defined by M and B
$R_{B\nu}$	length scale defined by B and viscous spreading
R_o	initial radial distance and half-length of base
R_l	transition length scale from inertial-buoyancy spreading to viscous-buoyancy spreading as defined in Tables 3.1.2 and 3.1.5
r	space variable
r_j	radius of radial surface buoyant jet
r_s	measuring location from the end of wall

$S(\gamma, m, n)$	coefficient in shock wave front propagation
S_c	channel slope
S_o	average distribution at free surface due to submerged discharge
T	measured temperature or theoretical oscillating period of inertial radial plume
T_a	temperature of ambient fluid
T_j	temperature of jet fluid
T_{ob}	observed oscillating period in density measurement
T'	fluctuation from mean temperature
t	time after initiation of discharge
t_{MB}	time scale defined by M and B
t_{Bv}	time scale defined by B and viscous spreading
t_o	dimensionless time scale from the initial collapse stage to the principal collapse stage, $R_o / \sqrt{g \Delta_1 h_o^{i+1}}$
t_1	transition time scale from inertial-buoyancy spreading to viscous-buoyancy spreading as defined in Tables 3.1.2 and 3.1.5
U	ambient current velocity or frontal velocity
U_d	density front velocity used by Larsen and Sørensen to estimate spreading field in a current
U_2	average fluid velocity in emptying cavity flow
u_{MB}	velocity scale defined by M and B
u_{QM}	velocity scale defined by Q and M
u_{QB}	velocity scale defined by Q and B
$u(r, t)$	average fluid velocity at time t and location r
$u(r, z)$	fluid velocity in horizontal direction
u_f	fluid velocity just behind the front
u_j	initial buoyant jet velocity

$u_m(r)$	horizontal fluid velocity at free surface $z = 0$
u'	fluctuation value of horizontal velocity
$V(t), V$	volume of spreading fluid or measured voltage
$V_j(t)$	total volume supplied at time t
V_o	initial total volume of spreading fluid
$W(r)$	turbulent tracer flux at r
w	width of channel or fluid velocity in z direction
w'	fluctuation value of vertical velocity
x	downstream distance in the direction of current or $x = 1 - \xi$ space variable
x_d	downstream edge position of initiation of surface field
x_e	upstream edge position of surface field
x_i	any independent variable number i
$y(x)$	half-width of surface field
z	vertical coordinate
z_m	maximum height of rise
$z_{1/2}(r)$	thickness at 50% value of the maximum density deficiency
α	unknown constant
$\alpha(T)$	thermal expansion coefficient at temperature T_c
β	inclined angle of frontal interface or some constant
β_o	initial frontal angle
$\Gamma(x)$	Gamma function of x
γ	specific gas constant
Δ	relative density difference, $\Delta = \frac{\rho_j - \rho_a}{\rho_j}$
$\Delta(r, z)$	relative deficiency at (r, z)

Δ_i	relative density difference Δ with $i=0$ and density-stratified ambient slope with $i=1$
$\Delta_m(r)$	maximum value of density deficiency
δ	super-elevation of surface spreading layer above free surface
δ_1	Rayleigh's unsteady laminar boundary layer thickness, $\sqrt{\nu_a t}$
ϵ	effective eddy viscosity or ambient density gradient, $\frac{-1}{\rho_s} \frac{d\rho_a(z)}{dz}$
ϵ_u	eddy viscosity
ϵ_c	eddy diffusivity of tracer c
ϵ_o	initial eddy diffusivity at origin of wastewater field
η	relative frontal displacement $R(t)$ to the initial length or radius R_o , $\eta = R(t)/R_o$
θ	angle between the ambient flow direction and the tangent at the boundary of wastewater field
θ_a	potential temperature of ambient air
θ_s	potential temperature of spreading air
Λ	decay coefficient, $\Lambda = \frac{\theta_a - \theta_s}{R_o^2}$
λ	dimensionless number relative to front velocity to average or head spreading layer thickness
ν	kinematic viscosity of spreading fluid (0.01 cm ² /sec)
ν_a	kinematic viscosity of ambient fluid
ν_m	average value of kinematic viscosity of two fluids of lock exchange flow
ν_s	kinematic viscosity of spreading fluid

ξ	dimensionless horizontal coordinate $\xi = r/R(t)$ relative to frontal length or $\xi = az/r$ dimensionless variable
π	3.14159
ρ	gas density, fluid density
ρ_a	mass density of ambient fluid
ρ_i	calculated diluted fluid density at source
ρ_j	density of discharge fluid
ρ_s	mass density of spreading fluid
ρ_u	mass density of upper ambient fluid layer of stably stratified fluid
ρ_1, ρ_2	mass density of lock exchange flow
$\bar{\rho} = (\rho_1 + \rho_2)/2$	average mass density of two fluids in lock exchange flow
$\Delta\rho_f$	density difference at density head
$\Delta\rho_n$	salinity difference between the frontal and the ambient fluids
Σ	summation of series
σ	standard deviation of concentration distribution
τ	dimensionless time, $t \sqrt{g\Delta_i h_i^{i+1}}/R_o$
τ_{zr}	turbulent shear stress at (r, z)
$T(t)$	spreading layer thickness scale
ϕ	arbitrary dimensionless function, dependent variable
$\phi(\xi)$	similarity distribution of average velocity
ϕ_1	dimensional self-similar velocity scale
ϕ^*	dimensionless function
χ_u	mixing length coefficient related to u
χ_c	mixing length coefficient related to c

ψ	stream function
$\Omega(t)$	mean velocity scale

SPECIAL NOTATION

\sim	proportional to
$=$	equal to
\approx	approximately equal to
\circ	differentiation with respect to t
prime (')	differentiation with respect to ξ or fluctuating part
[]	jump value of the term inside brackets
∞	infinity
$(\bar{\quad})$	mean

SUBSCRIPTS

$+$	limit from above
$-$	limit from below
$*$	normalized value

CHAPTER 1

INTRODUCTION

It is a common practice to dispose of treated wastewater, or cooling water from power plants, by discharging it into a large body of receiving water, such as the ocean, lakes, or rivers. In order to prevent the possible contamination of the ambient water, pollution control agencies usually establish requirements specifying the discharge concentration levels permissible within a given distance from the point of discharge. These permissible concentration levels can then be used to calculate the dilution of the discharge that is necessary. To gain the required dilution two types of submerged discharge facilities are frequently used: one is the single port discharge at the open end of an outfall pipeline and the other is a multi-port diffuser. The usual goal is rapid mixing to reduce the undesirable attributes of the discharge to a tolerable concentration before the discharge is fully diffused into a larger environmental scale by ambient turbulence.

The minimum dilution requirement for submerged outfall discharges usually considers only the dilution induced by the discharge momentum and buoyancy without regard for dilution subsequent to the discharge reaching a free surface or becoming trapped by ambient density-stratification. Minimum surface dilution is sometimes predicted on the basis of the dilution at the same elevation as if the discharge were in an infinitely

deep receiving water. However, the outfall effluent, which initially behaves like a positive buoyant jet, may reach the free surface and become a free surface horizontal flow. The residual buoyancy and the flow momentum then induce a horizontal flow producing further dilution regardless of whether the ambient fluid is in motion.

Since oceans and lakes are usually density-stratified, especially in the summer season, diluted effluent may be trapped at some submerged level of neutral buoyancy and then may spread laterally. Such a submerged wastewater field is favored for avoiding contamination of surface waters. Figures 1.1(a) and (b) show the configurations of the surface spreading flow and submerged spreading flow due to a horizontal single-port outfall discharge; Figures 1.2(a) and (b) depict those due to a multi-port diffuser discharge. The same internal spreading layers are also found in thermally stratified lakes as shown in Figure 1.3.

A similar, though inverted, situation occurs with marine barge sludge disposal, which can sink as a negatively buoyant plume and spread as a subsurface turbidity current, at the sea floor or some intermediate level as shown in Figure 1.4. Such bottom currents are also formed, for example, by turbid or cold rivers flowing into a reservoir or lake, or by the discharge of a relatively dense liquid, as shown in Figure 1.5.

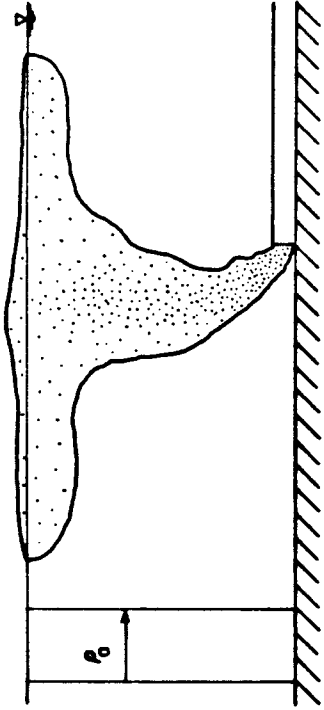


Figure 1.1(a) Surface density spread field from a horizontal single-port outfall discharge into a uniform environment.

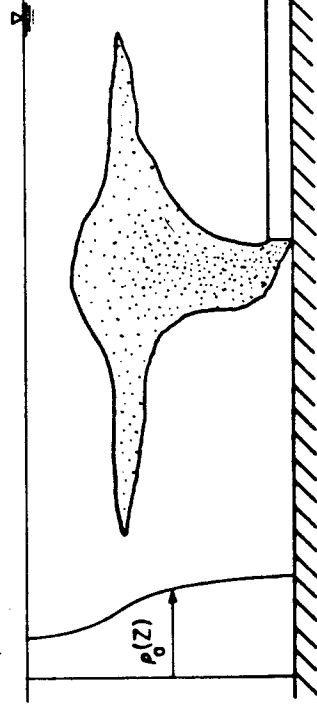


Figure 1.1(b) Submerged density spread field from a horizontal single-port outfall discharge into a density-stratified environment.

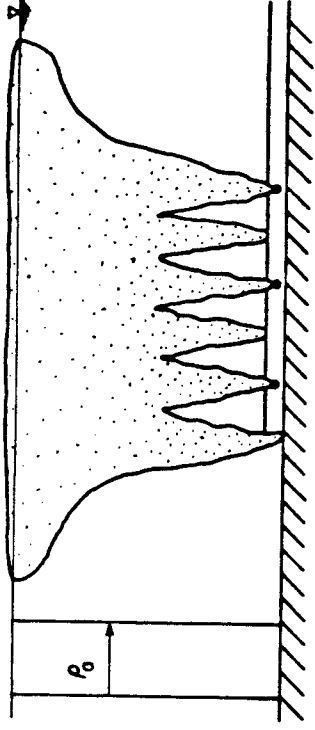


Figure 1.2(a) Surface density spreading field due to a multi-port diffuser discharge into a uniform environment.

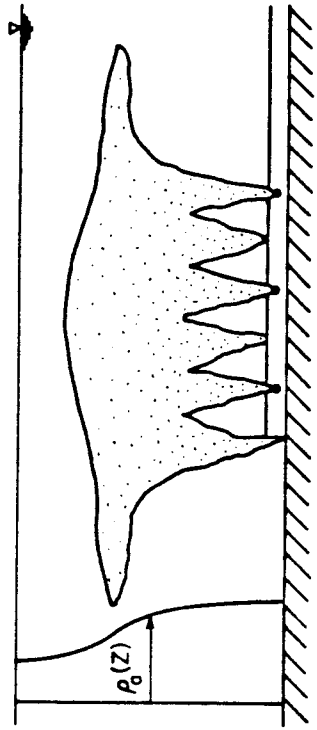


Figure 1.2(b) Submerged density spreading field due to a multi-port diffuser discharge into a density-stratified environment.

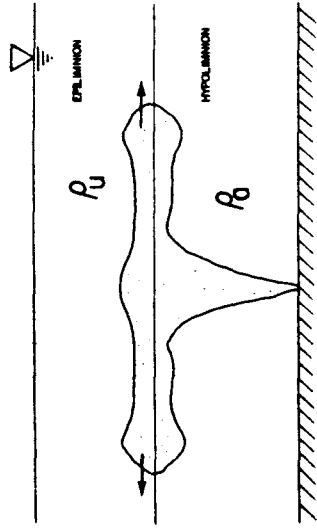


Figure 1.3 Submerged density field from a single-port outfall discharge spreading between two homogeneous layers of densities ρ_u and ρ_b (e.g. epilimnion and hypolimnion).

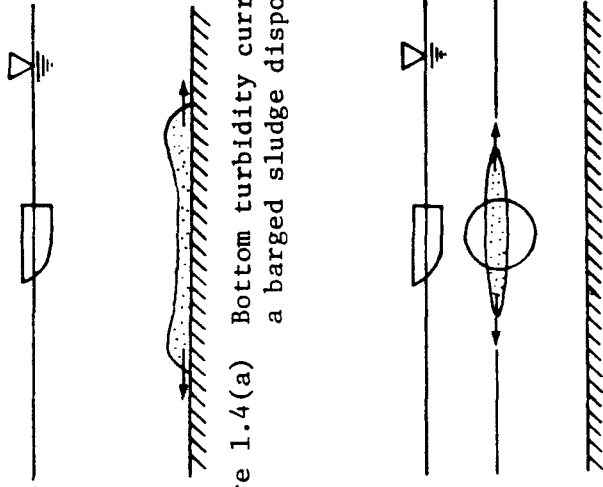


Figure 1.4(a) Bottom turbidity current from a barged sludge disposal.

Figure 1.4(b) Spreading turbidity current at the stably stratified interface from barged sludge disposal.

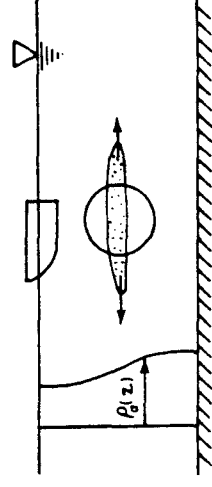


Figure 1.4(c) Spreading turbidity current at an intermediate level of density stratified ocean from barged sludge disposal.

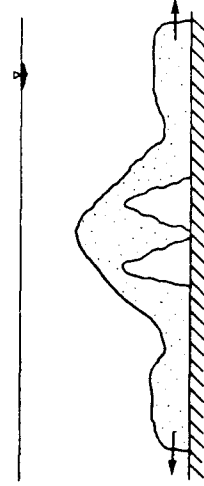


Figure 1.5 Dense bottom currents from a negatively buoyant discharge.

An analogous situation is found in the surface channel discharge of cooling water from power plants and also from large scale river flows into the ocean.

When there is a prevailing current the diluted discharge forms a wide downstream field, which may be found at the surface as shown in Figure 1.6, or lie below the surface for discharges trapped in a density stratification. Preventing the surface or subsurface wastewater field from reaching the shoreline involves predicting the size of this field. On the other hand, for cooling water discharges from nearshore power plants it may be preferable to have a wide surface field to accelerate the heat transfer to the atmosphere.

The object of the present investigation is to examine surface and subsurface buoyant spreading mechanisms for the wastewater fields due to submarine ocean outfalls discharging wastewater or cooling water, or the ocean barged disposal of sludge or dredge spoil. A review of previous studies of such gravity currents is given in Chapter 2.

In Chapter 3, theoretical analyses are presented for unsteady gravity-driven surface and subsurface spreading flows and nearfield surface buoyant jet mixing. A force scale analysis is used to derive a series of functions to describe both surface and submerged density spreading in a stagnant environment. In each asymptotic formula for frontal position there is one empirical coefficient. Similarity solutions of inviscid and viscous long

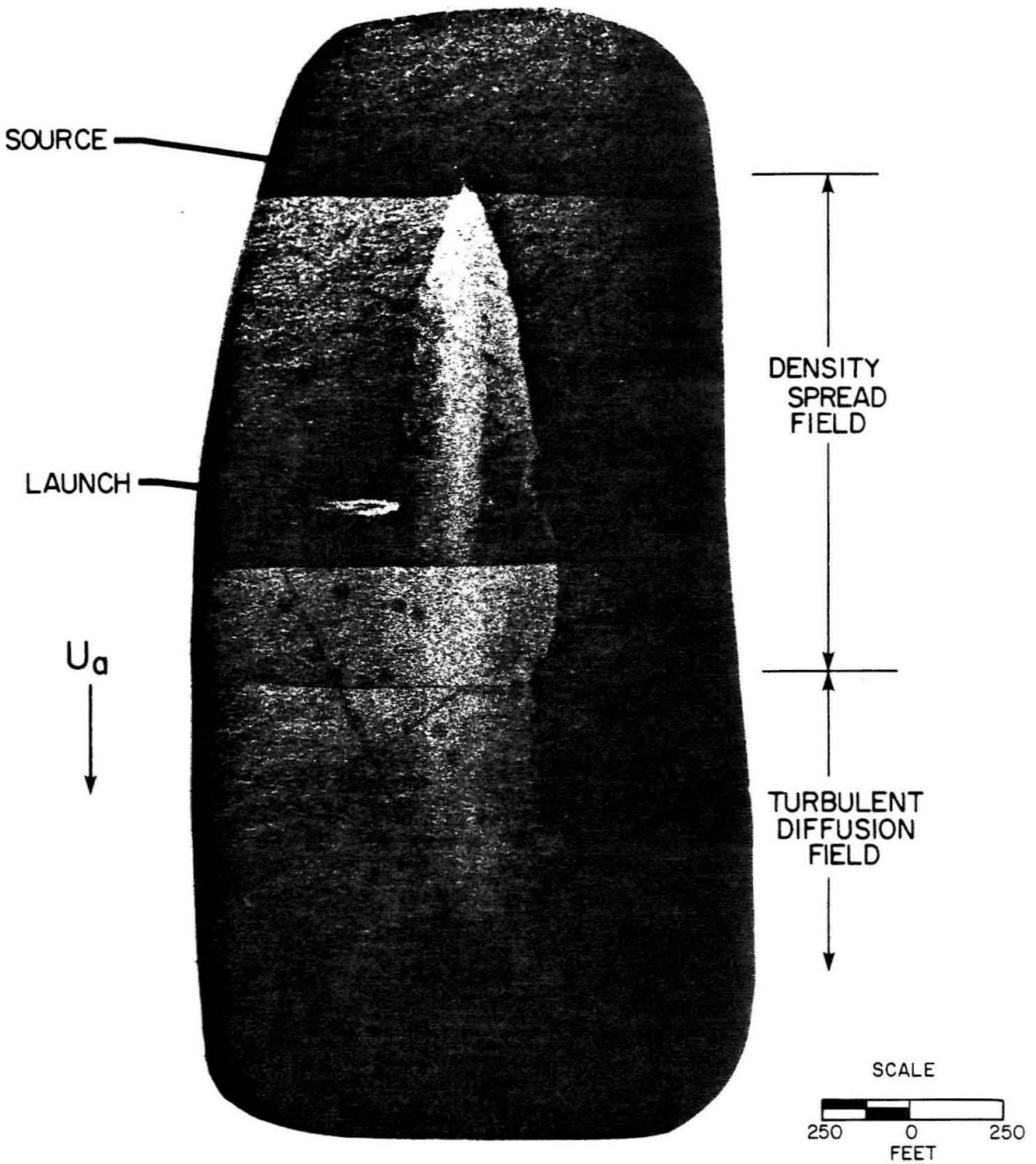


Figure 1.6 A wide surface density spreading field persisting for a long distance before oceanic turbulent diffusion takes over, aerial photograph taken by Foxworthy and Kneeling (1969) at Ventura Outfall on November 11, 1966.

wave approximation equations will be used to determine the unknown coefficients. The fluid velocity, the spreading layer thickness for the inertial and the viscous regimes of both surface and subsurface spreading flows will be described. Surface jet mixing of the nearfield spreading flow will be modelled using Prandtl's assumptions. Dimensional analysis is used to show the effect of initial conditions on the spreading currents.

Experimental studies of starting half radial surface buoyant jet flows, the full radial surface buoyant jet flow in a cross-current and nearfield surface jet mixing are described in Chapter 4. Two sets of experimental measurements on surface buoyant jet mixing were made: one for a full radial heated jet and the other for a half radial buoyant jet. Experimental results are presented in Chapter 5.

In Chapter 6, many previously published data of importance to the horizontal spreading problem are compared with present theoretical results. Examples of engineering applications will be presented in Chapter 7. A summary of conclusions and discussion is given in Chapter 8.

CHAPTER 2

REVIEW OF PREVIOUS STUDIES

2.1 Wastewater Field from Submarine Outfall Discharges2.1.1 Maximum Height of Rise and Spreading Level

When the receiving body of water is density-stratified, a diluted buoyant field can sometimes reach the free surface and spread outward to become a surface field, but it is more usually trapped at some neutrally buoyant level below the surface. If it is trapped, it then spreads laterally at that level as an intrusion layer and forms a submerged field.

To determine whether the diluted water will either become a spreading field at the free surface or at some submerged level, it is necessary to determine the maximum height of rise and the submerged spreading level for a submerged buoyant jet discharging into a density-stratified environment. Several previous investigations have studied the maximum rise problem both theoretically and experimentally and the terminal height of rise can be predicted reasonably well in terms of the parameters of the jet and the environment. These previous results are summarized in Table 2.1.1 in terms of the characteristic lengths appropriate to a turbulent jet or plume.

2.1.2 Observations of Spreading Flows

A diluted effluent, upon reaching the free surface, or some intermediate neutral buoyancy level, is deflected from

Table 2.1.1.1 Review of previous experiments on the buoyant round (n = 1) or plane (n = 0) jet rise into a stagnant linearly density-stratified environment.

Investigator	z_m/H_B (or $\frac{z_m}{H_M}$)		$Fr = \frac{M^2/h}{QD^{1/2}}$		$\frac{M\sqrt{gE}}{B}$		n	Maximum Height Definition	Observation Technique
	From	to	From	to	From	to			
Abraham and Eysink (1969)	4.47	5.20	7.94	17.5	0.849	2.40	1	Density gradient changing height	Lab. density measurement along upward fresh water jet flow by conductivity probe
Barday (1977)	3.07 3.70	3.40 4.11	∞ ∞	∞ ∞	∞ ∞	∞ ∞	1 0	Maximum penetration of dyed salt solution	Lab. photograph of downward dyed jet injection
Crawford and Leonard (1962)	3.18	4.43	2.43	3.41	0.0412	0.198	1	Temperature discontinuity height	Schlieren optical observation of upward discharging warm air in an ice skating rink
Davies (1959)	3.76	?	?	?	?	?	1	Top of the fire plume	Field photograph of oil fire plume in stratified atmosphere
Fan (1967)	3.94	4.76	19.1	56.3	1.80	5.28	1	Maximum penetration of dyed salt solution	Lab. photograph of downward dyed jet injection
Fox (1970)	4.75	8.20	38.2	324.0	1.71	30.22	1	Maximum penetration of dyed salt solution	Lab. photograph of downward dyed jet injection
Hayashi and Ito (1974)	?	?	101.4	?	?	?	1	Maximum penetration of dyed ethyl alcohol solution	Lab. photograph of upward dyed ethyl alcohol solution injection
Morton, Taylor and Turner (1956)	2.77	4.38	?	?	?	?	1	Maximum penetration of dyed salt solution	Lab. photograph of downward dyed salt solution injection
Sneck and Brown (1974)	3.75	?	?	?	0.10	3.16	1	Top of smoke plume by temperature profile measurement	Lab. temperature profile measurement of air smoke in thermal stratified wood-frame air chamber
Vehrencamp, Carpenter and Romie (1955)	2.54	3.46	?	?	?	?	1	Top of smoke plume	Field photographic record of black smoke from the domestic diesel burning in the desert

Note: $H_B = B \frac{1}{n+3} (gE)^{-1/2}$, $H_M = M \frac{1}{n+3} (gE)^{-1/2}$

vertical flow to nearly-horizontal flow, whereupon it spreads out uniformly. Descriptions on this spreading flow were reported by Rawn and Palmer (1929) on the basis of their laboratory measurements and field observations of four single-port ocean outfalls around southern California. They noted that the diameter of a rising column, when it impinges the free surface, is around one-third of the path length traveled, for both vertical and horizontal single-port discharging flows. The speed of the initial fronts generated by the submerged buoyant discharge were measured by recording the time at which the dyed discharge front passed a designated location. They found that the diameter of the front grew in proportion to the two-thirds power of time. In the subsequent motion, the dyed discharge frequently moved in a series of concentric waves, or annular rings, as described by Brooks (1952) in an unpublished report of his observations of seasonal ocean outfall operations at White's Point and Point Loma (see also Rawn, Bowerman, and Brooks, 1960). Each wave or ring was followed by an interval of apparently clear water. The waves continued for some distance from the rising column, and gradually merged to form a field of uniform color which remained well stratified. Brooks (1952) did, however, sometimes also observe a steady radial surface flow. This periodic unsteadiness in flow is apparently typical of such flows, for a similar series of the radial surface fronts were observed by Green *et al.* (1972) and Scarpace and Green (1973) in

their aerial photographs of the thermal plume from the surface thermal water discharge at Point Beach Power Plant on Lake Michigan and at three other power plants located at Port Washington, Sheboygan and Madison, Wisconsin. Some field measurements of temperature and velocity of heated discharges were conducted by Frigo *et al.* (1974) at the Point Beach, J. H. Campbell and Waukegan Power Plants located on Lake Michigan. Unknown coherent oscillating fluctuations in water temperature and velocity were observed with periods ranging from 2 to 20 minutes. It was believed that the long period of fluctuation might be due to the development of "radial thermal fronts" structure as observed by Scarpace and Green (1973). The same band structure was observed on a larger scale by McClimans (1978) in a radial oceanic front in a fjord at Trondheim, Norway, as shown in Figure 2.1.1.

According to the early observations by Rawn and Palmer (1929) the interface between a surface horizontal flow and the underlying fluid is not clearly defined close to the surface impingement point. The intensive interfacial mixing of the discharged water with the ambient water, and the periodic concentric wave behavior made it very difficult to measure the thickness of the spreading field. For both vertical and horizontal buoyant round jet discharge, the overall average of observations indicated that the thickness of the two-layer stratified flow was about one-twelfth of the length of travel of the effluent before it reached the free surface. Some



Figure 2.1.1.1 A series of radial oceanic fronts in a fjord observed by McClimans (1978).
The photograph from which this reproduction was made was taken by
T. A. McClimans, who graciously supplied a copy to the author.

laboratory observations of Frankel and Cumming (1965) indicated that the thickness of the stratified layer generated by a horizontal buoyant round jet discharge was around one-third of the total water depth. The same layer thickness to depth ratio checks fairly well with that found by Hart (1961) for a vertical buoyant round jet discharge in an almost stratified fluid. More recent laboratory experiments by Liseth (1970) and Liu (1976) showed that the two-dimensional stratified layer formed by a downward, or an upward, multi-port buoyant discharge into stagnant ambient water, never exceeded 30% of the total depth. Other experiments by Bühler (1974) showed that this two-dimensional bottom stratified layer occupied the lower 40% of the water depth. Roberts' (1977) results for a vertical line plume discharge show a ratio around 30%, which is close to the value predicted by Koh (1976), i.e., approximately one-third of the total ambient water depth.

When there is a slow prevailing ocean current the spreading flow has a well-defined upstream edge. According to Brooks' (1952) observations at White's Point and Point Loma, the stronger is the current, the closer the upstream interface is to the point of discharge. The boundary between the discharge and the ambient water also becomes sharper. The ambient current apparently rides under the sewage layer provided that the flowing layer is substantially thicker than the sewage layer. Downstream from the point of discharge the sewage moves as if it were part of the

overall current, but spreads laterally. Further mixing, due to the natural turbulence found in the ocean proceeds slowly both vertically and horizontally, and the diluted discharge ultimately becomes an almost non-buoyant tracer.

The variation of lateral surface spreading width before turbulent diffusion takes over was found by Foxworthy *et al.* (1966) to vary as the 0.78th power of downstream distance measured from the surface impingement point. An excellent photograph of the transition from gravitational spreading flow to the turbulent diffusion regime is shown in Figure 4 of Foxworthy and Kneeling (1969). (See Figure 1.6)

Very few field observations have been made examining submerged spreading flow and the subsequent dilution and diffusion. This is possibly because the diluted effluent is trapped beneath the sea surface and no immediate "visible" nuisance is produced. However, in a stably stratified atmosphere industrial discharges are often seen spreading at a neutral density level. In Figure 2.1.2(a) is a horizontal spreading plume due to the cooling tower discharge at John E. Amos Power Plant observed by Kramer and Seymour (1976). A series of discontinuous radially spreading fronts can also be seen in Figure 2.1.2(b).

Submerged spreading of a turbid cloud at the ocean bottom and at a strongly stratified interface due to ocean dumping of barged sludge was reported by Beyer (1955). No details of measurements



(b)

A series of discontinuous radially spreading front. (Courtesy of Kramer and Seymour, 1976)



(a)

Radially horizontal spreading cooling tower plume in a stably stratified atmosphere. (Courtesy of Kramer and Seymour, 1976)

Figure 2.1.2

were made. Ocean dumping of dredge spoil was surveyed by Gordon (1974) in one of the few published field studies of bottom turbidity currents. He found that after the sinking turbid plume reached the ocean bottom, it spread axisymmetrically over the sea floor and increased in diameter proportionally to the square root of time. The thickness of the turbid cloud at certain locations was observed to decrease as a function of time after initiation of dumping.

2.1.3 Unsteady Density Spread in a Stagnant Environment

As has been suggested by several investigators, such as Frankel and Cumming (1965), Jirka and Harleman (1973) and Lee *et al.* (1974), a starting or unsteady flow has three possible regions of flow: the submerged buoyant jet, the subsequent surface impingement and transition, and the horizontal spreading, as shown in Figures 2.1.3(a) and (b).

As noted previously, the surface spreading front on a motionless water surface, and due to a single port submarine outfall discharge, was observed by Rawn and Palmer (1929) in both the field and the laboratory and they found that the diameter of a floating dye plume grew as the two-thirds power of time.

Sharp (1969a,b) conducted similar experiments for both upward and downward horizontal buoyant round jets, as shown in Figures 2.1.4(a) and 2.1.4(b). Experimental data were plotted

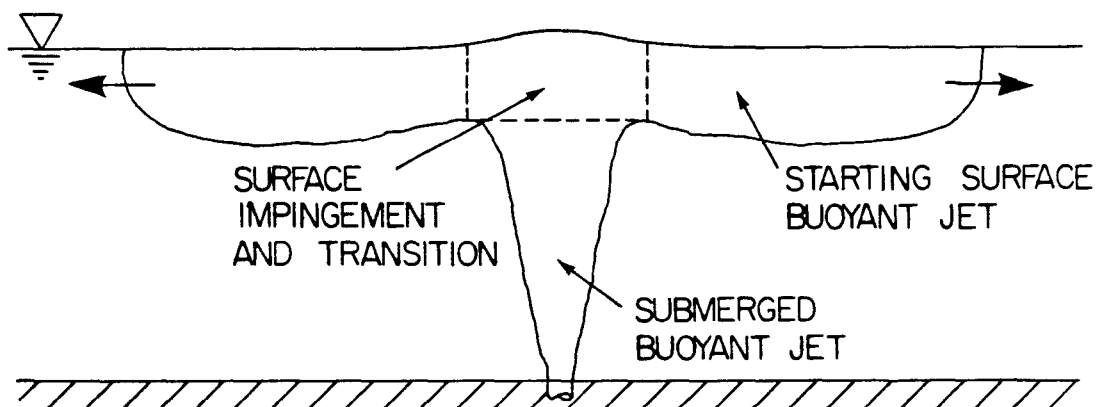


Figure 2.1.3(a) Flow regions resulting from a positive submerged buoyant round or plane jet discharging vertically upwards into a homogeneous environment.

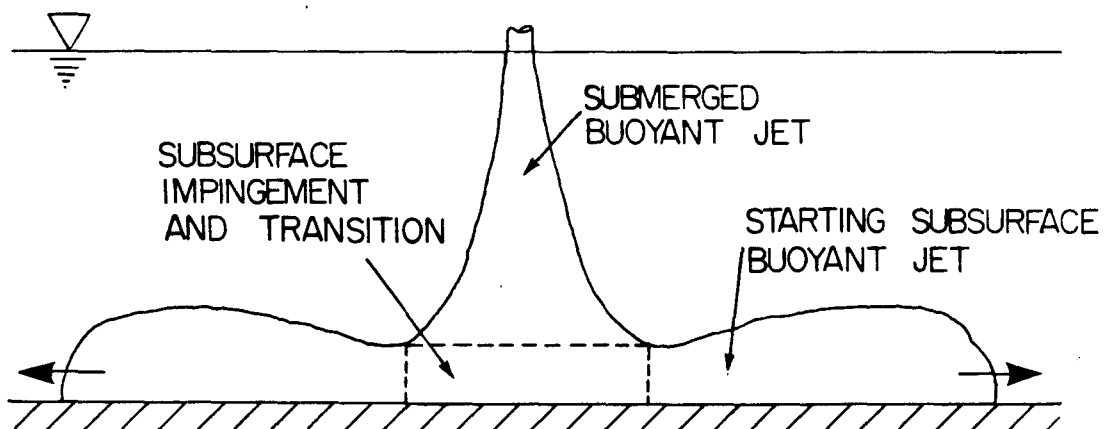


Figure 2.1.3(b) Flow regions resulting from a negative buoyant round or plane jet discharging vertically downwards into a homogeneous environment.

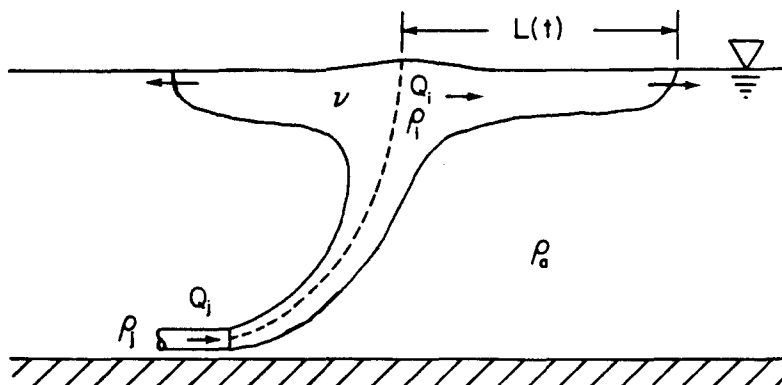


Figure 2.1.4(a) Free surface spreading front due to a submerged horizontal buoyant round jet discharge.

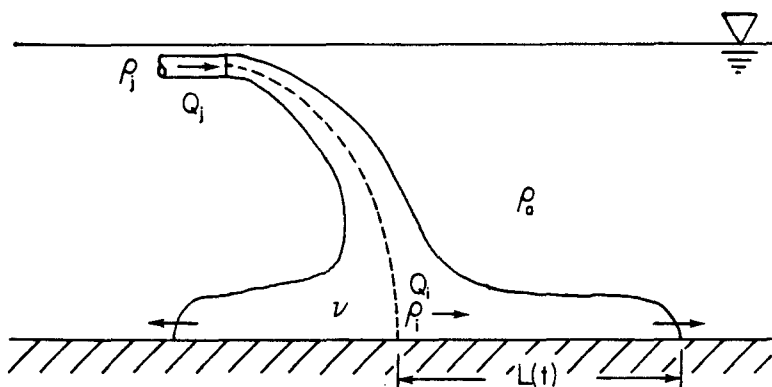


Figure 2.1.4(b) Bottom surface spreading front due to a horizontal buoyant round jet discharge.

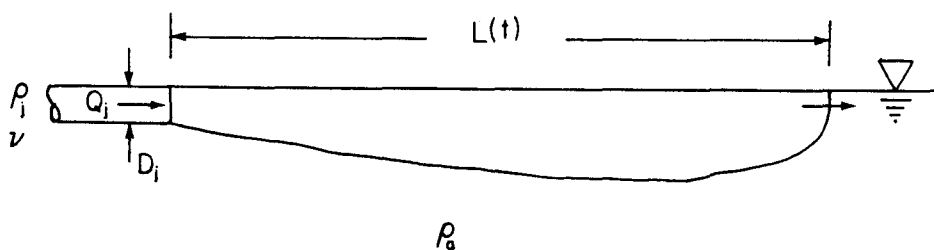


Figure 2.1.5 Unsteady spreading tip position at time t due to a buoyant pipe flow discharge, after Sharp (1971).

using three dimensionless parameters in the form:

$$\phi \left(\frac{Lg'^{1/5}}{Q_i^{2/5}}, \frac{tg'^{3/5}}{Q_i^{1/5}}, \frac{Q_i g'^{1/3}}{\nu^{5/3}} \right) = 0 \quad (2.1.1)$$

where L is the surface travel length of the spreading fluid on time t , Q_i is the volume flux at source of spread, which is calculated by multiplying the discharge volume flux Q_j with the average dilutions from the graphical solutions by Fan and Brooks (1969), g' is the reduced gravitational acceleration, $g \left| \frac{\rho_a - \rho_i}{\rho_a} \right|$, ρ_i is the calculated diluted fluid density at source of spread, ν is the kinematic viscosity of the spreading fluid and ϕ is an unknown function. Hart (1961) also performed small scale laboratory experiments. However, both failed to show clearly the different possible regions of flow that can occur.

Sharp (1971) extended his studies to surface spreading front due to a horizontal buoyant round jet discharge on the surface of a wider channel, as shown in Figure 2.1.5. A further dimensionless variable involving the properties of a discharge from a round pipe was added to those considered previously (2.1.1) to obtain:

$$\phi \left(\frac{Lg'^{1/5}}{Q_j^{2/5}}, \frac{tg'^{3/5}}{Q_j^{1/5}}, \frac{Q_i g'^{1/3}}{\nu^{5/3}}, \frac{D_j g'^{1/5}}{Q_j^{2/5}} \right) = 0 \quad (2.1.2)$$

where L is the spreading length from the discharging pipe on time t , D_j and Q_j are the diameter and the volume flux of the pipe discharge. The added dimensionless variable in Eq. (2.1.2), $\frac{D_j g^{1/5}}{Q_j^{2/5}}$, is related to the discharge Richardson number or Froude number of the pipe flow.

Experiments on radial spreading plumes due to a submerged vertical buoyant round jet discharge were performed by Chen and List (1976). After a very brief initial period the radially symmetric front increased in diameter with the three-quarters power of time and then broke sharply to a function of one-half power of time. The second regime was also confirmed by Anwar (1972). Both regimes were confirmed recently by Britter (1979) in the laboratory experiments on radially spreading gravity currents.

Roberts (1977) observed a similar two-stage spreading front from a submerged line plume discharge; the distance from discharge to front increased as a linear function of time t and then changed to $t^{4/5}$. This implied constant velocity of the plane spreading front, which depends only on the discharge buoyancy flux, was also found earlier by Liseth (1970) and Bühler (1974) for the flow from a multiport diffuser discharge with dense fluid.

Different time functions were noted by Chen and List (1976) for the radial surface spreading front produced by dumping a finite volume of liquid onto the free surface of a denser miscible liquid. The diameter of the spill grew as $t^{1/2}$

initially and then changed to $t^{1/8}$. Different time functions were also found by Almquist (1973) for a plane surface spreading front produced by the release of a finite volume of buoyant fluid: the distance grew initially as $t^{2/3}$ and then changed to $t^{1/5}$.

In order to study spreading rate for a plane front in a linearly density-stratified environment Maxworthy (1972) examined a neutrally buoyant horizontal slot jet into a density stratified fluid, as shown in Figure 2.1.6. After intensive mixing with ambient fluid occurred in the neighborhood of exit, the interflowing front distance increased as $t^{5/6}$ for the case of low source flow rate.

Similar experiments were also performed by Zuluaga-Angel *et al.* (1972) and Manins (1976a), but different growth rates of the interflowing wedge were found. Manins found the intrusion layer length to be a linear function of time. Zuluaga-Angel *et al.* found a three-quarters power of time. However, one of the experiments of Zuluaga-Angel *et al.* did show a wedge increasing its length in direct proportion to the time t and then changing to $t^{5/6}$ before reaching the end of the channel, as plotted in Figure 2.1.7. Thus no conclusive result has appeared for the submerged density spread due to a submerged buoyant round or plane jet discharge.

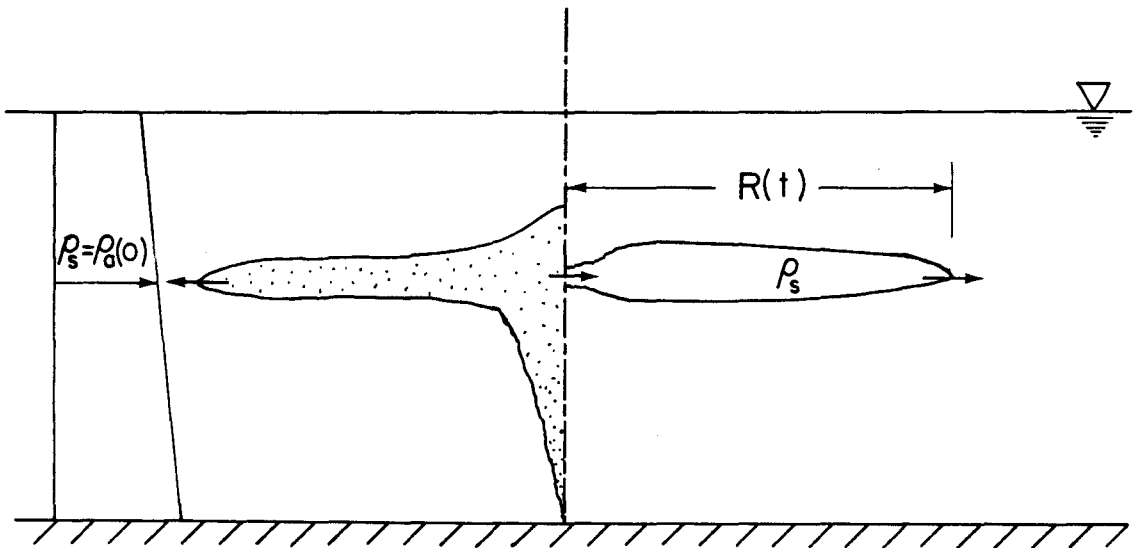


Figure 2.1.6 Simulation of submerged density spreading by a horizontal jet discharging at its own density level in a linearly density-stratified environment, after Maxworthy (1972).

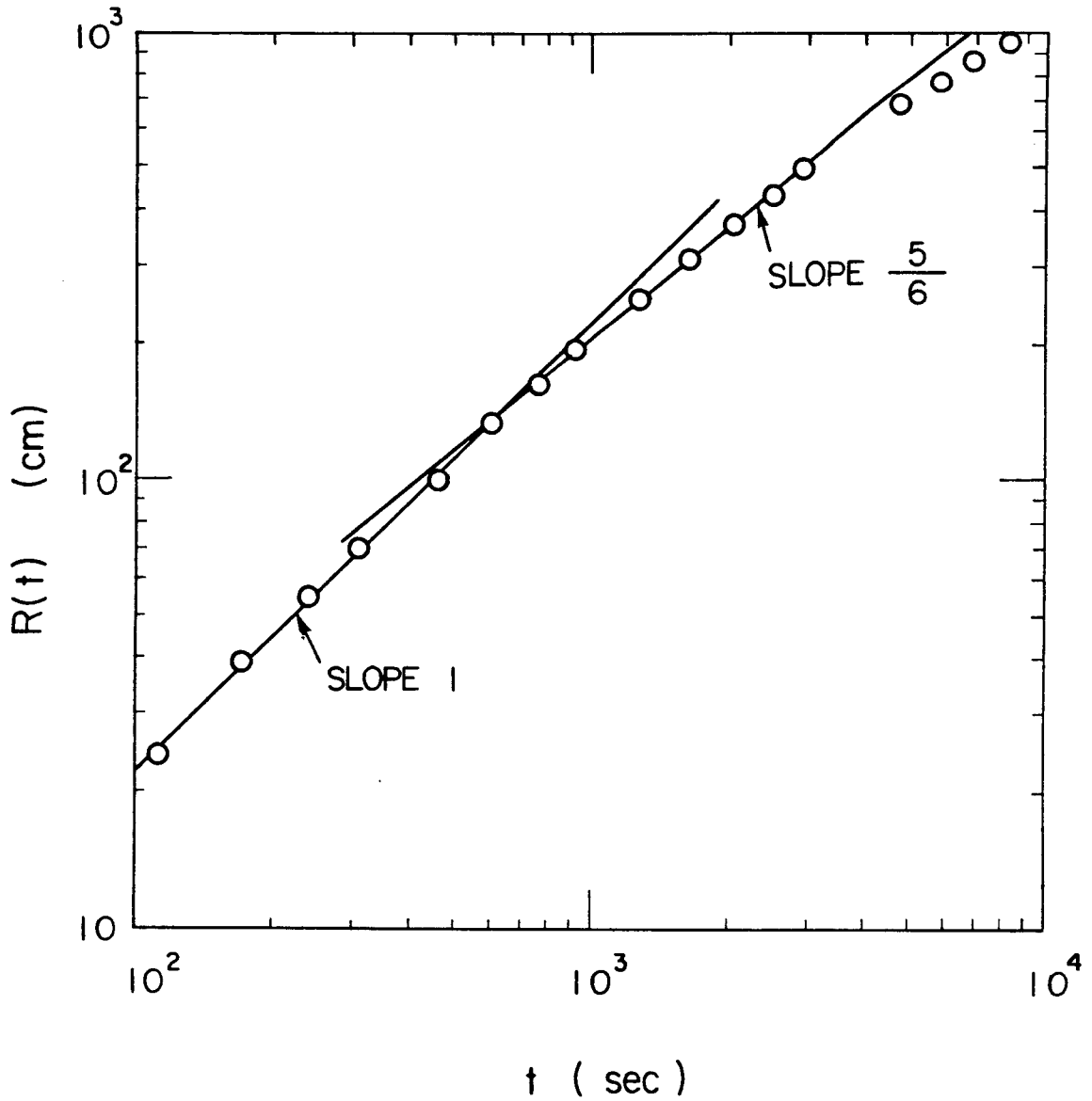


Figure 2.1.7 Growth history of the interflowing wedge front due to a horizontal slot jet discharging at a neutral buoyant level into a linearly density-stratified ambient, data from Zuluaga-Angel *et al.* (1972).

Wu (1965,1969) found different results for the submerged density spread due to a finite volume of homogeneous fluid collapsing at a neutral density level in a linearly density-stratified fluid, as shown in Figures 2.1.8(a) and (b). In a series of experiments three stages of interflowing wedge front were observed: an initial stage with $Nt < 2.5$, a principal stage with $3 < Nt < 25$, and the final stage with $Nt > 25$, where t is the time after initiating collapse and N is the Brunt-Väisälä frequency of the stratified ambient fluid. In the initial stage the interflowing wedge moved almost at a constant velocity, while in the later two stages the wedge front was decelerating during the spreading. Wu gave an empirical formula describing the front propagation in the initial stage as a function to time,

$$\frac{R(t)}{R_0} = 1 + 0.29(Nt)^{1.08} \quad , \quad (2.1.3)$$

and in the principal stage:

$$\frac{R(t)}{R_0} = 1.03(Nt)^{0.55 \pm 0.02} \quad (2.1.4)$$

where R_0 is the initial radius of the cylindrical section of the two-dimensional homogeneous fluid, $R(t)$ is the wedge length at time t . In the final stage, the distance to the front increased at a much slower rate than in the principal stage. The results

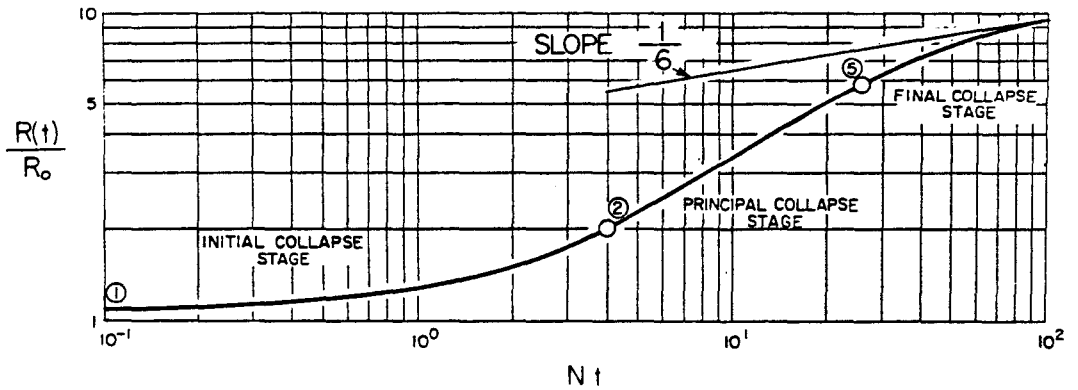


Figure 2.1.8(a) Three stages of plane submerged density front spread due to a finite volume of homogeneous fluid collapsing at a neutral level in a linearly density-stratified environment, after Wu (1965).

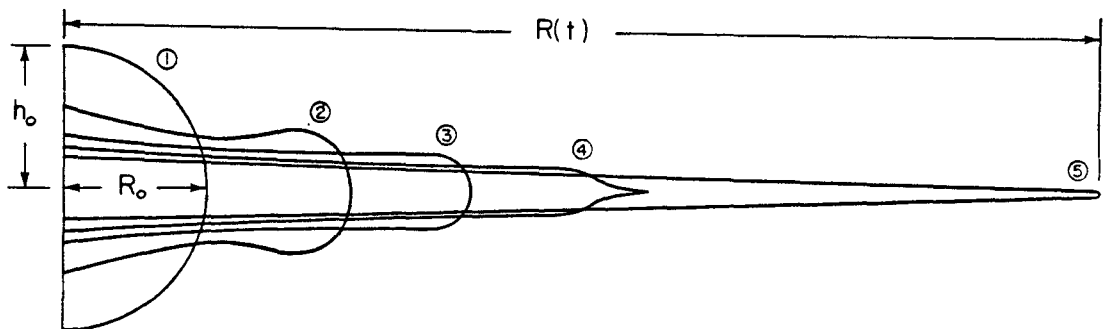


Figure 2.1.8(b) Sequential cross sections of plane submerged density front spread at various times, after Wu (1965).

given by Wu appear inconclusive. However, the front distances does appear asymptotically to grow in proportion to $t^{1/6}$ (see Figure 4 of Wu (1969) and Figure 2.1.8(a)).

Similar experiments were performed by van de Watering (1966) with a different apparatus. The dyed wedge was found to move in the initial stage as

$$\frac{R(t)}{R_0} = 1 + 0.16(Nt)^{0.94} \quad (2.1.5)$$

and as

$$\frac{R(t)}{R_0} = 1.02(Nt)^{0.34} \quad (2.1.6)$$

for the principal stage.

A simple force scale analysis and similarity solutions of long wave equations will be used later to derive these different power laws of time for both the surface and the submerged density spread.

2.2 Surface Wastewater Discharge in a Cross Current

2.2.1 Non-Buoyant Models

Non-buoyant wastewater field models are reviewed here. The models were developed by considering only the source strengths and the diffusion mechanisms and by neglecting any buoyancy effects.

The solution for a non-buoyant source in a uniform current is well-known in hydrodynamics (see for example, Milne-Thomson

(1969), pp. 480-481). The induced velocity field, as shown in Figure 2.2.1, is asymptotic far downstream, to a constant width, $\sqrt{\frac{Q}{\pi U}}$, where Q is the source strength, U is the current velocity. The upstream edge where the velocity vanishes, is located at a distance, $\frac{1}{2}\sqrt{\frac{Q}{\pi U}}$, upstream from the source. No further information about the tracer distribution is given.

The turbulent diffusion field from a line non-buoyant tracer source was developed by Brooks (1960) by neglecting the vertical and the longitudinal diffusion. A turbulent diffusion field is assumed to form as soon as the diluted effluent reaches the free surface. The downstream concentration is found to decay in both the transverse and stream directions. An overall sketch of this diffusion waste field is shown in Figure 2.2.2. The lateral spread of the waste field is found to be dependent on the variation of the scale of eddy diffusivity ϵ along the current direction. The three types of growing field widths that are found are:

$$\frac{L}{b} = \left(1 + \frac{24\epsilon_o}{Ub} \frac{x}{b} \right)^{1/2}, \quad (2.2.1)$$

$$\frac{L}{b} = 1 + \frac{12\epsilon_o}{Ub} \frac{x}{b} \quad (2.2.2)$$

and

$$\frac{L}{b} = \left(1 + \frac{24\epsilon_o}{3Ub} \frac{x}{b} \right)^{3/2}, \quad (2.2.3)$$

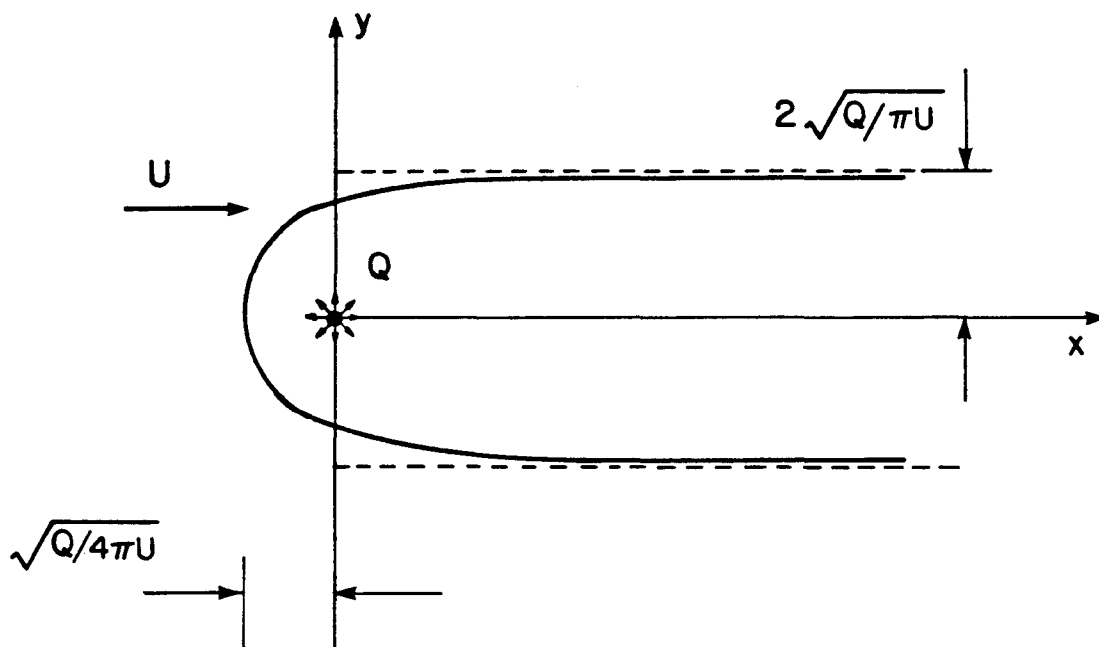


Figure 2.2.1 A non-buoyant and non-diffusive source in a uniform cross current.

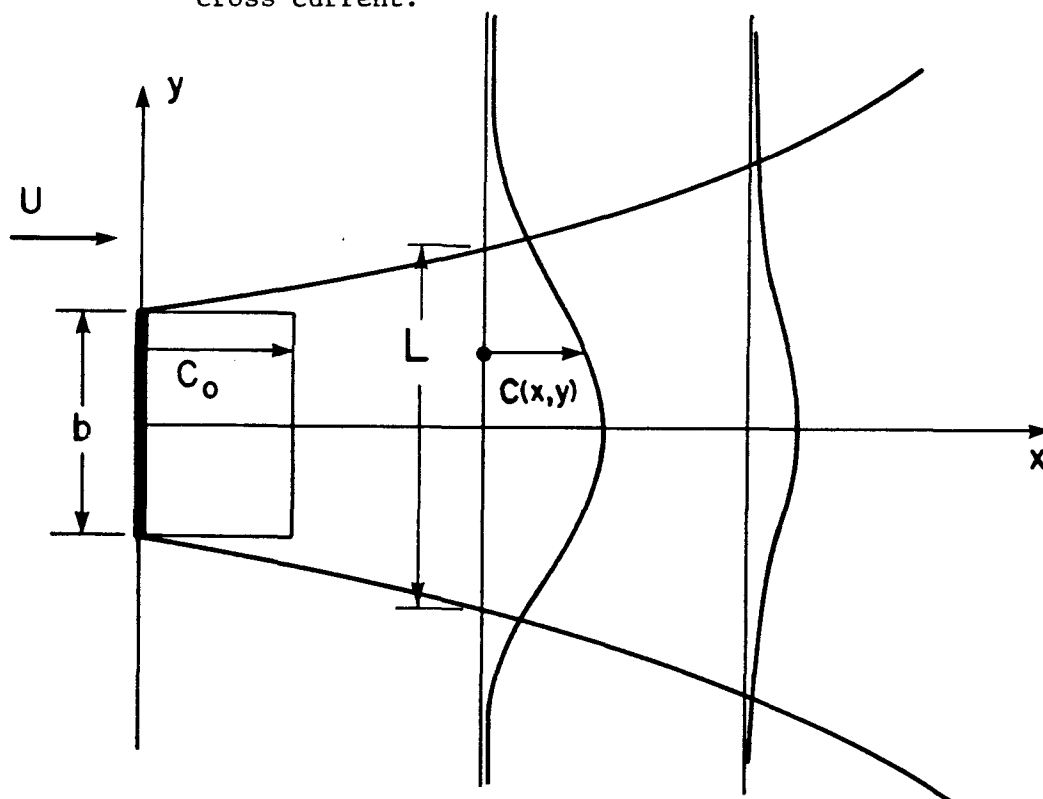


Figure 2.2.2 Schematic diagram for diffusive field from line-like diffuser in an ocean current, after Brooks (1960).

each corresponding to one of three types of eddy diffusivity functions assumed: (2.2.1) a constant, (2.2.2) a linear variation of the eddy diffusivity with the diffusion width, and (2.2.3) a four-thirds law of eddy diffusivity, where L is the nominal diffusion width defined as

$$L = 2\sqrt{3} \sigma \quad (2.2.4)$$

and σ is the standard deviation of the concentration distribution function at a given station downstream x , ϵ_0 is the initial eddy diffusivity value at the origin, where the initial width of the water field is assumed as b .

For the diffusion field from a single-port outfall discharge, mathematical models of the diffusion field, developed to describe the material distribution of an emission from a smoke stack in the atmosphere, are applicable. Frenkiel (1953) suggested that if the longitudinal dispersion is negligible, a theoretical steady plume model could be assembled by the superposition of an infinite number of overlapping circular patches, as shown in Figure 2.2.3(a), or one-dimensional slice elements, as shown in Figure 2.2.3(b). However, some field density and coliform concentration measurements by Foxworthy *et al.* (1966) and Foxworthy and Kneeling (1969), in the vicinity of submarine outfalls operated by Orange County Sanitation Districts, indicate turbulent diffusion differing from Gaussian profiles.

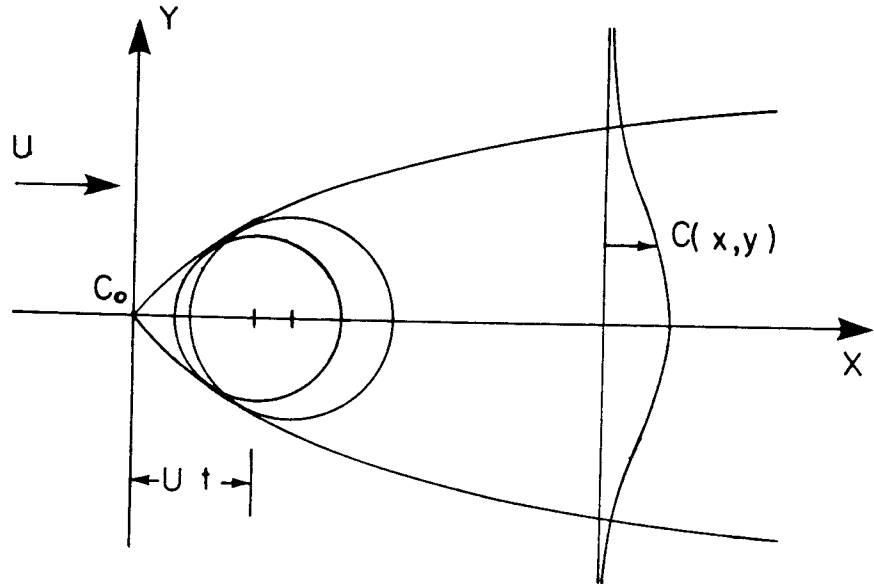


Figure 2.2.3(a) Superposition of a series of circular diffusion patches in a horizontal turbulent current.

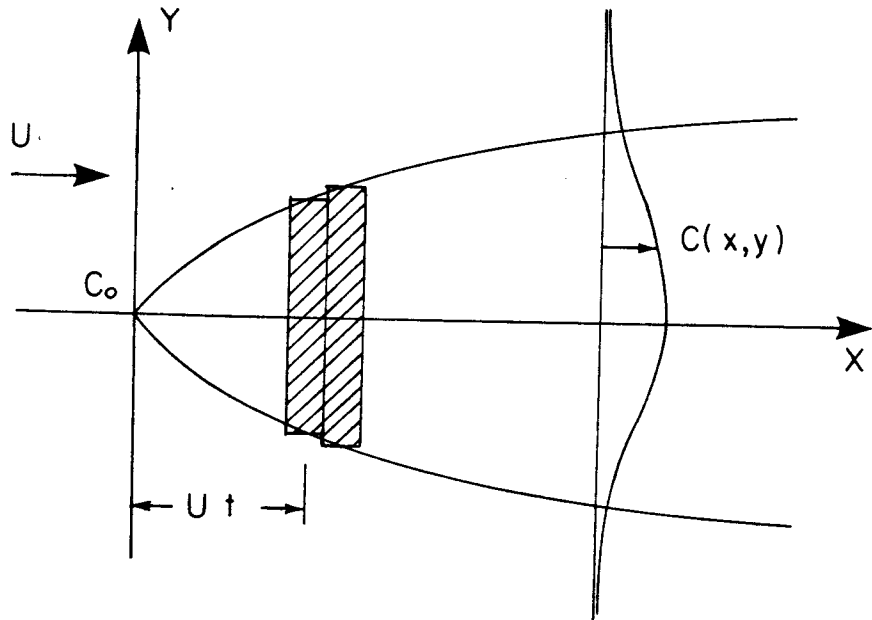


Figure 2.2.3(b) Superposition of a series of slices of diffusion elements in a horizontal turbulent current.

It is believed that this is due to the buoyancy forces and would indicate that the details of intermediate scale density spread dynamics are important to the study of large scale diffusion problems.

2.2.2 Surface Density Spread Models

To determine a non-diffusive surface wastewater field several environmental factors must be considered in addition to the discharge variables. Those include ocean currents, tides, wind, local climate, and bottom topography. Inclusion of all these factors together is difficult. Only the effect of a uniform prevailing current will be considered here.

A density spread model was given by Larsen and Sörensen (1968), Cederwall (1968), and Hydén and Larsen (1975). Harremöes (1967) used a similar model to consider the surface field due to a multi-port diffuser discharge.

Larsen and Sörensen assumed that there is a uniform thickness h of surface wastewater field at a location x , downstream from the release point, and that the density front propagates with a velocity

$$U_d = \lambda \sqrt{g \Delta h} \quad . \quad (2.2.5)$$

The boundary of the surface field will then be defined by the relationship

$$U \sin \theta = U_d \quad , \quad (2.2.6)$$

as shown in Figures 2.2.4(a) and (b), where the coefficient λ is chosen as 1.0 by Larsen and Sörensen (1968) and Harremöes (1967), and as 1.0 to 1.4 by Hydén and Larsen (1975). The angle θ was related to the half-width of the surface field by

$$\frac{dB}{dx} = \tan \theta \quad (2.2.7)$$

so that for small angles θ

$$U \frac{dB}{dx} = \lambda \sqrt{g\Delta h} \quad (2.2.8)$$

The continuity relationship implies that

$$2 B(x) h U = S_o Q \quad (2.2.9)$$

so that one gets the half-width equation in differential form as

$$B(x) \left(\frac{dB(x)}{dx} \right)^2 = \frac{\lambda^2 g \Delta S_o Q}{2U^3} \quad (2.2.10)$$

where Δ is the dimensionless density difference of the surface field is related to the value of the discharge fluid as

$$\Delta = \frac{\rho_a - \rho_s}{\rho_a} = \frac{\rho_a - \rho_j}{S_o \rho_a} \quad (2.2.11)$$

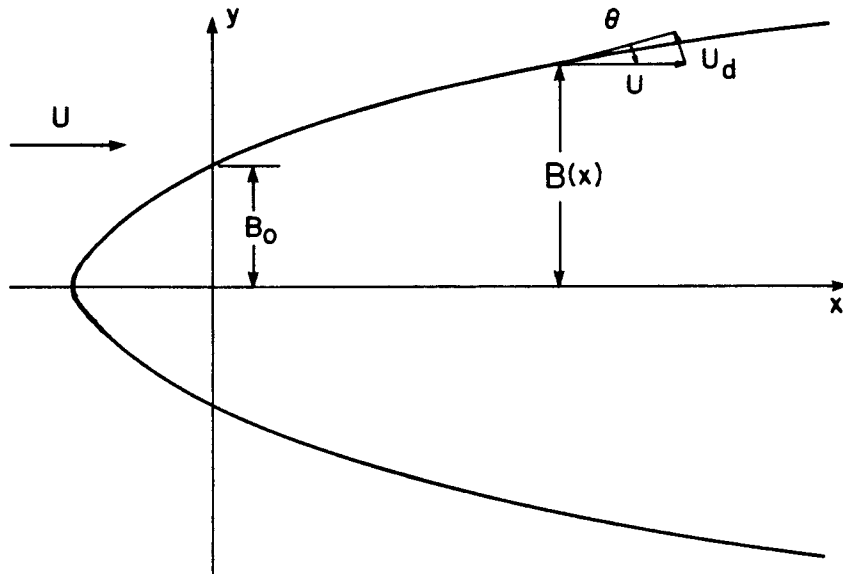


Figure 2.2.4(a) Top view of surface density spread field in a horizontal current.

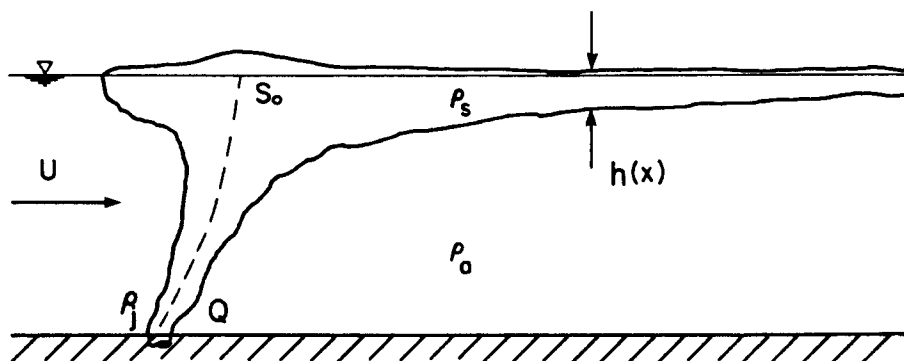


Figure 2.2.4(b) Central cross section along x direction of surface density spread field in a horizontal current.

Equation (2.2.12) after integration becomes

$$\frac{B(x)}{B_0} = \left(1 + \frac{3}{2} \frac{x}{B_0}\right)^{2/3} \quad (2.2.12)$$

in which

$$B_0 = \frac{\lambda^2 g \Delta S_0 Q}{2U^3} \quad (2.2.13)$$

The model described here is valid only when the current velocity does not exceed some maximum value since B_0 will vanish. In the case of low current speeds the longitudinal spreading velocity is no longer negligible, and Eq. (2.2.8) is not a good approximation of Eqs. (2.2.6) and (2.2.7).

The width of the field is mainly dependent on the velocity of the density front, which contains an unknown coefficient λ . Harremöes (1967) argued that a constant value of λ is doubtful since the front edge is observed to propagate with a vanishing thickness, which implies that the front velocity must vanish in Eq. (2.2.5). To overcome such deficiencies, other models are necessary.

Rawn and Palmer (1929) proposed the concept of a one-dimensional transverse spreading field superimposed on a uniform current as shown in Figure 2.2.5. Howland (1934) suggested that the experimental results of lock exchange flow by O'Brien and Chernov (1932)

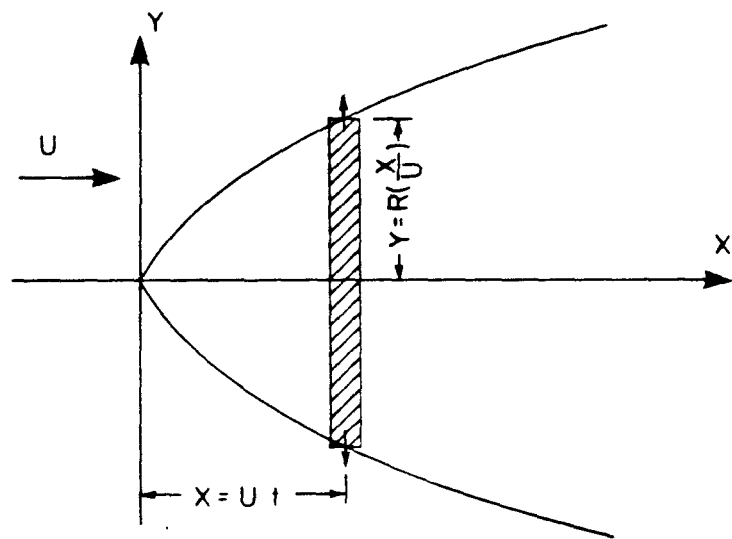


Figure 2.2.5 Side-spread model for the plume boundary of a surface wastewater field.

may be used to predict this side-spread velocity. The same concept was used by Koh (1976) and Roberts (1977) to determine the surface spreading from a finite length diffuser discharge. The same idea was also used by Lee (1971) to predict the surface oil slick due to an oil tanker accident.

According to this model the downstream width of the surface spreading field can be approximated by a Galilean transformation of an unsteady time function describing the plane density front motion in a stagnant ambient fluid. In other words, the sharp boundary of the spreading field can be described by just changing the time term t to a space term x/U in the solution for an instantaneous finite volume release. The details of these unsteady functions will be given in Section 3.1.

The above approach is a good approximation only when the longitudinal spreading velocity is negligible compared to the current velocity. Otherwise, a radially spreading front is a better approximation, as shown in Figure 2.2.6. The sharp density boundary of a surface wastewater field is in this case similar to the shock wave curve formed by a moving source. There is no upstream wedge in the critical or the supercritical flow case, when the current velocity is equal to or higher than the shock front velocity. In the subcritical flow case, there will be an upstream edge formed by the interaction of the current and the spreading flow.

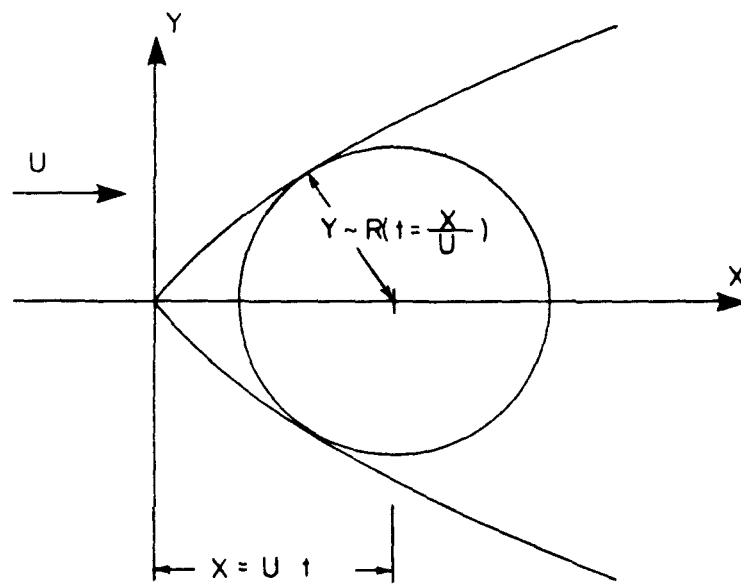


Figure 2.2.6 Radial spread model for the plume boundary of surface wastewater field.

2.3 Gravity-Driven Starting Flows

2.3.1 Formation of Gravity-Driven Flows

Gravity-driven flows occur both in nature and in engineering practice. They result from unsteady and non-uniform free-boundary motion caused by a density difference which may be due to:

- (1) A difference in concentration of dissolved solute, such as in saline wedges, or lock exchange flows as observed by O'Brien and Chernov (1932).
- (2) A difference in temperature, such as atmospheric cold fronts, land breezes after sundown, and katabatic winds in mountain valleys as observed by Margules (1906) and Schmidt (1910); sinking melted ice water advancing on the sea floor, (Sandstrom, 1908), the surface thermal plume of power plant cooling water discharge from a channel discharge (Scarpace and Green, 1973), and submerged outfall discharges (Sonnichsen, 1971).
- (3) Suspended solids, such as in an atmospheric dust storm (a "black blizzard"), turbidity currents of muddy river flows into reservoirs and lakes (Bell, 1942) or from ocean-barge dredge spoil disposal (Gordon, 1974), avalanches of powder snow (Seligman, 1962), and the base surge of misty air from an atomic bomb explosion in a shallow ocean (U.S. Atomic Energy Commission, 1950).

(4) Different constituent fluids such as damp gas motion in mining tunnels (Georgeson, 1942), oil slicks spreading on the sea surface (Smith, 1968), and dam break flows into a river channel (Schoklitsch, 1917).

(5) Combinations of the above items, such as muddy river plumes after rain storm (Bell, 1942), oceanic and estuarine fronts (Garvine, 1974 and McClimans, 1978), and vaporized liquified natural gas (Drake and Reid, 1977).

Thus, although there have been many investigations made of such unsteady flow problems, there is, as yet, no universal theory that can explain the results obtained. The above examples are considered in further detail.

2.3.2 Lock Exchange Flows

A lock exchange flow is produced by the removal of a vertical barrier separating two sections of a channel filled with fluids with a slight density difference, as shown in Figure 2.3.1. According to Yih's (1947) laboratory observations, two wedge-shape surge flows are found moving at the same speed but opposite direction. The average value of the initial

frontal velocity U , in terms of a Froude number, $F = \frac{U}{\sqrt{2g \frac{(\rho_2 - \rho_1)}{\rho_2 + \rho_1} H}}$,

is around 0.47, as shown in Table 2.3.1. The experimental value, $F = 0.47$, is 6% lower than the one predicted theoretically by Yih (1947), or Keulegan (1934), or by O'Brien and Chernov (1932).

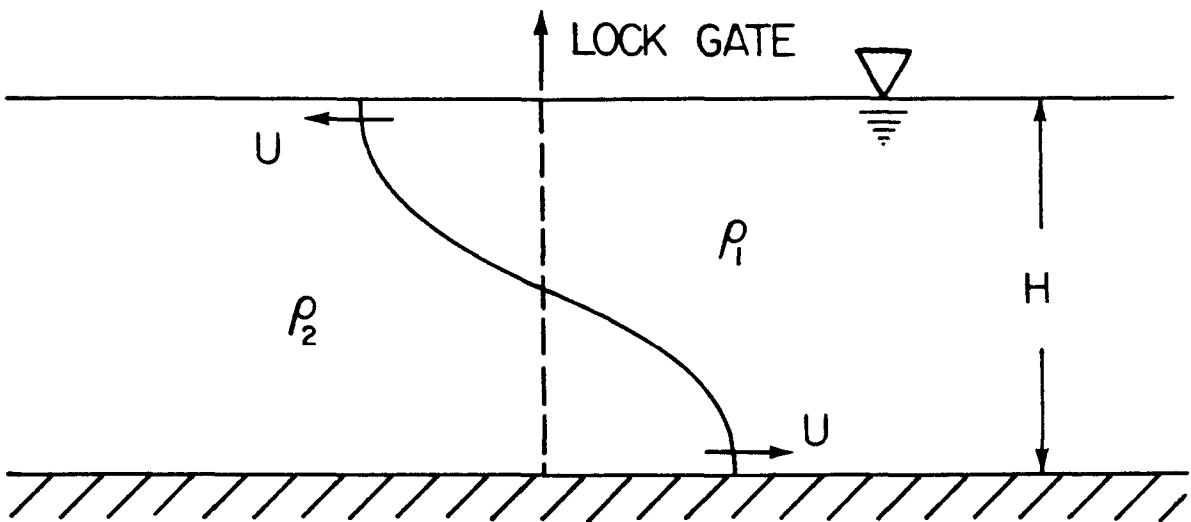


Figure 2.3.1 Lock exchange flow.

Table 2.3.1 Experimental studies on lock exchange flows.

Investigator	Water Tank			Water Depth R (cm)	Initial Length L_0 (cm)	Aspect Ratio H/L_0	Initial Density Disparity $\frac{\Delta\rho}{\rho_m}$	Channel Slope S_c	Relevant Reynolds Number	Initial Froude Number $F = \sqrt{\frac{g \Delta\rho}{\rho_2 - \rho_1} \frac{H}{\nu_m}}$	Density Difference Due to	Initial Front Velocity Observations
	Length L (cm)	Width B (cm)	Depth D (cm)									
Barr (1967)	8750	152	42	?	?	$0.07 \sim 0.56$?	0	?	?	?	overflow and underflow
Barr & Hassan (1963)	579.12 487.68 121.92	45.72 10.48 3.81	25.4 10.48 0.64	?	?	?	?	0	?	?	?	overflow and underflow
Keulegan (1957)	?	45.7 22.9 11.3 5.2 2.54	?	5.8 ~ 52	41.7 ~ 750	$0.07 \sim 0.30$	$0.005 \sim 0.150$	0	$U_h \epsilon \sim 175,000$ $3200 \epsilon \sim \frac{U_h}{\nu_m}$	$0.42 \sim 0.50$ average 0.462	Concentration difference in salinity and sugar	underflow
Middleton (1966)	500	15.4	50	$20 \sim 30.2$	28.3	$0.71 \sim 1.07$	$0.098 \sim 0.242$	0	?	$0.404 \sim 0.51$ average 0.44	Concentration difference in turbidity	underflow
O'Brien & Cherno (1932)	743.71	15.24	38.10	$12.19 \sim 36.58$	$9.75 \sim 54.56$	$0.13 \sim 3.08$	$0.015 \sim 0.101$	0	?	$0.46 \sim 0.59$	Concentration difference in salinity	underflow
Shwartz et al. (1973)	609.60	38.10	243.84	?	?	$0.05 \sim 10$	$0.0125 \sim 0.1478$	$0^* \sim 16^*$?	$0.25 \sim 0.5$	Concentration difference in salinity or turbidity	underflow
Simpson (1972)	150	30	30	6, 12, 24	20	$0.3 \sim 1.2$	$0.0015 \sim 0.0456$	0	$U_h \epsilon \sim 10,000$ $300 \epsilon \sim \frac{U_h}{\nu_m}$?	Concentration difference in salinity and sugar	underflow
Smith (1965)	1219.2	38.10	53.34	18.29	?	?	$0.002 \sim 0.005$	0	?	$0.50 \sim 0.60$	Concentration difference in salinity	overflow
Yih (1947)	304.8	30.48	60.96	$7.62 \sim 49.05$	152.40	$0.05 \sim 0.32$	$0.0005 \sim 0.0640$	0	?	average 0.47	Concentration difference in salinity	overflow and underflow

Keulegan (1957) performed several similar experiments, but with a relatively shorter lock length as shown in Figures 2.3.2(a) and (b). He found the saline front advancing at a constant velocity which depends only upon the initial water depth and the density difference of two fluids. The frontal Froude number, F , varied from 0.42 and 0.50. The average value was around 0.452, which is very close to Yih's result. O'Brien and Chernov (1932) also found the underflowing wedge front moved at a frontal Froude number that varied from 0.46 to 0.59. Smith (1965) found a variation from 0.50 to 0.60.

For longer travel, as shown in Figure 2.3.2(c), the underflowing front presented a head shape with a crest and trough. The ratio of the two heights, d_2/d_1 , (see Figure 2.3.3) was found to be almost a constant, 2.0, independent of the initial lock size, salinity difference, viscosity of the fluids, and the length of travel. The density head did not propagate with constant speed and in fact quickly decelerated. In other words, the lock exchange flow laws were not applicable. Keulegan (1957) used another Froude number

$$F_1 = \frac{U}{\sqrt{g \frac{2\Delta\rho_f d_1}{\rho_2 + \rho_1}}}$$

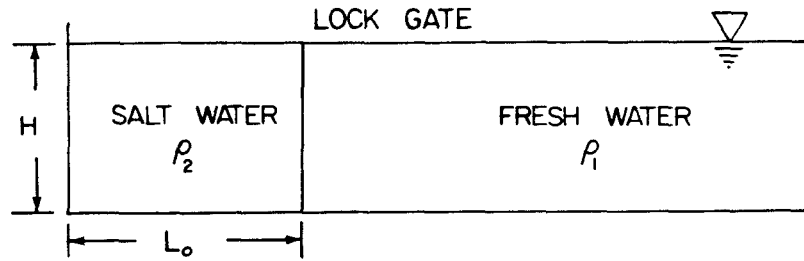


Figure 2.3.2(a) Lock and channel before removing gate.

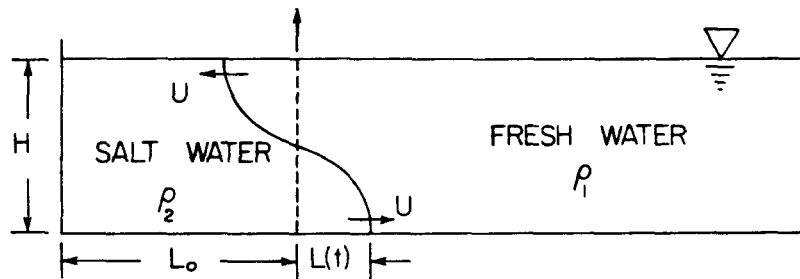


Figure 2.3.2(b) Advancing lock exchange flow.

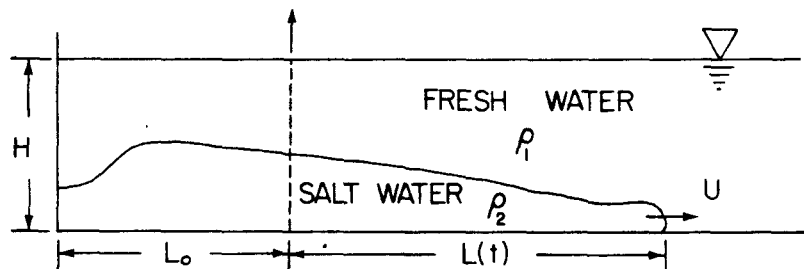


Figure 2.3.2(c) Finite-length exchange flow.

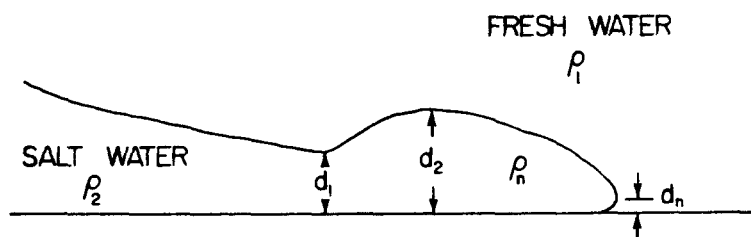


Figure 2.3.3 Idealized shape of saline front from finite-length lock exchange flow, after Keulegan (1957).

to describe the decaying frontal velocity, where $\Delta\rho_f$ is the local density difference at the front and d_1 is the trough height near the front. When the frontal Reynolds number, $Re_1 = \frac{Ud_1}{\nu_m}$, was greater than 400, the Froude number F_1 was constant (1.07). ν_m is the average value of the initial kinematic viscosity of the two fluids. But when the frontal Reynolds number Re_1 was less than 400, the Froude number F_1 was a function of the local Reynolds number Re_1

$$F_1 = 0.22 Re_1^{1/4} \quad . \quad (2.3.1)$$

The decelerating velocity was also observed by O'Brien and Chernoo (1932) for a saline front in a finite-length lock exchange flow.

The surge front from a finite-length turbid water lock exchange flow was observed by Middleton (1966). He found a constant velocity initially with the frontal Froude number, F , varying from 0.404 to 0.51 with an average value of 0.44. Similar rapid deceleration of the head at a longer travel distance was also noted by Middleton.

Shwartz *et al.* (1973) found that, for both saline and the turbidity flows from a finite-length lock on a horizontal bottom, and also with a mild bottom slope, the asymptotic decay of the frontal velocity U with distance traveled x was

$$U \sim x^{-1/2} \quad . \quad (2.3.2)$$

There is no clear explanation why this rapid deceleration occurs. Previous investigators have speculated that this may be due to viscous bottom friction, or side wall friction or the exhaustion of the supply of sediment caused by deposition of the suspended material.

A three-dimensional structure to the finite-length lock exchange flow was observed by Simpson (1972). A series of cleft and the lobe structures were seen to develop in the transverse direction to the "nose". The elevated height of the nose, d_n , was found as a function of frontal Reynolds number, $Re_3 = \frac{Ud_2}{\nu_s}$,

$$\frac{d_n}{d_2} = 0.61 Re_3^{-0.23 \pm 0.01} \quad (2.3.3)$$

where ν_s is the kinematic viscosity of the moving fluid. The lobe length between two clefts, ℓ , was found as a function of Reynolds number,

$$\frac{\ell}{d_2} = 7.4 Re_3^{-0.39 \pm 0.2} \quad (2.3.4)$$

Similar experiments for lock exchange flow connected to a wider channel, were also performed by Keulegan (1958). He found that a saline front intruding into a narrow channel also moved at a constant speed. The observed Froude number F was a function of the width ratio of the two channels. In the limiting case of a

river channel connected to an open sea, the saline front moved initially at a faster constant speed than that for a constant width channel. The average value of the frontal Froude number F was 0.57. The frontal head characteristics were also found to be different with the head being flatter and slightly longer. The ratio of the crest height, d_2 , to trough height, d_1 , was 2.16. The Froude number, F_1 , based on the head velocity and the trough height, d_1 , was 1.04 when the frontal Reynolds number, $Re_1 = \frac{Ud_1}{\nu_m}$, was greater than 550. For a frontal Reynolds number, Re_1 less than 550

$$F_1 = 0.206 Re_1^{1/4} \quad . \quad (2.3.5)$$

Similarly, it was found that

$$F_2 = \frac{U}{\sqrt{g \frac{\Delta\rho_f}{\bar{\rho}} d_2}} = 0.705 \quad (2.3.6)$$

when the frontal Reynolds number $Re_2 = \frac{Ud_2}{\nu_m}$ was greater than 1200 and

$$F_2 = 0.113 Re_2^{1/4} \quad (2.3.7)$$

when the frontal Reynolds number Re_2 was less than 1200.

2.3.3 Plane Surface Starting Buoyant Jets

Experimental studies on plane gravity currents have been performed by many investigators, as shown in Table 2.3.2. As shown in Figures 2.3.4(a) and (b), most of them produced a current by discharging horizontally a fluid of density ρ_j onto the free surface or bottom surface at one end of channel filled with a homogeneous fluid of density ρ_a . This type of density current is found to move at approximately a constant speed, even with viscosity drag effects.

The earliest experimental observations were made by meteorologists modeling atmospheric cold front propagation. Schmidt (1910) performed model experiments by discharging a salt solution onto a channel floor. An advancing saline front formed a nose, whose speed of advance depended on the salinity difference between the frontal and the ambient fluids, $\Delta\rho_n$, and the height of nose, h_n . Schmidt (1911) proposed that the frontal velocity, U , be expressed as

$$U = \lambda \sqrt{\Delta\rho_n h_n} \quad (2.3.8)$$

λ is a dimensional constant. A similar results was derived by Margules (1906) for modeling atmospheric cold front propagation by equating the change of potential energy to the change of kinetic energy.

Table 2.3.2 Experimental studies on plane gravity currents due to a constant rate of discharge at one end of channel.

Investigator	Channel		Ambient Fluid Depth h (cm)	Discharge Rate per Unit Width q (cm ² /sec)	Relative Density Excess $A = \frac{\Delta\rho}{\rho}$	Inlet Depth h_1 (cm)	Inlet Froude Number $Fr_1 = \frac{u_1}{\sqrt{g_0 h_1}}$	Kinematic Viscosity of Discharged Fluid ν_j (cm ² /sec)	Inlet Reynolds Number $Re = \frac{u_1}{\nu_j}$	Channel Bottom Slope S_c	$\frac{u}{h^{1/3}}$	Density Difference Due to	Gravity Currents Flow Observations
	Length (cm)	Width (cm)											
Abbott (1961)	?	?	?	?	0.29	?	?	?	?	0	?	Different constituent	Steady velocity measurement of paraffin oil front (overflow) spreading on fresh water
Almewati (1973)	487.7	12.7	45.72	0.945 ± 4.33	0.0036 ± 0.015	?	?	± 0.01	94.5 ± 433	0	average 1.15	Concentration difference in salinity	Time recording of dyed fresh water front (overflow) past the designated locations
Barr (1959)	518.16	45.72	?	4.40 ± 12.39	0.00247 ± 0.00270	5.35 2.67	~0.64 0.64 ± 1.06	± 0.01	440 ± 1240	0	1.10 ± 1.30	Temperature difference of fresh water	Sequential photograph of dyed heated front (overflow) at various times
Ball (1942)	152.4 304.8 457.2	5.72 25.4 38.1	25.4 25.4 86.4	?	0.0001 ± 0.0080	?	?	?	?	0.23% ± 8.0%	?	Concentration difference in salinity or suspended materials or sugar or salt or other substances and temperature difference	Dyed density currents underflows on sloping channel
Branstator (1940)	243.84	11.43	45.72	2.81 ± 4.30 2.35 ± 4.37	0.0020 ± 0.0134 0.0020 ± 0.0168	?	?	± 0.01	261 ± 430 235 ± 442 235 ± 437	0.003 0.010 0.013	0.72 ± 0.85 0.72 ± 0.85 0.77 ± 1.70	Concentration difference in salinity and fluorescein dye	Sequential photograph of underflow dyed front and velocity and thickness measurements of uniform flow behind the front
Ellison & Turner (1959)	500 200	15 10	20 60	?	?	?	?	?	?	0 0° ± 90°	?	Concentration difference in salinity	Dyed fresh water front overflows salt water front underflows down on inclined fresh water box
Georgescu (1942)	3048	152.4	182.88	19.51 ± 61.94 3.41 ± 64.72	0.78 10.43	?	?	?	?	1/10	1.06 ± 1.18 0.55 ± 0.81	Difference of mass, fluorescein and hydrogen from air	Measures mass velocity of inverted flow of hydrogen as front advancing upwards along the inclined gallery or the roof of the airway by taking pans the designated locations
Kesteven (1946)	?	?	?	15.51 ± 53.61	0.091 ± 0.0196	?	?	± 0.01	1550 ± 5360	0	0.64 ± 0.756 average 0.700	Concentration difference in salinity	Saline front (media) velocity measurements in still fresh water, salt water discharged vertically upwards (underflow)
Lane & Willcock (1965)	2286	60.96	121.92	15.33 49.24 ± 118.92	?	1.27 9.91	2.59 ± 13.30 0.56 ± 4.55	± 0.01	1533 4924 ± 11,900	0	?	Temperature difference of fresh water	Dyed heated fresh water front (overflow) velocity observations, velocity and layer thickness measurements of uniform flow behind front
McMillan (1966)	500	15.4	50	15.88 ± 56.44	0.0263 0.0557	?	?	0.0092 ± 0.01115	1560 ± 5840	0 ± 0.040	?	Concentration difference in salinity	Sequential photograph of dyed saline front at various times, velocity and thickness measurements of uniform flow behind front
Schmidt (1940)	181	4	31	?	?	?	?	?	?	0	?	Concentration difference in salinity	Dyed saline front (overflow) observations (underflow)
Williamson (1970)	3657.6	56.42	60.96	741.6 ± 1144	0.0023 ± 0.0120	?	?	± 0.01	74,100 ± 114,400	0 ± 0.542	1.045 ± 0.047	Concentration difference in salinity	Sequential photograph of dyed saline front (underflow) at various times
Wood (1966)	182.88	30.48	55.88	?	0.0033 ± 0.1160 0.0032 ± 0.146 0.0022 ± 0.1605 0.00296 ± 0.148 0.00197 ± 0.0680	?	?	?	?	0° 6° 28° 50° 90°	1.06 ± 0.10 1.24 ± 0.08 1.51 ± 0.17 1.53 ± 0.16 1.18 ± 0.14	Concentration difference in salinity	Sequential photograph of dyed salt front (underflow) at various times

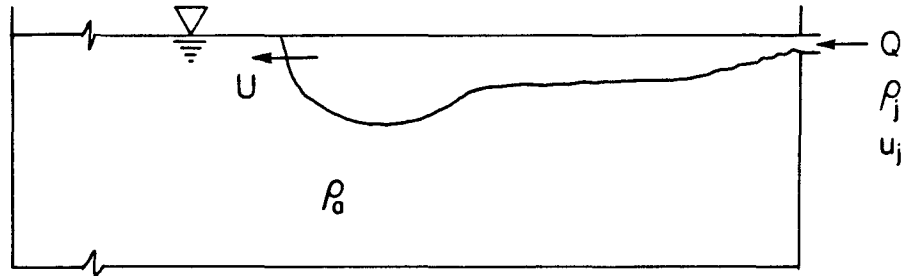


Figure 2.3.4(a) Forced free surface density currents.

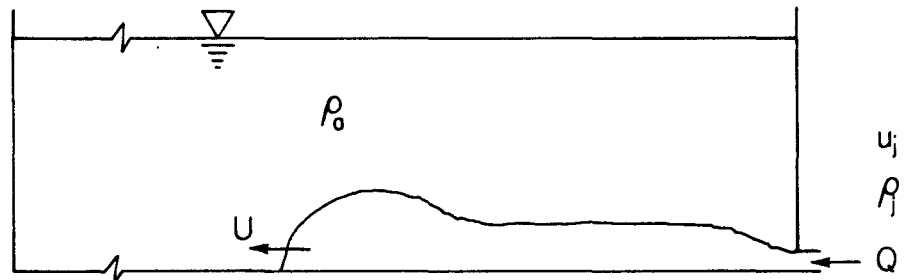


Figure 2.3.4(b) Forced bottom surface density currents.

Barr (1959) produced so-called plane "forced surface density currents" on the free surface of a flume, as in Figure 2.3.5. He found that sometimes a roller type front developed initially after the discharge and sometimes a faster moving and pointed wedge type front occurred, either initially or after some travel. No clear explanation was given for this behavior although surface tension effects were suspected.

Lean and Willock (1965) also performed similar experiments and found the front moved out initially with a nearly constant speed, with an intensive mixing region behind the front. The thickness of the surface layer increased away from the entry point, but downstream the surface layer changed to a uniform depth and there was little further mixing with the underlying cold water. The turbulence in the interfacial layer damped out smoothly to form a sharp interface. Lean and Willock found that a higher inlet Froude number flow always lead to a thicker uniform surface layer and that for an inlet Froude number less than about 1.0, the thickening of surface layer was slight. The local densimetric Froude numbers, $F_\ell = \frac{u}{\sqrt{g\Delta h}}$, were 0.69 to 1.14, which generally agrees with the results of Ellison and Turner (1959) for the case of negligible mixing.

Almquist (1973) also observed surface density front motion and the details of the experimental parameters are shown in Table 2.3.2, and in Koh (1976). The wedge-shape front grew

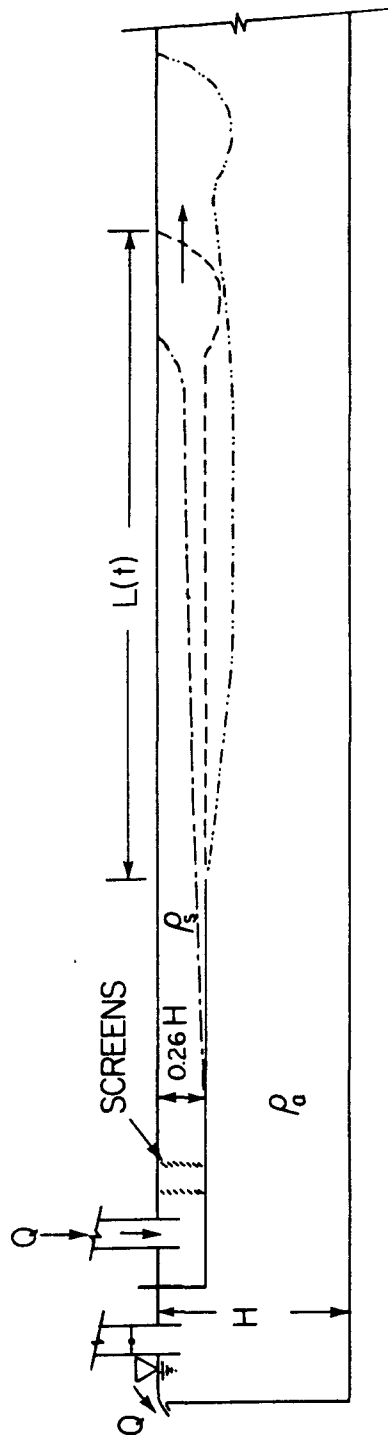


Figure 2.3.5 Surface density currents and discharging box used by Barr (1959).

first with time t , and then changed to $t^{4/5}$, as shown in Figure 2.3.6. The density fronts therefore propagated initially with a constant speed and then decelerated, which was consistent with the results of Barr (1959) and Lean and Willock (1965).

Density currents on the bottom were investigated by Bell (1942), who used saline flows to model the turbid river flow entering a reservoir. Middleton (1966) performed a series of experiments to investigate the sediment transport mechanism by the turbidity currents. A suspended sediment density current "head" was formed and after an initial acceleration this flowed at an approximately constant velocity down the sloping floor of a channel. The steeper the slope is, the longer the acceleration stage will be. Eventually the flow was decelerated to a nearly constant velocity and the head shape was preserved. Figure 12 of Middleton (1966) shows nearly uniform distributions of velocity and layer thickness in the flow behind the current head. Keulegan's (1957) results for density currents were also checked by Middleton. The Froude

number, $F_2 = \frac{U}{\sqrt{g \frac{2\Delta\rho}{\rho_j + \rho_a} d_2}}$, was found to vary from about 0.7

for the low slope case ($S_c = 0.005$) to about 0.8 to 0.9 for the high slope case ($S_c = 0.04$).

Similar experiments on a milder sloping floor were also performed by Braucher (1950). The front propagated with a constant velocity proportional to the cubic root of the buoyancy flux discharged, B . The value of this coefficient $\frac{U}{B^{1/3}}$,

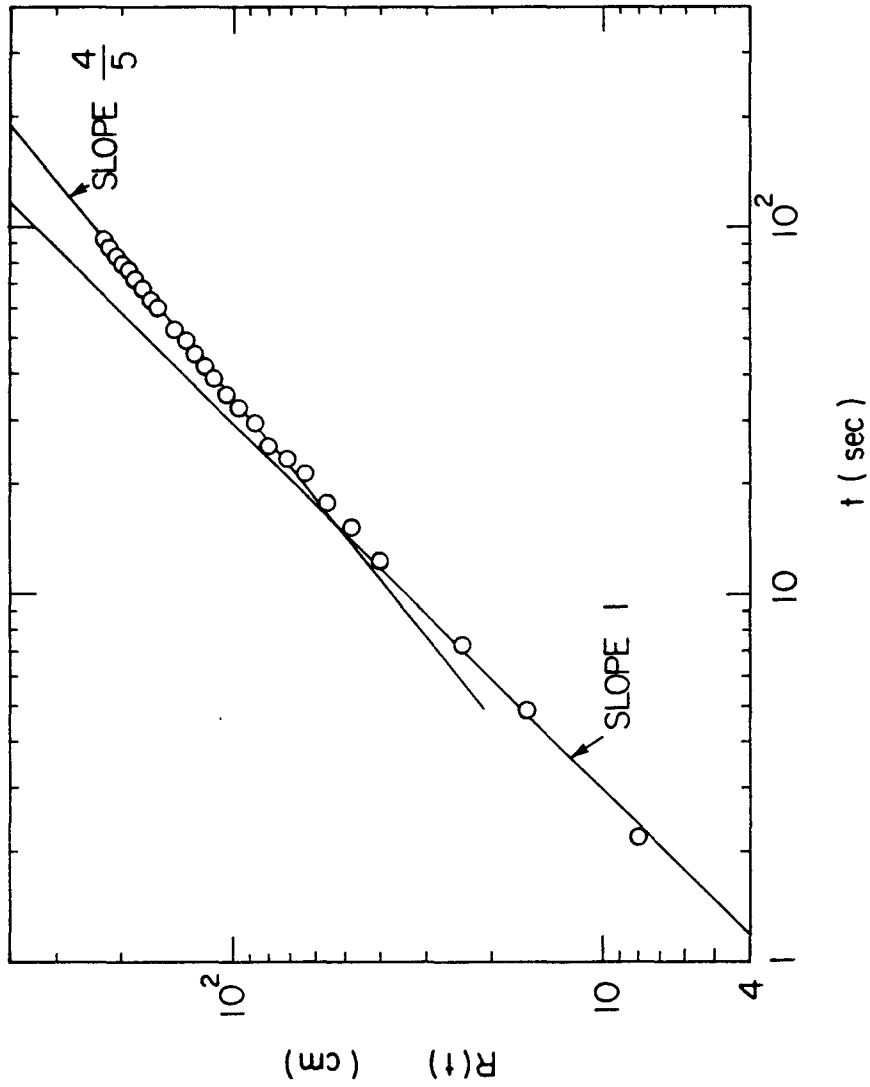


Figure 2.3.6 Growth history of starting free surface gravity currents, reproduced from Chen (1975). Experimental data from Almquist (1973).

as shown in Column 9 of Table 2.3.2, is found to vary slightly with channel slope.

Experimental studies of plane forced density current for a range of bottom slopes, (0° , 6° , 28° , 50° , 90°), were conducted by Wood (1965). All experimental results shown that after an initial period the magnitude of the constant frontal velocity was proportional to the cubic root of kinematic buoyancy flux with the coefficient a function of slope angle. This coefficient had its maximum value for a 50° slope and for the horizontal bottom the value was close to that observed by Wilkinson (1970).

Keulegan (1946) also performed this type of experiment but the discharge arrangement, as shown in Figure 2.3.7, lead to a wedge shape front instead of the head or the cap shape observed by Middleton (1966), Wood (1965), and Wilkinson (1970). Although a constant frontal velocity was also observed, the ratio of frontal velocity to the cubic root of buoyancy flux had an average value of around 0.700.

Georgeson (1942) studied frontal motion as a model of gas spreading in mining tunnels and found that the propagating velocity of the frontal edge was proportional to the cubic root of the rate of inflow and varied little with the travel distance along a sloping gallery roof. The ratios of the frontal velocity to the cubic root of the buoyancy flux have been re-calculated, as shown in Table 2.3.2, and vary from 1.06 to 1.18 for methane gas and from 0.55 to 0.81 for hydrogen.

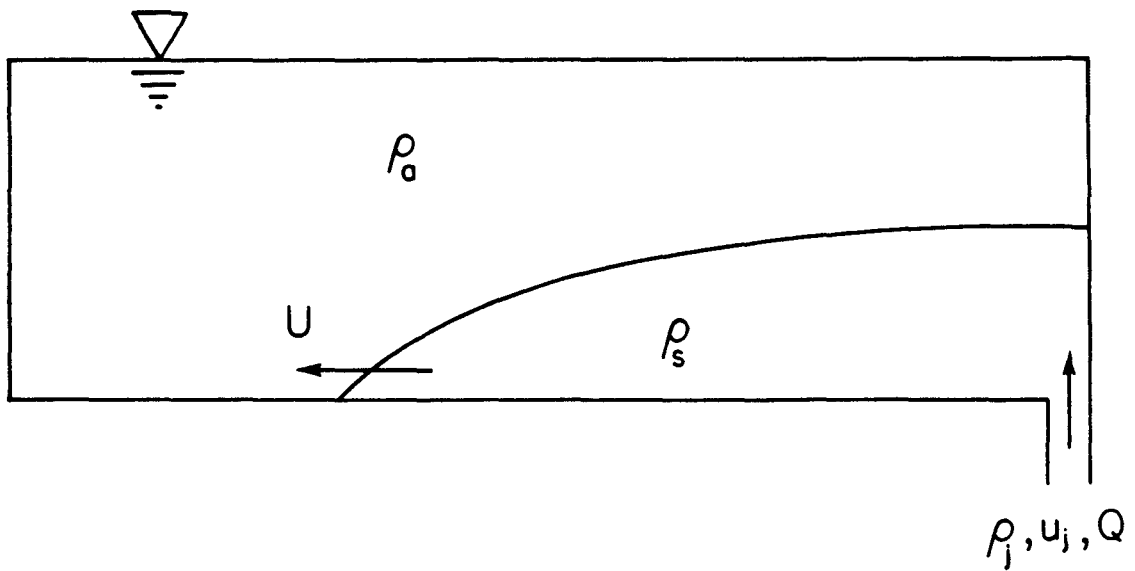


Figure 2.3.7 Advancing wedge on the bottom of a channel, after Keulegan (1946).

2.3.4 Von Kármán, Prandtl, and Benjamin Theories

Von Kármán (1940) made a pioneering theoretical study of bottom density currents propagating in an ambient fluid of infinite extent. The essential ideas are repeated in Yih (1965). Figure 2.3.8(a) shows the nature of a dense current advancing into a less dense fluid as viewed in a reference frame fixed relative to the ground. Figure 2.3.8(b) shows the current as viewed in a moving frame traveling with the front velocity U . In this moving frame the front becomes a stagnation point and the layer behind the front becomes a stationary layer under a uniform and steady flow with velocity U .

Applying the Bernoulli equation along a streamline in the ambient fluid in the neighborhood of the discontinuous interface between stagnation point X (subscript s) and the far downstream point Y (subscript ∞) gives

$$P_s = P_\infty + g \rho_a h_\infty + \frac{\rho_a}{2} U^2 \quad (2.3.9)$$

where P_s and P_∞ are pressures, ρ_a is the ambient fluid density, h_∞ is the thickness of the uniform layer at the far downstream point Y and U is the horizontal current velocity. Since the current is assumed steady, the application of Bernoulli's equation along another streamline on the other side of interface implies

$$P_s = P_\infty + g \rho_s h_\infty \quad (2.3.10)$$

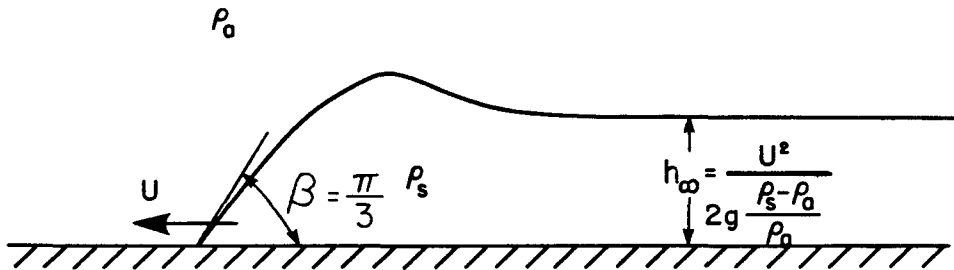


Figure 2.3.8(a) Configuration of a forced plane gravity current as viewed in a fixed reference frame to the ground.

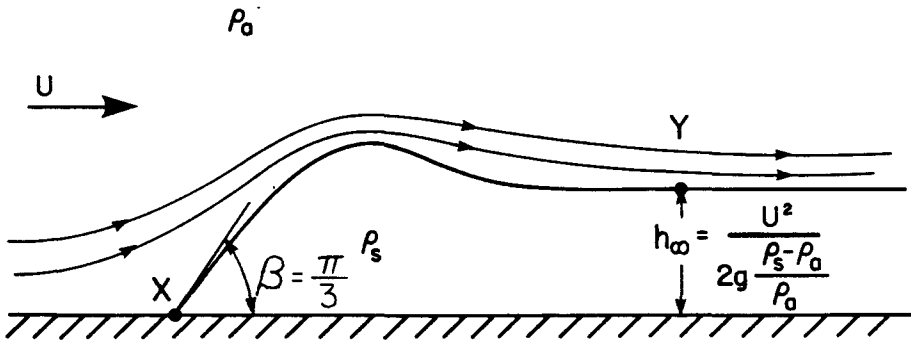


Figure 2.3.8(b) Configuration of a forced plane density wedge as viewed in a moving reference frame with the front, after von Kármán (1940).

where ρ_s is the fluid density of the arrested current. By equating the two pressure differences in Eqs. (2.3.9) and (2.3.10) one obtains

$$U^2 = 2g \frac{\rho_s - \rho_a}{\rho_a} h_\infty \quad (2.3.11)$$

$$\text{or } F_\infty = \frac{U}{\sqrt{g \left(\frac{\rho_s - \rho_a}{\rho_a} \right) h_\infty}} = \sqrt{2}.$$

Using free streamline theory, von Kármán (1940) also showed that the inclination angle of the frontal interface, β , must be at 60° to the horizontal. A similar angle was also derived by Stewart (1945) and Jeffreys (1952) using inviscid potential flow theory in polar coordinates. Rannie (1975) also derived the same angle, 60° , assuming an approximate profile in an infinitely deep ambient fluid. Von Kármán (1940) also suggested that there must be a head at the front which is thicker than the downstream layer. The head shape of the discontinuity surface has not yet been determined.

Ambient stratification effects on such currents were discussed by Kao (1976,1977). According to Kao's study, the velocity of an intruding uniform current at a level of neutral density in a stratified environment will be

$$U = \sqrt{g\epsilon} h_\infty, \quad (2.3.12)$$

where the ambient stratification $\epsilon = \frac{-1}{\rho_o} \frac{d\rho_a(z)}{dz}$ and $\rho_o = \rho_a(o)$ which is to say that the Richardson number

$$Ri = \frac{\sqrt{g\epsilon} h_\infty}{U} = 1 \quad . \quad (2.3.13)$$

An advancing density current propagating along a sharp interface between two infinitely deep homogeneous fluids, as shown in Figure 2.3.9, was studied by Engelund and Christensen (1969), Moshagen (1973), Thorpe (1973), and Kao (1977). On the basis of the Bernoulli theorem the front should move at a speed U ,

$$U^2 = 2 \frac{\rho_a - \rho_s}{\rho_s} \frac{\rho_s - \rho_u}{\rho_a - \rho_u} g h_\infty \quad . \quad (2.3.14)$$

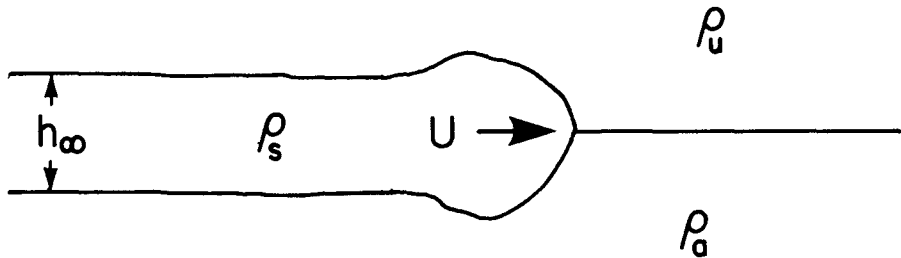


Figure 2.3.9 Internally spreading currents between a stably stratified interface.

The limiting case of a surface spreading current when the density ρ_u of the upper ambient fluid is small, i.e., ρ_u/ρ_a and $\rho_u/\rho_s \rightarrow 0$.

Then

$$U^2 = 2 \frac{\rho_a - \rho_s}{\rho_a} g h_{\infty} \quad . \quad (2.3.15)$$

Prandtl (1952) studied the rate of advance of atmospheric cold front, as shown in Figure 2.3.10(a). In a reference system of coordinates traveling at the same velocity as the front, the moving front is a stagnation point. He reasoned that pressure must be the same on both sides of the stagnation point so by neglecting the hydrostatic pressure terms, and equating the dynamic pressure, he found

$$\frac{1}{2} \rho_s (u_f - U)^2 = \frac{1}{2} \rho_a U^2 \quad , \quad (2.3.16)$$

which gives

$$\frac{u_f}{U} = 1 + \sqrt{\frac{\rho_a}{\rho_s}} \quad , \quad (2.3.17)$$

where U and u_f are the velocities respectively of the front and the fluid particle just behind the front, ρ_a and ρ_s are the densities of the ambient air and the cold air, as defined in Figure 2.3.10(b).

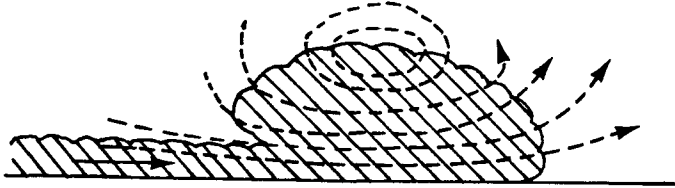


Figure 2.3.10(a) Advancing mass of cold air; actual flow relative to the ground, after Prandtl (1952).

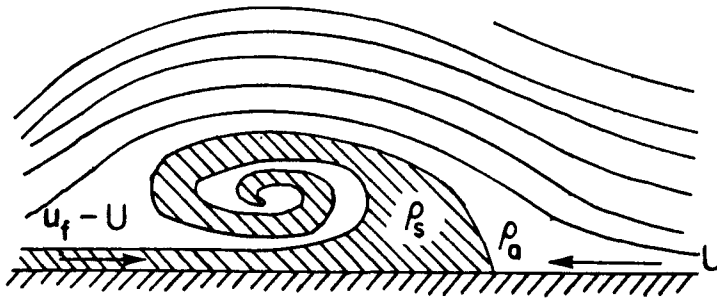


Figure 2.3.10(b) Advancing mass of cold air; idealized flow relative to the front, after Prandtl (1952).

Prandtl's theory implies that the cold front must advance at a velocity of about one half the velocity of a fluid particle behind it, since the density of the frontal air usually differs little from that of the ambient air. Thus, a roller-type stream is expected to be formed when the fluid behind the front is deflected upward at the front in a manner that is similar to the development of a starting jet flow. For the case of an avalanche, in which the density of the moving mixture of snow and cold air is considerably greater than that of the ambient air, the frontal velocity should become nearly equal to the fluid particle velocity. Prandtl claimed that the results of field observations by Koschmieder (1936) supported his Eq. (2.3.17). These ratios of the front velocity to the fluid velocity were also recalculated by Berson (1958) and the mean values varied from 0.50 to 0.62.

However, this simple theory does not agree with the laboratory experiment results obtained by Keulegan (1957), Ellison and Turner (1959), Wood (1965), and Middleton (1966). Neither does it agree with other field measurements of cold fronts by Clarke (1961). Wood (1965) suggested that Prandtl's neglect of the hydrostatic pressure terms in the steady layer behind the front accounts for the error in the result. Benjamin (1968) also argued that Prandtl's theory can only apply to the transient problem immediately following the release of a stream of dense fluid into a deep expanse of lighter fluid.

Benjamin (1968) studied the flow produced by a cavity emptying a two-dimensional box, as shown in Figure 2.3.11(a). In a reference frame moving with the same velocity as that of cavity tip, Benjamin considered the steady flow past a cavity, (as shown in Figure 2.3.11(b)). Benjamin balanced the total flow force, that is, the momentum flux plus pressure force, between the approaching and the receding streams and in this moving coordinate system the cavity tip becomes a stagnation point where the pressure can be chosen to be zero.

Applying Bernoulli's theorem along the free surface streamline downstream one obtains

$$U_2^2 = 2g(h_2 - h_\ell) \quad , \quad (2.3.18)$$

for the plane cavity flow, in which U_2 is the mean fluid flow speed downstream where the mean thickness is $(d - h_2)$, d is the total thickness of the box and h_ℓ is the unknown head loss between the approaching and the receding streams.

The total flow force P_u for upstream of the stagnation point is equal to the sum of the hydrodynamic pressure, $-\frac{1}{2} \rho_a U^2 d$, the hydrostatic pressure, $\frac{1}{2} \rho_a g d^2$, and the momentum flux, $\rho_a U^2 d$, i.e.

$$P_u = \frac{1}{2} \rho_a U^2 d + \frac{1}{2} \rho_a g d^2 \quad (2.3.19)$$

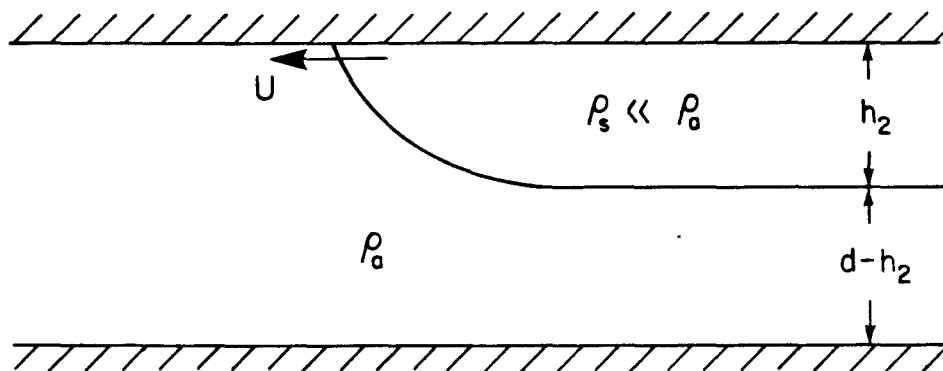


Figure 2.3.11(a) Cavity front moving at a constant velocity along a two-dimensional box.

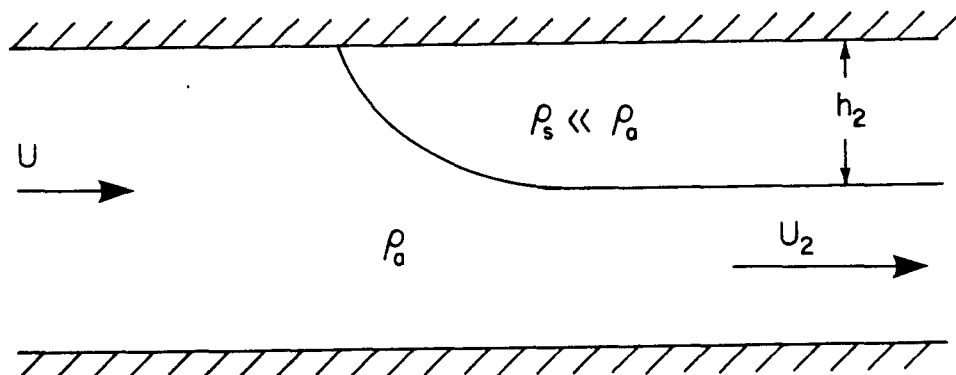


Figure 2.3.11(b) Arrested cavity front as viewed in a moving frame with the same velocity of front.

And the total flow force P_d far downstream is equal to the sum of the hydrostatic pressure force, $\frac{1}{2} \rho_a g (d - h_2)^2$, plus the momentum flux, $\rho_a U_2^2 (d - h_2)$, i.e.

$$P_d = \rho_a U_2^2 (d - h_2) + \frac{1}{2} \rho_a g (d - h_2)^2 \quad . \quad (2.3.20)$$

Equating the flow force terms and using the continuity relationship,

$$Ud = U_2 (d - h_2) \quad (2.3.21)$$

gives

$$U^2 = \frac{g h_2 (d - h_2) (2d - h_2)}{d(d + h_2)} \quad , \quad (2.3.22)$$

and

$$U_2^2 = \frac{g d h_2 (2d - h_2)}{(d - h_2) (d + h_2)} \quad . \quad (2.3.23)$$

Using Eqs. (2.3.22) and (2.3.23) one has the relevant Froude numbers

$$Fr_1 = \frac{U}{\sqrt{gh_2}} = \left[\frac{(1 - h_2/d)(2 - h_2/d)}{(1 + h_2/d)} \right]^{1/2} \quad , \quad (2.3.24)$$

$$Fr_2 = \frac{U}{\sqrt{gd}} = \left[\frac{(1 - h_2)(2 - h_2/d)(h_2/d)}{(1 + h_2/d)} \right]^{1/2} \quad , \quad (2.3.25)$$

and

$$Fr_3 = \frac{U_2}{\sqrt{g(d-h_2)}} = \left[\frac{(2-h_2/d)(h_2/d)}{(1+h_2/d)} \right]^{1/2} / (1-h_2/d) \quad (2.3.26)$$

Equating (2.3.18) and (2.3.23) gives the head loss term h_ℓ between the approaching and the receding streams as

$$h_\ell = \frac{h_2^2(d-2h_2)}{(d^2-h_2^2)} \quad (2.3.27)$$

This relationship gives $h_2 = d/2$ when $h_\ell = 0$, i.e., no head loss, and $h_2 < d/2$ when there is non-negative head loss. Without an energy source the case $h_2 > d/2$ is clearly impossible.

Benjamin (1968) recommended that all the equations derived here were still applicable to gravity currents by replacing g by g' , where $g' = g \left(\frac{\rho_a - \rho_s}{\rho_a} \right)$. Benjamin found that the equations so derived checked fairly well with the experimental measurements of lock exchange flows made by Keulegan (1958) and with measurements of forced gravity currents on a sloping floor by Braucher (1950), but not with the turbidity flow measurements on sloping bottoms made by Middleton (1966).

The energy loss Eq. (2.3.27) indicates that the possible range of the cavity flow thickness h_2 is from 0 to one-half of the box thickness and the possible ranges of Froude numbers, are from $\sqrt{2}$ to $\frac{1}{\sqrt{2}}$ for Fr_1 , from 0 to $\frac{1}{2}$ for Fr_2 , and from 0 to $\sqrt{2}$

for Fr_3 , depending on the depth ratio, $\frac{h_2}{d}$, of the receding streams. A fairly good comparison with Benjamin's theory for a plane propagating cavity flow was given by Ellis and Al-Khairulla (1974), as shown in Figure 2.3.12.

Benjamin (1968) extended his analysis to cavity flows propagating in a circular tube. In the limiting case without any surface tension and viscosity effects, the theory was confirmed fairly well by the experimental results of bubble motion in a circular tube by Zukoski (1966).

Using a hodograph transformation, Benjamin (1968) was also able to derive the actual shape of a free boundary for a two-dimensional arrested cavity. The inclined angle at the tip was found to be 60° just as von Kármán found, but no prominent "head" shape, as von Kármán suggested, was found.

Benjamin (1968) argued that there must be some separation and turbulence behind the crest point of the density head in order to balance the hydrodynamic force between the tip and a point far downstream. In the limit of infinite depth of ambient fluid, $h_2/d \rightarrow 0$, in Eq. (2.3.24), Benjamin has $\frac{U}{\sqrt{g'h_2}} = \sqrt{2}$, which was also derived by von Kármán earlier as $\frac{U}{\sqrt{g'h_\infty}} = \sqrt{2}$. Benjamin claimed that although von Kármán overlooked the energy loss, he obtained the right value with wrong reasoning.

Recently, many experimental measurements were made by Britter and Simpson (1978) and Simpson and Britter (1979) on an arrested density wedge produced by a continuous release of saline water into

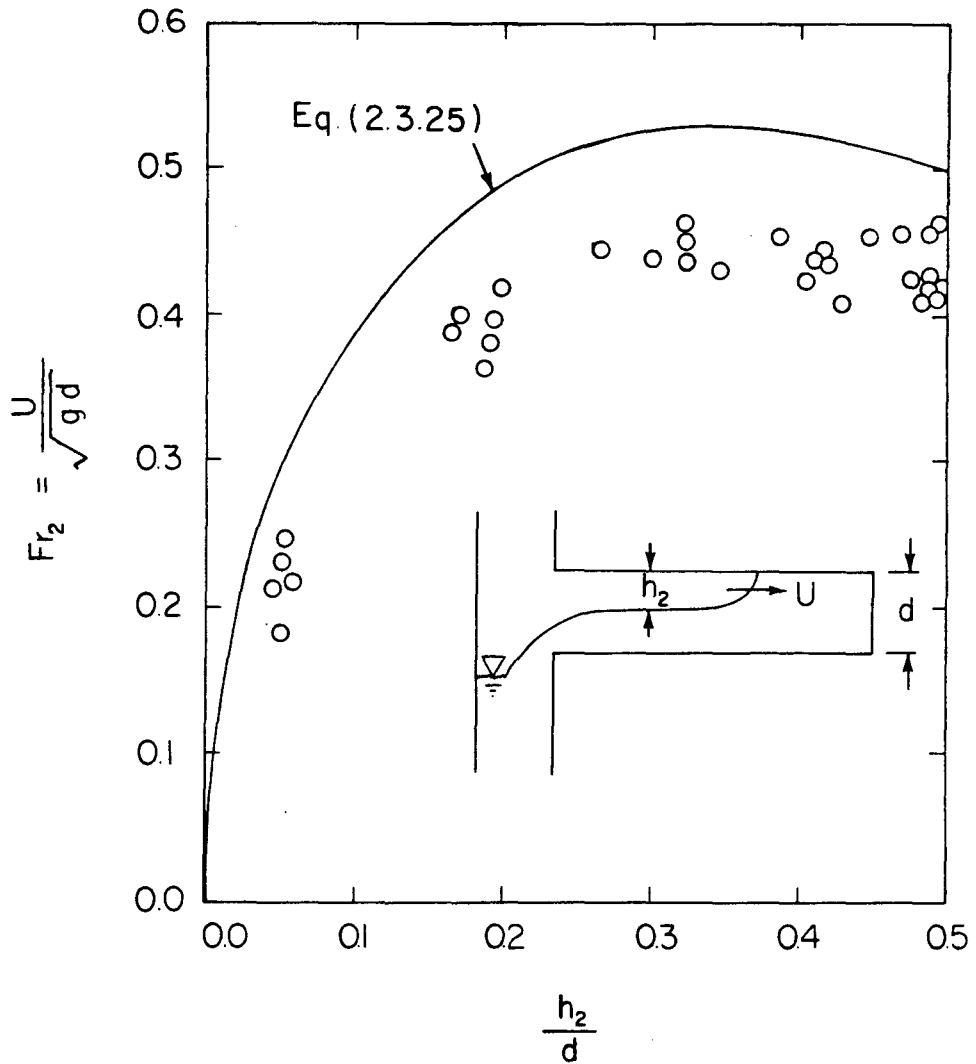


Figure 2.3.12 Comparison of theoretical solution (solid line) of Benjamin (1968) with the experimental results (open circles) of emptying cavity flow in an expansion gallery of surge tank by Ellis and Al-Khairulla (1974).

uniformly flowing fresh water. The wedge angle was found to be around $40 \pm 5^\circ$, which is smaller than the 60° predicted by von Kármán and others. Much higher values of the Froude numbers than those predicted by Benjamin's theory were found for the range of the relative depth, $0.0 < h_2/d < 0.3$. The trend of the experimental results is that the Froude number will go to a large value for the case of vanishing relative depth, $\frac{h_2}{d} = 0$, rather than the value, $\sqrt{2}$, predicted both by von Kármán and Benjamin. The difference between the experimental results by Britter and Simpson (1978) and the theoretical results by Benjamin is probably due to the downstream source condition.

2.4 Previous Analysis of Density Front Propagation

2.4.1 Spreading in a Homogeneous Environment

In Section 2.3, most of the density fronts discussed belonged to the class of lock exchange flows or to the plane forced surface density currents. Most were observed to propagate with constant speed and any deceleration was believed due to the effect of viscosity. The influence of other aspects of these problems, such as the source condition (a finite volume release or a continuous steady discharge), or radial motion, requires further discussion.

A force scale analysis was used by Fay (1969,1971) to study plane and radial spreading of an oil slick on the sea surface. He concluded that an oil front spreading from a finite volume

oil spill will be first driven by an unbalanced horizontal pressure force due to the buoyancy and then later by surface tension.

The spreading is retarded at first by inertial forces and then by the viscous force associated with an unsteady boundary layer growth in the ambient water. A similar force balance method was previously used by Langmuir (1933) to examine the extent of an oil film lens.

Chen and List (1976) used the same methods to analyze the frontal motion due to a steady submerged buoyant jet discharge and also that resulting from a finite volume surface release of miscible buoyant liquid. Two regimes were found for both cases, each with different time histories corresponding to a buoyancy-inertial spread and a buoyancy-viscous spread. In the finite volume release case the inertial density front grows at the same rate as that for a spreading oil slick, but the results are different in the viscous regime. The same force argument can be used to predict oil front motion resulting from a constant discharge spill and the results are quite different from the case of a finite volume release, (Waldman *et al.* (1972) and Chen (1975)).

In order to solve these problems for more than just the frontal position function, several direct numerical calculations of the Navier-Stokes equations have been used. Daly and Pracht (1968) and Vasiliev (1975) considered lock exchange flows, Kao *et al.* (1977,1978) plane forced surface density currents,

and Harlow and Welch (1965) and Sokolov (1972) some miscellaneous problems. Another approach, potential flow solution, was used by Penney and Thornhill (1952), to determine the inertial phase of flow of a squatting liquid column which was a different density from that of ambient fluid. Similar method was also used by Pohle (1952), for the dry-bed dam-break flow. Numerical calculations were performed by Meng and Thomson (1978) and Meng (1978) to study a mixed region collapsing in a stably density-stratified interface between two homogeneous fluids.

Nonlinear internal shallow water wave equations were developed by Penney and Thornhill (1952) to study the base surge flow due to an atomic bomb explosion in a shallow ocean. These long wave approximation equations were also used by Abbott (1961,1968) and Hoult (1972) to study inertial spreading of oil slicks. Numerical computations of the equations using the method of characteristics were performed by Penney and Thornhill (1952), Abbott (1961,1968) and Reid (as reported by Ichiye, 1972), but problems were found in specifying the source conditions and the initial and the boundary conditions at front. Other self-similar solutions of the long wave equations were used by Hoult and Suchon (1970), Fay (see Liang, 1971), and Fannelop and Waldman (1972) for finite volume oil spills.

Recently, Mei (1966) and Buckmaster (1977) considered the spreading flow of a sheet of viscous liquid down an inclined plane. The special case involving spread over a horizontal plane

was considered by S. H. Smith (1969b). He obtained similarity solutions to appropriate to an instantaneous point source and found that a liquid front moves over a horizontal bed with a decelerating velocity proportional to $t^{-4/5}$ for plane flow and proportional to $t^{-7/8}$ for radial flow.

More general solutions including varying source conditions are presented in the next chapter.

2.4.2 Spreading in a Linearly-Stratified Environment

Numerical studies for interflowing density fronts were made by Wessel (1969), Padmanabhan *et al.* (1970), Young and Hirt (1972), Vasiliev *et al.* (1972), Bell and Dugan (1974), Dugan *et al.* (1976), and Cerasoli (1978), as listed in Table 2.4.1. For the so-called "principal stage" region, Manins (1976b) and Kao (1977) showed that a plane submerged density front resulting from a volume of homogeneous fluid collapsing at a neutrally buoyant level in a linearly stratified environment will increase its horizontal length scale in proportion to $t^{1/2}$. However, the viscous long wave approximation by Padmanabhan *et al.* (1970) showed that it will increase as $t^{1/6}$ when time is very large. By an inverse analogy to selective withdrawal theory, Imberger *et al.* (1976) obtained different power laws for the plane intrusion layer. They found that in the absence of molecular diffusion, the interflowing wedge due to a horizontal slot jet discharge at a neutral buoyancy level in a linearly density-stratified environment will grow in proportion to the time t in the inertial-buoyancy

Table 2.4.1 Summary of previous theoretical studies of a plane (n = 0) or a radial (n = 1) submerged density front spreading in a linearly density-stratified environment due to a finite volume release (m = 0) or a continuous discharge (m = 1) at a neutral level.

Author	m	n	Numerical Solution	Analytical Solution	Asymptotic form of R(t)/R ₀	Valid Domain	Note
Bell and Dugan (1974)	0	0	-	$Nt = \frac{R}{R_0} \int_1^R \frac{1+t^{-4}}{1-t^{-2}} dt$	$\sim 1 + \frac{N^2 t^2}{4} - O(N^4 t^4)$	Initial Stage	Reynolds Number $Re_N = \frac{NR^2}{\nu s}$ is rather large
		1	-	$Nt = 2^{1/2} \frac{R}{R_0} \int_1^R \frac{1+2t^{-6}}{1+t^{-4}} dt$	$\sim 1 + \frac{N^2 t^2}{6} - O(N^4 t^4)$	Initial Stage	
Cerasoli (1978)	0	0	Numerical Calculation	-	?	?	
Dugan et al. (1976)	0	0	Finite Difference	-	$\sim 1 + \frac{1-\epsilon}{8} N^2 t^2$	Small Time	
Hartman and Lewis (1972)	0	0	-	-	$\sim 2 - \epsilon_s - 2(1 - \epsilon_s) \frac{J(Nt)}{Nt}$	Small Time	
Imberger et al. (1976)	1	0	Numerical Calculation	-	$\sim t^{1.04}$		
			-	Inverse Withdrawal Theory	$\sim t$	Inertial-buoyancy	Inflow momentum is small
					$\sim t^{5/6}$	Viscous-buoyancy	
		$\sim t^{3/4}$	Viscous-diffusion				
Kao (1974)	0	0	-	$\frac{R(t)}{R_0} = \sqrt{\frac{\pi}{2}} (Nt + c)^{1/2}$ c = integration constant - 1.0 ≤ c ≤ - 0.8	$\sim (Nt)^{1/2}$	Principal Stage	
Kao (1976)	0	0	-	$\frac{R(t)}{R_0} = 1 + \frac{N^2 t^2}{8} + O(N^4 t^4)$		Nt ≤ 2.05	
				$\frac{R(t)}{R_0} = \sqrt{\frac{\pi}{2}} (Nt - 0.57)^{1/2}$	$\sim (Nt)^{1/2}$	Nt ≥ 2.05	
Manins (1976a)	0	0	-	$\frac{R(t)}{h(o,o)} = (1 + 2Fr Nt)^{1/2}$	$\frac{R(t)}{R_0} = (\frac{5}{4} Nt)^{1/2}$	Principal Stage	Assume elliptical section and $Fr = \frac{\dot{R}(t)}{Nh(o,t)} = \frac{5}{8}$
Manins (1976b)	1	0	-	$R(t) = f\left(\frac{Q}{\nu}, Nt, \frac{h_1}{H}\right) N^{1/2} Q^{1/2} t$	$R(t) \sim N^{1/2} Q^{1/2} t$	Inertial-buoyancy	
Maxworthy (1972)	1	0	-	$R(t) \sim t^{1/6} Q^{2/3} t^{5/6}$	$\sim t^{5/6}$		Neglect diffusion
Mei (1969)	0	0	-	$R(t) = (1 + h^2(o,t)t^2)^{1/2}$		Initial Stage	Assume an elliptical initial section
Padmanabhan et al. (1970)	0	0	Finite Difference	-	$\sim t^{0.33}$	Inviscid, Nt ≤ 20	
					$\sim t^{0.33}$	Viscous, Nt ≤ 20	
			-	Viscous Long Wave Approximation	$\sim t^{1/6}$	Final Stage t >> 1	
Wessel (1969)	0	0	Numerical Calculation	-	$\sim 1 + 0.122(Nt)^{1.70}$	0 ≤ Nt ≤ 2.75	R ₀ is one-half the side of the initial square of mixed fluid
					$\sim 0.907(Nt)^{0.58}$	2.75 ≤ Nt ≤ 25	
Young and Hirt (1972)	0	0	MAC Method (Marker and Cell)	-	?	Initial and Principal Stage	
Zuluaga-Angel et al. (1972)	1	0	-	$R(t) \sim \frac{2/9 Q}{h^{5/6} \nu^{1/18}} (Nt)^{3/4}$	$\sim t^{3/4}$		

region, and then in proportion to $t^{5/6}$ in the viscous-buoyancy region. A linear function of time was also obtained by Manins (1976a) using a different approach. Mei (1969) found by using internal long wave approximations that a finite volume of homogeneous fluid collapsing initially in a linearly stratified ambient fluid will propagate asymptotically in proportion to t .

Although Manins (1976a,b) obtained two different power laws for interflowing fronts for two different source conditions, he (1976b) suggested that there must be some dynamic similitude between them. However, there is not, as yet, a unified theory which can show how the wide variety of power laws for interflowing fronts are related. A simple order of magnitude analysis will serve this role in the next chapter.

General self-similar solutions of long wave approximation are also presented for the inertial and the viscous phases of interflowing fronts, including the initial stage, the principal stage, and the final stage.

2.5 Further Mixing of Surface Spreading Flow

2.5.1 Description of Spreading Flow

When a round or slot buoyant jet flow reaches the free surface or the bottom, it may still have residual buoyancy and horizontal momentum which will cause it to spread out as a horizontal buoyant jet. For instance, in the two-dimensional case, Jirka and Harleman (1973) found that a two-dimensional

surface spreading flow moved out from the transition zone at an initial densimetric Froude Number F_i around 2.6, where

$$F_i = \frac{u_i}{\sqrt{g \frac{\rho_a - \rho_i}{\rho_i} h_i}}, \quad u_i \text{ and } h_i \text{ are respectively the mean}$$

velocity and the thickness of the spreading flow at the boundary of the transition zone, and the density of the spreading fluid is ρ_i .

Any residual horizontal momentum flux will drive the diluted water away from the surface intersection point and produces a secondary entrainment of ambient fluid during horizontal spreading. By contrast, residual buoyancy will gradually erode the capacity of the spreading fluid to mix with the ambient fluid and will force the less dense fluid into a thinner floating layer. Eventually, interfacial mixing will be reduced to a negligible amount and the interface will be sharpened. A two-layered stratified flow will be formed.

The initial region of the surface spreading flow was found by Jirka and Harleman to have rapidly increasing depth while the local densimetric Froude number decreased to a lower value. Intensive interfacial mixing with the ambient fluid occurred inside this region. Jirka and Harleman (1973) and Lee *et al.* (1974) suggested that this region formed an internal hydraulic jump. List (1977) preferred to call this increasing depth zone surface jet mixing rather than an internal hydraulic jump, since although the Froude number of the spreading flow is

reduced by an interfacial mixing process in the absence of a downstream control there can be no stably hydraulic jump. Some velocity measurements were made by Murota and Muraoka (1967) and Anwar (1972) and excess-density or temperature measurements by Anwar (1972) and Pryputniewicz and Bowley (1975).

Similar flow structures have been observed in other experimental studies of surface buoyant jet discharges, such as by Wood (1965,1967), Wilkinson and Wood (1971), Wilkinson (1970), Stefan (1972) in the plane jet case and Jirka *et al.* (1977) in the radial case. An intensive interfacial mixing zone was followed by a two-layered stratified flow where vertical entrainment was almost negligible. The plane jet mixing was found to be sensitive to changes in the discharge condition as well as in the downstream control. An internal hydraulic jump does occur in this jet mixing zone when the entrainment length is controlled by a broad-crested weir downstream (Wilkinson and Wood, 1971).

2.5.2 Surface Buoyant Jet Models

A radial surface jet model by Chao (1975) simulates the initial mixing zone of the surface spreading flow created by a vertical single port discharge. Following the wall jet solution by Glauert (1956), Chao derived the mean velocity field of the radial surface jet for both laminar and the turbulent flows. He found that there are similarity profiles for the radial velocity, and that the maximum mean surface

velocity decays in inverse proportion to the radial distance from the stagnation point, while the surface jet thickness increases linearly with the radial distance. Similar results for radial surface jet flow and surface buoyant jets were also derived earlier by Koh and Fan (1970) using an entrainment theory approach. However, no information about the surface jet dilution was presented.

An analytical solution for surface jet mixing, for both plane and radial surface jets, will be presented in the next chapter.

CHAPTER 3

THEORETICAL ANALYSIS

3.0 Introductory Note

In this chapter theoretical solutions describing gravity-driven surface and subsurface spreading currents, in both homogeneous and linearly density-stratified environments, due to a variable rate source will be presented. An order-of-magnitude analysis by a force-balance method is used to derive a series of asymptotic time functions for both the inertial and the viscous spreading regimes. Self-similar solutions of non-linear long wave equations are also used to examine these asymptotic formulae. For inertial spreading the solutions analogous to blast wave propagation and to gas cloud expansion are derived for the inertial-buoyancy spreading region and the initial stage. For viscous spreading a solution analogous to the "power-law" diffusion mechanism is derived. Solutions of surface jet mixing in the momentum jet regime are also derived on the basis of Prandtl's assumptions. Dimensional analysis will be used to consider the initial condition effects on the spreading mechanisms.

3.1 Force Scale Analysis for Density Currents3.1.1 Free Surface Spreading Currents

Suppose there is a pool of liquid with uniform density ρ_s floating on a liquid of infinite depth with a uniform density

ρ_a , ($\rho_s < \rho_a$), where the dimensionless density difference ratio Δ is $(\rho_a - \rho_s)/\rho_s$, as shown in Figure 3.1.1. At time t after

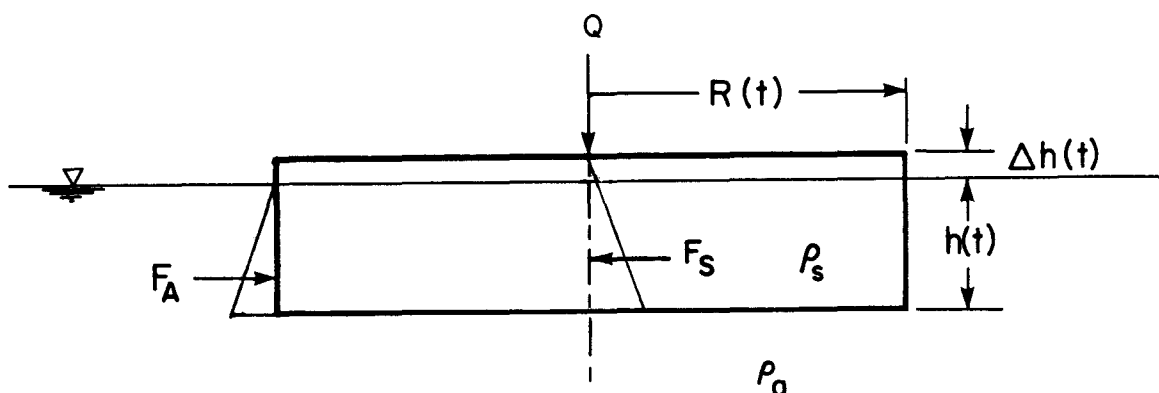


Figure 3.1.1 Idealized sketch of free surface spreading density currents.

starting the discharge Q , the average thickness of the spreading pool is $h = h(t)$ and the pool radius $R = R(t)$. Suppose the vertical acceleration is very small in comparison to the horizontal one, so that the pressure distribution will be hydrostatic. When the floating layer is in hydrostatic equilibrium in the vertical direction, the average super-elevation of the floating pool over the free surface is $\Delta h(t)$, which can be simply derived from the hydrostatic assumption. Assume that there is no molecular diffusion and a negligible amount of mixing through the interface, then the total volume of the surface layer, which is

proportional to $(1+\Delta)hR^{n+1}$, is fixed by the discharge. If the integrated source discharge is Qt^m , then the volume conservation equation is simply

$$Qt^m \sim R^{n+1} h \quad (3.1.1)$$

in which n is a parameter that denotes the plane ($n=0$) and the radial ($n=1$) cases, Q is the discharge rate, and m is a source parameter that denotes an instantaneous finite volume release ($m=0$) or a continuous steady source respectively ($m=1$). Q represents a finite volume V when $m=0$, and a constant discharge rate Q when $m=1$.

If the surface tension force is negligible, the driving force, F_p , at the plume front is the resultant of two horizontal pressure forces F_S and F_A , which are directed outwards and inwards at the front. These are

$$F_S \sim R^n \rho_s g h^2 (1+\Delta)^2 \quad (3.1.2)$$

$$F_A \sim R^n \rho_a g h^2 \quad (3.1.3)$$

and

$$F_P = F_S - F_A \sim R^n h^2 \rho_s g \Delta (1+\Delta) \quad (3.1.4)$$

There are two forces retarding the spreading plume: one is the inertial F_I which is proportional to the product of the plume mass with the acceleration

$$F_I \sim \rho_s h R^{n+1} (R/t^2) = \rho_s h R^{n+2} / t^2 \quad (3.1.5)$$

and the other is the viscous force. The viscous force may arise from two different mechanisms of interfacial shear. For example, an oil slick is usually very thin and its kinematic viscosity ν_s is much higher than that of the ambient fluid ν_a underneath the oil layer, thus the viscous force F_{VA} for a spreading oil slick can be approximated by the boundary layer shear in the ambient fluid, and

$$F_{VA} \sim R^{n+1} \rho_a \nu_a (R/t) / \delta_1 = R^{n+2} \rho_a \nu_a^{1/2} / t^{3/2} \quad , \quad (3.1.6)$$

where δ_1 is the Rayleigh's unsteady laminar boundary layer thickness $\sqrt{\nu_a t}$. For miscible fluids, the viscous force is dominated by the fully developed boundary layer in the plume fluid itself and we write

$$F_{VS} \sim R^{n+1} \rho_s \nu_s (R/t) / h = R^{n+2} \rho_s \nu_s / t h \quad . \quad (3.1.7)$$

From the comparison of the two possible retarding forces two different asymptotic regimes for the starting plume can be distinguished. In one, the inertial force dominates the viscous force and in the second, the viscous force is predominant. By balancing the driving force with either of the aforementioned retarding forces and introducing the average thickness h from the continuity relationship (3.1.1) the possible growth rates are derived. For a buoyancy-inertial plume

$$R(t) \sim (g\Delta Q)^{\frac{1}{n+3}} t^{\frac{m+2}{n+3}} \quad (3.1.8)$$

with an average thickness

$$h(t) \sim \frac{Q^{\frac{2}{n+3}}}{(g\Delta)^{\frac{n+1}{n+3}} t^{\frac{2(n-m+1)}{n+3}}} \quad (3.1.9)$$

For a miscible buoyancy-viscous plume

$$R(t) \sim \left(\frac{g\Delta Q^3}{\nu_s} \right)^{\frac{1}{3n+5}} t^{\frac{3m+1}{3n+5}} \quad (3.1.10)$$

and its average thickness

$$h(t) \sim \frac{Q \frac{2}{3n+5}}{\left(\frac{g\Delta}{v_s}\right)^{\frac{n+1}{3n+5}} t^{\frac{n-2m+1}{3n+5}}} \quad (3.1.11)$$

The inertial-buoyancy spread regime is therefore identical with that of a spreading oil slick. However, a different growth history is found in viscous-buoyancy spreading regime due to the different mechanisms of interfacial shear. The equations equivalent to Eqs. (3.1.10) and (3.1.11) are, in this regime,

$$R(t) \sim \left(\frac{g\Delta Q^2}{v_a^{1/2}}\right)^{\frac{1}{2(n+2)}} t^{\frac{4m+3}{4(n+2)}} \quad (3.1.12)$$

and

$$h(t) \sim \frac{Q \frac{1}{n+2}}{\left(\frac{g\Delta}{v_a}\right)^{\frac{n+1}{4(n+2)}} t^{\frac{3n-4m+3}{4(n+2)}}} \quad (3.1.13)$$

More details of spreading oil slicks are given in Fay (1969,1971), Hoult (1972), and Buckmaster (1973).

It is interesting to note that, from Eqs. (3.1.8) and (3.1.10), the starting surface plume does not necessarily propagate with a constant velocity except when $m = n + 1$ (with no viscous effect) and when $m = (3n + 4)/3$ (with a viscous effect). Table 3.1.1 gives the surface starting plume formulae for two conventional discharge

Table 3.1.1 Asymptotic formulae for starting surface plumes. (Chen, 1975).

Item Case	Source condition	Inertial plume	Viscous plume
Plane $n = 0$	Instantaneous finite volume release $m = 0$	$R(t) \sim (g\Delta V)^{1/3} t^{2/3}$	$R(t) \sim \left(\frac{g\Delta V^3}{\nu_s}\right)^{1/5} t^{1/5}$
	Steady continuous discharge $m = 1$	$R(t) \sim (g\Delta Q)^{1/3} t$	$R(t) \sim \left(\frac{g\Delta Q^3}{\nu_s}\right)^{1/5} t^{4/5}$
Radial $n = 1$	Instantaneous finite volume release $m = 0$	$R(t) \sim (g\Delta V)^{1/4} t^{1/2}$	$R(t) \sim \left(\frac{g\Delta V^3}{\nu_s}\right)^{1/8} t^{1/8}$
	Steady continuous discharge $m = 1$	$R(t) \sim (g\Delta Q)^{1/4} t^{3/4}$	$R(t) \sim \left(\frac{g\Delta Q^3}{\nu_s}\right)^{1/8} t^{1/2}$

conditions, corresponding to $m=0$ and $m=1$ for both plane and axisymmetric cases. The relevant length and time scales for normalizing experimental data as derived from Eqs. (3.1.8) and (3.1.10), are shown in Table 3.1.2. The frontal propagation velocities can be simply derived by differentiation. For the inertial regime the front velocity of the plume \dot{R} decays along with frontal travel distance according to

$$\dot{R}(R) \sim (g\Delta Q)^{\frac{1}{m+2}} R^{\frac{m-n-1}{m+2}} \quad . \quad (3.1.14)$$

In the viscous regime

$$\dot{R}(R) \sim \left(\frac{g\Delta Q^3}{\nu_s} \right)^{\frac{1}{3m+1}} R^{\frac{3m-3n-4}{3m+1}} \quad . \quad (3.1.15)$$

These are shown in Table 3.1.3 for the cases in which $n=0, 1$ and $m=0, 1$.

An alternative approach to the above, used by Koh and Fan (1970), employed the hydrodynamic drag force F_D ,

$$F_D \sim \rho_a R^n h \left(\frac{dR}{dt} \right)^2 \quad (3.1.16)$$

and the interfacial shear force F_{IS}

$$F_{IS} \sim \frac{\epsilon}{h} \left(\frac{dR}{dt} \right) \left(R^{n+1} - R_o^{n+1} \right) \quad (3.1.17)$$

Table 3.1.2 Length and time scales for surface density spreading.

Item Case	Source condition	Length Scale R_1	Time Scale t_1
Plane $n = 0$	Instantaneous finite volume release $m = 0$	$\left(\frac{g\Delta V^5}{v_s^2}\right)^{1/7}$	$\left(\frac{v^4}{(g\Delta)^2 v_s^3}\right)^{1/7}$
	Steady continuous discharge $m = 1$	$\frac{Q^2}{(g\Delta Q)^{1/3} v_s}$	$\frac{Q^2}{(g\Delta Q)^{2/3} v_s}$
Radial $n = 1$	Instantaneous finite volume release $m = 0$	$\left(\frac{g\Delta V^5}{v_s^2}\right)^{1/12}$	$\left(\frac{v}{g\Delta v_s}\right)^{1/3}$
	Steady continuous discharge $m = 1$	$\left(\frac{Q^5}{g\Delta v_s^3}\right)^{1/8}$	$\left(\frac{Q}{g\Delta v_s}\right)^{1/2}$

Table 3.1.3 Asymptotic formulae for surface density spreading front velocity as a function of frontal distance.

Item Case	Source condition	Inertial plume	Viscous plume
Plane n = 0	Instantaneous finite volume release m = 0	$\dot{R}(R) \sim (g\Delta V)^{1/2} R^{-1/2}$	$\dot{R}(R) \sim \left(\frac{g\Delta V^3}{\nu_s}\right) R^{-4}$
	Steady continuous discharge m = 1	$\dot{R}(R) \sim (g\Delta Q)^{1/3}$	$\dot{R}(R) \sim \left(\frac{g\Delta Q^3}{\nu_s}\right)^{1/4} R^{-1/4}$
Radial n = 1	Instantaneous finite volume release m = 0	$\dot{R}(R) \sim (g\Delta V)^{1/2} R^{-1}$	$\dot{R}(R) \sim \left(\frac{g\Delta V^3}{\nu}\right) R^{-7}$
	Steady continuous discharge m = 1	$\dot{R}(R) \sim (g\Delta Q)^{1/3} R^{-1/3}$	$\dot{R}(R) \sim \left(\frac{g\Delta Q^3}{\nu_s}\right)^{1/4} R^{-1}$

to express the two forces resisting spreading. Here ϵ is an effective viscosity coefficient and $R_0 = R(0)$. Since the dimensions of these two resisting forces, in Eqs. (3.1.16) and (3.1.17) are homogeneous respectively with those of the previously derived inertial force F_I and viscous force F_{VS} , the same results for frontal motion, as shown in Table 3.1.1, can be derived from this approach (see Koh (1976)).

3.1.2 Bottom Spreading Currents

A bottom starting plume can be viewed as an inverted version of the free surface plume without super-elevation Δh . The two retarding forces are the same as for the free surface case since the inertial force is still involved and the interfacial shear dominates the wall shear. As shown in Figure 3.1.2 the driving force F_P' for a starting bottom current is the resultant of two pressure forces F_S' and F_A' ,

$$F_S' \sim R^n \rho_s g h^2 \quad (3.1.18)$$

$$F_A' \sim R^n \rho_a g h^2 \quad (3.1.19)$$

and $F_P' = F_S' - F_A'$ so that F_P' has the same form as Eq. (3.1.4):

$$F_P' \sim R^n \rho_s h^2 g \Delta \quad (3.1.20)$$

and the free surface results may be applied directly.

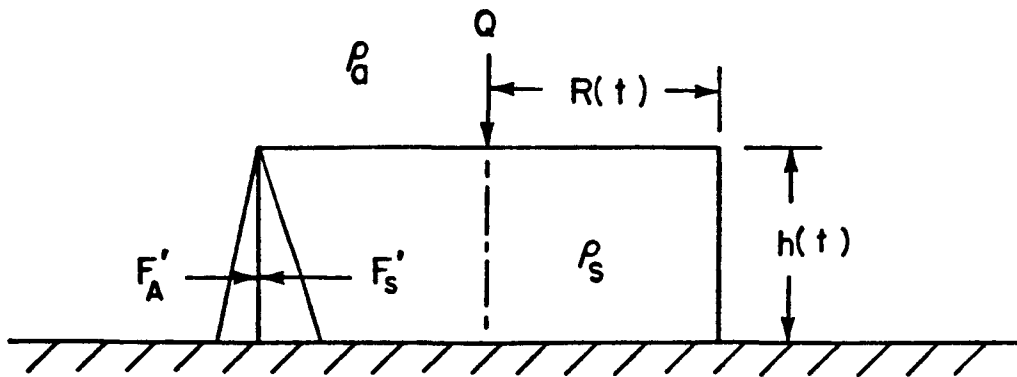


Figure 3.1.2 Idealized sketch of bottom spreading density currents.

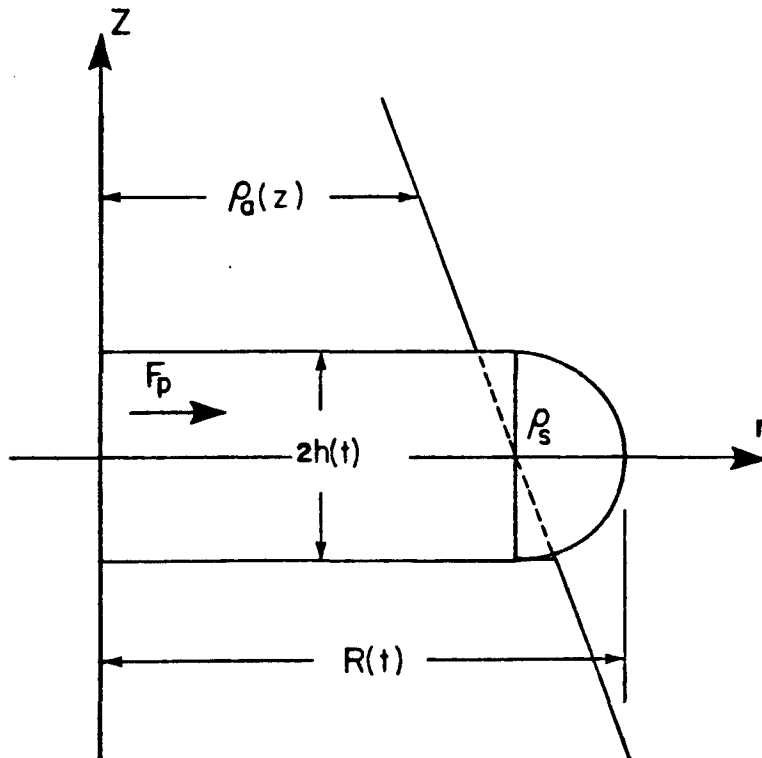


Figure 3.1.3 A homogeneous layer intruding at a neutral buoyant level into the linearly density-stratified ambient fluid.

3.1.3 Internal Density Currents

The driving force for submerged density currents is the unbalanced horizontal pressure force F_p . It is assumed that the internal current is homogeneous and is spreading at a neutral density level in a linearly stratified environment, as shown in Figure 3.1.3; the density difference between the current and the ambient stratified fluid is a linear function of depth. The total pressure force F_p in this case is proportional to the cubic power of the average thickness of the current rather than the square power as for surface and bottom spreading currents, i.e.

$$F_p \sim g \frac{d \rho_a(z)}{dz} h^3(t) R^n(t) \quad . \quad (3.1.21)$$

In the two dimensional case (for which $n=0$), the total pressure force is $\frac{1}{12} g \frac{d \rho_a(z)}{dz} h^3$, as derived by Kao (1974,1976).

The retarding forces for submerged density currents are the same as for free surface and bottom currents, i.e. the inertial force F_I and the viscous force F_{VS} as defined in Eqs. (3.1.5) and (3.1.7).

Equating the pressure force F_p with the inertial force F_I and cancelling the average thickness term h with the aid of the continuity relationship (3.1.1) enables the inertial spreading front to be expressed as a function of time t as

$$R(t) \sim (NQ)^{\frac{1}{n+2}} t^{\frac{m+1}{n+2}} \quad (3.1.22)$$

since $N = \sqrt{g\varepsilon}$. Equating the pressure force F_p to the viscous force F_{vs} , gives the radius of the viscous spreading front

$$R(t) \sim \left(\frac{N^2 Q^4}{v_s} \right)^{\frac{1}{2(2n+3)}} t^{\frac{4m+1}{2(2n+3)}} \quad (3.1.23)$$

Table 3.1.4 gives specific results for the various values of m and n . The average thickness $h(t)$ for the inertial spreading wedge can be written as

$$h(t) \sim \frac{Q^{\frac{1}{n+2}}}{N^{\frac{n+1}{n+2}} t^{\frac{3m+n+1}{n+2}}} \quad (3.1.24)$$

and for the viscous spreading wedge as

$$h(t) \sim \frac{Q^{\frac{1}{2n+3}}}{\left(\frac{N^2}{v_s} \right)^{\frac{n+1}{2(2n+3)}} t^{\frac{n+1-2m}{2(2n+3)}}} \quad (3.1.25)$$

The length and the time scales for normalizing experimental data are given in Table 3.1.5.

Table 3.1.4 Asymptotic formulae for submerged density spreading of an intrusion layer in a linearly density-stratified environment

Item Case	Source Condition	Inertial Submerged Spread	Viscous Submerged Spread
Plane $n = 0$	Finite Volume Release $m = 0$	$R(t) \sim (NV)^{1/2} t^{1/2}$	$R(t) \sim \left(\frac{N^2 V^4}{\nu_s} \right)^{1/6} t^{1/6}$
	Steady Continuous Discharge $m = 1$	$R(t) \sim (NQ)^{1/2} t$	$R(t) \sim \left(\frac{N^2 Q^4}{\nu_s} \right)^{1/6} t^{5/6}$
Radial $n = 1$	Finite Volume Release $m = 0$	$R(t) \sim (NV)^{1/3} t^{1/3}$	$R(t) \sim \left(\frac{N^2 V^4}{\nu_s} \right)^{1/10} t^{1/10}$
	Steady Continuous Discharge $m = 0$	$R(t) \sim (NQ)^{1/3} t^{2/3}$	$R(t) \sim \left(\frac{N^2 Q^4}{\nu_s} \right)^{1/10} t^{1/2}$

Table 3.1.5 Length and time scales of submerged density spread for normalization.

Item Case	Source Condition	Length Scale R_1	Time Scale t_1
Plane $n = 0$	Instantaneous finite volume release $m = 0$	$\left(\frac{NV^3}{v_s}\right)^{1/4}$	$\left(\frac{V}{N v_s}\right)^{1/2}$
	Steady continuous discharge $m = 1$	$\frac{Q^{3/2}}{N^{1/2} v_s}$	$\frac{Q}{N v_s}$
Radial $n = 1$	Instantaneous finite volume release $m = 0$	$\left(\frac{NV^3}{v_s}\right)^{1/7}$	$\left(\frac{V^2}{N^4 v_s^3}\right)^{1/7}$
	Steady continuous discharge $m = 1$	$\left(\frac{Q^3}{N v_s^2}\right)^{1/5}$	$\left(\frac{Q^2}{N^4 v_s^3}\right)^{1/5}$

3.2 Similarity Solutions for Inertial-Buoyancy Density Currents

The force scale analysis presented in Section 3.1 provides order of magnitude estimates of frontal trajectories for unsteady and non-uniform flows. However, in each power law growth rate there is an unknown coefficient that must be determined from experimental studies. Moreover, all of the fluid was assumed to move at the frontal velocity and the spreading layer thicknesses were assumed to be uniform. In this section two generalized shallow-water equations will be used to describe the inertial-buoyancy force balance for surface and the submerged density spreading flows in more detail. Taylor's (1950) self-similar technique for describing blast wave propagation is extended and used to find the unknown coefficients and the non-uniform features of the flows. The series of asymptotic formulae that were derived by the force scale analysis will be determined directly from the equations of motion.

The effects of finite dimensions will be considered for both the surface and the submerged spreading flow produced by a finite volume release, and the self-similar solutions are found to describe the early stage of flow before "shock wave" type propagation develops. This solution is similar to the expansion of a suddenly released finite volume of gas.

Theoretical results developed in this section will be compared with previously published numerical and experimental data in Chapter 6.

3.2.1 Longitudinal Internal Shallow-Water Wave Equations

We consider the two flow configurations as shown in Figures 3.2.1(a) and (b). At time t , there is a spreading pool with a horizontal extent $R(t)$ and layer thickness $h(r,t)$ at a radial distance r . If the horizontal length scale is much larger than the maximum vertical length scale, then the vertical acceleration and velocity will be smaller than the corresponding horizontal values. The pressure distribution is therefore hydrostatic and the horizontal velocity $u(r,t)$ is independent of the vertical direction z . At hydrostatic equilibrium the thickness of the surface pool above the water surface is

$$\delta(r,t) = \Delta h(r,t) \quad (3.2.1)$$

where the dimensionless density difference $\Delta = (\rho_a - \rho_s)/\rho_s$.

For a submerged spreading flow in a linearly density-stratified medium, as shown in Figure 3.2.1(c), the flows are assumed symmetrical. The coordinate system is chosen such that the origin is at the point of symmetry and $h(r,t)$ represents only one-half the thickness of the submerged spreading layer.

Using a long-wave approximation, two generalized shallow-water wave equations can be derived for these spreading flows (see Appendix A). First, the continuity equation is

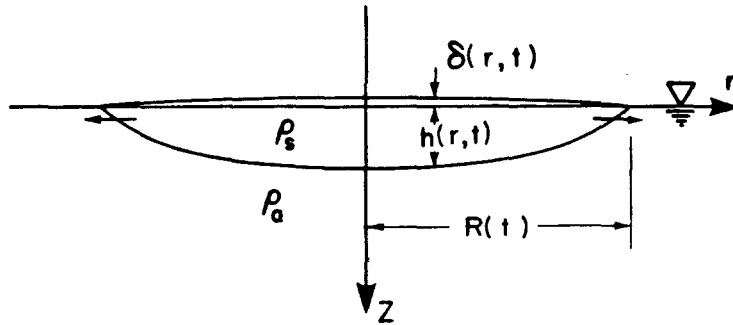


Figure 3.2.1(a) Coordinate system for free surface spreading flows.

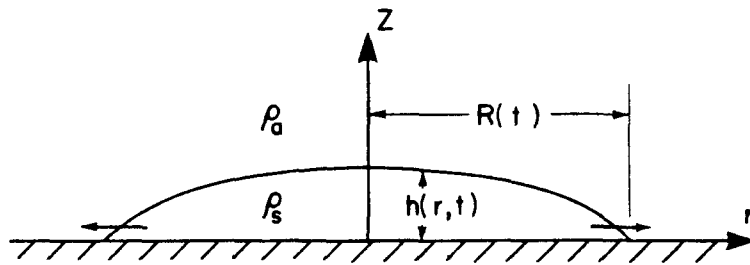


Figure 3.2.1(b) Coordinate systems for bottom spreading flows.

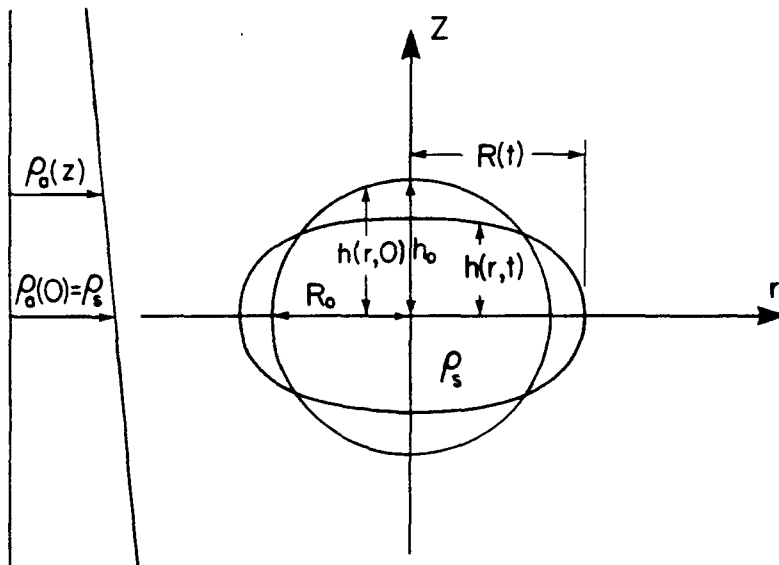


Figure 3.2.1(c) Coordinate system for submerged density flows.

$$\frac{\partial h}{\partial t} + \frac{1}{r^n} \frac{(\overline{r^n u h})}{\partial r} = \frac{\partial h}{\partial t} + \frac{\partial(\overline{uh})}{\partial r} + \frac{\overline{nuh}}{r} = 0 \quad (3.2.2)$$

and the horizontal momentum equation is

$$\frac{\partial u}{\partial t} + u \frac{\partial u}{\partial r} + g \Delta_i h^i \frac{\partial h}{\partial r} = 0 \quad (3.2.3)$$

where the parameter n denotes the case of plane spreading flow for $n=0$ and radial spreading flow when $n=1$. The parameter $i=0$ denotes surface and bottom spreading flows in a uniform environment. Submerged spreading flow in a linearly density-stratified environment is denoted by $i=1$.

$$\Delta_i = \begin{cases} \Delta & \text{for } i=0 \\ \frac{1}{\rho_s} \frac{d\rho_a}{dz} & \text{for } i=1 \end{cases}$$

By adding Eq. (3.2.2) multiplied by u and Eq. (3.2.3) multiplied by h the momentum equation can be rewritten as

$$\frac{\partial(\overline{uh})}{\partial t} + \frac{1}{r^n} \frac{(\overline{r^n u^2 h})}{\partial r} + g \Delta_i h^{i+1} \frac{\partial h}{\partial r} = 0 \quad (3.2.4)$$

Equation (3.2.4) is actually an energy equation for shallow-water waves.

Equations (3.2.2) and (3.2.3), with $i = 0$ and $n = 1$, were derived by Penney and Thornhill (1952) to study the base surge mist-air flow formed by an atomic bomb explosion in shallow water. Equations (3.2.2) and (3.2.3), with $i = 0$ and $n = 0$, are the general form of dam-break flow equations without friction effects, in which case the relative density difference Δ is unity. The same shallow water wave equations, with $i = 0$, were used by Hoult (1972) to study inertial spreading of an oil slick on the sea surface. Equations (3.2.2) and (3.2.3), with $i = 1$ and $n = 0$, were used by Mei (1969) to study the initial stage of collapse of a plane mixed region in a linearly density-stratified fluid.

3.2.2 Gas Dynamics Analogy

It is well-known (see Courant and Friedrichs (1948), pp. 32-35) that the two shallow-water wave equations (3.2.2) and (3.2.3), when $i = 0$, are similar to the equations of one-dimensional unsteady isentropic gas-dynamics.

$$\frac{\partial \rho}{\partial t} + u \frac{\partial \rho}{\partial r} + \rho \frac{\partial u}{\partial r} + \frac{n \rho u}{r} = 0 \quad , \quad (3.2.5)$$

$$\frac{\partial u}{\partial t} + u \frac{\partial u}{\partial r} + \frac{c^2}{\rho} \frac{\partial \rho}{\partial r} = 0 \quad (3.2.6)$$

when the specific gas constant γ is equal to 2, in which the sound speed $c = \sqrt{dp/d\rho}$ and the parameter n denotes the plane, cylindrical or spherical flow respectively when $n = 0, 1$, and 2 .

Following the study of Penney and Thornhill (1952), the characteristics equations for density spreading flows can therefore be written as

$$\left[\frac{\partial}{\partial t} + \left(u \pm \sqrt{g\Delta_i h^{i+1}} \right) \frac{\partial}{\partial r} \right] \left(u \pm \frac{2}{i+1} \sqrt{g\Delta_i h^{i+1}} \right) \pm \frac{nu \sqrt{g\Delta_i h^{i+1}}}{r} = 0 \quad (3.2.7)$$

The Riemann invariants along the characteristics curves,

$$\frac{dr}{dt} = u \pm \sqrt{g\Delta_i h^{i+1}} \quad (3.2.8)$$

are

$$u \pm \frac{2}{i+1} \sqrt{g\Delta_i h^{i+1}} \pm n \int^t \frac{u \sqrt{g\Delta_i h^{i+1}}}{r} dt = \text{constant} \quad , \quad (3.2.9)$$

or

$$u \pm \frac{2}{i+1} \sqrt{g\Delta_i h^{i+1}} \pm n \int^r \frac{u \sqrt{g\Delta_i h^{i+1}}}{u \pm \sqrt{g\Delta_i h^{i+1}}} \frac{dr}{r} = \text{constant} \quad . \quad (3.2.10)$$

With suitable initial and boundary conditions these equations may be solved numerically except when a jump discontinuity develops due to the non-linearity.

Similarity solutions for the blast wave propagation produced by an atomic bomb explosion were introduced independently by Taylor (1950), and Sedov (1957). Later, this self-similar technique was extended by several investigators, (see Rogers (1958), Freeman (1968), Dabora (1972), Pitkin (1977)), to solve the more general problem of the shock wave produced by a variable rate of energy release. Taylor and Sedov found that shock wave front propagated with a velocity that depends only on the specific energy release. The trajectory of the front is described as

$$R(t) = S(\gamma, m, n) \left(\frac{E}{\rho} \right)^{\frac{1}{n+3}} t^{\frac{m+2}{n+3}} \quad (3.2.11)$$

where the proportionality coefficient $S(\gamma, m, n)$ is found from an energy conservation condition. The similarity distributions for particle velocity, density and pressure were solved analytically and numerically.

Sedov's self-similar technique was used by Hoult and Suchon (1970) to study the inertial phase of spreading of a plane oil slick formed by the release of a finite volume of oil. However, their computed results are not in agreement with their experimental results. Later, Hoult (1972) revised the technique to use a different independent self-similar variable but problems were still met in specifying the boundary conditions and the similarity profile for the spreading layer thickness was not given for the radial spreading case. Similar difficulties were

also encountered by Fay (see Liang, 1971) and Fannelop and Waldman (1972).

Here, we use Taylor's self-similar technique, as extended by Rogers (1958), to resolve the general problems of a variable flow rate buoyant-discharge. However, first we must derive the correct Taylor's self-similar formulae and the necessary boundary conditions at the front.

3.2.3 Derivation of Self-Similar Formulae

Two methods of derivation will be given here. The first one is the method of separation of variables and the second one is the Taylor's method used for the blast wave propagation.

3.2.3.1 Method of Separation of Variables

Assume that the two unknowns, $u(r,t)$ and $h(r,t)$ in the shallow-water wave equations, have solutions in the following forms:

$$u(r,t) = \Omega(t) \phi(\xi) \quad , \quad (3.2.12)$$

$$h(r,t) = T(t) H(\xi) \quad , \quad (3.2.13)$$

where the dimensionless variable ξ is defined as $r/R(t)$, and $R(t)$ is the frontal position at time t , $\Omega(t)$ and $T(t)$, which will be determined later, are two unknown scale functions for mean velocity and spreading layer thickness, respectively.

Substituting the above into the shallow-water wave equations (3.2.2) and (3.2.3), one obtains

$$\frac{\overset{\circ}{R}\overset{\circ}{T}}{\Omega T} H - \frac{\overset{\circ}{R}}{\Omega} \xi H' + \phi H' + \phi' H + \frac{n\phi H}{\xi} = 0 \quad (3.2.14)$$

and

$$\frac{\overset{\circ}{R}\overset{\circ}{\Omega}}{\Omega^2} \phi - \frac{\overset{\circ}{R}}{\Omega} \xi \phi' + \phi \phi' + \frac{g\Delta_i T^{i+1}}{\Omega^2} H^i H' = 0 \quad , \quad (3.2.15)$$

in which " $\overset{\circ}{}$ " denotes the differentiation of a function with respect to time t and " $'$ " to the dimensionless variable ξ .

In order to have the assumed form of solutions given in Eqs. (3.2.12) and (3.2.13), one must let four unknown functions, $\overset{\circ}{R}/\Omega$, $\overset{\circ}{R}\overset{\circ}{\Omega}/\Omega^2$, $\overset{\circ}{R}\overset{\circ}{T}/\Omega T$ and $g\Delta_i T^{i+1}/\Omega^2$, be dimensionless. Choose unity for the first one $\overset{\circ}{R}/\Omega$. Then, the velocity scale will be the front velocity and the similarity assumption for mean velocity will become

$$u(r,t) = \Omega(t)\phi(\xi) = \overset{\circ}{R}(t)\phi(\xi) \quad . \quad (3.2.16)$$

The second function $\overset{\circ}{R}\overset{\circ}{\Omega}/\Omega^2$ will therefore automatically become a dimensionless number Λ that we call the decay coefficient,

$$\Lambda = \frac{\overset{\circ}{R}\overset{\circ}{\Omega}}{\Omega^2} = \frac{R(t)\overset{\circ}{\overset{\circ}{R}}(t)}{\overset{\circ}{R}^2(t)} \quad . \quad (3.2.17)$$

There are two kinds of self-similar solutions to choose for the spreading layer thickness. The first one is to set the fourth function $g\Delta_i T^{i+1}/\Omega^2$ to unity. That is to say that the length scale for the spreading layer thickness will be

$$T(t) = \left(\frac{\Omega^2}{g\Delta_i} \right)^{\frac{1}{i+1}} = \left(\frac{\overset{\circ}{R}^2(t)}{g\Delta_i} \right)^{\frac{1}{i+1}} . \quad (3.2.18)$$

In this case the third function $\overset{\circ}{RT}/\Omega T$ will automatically become a constant value that is related only to the decay coefficient, i.e.

$$\frac{\overset{\circ}{RT}}{\Omega T} = \frac{2}{i+1} \frac{\overset{\circ}{RR}}{\overset{\circ}{R}^2} = \frac{2}{i+1} \Lambda , \quad (3.2.19)$$

and the similarity assumption, Eq. (3.2.13) will become

$$h(r,t) = \left(\frac{\overset{\circ}{R}^2(t)}{g\Delta_i} \right)^{\frac{1}{i+1}} H(\xi) . \quad (3.2.20)$$

The second solution is to set the third function $\overset{\circ}{RT}/\Omega T$ to a constant value α , i.e.

$$\frac{\overset{\circ}{RT}}{\Omega T} = \frac{\overset{\circ}{RT}}{\overset{\circ}{RT}} = \frac{\overset{\circ}{\eta T}}{\overset{\circ}{\eta T}} = \alpha , \quad (3.2.21)$$

where the dimensionless frontal position $\eta = R(t)/R_0$, R_0 is the initial frontal length $R(0)$. From Eq. (3.2.21) one has the length scale for the spreading layer thickness

$$T(t) = T(0) \eta^\alpha(t) \quad , \quad (3.2.22)$$

where $T(0)$ is the initial length scale of the spreading layer thickness. By choosing $T(0) = h_1$, then the second solution for the spreading layer thickness becomes

$$h(r,t) = h_1 \eta^\alpha(t) H(\xi) \quad , \quad (3.2.23)$$

in which α is an unknown constant and h_1 is an initial layer scale thickness. For this case the fourth function, $g\Delta_1 T^{i+1}/\Omega^2$, will be a dimensionless number that is related only to the decay coefficient Λ .

The first set of similarity solutions, Eqs. (3.2.16) and (3.2.20), indicate that only the frontal velocity plays the role in defining the spreading layer thickness. In the second set, Eqs. (3.2.16) and (3.2.23), only the relative frontal length η is important. The first set thus is used to describe the far-field gravitational spreading problem where the front is so displaced from the origin of motion that the initial dimension is no longer important but not so far that viscous effects are negligible. The second set of solutions is appropriate for the near-field problem and will be considered in Section 3.2.7.

The first set of similarity solutions can also be derived by Taylor's (1950) approach to solving the blast wave propagation as extended by Latter (1955).

3.2.3.2 Taylor's Method

Assume that two unknowns, $u(r,t)$ and $h(r,t)$, have similarity solutions of the following forms:

$$u(r,t) = R^k(t)\phi_1(\xi) \quad , \quad (3.2.24)$$

$$h(r,t) = R^\ell(t)H_1(\xi) \quad , \quad (3.2.25)$$

where k and ℓ are two unknown integers that will be determined later, ϕ_1 and H_1 are two unknown functions that are also to be determined later.

Substituting above two assumptions in the shallow-water wave equations (3.2.2) and (3.2.3), one gets

$$R^{-k} \left(\ell H_1 - \xi H_1' \right) + \left(\phi_1' H_1 + \phi_1 H_1' + \frac{n\phi_1 H_1}{\xi} \right) = 0 \quad (3.2.26)$$

and

$$R^{-k} \left(k\phi_1 - \xi\phi_1' \right) + \phi_1\phi_1' + g\Delta_1 R^{(i+1)\ell-2k} H_1' = 0 \quad . \quad (3.2.27)$$

In order to homogenize both Eqs. (3.2.26) and (3.2.27) into dimensionless forms, one has to set

$$R^{-k} \overset{\circ}{R} = A \quad , \quad (3.2.28)$$

$$(i+1)\ell - 2k = 0 \quad , \quad (3.2.29)$$

and assume

$$\phi_1(\xi) = A\phi(\xi) \quad (3.2.30)$$

$$H_1(\xi) = \left(\frac{A^2}{g\Delta_i} \right)^{\frac{1}{i+1}} H(\xi) \quad (3.2.31)$$

in which A is a dimensional constant, and $\phi(\xi)$ and $H(\xi)$ are two dimensionless similarity functions. From Eqs. (3.2.24), (3.2.25), (3.2.28), (3.2.29), (3.2.30), and (3.2.31) two similarity solutions are derived as (see Appendix B for details of derivation)

$$u(r,t) = \overset{\circ}{R}(t)\phi(\xi) \quad (3.2.16)$$

and

$$h(r,t) = \left(\frac{\overset{\circ}{R}^2(t)}{g\Delta_i} \right)^{\frac{1}{i+1}} H(\xi) \quad . \quad (3.2.20)$$

The two similarity functions $\phi(\xi)$ and $H(\xi)$ are the dimensionless distributions of the relative mean particle velocity and the local Richardson number behind the front. For the uniform

environment case where $i=0$, the local Richardson number is clearly defined as

$$H(\xi) = Ri(r,t) = \frac{g\Delta h(r,t)}{\overset{\circ}{R}^2(t)} \quad (3.2.32)$$

and for the linearly stratified case where $i=1$, it is defined as

$$H(\xi) = Ri(r,t) = \frac{Nh(r,t)}{\overset{\circ}{R}(t)} \quad , \quad (3.2.33)$$

in which N is the Brunt-Väisälä frequency of the ambient stratification.

3.2.4 Evaluation of Self-Similar Solutions

3.2.4.1 General Derivation

The similarity assumptions (3.2.16) and (3.2.20) when substituted into the continuity and the momentum equations (3.2.2) and (3.2.3) reduce the two partial differential equations to two ordinary differential equations:

$$(\phi - \xi)H' + \frac{2}{i+1} \Lambda + \phi' + \frac{n\phi}{\xi} H = 0 \quad , \quad (3.2.34)$$

$$(\phi - \xi)\phi' + \Lambda\phi + H^i H' = 0 \quad , \quad (3.2.35)$$

in which ' denotes differentiation with respect to ξ , i.e. $d/d\xi$.

The decay coefficient $\Lambda = \overset{\circ}{R}\overset{\circ}{R}/\overset{\circ}{R}^2$ in Eqs. (3.2.34) and (3.2.35) can be derived from the frontal function $R(t)$.

Now suppose a buoyancy source supplies a time-varying volume $V_j(t)$ of fluid that may be positively, negatively, or neutrally buoyant. Then we have

$$V_j(t) = Q t^m \quad (3.2.36)$$

where $m=1$ denotes the case of a steady, constant rate discharge Q , and $m=0$ denotes the case of an instantaneous release of a finite volume $V_j = V$.

Assuming that the amount of interfacial mixing between the two fluids is negligible and also that free surface evaporation loss or bottom floor seepage is negligible, then the total volume $V(t)$ of the spreading layer at time t must equal the amount that has been supplied $V_j(t)$, i.e.

$$V(t) = V_j(t) \quad (3.2.37)$$

The total volume of a spreading layer at time t is

$$V(t) = \int_0^{R(t)} k_{in} h(r,t) r^n dr = \frac{k_{in} I_{imn} R(t)^{n+1} R(t)^{\frac{2}{i+1}}}{(g\Delta_i)^{\frac{1}{i+1}}}, \quad (3.2.38)$$

in which the integration constant in each case will be

$$I_{imm} = \int_0^1 \xi^n H(\xi) d\xi \quad , \quad (3.2.39)$$

and the shape factor k_{in} is defined as

$$k_{in} = \begin{cases} (i+1) & , \quad n=0 \\ (i+1)2\pi & , \quad n=1 \end{cases} \quad (3.2.40)$$

When the relative density difference Δ is rather small, i.e. for the case of free surface spreading of sewage or thermal water discharge, Eq. (3.2.38) is still a good approximation with an error to the order of Δ , but for a spreading oil slick, the relative density difference is not very small and the shape factor has to be multiplied for a factor $(1+\Delta)$ for correction, i.e.

$$k_{on} = \begin{cases} (1+\Delta) & , \quad n=0 \\ (1+\Delta)2\pi & , \quad n=1 \end{cases} \quad (3.2.41)$$

From the similarity assumptions (3.2.19) and the condition of volume conservation, one obtains the differential equation for the trajectory function,

$$R(t) \frac{(i+1)(n+1)}{2} \frac{dR(t)}{dt} = \left\{ \frac{(g\Delta_i)^{\frac{1}{i+1}} Q}{k_{in} I_{imn}} \right\}^{\frac{i+1}{2}} t^{\frac{m(i+1)}{2}}, \quad (3.2.42)$$

for both surface and submerged spreading flows. Integrating

Eq. (3.2.42) from $R=R(0)=R_0$ to $R=R(t)$ gives the frontal function,

$R(t) =$

$$\left\{ R_0^{\frac{(i+1)(n+1)+2}{2}} + \frac{(i+1)(n+1)+2}{m(i+1)+2} \left(\frac{B_i}{k_{in} I_{imn}} \right)^{\frac{i+1}{2}} t^{\frac{m(i+1)+2}{2}} \right\}^{\frac{2}{(i+1)(n+1)+2}}, \quad (3.2.43)$$

in which the generalized definition of kinematic or specific buoyancy flux B_i is

$$B_i = (g\Delta_i)^{\frac{1}{i+1}} Q = \begin{cases} g\Delta Q & , \quad i=0 \\ NQ & , \quad i=1 \end{cases} \quad (3.2.44)$$

When the initial size of the spreading pool is very small, i.e.

$$R_0/R(t) \ll 0(1) \text{ or } R_0^{\frac{(i+1)(n+1)+2}{2}} / B_i^{\frac{i+1}{2}} t^{\frac{m(i+1)+2}{2}} \ll 0(1), \text{ an}$$

asymptotic form for $R(t)$ is

$$R(t) = c_{imn} B_i \frac{i+1}{(i+1)(n+1)+2} t^{\frac{m(i+1)+2}{(i+1)(n+1)+2}}, \quad (3.2.45)$$

in which the coefficient in the asymptotic form c_{imn} is

$$c_{imn} = \left\{ \frac{(i+1)(n+1)+2}{m(i+1)+2} \right\}^{\frac{2}{(i+1)(n+1)+2}} / \left\{ k_{in} I_{imn} \right\}^{\frac{i+1}{(i+1)(n+1)+2}}. \quad (3.2.46)$$

The power law is a general form for describing inertial-buoyancy motion for both surface and submerged spreading currents due to a variable source of buoyant discharge. The decay coefficient Λ becomes

$$\Lambda = \frac{R(t)\ddot{R}(t)}{\dot{R}^2(t)} = \frac{(i+1)(m-n-1)}{m(i+1)+2} \quad (3.2.47)$$

The two non-linear ordinary differential equations for H and ϕ become

$$\frac{H'}{H} = \frac{\frac{n\phi(\phi-\xi)}{\xi} + \frac{(1-i)(m-n-1)}{m(i+1)+2} \phi - \frac{2(m-n-1)}{m(i+1)+2} \xi}{H^{i+1} - (\phi-\xi)^2} \quad (3.2.48)$$

$$\phi' = \frac{\frac{(i+1)(m-n-1)}{m(i+1)+2} \phi(\phi-\xi) - \left(\frac{2(m-n-1)}{m(i+1)+2} + \frac{n\phi}{\xi} \right) H^{i+1}}{H^{i+1} - (\phi-\xi)^2} \quad (3.2.49)$$

To solve these two differential equations for the similarity profiles two boundary conditions are needed and they are found from the shock discontinuities at the front.

3.2.4.2 Shock Conditions at Front

From continuity of mass, Eq. (3.2.2), and momentum Eq. (3.2.3) or energy Eq. (3.2.4), three shock conditions at the front can be derived:

$$U[h] = [uh] \quad , \quad (3.2.50)$$

$$U[u] = \left[\frac{1}{2} u^2 + \frac{g\Delta_1 h^{i+1}}{i+1} \right] \quad , \quad (3.2.51)$$

$$U[uh] = \left[u^2 h + \frac{g\Delta_1 h^{i+2}}{i+2} \right] \quad , \quad (3.2.52)$$

where [] denotes the jump value of the term inside brackets between the right-hand side (+ side) and the left-hand side (- side) of the discontinuity and $U = \dot{R}(t)$ is the frontal velocity. The derivation details for these three jump conditions are given in Appendix C.

Now, assume that the ambient fluid is stagnant, i.e. $u_a = u_+ = u(R_+, t) = 0$, and the spreading layer thickness there vanishes, i.e. $h_+ = h(R_+, t) = 0$. From Eq. (3.2.50), one has

$$U = \overset{\circ}{R}(t) = \frac{u_- h_- - u_+ h_+}{h_- - h_+} = u_- = u(R_-, t) \quad (3.2.53)$$

i.e.

$$\phi(1) = \frac{u(R, t)}{\overset{\circ}{R}(t)} = \frac{u(R_-, t)}{\overset{\circ}{R}(t)} = 1 \quad (3.2.54)$$

From Eqs. (3.2.51) and (3.2.53), one has

$$U = \overset{\circ}{R}(t) = \frac{\frac{1}{2} u_-^2 + \frac{g \Delta_i h_-^{i+1}}{i+1} - \frac{1}{2} u_+^2 - \frac{g \Delta_i h_+^{i+1}}{i+1}}{u_- - u_+} = \frac{1}{2} u_- + \frac{1}{i+1} \frac{g \Delta_i h_-^{i+1}}{u_-} \quad (3.2.55)$$

i.e.

$$H(1) = \frac{h(R, t)}{\left(\overset{\circ}{R}^2(t) / g \Delta_i \right)^{\frac{1}{i+1}}} = \left(\frac{g \Delta_i}{\overset{\circ}{R}^2(t)} \right)^{\frac{1}{i+1}} h(R_-, t) = \left(\frac{i+1}{2} \right)^{\frac{1}{i+1}} \quad (3.2.56)$$

Similarly, from Eqs. (3.2.52) and (3.2.53), one has

$$U = \overset{\circ}{R}(t) = \frac{u_-^2 h_- + \frac{g \Delta_i h_-^{i+2}}{i+2} - u_+^2 h_+ - \frac{g \Delta_i h_+^{i+2}}{i+2}}{u_- h_- - u_+ h_+} = u_- + \frac{1}{i+2} \frac{g \Delta_i h_-^{i+1}}{u_-} \quad (3.2.57)$$

i.e.

$$H(1) = \frac{h(R, t)}{\left(\frac{\overset{\circ}{R}^2(t)/g\Delta_i}{\overset{\circ}{R}^2(t)}\right)^{\frac{1}{i+1}}} = \left(\frac{g\Delta_i}{\overset{\circ}{R}^2(t)}\right)^{\frac{1}{i+1}} h(R, t) = 0 \quad (3.2.58)$$

Two kinds of front are therefore possible depending on whether momentum or energy is conserved: one is the wave front with a constant frontal Richardson number,

$$Ri_f = H(1) = \left(\frac{g\Delta_i}{\overset{\circ}{R}^2(t)}\right)^{\frac{1}{i+1}} h(R, t) = \left(\frac{i+1}{2}\right)^{\frac{1}{i+1}}, \quad (3.2.59)$$

and the other is the front with a vanishing frontal Richardson number,

$$Ri_f = H(1) = \left(\frac{g\Delta_i}{\overset{\circ}{R}^2(t)}\right)^{\frac{1}{i+1}} h(R, t) = 0 \quad (3.2.60)$$

Two kinds of moving surface fronts for the case $i=0$ were also found by Abbott and Torbe (1963) using the method of characteristics: one was called the wave front (or moving hydraulic jump or bore) propagating with a finite frontal Richardson number, the other was called the Saint Venant front propagating with a vanishing frontal Richardson number. According to their theoretical arguments, the front moving with

a vanishing frontal thickness occurs at the coincidence of two characteristics curves and the wave front moving with a finite frontal Richardson number occurs when one of the characteristics becomes time stationary. In the case of one fluid spreading over or under another, a wave front must always be formed as long as the velocities in both fluids are in the same direction. A spreading front formed by a shallow fluid layer flowing over or under another fluid of much greater depth will eventually develop into a moving wave front since it does not induce appreciable motion in ambient fluid.

The vanishing submerged frontal thickness in Eq. (3.2.58) when $i=1$ and $n=m=0$ was also derived by Mei (1969) for the initial stage of dynamic collapse of a mixed region in a linearly density-stratified environment.

3.2.5 Asymptotic Solutions for Surface Density Spreading

The asymptotic form of the frontal trajectory function in this category, $i=0$, has the same time-power function as for blast wave propagation produced by a variable rate of energy release,

$$R(t) = c_{\text{omn}} B_o \frac{1}{n+3} t^{\frac{m+2}{n+3}} \quad (3.2.61)$$

In this case the kinematic buoyancy flux, $B_o = B = g\Delta Q$, or the specific buoyant force per unit mass, $B_o = B = g\Delta V$, is analogous

to the specific power or energy release E/ρ in Eq. (3.2.11).

The coefficient c_{omn} ,

$$c_{\text{omn}} = \left\{ \frac{n+3}{(m+2) \sqrt{k_{\text{on}} I_{\text{omn}}}} \right\}^{\frac{2}{n+3}}, \quad (3.2.62)$$

can be determined from the integration constant I_{omn} of the self-similar thickness profiles $H(\xi)$ for each case n and discharge conditions m . The similarity distributions for spreading layer thickness and mean velocity can be solved analytically or numerically from the two reduced ordinary differential equations,

$$\frac{H'}{H} = \frac{\frac{m-n-1}{m+2} (\phi - 2\xi) + \frac{n\phi(\phi - \xi)}{\xi}}{H - (\phi - \xi)^2}, \quad (3.2.63)$$

$$\phi' = \frac{\frac{m-n-1}{m+2} \phi(\phi - \xi) - \left[\frac{2(m-n-1)}{m+2} + \frac{n\phi}{\xi} \right] H}{H - (\phi - \xi)^2}, \quad (3.2.64)$$

using two Rankine-Hugoniot type frontal boundary conditions,

$$H(1) = \frac{1}{2} \text{ and } \phi(1) = 1.$$

3.2.5.1 Plane and Radial Surface Density Spread from a Finite Volume Release

The ordinary differential equations in this case

($n = 0, 1$, and $m = 0$) become

$$(\phi - \xi) H' + H(-n-1 + \frac{n\phi}{\xi} + \phi') = 0 \quad (3.2.65)$$

and

$$(\phi - \xi) \phi' - \left(\frac{n+1}{2}\right) \phi + H' = 0 \quad (3.2.66)$$

Corresponding to the boundary conditions $\phi(1) = 1$ and $H(1)$ not specified, these equations have the solutions

$$\phi(\xi) = \xi \quad (3.2.67)$$

and

$$H(\xi) = \left(\frac{n+1}{4}\right) (\xi^2 - 1) + H(1) \quad (3.2.68)$$

The Saint Venant front condition, $H(1) = 0$, gives a negative value for $H(\xi)$ except at the front. The wave front condition, $H(1) = \frac{1}{2}$, gives the thickness distribution as

$$H(\xi) = \left(\frac{n+1}{4}\right) \xi^2 + \left(\frac{1-n}{4}\right) \quad (3.2.69)$$

Thus the integration constant

$$I_{oon} = \int_0^1 \xi^n H(\xi) d\xi = \frac{1}{(n+1)(n+3)} \quad (3.2.70)$$

and the spreading layer coefficient is

$$c_{oon} = \left(\frac{(n+1)(n+3)^3}{4 k_{on}} \right)^{\frac{1}{n+3}} \quad (3.2.71)$$

The plane inertial spreading front ($n = 0$) due to a finite volume release therefore grows asymptotically according to

$$R(t) = 1.890(g\Delta V)^{1/3} t^{2/3} \quad (3.2.72)$$

and the radial inertial spreading front ($n = 1$) grows asymptotically as

$$R(t) = 1.502(g\Delta V)^{1/4} t^{1/2} \quad (3.2.73)$$

The density wave front from a finite volume release therefore grows with the greatest thickness at the front and a continually decreasing thickness behind the front. No "density head" or "density nose" is given by this blast wave analogy solution. The whole spreading fluid acts as a stretching layer between the front and the origin. The front pulls the spreading fluid with the same velocity as the front at the frontal wall and a linear distribution of fluid particle velocity, proportional to its dimensionless location, ξ , occurs behind the front. The details of this spreading flow are shown in Figure 3.2.2.

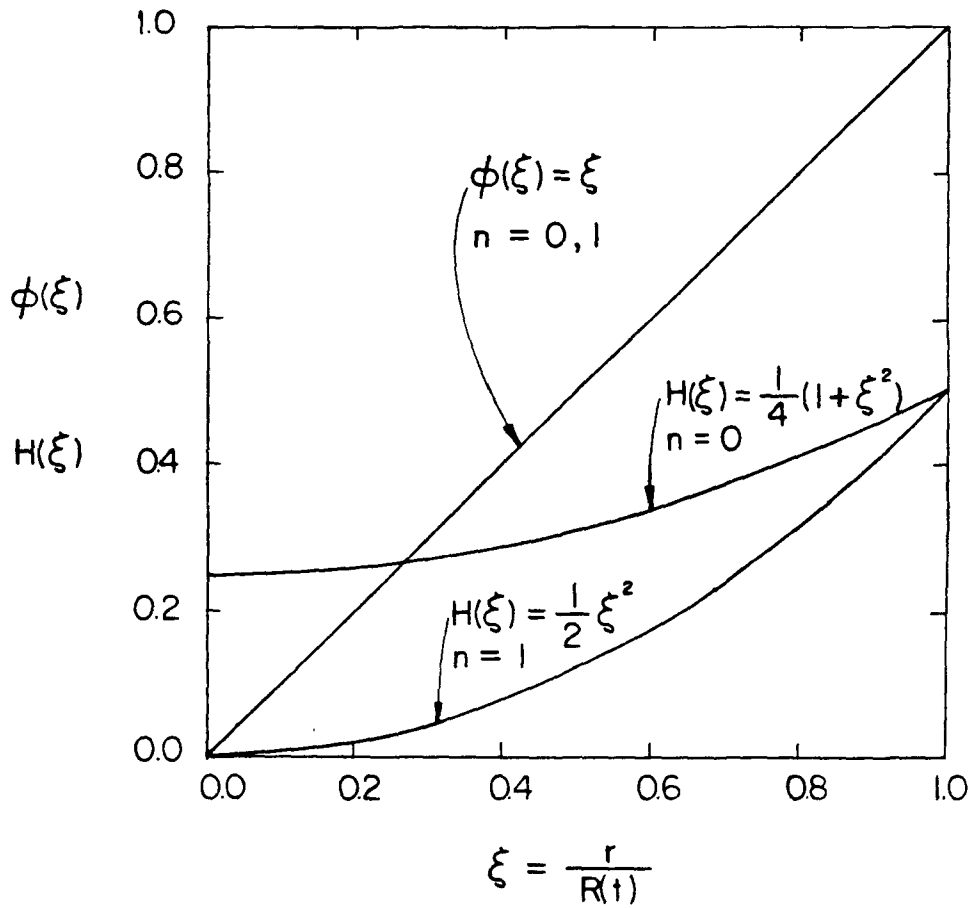


Figure 3.2,2 Self-similar velocity and thickness distributions of the plane and the radial inertial density wave front propagation due to a finite volume release of buoyant fluid.

This strong shock wave solution is applicable only when the density fronts are so far away from the origin point that the initial dimensions are negligible in comparison to the frontal distance. The initial dimension plays no further role in defining the length scale to the problem. In the case where the initial dimensions are important, the initial flow problem is totally different and will be discussed in Subsection 3.2.7.

3.2.5.2 Starting Two-Dimensional Stratified Flow

In this case $n = 0$ and $m = 1$ so that providing that $(\phi - \xi)^2 - H(\xi) \neq 0$, the two similarity equations in this case are

$$\phi'(\xi) = 0 \quad (3.2.74)$$

and

$$H'(\xi) = 0 \quad . \quad (3.2.75)$$

The non-trivial wave front solutions are

$$\phi(\xi) = 1 \quad (3.2.76)$$

and

$$H(\xi) = \frac{1}{2} \quad . \quad (3.2.77)$$

Hence the integration constant

$$I_{010} = \int_0^1 H(\xi) d\xi = \frac{1}{2} \quad (3.2.78)$$

and the coefficient for the two-dimensional inertial starting flow is

$$c_{010} = 2^{1/3} = 1.260 \quad , \quad (3.2.79)$$

i.e., the starting free surface inertial spreading flow grows as

$$R(t) = 1.260(g\Delta Q)^{1/3} t \quad , \quad (3.2.80)$$

where Q is the volume flux of the discharge. In the absence of any viscosity effect the two-dimensional starting flow therefore grows with a constant velocity which is proportional to the cubic root of the discharge buoyancy flux $B = g\Delta Q$.

The velocity and the thickness of a two-dimensional starting flow are therefore distributed in such a way that the local Richardson number $Ri(r,t)$ is uniformly distributed with a constant value 0.5 over the entire spreading length, i.e.

$$Ri(r,t) = \frac{g\Delta h(r,t)}{u^2(r,t)} = \frac{H(\xi)}{\phi^2(\xi)} = \frac{1}{2} \quad . \quad (3.2.81)$$

This is fully analogous to a two-dimensional propagating strong shock front driven by a continuous steady energy release, as derived by Rogers (1958). The shock wave front also propagates with a uniformly distributed velocity, density (pressure also) and Mach number.

3.2.5.3 Surface Radial Starting Plume

In this case $n=1$, $m=1$, and the two ordinary differential equations describing the similarity solution are

$$\phi'(\xi) = \frac{\frac{1}{3} \phi(\phi - \xi) + H\left(\frac{\phi}{\xi} - \frac{2}{3}\right)}{(\phi - \xi)^2 - H} \quad (3.2.82)$$

and

$$H'(\xi) = \frac{H\left\{\frac{1}{3}(\phi - 2\xi)\xi - \phi(\phi - \xi)\right\}}{\xi\{(\phi - \xi)^2 - H\}}, \quad (3.2.83)$$

These two differential equations were solved numerically at Caltech's Booth Computing Center by a program called "MODDEQ/Differential Equation Solver" using frontal boundary conditions $\phi(1) = 1$ and $H(1) = 1/2$. The numerical calculation is based on the method of Runge-Kutta-Gill with automatic error control. Two similarity profiles are shown in Figure 3.2.3. It is peculiar to see that there is an infinitely large fluid velocity inside the plume at the location $\xi = 0.753$. At this point the thickness vanishes and another internal ring forms after the former ring is dispatched.

The integration constant I_{011} as calculated by Simpson's rule is

$$I_{011} = \int_{0.753}^1 \xi H(\xi) d\xi = 0.09645 \quad (3.2.84)$$

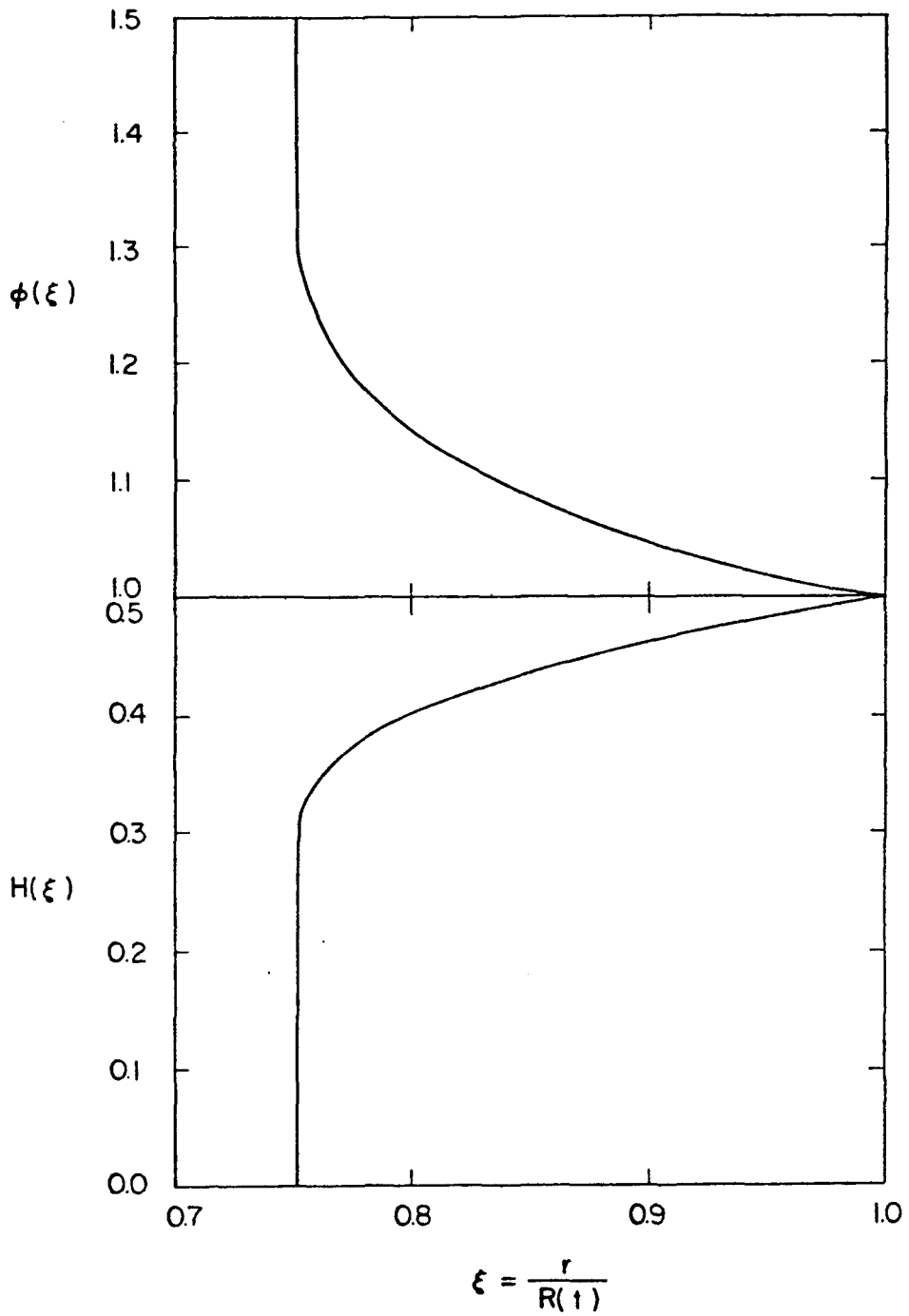


Fig. 3.2.3 Velocity and thickness distributions of a starting internal radial ring.

Thus, the coefficient for the radial starting plume is

$$c_{011} = \frac{(4/3)^{1/2}}{(k_{01} I_{011})^{1/4}} = 1.309 \quad . \quad (3.2.85)$$

The frontal bore therefore propagates outwards according to

$$R(t) = 1.309 (g\Delta Q)^{1/4} t^{3/4} \quad . \quad (3.2.86)$$

Suppose that there is a stationary observer located at a distance r from the surface buoyant source point. He will experience a series of internal ring fronts at a period T , which is

$$T = \frac{1}{(1.309)^{4/3}} \left(\frac{r^4}{g\Delta Q} \right)^{1/3} = 0.699 \left(\frac{r^4}{B} \right)^{1/3} \quad . \quad (3.2.87)$$

Velocity measurements at the same location r from the source point will have an oscillation in magnitude, which is coherent with an oscillation in density, at the same period T .

3.2.6 Asymptotic Solutions for Internal Density Spreading

The asymptotic Eq. (3.2.45) of the frontal trajectory function in this category, $i=1$, becomes

$$R(t) = c_{1mn} B_1^{\frac{1}{n+2}} t^{\frac{m+1}{n+2}} \quad , \quad (3.2.88)$$

in which the kinematic buoyancy flux $B_1 = NQ$ for the steady continuous discharge case, $m = 1$, and the specific buoyant force per unit mass $B_1 = NV$ for the finite volume case, $m = 0$. The coefficient c_{1mn} ,

$$c_{1mn} = \left\{ \frac{n+2}{(m+1) k_{in} I_{1mn}} \right\}^{\frac{1}{n+2}}, \quad (3.2.89)$$

can be determined from the integration of the self-similar thickness profile $H(\xi)$ for each case n and discharge conditions m . This self-similar thickness distribution $H(\xi)$ can be solved analytically or numerically from two ordinary differential equations,

$$\frac{H'}{H} = \frac{\frac{n\phi(\phi - \xi)}{\xi} - \frac{m-n-1}{m+1} \xi}{H^2 - (\phi - \xi)^2}, \quad (3.2.90)$$

$$\phi' = \frac{\frac{m-n-1}{m+1} \phi(\phi - \xi) - \left(\frac{m-n-1}{m+1} + \frac{n\phi}{\xi} \right) H^2}{H^2 - (\phi - \xi)^2} \quad (3.2.91)$$

with the boundary conditions $H(1) = 1$ and $\phi(1) = 1$.

3.2.6.1 Plane and Radial Submerged Density Spread from a Finite Volume Release

The ordinary differential equations in this case

($n = 0, 1$, and $m = 0$) become

$$H'(\phi - \xi) + H(\phi' + \frac{n\phi}{\xi} - n - 1) = 0 \quad (3.2.92)$$

and

$$\phi'(\phi - \xi) + HH' - (n+1)\phi = 0 \quad . \quad (3.2.93)$$

Corresponding to the boundary conditions $\phi(1) = 1$ and $H(1) = 1$, these equations have the solutions

$$\phi(\xi) = \xi \quad (3.2.94)$$

and

$$H(\xi) = \sqrt{(n+1)\xi^2 - n} \quad . \quad (3.2.95)$$

The half-thickness will be seen as a linear function of the dimensionless variable ξ for the plane flow, $n=0$,

$$H(\xi) = \xi \quad (3.2.96)$$

and for the radial flow, $n=1$, will be

$$H(\xi) = \sqrt{2\xi^2 - 1} \quad , \quad (3.2.97)$$

where the value exists only for $1/\sqrt{2} \leq \xi \leq 1$. A circular internal ring structure must be formed for this case which is different from that of radial surface spreading. Details of self-similar half-thickness

profiles are given in Figure 3.2.4. Therefore, the integration constant I_{1on} becomes

$$I_{1on} = \frac{1}{(n+1)(n+2)} \quad , \quad (3.2.98)$$

and the coefficient c_{1on} becomes

$$c_{1on} = \left\{ \frac{(n+1)(n+2)^2}{k_{1n}} \right\}^{\frac{1}{n+2}} \quad . \quad (3.2.99)$$

A plane inertial spreading front ($n=0$) due to a finite volume release therefore grows asymptotically according to

$$R(t) = (2NV)^{1/2} t^{1/2} \quad (3.2.100)$$

and the radial spreading front ($n=1$) grows asymptotically as

$$R(t) = \left(\frac{9}{2\pi} \right)^{1/3} (NV)^{1/3} t^{1/3} \quad . \quad (3.2.101)$$

For the special case of an initially cylindrical section of radius R_o , ($n=0$), the frontal position function will be

$$\frac{R(t)}{R_o} = \pi^{1/2} (Nt)^{1/2} \quad . \quad (3.2.102)$$

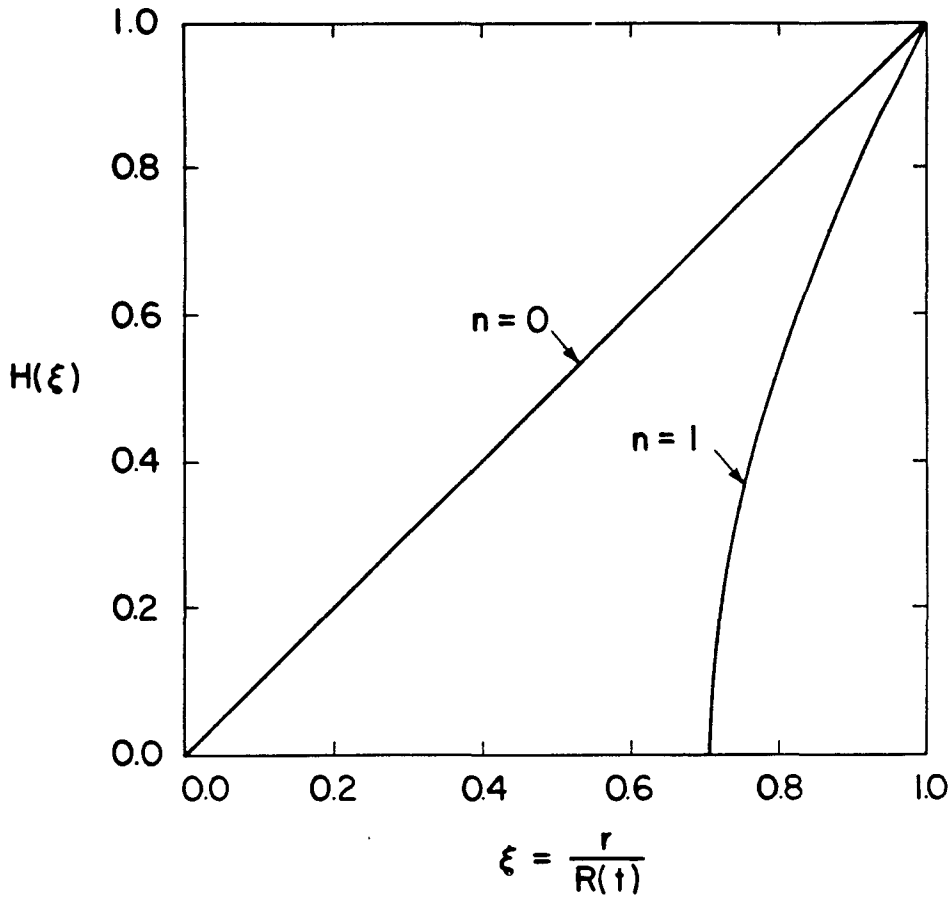


Figure 3.2.4 Similarity profiles of the half-thickness for a plane ($n=0$) and radial ($n=1$) interflowing layer resulting from a collapsing homogeneous mixed region at a neutral density level in a linearly stratified environment.

For an initially spherical section of radius R_0 , ($n=1$), the frontal position will be specified by

$$\frac{R(t)}{R_0} = 6^{1/3} (Nt)^{1/3} \quad . \quad (3.2.103)$$

3.2.6.2 Internal Plane Starting Layer (Continuous Flow)

Providing that $(\phi - \xi)^2 - H^2(\xi) \neq 0$, the two similarity solutions in this case ($n=0$ and $m=1$) are

$$H'(\xi) = 0 \quad (3.2.104)$$

and

$$\phi'(\xi) = 0 \quad . \quad (3.2.105)$$

The non-trivial wave front solutions for the half-thickness and the mean velocity of the intrusive layer are:

$$H(\xi) = \frac{Nh(r,t)}{\dot{R}(t)} = 1 \quad (3.2.106)$$

and

$$\phi(\xi) = \frac{u(r,t)}{\dot{R}(t)} = 1 \quad . \quad (3.2.107)$$

The integration constant in this case is

$$I_{110} = \int_0^1 H(\xi) d\xi = 1 \quad , \quad (3.2.108)$$

and the coefficient for the plane intrusive layer is

$$c_{110} = \frac{\sqrt{2}}{2} \quad . \quad (3.2.109)$$

An intrusion layer front resulting from a discharge at a neutral density level, with a discharge Richardson number $Ri_j = \frac{Nh_j}{u_j}$ of unity, will increase its displacement according to

$$R(t) = \frac{\sqrt{2}}{2} (NQ)^{1/2} t \quad , \quad (3.2.110)$$

where h_j is the half-thickness of the slot jet opening, u_j is the mean jet velocity and Q is the volume rate of discharge, $Q = 2u_j h_j$. When the jet Richardson number is less than unity, i.e. $Ri_j = \frac{Nh_j}{u_j} < 1$, there will be a region of mixing. This jet mixing will reduce the mean velocity to a lower value such that the flow will move at a Richardson number of unity. However, the total volume of the interflowing layer will be larger than the amount discharged. In this case the constant of proportionality in Eq. (3.2.110), $\frac{R(t)}{(NQ)^{1/2} t}$, will be greater than $1/\sqrt{2}$.

3.2.6.3 Internal Radial Starting Layer (Continuous Flow)

In this case $n=1$ and $m=1$ and the decay coefficient $\Lambda = -\frac{1}{2}$. Two reduced differential equations are obtained:

$$H' = \frac{\frac{1}{2} H\phi + H(\phi - \xi)\left(\frac{\phi}{\xi} - \frac{1}{2}\right)}{H^2 - (\phi - \xi)^2}, \quad (3.2.111)$$

and

$$\phi' = \frac{-\frac{1}{2}\phi(\phi - \xi) - H^2\left(\frac{\phi}{\xi} - \frac{1}{2}\right)}{H^2 - (\phi - \xi)^2}. \quad (3.2.112)$$

With the two boundary conditions, $\phi(1) = 1$ and $H(1) = 1$, these two differential equations were solved numerically using the subroutine "MODDEQ/Differential Equation Solver" at Caltech's Booth Computing Center. The subroutine is based on the method of Runge-Kutta-Gill with automatic control of error truncation. The two similarity profiles for mean velocity and half-thickness obtained for the spreading layer are shown in Figure 3.2.5.

It is peculiar to see that there is also an infinitely large fluid velocity inside the plume at the location $\xi = 0.6915$ where the half-thickness vanishes. Since the neutral density source is continuously discharged at the origin, a series of such internal rings should form after the first ring is dispatched.

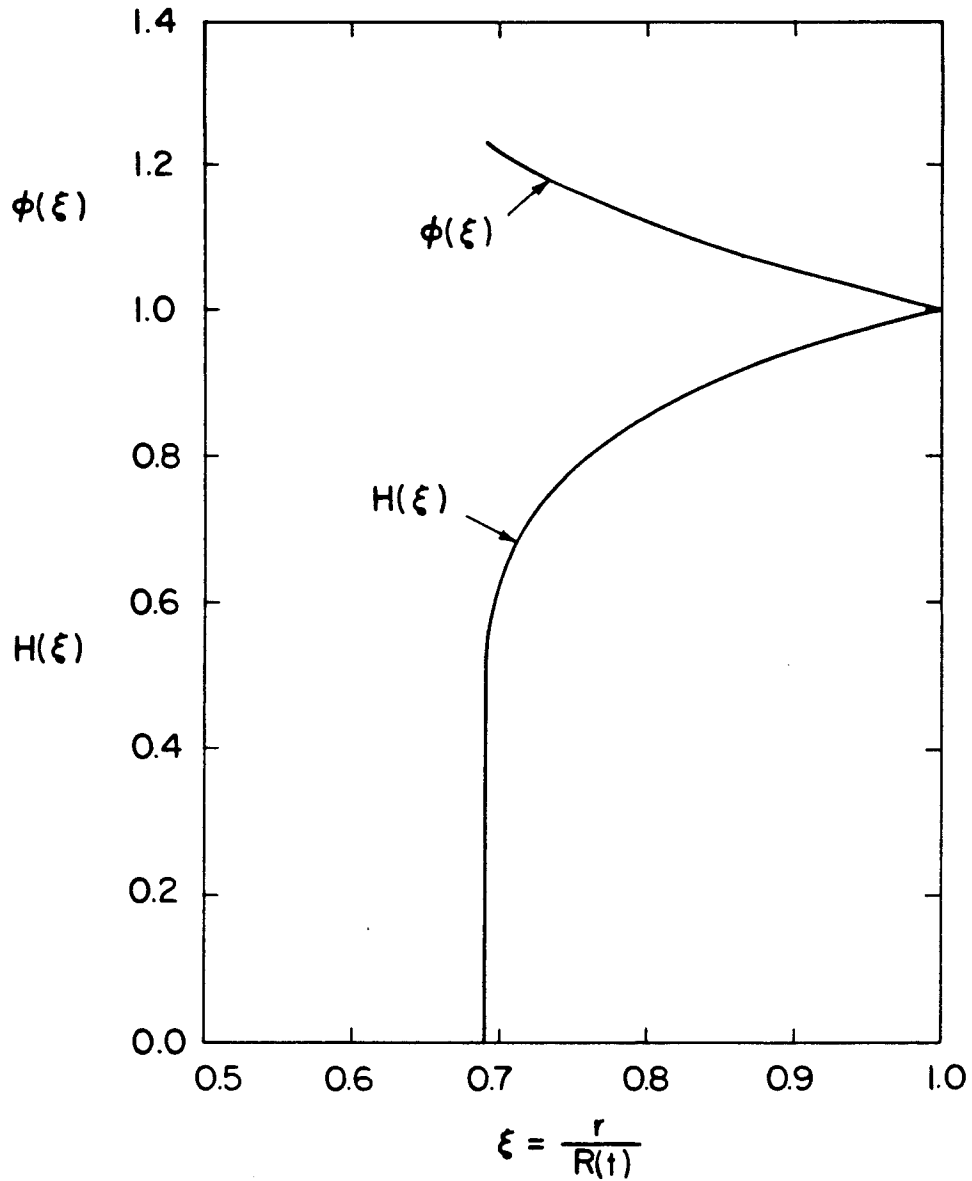


Figure 3.2.5 Similarity profiles of the average velocity and the half-thickness of interflowing radial ring due to a continuous release.

The coefficient of integration is computed using Simpson's rule as

$$I_{111} = \int_{0.6915}^1 \xi H(\xi) d\xi = 0.231 \quad . \quad (3.2.113)$$

and the radial front coefficient becomes

$$c_{111} = \left(\frac{3}{2 \times 4\pi \times 0.231} \right)^{1/3} = 0.802 \quad . \quad (3.2.114)$$

An internal ring front will therefore propagate according to

$$R(t) = 0.802 (NQ)^{1/3} t^{2/3} \quad . \quad (3.2.115)$$

Suppose there is a stationary observer located at a distance r from a submerged neutral density source discharging with a flow rate Q in linearly density-stratified environment for which the Brunt-Väisälä frequency is N . The observer will see a steady series of fronts passing at a period T

$$T = 1.391 \left(\frac{r^3}{NQ} \right)^{1/2} \quad . \quad (3.2.116)$$

3.2.7 Initial Stage of Density Spread

A spreading density front generated by release of a finite volume of liquid has an initial stage formed by the collapse of the volume. Subsequently the front formed develops

into the decelerating shock wave type propagation that was considered in the previous Subsections 3.2.5 and 3.2.6. As was discussed in Subsection 3.2.3.1 to solve the two shallow-water wave equations (3.2.2) and (3.2.3) in this case, similarity solutions for velocity and thickness were developed in the form

$$u(r,t) = \dot{R}(t)\phi(\xi) \quad (3.2.16)$$

and

$$h(r,t) = h_1 \eta^\alpha(t) H(\xi) \quad , \quad (3.2.23)$$

where ξ is the dimensionless variable $r/R(t)$ as before, η is the frontal position relative to the original radial length R_0 , i.e. $\eta = R(t)/R_0$, h_1 is the original characteristic thickness before spreading, and α is an unknown number. $\phi(\xi)$ and $H(\xi)$ are the similarity profiles for the mean velocity and the spreading layer thickness. Substitution of these two similarity solutions into the internal shallow water-wave Eqs. (3.2.2) and (3.2.3) gives

$$(\phi - \xi)H' + H(\phi' + \frac{n\phi}{\xi} + \alpha) = 0 \quad (3.2.117)$$

and

$$(\phi - \xi)\phi' + \Lambda\phi + \left(\frac{g\Delta_i h^{i+1}}{\dot{R}^2} \eta^{(i+1)\alpha} \right) H^i H' = 0 \quad , \quad (3.2.118)$$

where the decay coefficient Λ is equal to $\frac{\alpha}{R} \frac{R}{R^2}$ as before and $i=0$ for surface spreading and $i=1$ for internal spreading.

To homogenize the above equation (3.2.118), one must have that

$$\frac{g_i \Lambda_i h^{i+1}}{R^2} \eta^{(i+1)\alpha} = \beta \quad , \quad (3.2.119)$$

for some constant β , so that Eq. (3.2.118) becomes

$$(\phi - \xi)\phi' + \Lambda\phi + \beta H^i H' = 0 \quad . \quad (3.2.120)$$

Equations (3.2.117) and (3.2.120) have solutions (see Appendix D)

$$\phi(\xi) = \xi \quad (3.2.121)$$

$$H(\xi) = (1 - \xi^2)^{\frac{1}{i+1}} \quad (3.2.122)$$

satisfying

$$\phi(1) = 1 \quad (3.2.54)$$

$$H(1) = 0 \quad (3.2.58)$$

provided that constants α and β are chosen

$$\alpha = -(n+1) \quad , \quad (3.2.123)$$

$$\beta = \frac{(i+1)\Lambda}{2} \quad . \quad (3.2.124)$$

The characteristic thickness h_1 can be derived from a conservation of volume. The total volume of spreading fluid $V(t)$ must be equal to the total volume V_0 at the start of spreading. The relationship is

$$V(t) = V_0 \quad , \quad (3.2.125)$$

where

$$V_0 = \int_0^{R(0)} h(r,0) k_{in} r^n dr \quad (3.2.126)$$

and

$$V(t) = \int_0^{R(t)} h(r,t) k_{in} r^n dr = k_{in} h_1 R_0^{n+1} \int_0^1 \xi^n H(\xi) d\xi \quad . \quad (3.2.127)$$

It thus becomes possible to find the unknown length scale, h_1 ,

$$h_1 = \frac{V_0}{k_{in} R_0^{n+1} \int_0^1 \xi^n H(\xi) d\xi} = \frac{\int_0^{R_0} h(r,0) r^n dr}{R_0^{n+1} \int_0^1 \xi^n (1-\xi^2)^{\frac{1}{i+1}} d\xi} \quad . \quad (3.2.128)$$

The values of the original characteristic thickness scale h_1 are listed in Table 3.2.1 for spreading in a homogeneous environment ($i=0$) and in Table 3.2.2 for spreading in a linearly density-stratified environment ($i=1$). Thus, the unsteady and non-uniform thickness distribution $h(r,t)$ can be expressed explicitly as

$$\frac{h(r,t)}{h_1} \left\{ \frac{R(t)}{R_0} \right\}^{(n+1)} = H(\xi) = (1 - \xi^2)^{\frac{1}{i+1}} \quad . \quad (3.2.129)$$

These two similarity profiles for spreading fluid thickness are plotted in Figure 3.2.6 for $i=0$ and in Figure 3.2.7 for $i=1$. The thickness profile of an initial spreading layer in a homogeneous environment ($i=0$) is not an elliptical section as Longuet-Higgins (1972) expected. However, the thickness profile in a linear density-stratified environment ($i=1$) is an elliptical section which was also assumed by Mei (1969).

The frontal contact angle β with the horizontal bed (or the neutral water level) can be found from the following relationship,

$$\beta = \arctan \left\{ \frac{\partial h(R,t)}{\partial r} \right\} = \arctan \left\{ -2 \left(\frac{h_1}{R_0} \right) \left(\frac{R_0}{R(t)} \right)^{n+2} \right\} \quad (3.2.130)$$

for $i=0$ and

$$\beta = \arctan \left\{ \frac{\partial h(R,t)}{\partial r} \right\} = \arctan \{ \infty \} = \frac{\pi}{2} \quad (3.2.131)$$

Table 3.2.1 The original characteristic thickness scale h_1 for the initial stage of surface density spread in a homogeneous environment ($i=0$) expressed as a function of the initial shape of liquid volume before spreading.

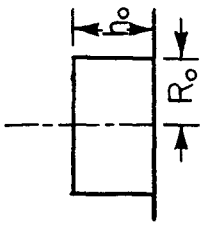
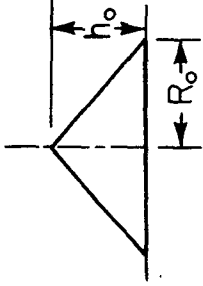
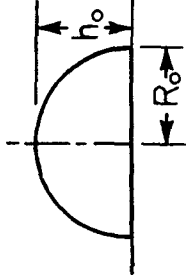
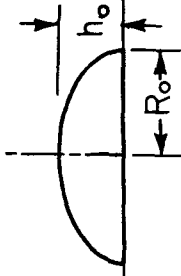
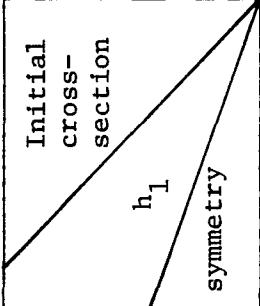
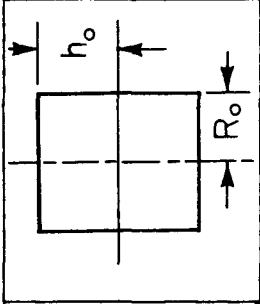
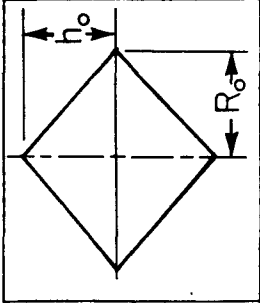
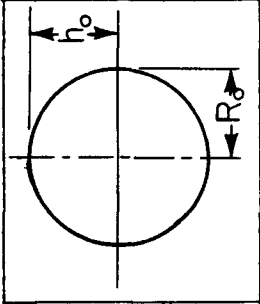
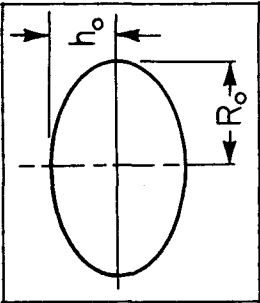
<p>Initial cross-section</p> <p>h_1</p> <p>symmetry</p>				
<p>plane</p> <p>$n=0$</p>	<p>rectangular column</p> <p>$\frac{3}{2} h_0$</p>	<p>triangular column</p> <p>$\frac{3}{4} h_0$</p>	<p>semi-cylindrical column</p> <p>$\frac{3\pi}{8} h_0$</p>	<p>semi-elliptic column</p> <p>$\frac{3\pi}{8} h_0$</p>
<p>radial</p> <p>$n=1$</p>	<p>circular cylinder</p> <p>$2 h_0$</p>	<p>triangular cone</p> <p>$\frac{2}{3} h_0$</p>	<p>hemi-sphere</p> <p>$\frac{4}{3} h_0$</p>	<p>semi-ellipsoid</p> <p>$\frac{4}{3} h_0$</p>

Table 3.2.2 The original characteristic thickness scale h_1 expressed as a function of initial cross-sections for the initial submerged density spread in a linearly density-stratified environment ($i=1$).

<p>Initial cross-section</p>  <p>h_1 symmetry</p>				
<p>plane $n = 0$</p>	<p>rectangular column $\frac{4}{\pi} h_0$</p>	<p>rhombic column $\frac{2}{\pi} h_0$</p>	<p>cylindrical column h_0</p>	<p>elliptic column h_0</p>
<p>radial $n = 1$</p>	<p>cylinder $\frac{3}{2} h_0$</p>	<p>double cone $\frac{1}{2} h_0$</p>	<p>sphere h_0</p>	<p>ellipsoid h_0</p>

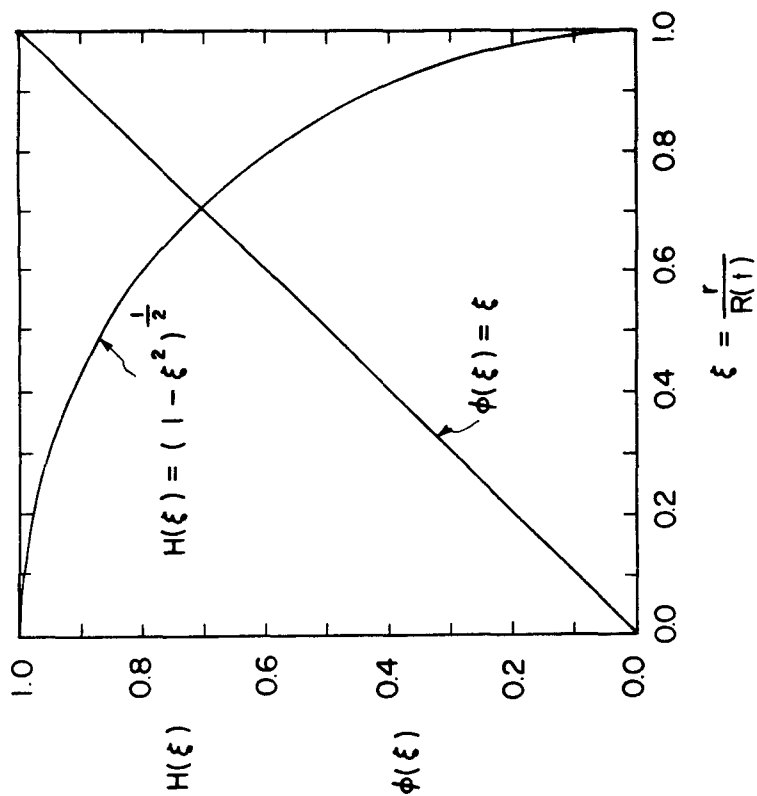


Figure 3.2.6 Similarity profiles for the mean horizontal velocity and the spreading layer thickness for the initial stage of surface density spreading in a homogeneous environment ($i=0$).

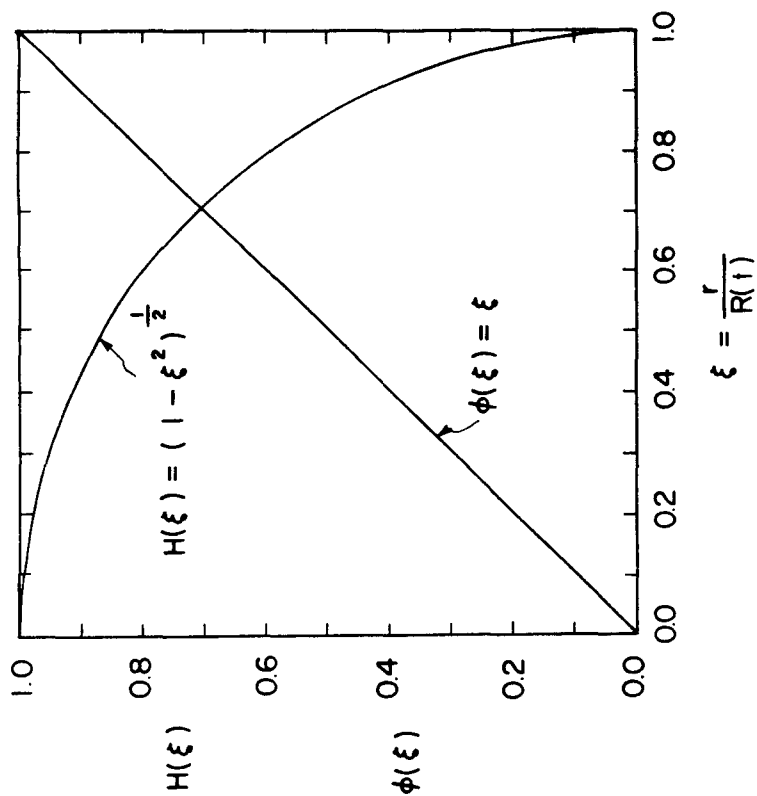


Figure 3.2.7 Similarity profiles for the average velocity and the half-thickness of interflowing submerged density spreading layer due to a finite volume release in a linearly density-stratified environment ($i=1$).

for $i=1$. This means that the internal wedge angle at the front is always perpendicular to the propagation direction at the neutral level for a stably stratified environment ($i=1$).

But more interesting, the frontal contact angle of inertial spreading in the homogeneous environment ($i=0$) is a function of: (i) the relative frontal distance $\eta = R(t)/R_0$; (ii) the initial shape of liquid volume; and (iii) the initial aspect ratio (or h_1/R_0) and also the case considered n . For a very long reservoir, $h_1/R_0 \rightarrow 0$, the initial value of β defined by

$$\beta_0 = \arctan \left\{ - \left(\frac{h_1}{R_0} \right) \right\} , \quad (3.2.132)$$

will be asymptotically zero, which coincides with the dry-bed break flow result obtained by Ritter (1892). For a long time,

$\left(\frac{h_1}{R_0} \right) \left(\frac{R_0}{R(t)} \right)^{n+2} \rightarrow 0$, so the frontal contact angle will be asymptotic to a constant value, 0, for a reservoir with finite aspect ratio.

The frontal trajectory function is determined by integration of the equation,

$$\frac{d^2 R(t)}{dt^2} = \frac{1}{2} \frac{dR^2}{dR} = \frac{2}{i+1} \frac{g \Delta_i h_1^{i+1}}{R_0} \left(\frac{R}{R_0} \right)^{-[(i+1)(n+1)+1]} , \quad (3.2.133)$$

Equation (3.2.133) can be rewritten as

$$\frac{d}{d\eta} \left(\frac{d\eta}{d\tau} \right)^2 = \frac{4}{i+1} \eta^{-[(i+1)(n+1)+1]} \quad , \quad (3.2.134)$$

where

$$\eta(\tau) = R(t)/R(0) = R(t)/R_0 \quad (3.2.135)$$

$$\tau = t \sqrt{g\Delta_i h_i^{i+1}} / R(0) \quad (3.2.136)$$

This equation is solved with initial conditions

$$\eta(0) = 1 \quad (3.2.137)$$

$$\frac{d\eta(0)}{d\tau} = 0 \quad (3.2.138)$$

to give

$$\tau = \left(\frac{i+1}{2} \right) (n+1)^{1/2} \int_1^\eta \frac{d\eta}{\left[1 - \eta^{-(i+1)(n+1)} \right]^{1/2}} \quad (3.2.139)$$

The normalized frontal velocity for large time is clearly

$$\frac{\dot{R}(t)}{\sqrt{g\Delta_i h_i^{i+1}}} = \frac{2}{(i+1)(n+1)^{1/2}} \quad (3.2.140)$$

For plane surface spreading in a homogeneous environment $n = 0$ and $i = 0$ so that Eq. (3.2.139) becomes

$$\tau = \frac{1}{2} \left\{ \eta^{1/2} (\eta - 1)^{1/2} + \ln [\eta^{1/2} + (\eta - 1)^{1/2}] \right\} \quad (3.2.141)$$

while for radial surface spreading in a homogeneous environment ($i = 0$ and $n = 1$) Eq. (3.2.139) becomes

$$\tau = \frac{\sqrt{2}}{2} (\eta^2 - 1)^{1/2} \quad . \quad (3.2.142)$$

For density stratified environments and internal spreading ($i = 1$ and $n = 0$) the plane spreading result is

$$\tau = (\eta^2 - 1)^{1/2} \quad (3.2.143)$$

and while for radial spreading the integral cannot be evaluated explicitly. In each of the above cases the characteristic length scale h_1 must be evaluated from the given initial shape of the spreading volume.

3.3 Similarity Solutions of Viscous-Buoyancy Density Currents

In this section the asymptotic functions describing both surface and submerged density currents in the viscous-buoyancy regime, which were derived by force scale analysis in Section 3.1, will be evaluated by a self-similar analysis. Exact solutions

analogous to point source solutions for nonlinear diffusion will be given for the first four cases. These correspond to a plane ($n=0$) or a radial ($n=1$) finite volume release ($m=0$) in a uniform ($i=0$) or a linearly density-stratified ($i=1$) environment. Series expansion solutions will be given for the continuous discharge cases ($m=1$). Self-similar distributions of thickness and velocity and the unknown numerical coefficients in the power law descriptions for the viscous spreading front will be found. A comparison of the results obtained with available experimental data will be presented in Chapter 6.

3.3.1 Nonlinear Long Wave Equations

The relevant long wave approximation equation for the viscous-buoyancy region of surface and submerged density spread is the " $(i+4)$ " power nonlinear diffusion equation,

$$\frac{\partial h}{\partial t} = \frac{g\Delta_i}{3(i+4)\nu} \frac{1}{r^n} \frac{\partial}{\partial r} \left(r^n \frac{\partial h^{i+4}}{\partial r} \right) \quad , \quad (3.3.1)$$

where $h=h(r,t)$ is the thickness of the spreading layer (for $i=0$), and is the half-thickness of an interflowing layer in a linearly density-stratified environment (for $i=1$), n is a parameter that denotes the radial case for $n=1$ and the plane case for $n=0$, ν is the kinematic viscosity of spreading fluid, $g\Delta_i$ denotes the reduced gravitational constant, $g(\rho_s - \rho_a)/\rho_s$, for $i=0$, and the square of Brunt-Väisälä frequency of ambient

density stratification, $N^2 = g\varepsilon = \frac{-g}{\rho_s} \frac{d\rho_a(z)}{dz}$, for $i=1$, in which ρ_a and ρ_s are mass densities of the ambient and the spreading fluid. The coordinate system of this spreading flow is that shown in Figure 3.2.1. (See Appendix E for the derivation of viscous long wave approximation equation.)

3.3.2 Derivation of Self-Similar Formula by the Method of Separation of Variables

Assume that the unknown spreading layer thickness $h(r,t)$ in the nonlinear long wave equation has solutions of the following form:

$$h(r,t) = T(t) H(\xi) \quad , \quad (3.3.2)$$

where the dimensionless variable ξ is defined as $r/R(t)$, $R(t)$ is the frontal position at time t , $T(t)$ is the unknown scale function for the spreading layer thickness and $H(\xi)$ is the similarity function to be determined.

Substituting Eq. (3.3.2) into Eq. (3.3.1) gives the ordinary differential equation

$$\frac{3R\dot{R}v}{g\Delta_i T^{i+3}} \left(\frac{\dot{R}T}{RT} \right) H - \frac{3R\dot{R}v}{g\Delta_i T^{i+3}} \xi H' = \frac{1}{\xi^n} \frac{d}{d\xi} \left(\xi^n \frac{dH^{i+4}}{d\xi} \right) \quad , \quad (3.3.3)$$

in which "°" denotes differentiation of a function with respect to time t and "·" differentiation with respect to the dimensionless variable ξ . In order to have a self-similar solution of Eq. (3.3.2), one must have the two terms, $\overset{\circ}{RRv}/g\Delta_i T^{i+3}$ and $R^2 v \overset{\circ}{T}/g\Delta_i T^{i+4}$, in the left-hand side of Eq. (3.3.3), be dimensionless and constant. For simplicity, choose the first term $\overset{\circ}{RRv}/g\Delta_i T^{i+3}$ equal to unity, so that the scale function $T(t)$ is

$$T(t) = \left(\frac{\overset{\circ}{RRv}}{g\Delta_i} \right)^{\frac{1}{i+3}} \quad (3.3.4)$$

Then the second term will automatically be a dimensionless number,

$$\frac{R^2 v \overset{\circ}{T}}{g\Delta_i T^{i+4}} = \frac{\overset{\circ}{RRv}}{g\Delta_i T^{i+3}} \left(\frac{\overset{\circ}{RT}}{\overset{\circ}{RT}} \right) = \frac{\overset{\circ}{RT}}{\overset{\circ}{RT}} = \frac{1+\Lambda}{i+3} \quad , \quad (3.3.5)$$

where the decay coefficient Λ is defined as $\Lambda = \overset{\circ}{RR}/R^2$ and can be determined from the frontal trajectory function $R(t)$. Therefore, Eq. (3.3.3) can be rewritten as

$$\frac{3(1+\Lambda)}{(i+3)} H - 3\xi H' = \frac{1}{(i+4)\xi^n} \frac{d}{d\xi} \left(\xi^n \frac{dH^{i+4}}{d\xi} \right) \quad . \quad (3.3.6)$$

Thus, the similarity solution for surface and submerged spreading layer thickness $h(r,t)$ has the form

$$h(r,t) = \left(\frac{R_0 v}{g \Delta_i} \right)^{\frac{1}{i+3}} H(\xi) \quad . \quad (3.3.7)$$

The same self-similar formula Eq. (3.3.7) can also be derived straightforwardly by substituting the Taylor's (1950) similarity assumption Eq. (3.2.25) into the nonlinear wave Eq. (3.3.1) (see Appendix E for details of derivation).

3.3.3 Derivation of General Self-Similar Solutions

If interfacial mixing and diffusion, and surface evaporation were negligible, then the total spreading volume $V(t)$ at time t must be equal to the volume that has been supplied $V_j(t)$. Since the total spreading volume at time t is

$$V(t) = \int_0^{R(t)} h(r,t) k_{in} r^n dr \quad , \quad (3.3.8)$$

where k_{in} is a shape function of i and n and is defined in Eqs. (3.2.40) and (3.2.41). The total volume supplied is assumed to be

$$V_j(t) = Q t^m \quad , \quad (3.3.9)$$

so that one obtains

$$R^{(n+1)(i+3)+1} \circ_R = \alpha \frac{g\Delta_i Q^{i+3}}{\nu} t^{(i+3)m} \quad , \quad (3.3.10)$$

where $\alpha = \frac{1}{(k_{in} I_{imn})^{i+3}}$, and the integration constant I_{imn} is defined as

$$I_{imn} = \int_0^1 \xi^n H(\xi) d\xi \quad (3.3.11)$$

which is a function of i , m , and n (since the similarity distribution $H(\xi)$ is a function of i , m , and n). Carrying out integration of Eq. (3.3.10) from $R=R_0$ to $R=R(t)$ and $t=0$ to $t=t$ gives the explicit form of frontal trajectory functions:

$$\frac{R(t)}{R_0} = \left\{ 1 + \frac{(n+1)(i+3)+2}{m(i+3)+1} \frac{\alpha g\Delta_i Q^{(i+3)}}{\nu} \frac{t^{m(i+3)+1}}{R_0^{(n+1)(i+3)+2}} \right\}^{\frac{1}{(n+1)(i+3)+2}} \quad . \quad (3.3.12)$$

When the spreading distance $R(t)$ is much larger than the initial length R_0 , i.e. $R(t) \gg R_0$ or equivalently when the time $t \gg$

$$\left\{ \frac{\nu R_0^{(n+1)(i+3)+2}}{g\Delta_i Q^{i+3}} \right\}^{\frac{1}{m(i+3)+1}} \quad , \quad \text{the asymptotic form of viscous-buoyancy}$$

spreading becomes

$$R(t) = b_{imn} \left(\frac{g \Delta_i Q^{i+3}}{v} \right)^{\frac{1}{(n+1)(i+3)+2}} t^{\frac{m(i+3)+1}{(n+1)(i+3)+2}}, \quad (3.3.13)$$

in which the coefficient b_{imn} is

$$b_{imn} = \left\{ \frac{(n+1)(i+3)+2}{m(i+3)+1} \right\}^{\frac{1}{(n+1)(i+3)+2}} / \left\{ k_{in} I_{imn} \right\}^{\frac{i+3}{(n+1)(i+3)+2}} \quad (3.3.14)$$

This function has exactly the same form as that derived by the force scale analysis in Section 3.1. The unknown coefficient mainly depends on the spreading layer thickness distribution which can be derived by integrating Eq. (3.3.6) with suitable boundary conditions.

From Eq. (3.3.13) the decay coefficient now is

$$\Lambda = \frac{\overset{\circ}{R}\overset{\circ}{R}}{\overset{\circ}{R}^2} = \frac{(i+3)(m-n-1) - 1}{m(i+3) + 1} \quad (3.3.15)$$

so that the ordinary differential equation for a viscous layer spreading thickness (Eq. (3.3.6)) becomes

$$\frac{3(2m-n-1)}{m(i+3)+1} H - 3\xi H' = \frac{1}{(i+4)\xi^n} \frac{d}{d\xi} \left(\xi^n \frac{dH^{i+4}}{d\xi} \right) \quad (3.3.16)$$

3.3.4 Solutions for Spreading from a Finite Volume Release

In this case ($m=0$) the ordinary differential Eq. (3.3.16) for surface and submerged spreading layer thickness is

$$- 3(n+1)H - 3\xi H' = \frac{1}{(i+4)\xi^n} \frac{d}{d\xi} \left(\xi^n \frac{dH^{i+4}}{d\xi} \right) \quad (3.3.17)$$

or

$$3(i+4) (\xi^{n+1} H)' + \left(\xi^n \frac{dH^{i+4}}{d\xi} \right)' = 0 \quad (3.3.18)$$

Integrating twice from $\xi=1$ to $\xi=\xi$ and using the boundary condition

$$H(1) = 0 \quad (3.3.19)$$

and assuming

$$H^{i+3}(1) H'(1) = 0 \quad (3.3.20)$$

gives the similarity distribution for spreading layer thickness as

$$H(\xi) = \left\{ \frac{3(i+3)}{2} \right\}^{\frac{1}{i+3}} (1-\xi^2)^{\frac{1}{i+3}} \quad (3.3.21)$$

which is consistent with Eq. (3.3.20). Thus the self-similar profile for the surface and submerged spreading layer thickness becomes

$$h(r,t) = \left(\frac{RRv}{g\Delta_i} \right)^{\frac{1}{i+3}} \left\{ \frac{3(i+3)}{2} (1 - \xi^2) \right\}^{\frac{1}{i+3}} \quad (3.3.22)$$

The shape of this thickness profile is shown in Figure 3.3.1 for the case of spreading in a homogeneous environment ($i = 0$) and in Figure 3.3.2 for the case of spreading in a linearly density-stratified environment ($i = 1$).

The integration constant I_{ion} is

$$I_{ion} = \left\{ \frac{3(i+3)}{2} \right\}^{\frac{1}{i+3}} \int_0^1 \xi^n (1 - \xi^2)^{\frac{1}{i+3}} d\xi \quad (3.3.23)$$

The special case $n = 1$, gives

$$I_{io1} = \left\{ \frac{3(i+3)}{2} \right\}^{\frac{1}{i+3}} \int_0^1 \xi (1 - \xi^2)^{\frac{1}{i+3}} = \left\{ \frac{3(i+3)}{2} \right\}^{\frac{1}{i+3}} \frac{3}{2(i+4)} \quad ; \quad (3.3.24)$$

and for $n = 0$,

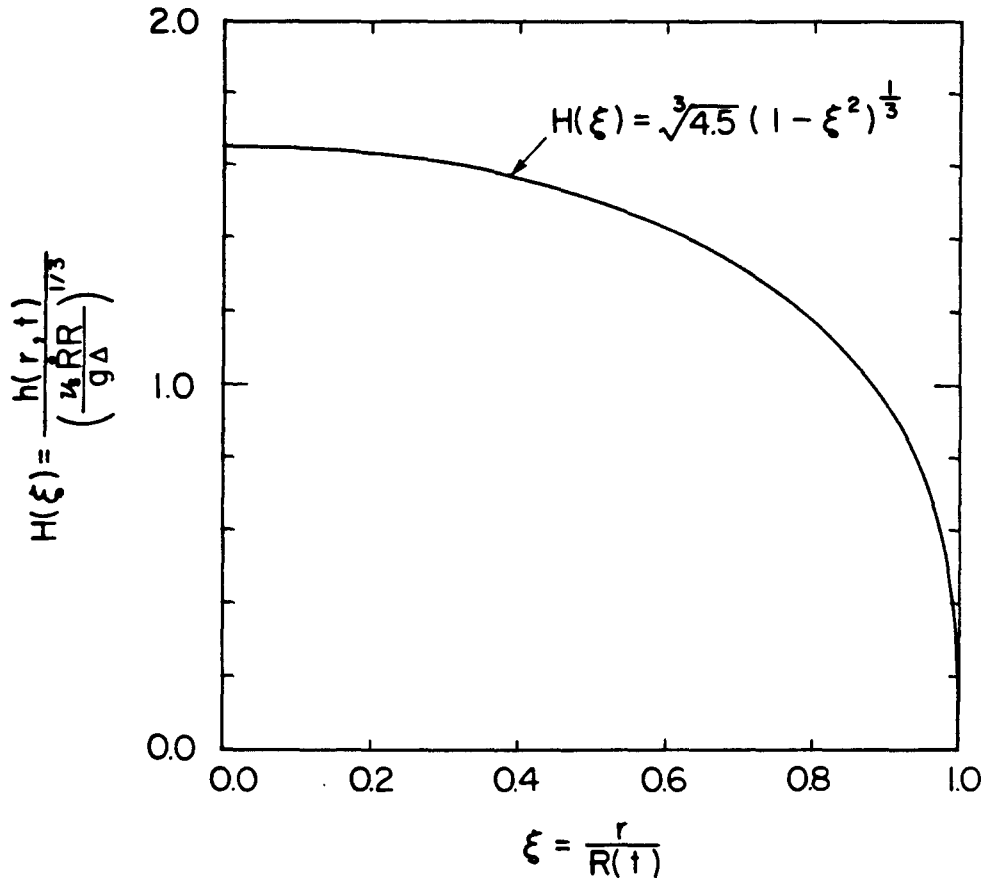


Figure 3.3.1 Self-similar thickness distribution of plane and radial viscous surface spread layer due to a finite volume release ($i=0$, $m=0$, $n=0$ and 1).

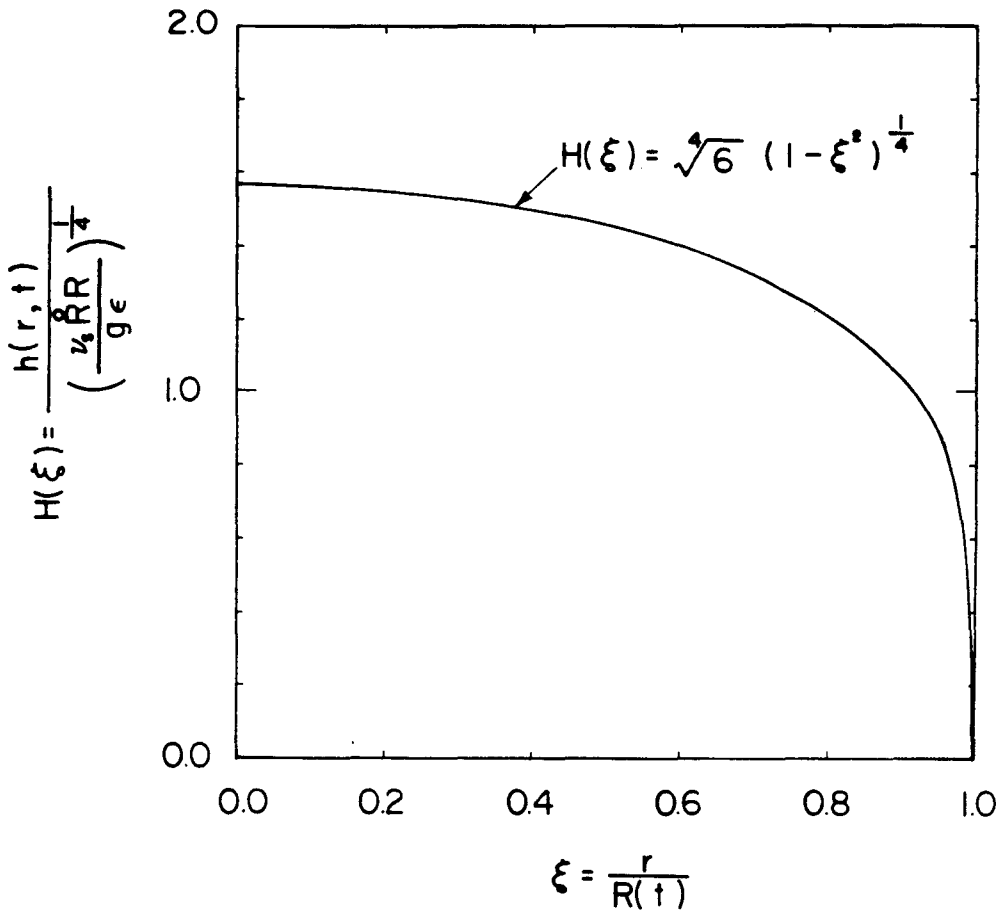


Figure 3.3.2 Self-similar thickness distribution of plane and radial viscous submerged density spread layer due to a finite volume release ($i=1$, $m=0$, $n=0$ and 1).

$$I_{i00} = \left\{ \frac{3(i+3)}{2} \right\}^{\frac{1}{i+3}} \int_0^{\frac{\pi}{2}} \cos^{\frac{i+5}{i+3}} \theta d\theta = \left\{ \frac{3(i+3)}{2} \right\}^{\frac{1}{i+3}} \frac{\Gamma\left(\frac{1}{2}\right) \Gamma\left(\frac{i+4}{i+3}\right)}{2\Gamma\left(\frac{3i+11}{2(i+3)}\right)}, \quad (3.3.25)$$

where $\Gamma(x)$ is the Gamma function of x . The approximate value of the integration constant I_{i0n} is listed in Table 3.3.1 for each case of i and n . The approximate value of the coefficient b_{i0n} in viscous-buoyancy spread Eq. (3.3.13) is then calculated and the viscous-buoyant trajectory function for each case i and n is listed in Table 3.3.2.

The frontal contact angle β defined by

$$\beta = \arctan \left\{ \frac{\partial h(R,t)}{\partial r} \right\} = \frac{\pi}{2} \quad (3.3.26)$$

for all time during viscous-buoyant spreading.

As derived in Appendix E, the horizontal velocity of a fluid particle will be given by

$$u(r,z,t) = - \frac{g\Delta_i h^{i+2}}{2\nu} \frac{\partial h}{\partial r} \left\{ 1 - \left(\frac{z}{h} \right)^2 \right\} \quad (3.3.27)$$

or

$$\frac{u(r,z,t)}{\dot{R}(t)} = \frac{3}{2} \xi \left\{ 1 - \left(\frac{z}{h} \right)^2 \right\} \quad (3.3.28)$$

Table 3.3.1 The value of the integration constant I_{ion} for surface and submerged spreading from a finite volume release ($m=0$).

I_{ion} <i>i</i>	<i>n</i> Plane Spreading <i>n</i> = 0	Radial Spreading <i>n</i> = 1
	In Homogeneous Environment <i>i</i> = 0	$\sqrt[3]{\frac{9}{2}} \int_{\infty}^{\frac{\pi}{2}} \cos^{5/3} \theta d\theta$ = 1.389
In Linearly Density-Stratified Environment <i>i</i> = 1	$\sqrt[4]{6} \int_{\infty}^{\frac{\pi}{2}} \cos^{3/2} \theta d\theta$ = 1.386	$\sqrt[4]{6} \cdot \frac{2}{5}$ = 0.626

Table 3.3.2 The frontal trajectory functions for the viscous-buoyant surface or submerged spreading due to a finite volume release ($m=0$).

i	R(t)	n	Plane Spreading	Radial Spreading
		n = 0	n = 1	
	In Homogeneous Environment i = 0		$1.133 \left(\frac{g\Delta V^3}{\nu} \right)^{1/5} t^{1/5}$	$0.779 \left(\frac{g\Delta V^3}{\nu} \right)^{1/8} t^{1/8}$
	In Linearly Density-Stratified Environment i = 1		$0.689 \left(\frac{N^2 V^4}{\nu} \right)^{1/6} t^{1/6}$	$0.552 \left(\frac{N^2 V^4}{\nu} \right)^{1/10} t^{1/10}$

as shown in Figure 3.3.3. The peak fluid particle velocity will therefore be 50% faster than the frontal velocity. The cross-sectional average fluid particle velocity is, however, continuous with the frontal velocity and still a linear function of location, since

$$\frac{u(r,t)}{\dot{R}(t)} = \frac{1}{h(r,t)} \int_0^{h(r,t)} \frac{u(r,z,t)}{\dot{R}(t)} dz = \xi \quad . \quad (3.3.29)$$

3.3.5 Plane Viscous Spreading Layer from a Continuous Discharge

Equation (3.3.16) in this case ($m=1$ and $n=0$) is

$$\left(H^{i+4} \right)'' = 3H - 3(i+4)\xi H' \quad . \quad (3.3.30)$$

According to the mathematical study by Gilding and Peletier (1976), there is no exact weak solution to Eq. (3.3.30). However, the solution was shown to exist and be unique. Moreover, it is bounded between a lower bound solution H_L ,

$$H_L(\xi) = \left\{ \frac{3(i+3)}{2} (1 - \xi^2) \right\}^{\frac{1}{i+3}} \quad (3.3.31)$$

and an upper bound solution H_U ,

$$H_U(\xi) = \left\{ \left[3(i+3) + \frac{3}{2} (1 - \xi) \right] (1 - \xi) \right\}^{\frac{1}{i+3}} \quad . \quad (3.3.32)$$

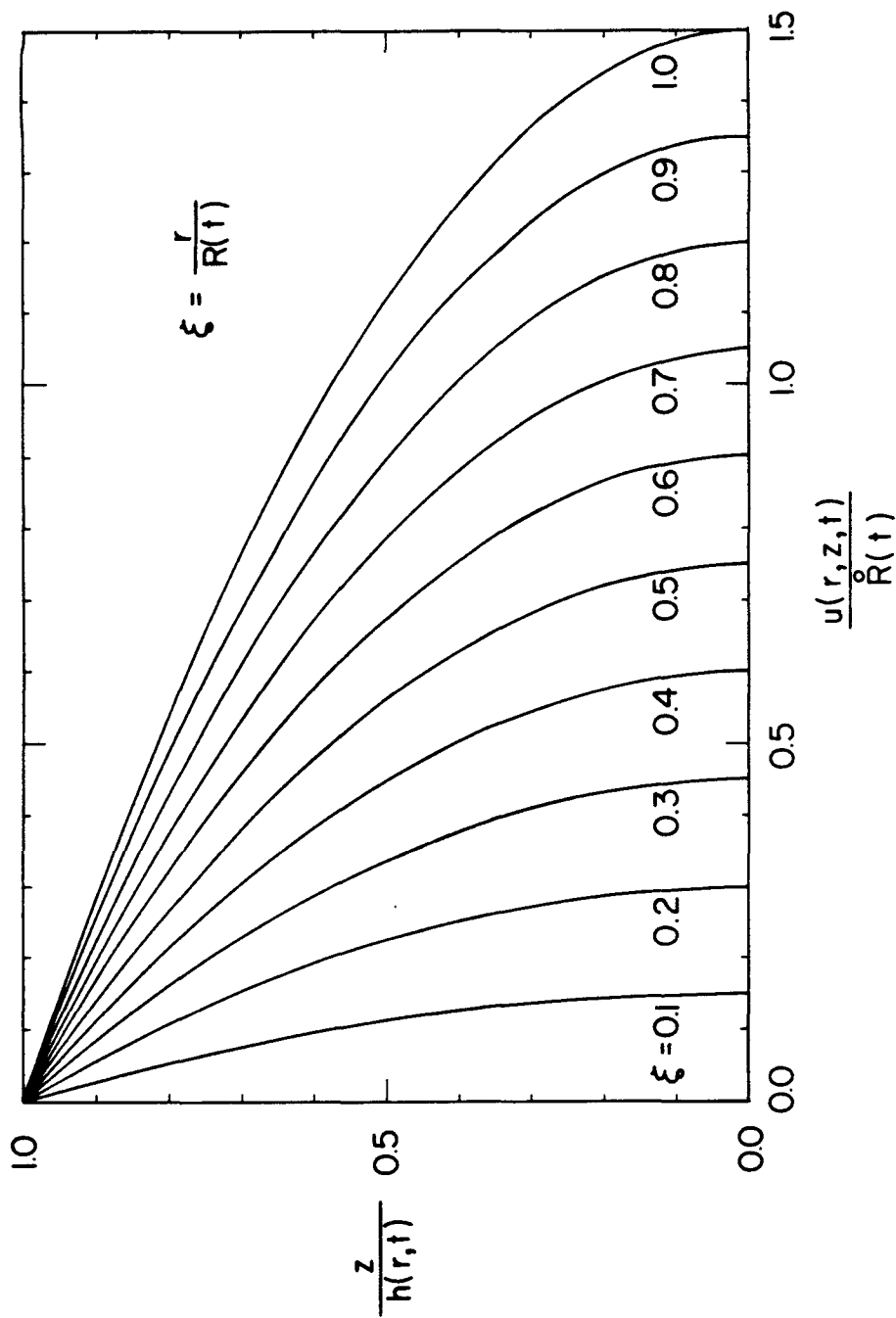


Figure 3.3.3 Self-similar distribution of plane and radial viscous surface ($i = 0$) or submerged ($i = 1$) spreading fluid velocity due to a finite volume release ($n = 0, 1$ and $m = 0$).

An approximate solution H_A between two bounds,

$$H_A(\xi) = \left\{ 3(i+3)(1-\xi) \right\}^{\frac{1}{i+3}}, \quad (3.3.33)$$

was given by Grundy (1979) with the method of phase plane analysis.

The approximate solution in Eq. (3.3.33) is actually a solution near the front as $\xi \rightarrow 1$. It can also be derived easily by integrating the simplified Eq. (3.3.30) twice near the front,

$$\left(H^{i+4} \right)'' \approx -3(i+4)H', \quad (3.3.34)$$

with two boundary conditions, $H(1) = 0$ and $H^{i+3}(1)H'(1) = 0$. The lower bound solution is the exact weak solution given in Eq. (3.3.21), which was derived in the Subsection 3.3.4.

Equation (3.3.30) can be rewritten in new form,

$$\frac{d^2f}{dx^2} = 3f^{\frac{1}{i+4}} + 3(i+4)(1-x) \frac{df}{dx}^{\frac{1}{i+4}}. \quad (3.3.35)$$

where $f(x) = H^{i+4}(\xi)$ and $x = 1 - \xi$. Assume that the solution of Eq. (3.3.35) has the following series expansion form near the front,

$$f(x) = [3(i+3)x]^{\frac{i+4}{i+3}} \left\{ 1 + \sum_{j=1}^{\infty} a_j x^j \right\}. \quad (3.3.36)$$

Substituting the series solution in Eq. (3.3.35) one can find the coefficients a_j . Two values, a_1 and a_2 , are found,

$$a_1 = \frac{-1}{2(i+4)(i+3)} \quad (3.3.37)$$

and

$$a_2 = \frac{2(i+4)^3 - 2(i+4)(i+3) - (i+3)}{[2(i+4)^2 + 4(3i+10)(i+3)(i+4) + (i+3)][2(i+4)^2(i+3)]} \quad (3.3.38)$$

The solution of Eq. (3.3.30) can be expressed up to the third order as

$$H(\xi) = [3(i+3)(1-\xi)]^{\frac{1}{i+3}} \left\{ 1 - \frac{(1-\xi)}{2(i+4)(i+3)} + \frac{2(i+4)^3 - 2(i+4)(i+3) - (i+3)}{[2(i+4)^2 + 4(3i+10)(i+3)(i+4) + (i+3)][2(i+4)^2(i+3)]} (1-\xi)^2 + \dots \right\}^{\frac{1}{i+4}} \quad (3.3.39)$$

Two self-similar profiles of plane spreading layer thickness are shown in Figure 3.3.4 for the homogeneous environment ($i=0$) case and in Figure 3.3.5 for the linearly density-stratified environment ($i=1$) case. The integration values I_{i10} are given in Table 3.3.3 and the coefficients b_{i10} in the asymptotic form of frontal trajectory functions are given in Table 3.3.4.

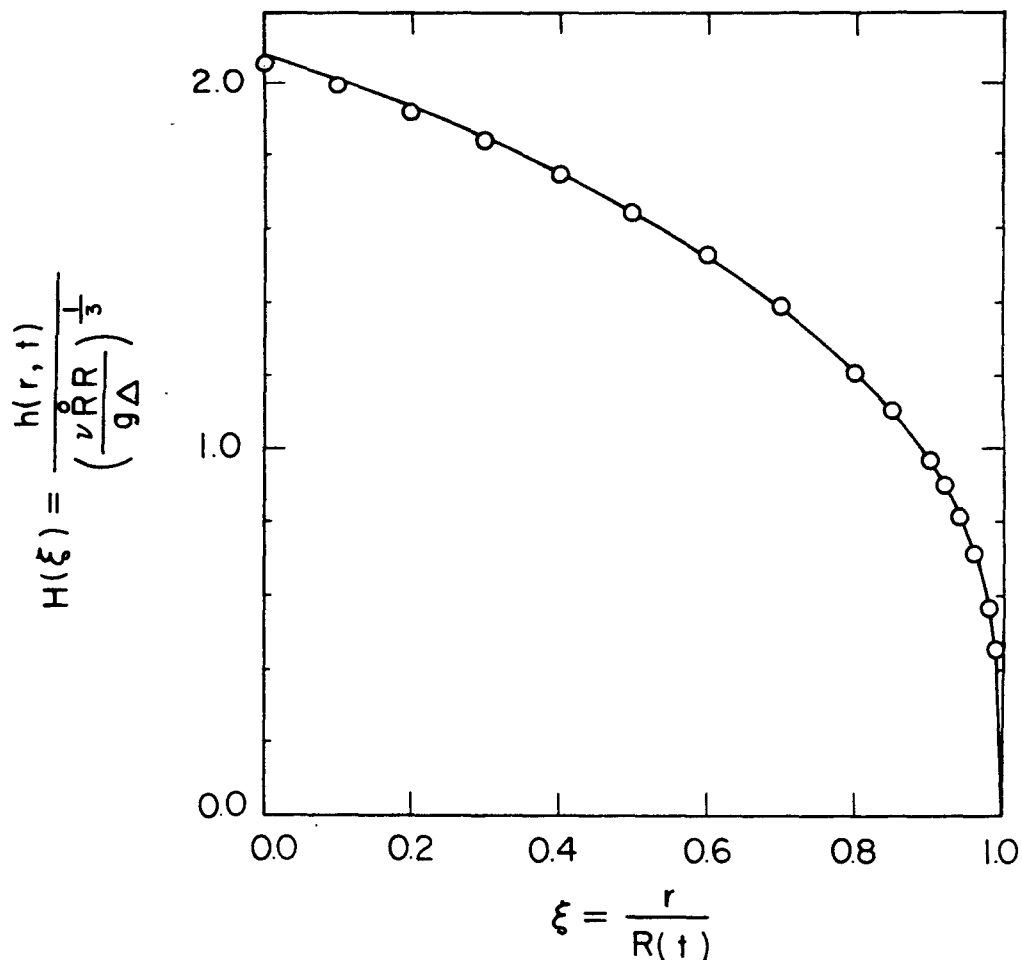


Figure 3.3.4 Self-similar thickness distribution of plane viscous surface spread layer due to a constant rate of discharge into a homogeneous environment ($i = 0$, $m = 1$, $n = 0$). Solid line denotes the first approximation, and open circles denote the third approximation.

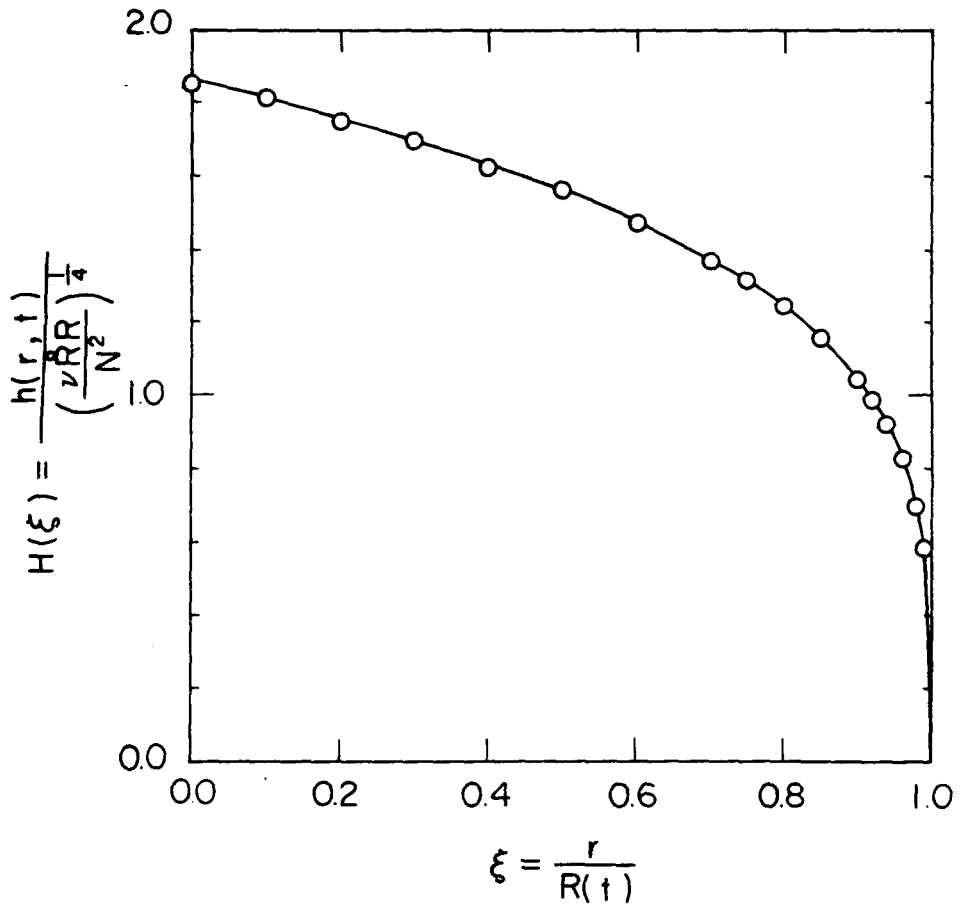


Figure 3.3.5 Self-similar half-thickness distribution of plane viscous submerged density spread layer due to a constant rate of discharge into a linearly density-stratified environment ($i = 1, m = 1, n = 0$). Solid line denotes the first approximation and open circles denote the third approximation.

Table 3.3.3 Integration values I_{i10} for plane viscous-buoyancy spreading currents due to a continuous steady discharge plume.

I_{i10} derived from	i	Uniform Environment	Linearly Density- Stratified Environment
		$i = 0$	$i = 1$
Upper bound of solution $H_u(\xi)$		1.6078	1.5140
Lower bound of solution $H_L(\xi)$		1.3890	1.3679
1st term approximate solution of $H(\xi)$		1.5600	1.4889
2nd term approximate solution of $H(\xi)$		1.5507	1.4848
3rd term approximate solution of $H(\xi)$		1.5510	1.4849

Table 3.3.4 Coefficients b_{i10} for the plane viscous-buoyancy spreading currents to a continuous steady discharge plume.

b_{i10} derived from	i	Uniform Environment	Linearly Density- Stratified Environment
		$i = 0$	$i = 1$
Upper bound of solution $H_u(\xi)$		0.7864	0.4925
Lower bound of solution $H_L(\xi)$		0.8585	0.5270
1st term approximate solution of $H(\xi)$		0.8008	0.4980
2nd term approximate solution of $H(\xi)$		0.8036	0.4990
3rd term approximate solution of $H(\xi)$		0.8036	0.4989

The series solutions are convergent very fast over all the domain between 0 and 1. Therefore, the solutions derived from the third term approximation are good enough for comparison. The frontal trajectory functions can be expressed as

$$R(t) = 0.8036 \left(\frac{g\Delta Q^3}{\nu} \right)^{1/5} t^{4/5} \quad (3.3.40)$$

for the spreading currents in the homogeneous environment ($i=0$) and as

$$R(t) = 0.4989 \left(\frac{N^2 Q^4}{\nu} \right)^{1/6} t^{5/6} \quad (3.3.41)$$

for the spreading currents in the linearly density-stratified environment ($i=1$).

3.3.6 Radial Viscous Spreading Layer from a Continuous Discharge

Equation (3.3.16) in this case ($m=1$ and $n=1$) is

$$\frac{d}{d\xi} \left(\xi \frac{dH^{i+4}}{d\xi} \right) = -3(i+4)\xi^2 \frac{dH}{d\xi} \quad (3.3.42)$$

The simplified Eq. (3.3.42) near the front can be expressed in the same form given in Eq. (3.3.34). Thus, the approximate solution near the front is also of the same form in Eq. (3.3.33).

Rewrite Eq. (3.3.42) in the form,

$$(1-x) \frac{d^2 f}{dx^2} - \frac{df}{dx} = 3(i+4)(1-x)^2 \frac{df}{dx} \frac{1}{i+4}, \quad (3.3.43)$$

where $f(x) = H^{i+4}(\xi)$ and $x = 1 - \xi$. Assume that the solution of Eq. (3.3.43) can also be expressed in the series expansion form about the solution near the front, i.e. Eq. (3.3.36). Substituting the power series expansion Eq. (3.3.36) in Eq. (3.3.43), one can find the coefficients a_j . Two values, a_1 and a_2 , are found,

$$a_1 = \frac{(i+2)}{2(i+3)} \quad (3.3.44)$$

and

$$a_2 = \frac{(i+2)}{2(i+3)} \left\{ \frac{(i+2)(i+5) + 2(4i+13)(i+3)(i+4)}{2(i+4)^2 + (i+3) + 4(3i+10)(i+3)(i+4)} \right\} + \frac{2(i+4)^2}{\{2(i+4)^2 + (i+3) + 4(3i+10)(i+3)(i+4)\}} \quad (3.3.45)$$

Thus, the self-similar function $H(\xi)$ can be expressed up to the third order as

$$H(\xi) = \left\{ 3(i+3)(1-\xi) \right\}^{\frac{1}{i+3}} \left\{ 1 + \frac{(i+2)}{2(i+3)} (1-\xi) + a_2 (1-\xi)^2 + \dots \right\}^{\frac{1}{i+4}} \quad (3.3.46)$$

Two self-similar profiles of radial spreading layer thickness are shown in Figure 3.3.6 for the homogeneous environment ($i = 0$) case and in Figure 3.3.7 for the linearly density-stratified environment ($i = 1$) case. The integration values I_{i11} are given in Table 3.3.5 and the coefficients b_{i11} in the asymptotic form of frontal trajectory functions are given in Table 3.3.6.

The series solutions are also convergent rather fast all over the domain between 0 and 1. Therefore, the frontal trajectory function can be expressed as

$$R(t) = 0.63 \left(\frac{g\Delta Q^3}{\nu} \right)^{1/8} t^{1/2} \quad (3.3.47)$$

for the radial spreading currents in the homogeneous environment ($i = 0$) and as

$$R(t) = 0.45 \left(\frac{N^2 Q^4}{\nu} \right)^{1/10} t^{1/2} \quad (3.3.48)$$

for the radial spreading currents in the linearly density-stratified environment ($i = 1$).

3.4 Further Mixing of Surface Spreading Flow

3.4.0 Introductory Note

After a discharged effluent reaches a free surface or the bottom, the momentum flux causes an increase in pressure which together with any buoyancy flux causes the diluted effluent to

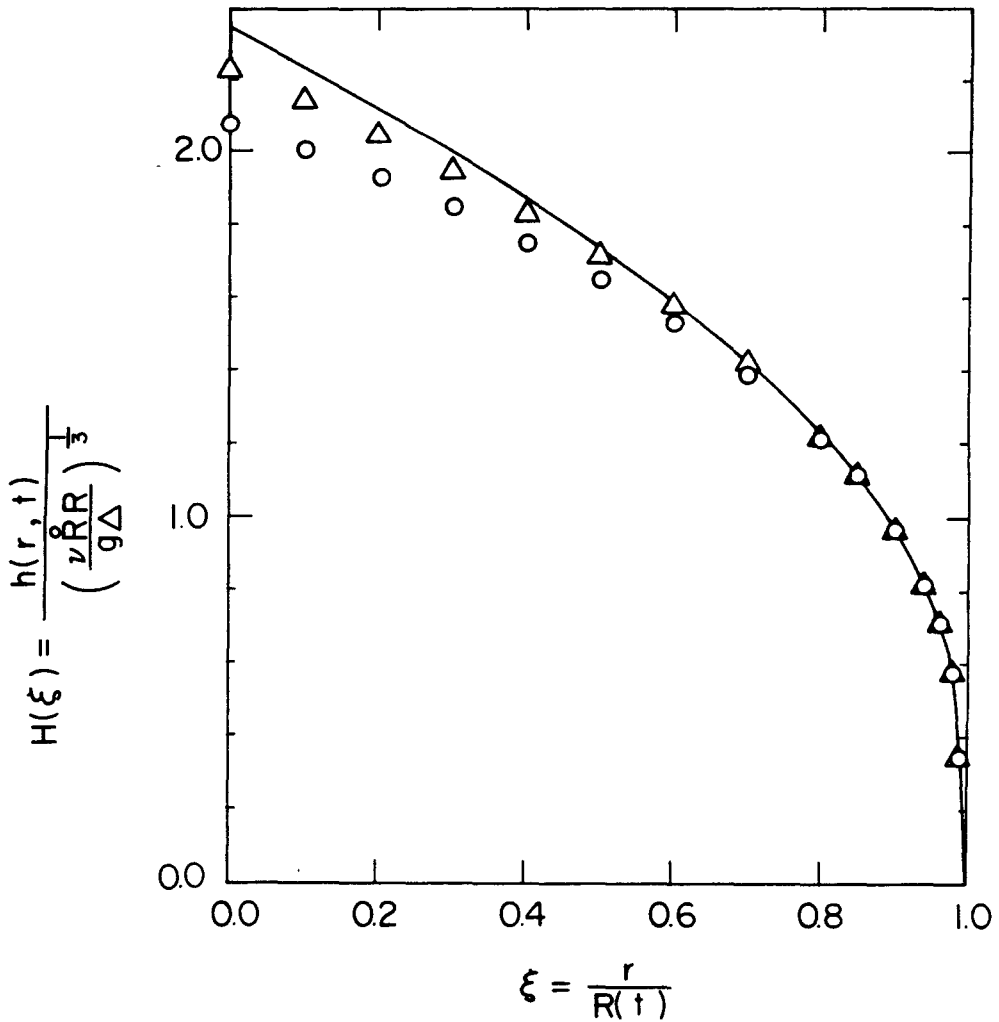


Figure 3.3.6 Self-similar thickness distribution of radial viscous surface spread layer due to a constant rate of discharge into a homogeneous environment ($i = 0$, $m = 1$, $n = 1$). Solid line denotes the third term approximation, open circles, the first term approximation, and triangles, the second term approximation.

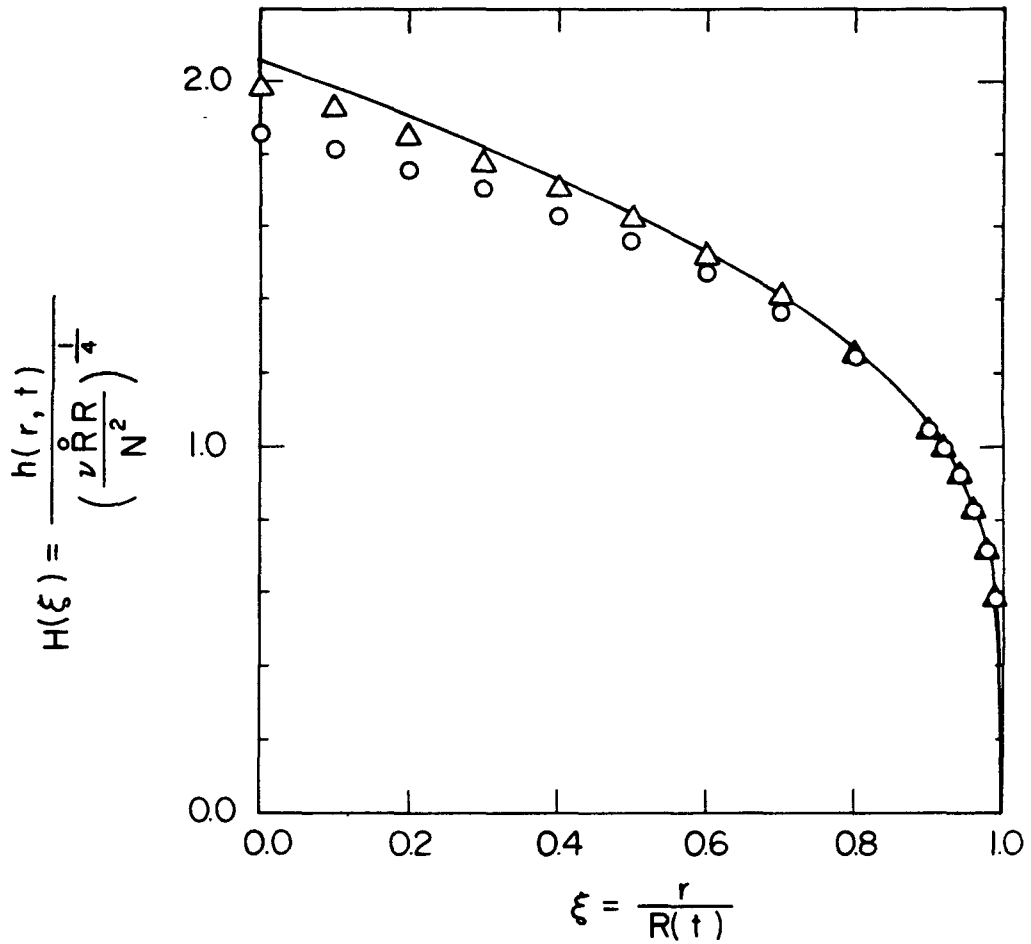


Figure 3.3.7 Self-similar half-thickness distribution of radial viscous submerged density spread layer due to a constant rate of discharge into a linearly density-stratified environment ($i=1, m=1, n=1$). Solid line denotes the third term approximation, open circles, the first term approximation, and triangles, the second term approximation.

Table 3.3.5 Integration values I_{i11} for the radial viscous-buoyancy spreading currents due to a continuous steady discharge plume.

I_{i11} derived from	i	Uniform Environment	Linearly Density- Stratified Environment
		$i = 0$	$i = 1$
1st term approximation of $H(\xi)$		0.6686	0.6618
2nd term approximation of $H(\xi)$		0.6895	0.6795
3rd term approximation of $H(\xi)$		0.6977	0.6858

Table 3.3.6 Coefficients b_{i11} for the radial viscous-buoyancy spreading currents due to a continuous steady discharge plume.

b_{i11} derived from	i	Uniform Environment	Linearly Density- Stratified Environment
		$i = 0$	$i = 1$
1st term approximation of $H(\xi)$		0.6366	0.4593
2nd term approximation of $H(\xi)$		0.6293	0.4545
3rd term approximation of $H(\xi)$		0.6265	0.4528

flow horizontally. The pressure gradient induced by the momentum flux makes the initial regime of horizontal flow behave as a surface jet and therefore causes a considerable amount of mixing with the ambient fluid beneath it, as shown in Figure 3.4.1(a). Further away from the impact point the buoyancy effects due to any small density difference become more important. The buoyancy gradually reduces the vertical mixing to a negligible amount and eventually produces a two-layer stratified flow. The behavior is therefore quite different from a vertical submerged buoyant jet.

The mixing due to both plane and radial buoyant jets, as shown in Figure 3.4.1(b), will be discussed in this section.

3.4.1 Turbulent Surface Jet Mixing

Suppose there is a radial or plane momentum source located at the origin of an r - z coordinate system in the free surface, as shown in Figure 3.4.2. The steady jet flow produced is assumed turbulent so that the molecular transport quantities are neglected. With the usual boundary layer assumptions the continuity, horizontal momentum, and mass conservation equations for mean jet flow can be written as

$$\frac{1}{r^n} \frac{\partial(r^n u)}{\partial r} + \frac{\partial w}{\partial z} = 0 \quad , \quad (3.4.1)$$

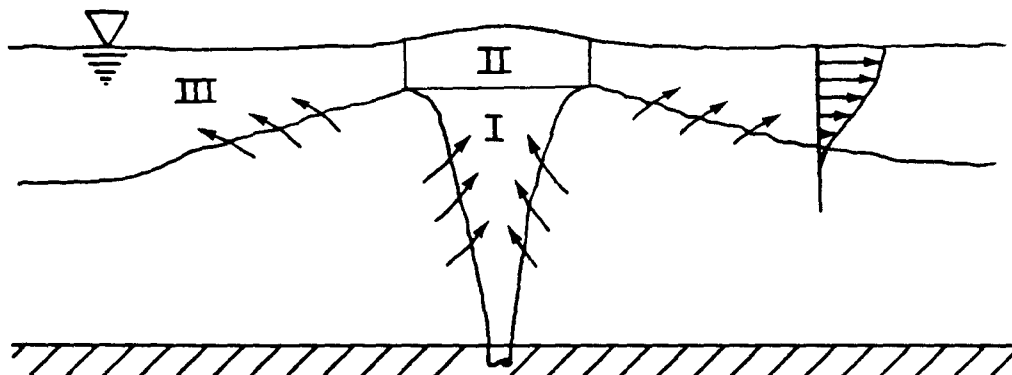


Figure 3.4.1(a) Flow regimes of an outfall discharge (soon after startup):
 I: Submerged buoyant jet flow,
 II: Surface transition,
 III: Surface buoyant jet flow.

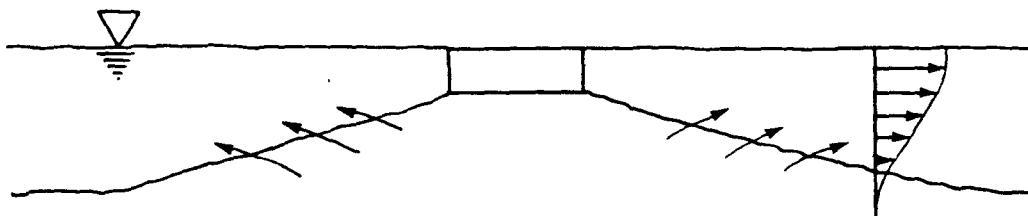


Figure 3.4.1(b) A surface buoyant jet flow model with finite dimension of discharge (soon after startup).

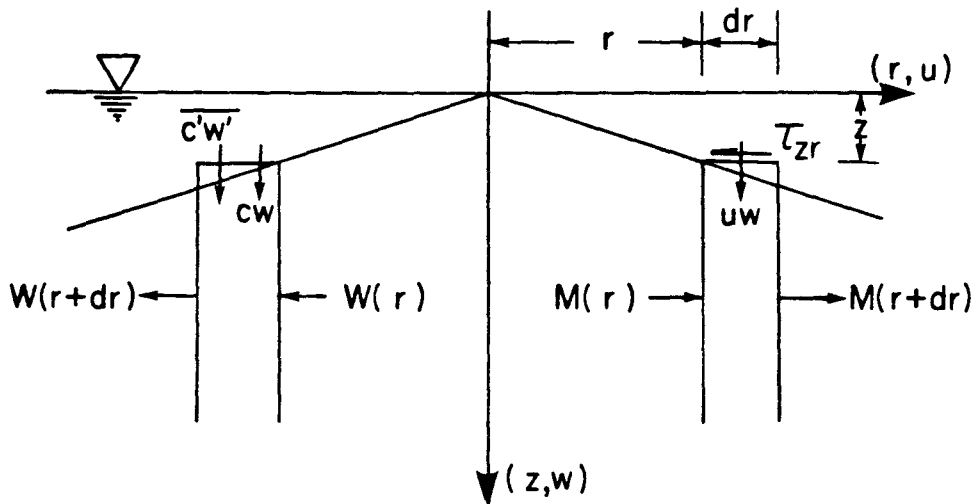


Figure 3.4.2 Point source surface jet nomenclature,

$$M(r) = \int_{\infty}^z \rho k_{on} r^n u^2 dz, \quad M(r+dr) = M(r) + dM(r)$$

$$W(r) = \int_{\infty}^z k_{on} r^n cw dz, \quad W(r+dr) = W(r) + dW(r).$$

$$u \frac{\partial u}{\partial r} + w \frac{\partial u}{\partial z} = \frac{\partial}{\partial z} \left(\frac{\tau_{zr}}{\rho} \right) \quad , \quad (3.4.2)$$

$$u \frac{\partial c}{\partial r} + w \frac{\partial c}{\partial z} = \frac{\partial}{\partial z} (W) \quad , \quad (3.4.3)$$

where u and w are the time-averaged velocities in the horizontal and the vertical direction, respectively; c is the relative mean temperature or mean density difference; τ_{zr} is the turbulent shear stress and W is the turbulent flux of c at horizontal position r and depth z , $n=0$ denotes the plane surface jet flow, and $n=1$ the radial surface jet flow. The ambient fluid is assumed infinitely deep.

Assume that the time-averaged horizontal velocity $u(r,z)$ has a similarity solution of the form

$$u(r,z) = u_m(r)f(\xi) \quad (3.4.4)$$

where the mean velocity at free surface $u(r,0) = u_m(r)$ and the dimensionless similarity variable $\xi = az/r$. The exact form of the maximum free surface velocity $u_m(r)$ can be derived from the condition of horizontal momentum conservation, namely that,

$$\int_0^\infty \rho k_{on} r^n u^2 dz = \frac{\rho_j k_{on} r^{n+1} u_m^2}{a} \int_0^\infty f^2(\xi) d\xi = \rho_j M \quad , (3.4.5)$$

where the initial kinematic momentum jet flux $M = k_{on} r_j^n h_j u_j^2$ and $k_{00} = 1$ for $n = 0$ and $k_{01} = 2\pi$ for $n = 1$ and the subscript j implies the initial jet values. Thus,

$$u_m(r) = \frac{J}{r^{(n+1)/2}} \quad , \quad (3.4.6)$$

where $J = \left\{ aM/k_{on} \int_0^\infty f^2(\xi) d\xi \right\}^{1/2}$ or simply in terms of the discharge jet dimensions and jet velocity u_j :

$$\frac{u_m(r)}{u_j} = \sqrt{\frac{a}{\int_0^\infty f^2(\xi) d\xi}} \frac{\sqrt{r_j^n h_j}}{r^{(n+1)/2}} \quad . \quad (3.4.7)$$

A Stokes' stream function can be derived from the Eq. (3.4.1),

$$u(r,z) = \frac{1}{r^n} \frac{\partial \psi}{\partial z} \quad , \quad (3.4.8)$$

$$w(r,z) = -\frac{1}{r^n} \frac{\partial \psi}{\partial r} \quad , \quad (3.4.9)$$

to give

$$\psi(r,z) = \frac{u_m(r) r^{n+1}}{a} F(\xi) \quad , \quad (3.4.10)$$

where $F(\xi) = \int_{\infty}^{\xi} f(\xi) d\xi$. Therefore the vertical mean velocity can be deduced as

$$w(r, z) = \frac{u_m(r)}{a} \left\{ \xi F'(\xi) - \frac{n+1}{2} F(\xi) \right\} \quad (3.4.11)$$

and the vertical gradient of the mean horizontal velocity as

$$\frac{\partial u(r, z)}{\partial z} = \frac{a u_m(r)}{r} F''(\xi) \quad (3.4.12)$$

where the prime denotes differentiation with respect to ξ .

Two unknown values of turbulent quantities in Eqs. (3.4.2) and (3.4.3), τ_{zr}/ρ and W , are assumed as

$$\frac{\tau_{zr}}{\rho} = - \overline{u'w'} = \epsilon_u \frac{\partial u}{\partial z} \quad (3.4.13)$$

$$W = \overline{c'w'} = - \epsilon_c \frac{\partial c}{\partial z} \quad (3.4.14)$$

by introducing two eddy viscosity terms, ϵ_u and ϵ_c , value primes denote fluctuations from the mean values. Following Prandtl-Tollmien's two assumptions are made for the two eddy viscosity terms:

$$\epsilon_u = \ell_u^2 \left| \frac{\partial u}{\partial z} \right|, \quad (3.4.15)$$

$$\epsilon_c = \ell_u \ell_c \left| \frac{\partial u}{\partial z} \right|, \quad (3.4.16)$$

where ℓ_u and ℓ_c are Prandtl's mixing length for the momentum and the tracer transfer,

$$\ell_u = c_u r \quad (3.4.17)$$

$$\ell_c = c_c r \quad (3.4.18)$$

in which c_u and c_c are two unknown coefficients. In short, Prandtl-Tollmien assumptions for two eddy viscosity terms are

$$\epsilon_u = K_u r^2 \left| \frac{\partial u}{\partial z} \right|, \quad (3.4.19)$$

$$\epsilon_c = K_c r^2 \left| \frac{\partial u}{\partial z} \right|, \quad (3.4.20)$$

where two unknown numbers K_u and K_c are related to $K_u = c_u^2$ and $K_c = c_u c_c$.

An alternate approach is, following Prandtl-Görtler (1942), to assume that

$$\epsilon_u = \chi_u b_u(r) u_m(r) \quad , \quad (3.4.21)$$

$$\epsilon_c = \chi_c b_c(r) u_m(r) \quad , \quad (3.4.22)$$

where $b_u(r)$ and $b_c(r)$ are two mixing thickness scales that are defined as

$$b_u(r) = k_u r \quad (3.4.23)$$

$$b_c(r) = k_c r \quad , \quad (3.4.24)$$

implying that the eddy viscosity terms are expressed as

$$\epsilon_u = K_u r u_m(r) \quad (3.4.25)$$

$$\epsilon_c = K_c r u_m(r) \quad , \quad (3.4.26)$$

where two unknown numbers K_u and K_c are related to $K_u = \chi_u k_u$ and $K_c = \chi_c k_c$ in Prandtl-Görtler assumption.

Substituting the Prandtl-Tollmien assumptions, Eqs. (3.4.13) and (3.4.19), into the integral form of horizontal momentum equation,

$$uw + \frac{1}{r^n} \frac{\partial}{\partial r} \int_{\infty}^z r^n u^2 dz - \frac{\tau_{zr}}{\rho} = 0 \quad , \quad (3.4.27)$$

given the ordinary differential equation,

$$F''^2(\xi) - F(\xi)F'(\xi) = 0 \quad , \quad (3.4.28)$$

where $a = \sqrt[3]{\frac{n+1}{2K_u}}$ from derivation of Eq. (3.4.28). With boundary conditions at the free surface of $u(r,0) = u_m(r)$, $w(r,0) = 0$ and at depth $u(r,\infty) = w(r,\infty) = 0$, i.e. $F'(0) = 1$ and $F(0) = F(\infty) = F'(\infty) = 0$, the similarity profile for mean velocity is obtained by integrating Eq. (3.4.28) as shown in Table 3.4.1.

The mean tracer distribution of the turbulent jet flow is found from the self-similar distribution assumed to be of the form

$$c(r,z) = c_m(r)\theta(\xi) \quad , \quad (3.4.29)$$

where the longitudinal tracer distribution at the free surface $c(r,0) = c_m(r)$. The total amount of tracer loss through the free surface is assumed very small so that the total integral amount of tracer distribution should be conserved at each radial location r , i.e.

Table 3.4.1 Prandtl-Tollmien similarity solutions of turbulent surface jet flows.

ξ	$\frac{u(r,z)}{u_m(r)} = F'(\xi)$	$F(\xi)$	$\frac{aw(r,z)}{u_m(r)} = \xi F'(\xi) - \frac{n+1}{2} F(\xi)$	
			Plane Surface Jet $n = 0$	Radial Surface Jet $n = 1$
0.0	1.000	0.000	0.000	0.000
0.1	0.979	0.100	0.048	-0.002
0.2	0.940	0.200	0.088	-0.012
0.3	0.897	0.287	0.126	-0.018
0.4	0.842	0.370	0.152	-0.033
0.5	0.782	0.450	0.166	-0.059
0.6	0.721	0.520	0.173	-0.087
0.7	0.660	0.590	0.167	-0.128
0.8	0.604	0.650	0.158	-0.167
0.9	0.538	0.710	0.129	-0.226
1.0	0.474	0.760	0.094	-0.286
1.1	0.411	0.810	0.047	-0.358
1.2	0.357	0.860	-0.002	-0.432
1.3	0.300	0.880	-0.050	-0.490
1.4	0.249	0.910	-0.106	-0.561
1.5	0.200	0.930	-0.165	-0.630
1.6	0.165	0.950	-0.211	-0.686
1.7	0.125	0.960	-0.268	-0.748
1.8	0.095	0.965	-0.312	-0.794
1.9	0.067	0.970	-0.358	-0.843
2.0	0.046	0.980	-0.398	-0.888
2.1	0.030	0.985	-0.430	-0.922
2.2	0.020	0.990	-0.451	-0.946
2.3	0.009	0.995	-0.477	-0.974
2.4	0.000	1.000	-0.500	-1.000

$$\int_{\infty}^0 k_{on} r^n cu dz = \frac{k_{on} r^{n+1} c_m(r) u_m(r)}{a} \int_{\infty}^0 f(\xi) \theta(\xi) d\xi = c_j Q \quad , \quad (3.4.30)$$

where c_j is the initial jet tracer concentration and Q is the jet discharge rate, $Q = k_{on} r_j^n h_j u_j$. Therefore, the maximum tracer distribution is decaying according to

$$\frac{c_m(r)}{c_j} = \frac{\sqrt{a \int_{\infty}^0 f^2(\xi) d\xi}}{\int_{\infty}^0 f(\xi) \theta(\xi) d\xi} \cdot \sqrt{\frac{r_j^n h_j}{r^{n+1}}} \quad . \quad (3.4.31)$$

Substituting the Prandtl-Tollmien assumption Eq. (3.4.14) with Eq. (3.4.20) in the integral form of tracer equation,

$$cw + \frac{1}{r^n} \frac{\partial}{\partial r} \int_{\infty}^z r^n cu dz - W = 0 \quad , \quad (3.4.32)$$

gives

$$\frac{K_c}{K_u} F''(\xi) \theta'(\xi) - F(\xi) \theta(\xi) = 0 \quad . \quad (3.4.33)$$

By the aid of Eq. (3.4.28), Eq. (3.4.33) can be written as

$$\frac{K_c}{K_u} \frac{\theta'(\xi)}{\theta(\xi)} = \frac{F(\xi)}{F''(\xi)} = \frac{F'(\xi)}{F'(\xi)} \quad , \quad (3.4.34)$$

Integrating Eq. (3.4.34) providing with boundary conditions $\theta(0) = 1$ and $F'(0) = 1$ from $c_m(r) = c(r,0)$ and $u_m(r) = u(r,0)$ gives the self-similar distribution $\theta(\xi)$ for mean tracer as a power function of mean velocity distribution,

$$\theta(\xi) = [F'(\xi)]^{K_c/K_u} = f^{K_c/K_u}(\xi) \quad . \quad (3.4.35)$$

Thus, the mean tracer distribution is expressed as

$$\frac{c(r,z)}{c_j} = \frac{\sqrt{a \int_{\infty}^0 f^2(\xi) d\xi}}{\int_{\infty}^0 f(\xi) \theta(\xi) d\xi} \frac{\sqrt{r_j^n h_j} f^{K_c/K_u}(\xi)}{r^{\frac{n+1}{2}}} \quad . \quad (3.4.36)$$

Similarly, using the Prandtl-Görtler assumptions Eqs. (3.4.13) and (3.4.14) with Eqs. (3.4.25) and (3.4.26) in the integral form of horizontal momentum Eq. (3.4.27), gives

$$2F(\xi)F'(\xi) + F''(\xi) = 0 \quad (3.4.37)$$

with $a = \sqrt{\frac{n+1}{4K_u}}$. The tracer equation (3.4.32) becomes

$$\theta'(\xi) + 2 \frac{K_u}{K_c} F(\xi)\theta(\xi) = 0 \quad (3.4.38)$$

Integrating Eq. (3.4.37) twice with boundary condition $F'(0) = 1$ and $F(0) = 0$, gives

$$F(\xi) = \tanh \xi \quad . \quad (3.4.39)$$

The similarity distribution of a mean horizontal velocity in dimensionless form is therefore

$$\frac{u(r,z)}{u_m(r)} = F'(\xi) = \text{sech}^2 \xi \quad (3.4.40)$$

From Eqs. (3.4.37) and (3.4.38)

$$\frac{\theta'(\xi)}{\theta(\xi)} = -2 \frac{K_u}{K_c} F = \frac{K_u}{K_c} \frac{F''(\xi)}{F'(\xi)} \quad . \quad (3.4.41)$$

Integration of Eq. (3.4.41) with boundary conditions $\theta(0) = F'(0) = 1$ gives

$$\theta(\xi) = F'^{K_u/K_c}(\xi) = [\text{sech}^2(\xi)]^{K_u/K_c} \quad . \quad (3.4.42)$$

Thus, the mean tracer distribution is expressed as

$$\frac{c(r,z)}{c_j} = \frac{\sqrt{a \int_{-\infty}^0 f^2(\xi) d\xi}}{\int_{-\infty}^0 f(\xi) \theta(\xi) d\xi} \frac{\sqrt{r_j^n h_j}}{r^{\frac{n+1}{2}}} \operatorname{sech}^{2K_u/K_c}(\xi) \quad (3.4.43)$$

The two mean tracer distributions, Eqs. (3.4.35) and (3.4.42), derived from the Prandtl-Tollmien and Prandtl-Görtler assumptions, therefore do not necessarily coincide with the mean horizontal velocity distribution $f = F'(\xi)$ except when two mixed coefficients K_u and K_c are equal. As shown in Figure 3.4.3 in this case the profiles of mean horizontal velocity and mean tracer distribution derived from the two assumptions give values close to each other.

3.5 Dimensional Analysis

The advantage of using kinematic fluxes instead of the actual physical dimensions to describe the general time-mean properties of a submerged buoyant jet has been demonstrated by List and Imberger (1973). The same dimensional methods may be used to solve the problem of a horizontal turbulent surface buoyant jet.

3.5.1 Radial Surface Buoyant Jet

As shown in Figure 3.5.1 a radial surface buoyant jet discharges a fluid of uniform density ρ_j and temperature T_j at the free surface of a large body of water of density ρ_a

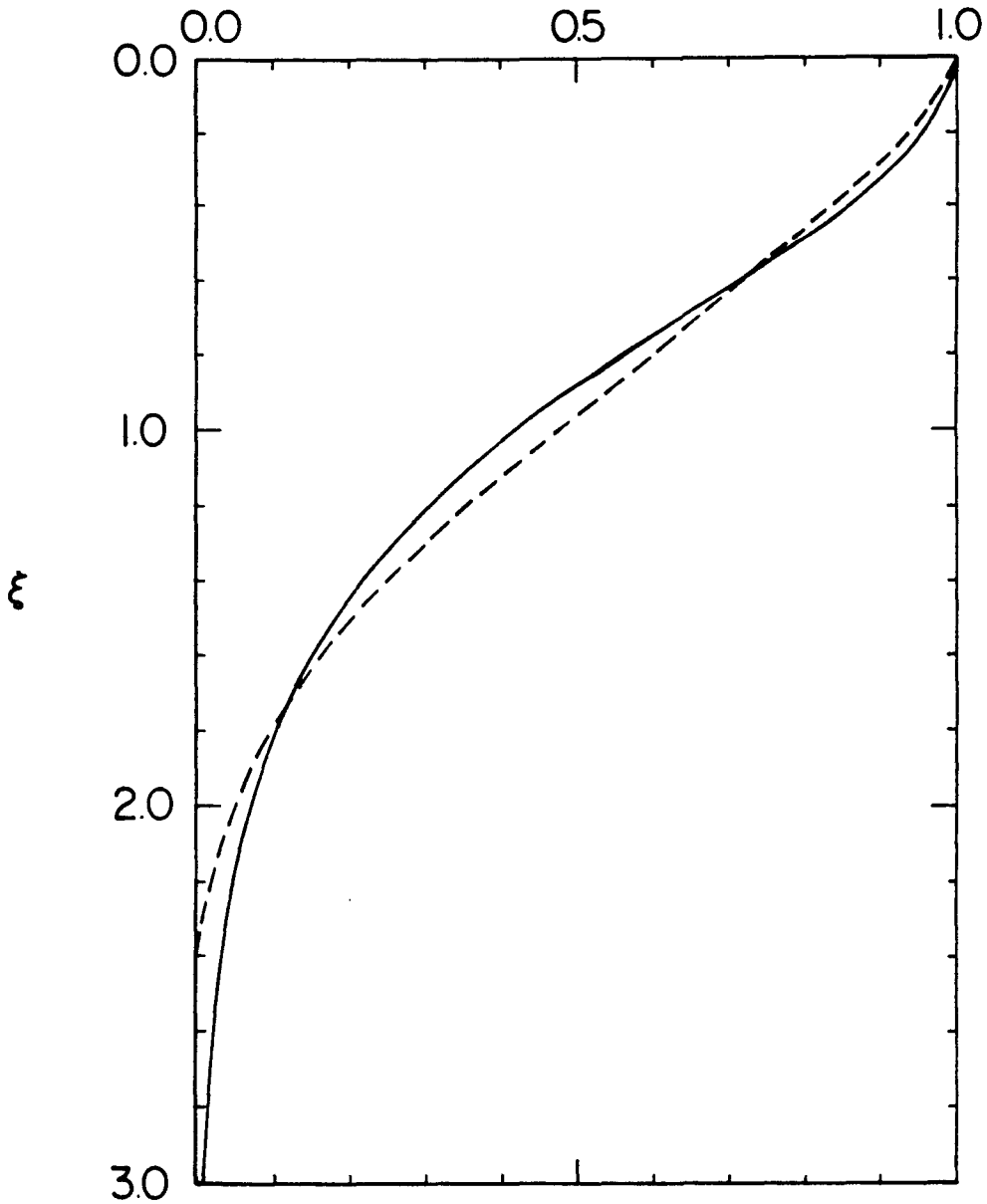
$$F'(\xi), \theta(\xi)$$


Figure 3.4.3 Two self-similar profiles of mean horizontal velocity, $F'(\xi) = u(r, z)/u_m(r)$, and mean tracer when $K_u = K_c$, $\theta(\xi) = c(r, z)/c_m(r)$. Dash line indicates the solution derived from the Prandtl-Tollmien assumption and solid line from the Prandtl-Görtler assumption.

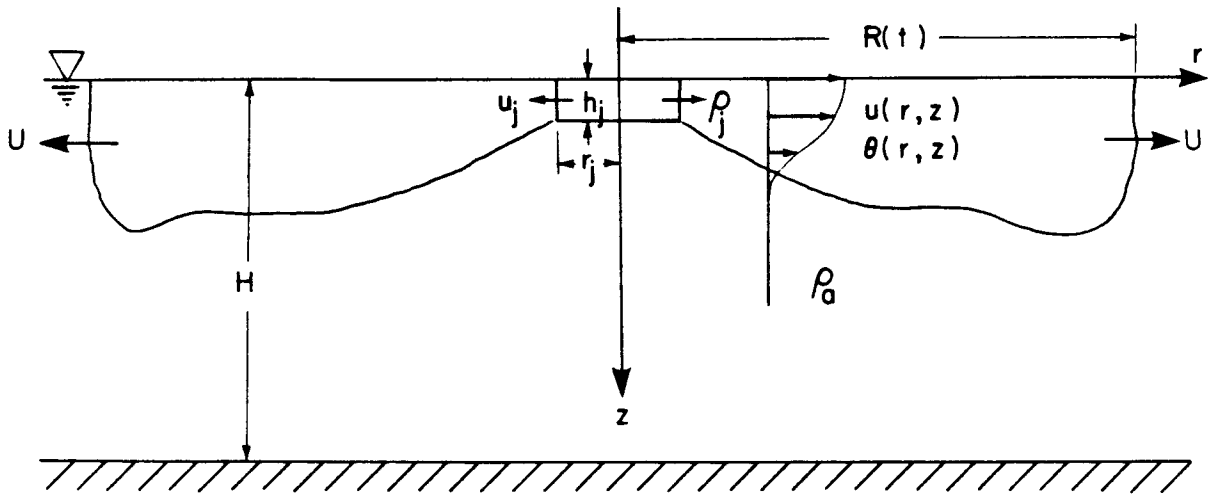


Figure 3.5.1 Sketch of a radial surface buoyant jet.

and temperature T_a . The jet originates from a circular slot of radius r_j and thickness h_j . For the case of stationary ambient fluid and when surface tension is neglected, there are $(8+i)$ independent variables to describe this buoyant jet flow so that any dependent variable ϕ is given by

$$\phi = \phi(x_i, r_j, h_j, u_j, \rho_a, \rho_j, g, \nu, H) \quad , \quad (3.5.1)$$

where H is the depth of the ambient fluid, x_i are the space or the time independent variables which can be r, z, t , or r and z , or only t , ν is the kinematic viscosity of the discharging fluid. It is assumed that the density difference between the discharged fluid and the ambient fluid is sufficiently small in comparison to some reference density, say ρ_j , that the density difference is only important in the body force term of the jet flow.

Now, four independent variables r_j , h_j , u_j , and $g\Delta = g(\rho_a - \rho_j)/\rho_j$ are transformed into three kinematic flux variables, Q , M , B , and one physical dimension of the jet, either r_j or h_j , so that

$$\phi = \phi(x_i, Q, M, B, r_j \text{ or } h_j, H, \nu) \quad , \quad (3.5.2)$$

in which the volume flux $Q = 2\pi r_j h_j u_j$, the momentum flux $M = Q u_j$ and the buoyancy flux $B = g\Delta Q$. The dimensions corresponding to each flux are respectively as L^3/T , L^4/T^2 and L^4/T^3 . There are three length scales associated with any combination of two

flux variables, as given in Table 3.5.1. Each length scale has its own meaning. For example, l_{MB} is the length scale located where the momentum flux produced by the buoyancy will begin to dominate the initial discharge momentum flux M . Thus, two regimes of flow, which are dominated respectively by the momentum flux M and by the buoyancy flux B , are roughly separated at a distance from the origin of order l_{MB} . Other time scales and velocity scales can also be derived from the similar combinations of any two fluxes, as given in Table 3.5.1.

The densimetric Froude number Fr (or the inverse square root of Richardson number Ri) of the buoyant jet flow is defined as the ratio of two length scales, l_{MB} and l_{QM} , i.e.

$$Fr = \frac{l_{MB}}{l_{QM}} = \frac{M^{5/4}}{QB^{1/2}} = \frac{u_j}{\sqrt{g\Delta\sqrt{2\pi r_j h_j}}} \quad (3.5.3)$$

Similarly, it is found that the ratio of any other two length scales, time scales, or velocity scales also forms a power of Froude number Fr .

To characterize the turbulent flow two Reynolds numbers are defined. The first is the Reynolds number of the jet flow Re_j ,

$$Re_j = \frac{u_{QM} l_{QM}}{\nu} = \frac{u_{MB} l_{MB}}{\nu} = \frac{M^{1/2}}{\nu} = \frac{u_j \sqrt{2\pi r_j h_j}}{\nu} \quad (3.5.4)$$

Table 3.5.1 Length, time, and velocity scales of a radial surface buoyant jet.

Fluxes Items Scales	Combinations of		
	Q and M	M and B	Q and B
Length scale	$\ell_{QM} = \frac{Q}{M^{1/2}}$ $= (2\pi r_j h_j)^{1/2}$	$\ell_{MB} = \frac{M^{3/4}}{B^{1/2}}$ $= \frac{(2\pi r_j h_j)^{1/4} u_j}{(g\Delta)^{1/2}}$	$\ell_{QB} = \frac{Q^{3/5}}{B^{1/5}}$ $= \frac{(2\pi r_j h_j u_j)^{2/5}}{(g\Delta)^{1/5}}$
Time scale	$t_{QM} = \frac{Q^2}{M^{3/2}}$ $= \frac{(2\pi r_j h_j)^{1/2}}{u_j}$	$t_{MB} = \frac{M}{B}$ $= \frac{u_j}{g\Delta}$	$t_{QB} = \frac{Q^{4/5}}{B^{3/5}}$ $= \frac{(2\pi r_j h_j u_j)^{1/5}}{(g\Delta)^{3/5}}$
Velocity scale	$u_{QM} = \frac{M}{Q}$ $= u_j$	$u_{MB} = \frac{B^{1/2}}{M^{1/4}}$ $= (g\Delta)^{1/2} (2\pi r_j h_j)^{1/4}$	$u_{QB} = \frac{B^{2/5}}{Q^{1/5}}$ $= (g\Delta)^{2/5} (2\pi r_j h_j u_j)^{1/5}$

which indicates the turbulence level in the jet flow regime and the second is the Reynolds number of the plume flow Re_p ,

$$Re_p = \frac{u_{QB} l_{QB}}{\nu} = \frac{Q^{2/5} B^{1/5}}{\nu} = \frac{(g\Delta)^{1/5} (2\pi r_j h_j u_j)^{3/5}}{\nu}, \quad (3.5.5)$$

which indicates the turbulence level in the plume region. The ratio of these two Reynolds numbers is also a function of the Froude number,

$$\frac{Re_j}{Re_p} = \frac{M^{1/2}}{Q^{2/5} B^{1/5}} = Fr^{2/5}. \quad (3.5.6)$$

This implies that Froude number and one or the other Reynolds number is necessary to model the whole regime of buoyant jet flow. Different levels of turbulence in the plume flow downstream may result depending on the jet Reynolds number, which is generally neglected in jet flows since it is very large.

From Buckingham π -theorem $(7 + i) - 2 = (5 + i)$ dimensionless terms can be formed to describe the flow problem given in Eq. (3.5.2). The first two π -terms are the densimetric Froude number Fr and the jet or the plume Reynolds number. There is no difference in choosing r_j or h_j to be normalized by the length scale l_{QM} , since the resultant dimensionless terms are reciprocal to each other, i.e.

$$\frac{r_j}{\ell_{QM}} = \sqrt{\frac{r_j}{2\pi h_j}} \quad (3.5.7)$$

and

$$\frac{h_j}{\ell_{QM}} = \sqrt{\frac{h_j}{2\pi r_j}} \quad , \quad (3.5.8)$$

and describe the aspect ratio r_j/h_j of the jet. One more π -term is the relative depth of ambient fluid H/h_j . The other $(1+i)$ terms can be formulated by suitable normalization with the length, time, or velocity scales an appropriate choice depending on the problem being considered. Thus, Eq. (3.5.2) can be rewritten in dimensionless form,

$$\phi^* = \phi^*(x_i^*, Fr, Re, r_j/h_j, H/h_j) \quad , \quad (3.5.9)$$

in which x_i^* and ϕ^* denote the dimensionless independent and dependent variables, the Reynolds number Re can be Re_j or Re_p .

Consider the initiation flow for a radial buoyant surface jet. The independent variable x_i in this case is time t and the dependent variable is $R(t)$, the growth history of the radial tip. The dimensionless equation becomes

$$R^*(t^*) = \phi(t^*, Fr, Re, r_j/h_j, H/h_j) \quad , \quad (3.5.10)$$

where R^* and t^* are suitable normalized values of $R(t)$ and t .

When the dimensionless length $R(t)/\ell_{MB}$ or the dimensionless time t/t_{MB} is much less than unity, there is a region of starting jet flow, i.e.

$$R(t) = M^{1/4} t^{1/2} \phi(Fr, Re, r_j/h_j, H/h_j) \quad (3.5.11)$$

Similarly, there is a region of inertial plume flow,

$$R(t) = B^{1/4} t^{3/4} \phi(Fr, Re, r_j/h_j, H/h_j) \quad (3.5.12)$$

when $t_{MB} < t < t_{Bv}$ or $R_{MB} < R(t) < R_{Bv}$. Subsequently there is a region of viscous plume flow

$$R(t) = \left(\frac{g\Delta Q^3}{\nu} \right)^{1/8} t^{1/2} \phi(Fr, Re, r_j/h_j, H/h_j) \quad (3.5.13)$$

when $t_{Bv} < t$. All the coefficients for starting jets, inertial plumes, and viscous plume flows are functions of the densimetric Froude number, a Reynolds number, the aspect ratio and the relative depth of ambient fluid. The limiting values for two starting plume coefficients were given in Sections 3.2 and 3.3 respectively as c_{011} and b_{011} . The time scale t_{Bv} and the length scale R_{Bv} are proportional to the values t_1 and R_1 given in Table 3.1.2.

3.5.2 Surface and Submerged Horizontal Buoyant Jets

The derivations of the dimensionless parameter in Subsection 3.5.1 can be extended to the case of a plane surface buoyant jet and to plane or radial submerged buoyant jets. The latter two cases involve the discharging of a fluid into a linearly density-stratified environment at a neutral density level. In these cases the general definitions for the volume flux Q , the momentum flux M , and the buoyancy flux B are given in Table 3.5.2. The general form of Eq. (3.5.2) can be written as

$$\phi = \phi(x_i, Q, M, B, \nu, H, nr_j) \quad . \quad (3.5.14)$$

In the plane jet case there is one less independent variable r_j , since the coordinate system can be shifted to eliminate the jet length r_j .

Just as found in the previous section, there are three possible starting flow regimes for the initiation flow, viz. a starting jet flow,

$$R(t) \sim M^{\frac{1}{n+3}} t^{\frac{2}{n+3}} \quad (3.5.15)$$

a starting inertial plume flow,

Table 3.5.2 Definitions of volume, momentum, and buoyancy fluxes for a horizontal surface or submerged buoyant plane or radial jet.

Items Fluxes	Definition	Dimensions
Volume flux Q	$2^i u_j h_j (2\pi r_j)^n$	$\frac{L^{n+2}}{T}$
Momentum flux M	$2^i u_j^2 h_j (2\pi r_j)^n$	$\frac{L^{n+3}}{T^2}$
Buoyancy flux B	$(g\Delta_i)^{\frac{1}{i+1}} 2^i u_j h_j (2\pi r_j)^n$	$\frac{\frac{(n+1)(i+1)+2}{i+1} L}{\frac{i+3}{T^{i+1}}}$

$$R(t) \sim_B \frac{1}{(n+1)(i+1)+2} \frac{i+3}{t^{(n+1)(i+1)+2}} \quad (3.5.16)$$

and a starting viscous plume flow,

$$R(t) \sim \left(\frac{g\Delta_i Q^{i+3}}{\nu} \right)^{\frac{1}{(n+1)(i+3)+2}} \frac{i+4}{t^{(n+1)(i+3)+2}} \quad (3.5.17)$$

Two time scales, t_{MB} and t_{Bv} , and two length scales, R_{MB} and R_{Bv} , can be derived from the above three equations (3.5.15), (3.5.16), and (3.5.17) to distinguish the three regimes of starting flow and steady flow, as shown in Figure 3.5.2.

However, not all three regimes necessarily exist in a starting flow or in a steady buoyant jet flow. For example, when the ratio of t_{Bv}/t_{MB} is very small, there is no starting inertial plume regime. Similarly, there is no inertial plume regime, when R_{Bv}/R_{MB} is very small.

3.5.3 Dynamic Collapse

The dynamic collapse of a homogeneous mass in a linearly density-stratified environment ($i=1$) or for the squatting of a liquid column in a uniform environment ($i=0$) may be similarly described. There are three flow regimes as shown in Figure 3.5.3. There is an initial stage, a principal flow stage, and a final spreading stage. Two time scales,

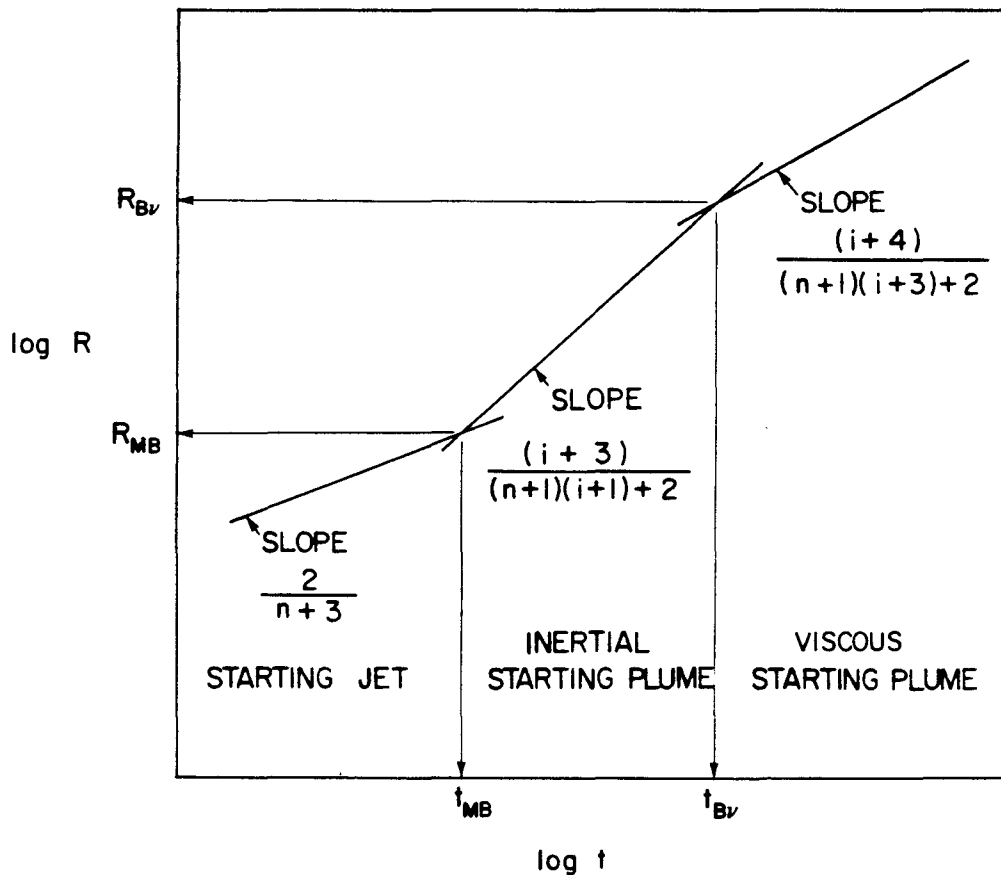


Figure 3.5.2 Three regimes of starting surface or submerged buoyant jet flow.

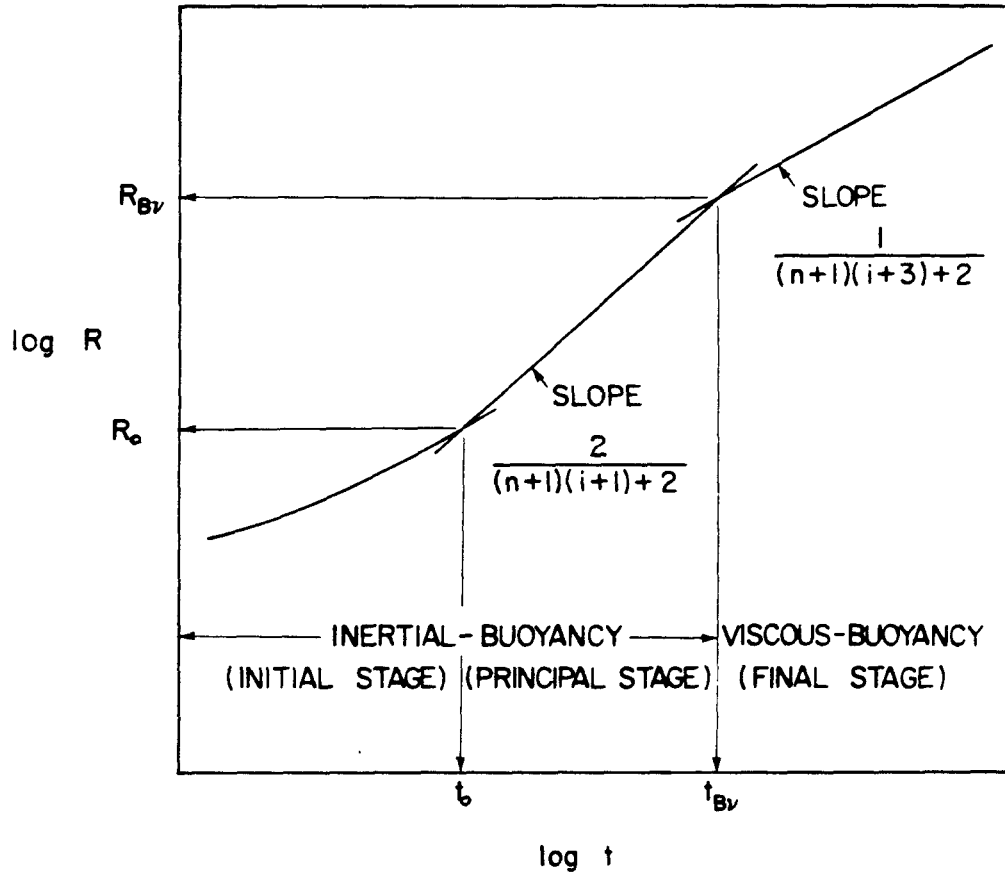


Figure 3.5.3 Three stages of dynamic collapse flows.

$t_o = R_o / \sqrt{g\Delta_1 h_o^{i+1}}$ and t_{Bv} , and two length scales R_o and R_{Bv} , can be developed to distinguish the three regimes although as before, not all three regimes necessarily exist. For example, when the ratio of R_{Bv} to R_o (or t_{Bv} to $t_o = R_o / \sqrt{g\Delta_1 h_o^{i+1}}$) is rather small, there is no principal stage.

The relationship of R_{Bv} and t_{Bv} to R_1 and t_1 , which were given in Tables 3.1.2 and 3.1.5, are given in Table 3.5.3 for $i=0$ and in Table 3.5.4 for $i=1$. The limiting values of two ratios, R_{Bv}/R_1 and t_{Bv}/t_1 , from the long wave solutions are also given.

3.5.4 Radial Surface Buoyant Jet in a Cross Current

The above analysis can be extended to describe spreading in a crossflow. If U is the magnitude of horizontal current velocity, and x is the downstream distance from the source then substituting t for x/U in Eqs. (3.5.11) and (3.5.12) gives the width of (inertial) surface wastewater field, $y(x)$,

$$y(x) \sim M^{1/4} \left(\frac{x}{U} \right)^{1/2} \quad (3.5.18)$$

and

$$y(x) \sim B^{1/4} \left(\frac{x}{U} \right)^{3/4} \quad (3.5.19)$$

The location of the upstream edge from the center of a radial buoyant jet x_e , can be derived from balancing the

Table 3.5.3 The ratio of R_{Bv} to R_1 and t_{Bv} to t_1 when $i = 0$.

ratio		$\frac{R_{Bv}}{R_1}$	$\frac{t_{Bv}}{t_1}$
		n	m
Plane currents $n = 0$	Instantaneous release $m = 0$	$\left(\frac{b_{000}^{10}}{c_{000}^3}\right)^{1/7} = 0.910$	$\left(\frac{b_{000}}{c_{000}}\right)^{15/7} = 0.334$
	Continuous discharge $m = 1$	$\frac{b_{010}^5}{c_{010}^4} = 0.133$	$\left(\frac{b_{010}}{c_{010}}\right)^5 = 0.106$
Radial currents $n = 1$	Instantaneous release $m = 0$	$\left(\frac{b_{001}^4}{c_{001}}\right)^{1/3} = 0.626$	$\left(\frac{b_{001}}{c_{001}}\right)^{8/3} = 0.174$
	Continuous discharge $m = 1$	$\frac{b_{011}^3}{c_{011}^2} = 0.143$	$\left(\frac{b_{011}}{c_{011}}\right)^4 = 0.0523$

Table 3.5.4 The ratio of R_{Bv} to R_1 and t_{Bv} to t_1 when $i=1$.

n	ratio m	$\frac{R_{Bv}}{R_1}$	$\frac{t_{Bv}}{t_1}$
		Plane currents n = 0	Instantaneous release m = 0
	Continuous discharge m = 1	$\frac{b_{110}^6}{c_{110}^5} = 0.0874$	$\left(\frac{b_{110}}{c_{110}}\right)^6 = 0.124$
Radial currents n = 1	Instantaneous release m = 0	$\left(\frac{b_{101}^{10}}{c_{101}^3}\right)^{1/7} = 0.407$	$\left(\frac{b_{101}}{c_{101}}\right)^{30/7} = 0.0469$
	Continuous discharge m = 1	$\frac{b_{111}^4}{c_{111}^3} = 0.0816$	$\left(\frac{b_{111}}{c_{111}}\right)^6 = 0.0325$

starting flow velocity with the ambient current velocity, to give

$$x_e = \frac{1}{2} d^2 \frac{M^{1/2}}{U} \quad (3.5.20)$$

and

$$x_e = \left(\frac{3}{4} c^{4/3} \right)^3 \frac{B}{U^3} \quad , \quad (3.5.21)$$

in which d is the starting jet coefficient $R(t)/M^{1/4} t^{1/2}$ in Eq. (3.5.11) and c is the inertial starting plume coefficient $R(t)/B^{1/4} t^{3/4}$ in Eq. (3.5.12).

From Eqs. (3.5.15), (3.5.16), and (3.5.17) similar relations can also be derived for the internal spreading of a submerged wastewater field ($i=1$).

CHAPTER 4

EXPERIMENTAL STUDIES AND APPARATUS

4.0 Introduction

Many experimental studies have been made on the unsteady phase of plane gravitation-driven spreading flows, and a systematic review of previous studies on these subjects was presented in Chapter 2. The theoretical results developed in Chapter 3 will be compared with these previous experimental results in Chapter 6.

In this chapter experiments on radial surface buoyant jets are described. Apparently no previous experiments of this type have been performed, at least none seem to be described in the research literature. The experiments to be described were performed to determine the effect of initial jet momentum on the jet mixing by evaluating the density distributions. Conductivity measurements will be described in which a periodic radial spreading motion develops, as predicted by the analysis in Chapter 3. Surface buoyant jet flows were also performed in which the buoyant surface flow field prevailing in a steady cross current was measured.

4.1 Surface Buoyant Jet4.1.1 Experimental Set-Up

The experiments were conducted in a square tank (4.0 meters by 4.0 meters) one meter deep filled with tap

water to a depth of 75 centimeters. A half-radial buoyant jet flow was generated by discharging blue-dyed buoyant water from a half-cylindrical chamber combining flow-straightening rings a half-circular slot 9.962 cm in radius and 0.3175 cm wide (see Figure 4.1.1 for details). A constant head tank was used to provide the pressure necessary to drive the radial jet and a calibrated precision bore flow meter (tube number B6-27-10/27 manufactured by Fischer & Porter Corporation) was used to regulate the flow rate with an accuracy of 1%. Another flow meter was connected to a drain pump and was set to a flow rate equal to the discharge simultaneously in order to keep the free surface at a constant depth during the experiment. The overall experimental set-up is shown in Figure 4.1.2.

Before running each experiment, the effluent fluid was mixed well and cooled to a temperature close to that of the tank water. Both temperatures of the discharging fluid, and tank water were checked with a thermometer (graduated in 0.1°C intervals and read to $\pm 0.02^\circ\text{C}$).

4.1.2 Density and Dilution Measurements

The discharged fluid was a mixture of tap water, methanol, sodium chloride (Food grade 999 salt supplied by Morton Salt Company) and a small amount of blue dye (blue concentrate supplied by 7-K Color Corp) for flow visualization. The sodium chloride was the tracer. The concentration change due to mixing was measured by a calibrated conductivity probe

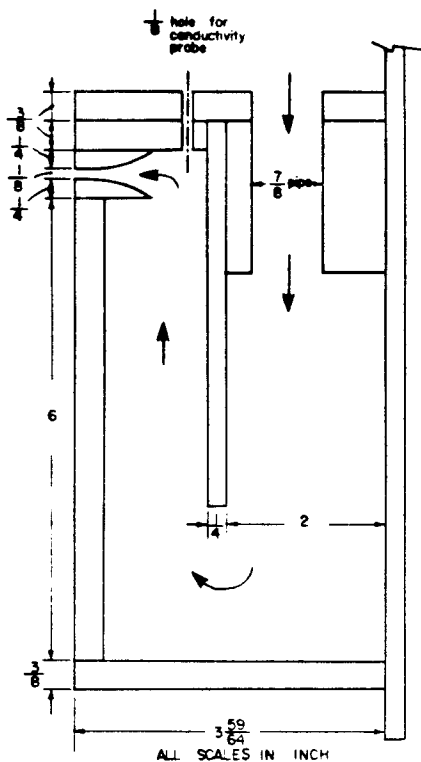


Figure 4.1.1 Cross section of the half-radial discharging box.

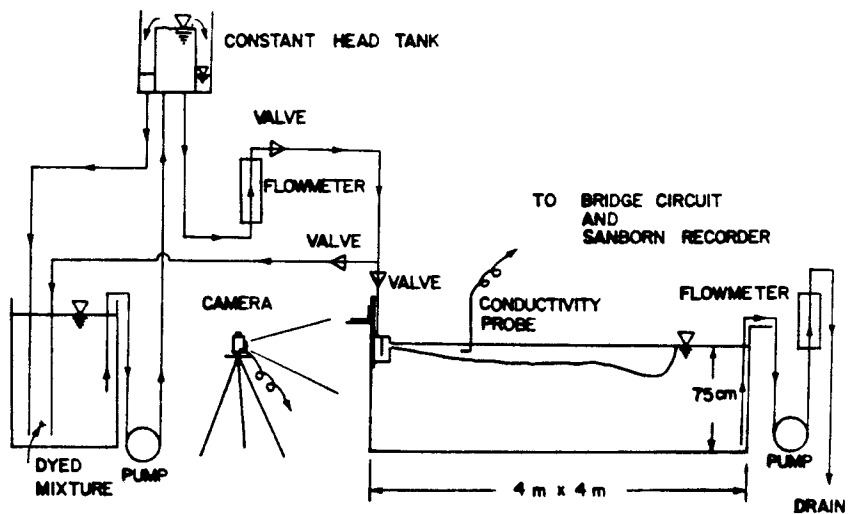


Figure 4.1.2 Overall experimental set-up for the half-radial surface buoyant jet.

(shown in Figure 4.1.3), forming part of a Wheatstone bridge circuit. The response of concentration change was measured as a conductivity change, which was recorded on a strip chart via a Sanborn analog recorder (Model 150).

The conductivity probe was mounted on a carriage, and could be moved vertically with an accuracy to 0.01 cm and radially to 0.10 cm. The probe electrodes were cleaned regularly and platinized using a platinum chloride solution. The probe was immersed in distilled water when not in use.

Before experiments were performed, the values of specific gravity of both the effluent and the tank water were measured by a specific gravity hydrometer (specified as ASTM 151H) in a graduated plastic cylinder (1000 c.c.). The accuracy of the specific gravity measured by hydrometer is within ± 0.0002 . A calibration curve was plotted for the conductivity probe by diluting the effluent fluid with the tap water in the tank (in a series of proportion of 1/2, 1/4, 1/8, 1/16, 1/32...). A typical calibration curve for the conductivity probe is shown in Figure 4.1.4.

4.1.3 Photographic Equipment

Side-view photographs of the discharge flow were taken with a Nikon F camera equipped with a 17 mm lens and mounted on a tripod in front of glass-side wall of tank. The camera was equipped with a motor drive which was connected via a cable to the timer of the Sanborn recorder, so that the strip

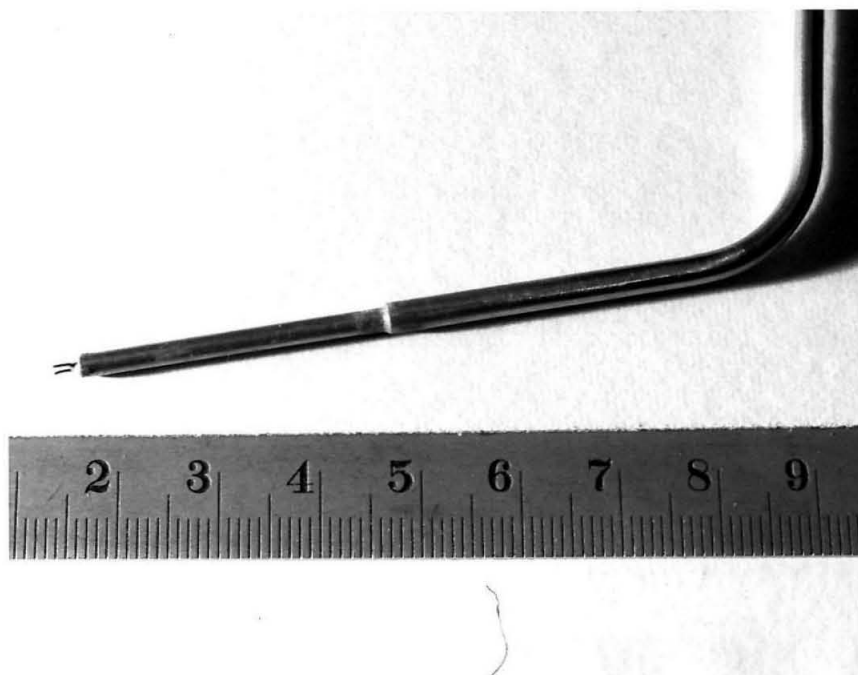


Figure 4.1.3 Photograph of a conductivity probe.

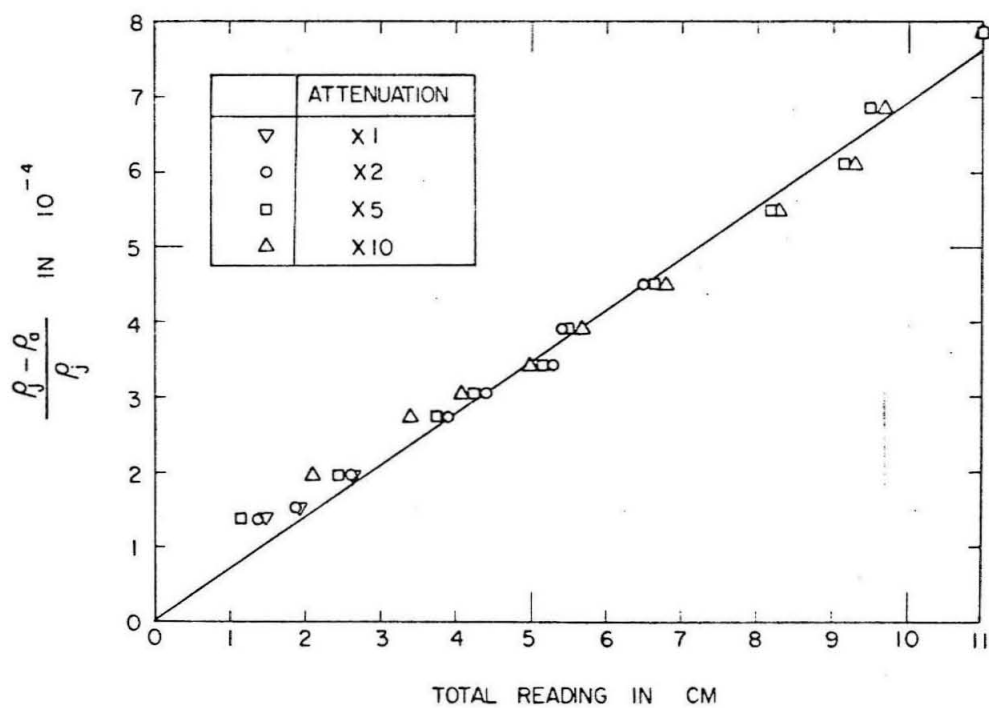


Figure 4.1.4 Typical calibration curve of conductivity probe (Run No. 10/27/77).

chart was marked as each photograph was taken. The photographs were scales from a projected image of the film negative using the known dimensions of the discharge box.

4.2 Radial Surface Heated and Buoyant Jets

4.2.1 General Experimental Set-Up

Two series of radial jet experiments were performed in a rectangular recirculating flow basin. The first set was for a heated radial surface jet in a stagnant environment. The second was set for a buoyant radial surface jet in a uniform steady current.

The test basin (36 feet long, 20 feet wide, and about 16 inches deep) is described in detail in Koh *et al.* (1974). The bottom of the basin is a uniform white sand (median diameter 0.8 mm) and for the experiments it was leveled to within ± 1 mm of horizontal by use of a grader rolling on steel rails at each side of the tank. The recirculation system consists of two pumps which allow the simulation of a wide range of current speeds. The average current speed was measured by timing cross-shaped lucite drogues (1 inch high and 2 inches long) while traveling a known distance in the tank. Five manifolds in both ends of basin were adjusted to guarantee the horizontal uniformity of the cross current. Two swimming pool skimmers were used to clean the free surface film from the water in the basin.

The general set-up for the radial surface heated jet experiments is shown in Figure 4.2.1. The flow injection system is essentially similar to that for the half-radial surface buoyant jet experiments shown in Figure 4.1.2, except an electrical heater was included to provide hot water at a constant temperature at the circular slot jet (7.62 cm radius and 0.3175 cm thick) generating the radial flow. Two precision bore flowmeters (Tube number FP-1-35-G-10/27 manufactured by Fischer & Porter Corp.) were used. In the observations of a radial surface buoyant jet in a cross current the discharge was a mixture of tap water with methanol and a small amount of blue dye for flow visualization. The overall experimental set-up is similar to that shown in Figure 4.1.2.

4.2.2 Temperature Measurements

Six fast-response thermistors were used for temperature measurements in the heated jet experiments and their characteristics are given in Table 4.2.1. Each thermistor was insulated and

Table 4.2.1 Fast-response thermistor characteristics

Type	Bead Diameter	Dissipation Constant-Still Water at 25°C	Time Constant in Moving Water	Resistance at 25°C
Small head Veco thermistors type 52A26	0.35 mm	0.75 mw/°C	27 or 45 milliseconds	~200 KΩ

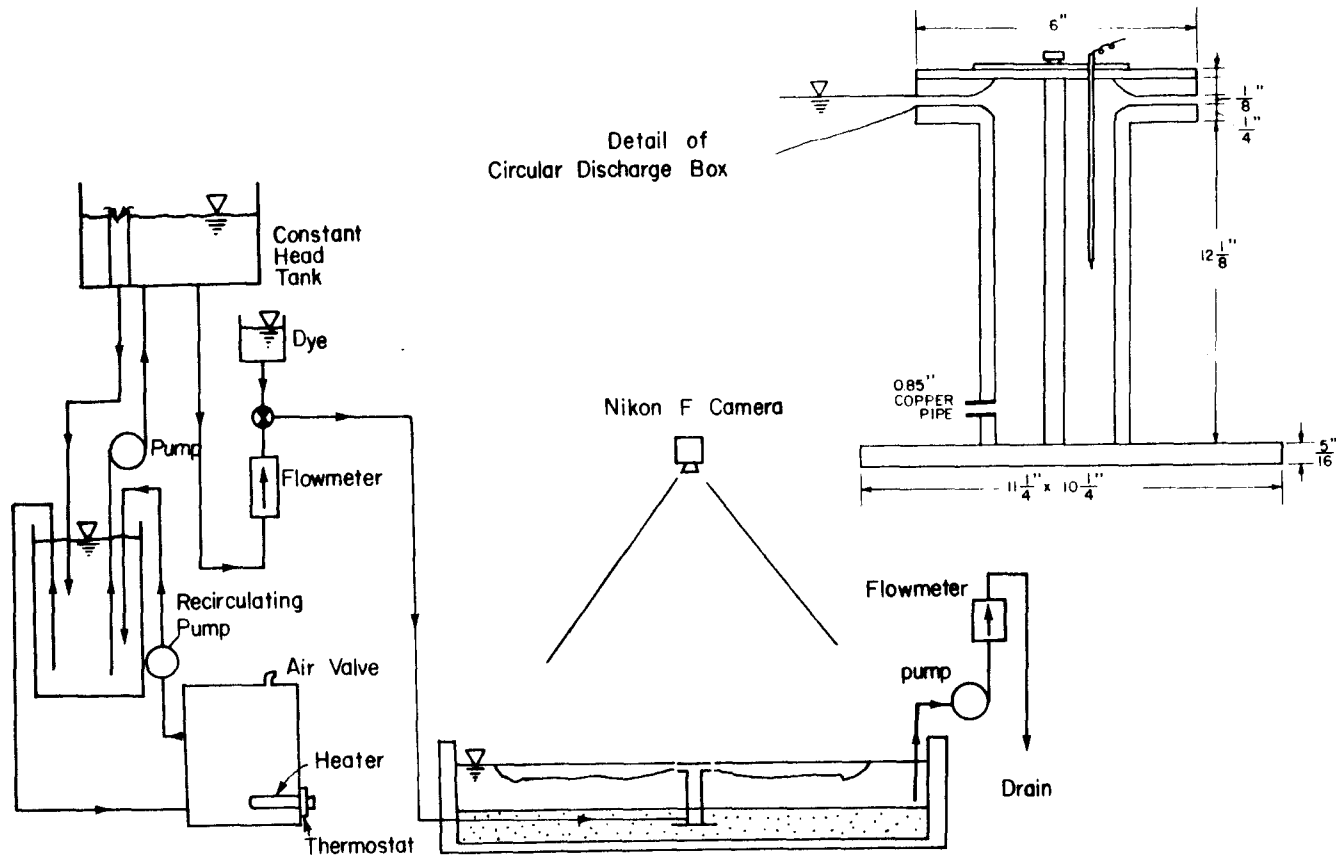


Figure 4.2.1 Overall experimental set-up for radial surface heated jet.

mounted in a stainless steel tube. One thermistor was installed inside the discharging chamber to record the initial temperature of the jet fluid. The other five formed an equally spaced vertical rake as shown in Figure 4.2.2. The rake was mounted on a carriage so that it could be moved in the radial direction (accurate to ± 0.10 cm) and vertically perpendicular to the free surface (accurate to ± 0.01 cm).

The thermistor response to temperature was measured with a bridge circuit designed by Gartrell (1979), as shown in Figure 4.2.3. A dual operational amplifier (Texas Instruments, SN558) was used to buffer, amplify and low-pass filter the signal from the bridge. All resistors used in the circuit were precision metal-film or wire-wound resistors. The electrical current passing through the thermistor was approximately 4.0×10^{-6} amperes so that the ohmic dissipation of the thermistor was approximately 2×10^{-6} watts. Hence the self-heating of thermistor was about 0.003°C by using the dissipation constant given in Table 4.2.1.

The amplified signal response was about 1.0 volt/ $^{\circ}\text{C}$, and the output of the circuit could be offset so that the zero-level output would correspond to a convenient temperature level. Six bridge circuits were connected in parallel to a DC power supply (± 15 volts) and were housed in a grounded aluminum box. The drift of the thermistor circuit was less than 10 mV over an extended period, giving the thermistor an accuracy of better than

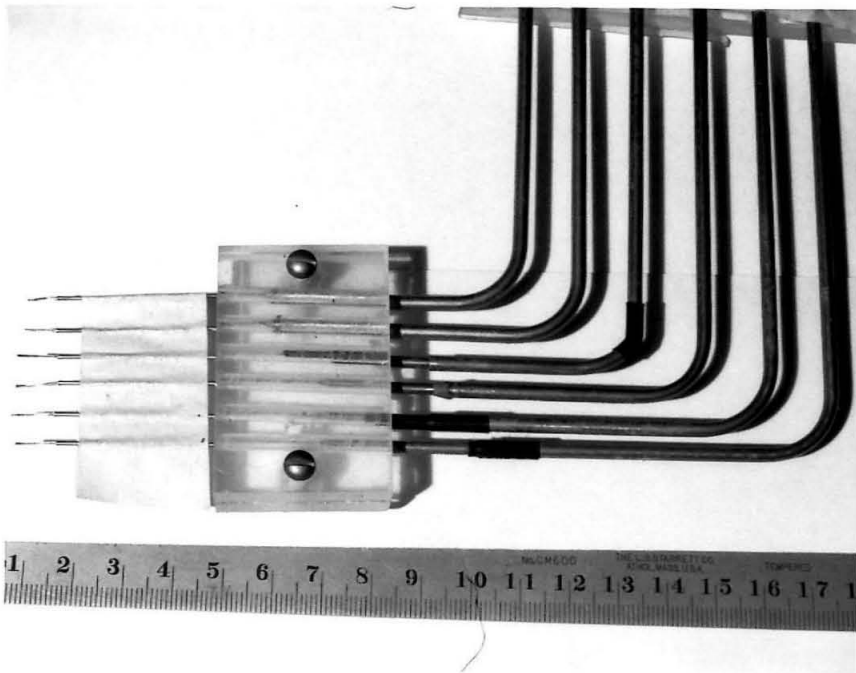


Figure 4.2.2 Photograph of a rake of five fast-response thermistors.

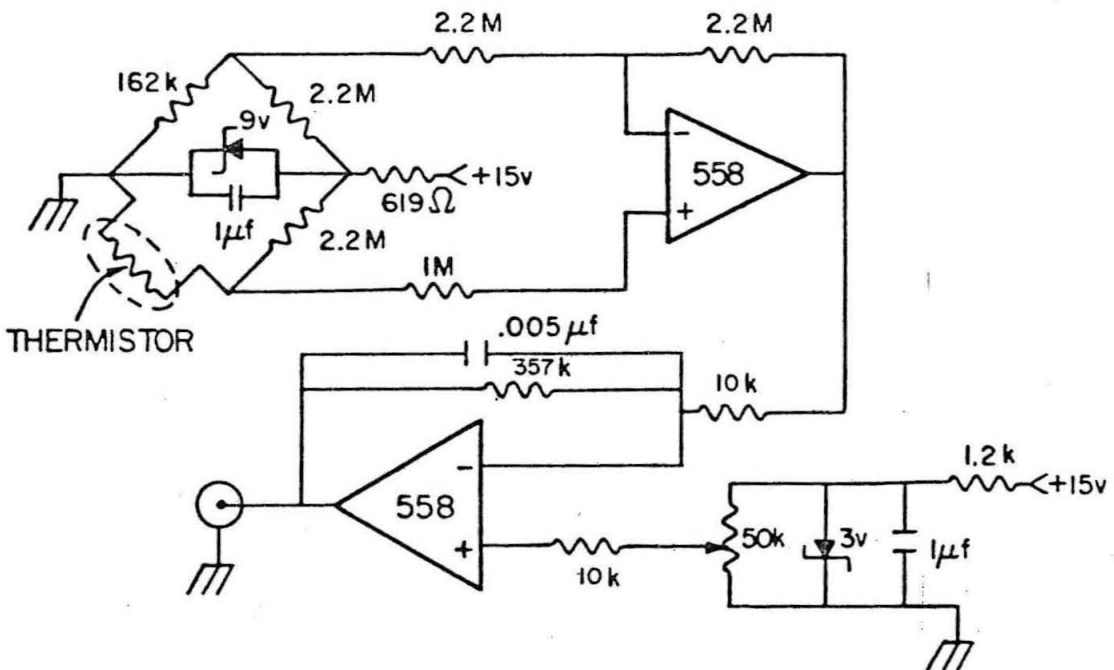


Figure 4.2.3 Fast-response thermistor circuit designed by Gartrell (1979).

0.01°C. A buffer circuit made from an integrated circuit operational amplifier (Texas Instruments SN741), as shown in Figure 4.2.4, followed the thermistor circuit and was used to increase the input impedance of the analog-to-digital converter system to about 1 megohm.

Each analog output voltage was fed into one channel of an eight channel analog-to-digital data acquisition system (manufactured by Digital Data System) which digitized the information and packed it on magnetic tape. Data written on the magnetic type were retrieved and processed at Caltech's Booth Computer Center with the IBM 370/168 high speed digital computer. The sample time of the A/D system was set at 150 seconds and the sample rate at 10 samples per second. The total length of the measurement records was 2 minutes for each location.

Each thermistor was individually calibrated with the same bridge circuit and same cable as in experiment. A third-order polynomial was fitted, in a least-square sense, to the calibrated data so that

$$T = a_0 + a_1 V + a_2 V^2 + a_3 V^3 \quad , \quad (4.2.1)$$

where T is the temperature in °C, V the analog output from the bridge in volts, and a_j , $j = 0,1,2,3$, are regression coefficients. Typical calibration curves along with calibration data are shown in Figure 4.2.5.

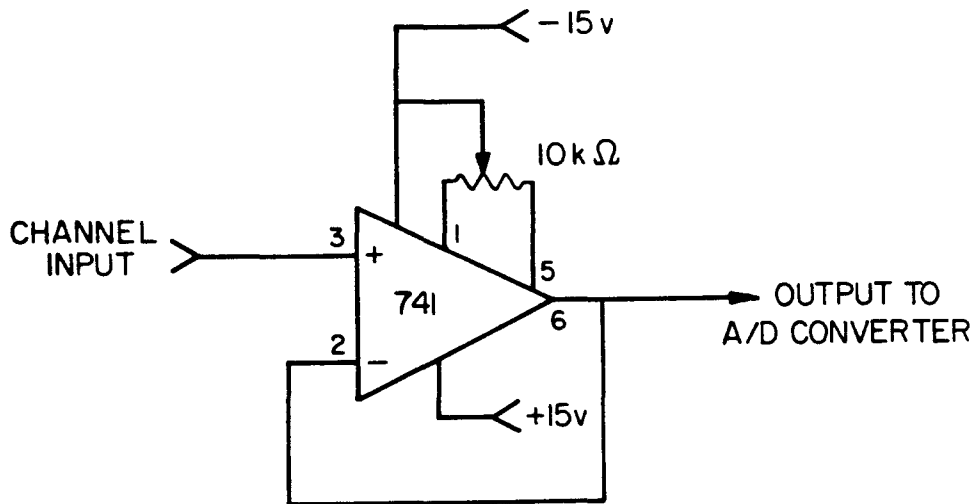


Figure 4.2.4 Buffer circuit for A/D converter from Gartrell (1979).

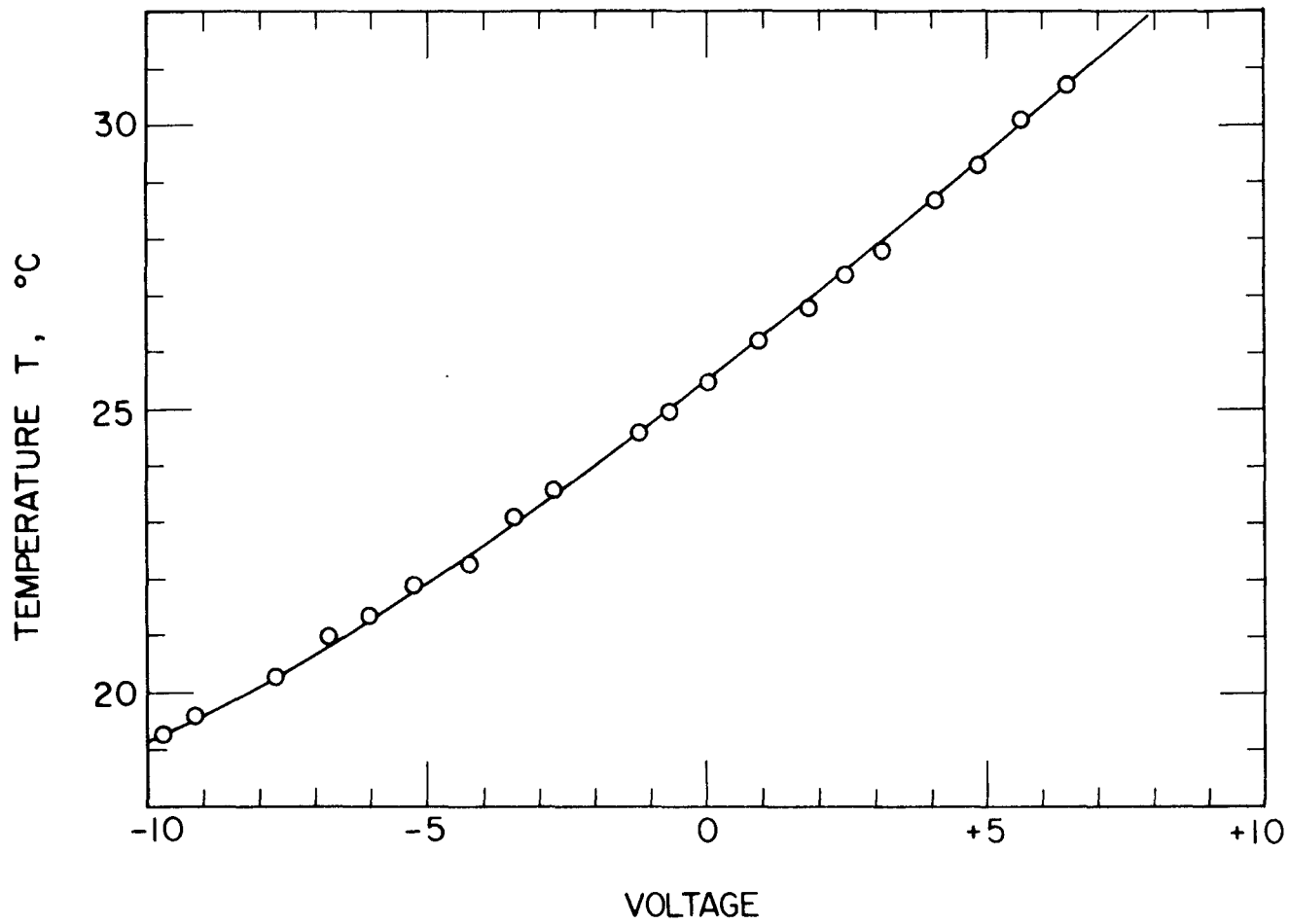


Figure 4.2.5 Typical calibration curve for fast-response thermistor.

4.2.3 Overhead Photographs

Overhead photographs of the dyed buoyant surface flow field were taken with a Nikon F camera equipped with a wide angle lens (17 mm). The camera was equipped also with motor drive so that it could be triggered remotely. The scale of flow field was read from the negative image by comparing the known spacing between two fiducial marks on the sand floor of the basin. The upstream edge position was also checked with direct measurement with a steel scale. Elapsed time photographs were also taken for some experiments involving initiation of flow in a steady cross current.

CHAPTER 5
EXPERIMENTAL RESULTS

5.1 Half-Radial Surface Buoyant Jet

A total of thirty experiments were performed using the apparatus described in the previous chapter. The relevant data are given in Table 5.1.1. These experiments covered the range of initial jet conditions as shown in Table 5.1.2. The densimetric Froude number Fr ranged from 2.80 to 25.0, the jet Reynolds number $Re = Re_j$ from 5040 to 13,700, and the ratio of two length scales, R_1/ℓ_{QM} , from 31.64 to 72.28 (or equivalently, Re/Fr^2 from 29.5 to 645.6). These dimensionless numbers were defined in Section 3.5 as

$$Fr = \frac{\ell_{MB}}{\ell_{QM}} = \frac{M^{5/4}}{QB^{1/2}} \quad , \quad (5.1.1)$$

$$Re_j = \frac{u_{MB} \ell_{MB}}{v_j} = \frac{M^{1/2}}{v} \quad , \quad (5.1.2)$$

$$\frac{R_1}{\ell_{QM}} = (Fr^2 \cdot Re^3)^{1/8} = \left(\frac{M^4}{v^3 Q^2 B} \right)^{1/8} \quad , \quad (5.1.3)$$

$$\frac{Re}{Fr^2} = \left(\frac{R_1}{\ell_{MB}} \right) = \frac{Q^2 B}{v M^2} \quad , \quad (5.1.4)$$

Table 5.1.1 Summary of data for starting half-radial surface buoyant jet experiments,
 $r_j = 9.962$ cm, $h_j = 0.3175$ cm and $H = 75.0$ cm.

Run No.	T_a (°C)	T_j (°C)	ρ_a (gm/cm ³)	ρ_j (gm/cm ³)	Δ (10 ⁻³)	u_j (cm/sec)	Q (cm ³ /sec)	M (cm ⁴ /sec ²)	B (cm ³ /sec ⁴)	Density Measurements
8/23/77	-	-	0.9990	0.9970	2.0	30.70	610	18,724	1,199.2	No
24	-	-	0.9994	0.9988	1.6	20.13	400	8,052	627.2	No
26	25.05	25.05	0.9994	0.9971	2.3	28.38	564	16,000	1,272.0	Yes
28	25.90	27.35	0.9990	0.9985	0.5	28.38	564	16,000	276.6	Yes
29	25.40	25.40	0.9990	0.9984	0.6	28.38	564	16,000	332.0	Yes
30	25.95	25.70	0.9990	0.9985	0.5	21.34	424	9,046	208.0	Yes
31	25.60	25.80	0.9990	0.9986	0.4	15.90	316	5,024	124.0	Yes
9/01/77	25.30	25.45	0.9990	0.9987	0.3	17.21	342	5,886	100.6	Yes
06	24.80	25.80	0.99905	0.9975	1.65	18.84	374.4	7,054	605.9	Yes
19	24.75	24.70	0.9991	0.9958	3.3	17.61	350	6,164	1,132.9	No
20	24.60	23.90	0.9991	0.99635	2.75	16.35	320	5,315	876.7	No
21	24.40	24.45	0.99915	0.99505	4.1	15.92	316.4	5,038	1,272.4	No
22	24.65	25.00	0.99915	0.9954	3.75	11.32	225	2,548	827.6	Yes
27	23.50	24.70	0.9996	0.9972	2.4	11.32	225	2,548	529.4	No
28	24.60	24.60	0.9990	0.00715	1.85	11.75	233.6	2,746	424.0	Yes
10/05/77	23.70	24.70	0.9992	0.0071	2.1	15.92	316.4	5,038	651.7	Yes
10	23.50	24.60	0.99945	0.00735	2.1	15.92	316.4	5,038	651.7	Yes
14	23.90	24.40	0.9995	0.9984	1.1	15.92	316.4	5,038	341.2	Yes
17	24.30	24.70	0.9995	0.9984	1.1	15.92	316.4	5,038	341.2	Yes
22	23.10	24.20	0.9992	0.9980	1.2	16.71	332.0	5,547	459.9	Yes
24	23.60	24.60	0.9995	0.9980	1.5	20.50	407.4	8,352	599.2	Yes
27	23.40	25.00	0.9995	0.9984	1.1	21.94	436.0	9,566	470.2	Yes
29	22.90	24.20	0.9995	0.9988	0.7	17.51	348.0	6,094	238.8	Yes
11/01/77	22.70	23.60	0.9995	0.9994	0.1	16.53	328.4	5,429	32.2	Yes
04	22.70	23.80	0.9995	0.9991	0.4	19.83	394.1	7,817	154.6	Yes
13	21.90	23.00	0.9995	0.9991	0.4	26.44	525.3	13,891	206.0	No
16	22.35	23.85	0.9998	0.9989	0.9	19.83	393.9	7,811	347.5	Yes
20	-	-	0.9997	0.9988	0.9	19.83	394.1	7,816	347.7	Yes
29	21.90	23.20	0.9998	0.9974	2.4	17.00	337.3	5,741	794.4	No
12/12/77	20.80	22.60	1.0000	0.9980	2.0	15.55	309.0	4,804	605.6	Yes

Table 5.1.2 Summary of calculated data for starting half-radial surface buoyant jet experiments.

Run No.	l_{MB} (cm)	t_{MB} (sec)	Fr	Re	Re/Fr ²	$\frac{R_1}{l_{QM}}$	$\frac{R(t)}{M^{1/4} t^{1/2}}$	$\frac{R(t)}{B^{1/4} t^{3/4}}$	$\frac{R(t)}{\left(\frac{g\Delta Q^3}{\nu}\right)^{1/8} t^{1/2}}$
8/23/77	46.22	15.61	10.37	13,684	127.3	63.83	1.05	-	-
24	33.94	12.84	7.61	8,973	154.8	50.44	-	-	-
26	39.90	12.58	8.95	12,652	158.0	59.73	1.04	-	-
28	85.56	57.86	19.19	12,652	34.4	72.28	1.03	-	-
29	30.75	48.22	17.52	12,652	41.3	70.65	1.11	1.04	-
30	64.32	43.50	14.43	9,511	45.7	60.48	1.04	-	-
31	53.60	40.52	12.02	7,089	49.1	51.75	-	-	-
9/01/77	66.98	58.48	15.03	7,672	34.0	56.37	1.06	-	-
06	31.27	11.64	7.01	8,399	170.7	48.20	1.07	-	-
19	20.67	5.44	4.64	7,851	365.3	42.38	1.30	0.93	-
20	21.02	6.06	4.71	7,290	317.8	41.55	1.40	1.00	-
21	16.76	3.96	3.76	7,097	502.0	38.72	1.32	0.84	0.725
22	12.46	3.08	2.80	5,047	645.6	31.64	1.53	0.77	-
27	15.58	4.81	3.49	5,047	413.0	33.46	1.43	-	-
28	18.42	6.48	4.13	5,240	306.8	35.38	1.30	0.85	0.777
10/05/77	23.42	7.73	5.25	7,097	257.1	42.10	1.25	0.80	0.713
10	23.42	7.73	5.26	7,097	257.1	42.10	1.15	0.75	-
14	32.37	14.76	7.26	7,097	134.6	45.65	1.12	-	-
17	32.37	14.76	7.26	7,097	134.6	45.65	1.05	0.70	-
22	29.97	12.06	6.72	7,447	164.8	45.59	1.18	0.78	-
24	35.69	13.94	8.00	9,139	142.6	51.43	1.07	0.71	-
27	44.60	20.34	10.00	9,780	97.7	55.78	1.02	0.70	-
29	44.63	25.51	10.01	7,806	77.9	51.26	1.07	0.81	-
11/01/77	111.44	168.57	25.00	7,368	11.8	63.06	0.95	0.88	-
04	66.87	50.57	15.00	8,842	39.3	59.43	1.04	0.89	-
13	89.15	67.43	20.00	11,785	29.5	71.13	1.08	0.88	-
16	44.57	22.48	10.00	8,838	88.4	53.69	1.07	0.77	-
20	44.57	22.48	10.00	8,841	88.4	53.70	1.05	0.78	-
29	23.40	7.23	5.26	7,577	274.8	43.14	1.30	0.85	-
12/12/77	23.45	7.93	5.26	6,931	250.6	41.74	-	-	-

in which the kinematic viscosity of the jet fluid, ν , is assumed a constant at $0.01 \text{ cm}^2/\text{sec}$ in all of the calculations.

In these experiments the aspect ratio of jet dimensions, h_j/r_j , was fixed at 0.03187 while the relative depth of ambient fluid, H/h_j , was also fixed at value of 236.2, corresponding to relatively deep water.

5.1.1 Starting Half-Radial Surface Buoyant Jet

Typical side-view photographs of a starting half-radial surface buoyant jet are shown in Figure 5.1.1(a), (b), and (c). Figure 5.1.1(a) shows a starting buoyant jet at an initial Froude number, $Fr = 5.25$. Figure 5.1.1(b) shows that with a Froude number $Fr = 10.0$ and Figure 5.1.1(c) is for $Fr = 15.0$. These photographs show the typical behavior of such jets. The jet is initiated with a frontal head that is thicker with larger Froude number. Just behind the front there is a vortex growing and traveling with the front until at some point the vortex collapses, as shown in Figure 5.1.1(c).

The growth histories of the radial fronts, as determined by the photographic methods described in the previous chapter are shown in Figure 5.1.2. This graph is a logarithmic plot of front radius $R(t)$ as a function of time from release. It is clear that the data fall into two categories corresponding to a slope of $1/2$ or a slope of $3/4$. However, some of the data show an initial slope of $1/2$ followed by a slope of $3/4$ leading

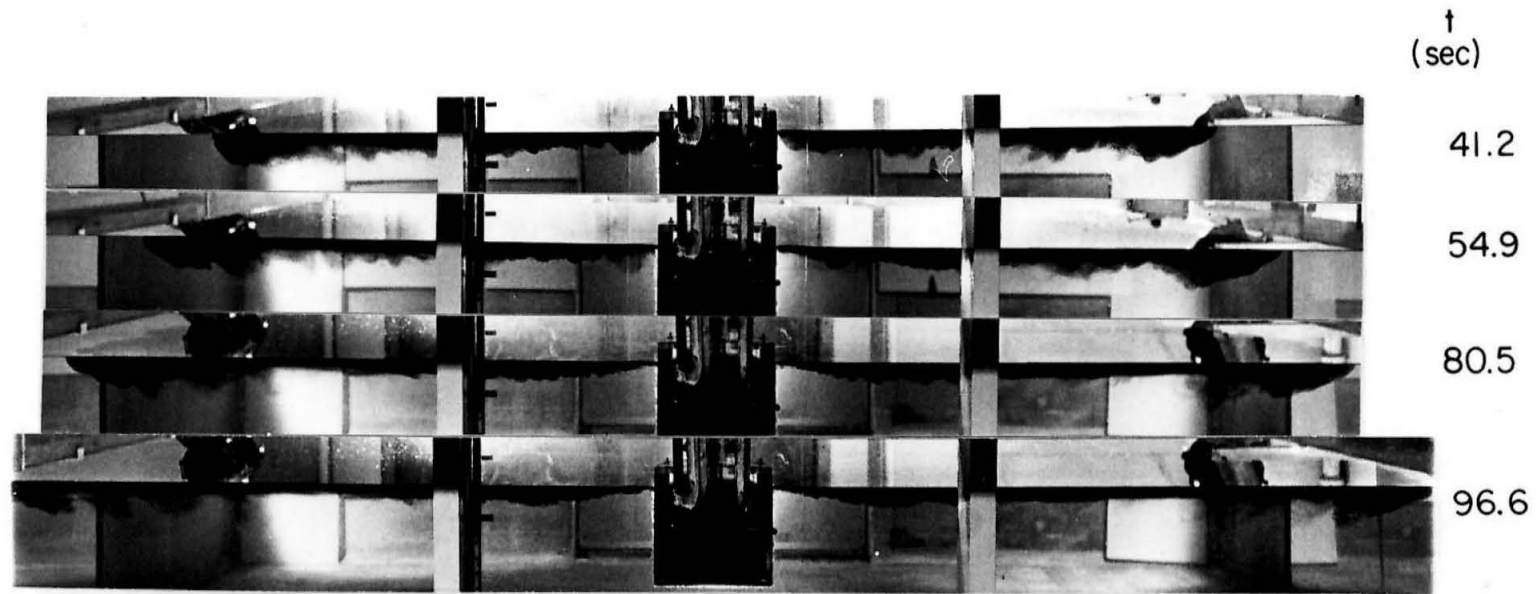


Figure 5.1.1 Cross sections of half-circular front at various time t after initiation of discharge (a) Run No. 10/5/77, $Fr = 5.25$, $Re = 7100$.

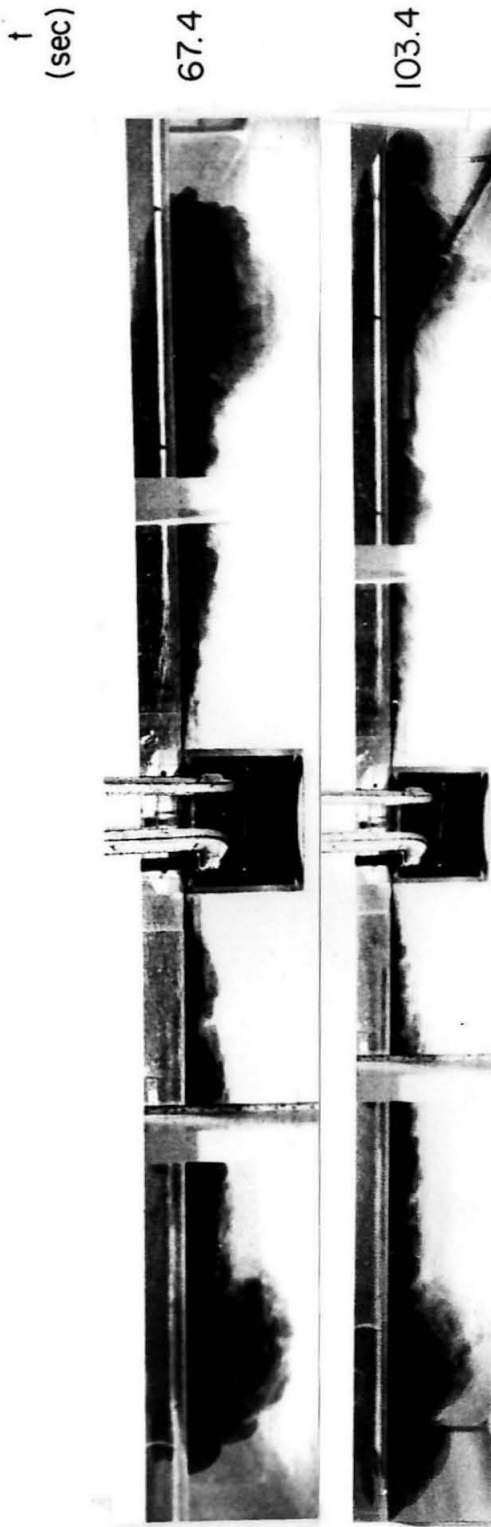
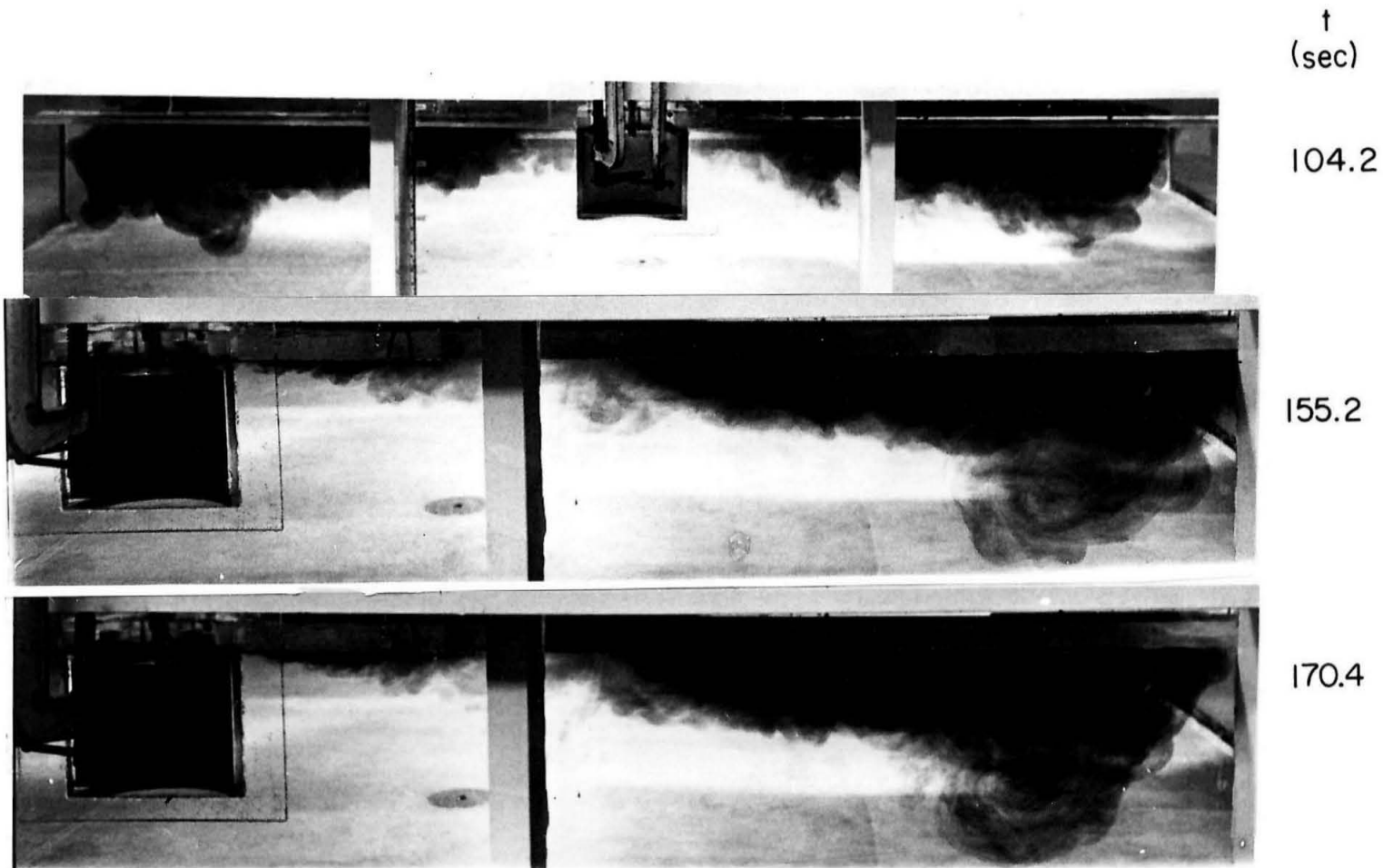


Figure 5.F.1(b) Run No. 11/16/77, Fr = 10.0, Re = 8840.



t
(sec)

104.2

155.2

170.4

223

Figure 5.1.1(c) Run No. 11/4/77, Fr = 15.0, Re = 8840.

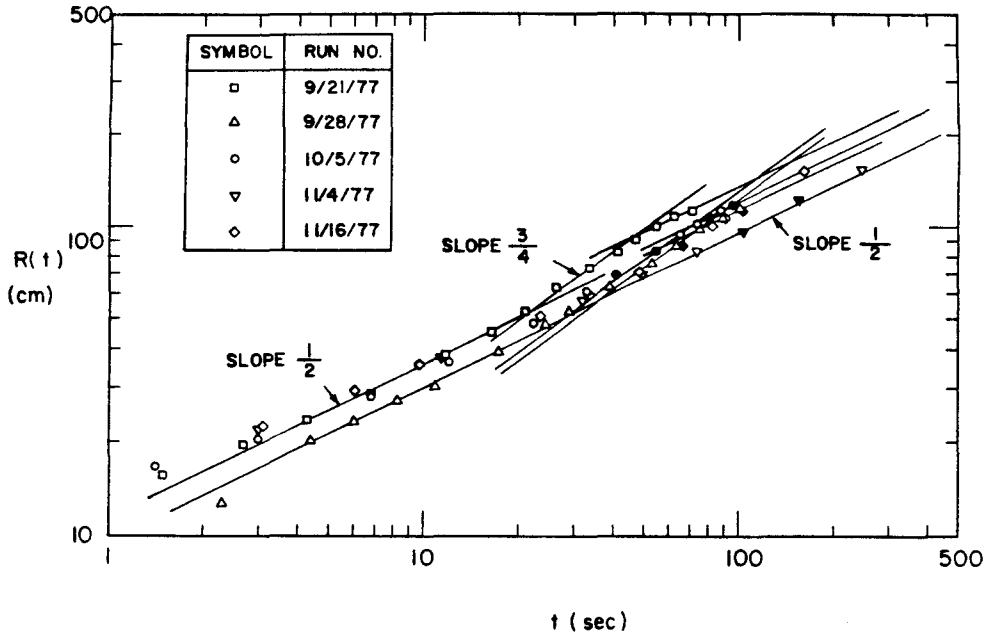


Figure 5.1.2 Growth history of starting radial surface turbulent buoyant jet flow. Closed symbols indicate the photographs are shown in Figure 5.1.1.

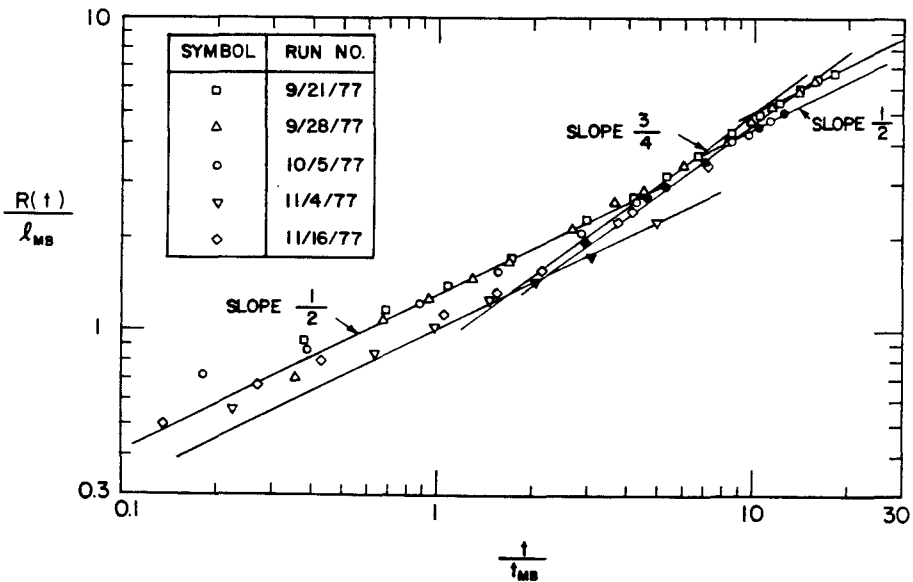


Figure 5.1.3 Normalized growth history of starting radial surface turbulent buoyant jet flow. Closed symbols indicate the photographs are shown in Figure 5.1.1.

to a further slope of 1/2. According to the discussion in Chapter 3 these can be categorized, respectively, a starting jet, a starting inertial plume, and a starting viscous plume.

The data in Figure 5.1.2 are replotted in Figure 5.1.3 in a normalized form, where length scales have been made relative to l_{MB} and the time scale by t_{MB} . These normalized data do not show a common curve for all three segments, as is to be expected, since the coefficients in each relation are not necessarily constant.

From the dimensional analysis given in Eq. (3.5.11) the coefficients for starting turbulent surface jet flows are a function of initial Froude number and Reynolds number,

$$\frac{R(t)}{M^{1/4} t^{1/2}} = \phi(Fr, Re) \quad . \quad (5.1.5)$$

The relationship of the jet coefficient to Reynolds number is shown in Figure 5.1.4(a) and to the densimetric Froude number in Figure 5.1.4(b). The value of starting jet coefficient decreases with increasing Froude number and it begins to approach to an asymptotic value around 1.05 when the Froude number is greater than 10. That means that the buoyancy enhances the initiation jet flow when the Froude number is less than 10. At a Froude number higher than 10 the buoyancy plays a less important role in initiation of flow so that starting turbulent buoyant jet flows can be described by the asymptotic formula,

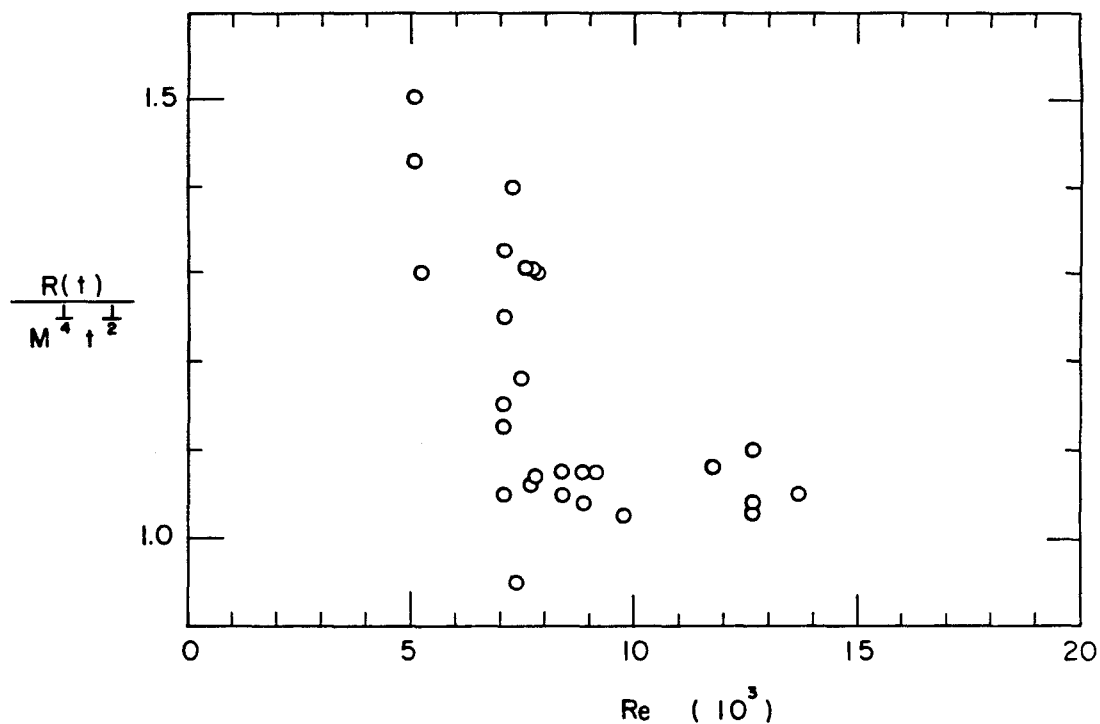


Figure 5.1.4(a) Relation of starting jet coefficient to jet Reynolds number.

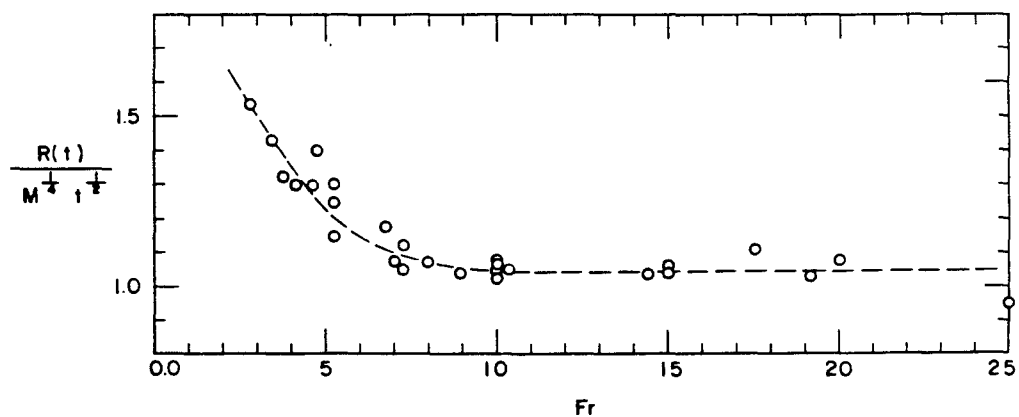


Figure 5.1.4(b) Relation of starting jet coefficient to radial jet Froude number.

$$R(t) = 1.05 M^{1/4} t^{1/2} \quad . \quad (5.1.6)$$

From Eq. (3.5.12) the starting radial plume coefficient will also be a function of initial Froude number and Reynolds number, i.e.

$$\frac{R(t)}{B^{1/4} t^{3/4}} = \phi(\text{Fr}, \text{Re}) \quad . \quad (5.1.7)$$

As shown in Figure 5.1.5(a) there is no systematic dependence of the starting plume coefficient on Reynolds number. Figure 5.1.5(b) and (c) shown the relation of starting plume coefficient to Froude number and $R_1/\ell_{QM} = (\text{Re}^3 \cdot \text{Fr}^2)^{1/8}$. All the values of the starting plume coefficients are between 1.04 and 0.70, which is lower than theoretical results 1.31, given in Subsection 3.2.6. Momentum and viscosity effects may be the possible reasons.

Only three values of viscous starting plume coefficient are found (0.713, 0.725, 0.777) as listed in the final column of Table 5.1.2. These values are about 15% higher than the theoretical result, 0.63 obtained from viscous long wave solution. There are insufficient data to show the dependence on the initial Froude and Reynolds numbers, i.e.

$$\frac{R(t)}{\left(\frac{g\Delta Q^3}{\nu}\right)^{1/8} t^{1/2}} = \phi(\text{Fr}, \text{Re}) \quad . \quad (5.1.8)$$

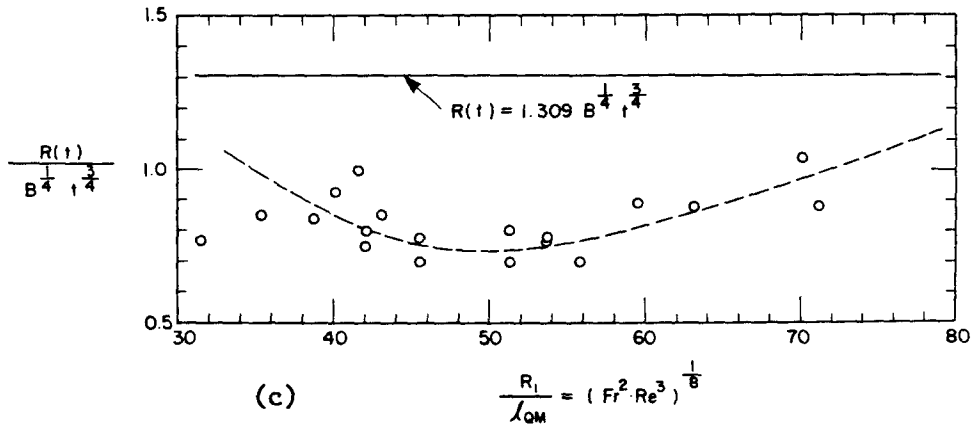
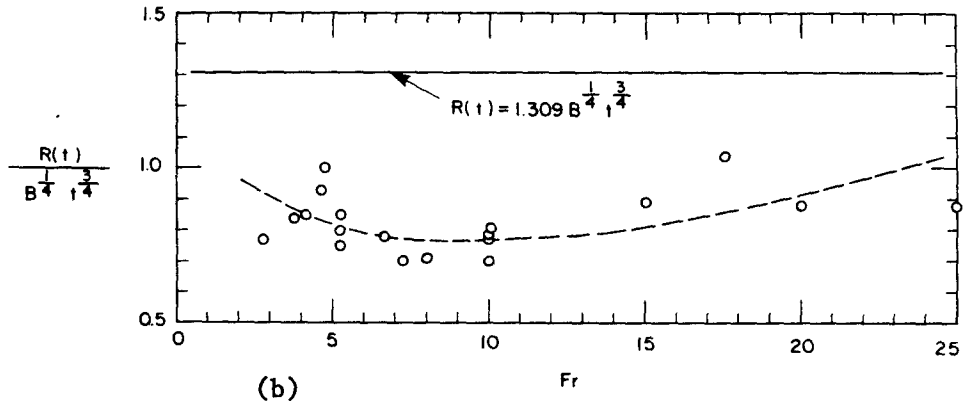
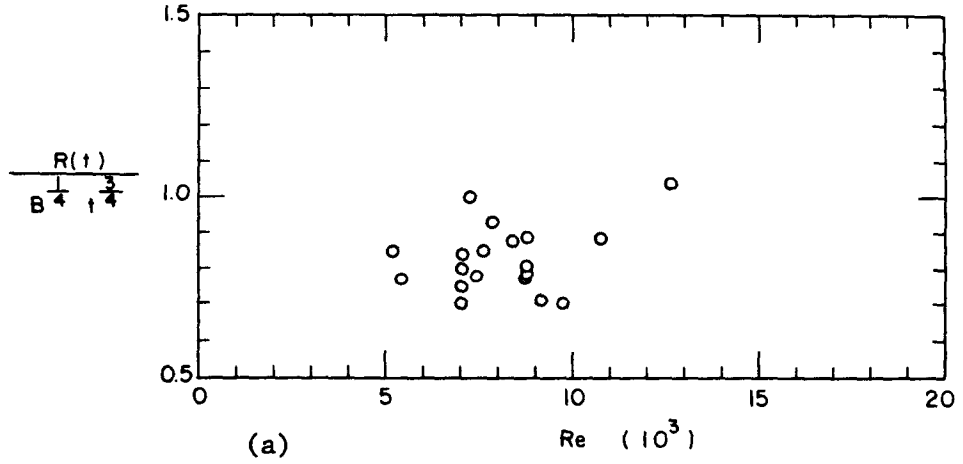


Figure 5.1.5 Relation of radial starting plume coefficient to (a) jet Reynolds number, (b) Froude number, (c) R_1/l_{QM} .

Without any initial effects, such as momentum jet mixing, ϕ will approach to the theoretical value, 0.63, as the dimensionless ratio R_1/ℓ_{QM} tends to be small.

Three similarity profiles for viscous spreading currents are compared with viscous long wave solution, as shown in Figure 5.1.6. The experimental profiles are all thicker than the theoretical profile and there is a prominent head at the front and some internal waves behind the front. The greater profile thickness may be due to jet mixing and possibly some error due in the kinematic viscosity value. The spreading currents thickness scale $T(t)$ in this case is independent of time t , i.e.,

$$T(t) = \left(\frac{RR\dot{v}}{g\Delta} \right)^{1/3} = \left(\frac{\phi^2}{2} \right)^{1/3} \left(\frac{vQ}{g\Delta} \right)^{1/4}, \quad (5.1.9)$$

in which ϕ is the viscous spreading plume coefficient given in Eq. (5.1.8) and v is assumed as $0.01 \text{ cm}^2/\text{sec}$. This thickness scale was also found independent of time by the force scale analysis (see Eq. (3.1.11)). Although the thickness scale for two-layered radial stratified flow is independent of time, in an infinite extent of ambient water, it does not mean that the thickness of flow is also uniformly distributed in all space (see Figure 5.1.6).

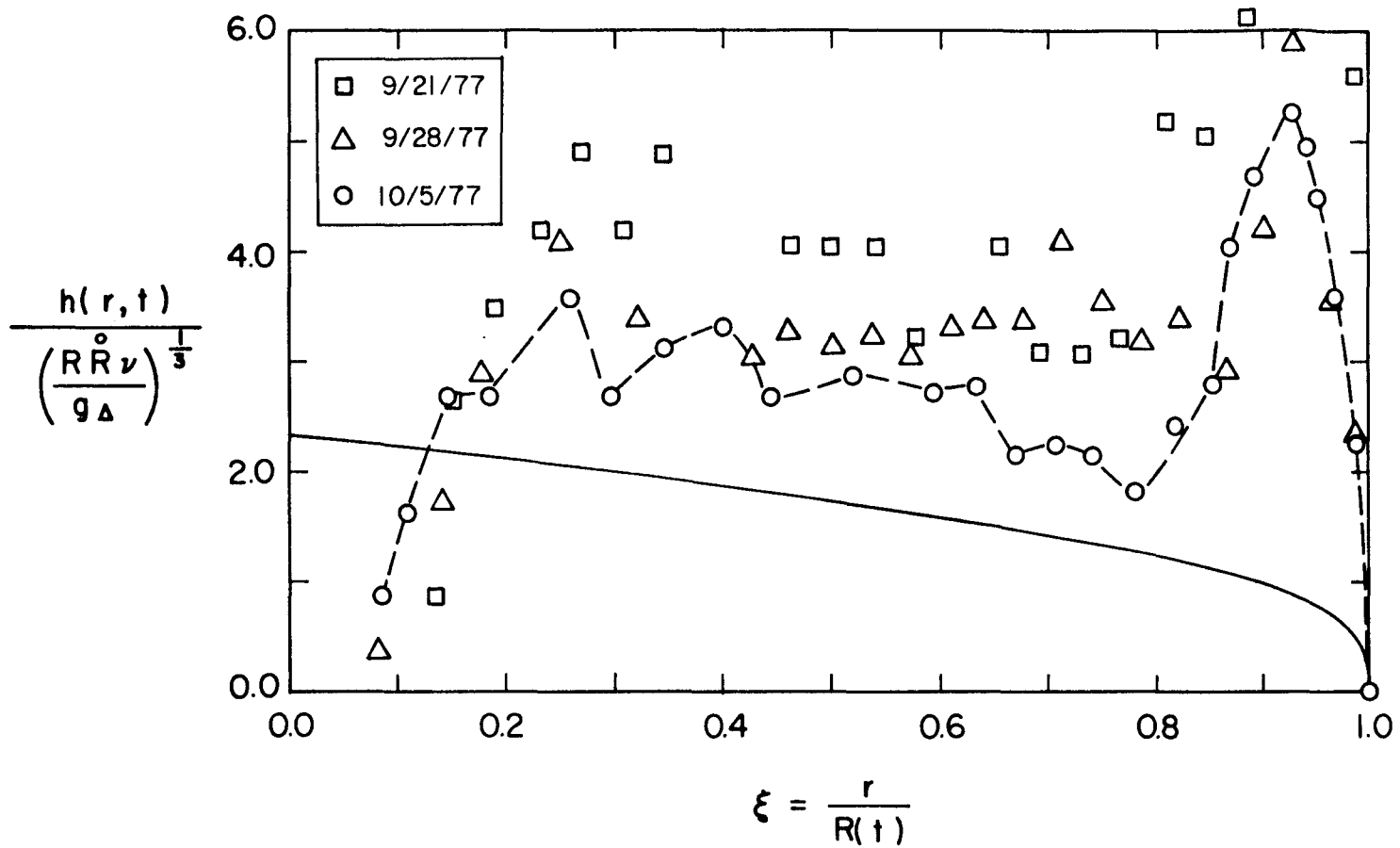


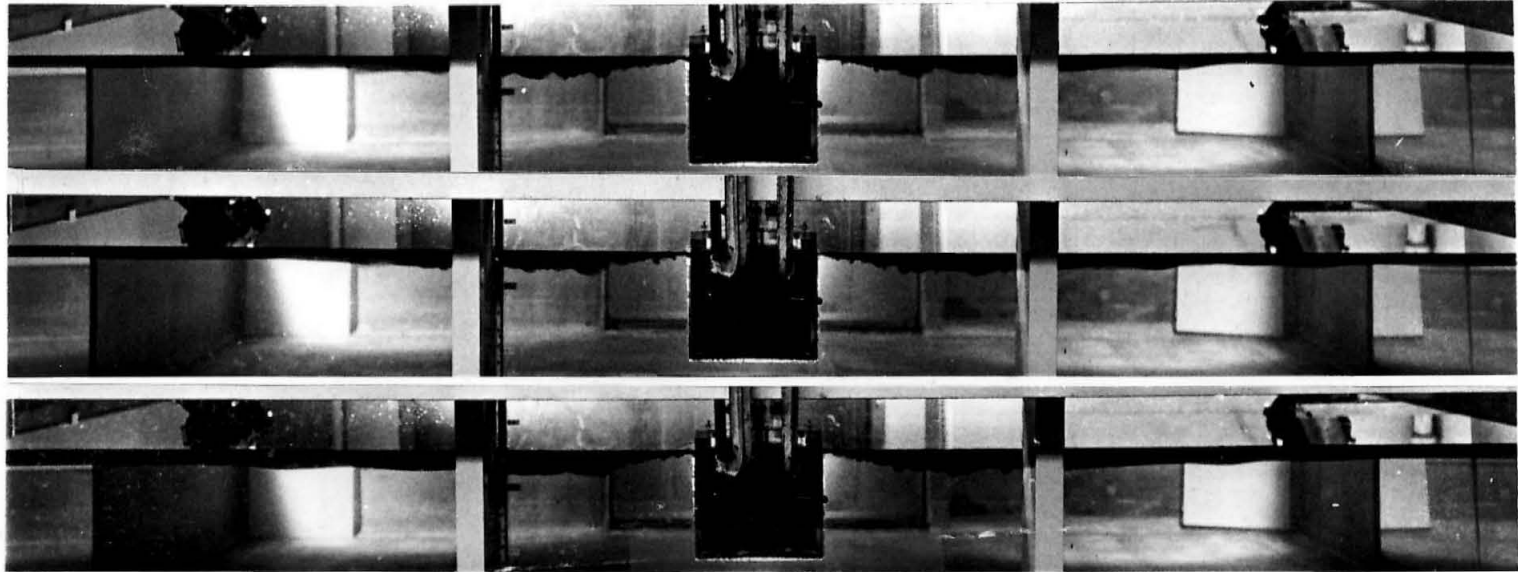
Figure 5.1.6 Similarity profiles of viscous radial surface spreading currents at time t (71.4 seconds for No. 9/21/77, 101.7 for 9/28/77, and 96.6 for 10/5/77) after discharge.

5.1.2 Density Measurements

Figure 5.1.7(a) shows a two-layered radial stratified flow being formed from a radial surface buoyant jet discharge at $Fr = 5.25$. The first photograph ($t = 200.5$ seconds) in Figure 5.1.7(a) was taken when the circular front just touched two side-walls (see Figure 5.1.1(a) for reference). The surface jet thickness became constant at a distance which was approximately the length scale ℓ_{MB} as indicated. It then collapsed to produce circular interfacial waves which were damped out quickly. After the circular front touched all the walls of the tank, the surface layer thickness kept increasing. The circular surface jet zone then looked like a circular internal hydraulic jump followed by a series of undular internal waves with a circular plan form.

Figure 5.1.7(b) shows the surface flow field produced by the half-radial surface buoyant jet with $Fr = 10.0$ and Figure 5.1.7(c) with $Fr = 15.0$. In those two cases the circular jet mixing also began to collapse at a distance which is roughly equal to ℓ_{MB} . However, more violent jet mixing and a propagating wavy interface made it difficult to locate the exact point of the jet collapse.

Typical records of density measurements as recorded by a conductivity probe are shown in Figure 5.1.8. The turbulent fluctuation was found to decrease as the depth of measurement increased at any radial distance. Mean values of density at a given radius were obtained by dividing these depth-density curves into two regions having equal area. The distribution of fluid



$t = 200.5$
 262.6
 472.0 seconds

$l_{MB} = 23.42$ cm

Figure 5.1.7 Radial stratified flow due to a half-radial surface buoyant jet discharge
 (a) Run No. 10/5/77.

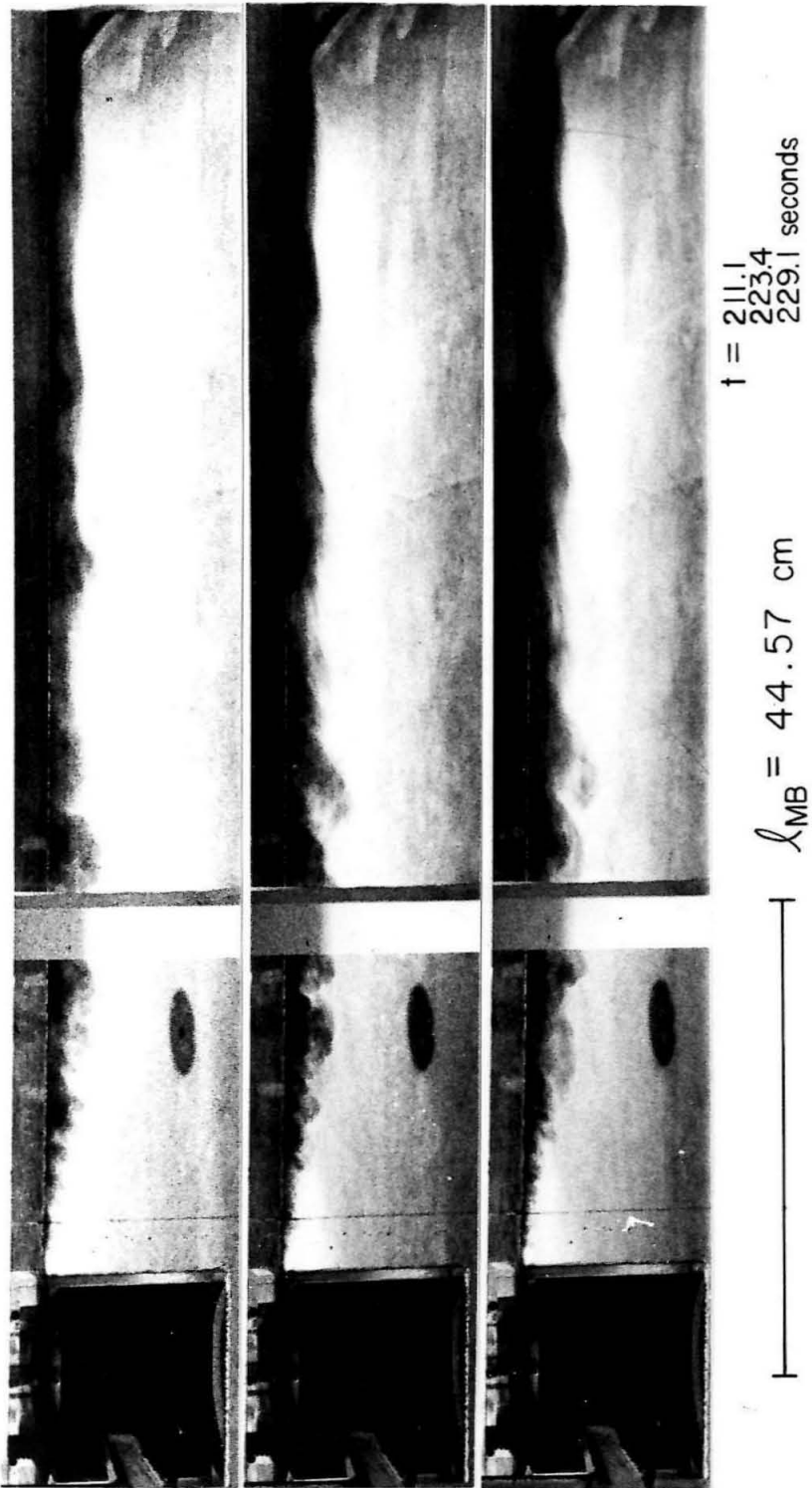
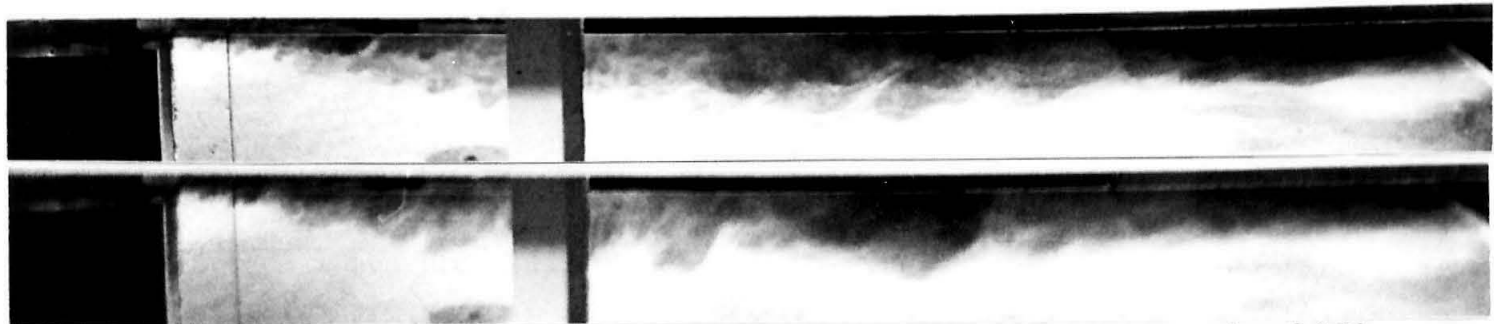
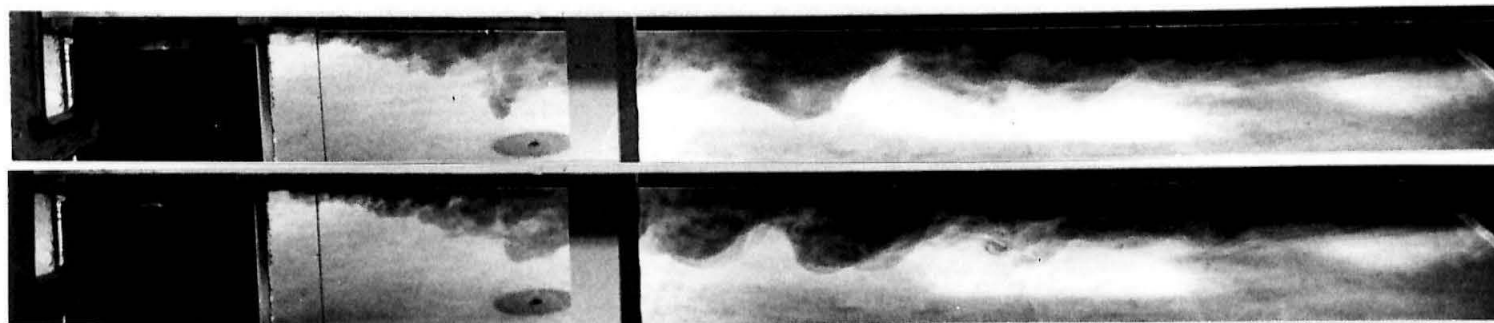


Figure 5.1.7(b) Run No. 11/16/77



$t = 247.0$
 286.9 seconds



$l_{MB} = 66.87$ cm , $t = 330.3$
 344.1 seconds

Figure 5.1.7(c) Run No. 11/4/77

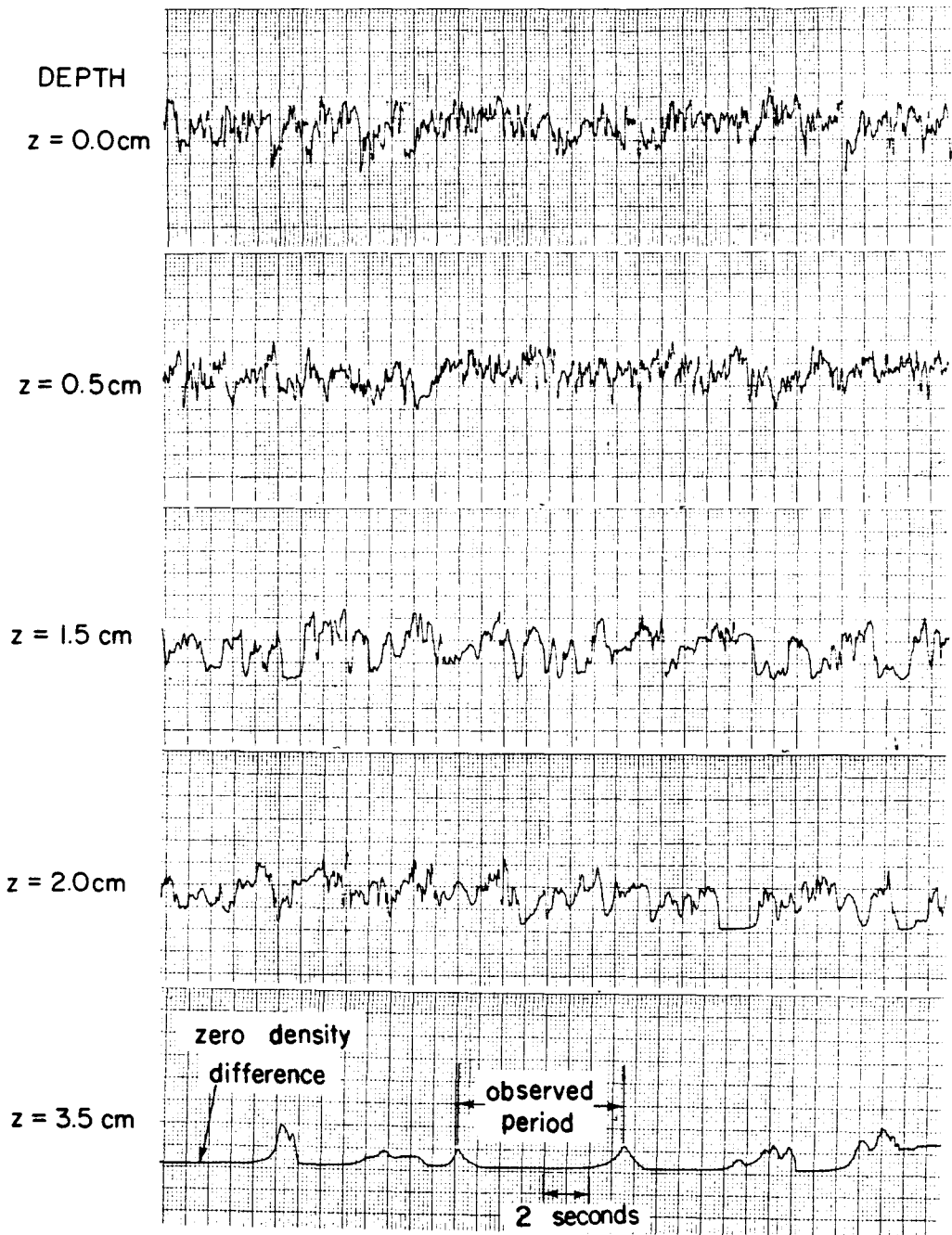


Figure 5.1.8 Density measurements of a half-radial surface buoyant jet (Run No. 10/27/77) with $Fr = 10.00$ at a radial distance $r = 32.39$ cm (or $r/l_{MB} = 0.726$).

density difference on depth at three radial locations are shown in Figure 5.1.9, in which circles denote the mean density difference and a bar denotes the maximum and the minimum values.

In Figure 5.1.10 the relative mean density difference, $\Delta(r,z)/\Delta_m(r)$ plotted against normalized depth $z/z_{1/2}(r)$, is compared with the similarity tracer distribution given by the radial surface jet solution in Section 3.4. The half-thickness $z_{1/2}(r)$ is defined as the thickness where the relative density difference is half of the maximum value $\Delta_m(r)$ at the free surface. In this case the discharge Froude number is $Fr = 10.0$. The maximum values of mean density difference, $\Delta_m(r)$, are found to agree fairly well with the radial jet solution, i.e. the density deficiency decays inversely proportional to the radial distance r , as shown in Figure 5.1.11. However, the half-thickness $z_{1/2}(r)$ is a linear function of radial distance r for the region where the buoyancy effects do not become important, i.e., where $r/\ell_{MB} < 1$, as shown in Figure 5.1.12.

Similar results are shown in Figures 5.1.13, 5.1.14, and 5.1.15 for a radial surface buoyant jet with a lower densimetric Froude number, $Fr = 5.26$. In this case it is hard to find a linear growth function of half-thickness $z_{1/2}(r)$. It approaches to a constant thickness without any sharp collapse from the jet regime.

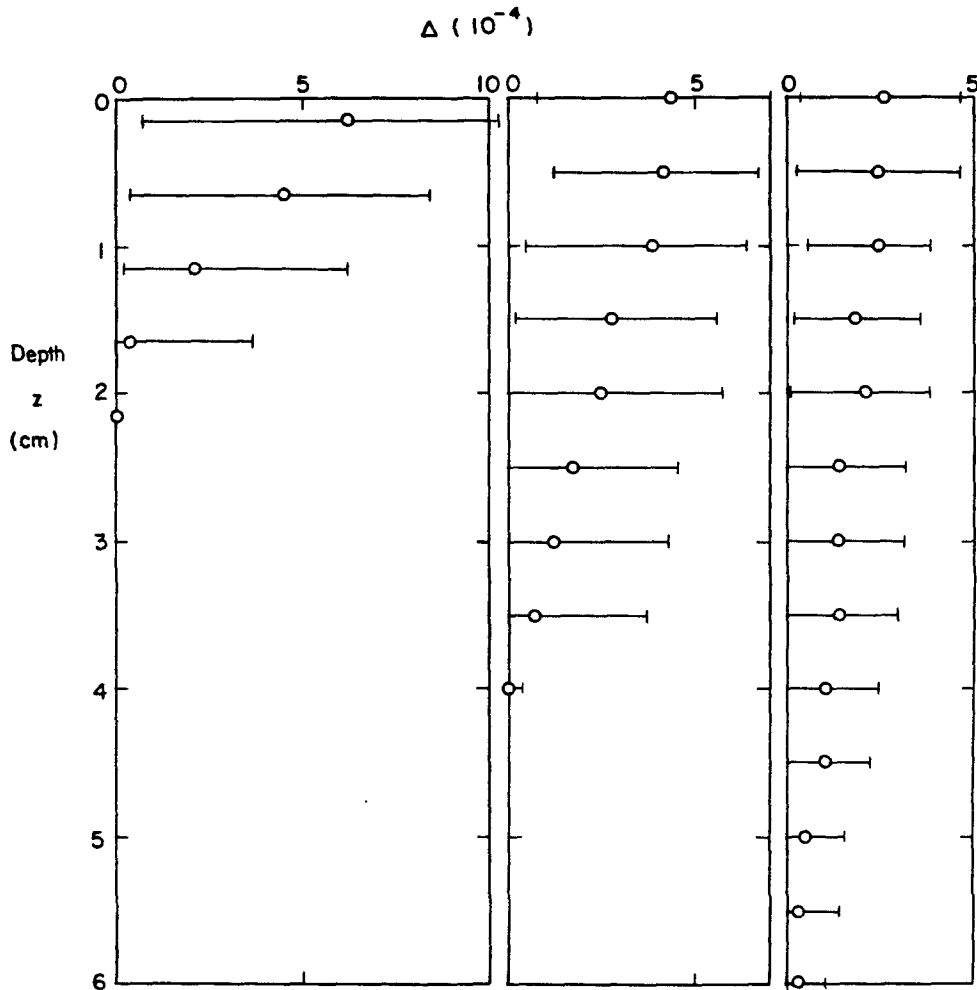


Figure 5.1.9 Distributions of relative density difference respectively at a distance $r = 17.15$, 32.39 , and 67.95 cm (or $r/\lambda_{MB} = 0.384$, 0.726 , and 1.523) for a radial surface flow field (Run No. 10/27/77).

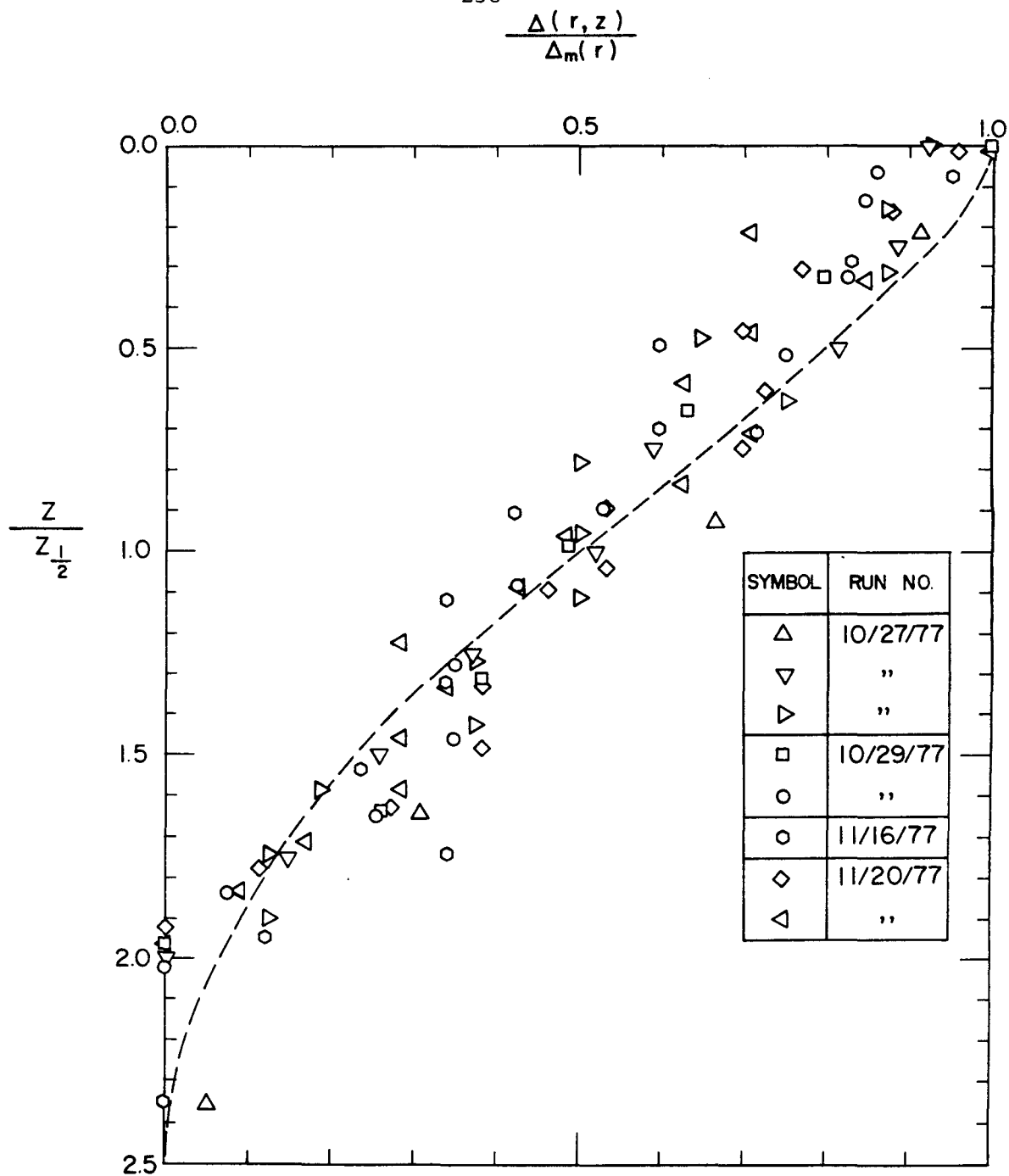


Figure 5.1.10 Self-similar distribution of relative density deficiency. Dotted line denotes Prandtl-Tollmien's solution.

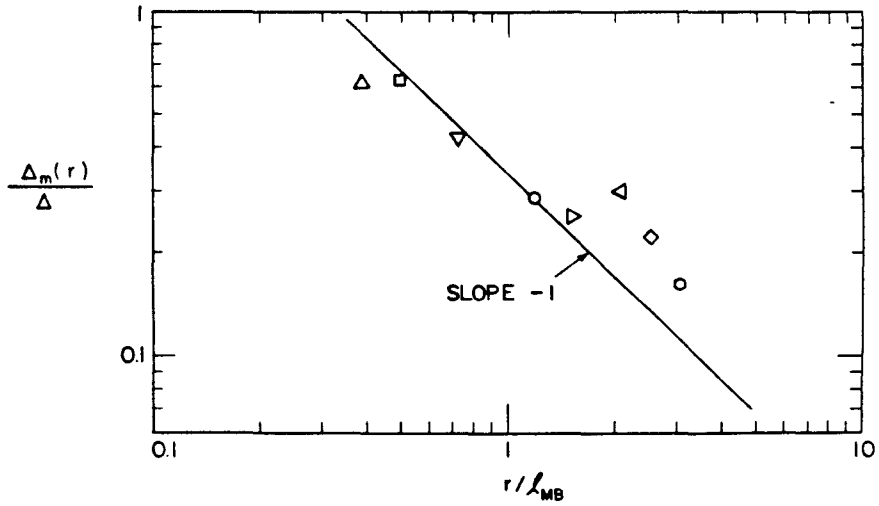


Figure 5.1.11 Relation of the maximum value of relative density deficiency to the radial distance. Symbols are defined in Figure 5.1.10.

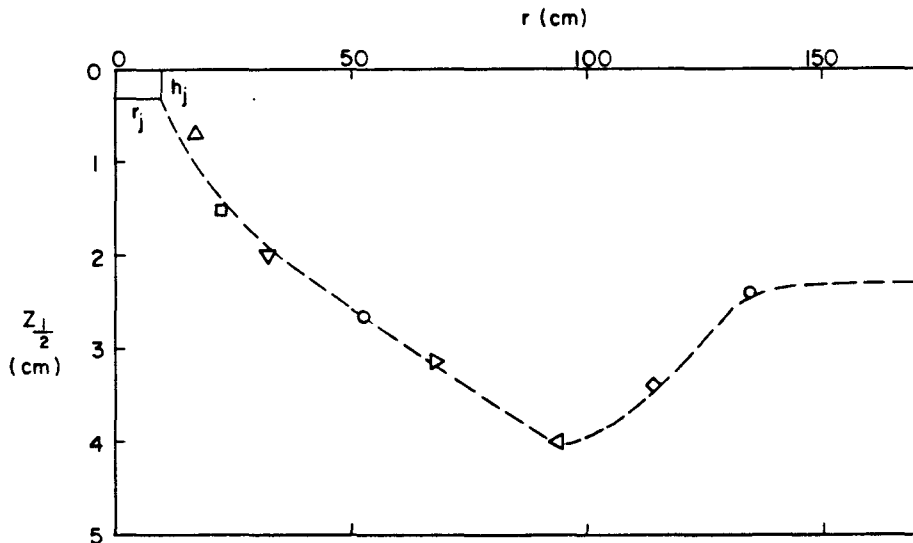


Figure 5.1.12 Relation of the half-thickness to the radial distance. Symbols are defined in Figure 5.1.10.

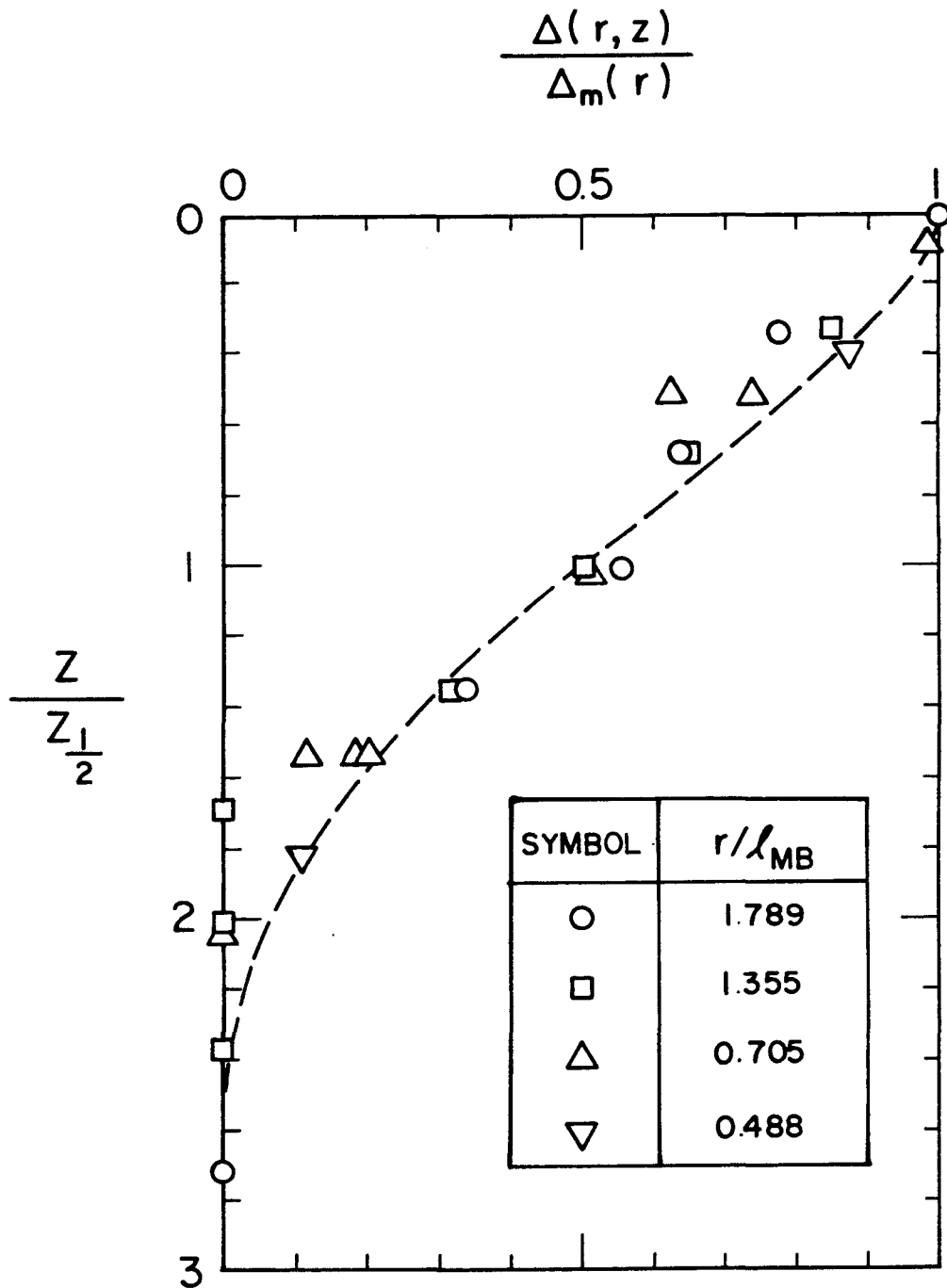


Figure 5.1.13 Self-similar distribution of relative density deficiency (Run No. 10/10/77, $Fr = 5.26$).

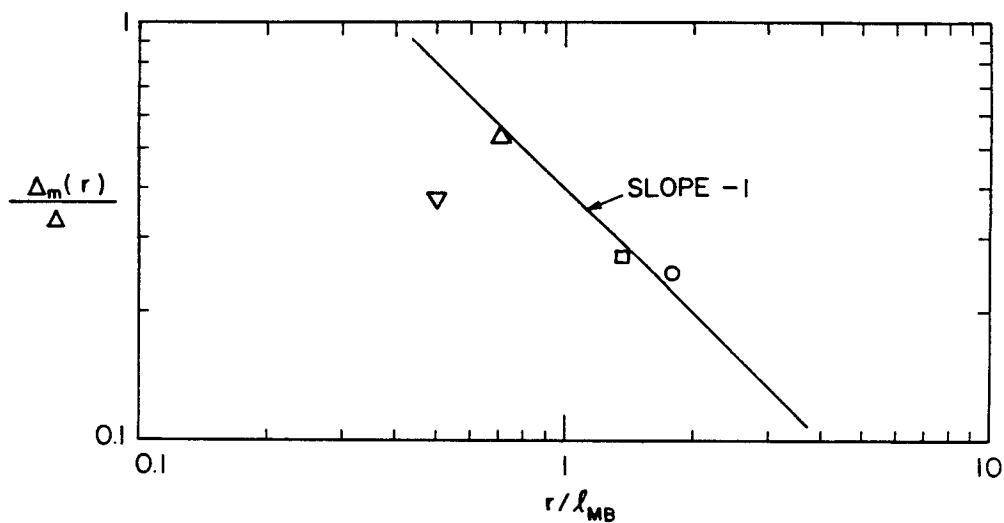


Figure 5.1.14 Relation of the maximum value of relative density deficiency to the radial distance. Symbols are defined in Figure 5.1.13.

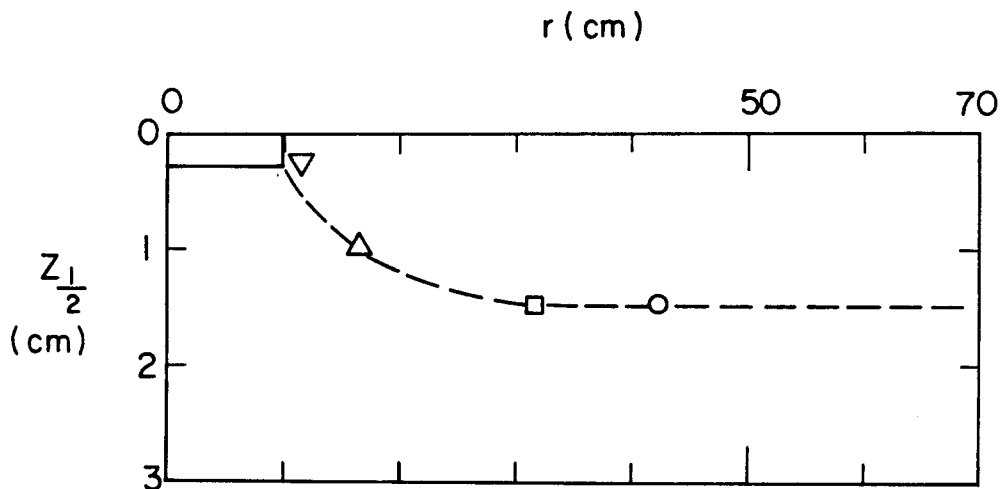


Figure 5.1.15 Relation of the half-thickness to the radial distance. Symbols are defined in Figure 5.1.13.

5.1.3 Periodic Feature

The analysis in Chapter 3 predicted the existence of a periodic wave feature in the buoyancy-inertial regime of flow. However, only a weakly periodic radial surface plume was observed in these experiments. Since there is intensive surface jet mixing in the upstream and strong viscous effects in the downstream, most of the periodic feature can only be observed in the position close to the interface. The period record as shown in the last record of Figure 5.1.8 results from breaking internal waves which form travelling mixing billows. The billows then collapse into a series of circular internal waves.

In Figure 5.1.16 all the observed periods T_{ob} are compared reasonably well with the predicted value T as given by Eq. (3.2.87). The details of the measurements are presented in Table 5.1.3.

5.2 Radial Heated Surface Jet

Four radial heated surface jet experiments were performed as listed in Table 5.2.1. In these experiments the density variations are produced by the temperature variations specified by the equation,

$$\frac{1}{\rho(T)} \frac{d\rho(T)}{dT} = \alpha(T) \quad , \quad (5.2.1)$$

where $\rho(T)$ is the fluid density at temperature $T^\circ\text{C}$, $\alpha(T)$ is the thermal expansion coefficient ($1/^\circ\text{C}$) at temperature $T^\circ\text{C}$.

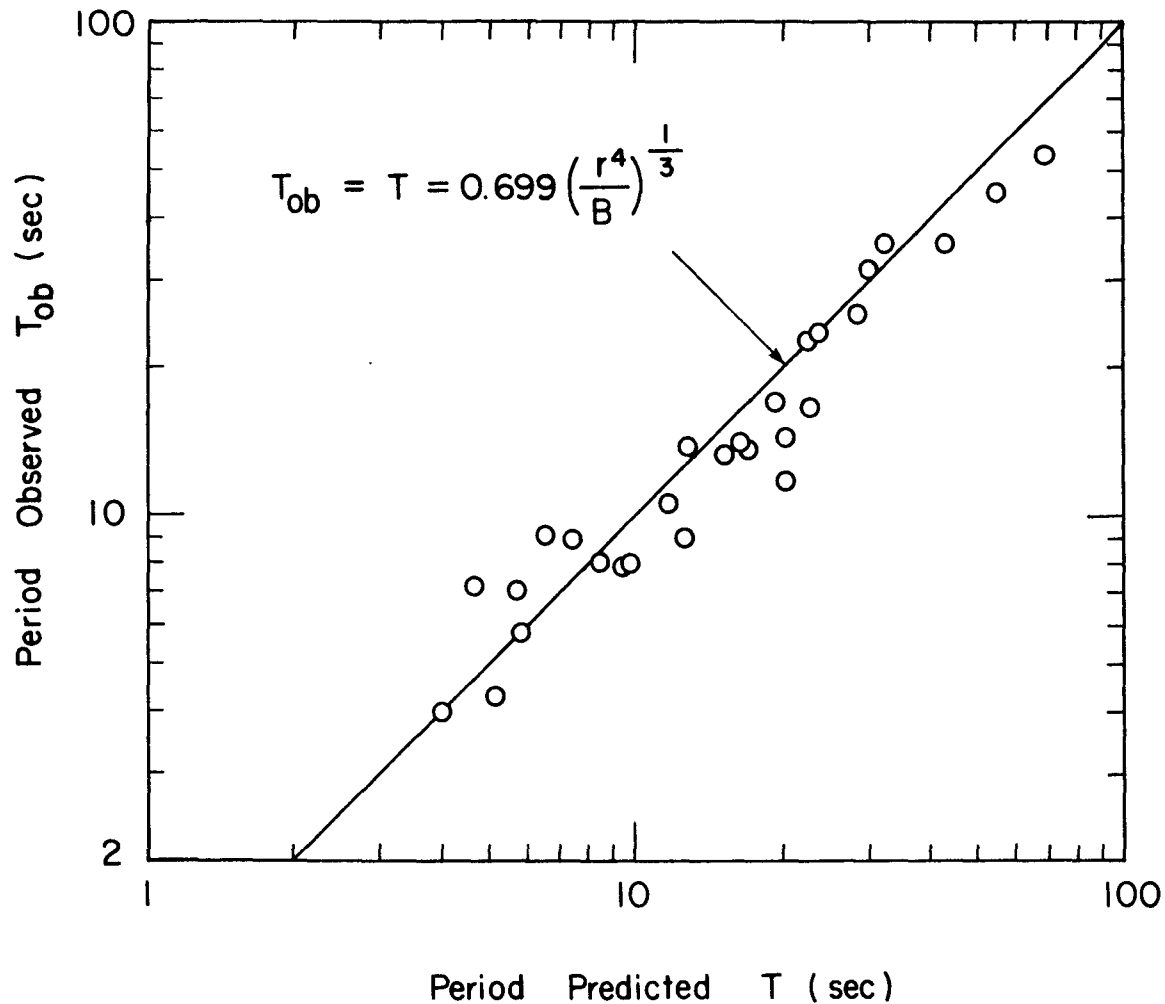


Figure 5.1.16 Comparison of the observed period with the predicted value T given by Eq. (3.2.87).

Table 5.1.3 Summary of observed and predicted periods.

Run No.	B (cm ⁴ /sec ³)	Location of Measurement			T _{ob} (sec)	T (sec)
		r (cm)	r/ℓ _{MB}	z (cm)		
8/26/77	1272	29.21	0.732	2.30	5.8	5.80
8/28/77	276.6	44.45	0.520	5.46	13.5	16.90
"	"	29.21	0.340	1.96	8.0	9.65
9/1/77	100.7	39.37	0.588	3.96	11.8	20.10
9/6/77	605.9	29.21	0.934	2.40	9.0	7.40
"	"	59.69	1.909	3.90	17.0	19.30
10/10/77	651.5	41.91	1.789	2.50	10.6	11.70
10/14/77	341.2	17.78	0.549	2.11	7.2	4.64
"	"	22.86	0.706	2.50	9.1	6.49
"	"	38.10	1.177	2.50	13.8	12.80
"	"	53.34	1.648	4.00	14.4	20.10
10/17/77	341.2	27.94	0.863	2.50	8.0	8.48
"	"	43.18	1.334	3.50	13.2	15.20
"	"	68.58	2.119	3.50	25.6	28.10
10/22/77	459.9	17.15	1.453	1.20	4.0	4.00
"	"	22.23	1.883	2.20	7.0	5.66
"	"	62.87	5.328	2.70	16.4	22.60
10/24/77	599.2	66.04	1.850	2.00	4.3	5.18
"	"	52.71	1.477	4.00	14.0	16.40
10/27/77	470.2	32.39	0.726	3.50	7.9	9.28
10/29/77	238.9	52.71	1.181	4.37	22.7	22.30
11/16/77	347.5	134.62	3.020	4.68	53.5	68.60
11/20/77	347.7	114.30	2.560	6.05	45.0	55.10
"	"	93.98	2.110	5.05	35.53	42.50
11/29/77	794.4	93.98	4.020	3.43	35.50	32.30
12/12/77	605.6	69.85	2.979	2.66	23.40	23.80
"	"	83.82	3.574	2.66	31.20	30.30

Table 5.2.1 Summary of experiments on radial surface heated jet in a stagnant environment.

RUN NO.	T_a (°C)	T_j (°C)	v_j (10^{-2} cm ² /sec)	$\alpha(T_j)$ (10^{-4})	Δ (10^{-3})	B (cm ⁴ /sec ³)	l_{MB} (cm)	Fr = $\frac{M^{5/4}}{QB^{1/2}}$	Re _j = $\frac{M^{1/2}}{v_j}$	Re _j /Fr ² = $\frac{BQ^2}{v_j M^2}$	$R_1/l_{QM} =$ $\left(\frac{M^4}{v_j^3 Q^2 B}\right)^{1/8}$
10/17/78	21.5	26.4	0.7955	2.748	1.346	422.2	36.19	9.28	10320	119.8	55.85
10/18/78	21.0	25.3	0.8138	2.646	1.138	356.8	39.36	10.10	10090	98.94	56.55
10/19/78	20.9	30.2	0.7378	3.081	2.865	898.5	24.81	6.36	11120	274.8	52.27
10/20/78	21.4	30.8	0.729	3.131	2.943	923.0	24.47	6.28	11250	285.7	52.33

Note: $r_j = 3$ in. (7.62 cm), $h_j = 1/8$ in. (0.3175 cm), $l_{QM} = \sqrt{2\pi r_j h_j} = 3.899$ cm

$$Q = 320 \text{ cm}^3/\text{sec}$$

$$u_j = Q/2\pi r_j h_j = 21.05 \text{ cm/sec}$$

$$M = Qu_j = 6736.3 \text{ cm}^4/\text{sec}^3$$

$$\alpha(T_j) = (-0.773 + 0.19 T_j - 0.0027 T_j^2 + 0.000021 T_j^3) \times 10^{-4}$$

For pure water an algebraic expression for the thermal expansion is given by Batchelor (1970) as

$$\alpha(T) = (-0.773 + 0.19 T - 0.0027 T^2 + 0.000021 T^3) \times 10^{-4} \quad (5.2.2)$$

which is plotted in Figure 5.2.1 as a solid curve. The values of kinematic viscosity of the hot water discharged are given in Figure 5.2.2,

$$\nu_j(T) = (1.745 - 0.0468 T + 0.0005823 T^3 - 0.2614 \times 10^{-5} T^3) \times 10^2 \text{ cm}^2/\text{sec}, \quad (5.2.3)$$

which is from the data also given by Batchelor (1970).

In these experiments the ambient water depth H was kept at 17.78 cm (7 inches). The relative depth of ambient water, H/h_j , was then fixed at 56 and the aspect ratio of the jet, h_j/r_j , was fixed at 1/24. The maximum value of the temperature excess at radial distance r , defined by

$$\frac{\Delta T_m}{\Delta T_j} = \frac{T(r,0) - T_a}{T_j - T_a}$$

was found to decay proportionally with the inverse of r , as shown by the data plotted in Figures 5.2.3 and 5.2.4. However,

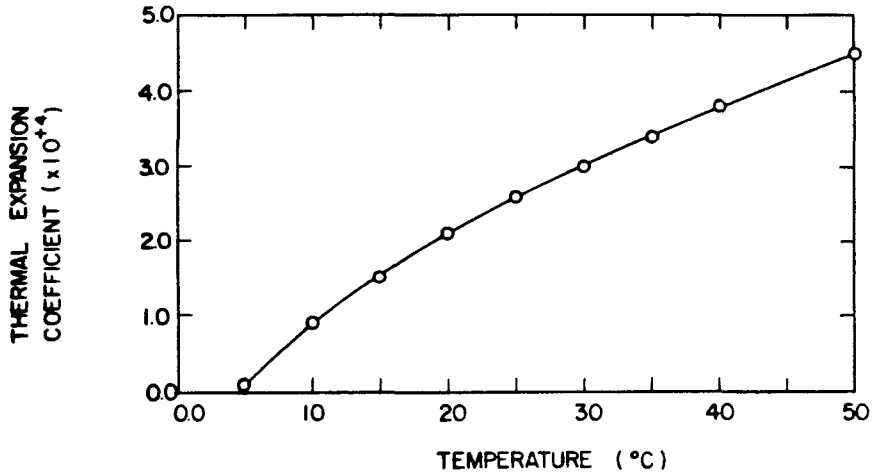


Figure 5.2.1 Thermal expansion coefficient of water as a function of temperature after Kotsovinos (1975).

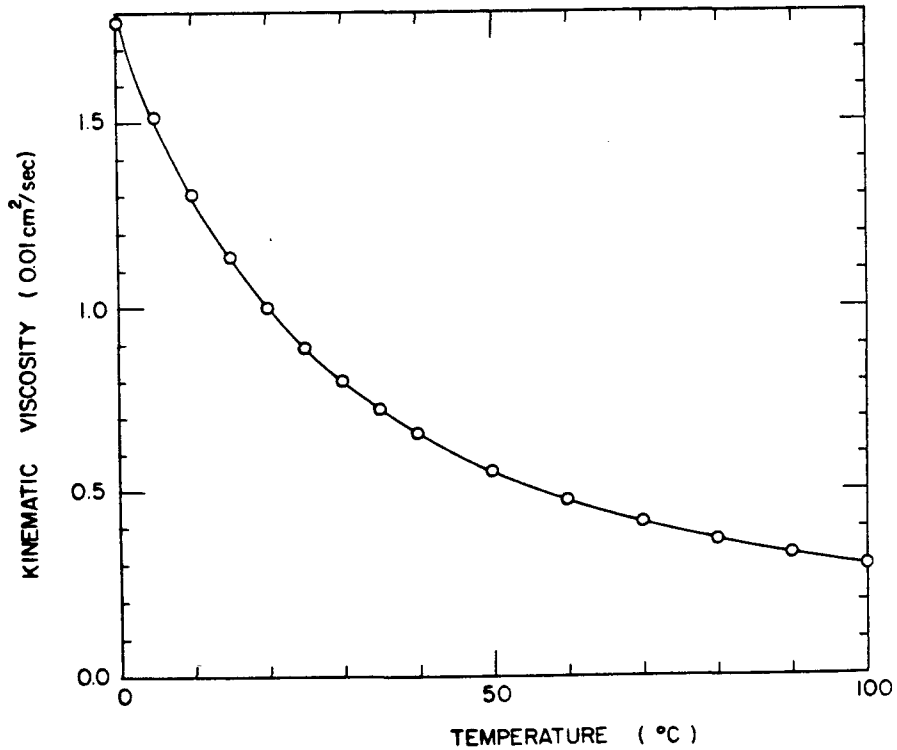


Figure 5.2.2 Kinematic viscosity of water as a function of temperature.

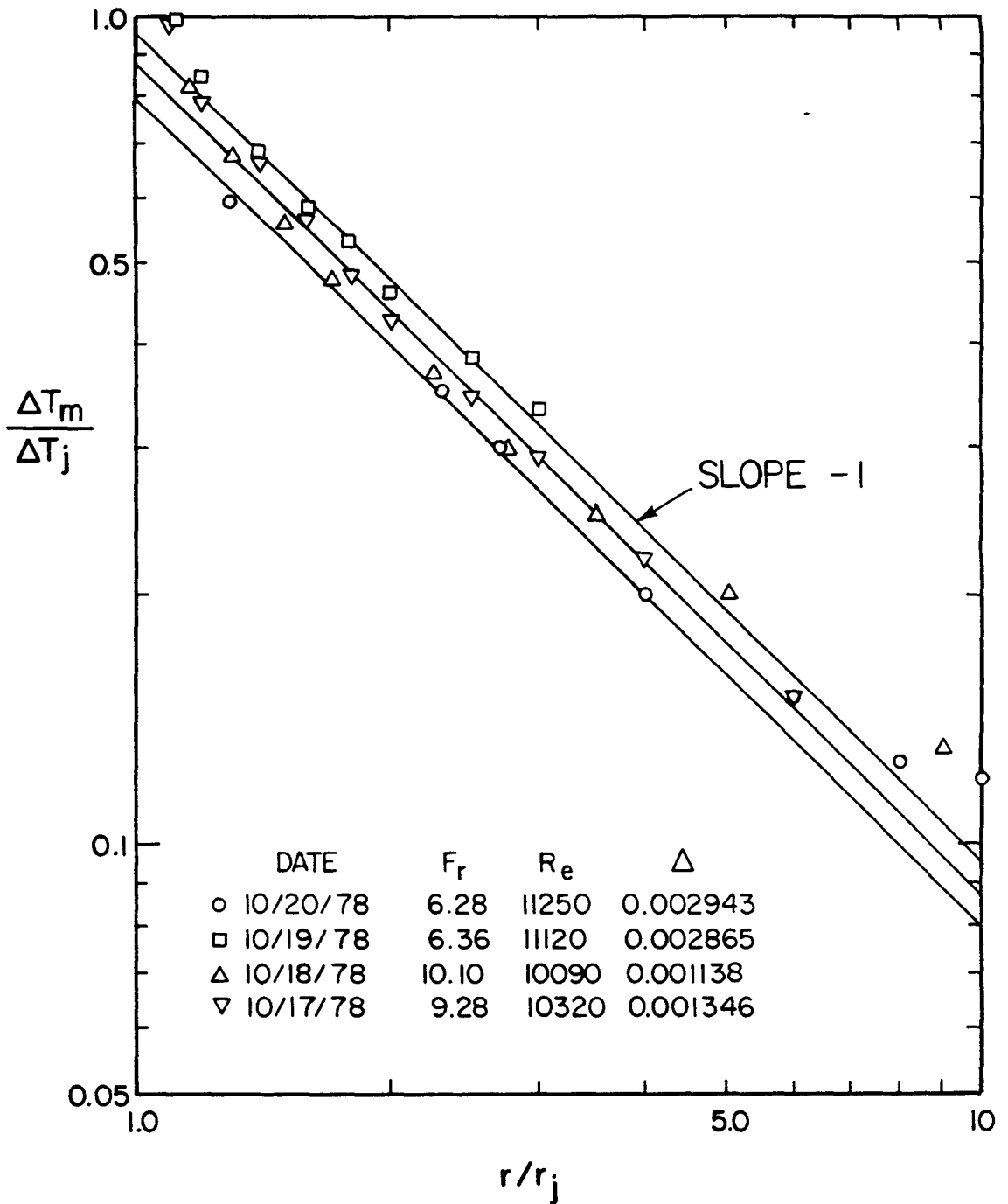


Figure 5.2.3 Relation of the maximum value of relative mean temperature excess to the relative radial distance r/r_j .

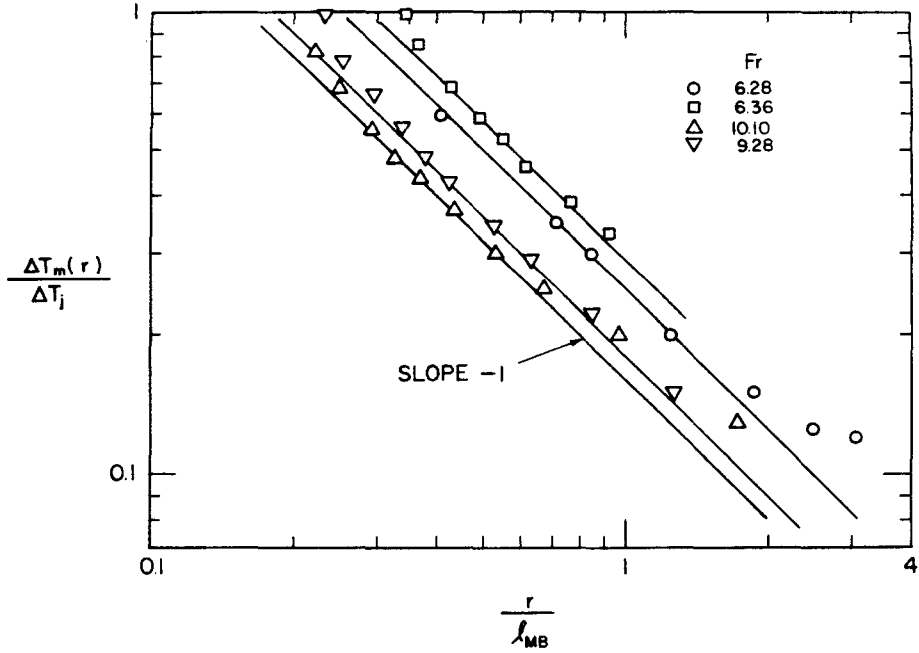


Figure 5.2.4 Relation of the maximum value of relative mean temperature excess to the normalized radial distance r/λ_{MB} .

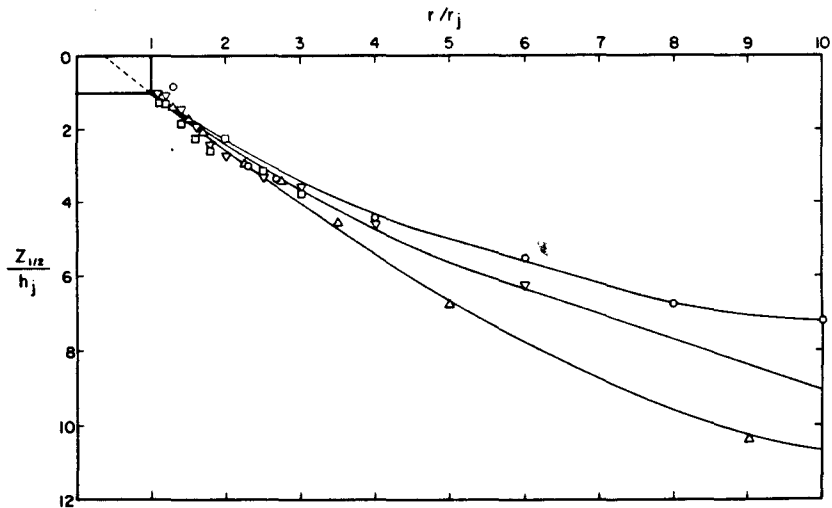


Figure 5.2.5 Relation of the normalized half-thickness to the normalized radial distance. Symbols are defined in Figure 5.2.4.

while the decay exponent of -1 is clearly independent of Froude number the coefficient of proportionality is not.

The half-thickness $z_{1/2}(r)$ of the time averaged mean temperature excess above the ambient temperature is not a linear function of the radial distance r . In Figure 5.2.5, it is clear that the relative half-thickness, $z_{1/2}(r)/h_j$ is a concave upwards curve and is deflected and the deflection is more rapid for a lower Froude number which implies it is due to a buoyancy effect.

The time averaged mean temperature excess is found to have a self-similar distribution, as shown in Figure 3.2.6(a), (b), (c), and (d). It is very close to the Prandtl-Tollmein's solution obtained when the two coefficients, K_u and K_c , are equal as discussed in Chapter 3.

One profile of the intensity of turbulent temperature fluctuations is shown in Figure 5.2.7. The maximum value of turbulent intensity, $\sqrt{T'^2/\Delta T_m}$, seems to increase with increasing radial distance r/r_j and the location of the maximum turbulent intensity deepens with increasing radial distance.

5.3 Radial Surface Buoyant Jet in a Cross Current

Experiments were performed to evaluate the performance of a buoyant radial surface jet in a cross current. The primary purpose of the experiments was to determine the relative importance of the jet momentum and buoyancy fluxes.

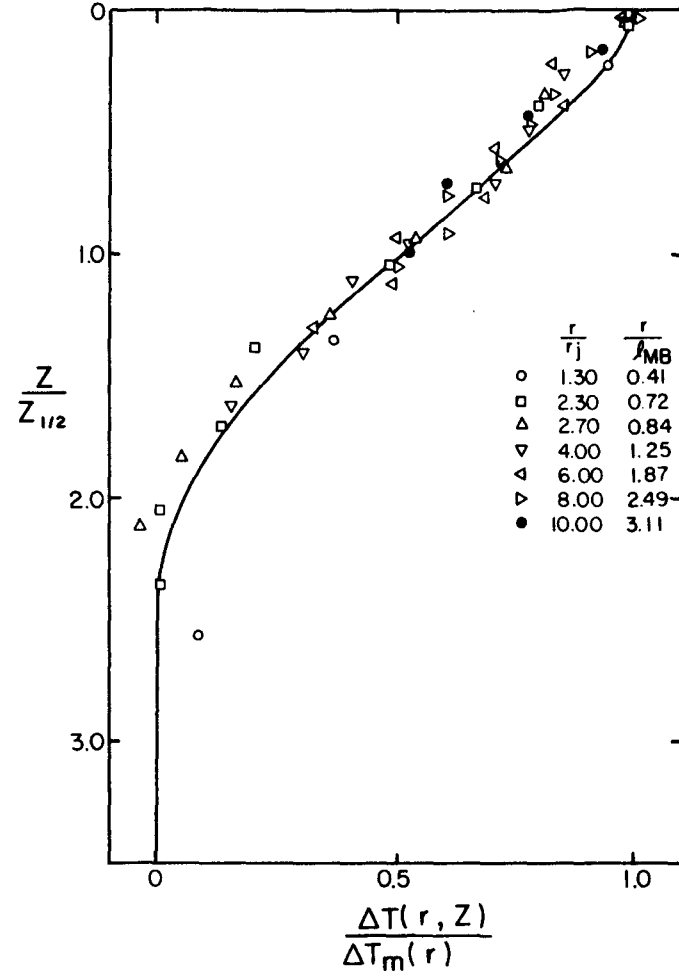
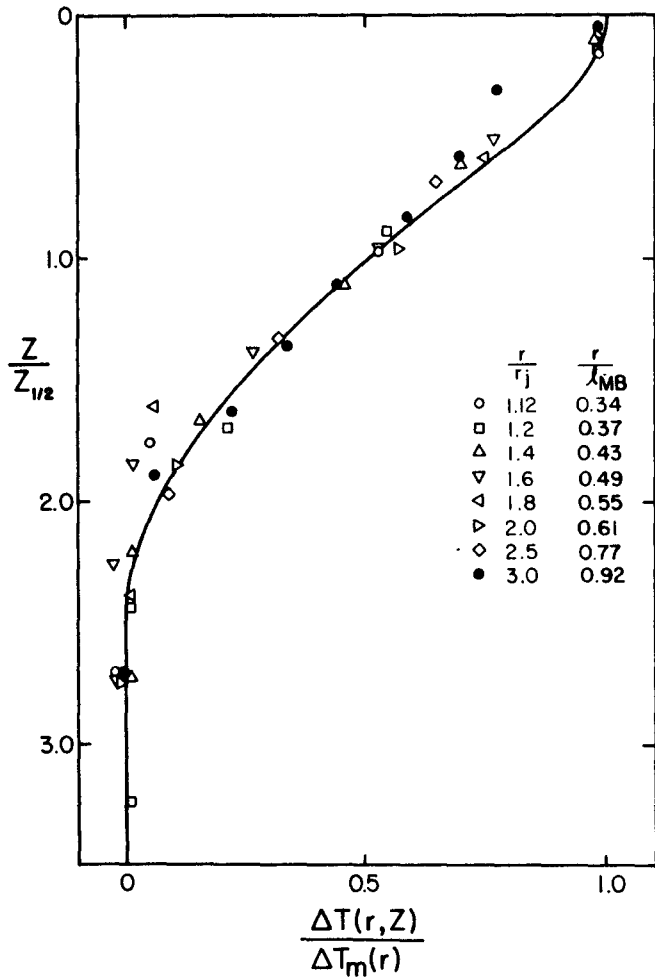
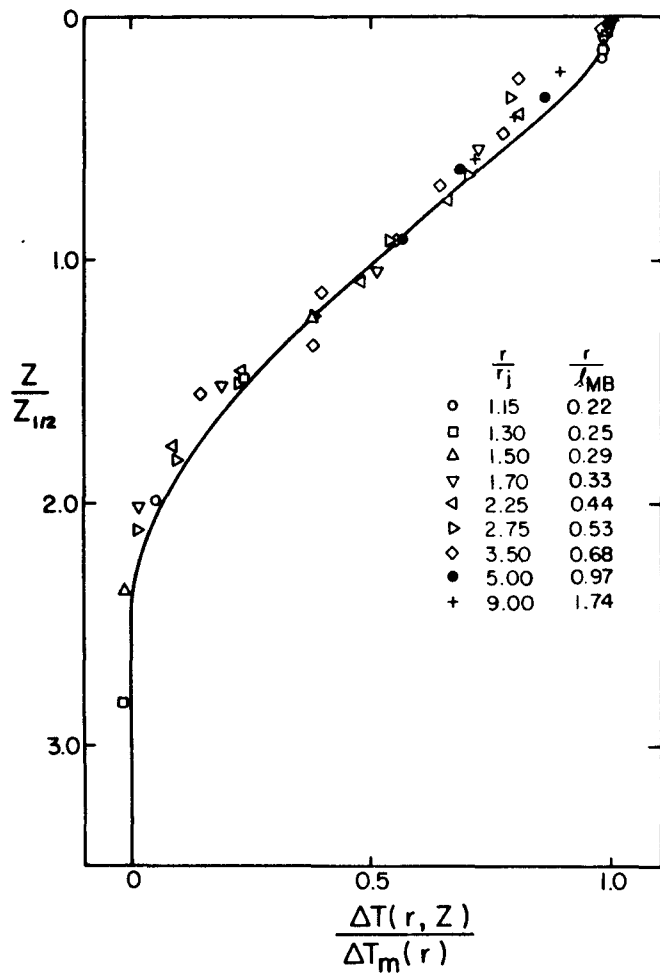
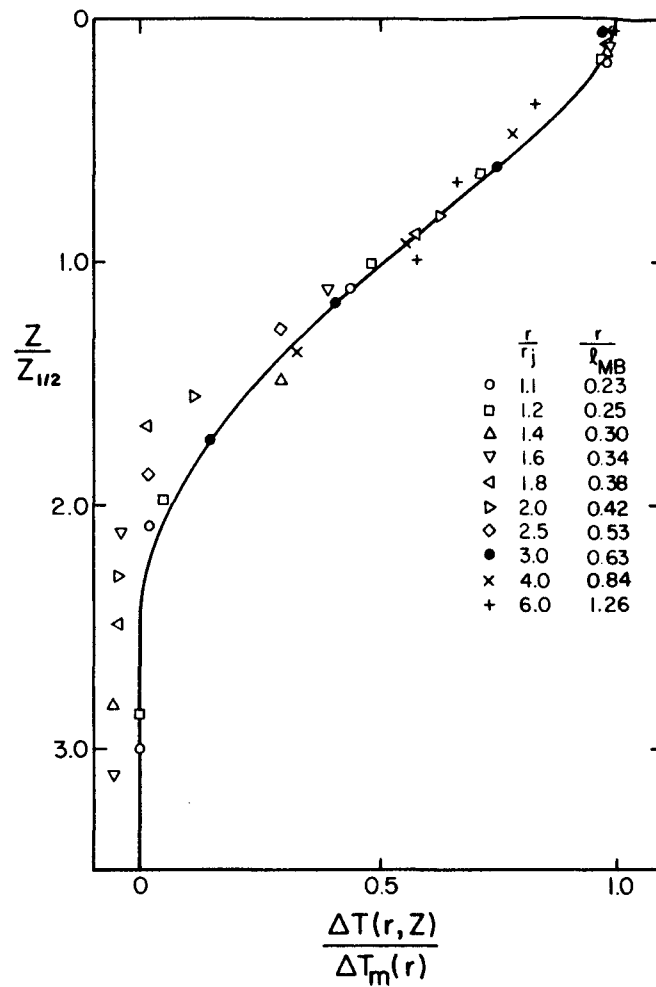


Figure 5.2.6 Self-similar relative mean temperature excess above the ambient temperature. Solid line denotes the Prandtl-Tollmien solution given in Chapter 3.
 (a) Run No. 10/19/78, $Fr = 6.36$. (b) Run No. 10/20/78, $Fr = 6.28$.



(c) Run No. 10/18/78, Fr = 10.10.



(d) Run No. 10/17/78, Fr = 9.28.

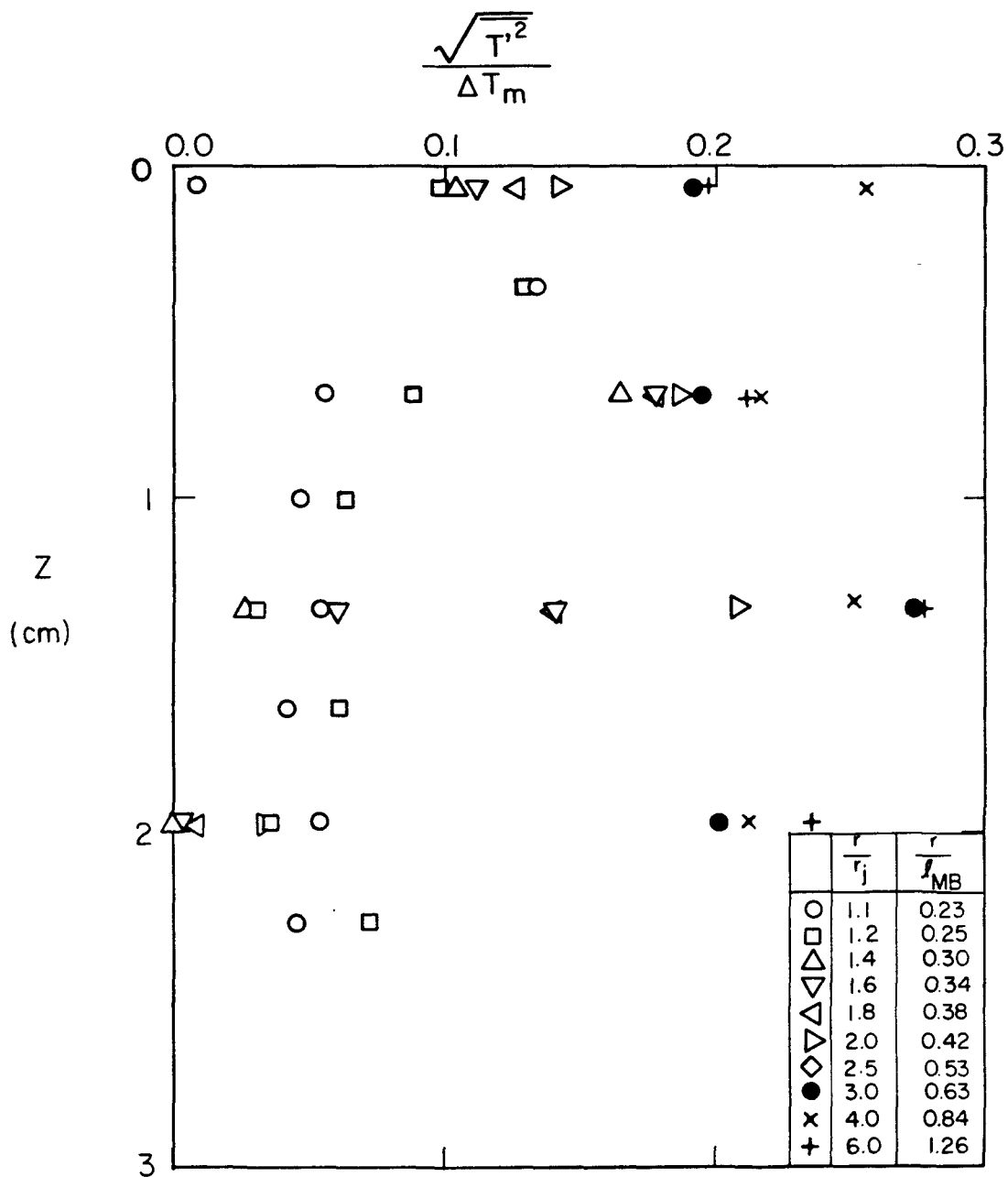


Figure 5.2.7 Profiles of the intensity of turbulent temperature fluctuations for radial surface heated jet (Run No. 10/17/78) versus depth and relative radial distance.

As listed in Table 5.3.1 seventeen experiments were performed and in all the tests the ambient water depth was maintained at $H = 19.81$ cm with a circular slot jet thickness of $h_j = 0.3175$ cm (1/8 inch). The relative depth of water was therefore constant at $H/h_j = 62.4$ for all experiments.

A typical development of initiation flow pattern to a well-developed flow field due to a radial surface buoyant jet discharge in a cross current is shown in Figure 5.3.1. The downstream edge position x_d in the current direction can be simply predicted by the superposition of a radial surface buoyant jet front and a uniform current. Therefore, the downstream edge grows as a starting jet flow followed by a starting plume flow, but with the velocity relative to the free stream, i.e.

$$R(t) = x_d - Ut \quad , \quad (5.3.1)$$

where U is the current speed.

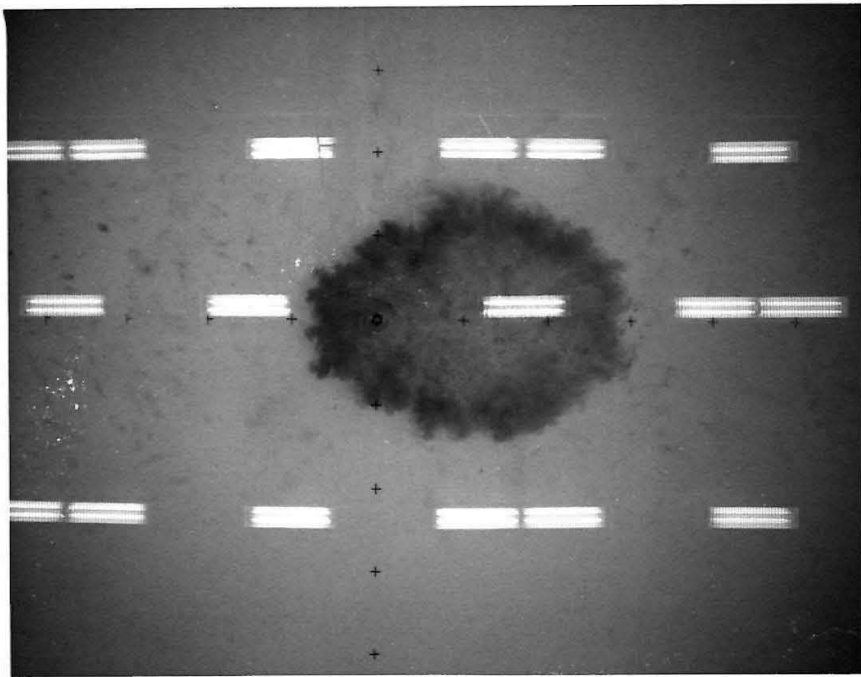
When the downstream displacement is plotted against time as in Figure 5.3.2 it is clearly seen that two different spreading regimes are distinguishable. One is the starting jet flow which specifies a jet coefficient defined by

$$\frac{R(t)}{M^{1/4} t^{1/2}} = \frac{x_d - Ut}{M^{1/4} t^{1/2}} \quad . \quad (5.3.2)$$

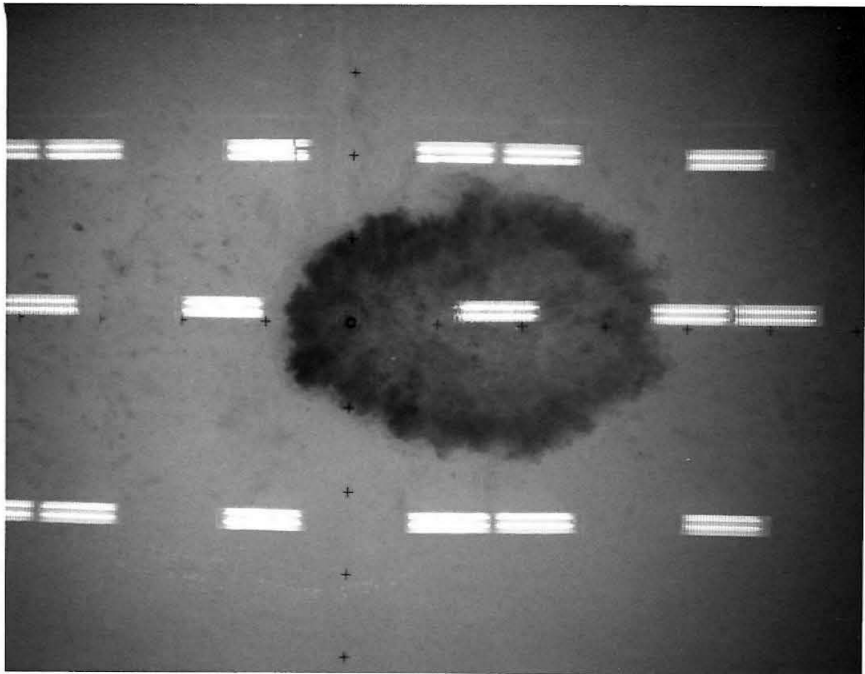
In the four tests where this is appropriate the coefficient varies from 1.22 to 1.45. The other regime is the inertial starting

Table 5.3.1 Summary of experimental data for a radial surface buoyant jet in a cross current.

Run No.	U (cm/sec)	ρ_a (gm/cm ³)	ρ_j (gm/cm ³)	Δ (10 ⁻⁴)	Q (cm ³ /sec)	u_j (cm/sec)	M (cm ⁴ /sec ²)	B (cm ⁴ /sec ³)	Fr	Re
2/23/78	0.920	0.9991	0.9987	4.005	328.0	21.58	7080	128.7	17.4	8400
2/27/78	"	0.9997	0.9985	12.018	"	"	"	386.3	10.1	"
3/02/78	0.962	1.000	0.9985	15.020	"	"	"	482.9	9.0	"
3/05/78	"	0.9997	0.9988	9.011	325.3	21.40	6970	287.3	11.5	8340
3/06/78	"	1.000	0.9990	10.010	328.0	21.58	7080	321.8	11.0	8400
3/06/78a	"	0.9995	0.9988	7.008	"	"	"	225.3	13.2	"
3/07/78	0.926	0.9998	0.9989	7.010	202.7	13.33	2700	179.0	7.2	5200
3/07/78a	0.949	0.9999	0.9985	14.523	328.0	21.58	7080	466.8	9.2	8400
3/08/78	0.933	0.9999	0.9989	10.011	202.7	13.33	2700	198.8	6.8	5200
3/09/78	0.933	1.000	0.9993	7.005	328.0	21.58	7080	225.2	13.2	8400
3/21/78	1.00	0.9996	0.9995	1.001	315.4	20.75	6540	30.9	33.5	8090
3/22/78	"	0.9995	0.9991	4.004	"	"	"	123.8	16.8	"
3/22/78a	"	"	0.9990	5.005	"	"	"	154.7	15.0	"
3/27/78	"	0.9997	0.9995	2.001	320	21.05	6740	62.8	24.1	8200
3/28/78	"	0.9994	0.9992	1.501	376	24.73	9300	55.3	32.7	9640
3/29/78	"	0.9997	0.9973	24.568	320	21.05	6740	770.4	6.9	8200
4/10/78	"	1.000	0.9992	8.006	376	24.73	9300	295.0	14.1	9640

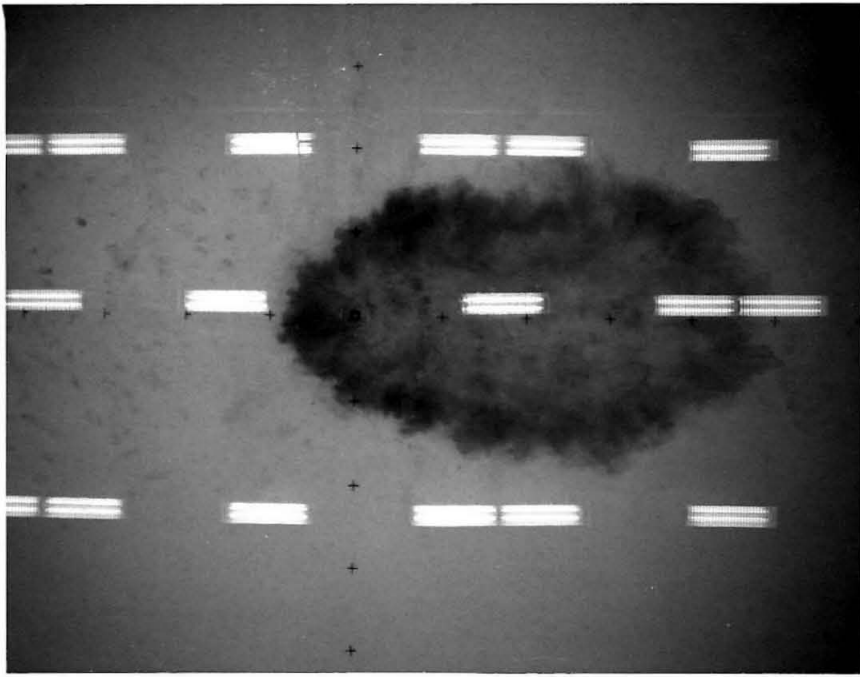


(a)

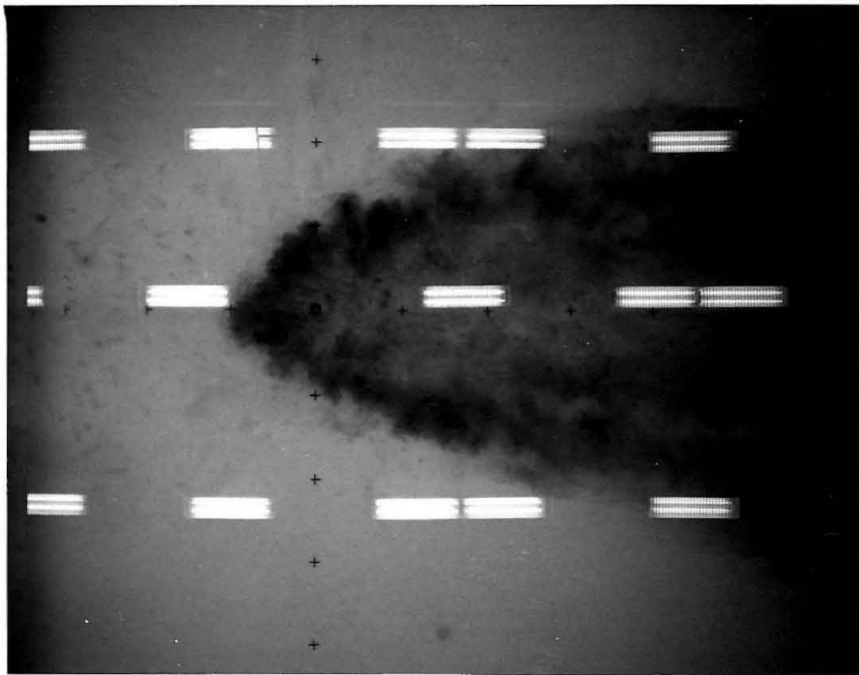


(b)

Figures 5.3.1(a,b) Photographs of the development of a surface flow due to a radial surface buoyant jet in a cross current (Run No. 4/10/77). (a) $t = 35$, (b) $t = 80$ seconds after initiation of discharge.



(c)



(d)

Figures 5.3.1(c,d) Photographs of the development of a surface flow due to a radial surface buoyant jet in a cross current (Run No. 4/10/77). (c) $t = 110$, (d) $t = 485$ seconds after initiation of discharge.

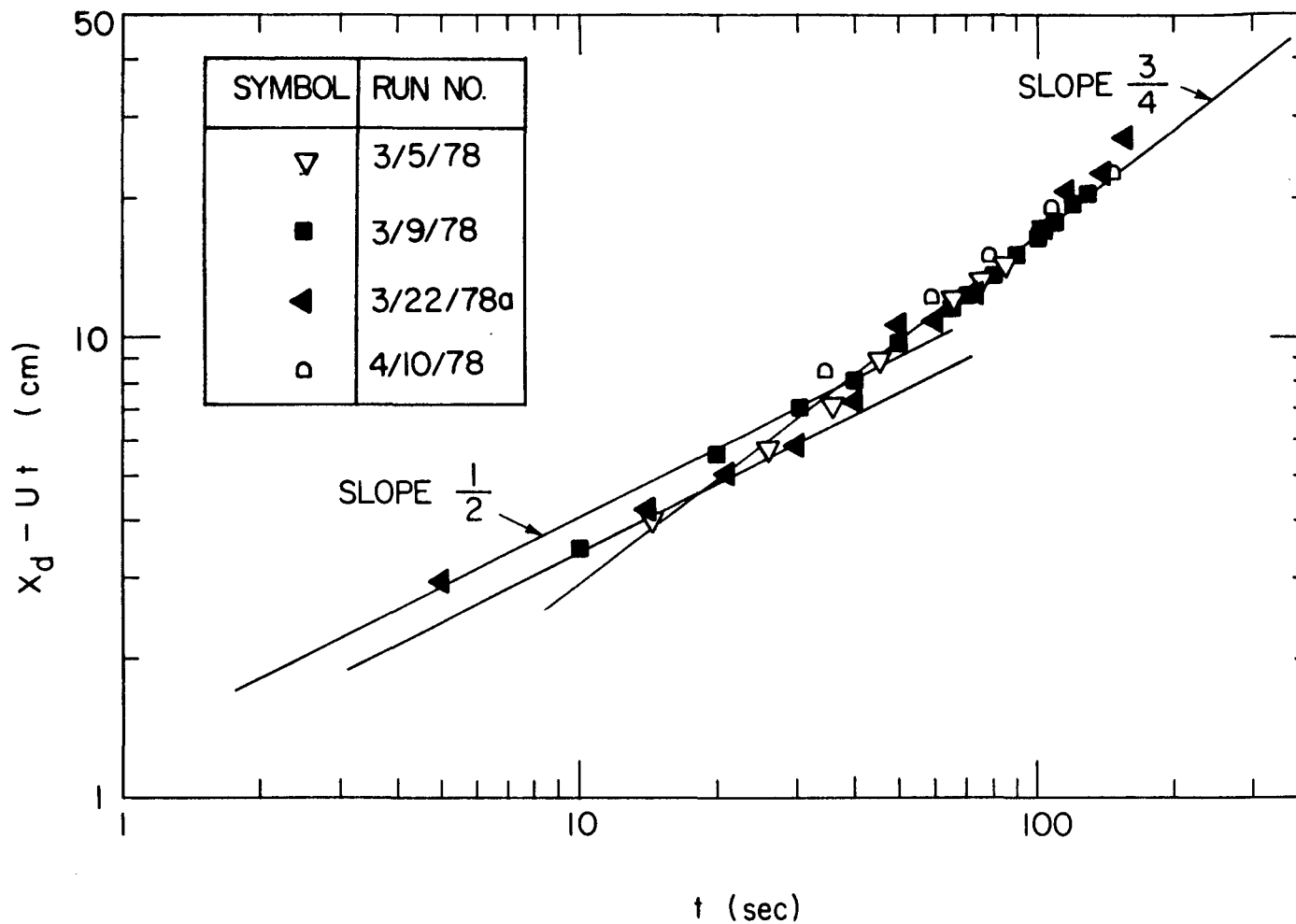


Figure 5.3.2 Growth histories of the downstream edge of an initiating surface field.

plume (slope 3/4) for which the starting plume coefficients, defined by

$$\frac{R(t)}{B^{1/4} t^{3/4}} = \frac{x_d - Ut}{B^{1/4} t^{3/4}}, \quad (5.3.3)$$

vary from 1.24 to 1.44.

In general, the location of the upstream edge of radial buoyant jet in a crossflow is specified by

$$\frac{x_e}{B/U^3} = \phi \left(\frac{U^2}{B/M^{1/2}}, Re, Fr, H/h_j \right) \quad (5.3.4)$$

Where M and B are specific or kinematic fluxes of momentum and buoyancy. It was shown in Section 3.5.4 that the asymptotic solutions corresponding to a radial momentum jet is

$$x_e = \frac{d^2}{2} \frac{M^2}{U} \quad (5.3.5)$$

and

$$x_e = \left(\frac{3}{4} c^{4/3} \right)^3 \frac{B}{U^3} \quad (5.3.6)$$

for a radial surface plume. d and c are respectively the coefficients of spreading defined by jets and plumes in the absence of a crossflow that

$$d = \frac{R(t)}{M^{1/4} t^{1/2}} \quad (5.3.7)$$

and

$$c = \frac{R(t)}{B^{1/4} t^{3/4}} \quad (5.3.8)$$

Figure 5.3.3 is a plot of the upstream position x_e normalized by B/U^3 and it shows how the upstream position varies from a jet flow to a plume flow. The upstream displacement was actually found to fluctuate between a maximum and a minimum value which is denoted by bars on the figure. The straight lines are shown for $d = 1.05$ and $c = 0.75$.

Figure 5.3.4 is a logarithmic plot of the surface half-width produced by a radial buoyant jet. The surface field also shows the transition from a jet flow to a plume flow. For Run No. 3/22/78a, the appropriate dimensionless numbers for each range of half-width of the surface field are found to be

$$\frac{y}{M^{1/4} (x/U)^{1/2}} = 1.06 \quad , \quad (5.3.9)$$

$$\frac{y}{B^{1/4} (x/U)^{3/4}} = 0.76 \quad , \quad (5.3.10)$$

and

$$\frac{y}{\left(\frac{g\Delta Q^3}{\nu}\right)^{1/8} \left(\frac{x}{U}\right)^{1/2}} = 0.85 \quad . \quad (5.3.10)$$

The value of kinematic viscosity ν was assumed to be $0.01 \text{ cm}^2/\text{sec}$.

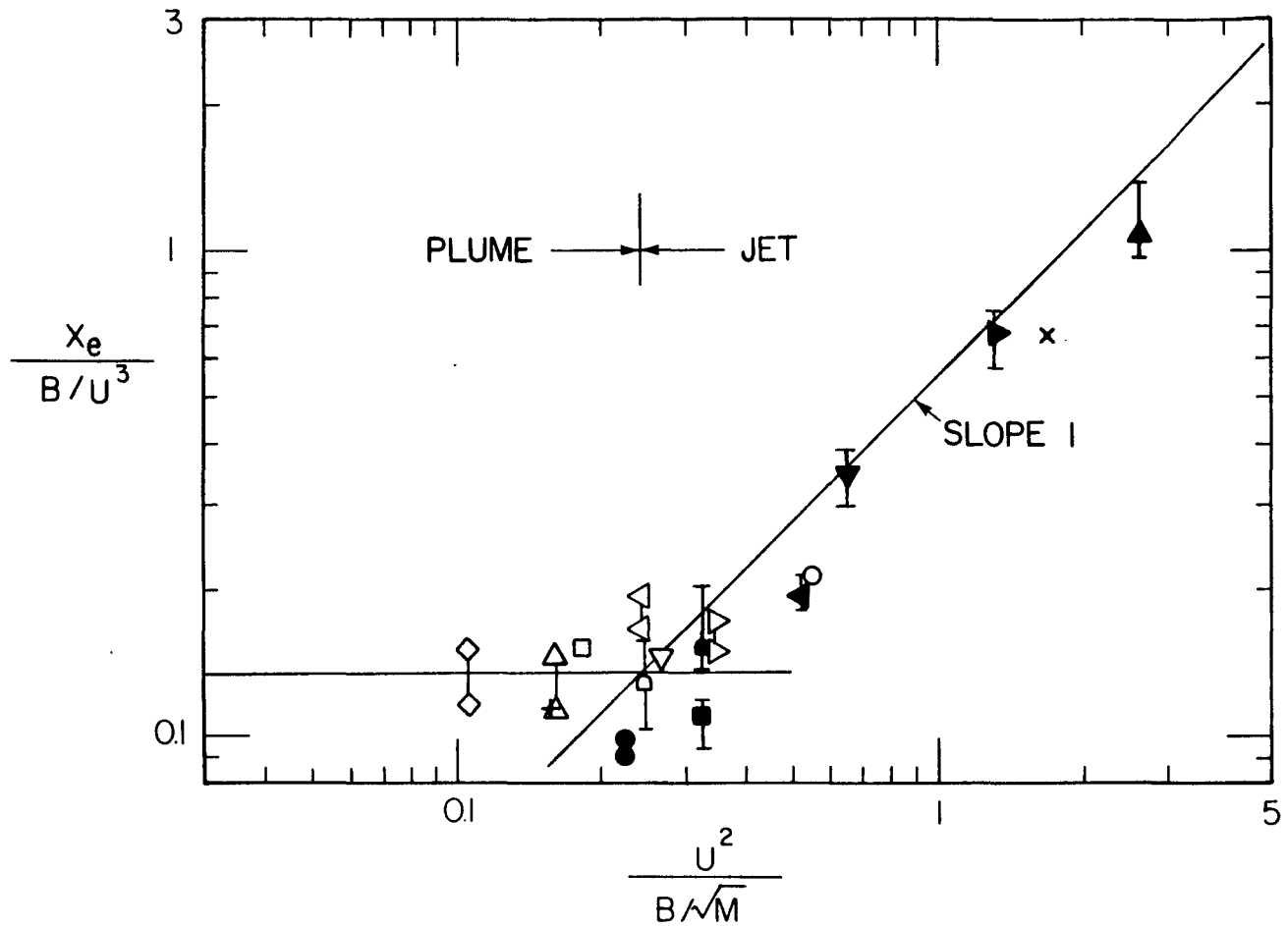


Figure 5.3.3 Upstream edge position of surface buoyant field. Symbols are defined in Table 5.3.2.

Table 5.3.2 Calculation of upstream edge position.

Symbol	Run No.	$\frac{U^2}{B/M^{1/2}}$	$\frac{x_e}{B/U^3}$		
			Minimum	Median	Maximum
○	2/23/78	0.553	-	0.216	-
□	2/27/78	0.184	-	0.152	-
△	3/02/78	0.161	-	0.112	0.145
▽	3/05/78	0.269	-	0.142	-
◁	3/06/78	0.242	0.168	-	0.197
▷	3/06/78a	0.345	0.150	-	0.170
◻	3/07/78	0.249	0.101	0.130	0.158
+	3/07/78a	0.162	-	0.100	0.112
●	3/08/78	0.228	0.0935	-	0.0987
■	3/09/78	0.325	0.0963	0.110	0.119
▲	3/21/78	2.616	0.970	1.099	1.293
▼	3/22/78	0.654	0.299	0.347	0.388
◀	3/22/78a	0.523	0.181	0.194	0.213
▶	3/27/78	1.308	0.590	0.669	0.701
×	3/28/78	1.743	-	0.687	-
◇	3/29/78	0.106	0.117	-	0.151
●	4/10/78	0.327	0.136	0.153	0.207

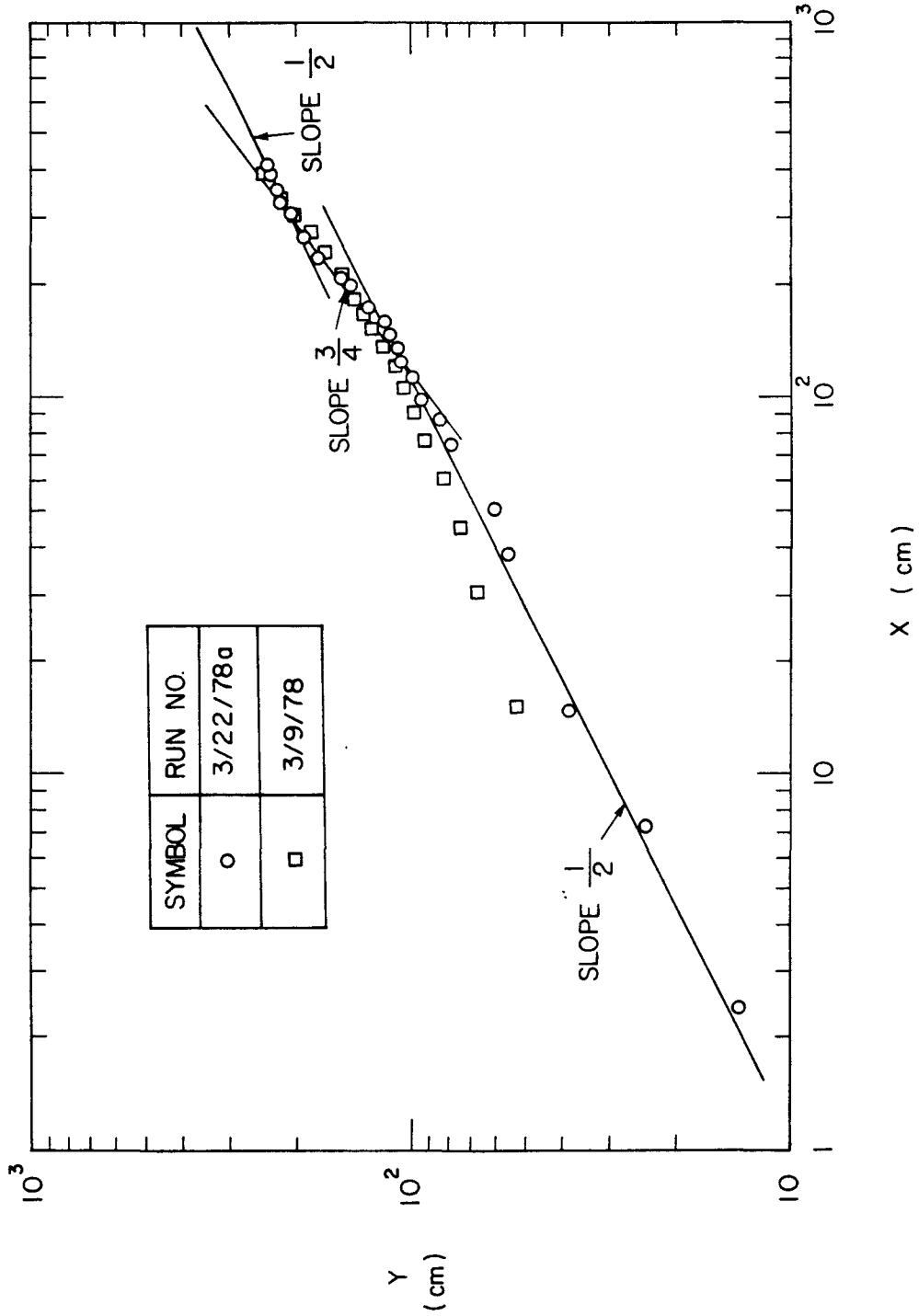


Figure 5.3.4 Growth of a surface buoyant field measured from upstream edge.

CHAPTER 6

COMPARISONS WITH PREVIOUS STUDIES

In this chapter theoretical solutions derived in Chapter 3 will be compared with the results of previous experimental studies. The first section discusses spreading currents in a homogeneous environment ($i = 0$) and in the second section those in a linearly density-stratified environment ($i = 1$).

6.1 Spreading Currents in Homogeneous Environment6.1.1 Plane Current from a Finite Volume Release

From the theoretical results previously developed for this case a plane current (after a brief initial period) will advance asymptotically according to the regime described by

$$R(t) = 1.890 (g\Delta V)^{1/3} t^{2/3} \quad (6.1.1)$$

for an inertial-buoyancy balanced flow and according to

$$R(t) = 1.133 \left(\frac{g\Delta V^3}{\nu} \right)^{1/5} t^{1/5} \quad (6.1.2)$$

for a viscous-buoyancy balanced flow without any mass diffusion.

Table 6.1.1 lists twenty experiments performed by Almquist (1973). In these experiments a tilting partition plate separated

Table 6.1.1 Summary of experiments performed by Almquist (1973) on the plane surface currents due to a finite volume release.

Symbol	Run No.	ρ_a (gm/cm ³)	ρ_b (gm/cm ³)	$\frac{\rho_a - \rho_b}{\rho_b}$ (10 ⁻³)	V (in ²)	R ₀ (in)	h ₀ (in)	$\frac{\sqrt{g\Delta h_0} h_0}{v}$	$\frac{R(t)}{(g\Delta v)^{1/3} t^{2/3}}$	$\frac{R(t)}{\left(\frac{g\Delta v^3}{v}\right)^{1/5} t^{1/5}}$
△	1	1.018	1.014	3.945	4.5	2.12	4.25	7.51	1.580	1.720
▽	2	"	"	"	8.0	2.83	5.65	11.51	1.750	1.610
●	3	"	"	"	4.0	2.00	4.00	6.86	1.571	1.630
○	4	"	"	"	2.0	1.414	2.83	4.08	1.493	1.810
●	5	"	1.009	8.920	3.0	1.732	3.46	8.30	1.564	1.660
▷	6	"	"	"	1.0	1.00	2.00	3.65	1.430	1.881
▲	7	"	1.015	2.956	1.0	1.00	"	2.10	1.471	1.897
▲	8	"	"	2.956	3.0	1.732	3.46	4.78	1.455	1.670
■	9	"	"	"	9.0	3.00	6.00	10.91	1.695	1.730
○	10	"	1.009	8.920	"	"	"	18.95	1.696	1.710
▽	1B	1.020	1.004	15.936	4.5	2.12	4.25	15.10	1.820	1.730
◆	2B	"	"	"	9.0	3.00	6.00	25.33	1.808	1.726
○	3B	"	"	"	18.0	4.24	8.49	42.63	1.835	-
○	4B	"	1.012	7.905	4.5	2.12	4.25	10.63	1.762	1.700
○	5B	"	"	"	18.0	4.24	8.49	30.02	1.760	-
+	6B	"	"	"	9.0	3.00	6.00	17.84	1.840	1.730
△	7B	1.0217	1.0177	3.930	2.0	1.414	2.83	4.07	1.377	1.700
◇	8B	"	"	"	4.5	2.12	4.25	7.50	1.550	1.760
□	9B	"	"	"	9.0	3.00	6.00	12.58	1.666	1.635
×	10B	"	"	"	18.0	4.24	8.49	21.17	1.740	1.540

Note: Initial aspect ratio $h_0/R_0 = 2.00$.

a right-triangular section of volume V per unit width from the ambient fluid. The triangular section had an initial horizontal length R_0 on one side and an initial vertical thickness h_0 on the other side. The plate was removed and the time when the dyed front passed through several fixed locations was recorded. The growth histories of twenty fronts are plotted in Figure 6.1.1. Two slopes are apparent: one is $2/3$, which is appropriate for inertial-buoyancy spreading, and the other is $1/5$ which is appropriate for the viscous-buoyancy spreading. A normalized plot of the twenty experiments is shown in Figure 6.1.2, however, all of the experimental points do not collapse into a single curve. Equation (6.1.1) is found to be an upper limit for inertial-buoyancy spreading. Equation (6.1.2) gives a low estimate for the viscous-buoyancy spreading. (The value of the kinematic viscosity of spreading fluid was assumed to be $\nu = 0.01 \text{ cm}^2/\text{sec}$ for all calculations).

An understanding of the variations of the coefficients in Eqs. (6.1.1) and (6.1.2) is apparent from a dimensional analysis. The growth histories of a frontal trajectory can be described by

$$\frac{R(t)}{R_1} = \phi \left(\frac{t}{t_1}, \frac{R_1}{R_0}, \frac{h_0}{R_0} \right), \quad (6.1.3)$$

in which the time and the length scales $t_1 = \left(\frac{\nu^4}{(g\Delta)^2} \right)^{1/7}$ and $R_1 = \left(\frac{g\Delta V^5}{\nu^2} \right)^{1/7}$ are as listed in Table 3.1.2. The second

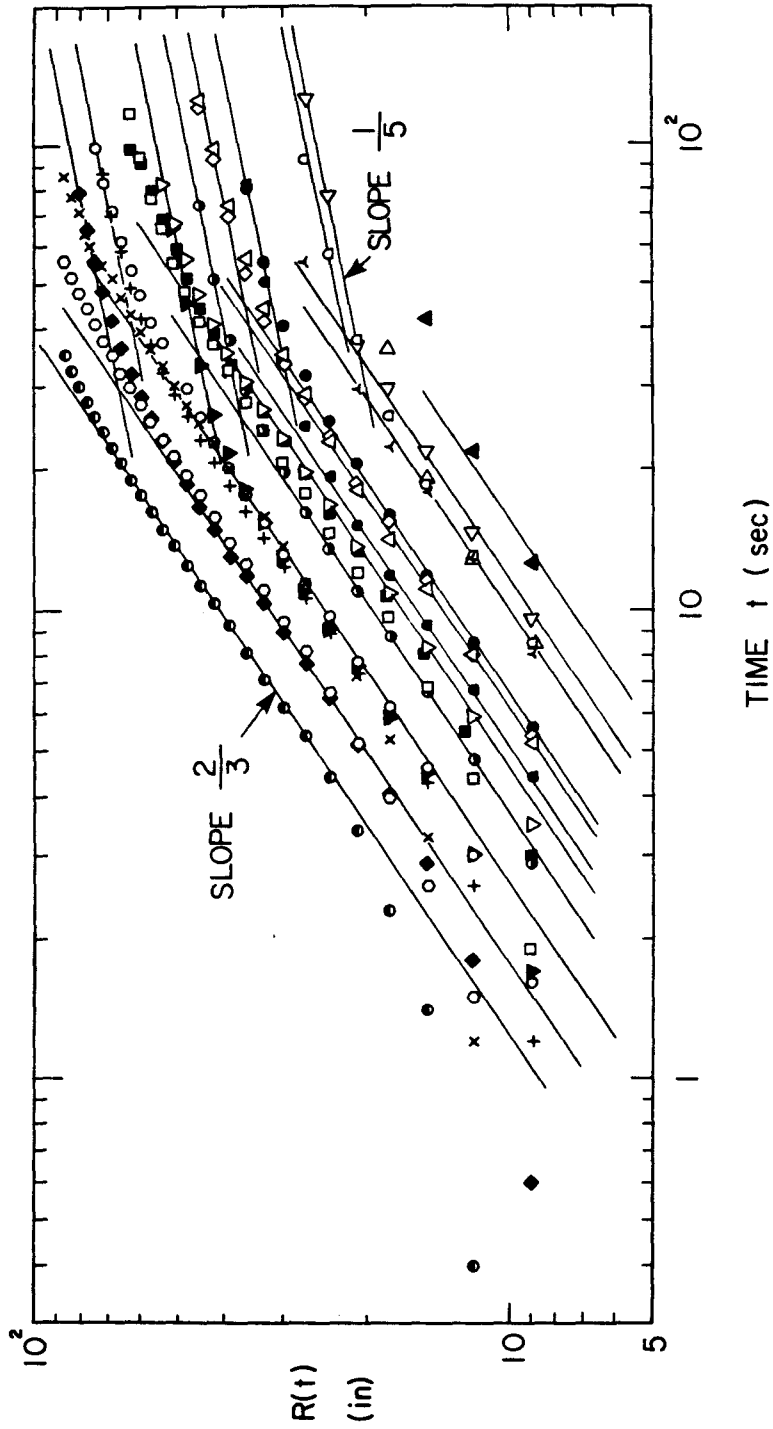


Figure 6.1.1 Growth histories for plane surface spreading currents due to a finite volume release. Experimental data are from Almquist (1973). Symbols are defined in Table 6.1.1.

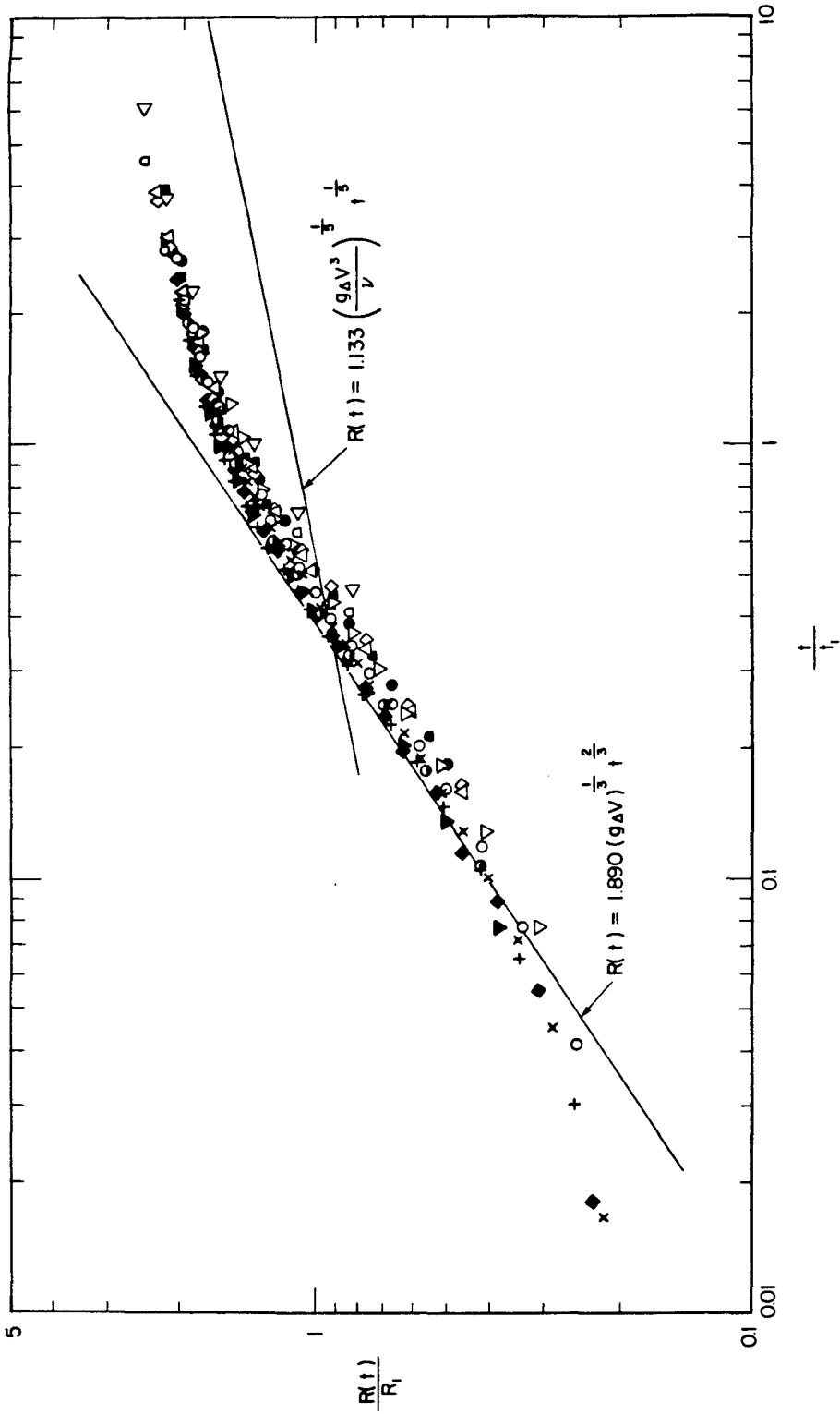


Figure 6.1.2 Normalized growth histories of plane surface spreading currents due to a finite volume release. Symbols are defined in Table 6.1.1.

$$R_1 = \left(\frac{g\Delta V^5}{\nu} \right)^{1/7} \quad \text{and} \quad t_1 = \left(\frac{V^4}{(g\Delta)^2 \nu^3} \right)^{1/7}$$

dimensionless number, R_1/R_0 , represents the viscosity effect in terms of ratio of the two length scales, R_1 and R_0 . The ratio is

$$\frac{R_1}{R_0} = \frac{\left(\frac{g\Delta V^5}{\nu^2}\right)^{1/7}}{R_0} = \left(\frac{1}{2} \frac{g\Delta h_0^3 h_0^2}{\nu^2 R_0^2}\right)^{1/7} \quad (6.1.4)$$

which contains a Reynolds number $\sqrt{g\Delta h_0} h_0/\nu$ and an aspect ratio of the initial geometry h_0/R_0 . The aspect ratio h_0/R_0 in these experiments was kept at 2.0. Therefore, when the length scale ratio $R_1/R_0 \rightarrow \infty$, an inviscid buoyant spreading current will result. In this case the coefficients which have the following form

$$\frac{R(t)}{(g\Delta V)^{1/3} t^{2/3}} = \phi\left(\frac{\sqrt{g\Delta h_0} h_0}{\nu}, \frac{h_0}{R_0}\right), \quad (6.1.5)$$

will approach the limiting value c_{ooo} as shown in Figure 6.1.3 and as given in Eq. (6.1.1). Similarly, when the length scale ratio $R_1/R_0 \rightarrow 0$, the flow will begin with a viscous current. The coefficient for a viscous-buoyancy spreading current,

$$\frac{R(t)}{\left(\frac{g\Delta V^3}{\nu}\right)^{1/5} t^{1/5}} = \phi\left(\frac{\sqrt{g\Delta h_0} h_0}{\nu}, \frac{h_0}{R_0}\right), \quad (6.1.6)$$

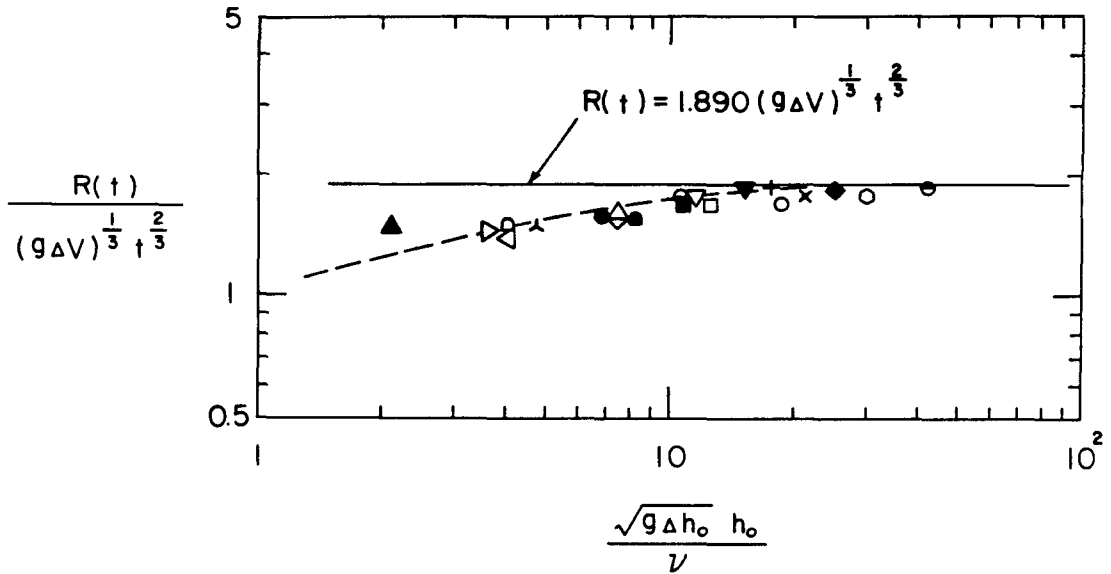


Figure 6.1.3 Coefficients of inertial-buoyancy spreading currents expressed as a function of Reynolds number $\sqrt{g\Delta h_o} h_o/\nu$.

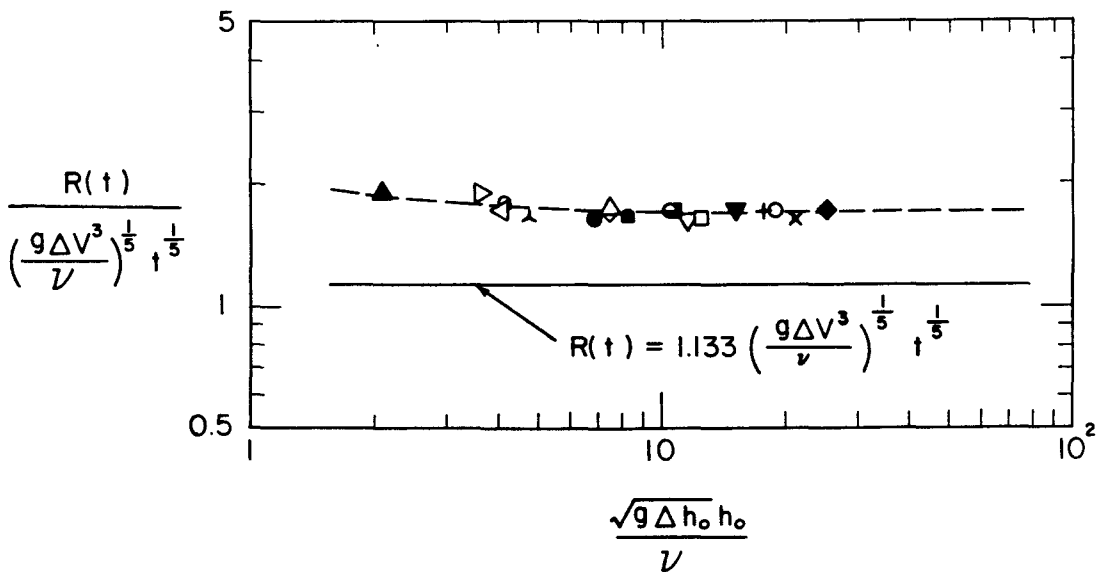


Figure 6.1.4 Coefficients of viscous-buoyancy spreading currents expressed as a function of Reynolds number $\sqrt{g\Delta h_o} h_o/\nu$.

will approach to the limiting value b_{000} given in Eq. (6.1.2). The fact that the data in Figure 6.1.4 lie above the data specified by Eq. (6.1.6) may be due to the error of assuming a constant value of kinematic viscosity of spreading fluid $\nu = 0.01 \text{ cm}^2/\text{sec}$ for all computations, although this is unlikely because of the fact that the experimental data are all very consistent.

A similar set of experiments were performed by Keulegan (1957) although the details of the initial flow are somewhat different. His experiments involved the density front produced by a finite length lock exchanging fluid with a semi-infinite channel. This flow eventually produces a rapidly decelerating velocity due both to the viscous effects and the fact that there is a finite volume of fluid spreading. Keulegan made observations of the frontal velocity at different locations rather than observing the frontal travel as a function of time. In this case it is best to rewrite Eq. (6.1.2) in the form (see also Eq. (3.1.15) with $n = m = 0$).

$$U(R) = \dot{R}(R) = 0.373 \left(\frac{g\Delta V^3}{\nu R^4} \right) \quad , \quad (6.1.7)$$

which may be used to describe the decelerating flow. Equation (6.1.7) rewritten in terms of lock variables, as defined in Figure 2.3.2, is

$$\frac{U(R)}{\sqrt{g\Delta H}} = 0.373 \frac{\sqrt{g\Delta H} H}{\nu} \left(\frac{L_0}{H}\right)^3 \left/\left(\frac{R}{H}\right)^4\right. , \quad (6.1.7a)$$

in which $R(t) = L(t) + L_0$ and H is the initial lock fluid depth.

Figure 6.1.5 shows that the frontal velocity decays with travel distance as the distance to the -4 power anticipated by Eqs. (6.1.7) and (6.1.7a). Equation (6.1.7a) compares very well with one set of experiments (denoted by circles). The initial Reynolds number $\sqrt{g\Delta H} H/\nu$ is approximately equal to that given by Keulegan (1957), $\sqrt{g\Delta H} H/\nu_m$, where ν_m is the mean value of kinematic viscosity of both ambient and saline fluids and the dimensionless distance R/H is approximately equal to L/H when $R(t) \gg L_0$.

Middleton (1966) performed similar experiments using turbidity currents, however, Eq. (6.1.7a) overestimates the velocity of the currents produced. The theoretical value, $U(R)/\sqrt{g\Delta H}$, (denoted by dotted line in Figure 6.1.6) is about ten times the value actually observed at the same location L/H . The simplest explanation for the discrepancy is the rapid settling of suspension which reduces the relative density difference to a value about 1% of the initial value.

From Subsection 3.2.4 we know that Eq. (6.1.1) is valid only when the initial relative density difference is much smaller than the order of 0.1. Otherwise, the coefficient in Eq. (6.1.1)

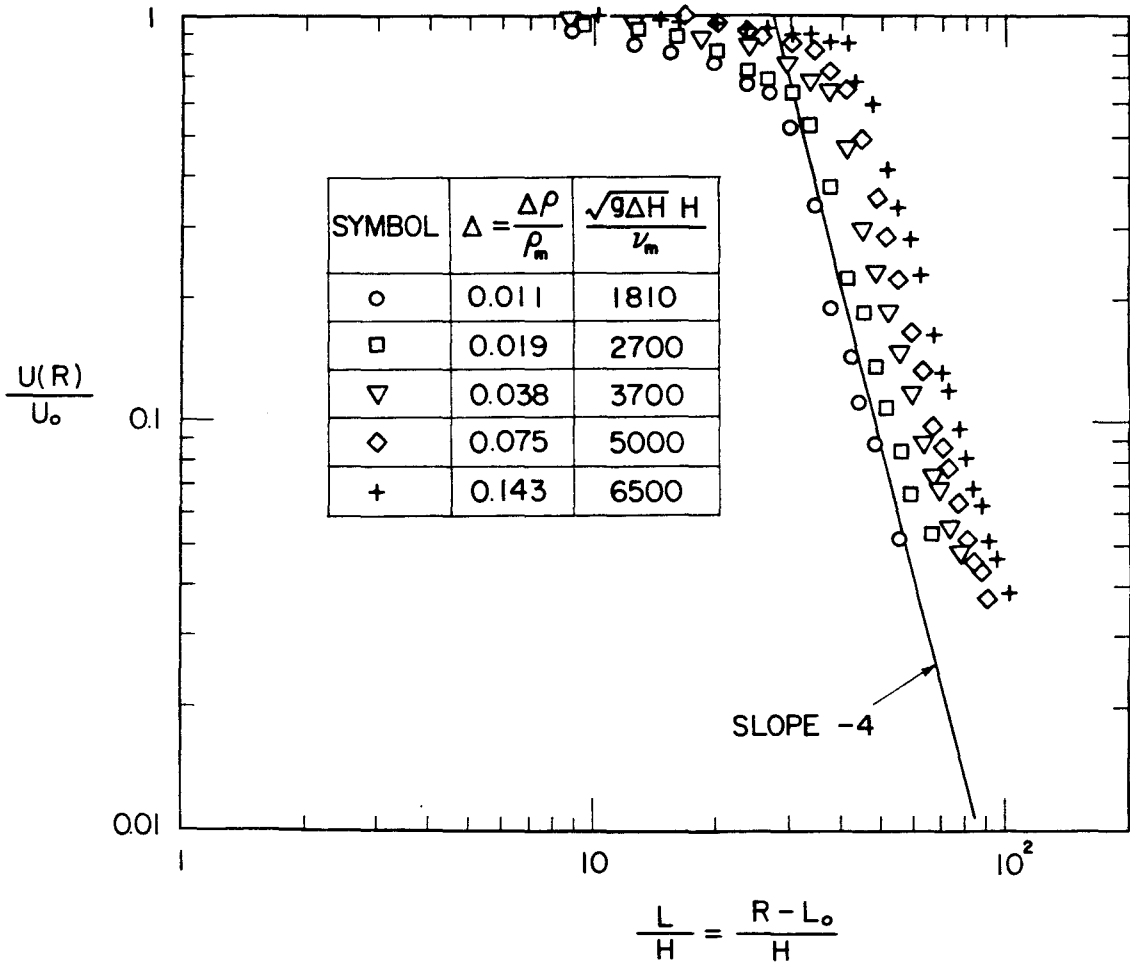


Figure 6.1.5 Frontal velocity decay of density currents from a finite-length lock exchange flow, experimental data from Figure 3 of Keulegan (1957). $H = 5.8$ cm, $L_0 = 41.7$ cm, and width of channel = 2.54 cm.

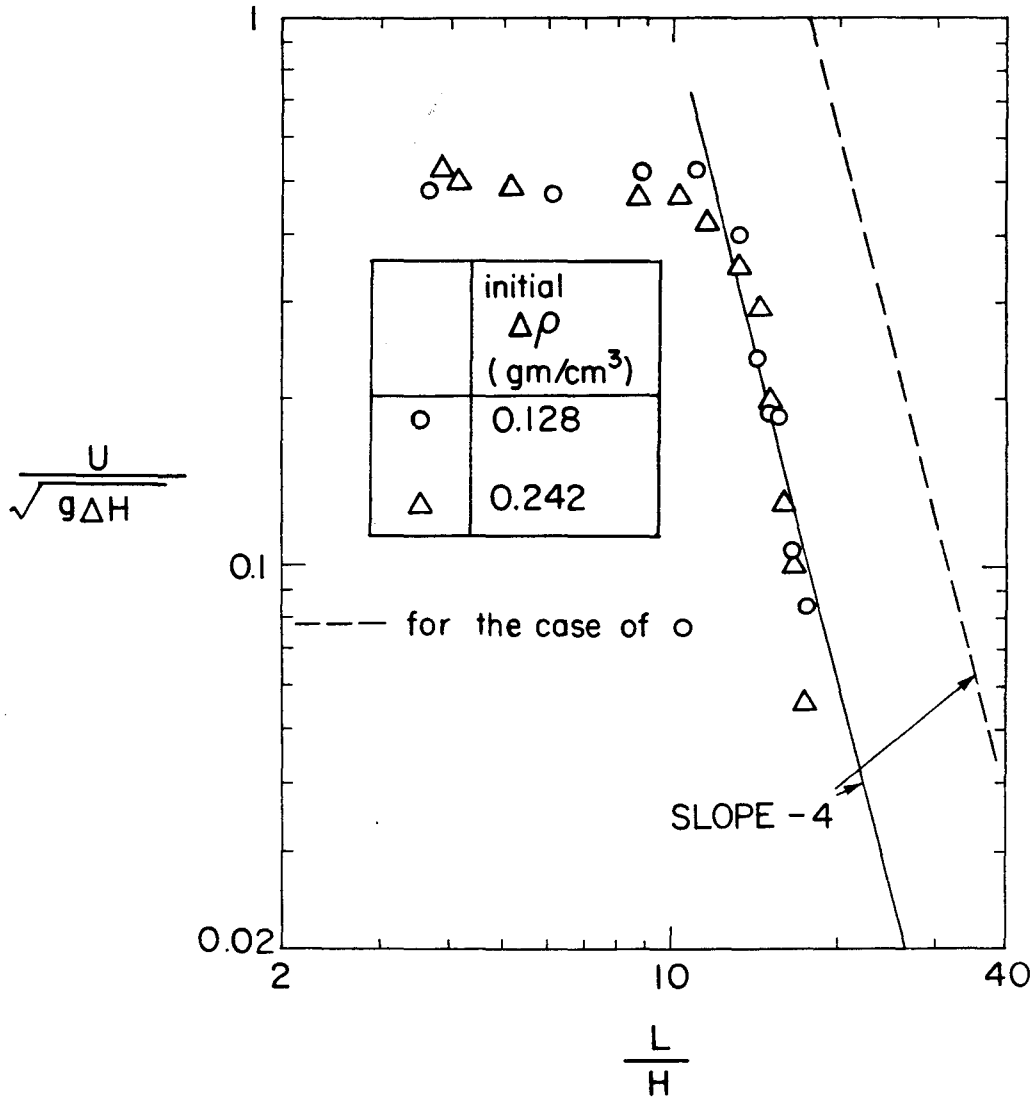


Figure 6.1.6 Frontal velocity decay of turbidity currents from a finite-length lock exchange flow, experimental data from Figure 10 of Middleton (1966). $H = 20.3$ cm, $L_o = 28.3$ cm, width of channel = 13.83 cm, and average settling velocity of suspension = 0.9 cm/sec.

needs correcting to the form

$$R(t) = \frac{1.890}{(1+\Delta)^{1/3}} (g\Delta V)^{1/3} t^{2/3} \quad . \quad (6.1.8)$$

For example, in the case of a spreading oil slick the relative density difference is $\Delta = 0.136$ for an experiment by Liang (1971). In this case Eq. (6.1.8) will be corrected to

$$R(t) = 1.811 (g\Delta V)^{1/3} t^{2/3} \quad . \quad (6.1.9)$$

However, as shown in Figure 6.1.7(a) the theoretical value given by Eq. (6.1.9) is still slightly higher than experimental observation. The reason, for this is not clear. Measurements of the spreading layer thickness $h(r,t)$ are of two types. One is a "wave-gage-type" measurement by fixing the measurement location and varying observation time. The other is a "photographic type" measurement performed by fixing the time and observing the spatial location of the front. Results for plane currents obtained by using the first technique will be discussed here. Results for the radial current case obtained with the second method will be discussed in the next subsection, 6.1.2.

The similarity profile of inertial buoyancy spreading layer thickness due to a finite volume release was derived in Section 3.2.5 as

$$h(r,t) = \frac{\dot{R}^2(t)}{4g\Delta} \left\{ 1 + \left(\frac{r}{R(t)} \right)^2 \right\} \quad , \quad (6.1.10)$$

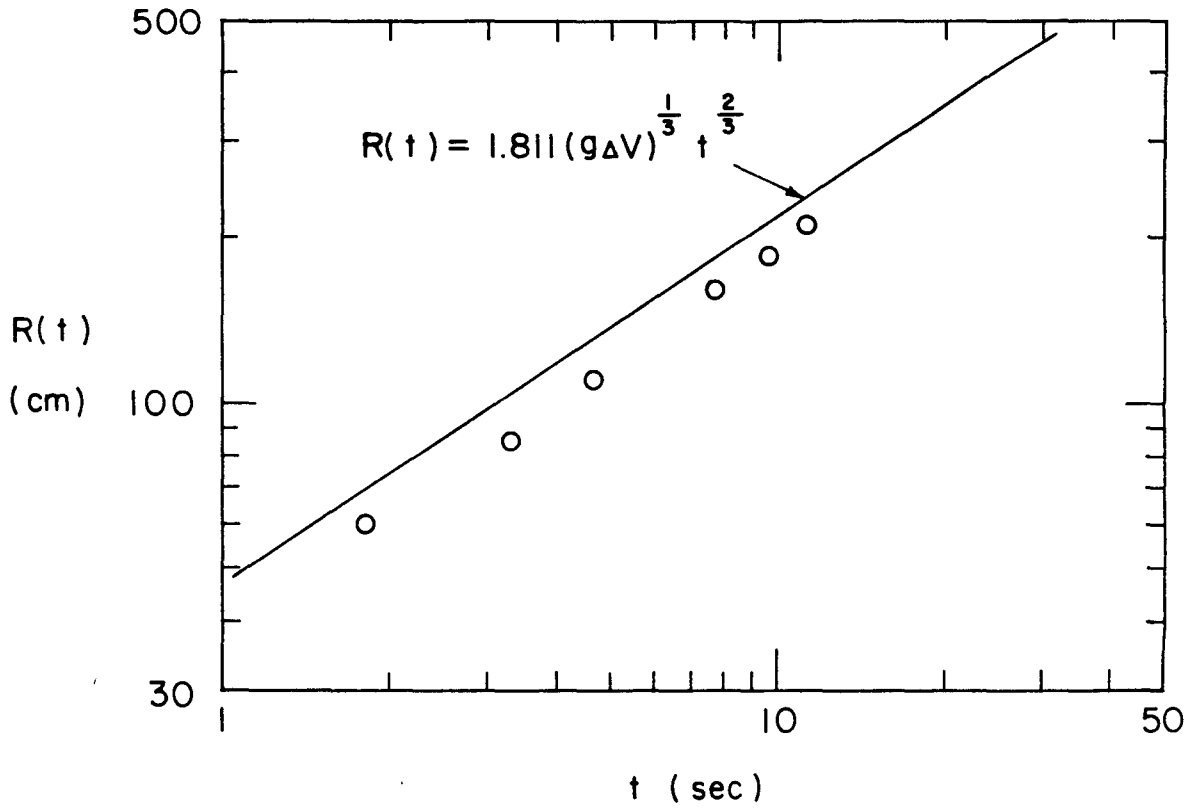


Figure 6.1.7(a) Frontal trajectory for an inertial-buoyancy oil slick spreading in a channel, data from Run No. 1 of Liang (1971). $V = 131.2 \text{ cm}^2$, $\Delta = 0.136$.

for which the frontal displacement function $R(t)$ is in Eq. (6.1.8). For a spreading oil slick the inertial layer thickness measured by photocell equipment located at r_s is actually the total thickness $h + \delta = (1 + \Delta)h$ so that the thickness as measured by Liang (1971) is of the form

$$h(r_s, t) = \frac{c^2}{9} \frac{v^{2/3}}{(g\Delta)^{1/3} t^{2/3}} \left\{ 1 + \left(\frac{r_s}{c(g\Delta v)^{1/3} t^{2/3}} \right)^2 \right\} \quad (6.1.11)$$

The value c can be computed from $c = R(t)/(g\Delta v)^{1/3} t^{2/3}$. Thus, the spreading layer thickness at one fixed location, r_s , will decay proportionally to $t^{2/3}$. Figure 6.1.7(b) shows that the agreement of the similarity solution (6.1.11) with three experimental observations by Liang (1971) is fairly good except for a damping internal wave train behind the steep front.

The collapse of a mixed region at a stably stratified interface can be viewed as a combination of two surface spreading currents. As shown in Figure 6.1.8 the numerical calculation performed by Meng and Thomson (1978) supports this assumption. The density front displacement grows proportionally to $t^{2/3}$ rather than as a linear time function.

6.1.2 Radial Current from a Finite Volume Release

After an initial stage the radial spreading current produced by a finite volume release grows asymptotically according to

$$R(t) = 1.502 (g\Delta v)^{1/4} t^{1/2} \quad (6.1.12)$$

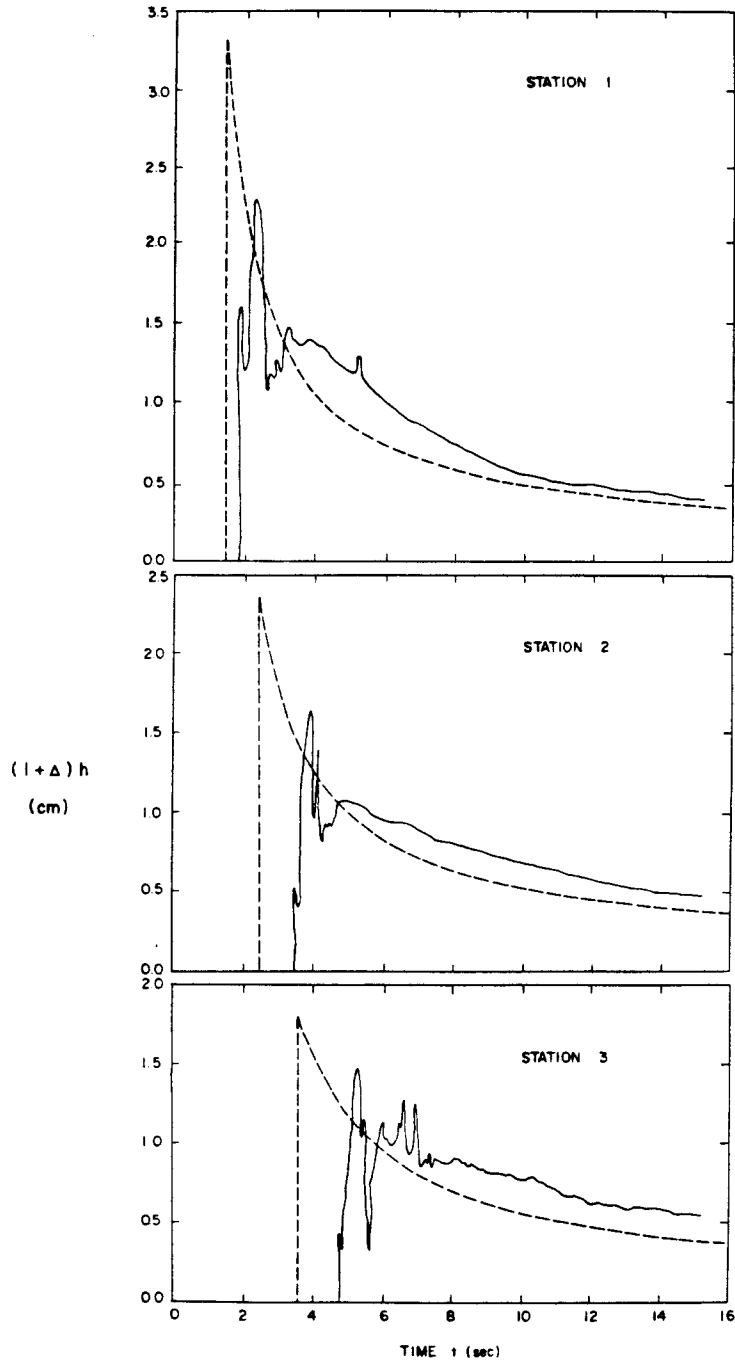


Figure 6.1.7(b) "Wave gage" measurements (in solid curve) of inertial oil slick spreading thickness by photocell equipment located at three locations (60, 85, 110 cm from end wall of channel for Station no. 1, 2, 3). Dotted curves indicate prediction by similarity solutions, data from Liang (1971).

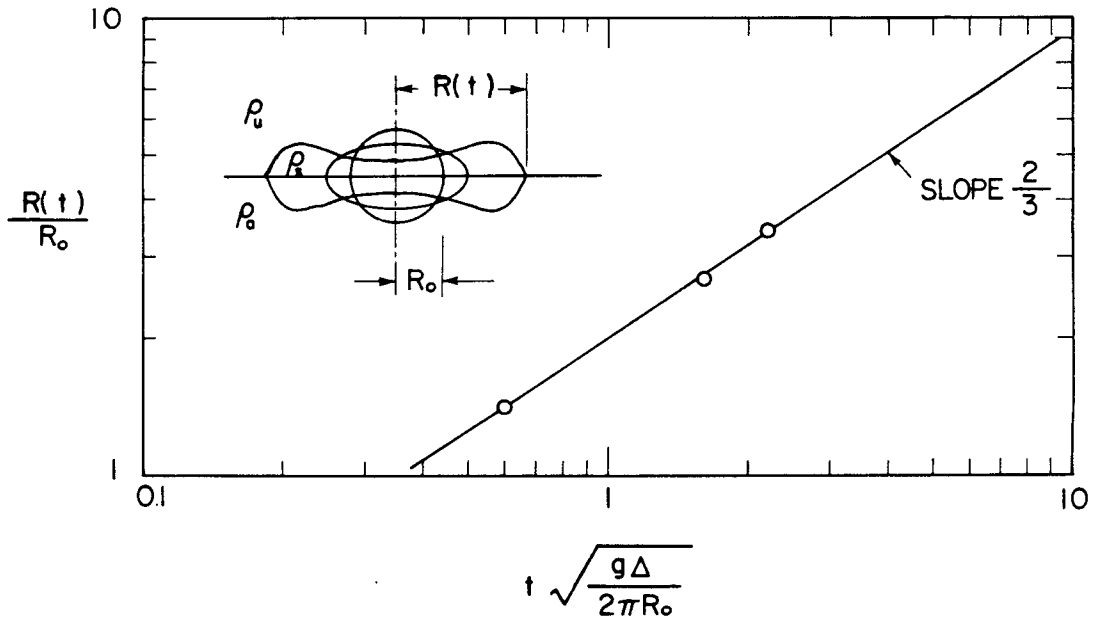


Figure 6.1.8 Dynamic collapse of a homogeneous region at a stably stratified interface. Numerical calculation data from Figure 7 of Meng and Thomson (1978).

for the inertial-buoyancy stage and then according to

$$R(t) = 0.779 \left(\frac{g\Delta V^3}{\nu} \right)^{1/8} t^{1/8} \quad (6.1.13)$$

for the viscous-buoyancy stage. Experimental results by Chen and List (1976) showed that two such regions of flow do exist but they found higher coefficients in both equations which can be ascribed to mixing.

As previously discussed for an oil slick, spreading in inertial stage, Eq. (6.1.12) needs an adjusted coefficient to give

$$R(t) = \frac{1.502}{(1+\Delta)^{1/4}} (g\Delta V)^{1/4} t^{1/2} \quad (6.1.14)$$

For the experiments by Abbott (1961) shown in Figure 6.1.9(a), $\Delta = 0.250$ and Eq. (6.1.14) becomes

$$R(t) = 1.240 (g\Delta V)^{1/4} t^{1/2} \quad (6.1.15)$$

Figure 6.1.9(b) shows that the agreement of Eq. (6.1.15) with the observations made by Abbott (1961) is very good. Figure 6.1.9(c) shows the comparison of similarity profiles developed in Subsection 3.2.5 with observations given in Figure 6.1.9(a).

The similarity profile for thickness of a radial spreading layer was computed as

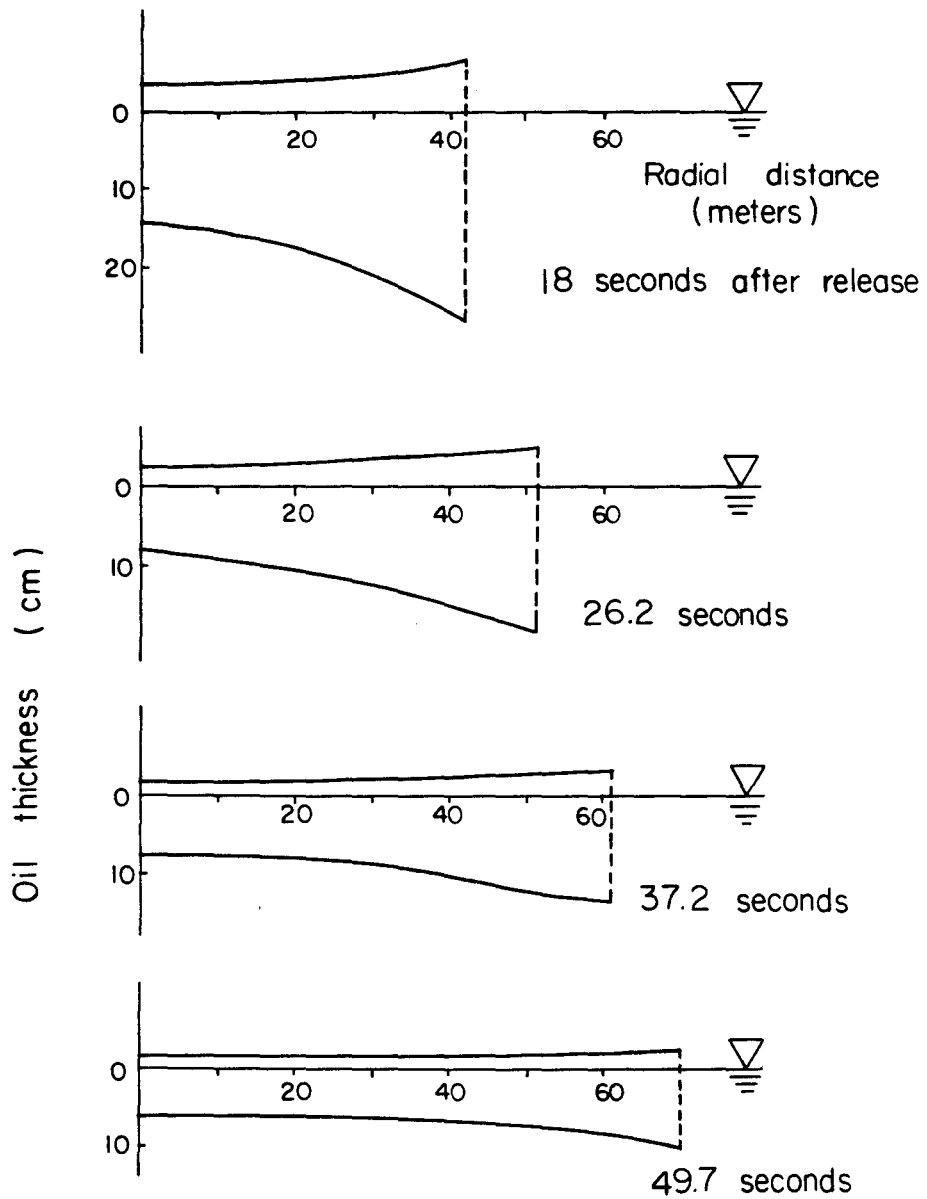


Figure 6.1.9(a) Oil spreading sections at four times after release of 1500 cubic meters of oil (1200 tons). Data from Abbott (1961).

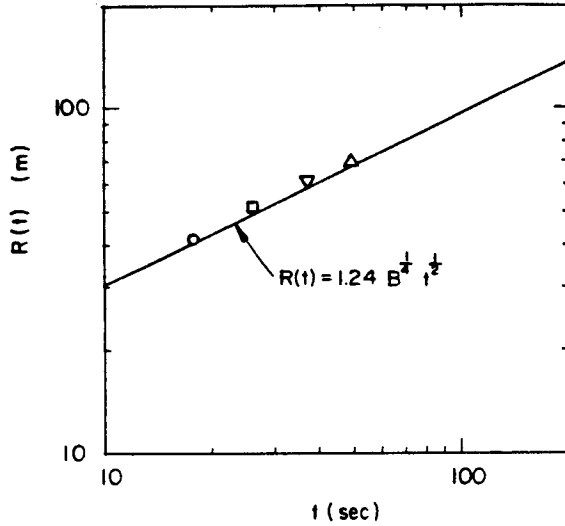


Figure 6.1.9(b) Growth history of inertial-buoyancy radial oil spreading front. Data from Figure 6.1.9(a).

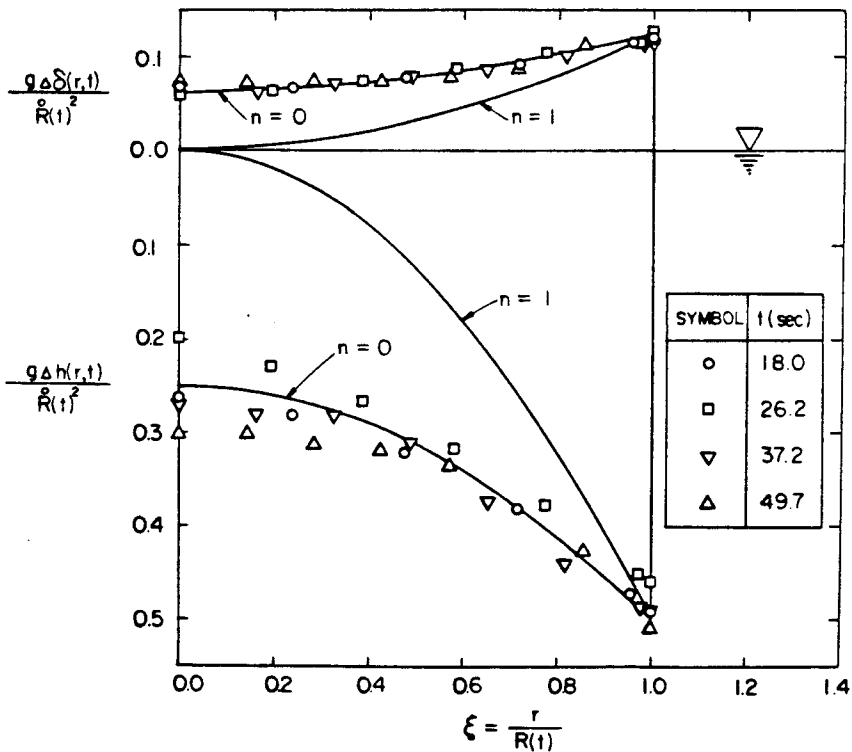


Figure 6.1.9(c) Comparison of oil spreading layer thickness given in Figure 6.1.9(a) with similarity profiles ($n=0$ denotes plane case, Eq. (6.1.10) and $n=1$ denotes radial case, Eq. (6.1.17)).

$$h(r,t) = \frac{\dot{R}^2(t)}{2g\Delta} \left\{ \frac{r}{R(t)} \right\}^2 \quad (6.1.16)$$

for each time t . In dimensionless form, this may be written as

$$\frac{g\Delta h(r,t)}{\left(\frac{1}{2} cB^{1/4} t^{-1/2}\right)^2} = \frac{1}{2} \left\{ \frac{r}{R(t)} \right\}^2, \quad (6.1.17)$$

in which the total buoyant force per unit mass $B = g\Delta V$ and $c = R(t)/B^{1/4} t^{1/2}$ for each instant time t after release. The superelevation $\delta(r,t)$ over free surface is equal to $\Delta h(r,t)$.

Although the frontal Richardson number, $g\Delta h(R,t)/\dot{R}^2(t)$ is found to agree with the theoretical value of 0.5, the spreading layer thickness follows the plane front solution ($n = 0$ in Figure 6.1.9(c)) rather than the radial solution ($n = 1$) given by Eq. (6.1.16). It is not clear how this result comes about.

In order to consider the results of Martin and Moyce (1952) for the radial spreading problem, Eqs. (6.1.12) and (6.1.13) are rewritten as

$$\frac{\dot{R}(R)}{\sqrt{g\Delta h_0}} = 2.00 \frac{R_0}{R(t)} \quad (6.1.18)$$

and

$$\frac{\dot{R}(R)}{\sqrt{g\Delta h_0}} = 0.526 \text{Re} \cdot \text{Ar} \cdot \left\{ \frac{R_0}{R(t)} \right\}^7, \quad (6.1.19)$$

in which R_0 and h_0 are the initial radii and the initial height of circular column before spreading. The Reynolds number $Re = \sqrt{g\Delta h_0} h_0 / \nu$ and Ar is the aspect ratio h_0/R_0 , ν is the kinematic viscosity of the spreading fluid and is assumed to be $0.01 \text{ cm}^2/\text{sec}$ in the calculations. Figures 6.1.10(a) and (b) show that Eq. (6.1.18) is an upper limit for inertial spreading and Eq. (6.1.19) is a lower limit for viscous spreading. Similar experiments were also performed by Hoge and Brooks (1951), however, there is insufficient information on the experiments to perform a comparison.

For the viscous spreading front, as described by Eq. (6.1.13), the frontal velocity decelerates proportionally to $t^{-7/8}$, which agrees with a similarity solution found by Smith (1969b). One experiment performed using syrup on a flat aluminum surface appears to confirm this basic result, as shown in Figure 6.1.11.

6.1.3 Plane Current from Continuous Steady Discharge

In this case the density front advances at an asymptotically constant velocity according to

$$R(t) = 1.260 (g\Delta Q)^{1/3} t \quad (6.1.20)$$

in the inertial-buoyancy stage and according to

$$R(t) = 0.804 \left(\frac{g\Delta Q^3}{\nu} \right)^{1/5} t^{4/5} \quad (6.1.21)$$

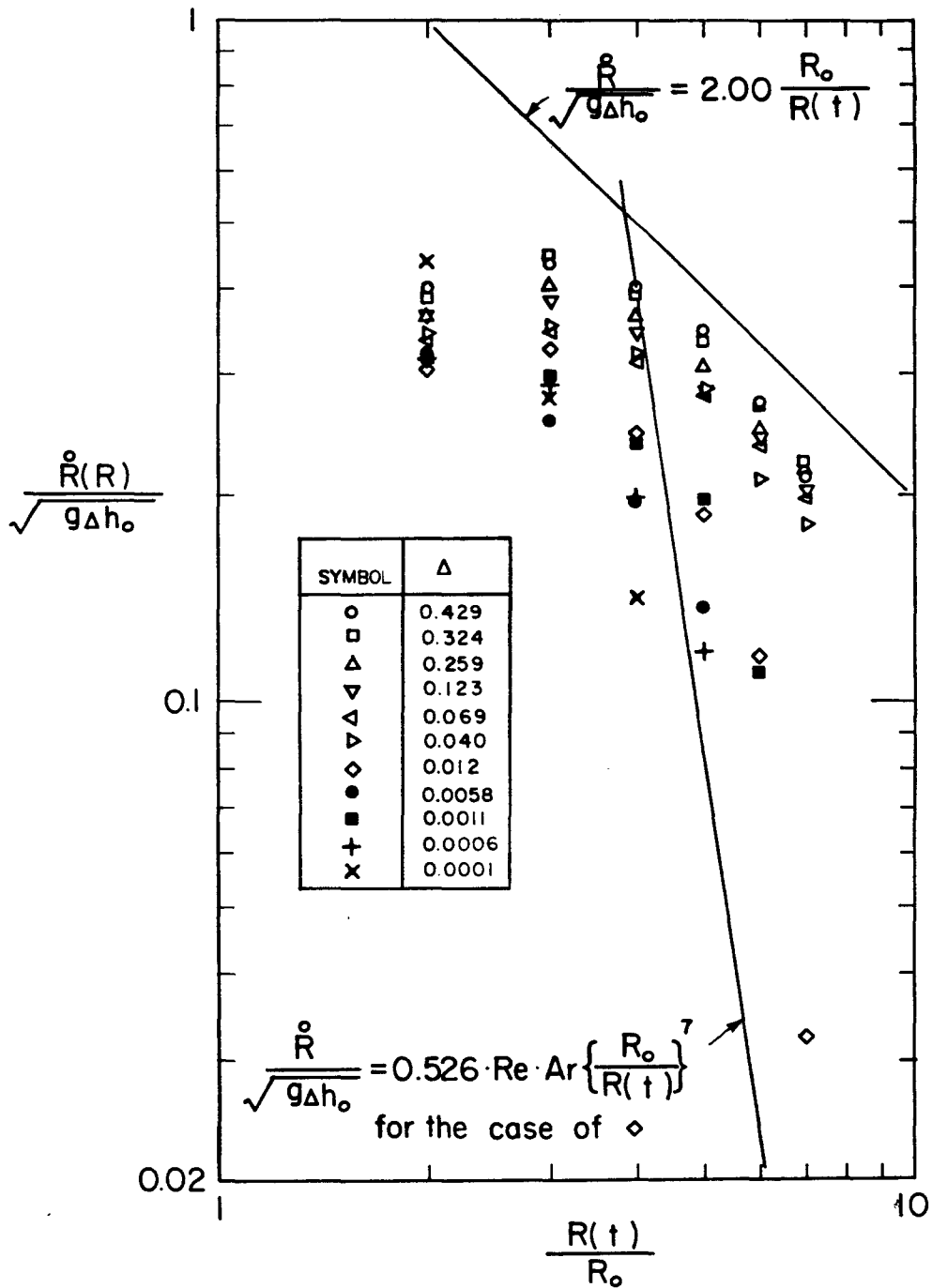


Figure 6.1.10(a) Radial gravity currents produced from circular lock exchange flow. The aspect ratio $Ar = 2$ and the initial radius $R_0 = 3.45$ cm, data from Table 1 of Martin and Moyce (1952, Part V).

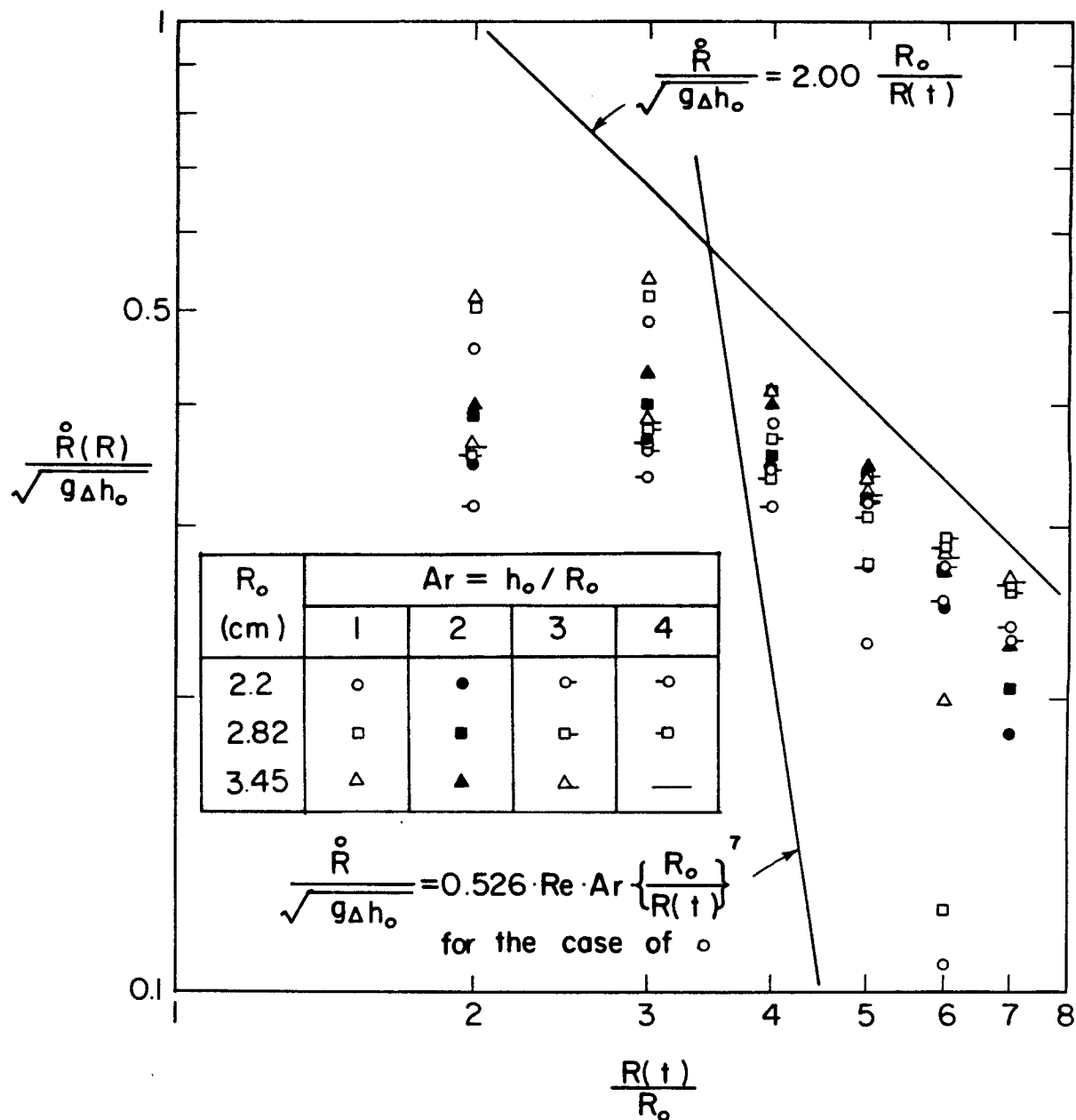


Figure 6.1.10(b) Radial gravity currents produced from circular lock exchange flow. The initial relative density difference $\Delta = 0.428$, data from Table 2 of Martin and Moyce (1952, Part V).

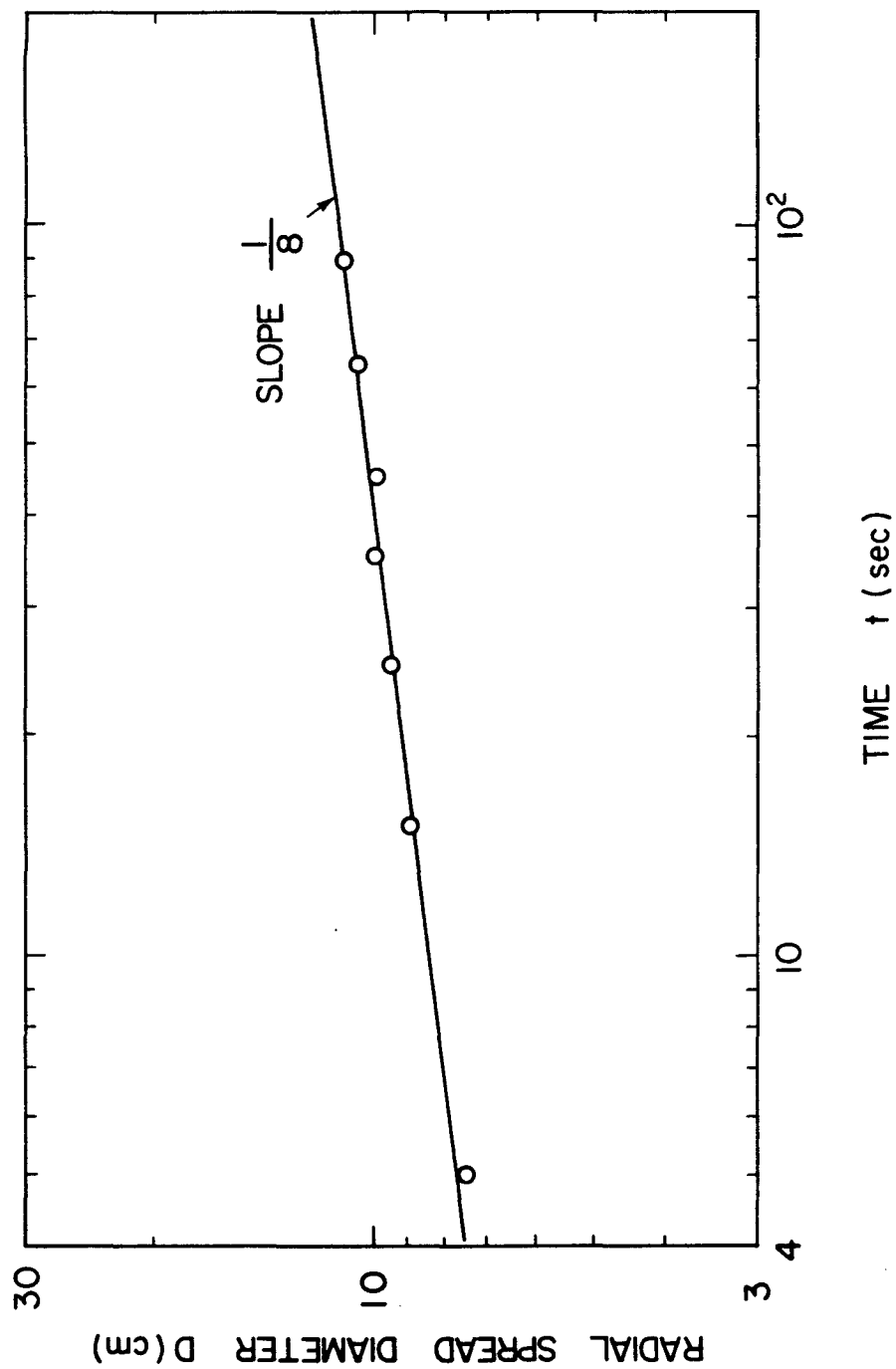


Figure 6.1.11 Growth history of a volume of syrup spreading on the shining face of aluminum foil.

in the viscous-buoyancy stage. These results apply after a short period in a starting jet regime.

Figure 6.1.12(a) shows the agreement of these results with experimental results by Barr (1959) (Experimental apparatus was shown in Figure 2.3.5). There appears to be some initial starting jet flows before approaching the plume flows. Figure 6.1.12(b) also shows agreement with another set of experimental results by Almquist (1973) who used a different discharge apparatus from Barr's (1959) (see Koh (1976)). Figure 6.1.13 also shows the agreement with Eqs. (6.1.20) and (6.1.21) of plane density currents propagating on a flat bottom as measured by Wood (1965) and Wilkinson (1970). There is insufficient information given by above three investigators to determine the dependency of the coefficients on the discharge Froude number and Reynolds number as discussed previously.

$$\frac{R(t)}{M^{1/3} t^{2/3}} \text{ or } \frac{R(t)}{(g\Delta Q)^{1/3} t} \text{ or } \frac{R(t)}{\left(\frac{g\Delta Q^3}{\nu}\right)^{1/5} t^{4/5}} = \phi(\text{Fr}, \text{Re} \text{ or } R_1/\ell_{QM}) \quad , \quad (6.1.22)$$

where $\text{Fr} = u_j/\sqrt{g\Delta h_j}$, $\text{Re} = u_j h_j/\nu$ and $R_1/\ell_{QM} = R_1/h_j = \text{Fr}^{2/3} \cdot \text{Re}$.

Plane surface currents, which were produced by a horizontal buoyant surface discharge from a circular pipe into a channel of motionless ambient water as illustrated in Figure 2.1.5 were observed by Sharp (1971). Four dimensionless numbers,

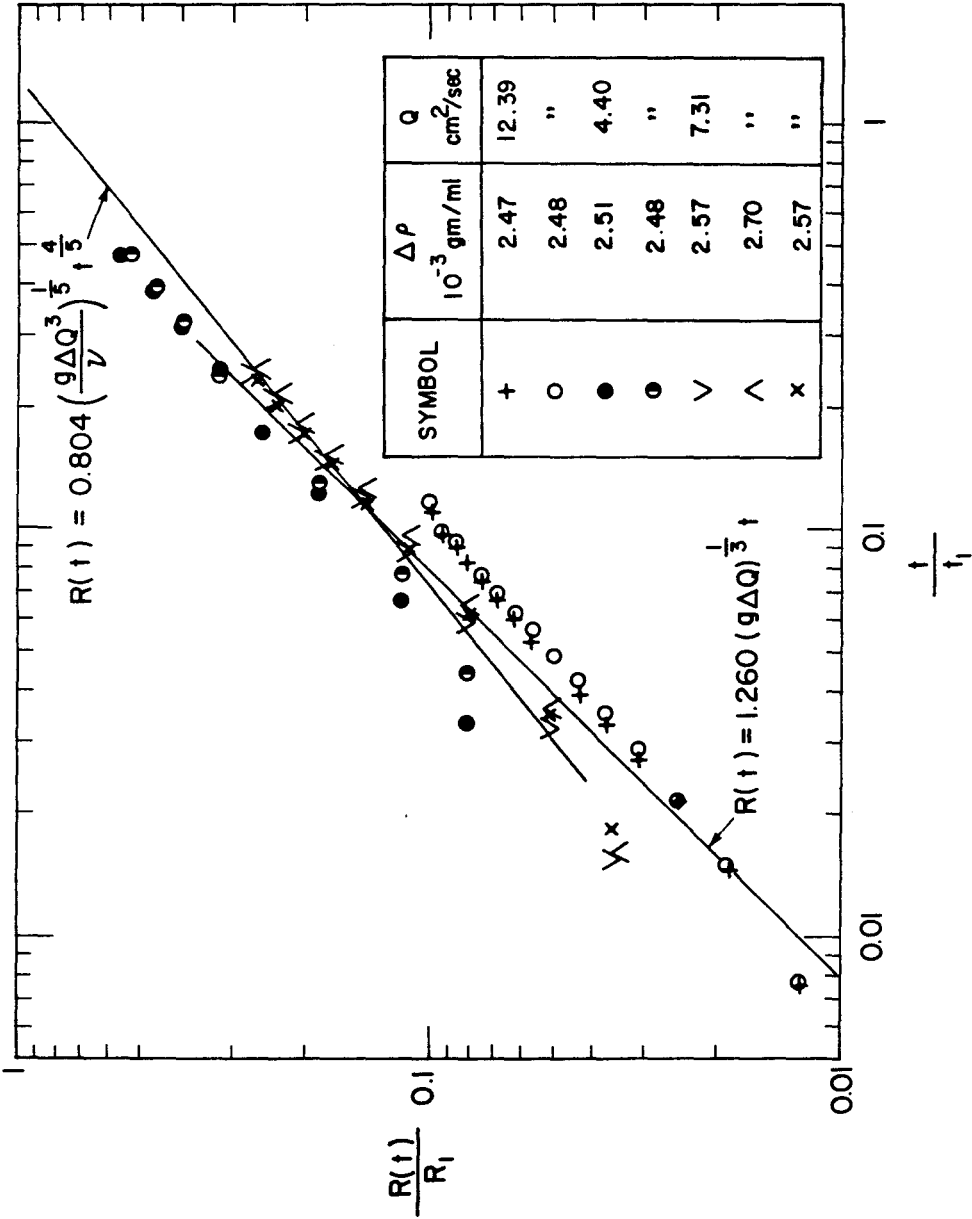


Figure 6.1.12(a) Plane surface spreading currents from a continuous steady discharge, data from Barr (1959).

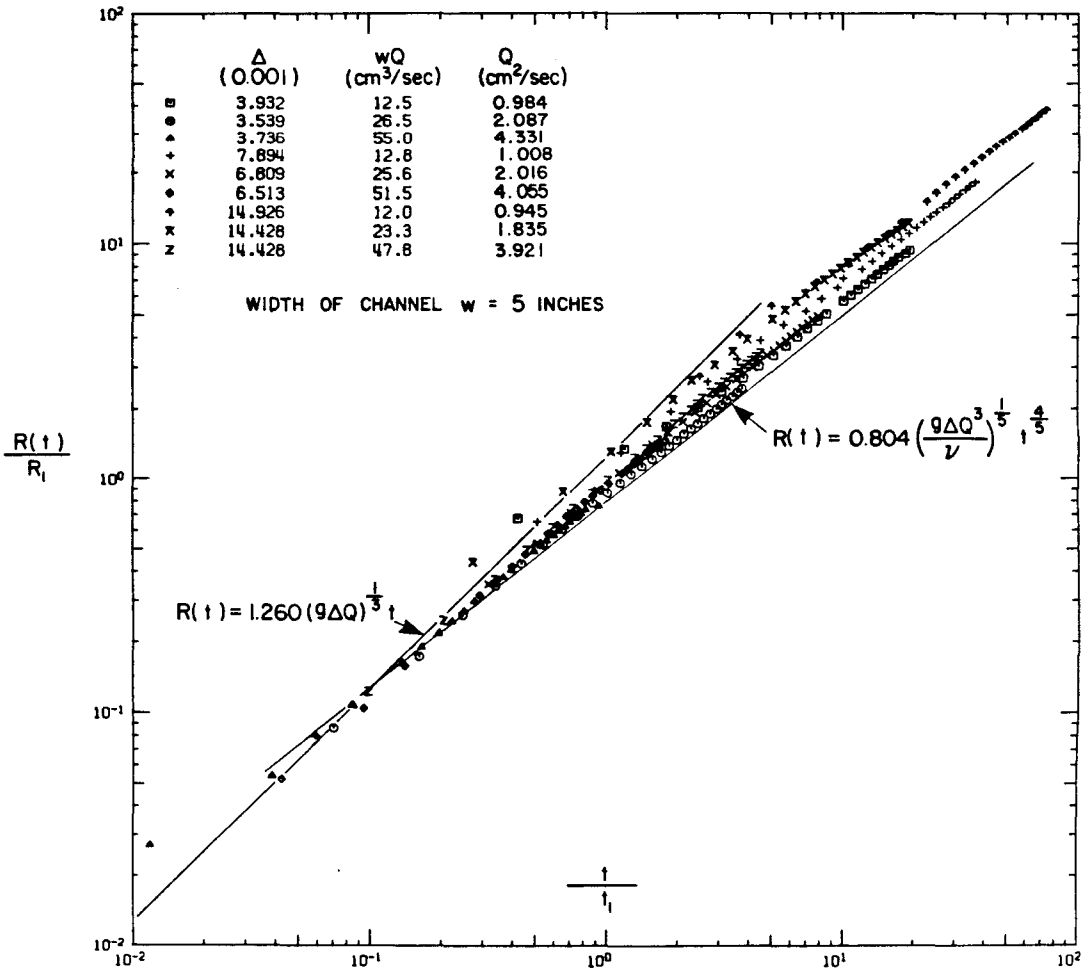


Figure 6.1.12(b) Plane surface spreading currents from a continuous steady discharge, data from Almqvist (1973).

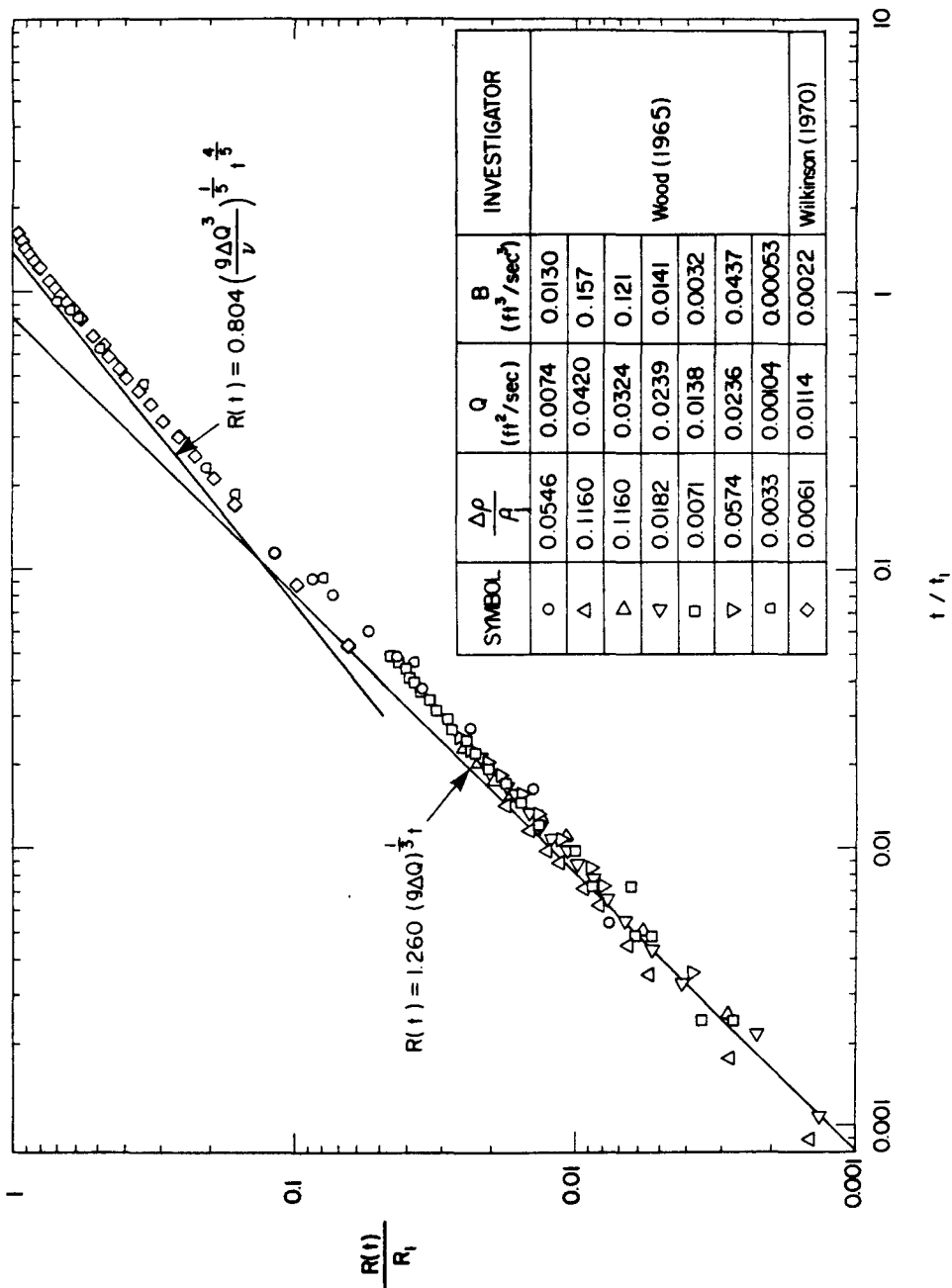


Figure 6.1.13 Plane bottom spreading currents from a steady continuous discharge.

$$\phi \left(\frac{L(g')^{1/5}}{Q_j^{2/5}}, \frac{t(g')^{3/5}}{Q_j^{1/5}}, \frac{Q(g')^{1/3}}{v^{5/3}}, \frac{D_j(g')^{1/5}}{Q_j^{2/5}} \right) = 0 \quad , \quad (6.1.23)$$

were used to describe these currents, in which the definition of each variable is given in Eq. (2.1.2). Sharp (1971) used at least two figures to illustrate Eq. (6.1.23). However, by using the following transformations,

$$\frac{t \ v \left(g' \frac{Q_j}{D_j} \right)^{2/3}}{\left(\frac{Q_j}{D_j} \right)^2} = \frac{t(g')^{3/5}}{Q_j^{1/5}} \cdot \left(\frac{Q_j(g')^{1/3}}{v^{5/3}} \right)^{-3/5} \cdot \left(\frac{D_j(g')^{1/5}}{Q_j^{2/5}} \right)^{4/3} \quad , \quad (6.1.24)$$

$$\frac{L \ v \left(g' \frac{Q_j}{D_j} \right)^{1/3}}{\left(\frac{Q_j}{D_j} \right)^2} = \frac{L(g')^{1/5}}{Q_j^{2/5}} \cdot \left(\frac{Q_j(g')^{1/3}}{v^{5/3}} \right)^{-3/5} \cdot \left(\frac{D_j(g')^{1/5}}{Q_j^{2/5}} \right)^{5/3} \quad , \quad (6.1.25)$$

it is seen that the dimensionless length and time scales R/R_1 and t/t_1 are contained within Eq. 6.1.23. Using these variables, all the experimental data given by Sharp (1971) can be plotted in one figure as shown in Figure 6.1.14. Two slopes, 1 and 4/5, can also be seen to indicate the inertial and the viscous starting plumes.

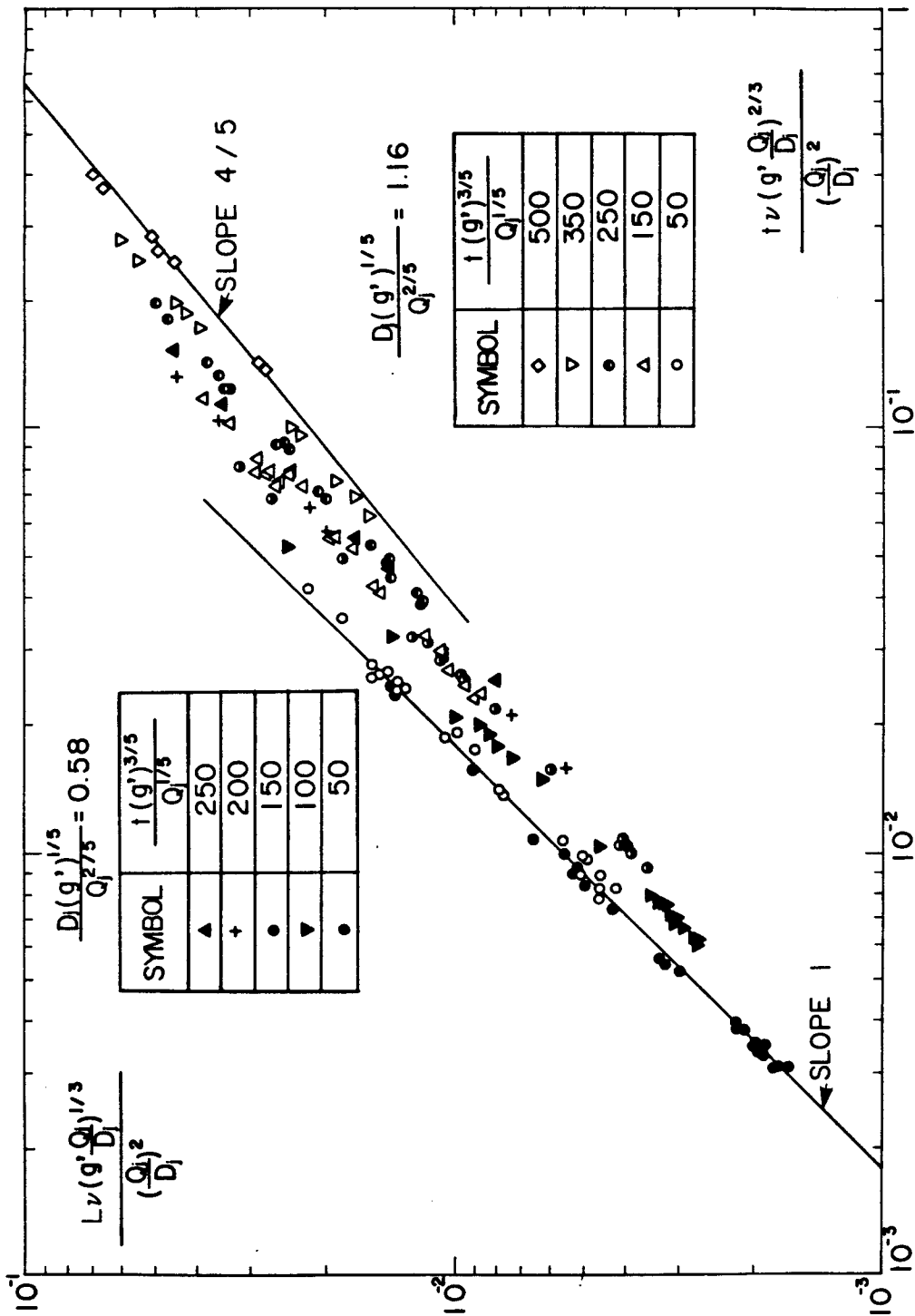


Figure 6.1.14 Unsteady surface spreading currents in a channel due to a buoyant pipe flow discharge, data from Sharp (1971).

From Eq. (6.1.20) we know that inertial-buoyancy spreading currents will propagate at a constant velocity which is proportional to the cubic root of kinematic buoyancy flux, i.e.

$$\overset{\circ}{R}(t) = 1.260 (g\Delta Q)^{1/3} \quad . \quad (6.1.26)$$

Such constant horizontal surface spreading velocities were observed by Bühler (1974) and Roberts (1977) when a submerged line plume reached the bottom or a free surface. From Eq. (6.1.26) the theoretical value of $\overset{\circ}{R}/(2g\Delta_j Q_j)^{1/3}$ (since the submerged buoyancy flux is two times that of a one-sided spreading plume) will be

$$\frac{\overset{\circ}{R}}{(2g\Delta_j Q_j)^{1/3}} = 1.26 \left(\frac{g\Delta Q}{2g\Delta_j Q_j} \right)^{1/3} \approx 1.0 \quad , \quad (6.1.27)$$

when the buoyancy flux is assumed conserved. The average value of experimental results is 0.66 from Bühler (1974) and 0.68 from Roberts (1977). It is not clear why these values are lower than predicted.

For the viscous spreading regime, Eq. (6.1.21) can be rewritten as

$$\frac{R(t)}{(2g\Delta_j Q_j)^{1/3} t} = \frac{0.804}{2^{1/3}} \left(\frac{Q}{Q_j} \right)^{2/5} \left(\frac{g\Delta Q}{g\Delta_j Q_j} \right)^{1/5} \left(\frac{Q_j}{(g\Delta_j Q_j)^{1/3} H} \right)^{2/5} \left(\frac{vt}{H^2} \right)^{1/5} \quad .$$

(6.1.28)

From Roberts (1977) the experimental range of $(Q_j/(2g\Delta_j Q_j)^{1/3} H)^{2/5}$ varies from 0.0972 to 0.229. Thus, Eq. (6.1.28) becomes

$$\frac{R(t)}{(2g\Delta_j Q_j)^{1/3} t} = (0.062 \sim 0.146) \left(\frac{Q}{Q_j}\right)^{2/5} \left(\frac{\nu t}{H^2}\right)^{-1/5} \quad (6.1.29)$$

when the buoyancy flux is assumed conserved, i.e. $g\Delta Q = g\Delta_j Q_j$.

The experimental results for viscous spreading reported by Roberts (1977) give

$$\frac{R(t)}{(2g\Delta_j Q_j)^{1/3} t} = 0.27 \left(\frac{\nu t}{H^2}\right)^{-1/5} \quad (6.1.30)$$

The difference is believed mainly due to the mixing occurring before the plume reaches the free surface, so that Q/Q_j is significantly greater than 1.

Numerical calculations of plane overflowing and underflowing currents in a finite depth of ambient fluid were performed by Kao *et al.* (1977,1978) using the full Navier-Stokes and diffusion equations. The range of calculations for surface currents varied from a starting jet flow to a starting plume flow. The local Richardson number $Ri(r,t) = g\Delta h(r,t)/u^2(r,t)$ for the surface flows was found to be roughly constant at 1.00. However, no further information is available for comparison with the similarity solutions given above.

6.1.4 Radial Current from Continuous Steady Discharge

In this case the spreading front advances asymptotically according to

$$R(t) = 1.309 (g\Delta Q)^{1/4} t^{3/4} \quad (6.1.31)$$

for the inertial-buoyancy stage and according to

$$R(t) = 0.63 \left(\frac{g\Delta Q^3}{\nu} \right)^{1/8} t^{1/2} \quad (6.1.32)$$

for the viscous-buoyancy stage.

These two stages of flow for surface currents were investigated by Chen and List (1976). The spreading currents were produced by a submerged buoyant round jet discharging vertically into a uniform stagnant environment. Typical flow patterns produced by radial surface spreading currents are shown in Figures 6.1.15(a), (b), and (c). Figure 6.1.15(a) shows the radial two-layered stratified flow formed behind a circular front. Figure 6.1.15(b) shows a band of radial stratified flow formed behind the circular front and connected to a radial surface jet zone (also note that the circular surface wave formed by the impingement of submerged jet on the free surface). Figure 6.1.15(c) shows the formation of a series of travelling circular rings behind the outer front. The rings are smoothed out gradually by viscous effects to form a stratified radial surface flow. The ratio of radii of two sequential dark streaks is found to be from 0.70 to 0.77, which is close to the theoretical value 0.753 found in Subsection 3.2.5.3.

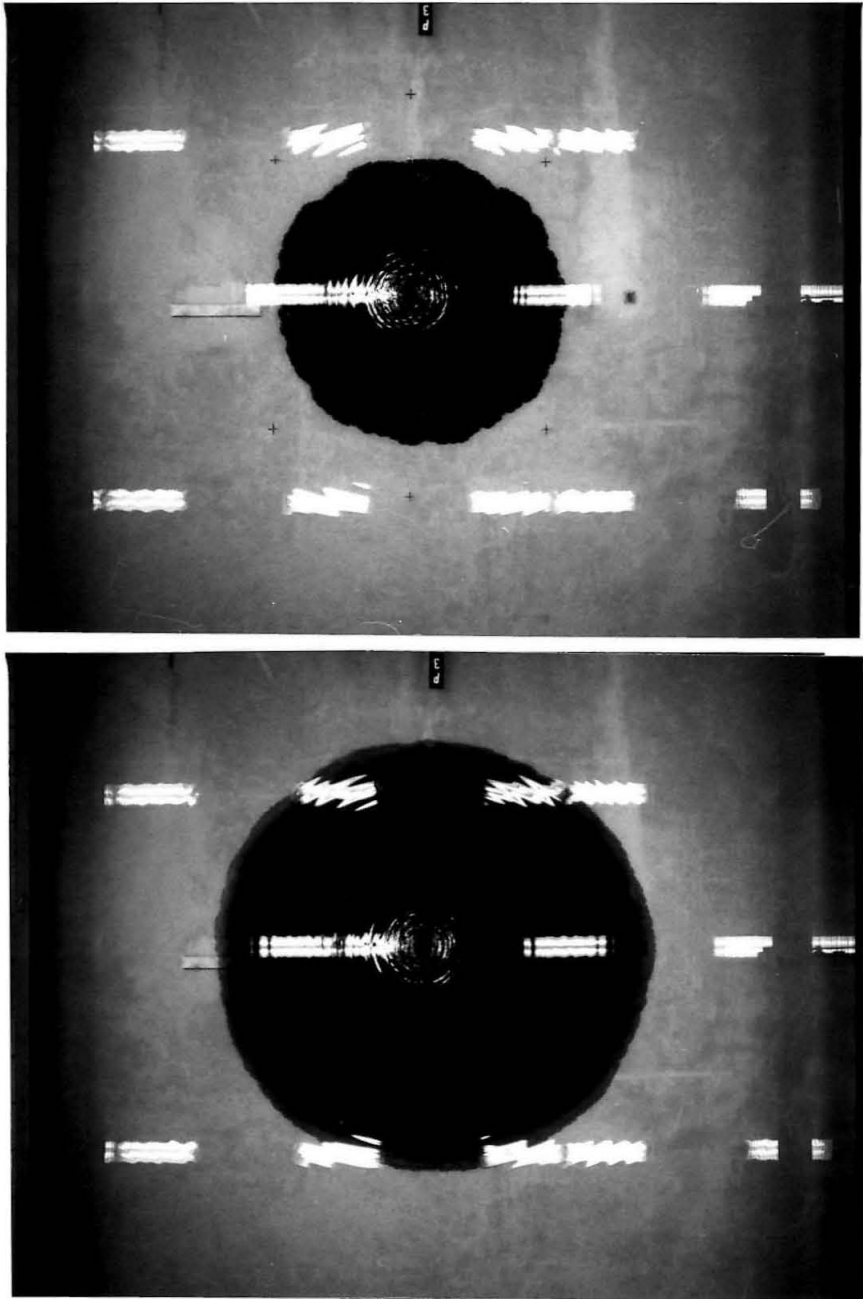


Figure 6.1.15(a) Radial surface stratified flow formed after the diluted effluent reached the free surface (77.9 and 155.5 seconds later). Due to a submerged buoyant round jet ($d_j = 0.586$ cm, $\Delta = 0.0170$, $Q_j = 40.8$ cm³/sec) discharged vertically into a uniform stagnant environment ($H = 11.72$ cm).

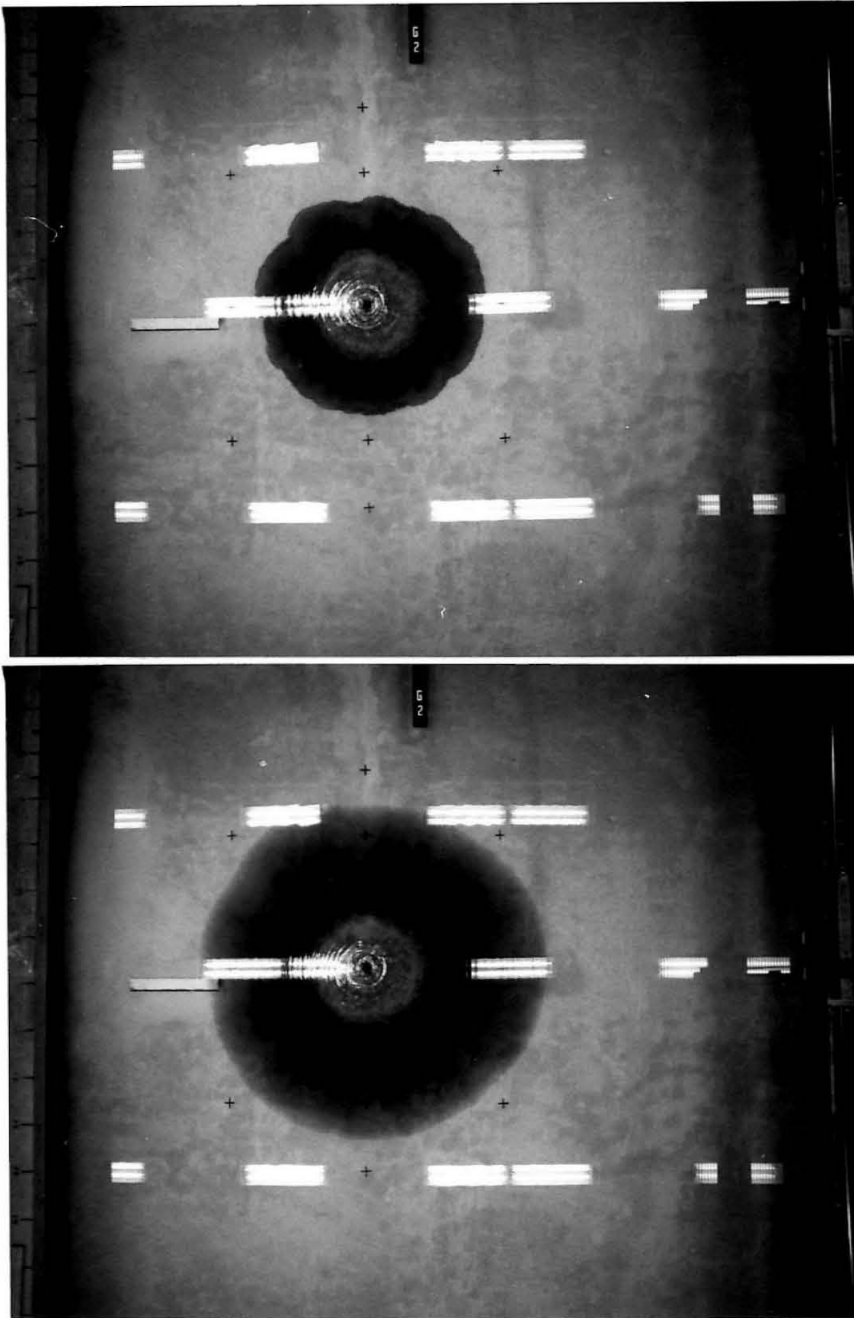


Figure 6.1.15(b) A band of radial surface stratified flow formed after the diluted effluent reached the free surface (70.5 and 166.5 seconds later). Due to a submerged buoyant round jet ($d_j = 0.586$ cm, $\Delta = 0.0142$, $Q_j = 18.9$ cm³/sec) discharged vertically into a uniform stagnant environment ($H = 6.19$ cm).

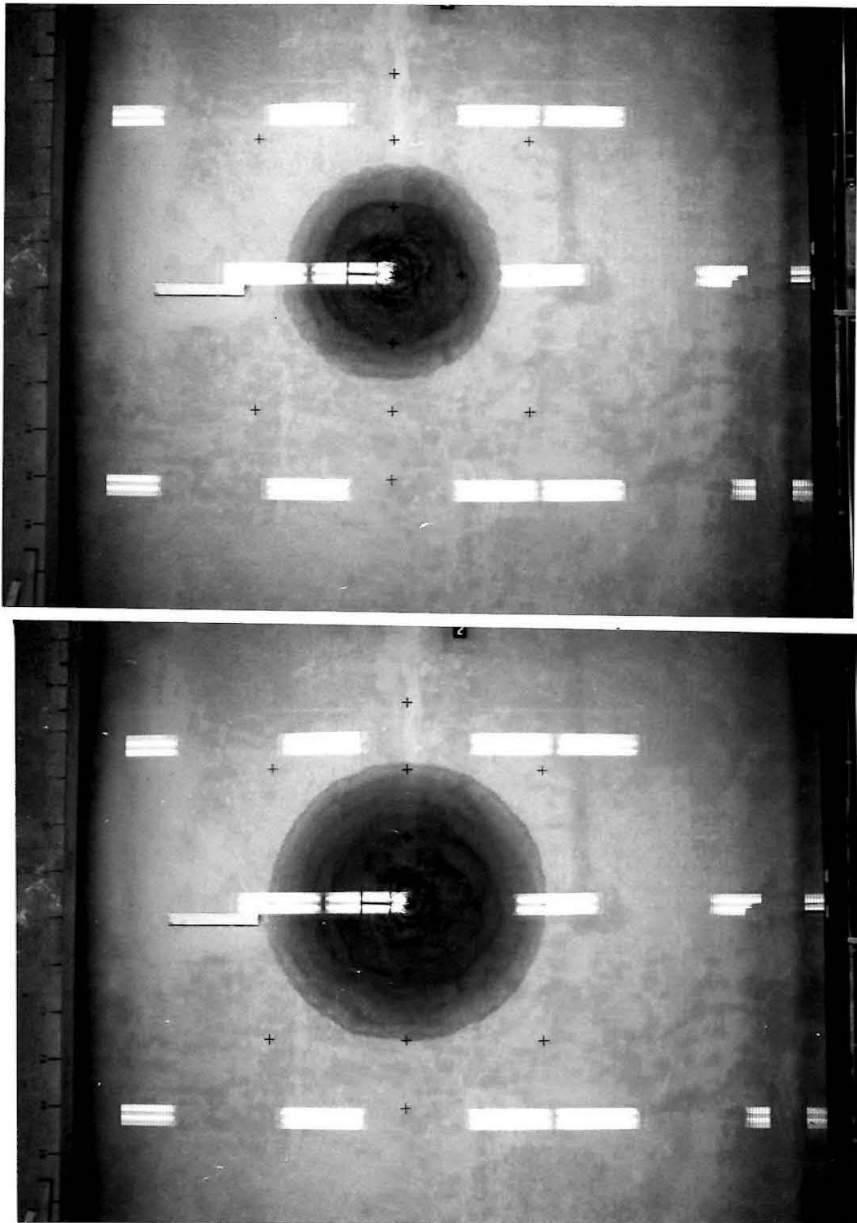


Figure 6.1.15(c) A series of outward travelling circular internal waves formed after the diluted effluent reached the free surface (79.1 and 121.6 seconds later). Due to a submerged buoyant round jet ($d_j = 0.586$ cm, $\Delta = 0.1092$, $Q_j = 4.5$ cm³/sec) discharged vertically into a uniform stagnant environment ($H = 23.41$ cm).

The spreading stage of each photograph presented in Figure 6.1.15 is shown in Figure 6.1.16 by solid symbols.

Britter (1979) performed experiments on bottom spreading radial gravity currents and Eqs. (6.1.31) and (6.1.32) rewritten as

$$\frac{R(t)}{(g\Delta Q)^{1/4} t^{3/4}} = 1.309 \quad (6.1.33)$$

for the inertial-buoyancy spreading currents, and as

$$\frac{R(t)}{(g\Delta Q)^{1/4} t^{3/4}} = 0.63 \left\{ \frac{t(\nu g\Delta Q)^{1/2}}{Q} \right\}^{-1/4} \quad (6.1.34)$$

for the viscous-buoyancy spreading currents agree well with his experimental data for the viscous region as shown in Figure 6.1.17. However, the theoretical value of the constant in the inertial spreading stage is greater than that observed.

Many experimental data describing radial surface and bottom density currents have been analyzed by Sharp (1969a,b), using the following dimensionless form (previously given in Eq. (2.1.1)),

$$\phi \left(\frac{L(g')^{1/5}}{Q_i^{2/5}}, \frac{t(g')^{3/5}}{Q_i^{1/5}}, \frac{Q_i(g')^{1/3}}{\nu^{3/5}} \right) = 0 \quad (6.1.35)$$

in which Q_i is the calculated volume flux at the surface origin of spreading. Using the following transformations,

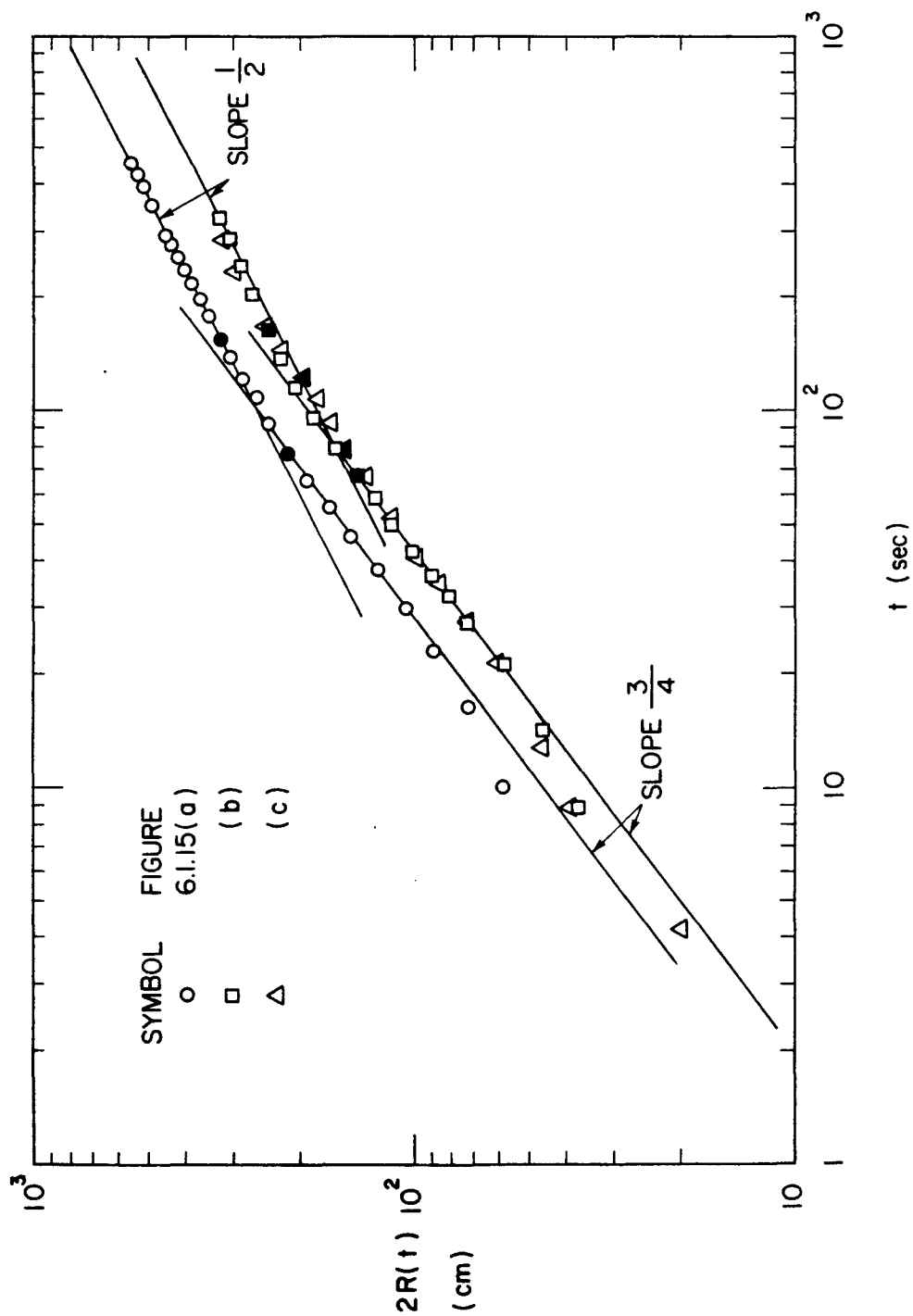


Figure 6.1.16 Growth histories of radial surface spreading fronts shown in Figures 6.1.15(a), (b), and (c).

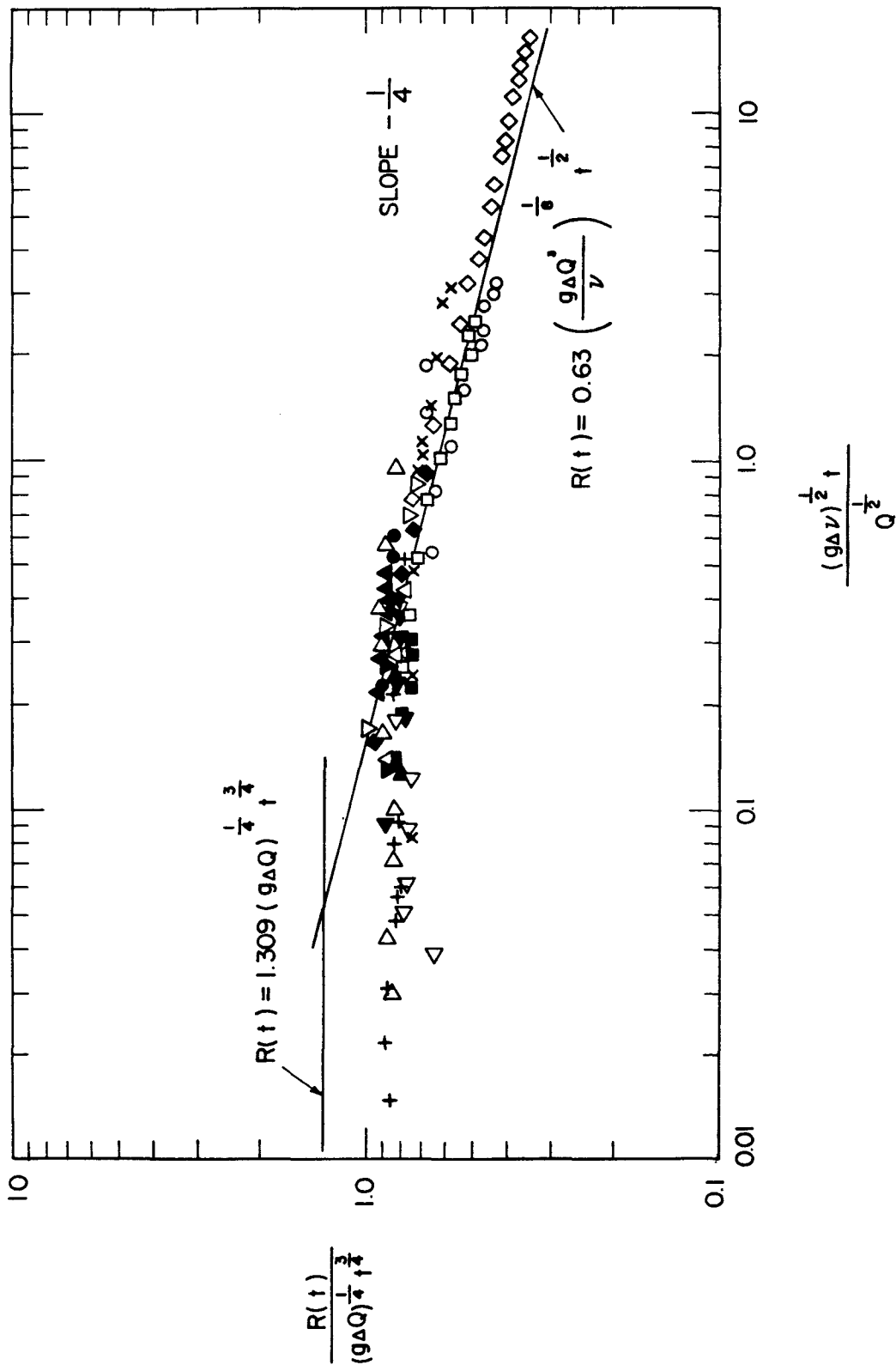


Figure 6.1.17 Growth histories of bottom radial gravity currents, data from Britter (1979).

$$\frac{L}{(g'Q_i)^{1/4} t^{3/4}} = \left\{ \frac{L(g')^{1/5}}{Q_i^{2/5}} \right\} \cdot \left\{ \frac{t(g')^{3/5}}{Q_i^{1/5}} \right\}^{-3/4} \quad (6.1.36)$$

and

$$\frac{t(vg'Q_i)^{1/2}}{Q_i} = \left\{ \frac{t(g')^{3/5}}{Q_i^{1/5}} \right\} \cdot \left\{ \frac{(g')^{1/3} Q_i}{v^{5/3}} \right\}^{-3/10}, \quad (6.1.37)$$

all of Sharp's data can be replotted as in Figure 6.1.18 for the surface currents, and as in Figure 6.1.19 for the bottom currents. Since the experimental frontal position $L(t)$ is not exactly the same value as $R(t)$, there are some deviations, however, the agreement with Eqs. (6.1.33) and (6.1.34) is generally fairly good. It is clear that most of Sharp's experiments were performed in the transition region.

McMinn and Golden (1973) studied the spreading of crude oil on ice, as shown in Figure 6.1.20. Equation (6.1.32) also predicts radial spreading of crude oil reasonably well. A surface buoyant discharged from a boundary can be viewed as an inertial plane current in the near field and as a radial viscous current in the far field. The spreading front therefore will eventually increase its distance from the boundary in proportion to $t^{1/2}$. As shown in Figure 6.1.21 the experimental data from Barr (1959) and Hayashi and Shuto (1967) for such a boundary discharge show this to be the case.

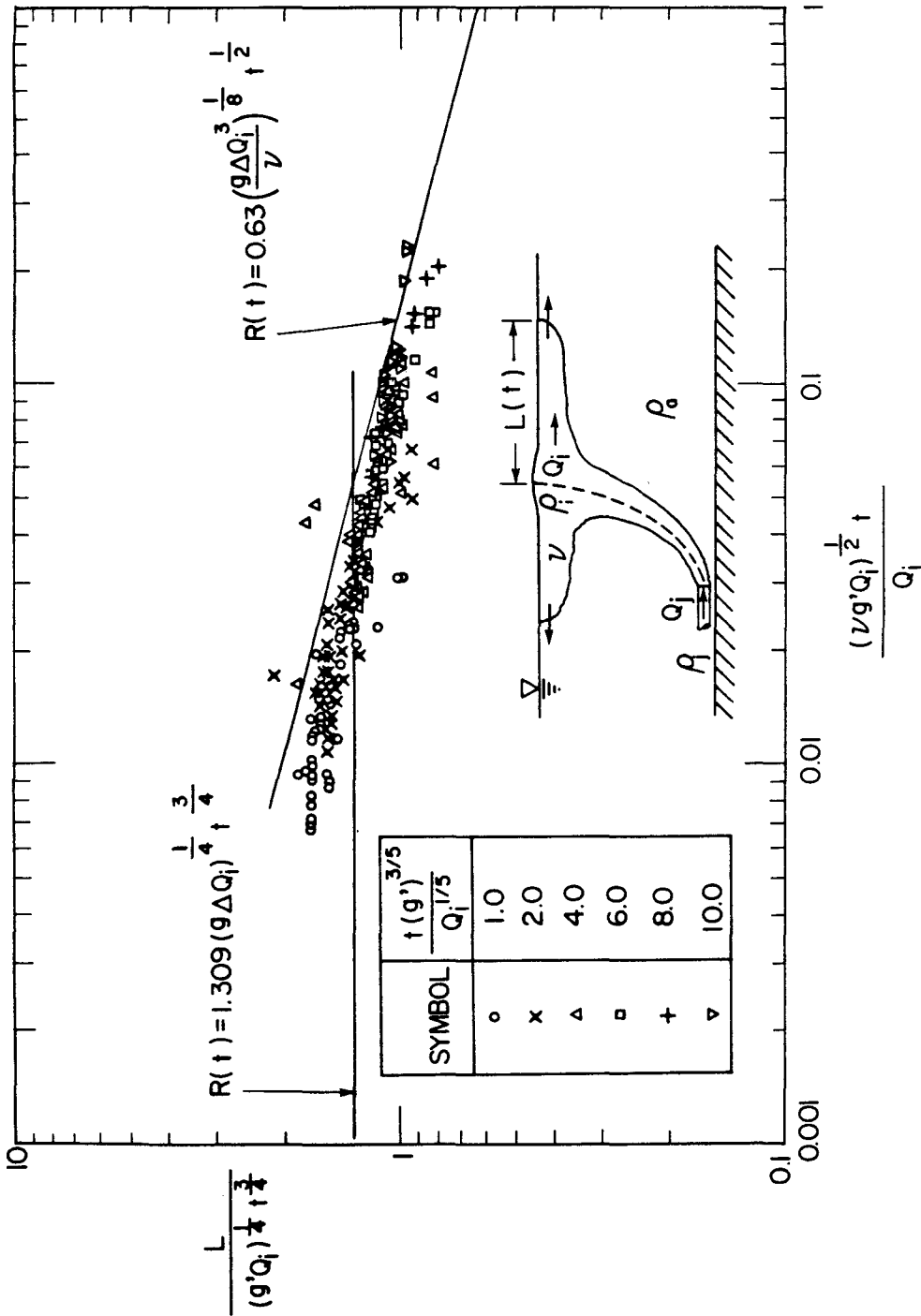


Figure 6.1.18 Growth history of radial surface spreading fronts due to a submerged buoyant round jet discharging horizontally into a uniform stagnant environment, data from Sharp (1969a).

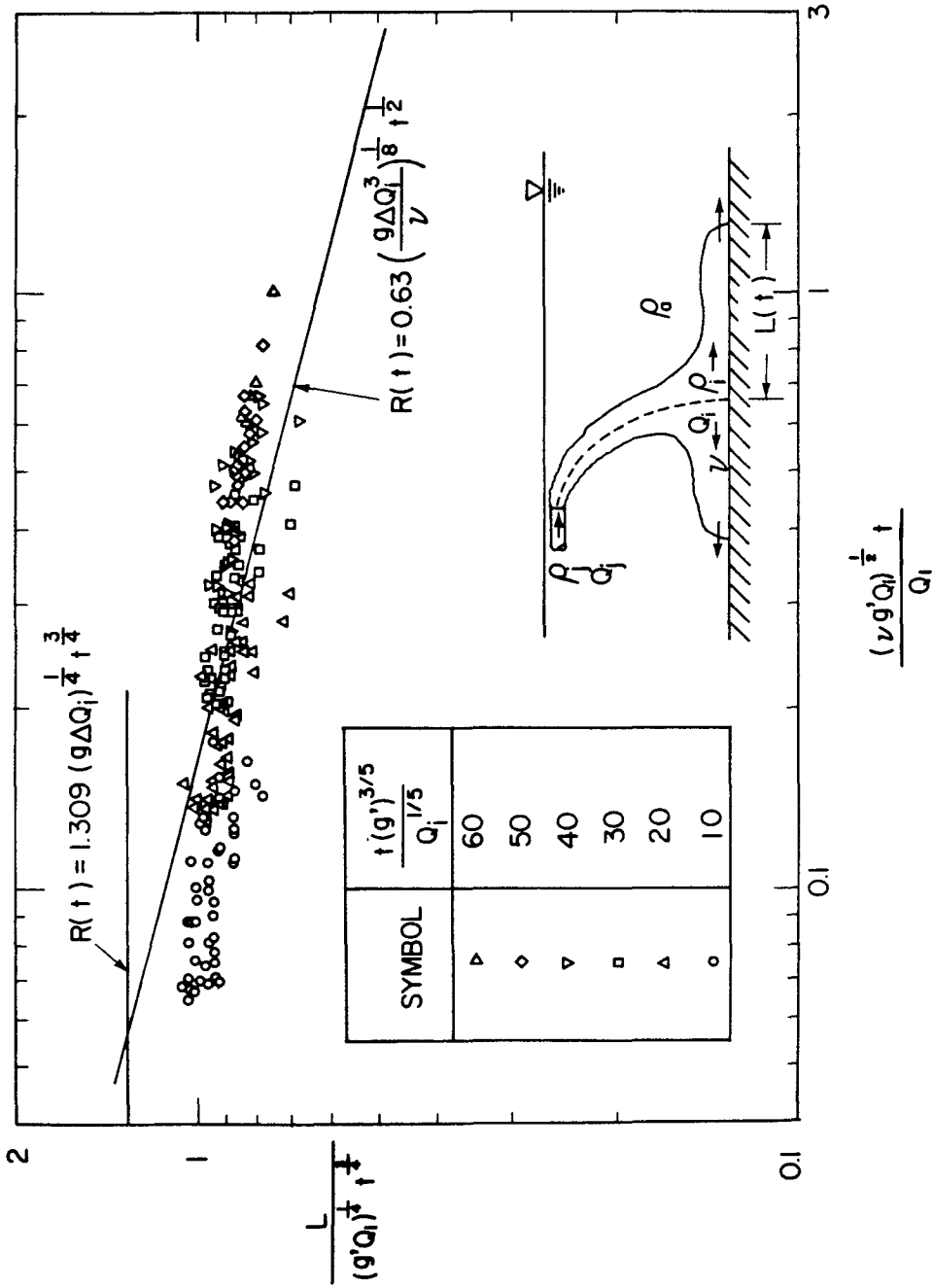


Figure 6.1.19 Growth history of radial bottom gravity currents due to a submerged buoyant round jet discharge horizontally into a uniform stagnant environment, data from Sharp (1969b).

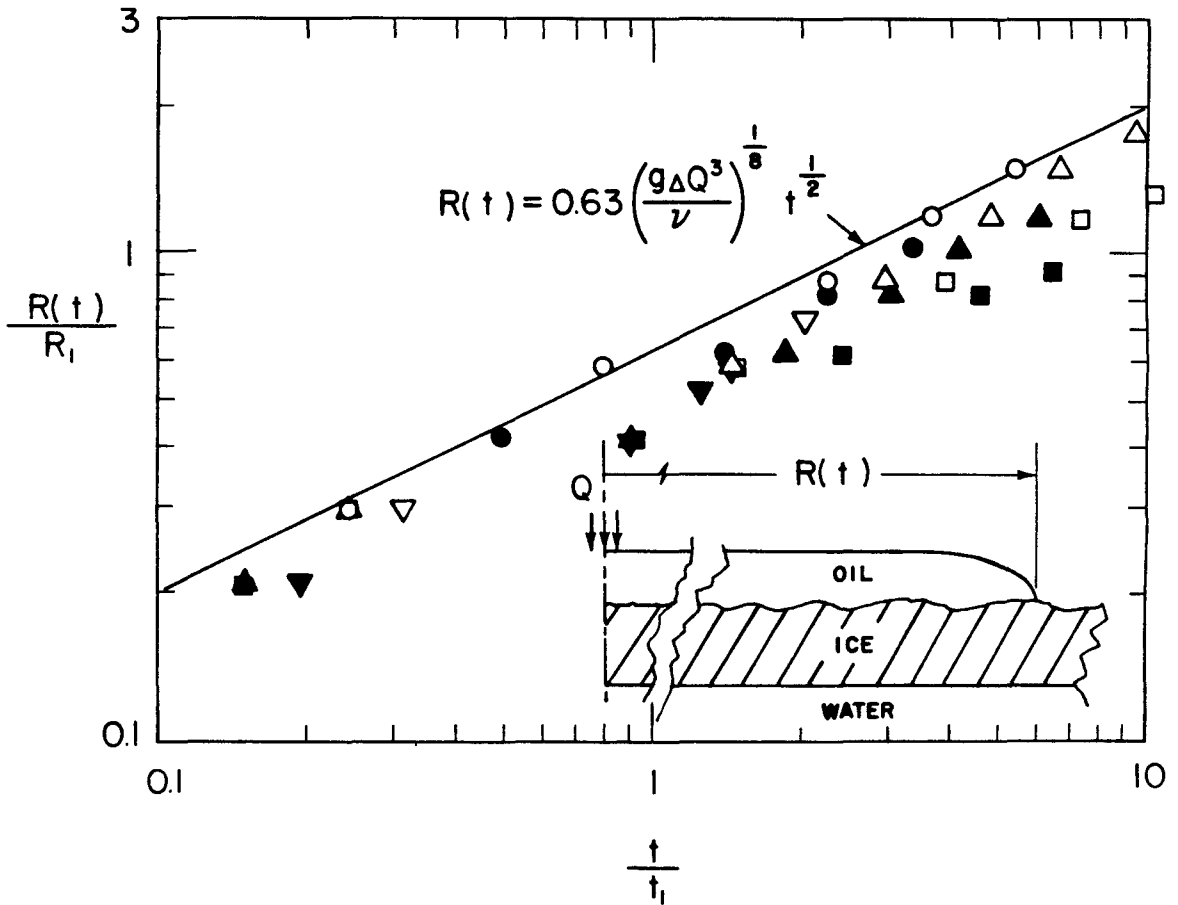


Figure 6.1.20 Radial spreading rate of crude oil on ice. The kinematic viscosity ν of crude oil is assumed as $60 \text{ cm}^2/\text{sec}$ for open symbols and as $23.1 \text{ cm}^2/\text{sec}$ for solid symbols. Data are from McMinn and Golden (1973).

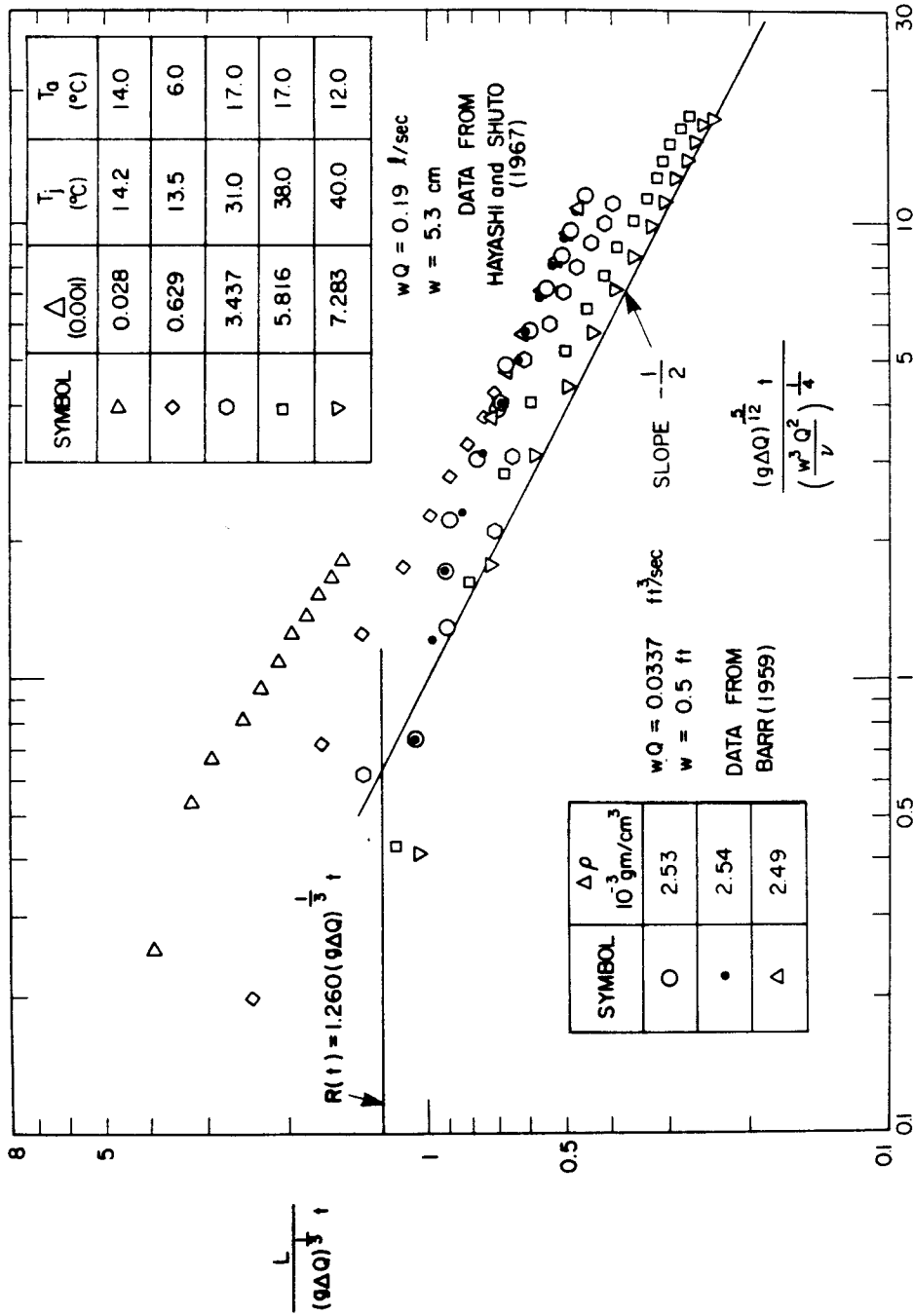


Figure 6.1.21 Growth history of surface spreading front at centerline of boundary buoyant surface discharge, data from Barr (1959) and Hayashi and Shuto (1967).

6.1.5 Initial Stage of Finite Volume Release

The initial collapse of a liquid column in a homogeneous environment was found to have a self-similar thickness profile, previously derived from the shallow-water wave equations, given by

$$\frac{h(r,t)}{h_1} \eta^{n+1} = 1 - \xi^2 \quad , \quad (6.1.38)$$

where $n=0$ for plane currents and $n=1$ for radial currents. The thickness scale h_1 is dependent on the initial shape of liquid column and examples are listed for reference in Table 3.2.1.

The relative frontal position $\eta = R(t)/R_0$, grows as

$$\frac{t\sqrt{g\Delta h_1}}{R_0} = \frac{1}{2} \left\{ \eta^{1/2} (\eta - 1)^{1/2} + \ln[\eta^{1/2} + (\eta - 1)^{1/2}] \right\} \quad (6.1.39)$$

for the plane currents and as

$$\frac{t\sqrt{g\Delta h_1}}{R_0} = \frac{1}{\sqrt{2}} (\eta^2 - 1)^{1/2} \quad (6.1.40)$$

for the radial currents (see Section 3.2.7).

As for plane-symmetric flows the thickness scale $h_1 = \frac{3}{2} h_0$ for a rectangular section and $h_1 = \frac{3\pi}{8} h_0$ for a semi-circular section.

Martin and Moyce (1952, part IV) made many laboratory observations of the collapse of a liquid column in air ($\Delta = 1$).

Figure 6.1.22(a) shows a sketch of three typical photographic sections taken during collapse of a liquid column with an initially rectangular section. Figure 6.1.22(b) shows the comparison of the self-similar profile given by Eq. (6.1.38) (with $n = 0$) with these three observations. The growth history of a plane front formed during collapse of a rectangular column is shown in Figure 6.1.23. It is interesting to note that the theoretical curve overestimates the displacement. The smaller the aspect ratio h_0/R_0 of the initial rectangular section is, the closer are the experimental data points to the theoretical curve. Two cases with initial aspect ratio $h_0/R_0 = 1$ begin to show deceleration with a change in slope of the displacement curve to $2/3$ (i.e. $R(t) \sim t^{2/3}$) around $t\sqrt{gh_0}/R_0 = 6$. In the one case with an aspect ratio $h_0/R_0 = 4$ the plane front shows a constant velocity up to $t\sqrt{gh_0}/R_0 = 20$. Figure 6.1.24 also shows the theory overestimates the displacement for the collapse of a semi-circular column section. The reason may be due to an insufficient description by the shallow-water wave equations of the initial stage of the collapse since the vertical acceleration is not small in this stage of the flow.

The radial front displacement produced by the collapse of a vertical cylindrical column is plotted in Figure 6.1.25. The theory also overestimates the observed displacement. The displacement also appears to be dependent on the initial aspect ratio as shown in Figure 6.1.25.

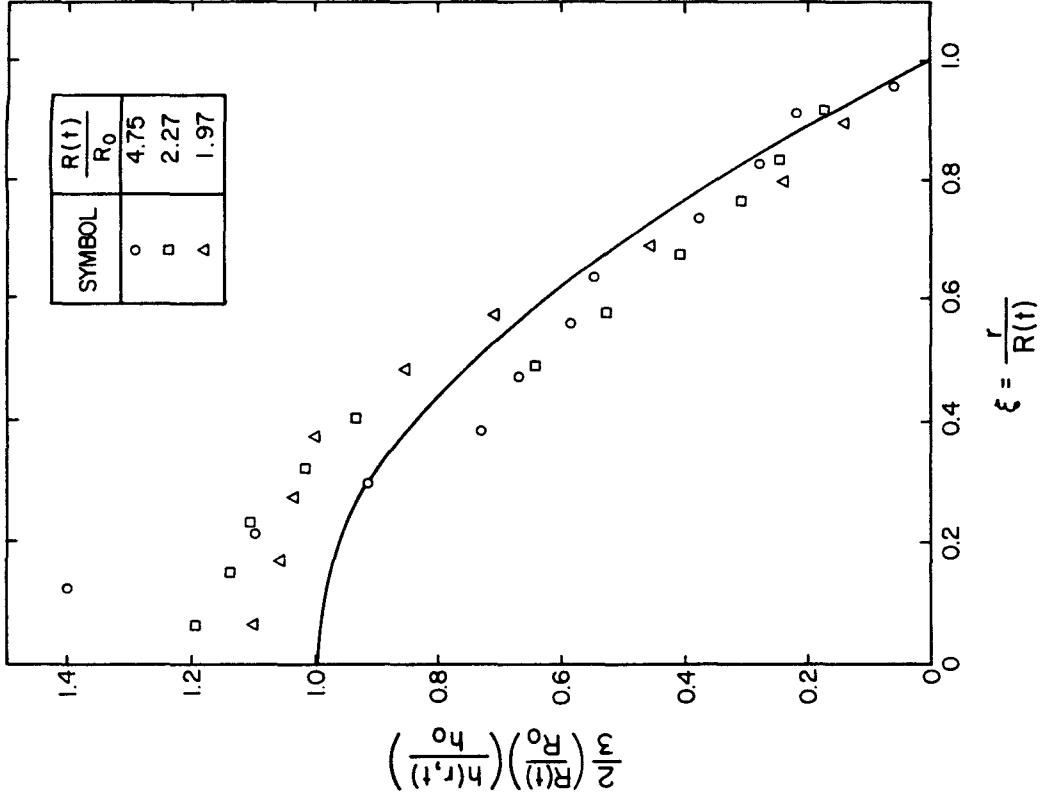


Figure 6.1.22(b) Calculated self-similar profiles of initial collapse shows in Figure 6.1.22(a).

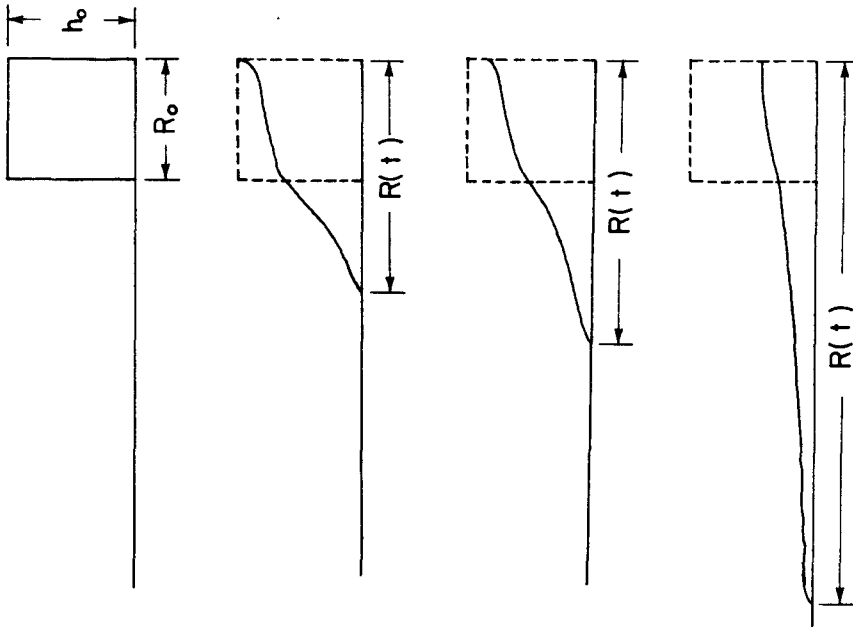


Figure 6.1.22(a) Initial collapse of a rectangular shape column, line sketch of a photograph from Martin and Moyce (1952, Part IV).

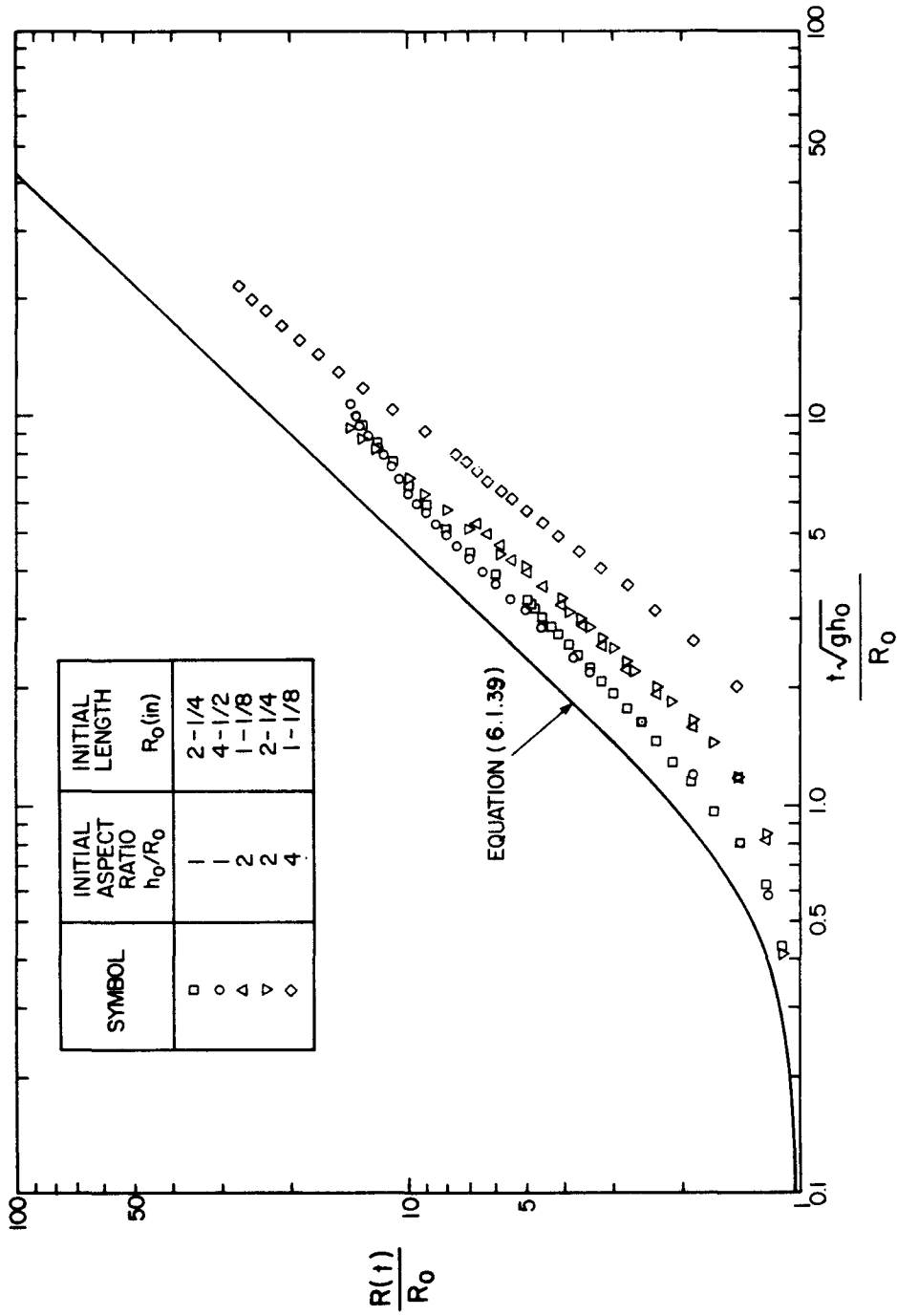


Figure 6.1.23 Growth history of plane front during initial collapse of a liquid column with rectangular section ($h_1 = 3h_0/2$ in Eq. (6.1.39)). Data from Tables 1, 2, and 3 of Martin and Moyce (1952, part IV).

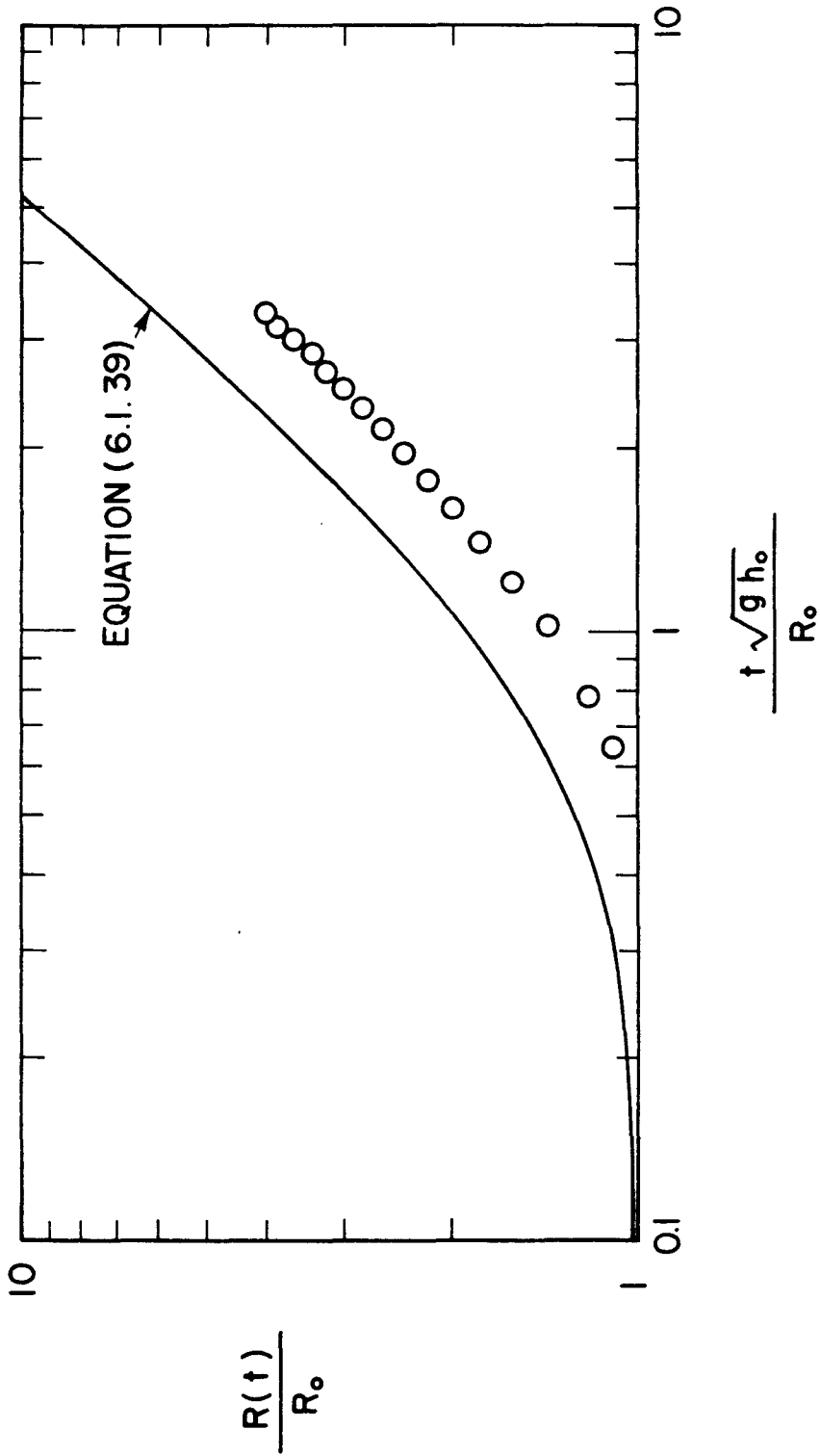


Figure 6.1.24 Growth history of plane front during initial collapse of a liquid column with semi-circular section ($h_1 = \frac{3\pi}{8} h_0$ in Eq. (6.1.39)) ($R_0 = 2$ inches), data from Table 4 of Martin and Moyce (1952, part IV).

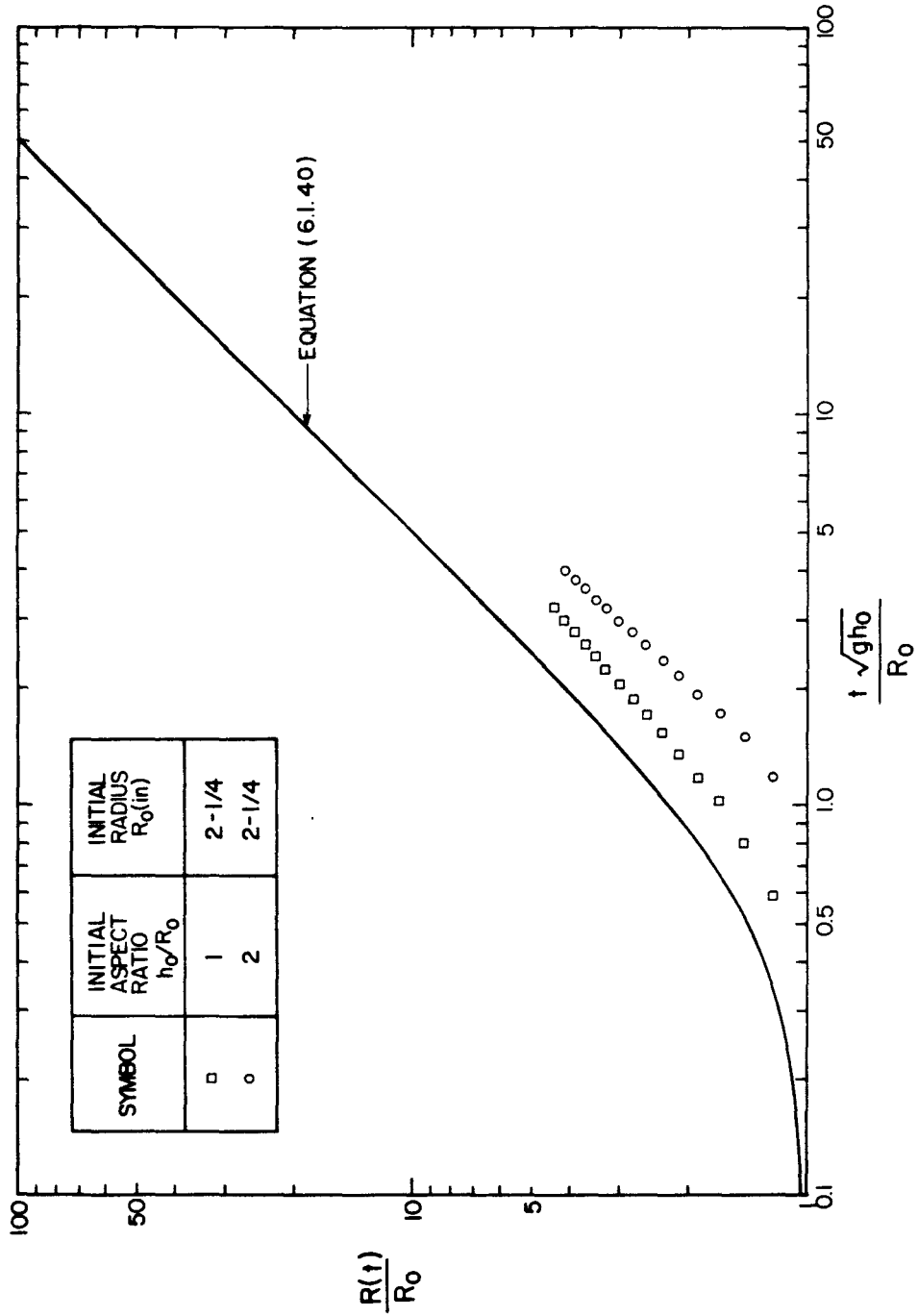


Figure 6.1.25 Growth history of radial front during initial collapse of a liquid column with vertical circular cylinder ($h_1 = 2h_0$ in Eq. (6.1.40)), data from Table 5 of Martin and Moyce (1952, part IV).

Although the theoretical frontal trajectory displacement functions Eqs. (6.1.39) and (6.1.40) are only asymptotic limits valid when the initial aspect ratio is small, the self-similar thickness profile compares very well with the results of numerical calculations with finite difference method and the method of characteristics as shown in Figures 6.1.26, 6.1.27, and 6.1.28.

6.2 Spreading Currents in Linearly Stratified Environment

In the first subsection the results of experimental studies and numerical calculations for a plane mixed region collapsing in a linearly density-stratified environment will be compared with the theoretical solutions that were developed in Chapter 3. Other experimental results for a plane starting intrusion layer due to a horizontal slot discharge into a linearly density-stratified environment will be examined in Subsection 6.2.2. There are no experimental results available for the radial submerged spreading case.

6.2.1 Plane Submerged Current from a Finite Volume Release

In Sections 3.2 and 3.3 a three-stage description was developed for a front advancing at its own density level in a linearly density-stratified environment. It is given by the case $i = 1, n = m = 0$. In particular the front due to collapse of a finite volume of homogeneous fluid is described by:

(I) Initial Stage

$$R(t) = (R_o^2 + h_1^2 g \epsilon t^2)^{1/2} \quad (6.2.1)$$

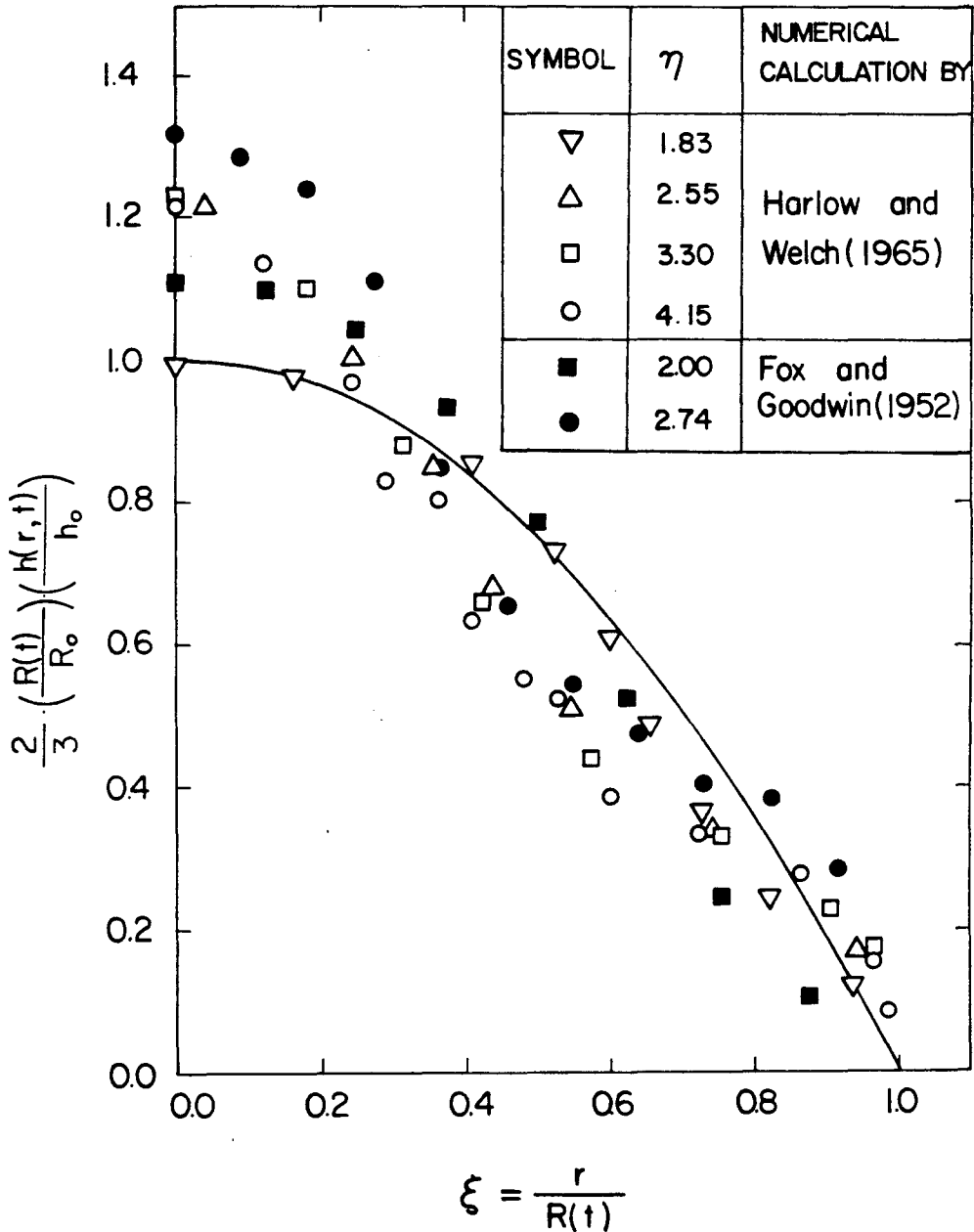


Figure 6.1.26 Comparison of self-similar profile with numerical calculation results by Harlow and Welch (1965) and Fox and Goodwin (1952) for the collapse of a plane symmetrical column in vacuo, initially rectangular at rest, at various relative distance $\eta = R(t)/R_0$.

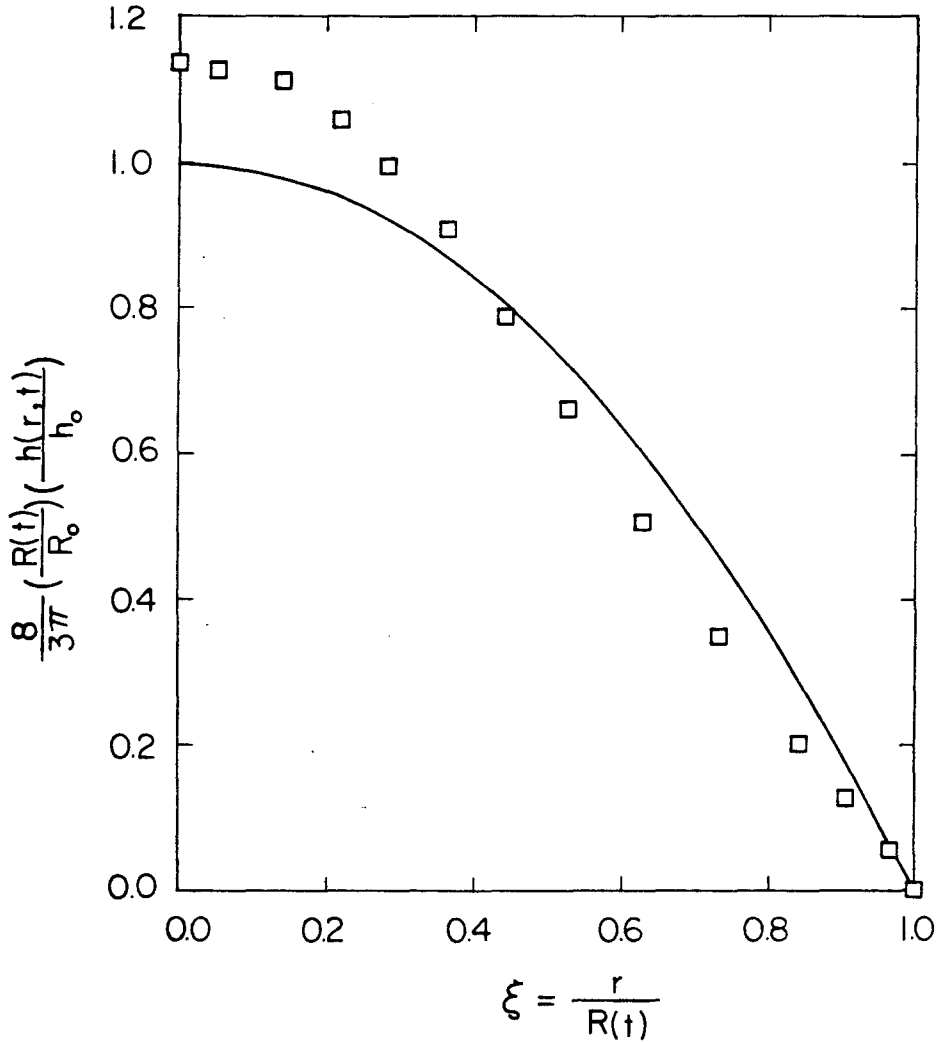


Figure 6.1.27 Comparison of self-similar profile with numerical calculation results by the method of characteristics by Penney and Thornhill (1952) for the collapse of an initially semi-cylindrical section column at rest at specific time $t \sqrt{\frac{g}{h_0}} = 0.8$ or $\eta = R(t)/R_0 = 1.78$.

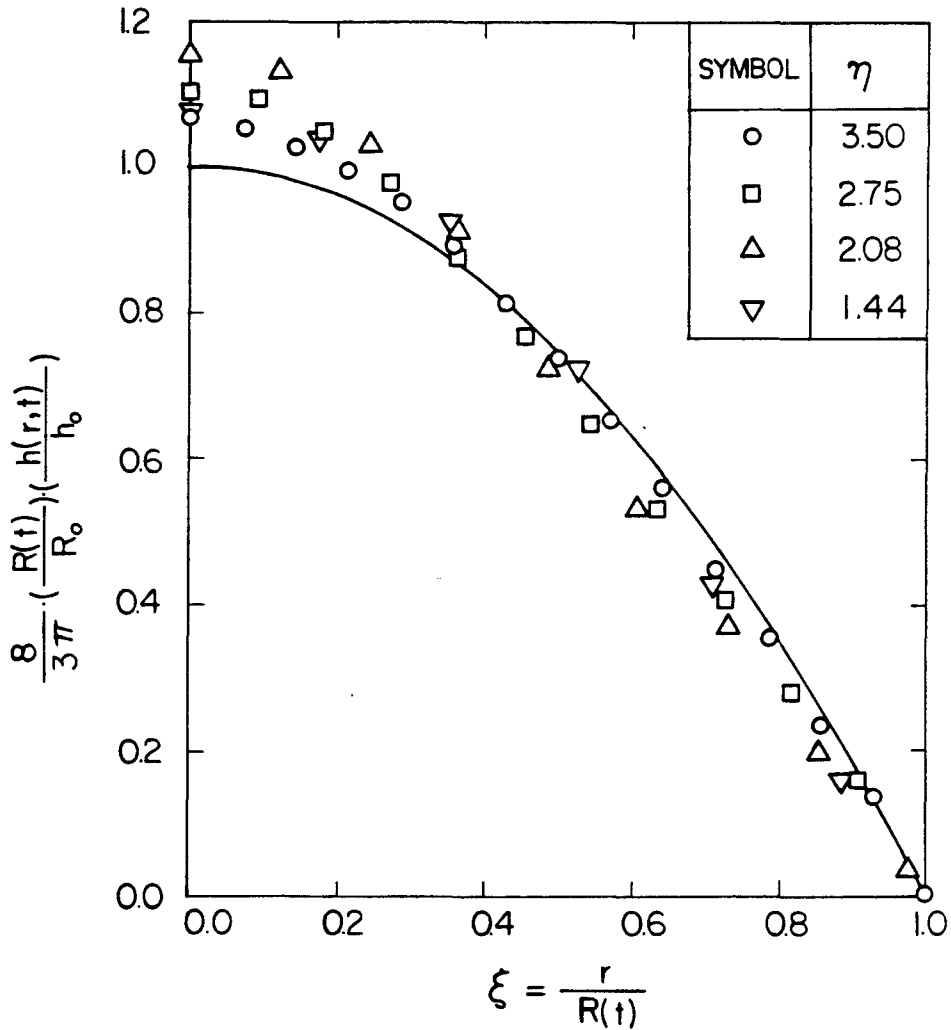


Figure 6.1.28 Comparison of self-similar profile with numerical calculation results by the method of characteristics by Penney and Thornhill (1952) for the collapse of an initially semi-elliptic column at rest at various time $\frac{t\sqrt{gh_0}}{R_0} = 0.5, 1.0, 1.5, \text{ and } 2.0$ or various relative distance $\eta = R(t)/R_0 = 1.44, 2.08, 2.75, \text{ and } 3.50$.

(II) Inertial-Buoyancy Balance Region

$$R(t) = (2NV)^{1/2} t^{1/2} \quad , \quad (6.2.2)$$

(III) Viscous-Buoyancy Balance Region

$$R(t) = 0.69 \left(\frac{g \epsilon V^4}{\nu_s} \right)^{1/6} t^{1/6} \quad (6.2.3)$$

where R_0 and h_0 are the initial horizontal and vertical length scale, V is the initial half-volume of homogeneous fluid, $R(t)$ is the horizontal extent at time t , ν_s the kinematic viscosity of the spreading fluid. The thickness scale h_1 is dependent on the initial shape of spreading fluid and is listed in Table 3.2.2. For an initially semi-circular cross-section, the value of h_1 is equal to h_0 . In this case, the horizontal length scale R_0 and the vertical length scale h_0 are both equal to the initial radius of the semi-circular section. The volume per unit width of the semi-circular section is equal to $V = \frac{\pi R_0^2}{2}$. Formulae for the three stages of spreading flow will, in this case be simplified to:

$$(I) \quad \frac{R(t)}{R_0} = \left\{ 1 + (Nt)^2 \right\}^{1/2} \quad , \quad (6.2.4)$$

$$(II) \quad \frac{R(t)}{R_0} = \pi^{1/2} (Nt)^{1/2} \quad , \quad (6.2.5)$$

$$(III) \quad \frac{R(t)}{R_0} = 0.93 \left(\frac{NR_0^2}{\nu_s} \cdot Nt \right)^{1/6} \quad , \quad (6.2.6)$$

in which the dimensionless parameter $\frac{NR_o^2}{v_s}$ on the right-hand side of Eq. (6.2.6) is a Reynolds number Re_N .

The three stages of submerged spreading flows are illustrated clearly in Figure 6.2.1. For a volume of semi-circular cross-section fluid with a Reynolds number Re_N greater than 500, the interflowing front will have three complete stages of flows which have been previously described by Wu (1965) as: the initial collapse stage, the principal collapse stage, and the final collapse stage. With an initial Reynolds number between 500 and 5, only two stages will exist for the flow (the principal stage is excluded). For an initial Reynolds number less than 5 there is only one final collapse stage.

The dimensionless transition time from the initial stage to the principal stage is about $Nt = 2.8$ and the dimensionless transition length is about $R(t)/R_o = 3.0$. However, the dimensionless transition time and length from the principal stage to the final stage are dependent on the initial Reynolds number Re_N . The larger the Reynolds number is, the longer the transition time and the transition length are.

For an initially rectangular shape of plane mixed region, three stages of collapse can be expressed:

(I) Initial Stage

$$\frac{R(t)}{R_o} = \left\{ 1 + \left(\frac{4}{\pi} \right)^2 \cdot \left(\frac{h_o}{R_o} \right)^2 N^2 t^2 \right\}^{1/2}, \quad (6.2.7)$$

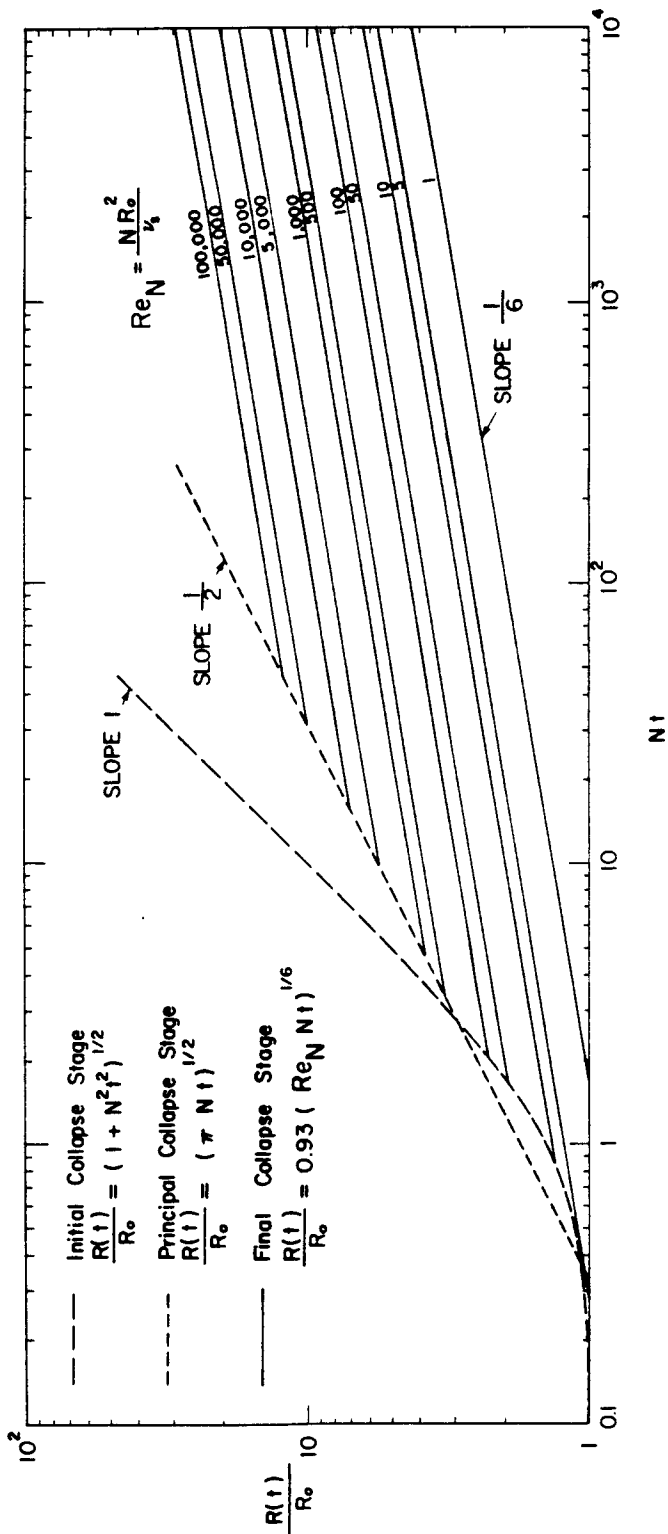


Figure 6.2.1 Three spreading stages of a plane mixed region collapsing in a linearly density-stratified environment.

(II) Principal Stage (Inertial-Buoyancy Balance)

$$\frac{R(t)}{R_o} = 2 \left(\frac{h_o}{R_o} \right)^{1/2} (Nt)^{1/2} , \quad (6.2.8)$$

(III) Final Stage (Viscous-Buoyancy Balance)

$$\frac{R(t)}{R_o} = 1.10 \cdot \left(\frac{h_o}{R_o} \right)^{1/3} \left(\frac{Nh_o^2}{v_s} \cdot Nt \right)^{1/6} , \quad (6.2.9)$$

in which R_o and h_o are now respectively the one-half length of the horizontal and the vertical sides of the rectangular section. The ratio of these two length scales, h_o/R_o , is the aspect ratio of the initial shape and the initial Reynolds number now is defined as $Re_N = \frac{Nh_o^2}{v_s}$ where the velocity scale is Nh_o and the length scale is h_o .

For the special case when the aspect ratio h_o/R_o is unity, i.e. the initial shape is square, and the three collapse stages are described by:

$$(I) \quad \frac{R(t)}{R_o} = \left\{ 1 + \left(\frac{4}{\pi} \right)^2 N^2 t^2 \right\}^{1/2} \quad (6.2.10)$$

$$(II) \quad \frac{R(t)}{R_o} = 2(Nt)^{1/2} \quad (6.2.11)$$

$$(III) \quad \frac{R(t)}{R_o} = 1.10 \cdot \left(\frac{Nh_o^2}{v_s} \cdot Nt \right)^{1/6} \quad (6.2.12)$$

Consider only the inertial-buoyancy and the viscous-buoyancy regions. A more general way to normalize the experimental data is by using the length scale $R_1 = \left(\frac{NV^3}{v_s} \right)^{1/4}$ and the time scale $t_1 = \left(\frac{V}{Nv_s} \right)^{1/2}$ as listed in Table 3.1.5. Then the intercept of two oblique lines given by Eqs. (6.2.2) and (6.2.3) will be at the point where the vertical ordinate is $R/R_1 = 0.481$ and the horizontal abscissa is $t/t_1 = 0.487$ as listed in Table 3.5.4.

Two sets of experimental data are available for comparison: Wu (1965,1969) and van de Watering (1966). Both experiments were originally performed to study the collapse of a turbulent wake in a density-stratified fluid. A semi-circular or circular homogeneous mixed region was prepared to simulate a uniform parcel of turbulent wake. Sequential pictures were taken as soon as the mixed region began to collapse. Thus, a history of horizontal spread was obtained by measuring the horizontal spreading length as a function of time.

A comparison by Mei (1969) of the theoretical solution for the initial collapse stage of a circular mixed region with the experimental results by Wu (1965) was found to be fairly good for dimensionless time Nt between 0 and 1. The theoretical curve shown in Figure 2 of Mei (1969) actually is the same curve given by Eq. (6.2.4). When the dimensionless time Nt is greater than 1, the theoretical solution overestimates the experimental results. The reason why the error is introduced is that the data probably lie in the so-called principal collapse stage.

In Figure 6.2.2, the comparison of two theoretical solutions with the experimental results is presented for the transition behavior from the initial collapse stage to the final collapse stage. All the experimental data are from Figure 16 of van de Watering (1966). The Reynolds number Re_N for each run is calculated to check its effect on submerged density spread. Since the kinematic viscosity of the spreading fluid was not given, it is assumed to be the same as that of pure water, $0.01 \text{ cm}^2/\text{sec}$. A log-log plotting of the data shows that the experimental results follow the theoretical prediction in the initial stage very well. For the final stage, or the viscous-buoyancy balanced spread, a slower growth rate of horizontal spread is found according to the $1/6$ power of t as shown. Most of the experimental results by van de Watering (1966) are in the lower Reynolds number Re_N range. Therefore, from the theoretical solution shown in Figure 6.2.1 it is known that the horizontal front moves as such a rate that it does not pass through the principal collapse stage. This is probably the reason why a false conclusion (see Eq. (2.1.6)) was drawn by van de Watering (1966) in his description of the principal collapse stage.

Figure 6.2.3 shows the transition from the principal collapse stage to the final collapse stage for eleven experiments by Wu (1965). The two different stages are noted by the sharp change of slope from $1/2$ to $1/6$ in the log-log plot of growth history for a horizontally spreading front. All the data are from

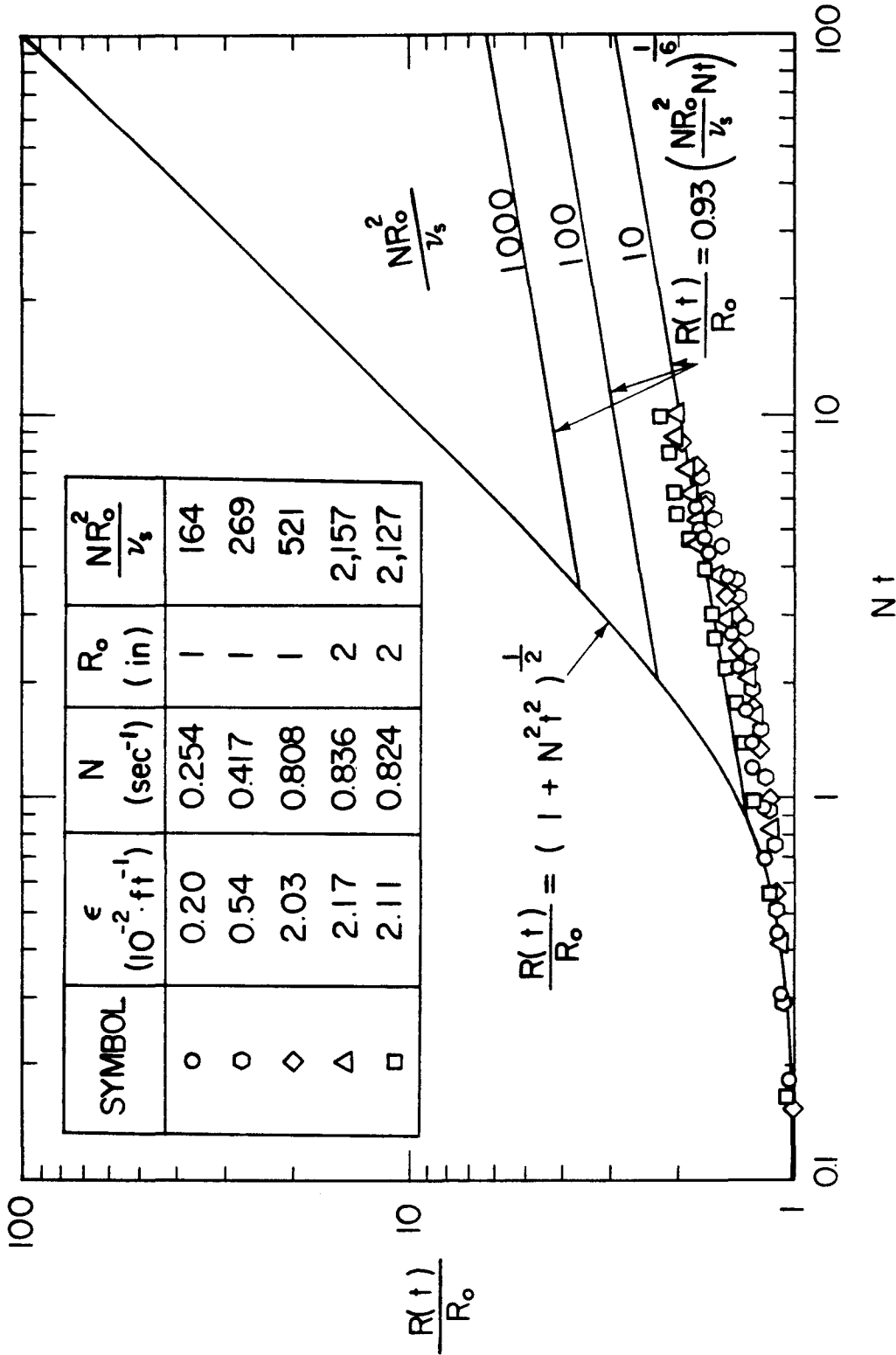


Figure 6.2.2 Comparison of theoretical solutions (the initial and the final collapse stages) for submerged density spreading front with experimental results by van de Watering (1966) on a plane mixed region collapsing in a linearly density-stratified environment.

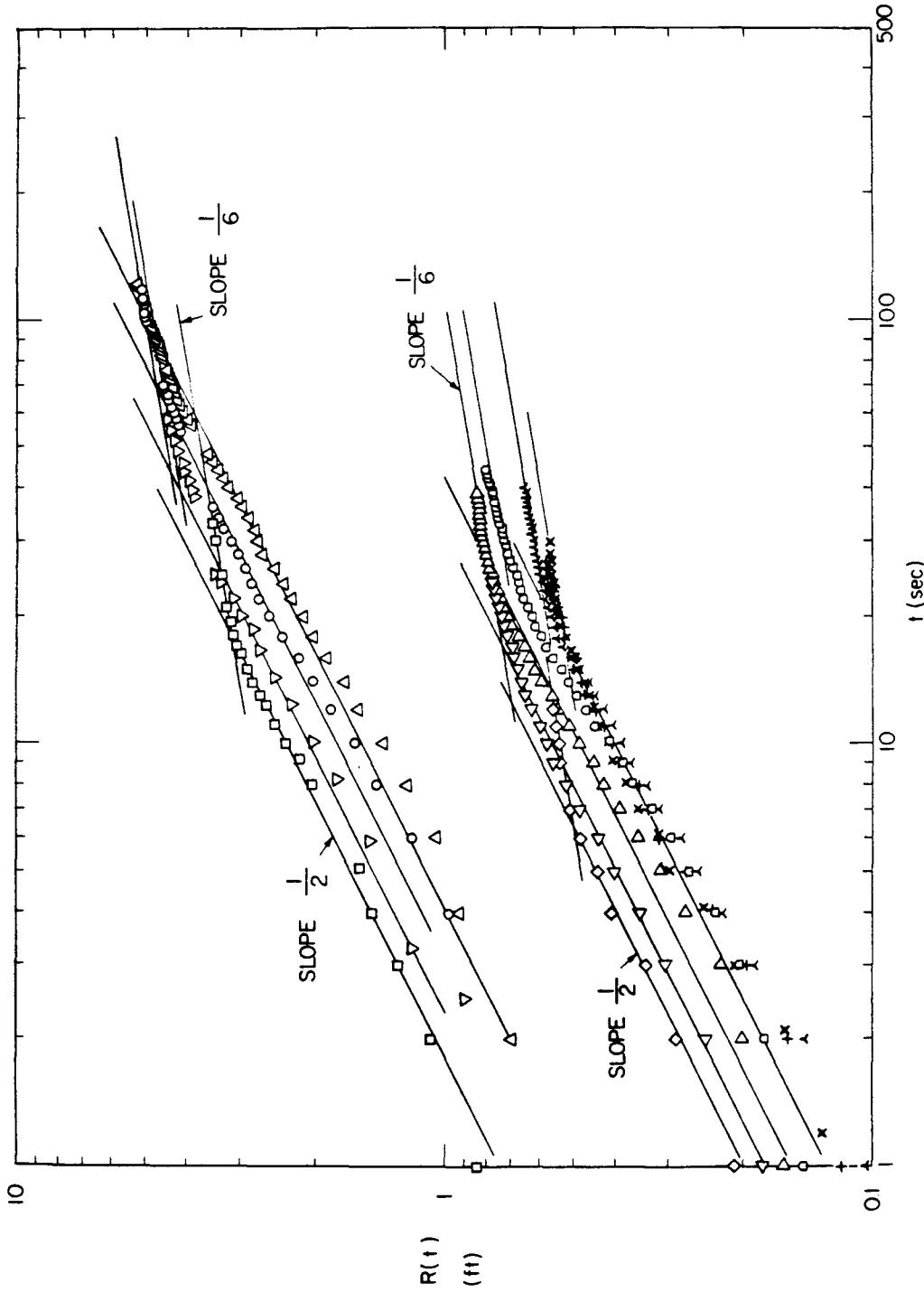


Figure 6.2.3 Eleven cases of growth history for submerged density spread front due to a plane mixed region collapsing in a linearly density-stratified environment. Data are taken from Figures 10, 11, and 12 of Wu (1965). Details of experimental parameters for each case are shown in Table 6.2.1.

Figures 10, 11, and 12 of Wu (1965). Details of experimental parameters for each run are given in Table 6.2.1.

The data shown in Figure 6.2.3 are normalized in two ways. One is shown in Figure 6.2.4 along with Eqs. (6.2.5) and (6.2.6). The other is shown in Figure 6.2.5 with Eqs. (6.2.2) and (6.2.3). Although the theoretical solutions predict very well the power laws of growth for the submerged spreading rate for both initial and final collapse stages, there is some discrepancy in the magnitude of coefficients in the two equations (6.2.2) and (6.2.3). The variations in the coefficient are found to depend on the initial size of the mixed region and the Reynolds number Re_N (for data presentation the kinematic viscosity of the spreading fluid is assumed to be $0.01 \text{ cm}^2/\text{sec}$ for all the eleven cases). As shown in Figure 6.2.6 the theoretical value of the coefficient ($\sqrt{2}$) for inertial-buoyancy spreading is an upper limit for the eleven experimental results. For each initial size of homogeneous mixed region the coefficient for inertial spreading forms a curve which is asymptotic to the upper limit at the lower Reynolds number Re_N . Although there are not enough data available to show the value of Reynolds number where the intercept to the upper limit occurs, some idea can be gained from Figure 6.2.6. The larger the initial size, the larger the intercept Reynolds number will be. Similar results are also seen in Figure 6.2.7 for the coefficient for the final collapse stage. The only difference is that the theoretical value for the viscous-buoyancy

Table 6.2.1 Experimental parameters related to Figures 6.2.3, 6.2.4, 6.2.5, 6.2.6, and 6.2.7.

Symbol	R_o (in)	N (sec ⁻¹)	$\frac{NR_o^2}{v_s}$	$\frac{R(t)}{(Nvt)^{1/2}}$	$\frac{R(t)}{\left(\frac{N^2v^4}{v_s} t\right)^{1/6}}$	Source from Wu (1965)	
						Run No.	Figure
□	6	1.612	37,440	0.92	0.46	9	12
▽	"	1.115	25,900	1.01	0.59	3	
○	"	0.706	16,400	1.14	0.71	1	
△	"	0.511	11,860	1.18	0.75	4	11
×	0.875	1.764	870	1.08	0.97	33	
+	"	1.162	570	1.29	1.13	31	
∧	"	0.904	450	1.40	1.29	30	10
◇	1.375	1.764	2,150	1.03	0.60	1	
▽	"	1.042	1,270	1.26	0.88	6	
▷	"	0.644	790	1.37	1.04	10	
○	"	0.321	390	1.40	1.21	12	

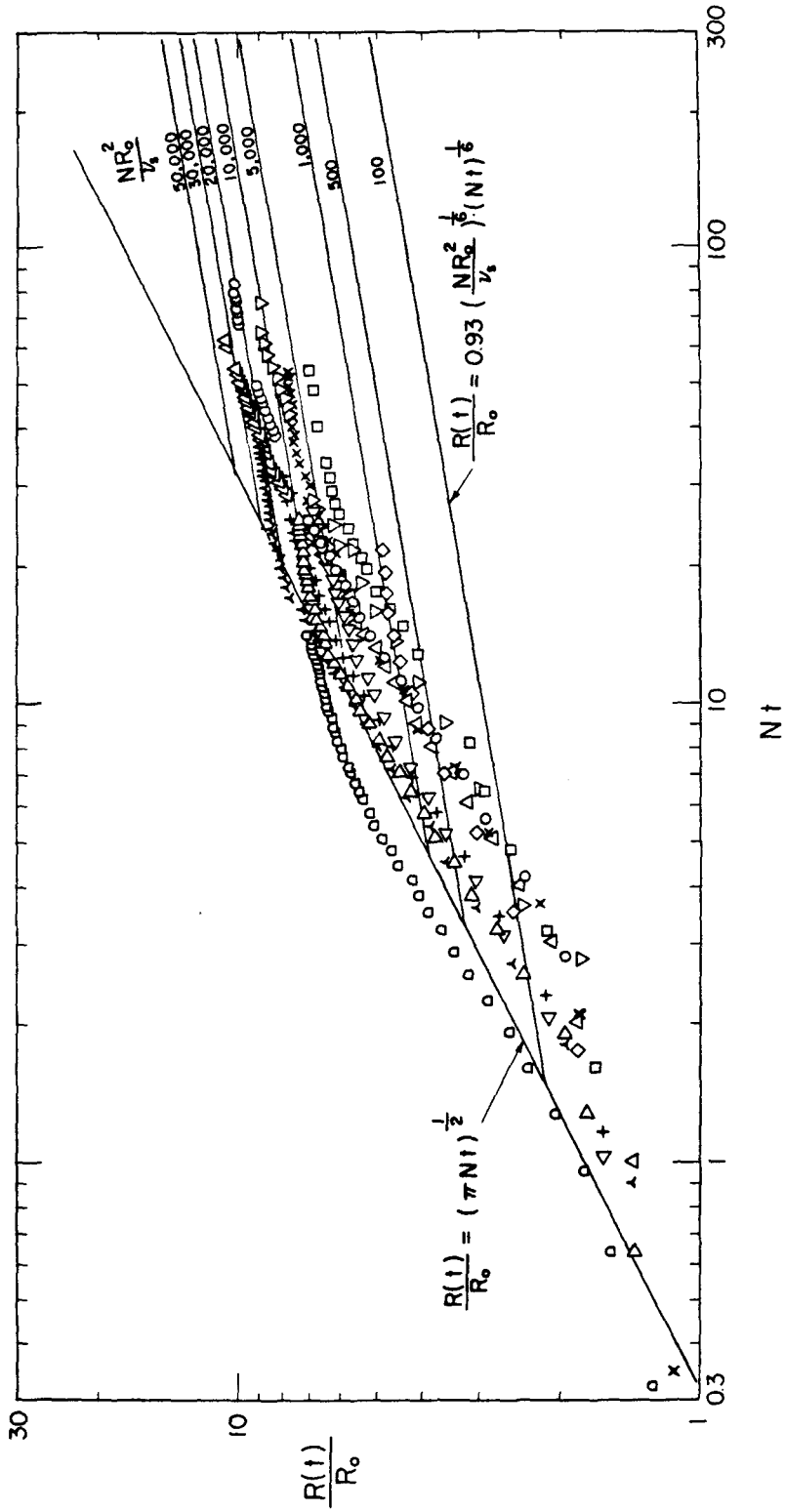


Figure 6.2.4 A plane mixed region collapsing in a linearly density-stratified environment. Comparison of theoretical solutions (the principal and the final collapse stages) for submerged density spreading front with experimental results by Wu (1965).

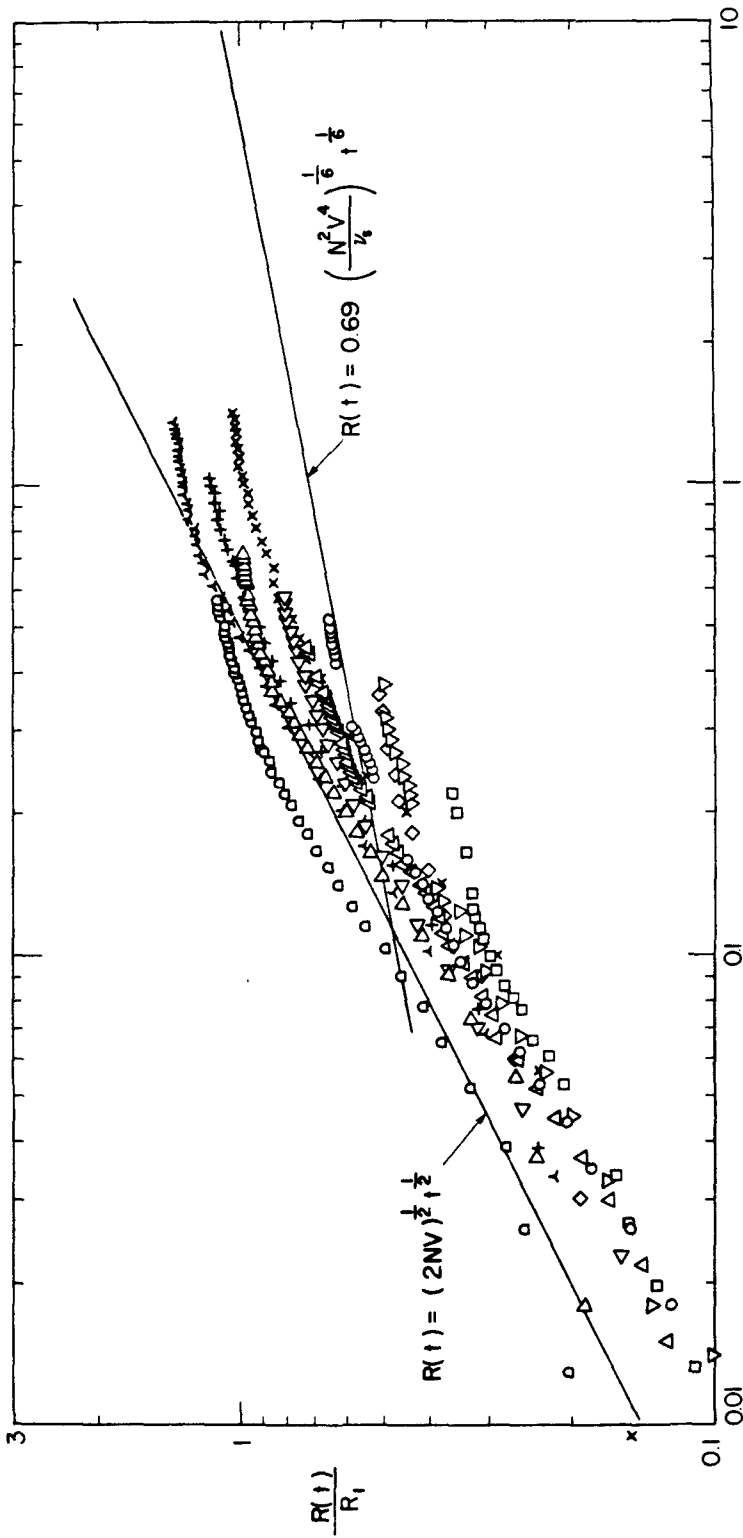


Figure 6.2.5 A plane mixed region collapsing in a linearly density-stratified environment. Comparison of theoretical solutions for submerged density spreading front (the inertial-buoyancy and the viscous-buoyancy regions) with experimental results by Wu (1965).

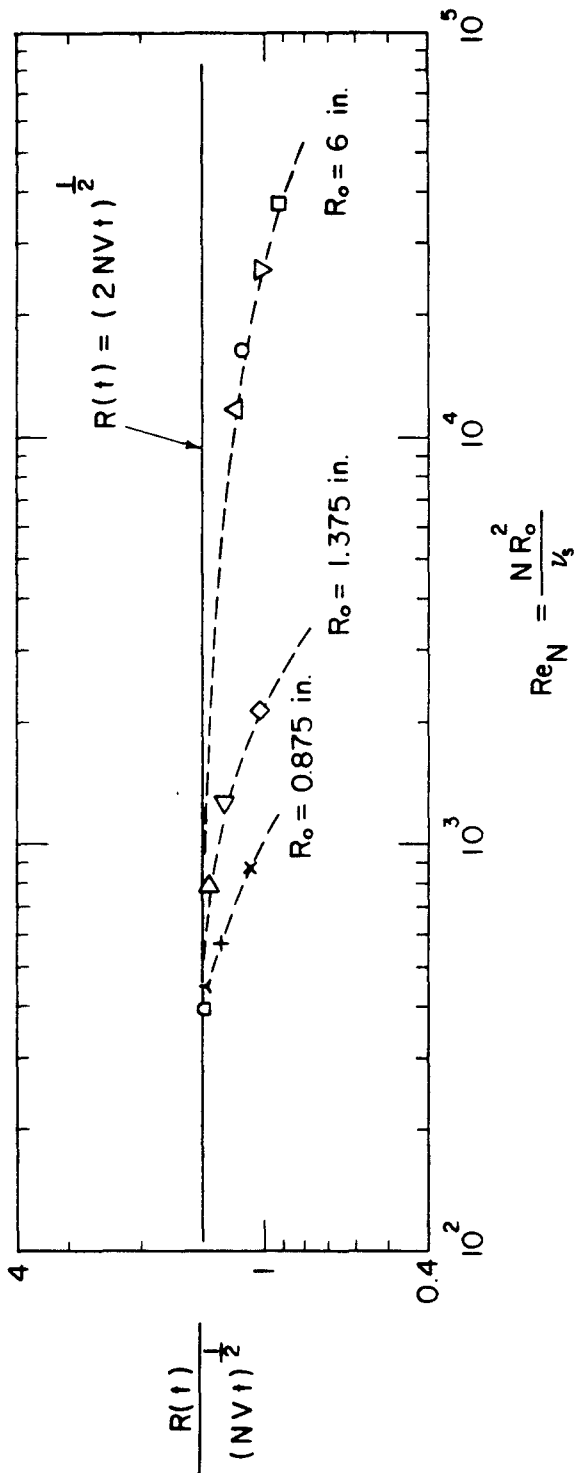


Figure 6.2.6 Coefficient of the principal collapse stage (the inertial-buoyancy submerged spread) as a function of Reynolds number Re_N and the initial radius of semi-circular or circular mixed region.

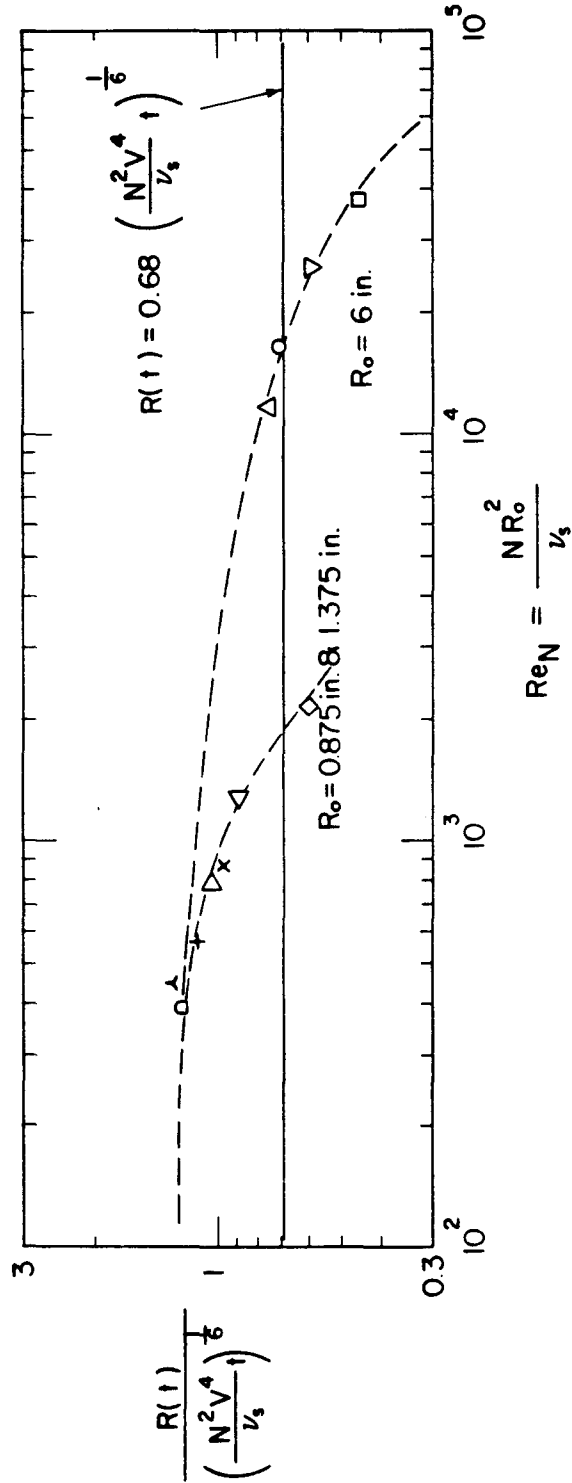


Figure 6.2.7 Coefficient of the final collapse stage (the viscous-buoyancy submerged spread) as a function of Reynolds number Re_N and the initial size of semi-circular or circular mixed region.

spreading coefficient is almost at the middle value of the experimental results.

Other experimental data for comparison with the theoretical solutions for the final collapse stage are taken from Tables 1 and 2 of Wu (1965). The value of upper tangent points of the principal collapse stage are re-calculated and plotted in Figure 6.2.8. (Details of the re-calculation are given in Table 6.2.2.) Equation (6.2.6) obviously is an upper limit for all 26 experimental points.

Several numerical calculations were performed using various methods by Cerasoli (1978), Dugan *et al.* (1976), Meng (1978), Padmanabhan *et al.* (1970), Wessel (1969), and Young and Hirt (1972). All investigators claim that their numerical results are in agreement with the experimental results by Wu (1965,1969), although only Young and Hirt (1972) give all the details of the numerical parameters as shown in Table 6.2.3. Most results of the numerical studies predict values lower than the theoretical solution in the inertial-buoyancy spread region, with the exception of the study by Padmanabhan *et al.* (1970), as shown in Figure 6.2.9. There is no way to compare the numerical results with the experimental results obtained by Wu (1965,1969) for the principal or the final collapse stage, since information such as the initial size and the Reynolds number Re_N are not given. The inertial-buoyancy spread coefficient calculated by Young and Hirt (1972) is around 0.98 for the Reynolds number $Re_N = 301$ and the

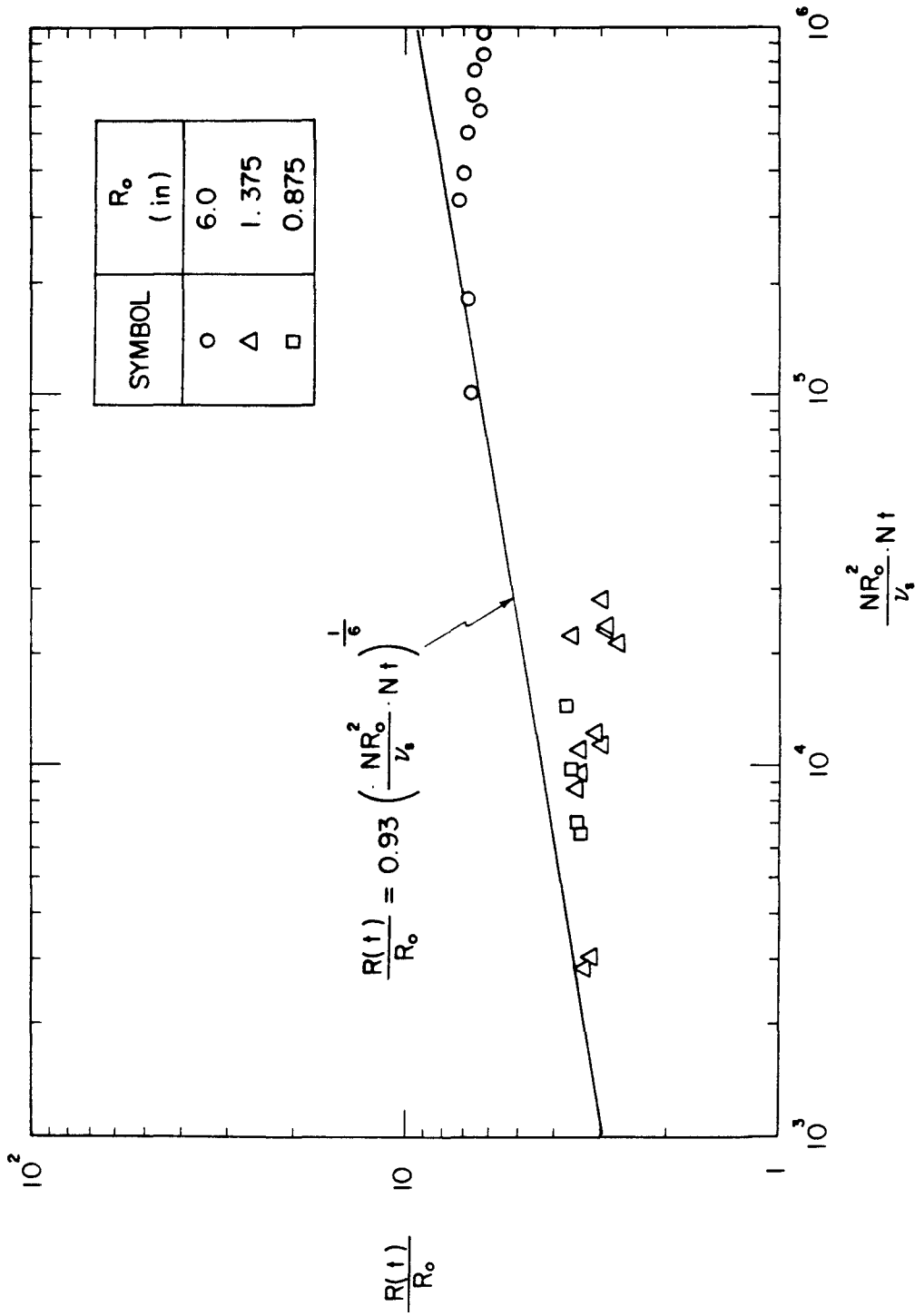


Figure 6.2.8 Plane mixed region in a linearly density-stratified environment: comparison of theoretical solution with experimental results by Wu (1965), for an interflowing front in the final collapse stage. Detail of re-calculation is shown in Figure 6.2.2.

Table 6.2.2 Re-calculation of experimental data for the final collapse stage of a plane mixed region in a linearly density-stratified environment. Data are taken from the upper tangent points of principal collapse stage in Tables 1 and 2 of Wu (1965).

R_o (in)	$\epsilon = \frac{-1}{\rho_s} \frac{d\rho_a}{dz}$ (ft ⁻¹)	$N = (g\epsilon)^{\frac{1}{2}}$ (sec ⁻¹)	$\frac{R(t)}{R_o}$	Nt	$\frac{Re}{Fr} = \frac{Nr_o^2}{\nu_s}$ (10 ³)	$\frac{Re}{Fr} Nt$ (10 ³)	Mixed Region Produced by		
6.00	0.00204	0.254	6.7	17.0	5.894	100.1	Wall-mixer		
	0.00401	0.359	6.8	22.0	8.335	183.4			
	0.00801	0.511	7.2	28.0	11.86	332.1			
	0.01549	0.707	7.0	24.0	16.41	393.8			
	0.02334	0.866	6.9	25.0	20.12	502.9			
	0.03101	1.000	6.3	25.0	23.20	580.6			
	0.03861	1.115	6.6	25.0	25.89	647.3			
	0.04578	1.214	6.6	27.0	28.21	761.5			
	0.08070	1.612	6.2	26.0	37.44	973.4			
	0.09210	1.722	6.2	21.0	40.00	840.0			
1.375	0.0966	1.764	2.7	10.0	2.15	21.52	Paddle-mixer		
	0.0814	1.619	3.0	14.5	1.97	28.63			
	0.0660	1.458	2.9	13.2	1.78	23.47			
	0.0550	1.331	2.9	14.5	1.62	23.54			
	0.0419	1.162	3.6	16.0	1.42	22.68			
	0.0337	1.042	3.1	9.6	1.27	12.20			
	0.0254	0.904	3.0	10.5	1.10	11.58			
	0.0213	0.828	3.4	11.0	1.01	11.11			
	0.0171	0.742	3.4	11.0	0.91	9.96			
	0.0129	0.645	3.5	11.0	0.79	8.65			
	0.0043	0.372	3.3	6.3	0.45	2.86			
	0.0032	0.321	3.2	7.8	0.39	3.05			
	0.875	0.0966	1.764	3.7	16.7	0.87		14.55	Paddle-mixer
		0.0659	1.456	3.6	13.6	0.72		9.78	
0.0419		1.162	3.5	12.2	0.57	7.00			
0.0254		0.904	3.4	15.0	0.45	6.70			

Table 6.2.3 Parameters of numerical calculations related to Figure 6.2.9.

Symbol	ϵ	N (sec ⁻¹)	R ₀ (cm)	v _s	$\frac{NR^2}{D}$ v s	Source	Numerical Method
△	0.0209 ft ⁻¹ (0.187 °C/cm)	0.820	?	?	?	Figure 13 Cerasoli (1978)	Finite Difference Method
○	?	?	?	0	?	Figure 4	Finite Difference Method
●	?	?	?	?	?	Figure 3	
▽	?	0.006	?	?	?	Figure 7	Vortex-in-Cell Method
▽	0.01549 ft ⁻¹	0.7062	?	1.2 × 10 ⁻⁵ ft ² /sec	?	Table 1	Primitive Variable Decomposition Method
▼	0.00810 ft ⁻¹	0.5107	?				
◇	?	0.25	?	?	?	Figure 1	Finite Difference Equations
□	0.001 cm ⁻¹	0.990	15.6	0.8 cm ² /sec	301	Figure 1 Young and Hirt (1972)	Marker-and-Cell Method

initial radius of circular section $R_0 = 15.6$ cm. It can be seen that it is a little lower than the experimental results by Wu given in Figure 6.2.6. Three cases of transition from the principal collapse stage to the final collapse stage were given by Padmanabhan *et al.* (1970) and Dugan *et al.* (1976). Unfortunately, no comparison between theoretical and experimental results in the final collapse stage is possible, since the value of initial size of mixed region was not given. Similarly, there is insufficient information available about the experiments reported by Amen and Maxworthy (1980) to compare their results with the present theories.

6.2.2 Plane Submerged Current from Continuous Steady Discharge

From the theoretical results and dimensional arguments of Chapter 3, it is known that in the absence of any diffusion effects there are three possible successive growth rates for a submerged intrusion front due to a horizontal slot buoyant jet discharging into a linearly density-stratified environment.

These three stages are:

(I) Starting Jet

$$R(t) \sim M^{1/3} t^{2/3} \quad , \quad (6.2.13)$$

(II) Inertial Starting Plume (or Inertial-Buoyancy Balanced Spread), $B_1 = NQ$,

$$R(t) = \frac{\sqrt{2}}{2} B_1^{1/2} t \quad , \quad (6.2.14)$$

(III) Viscous Starting Plume (or Viscous-Buoyancy Balanced Spread)

$$R(t) = 0.499 \left(\frac{N^2 Q^4}{v_s} \right)^{1/6} t^{5/6} \quad . \quad (6.2.15)$$

It should be noted that not all three stages of spreading are necessarily present in any given discharge situation. Also, end wall effects may modify these results. The results depend on three dimensionless parameters. The first is the Richardson number, $Ri_j = Nh_j/u_j$, which is used to classify whether the starting flow is a starting jet or a starting plume. The second is the Reynolds number, $Re_j = Q/v_s$, which is used to determine whether the discharge flow is turbulent or laminar initially. The third is also a Reynolds number, $Re_v = (NQ)^{1/2} h_j/v_s$, which is used to determine whether there exists an inertial plume regime or not. Excluding the case of a starting laminar jet, all three stages of spreading front exist only when the initial discharge Richardson number Ri_j is rather small and two Reynolds numbers, Re_j and Re_v , are simultaneously large. If the discharge Richardson number, Ri_j , is large and the two Reynolds numbers are both small, there will exist only the viscous starting plume stage (or more precisely, when R_1/ℓ_{QM} is very small, $R_1/\ell_{QM} = \left(\frac{u_j}{N^2 h_j} \right)^{1/2} \cdot \frac{u_j h_j}{v}$). There are two other combinations of these three parameters for the two other flow patterns. The details are given in Table 6.2.4.

Table 6.2.4 Four flow patterns for a plane intrusion layer due to different combinations of three dimensionless numbers.

Dimensionless Numbers Condition Flow Patterns	Discharge Richardson Number $Ri_j = \frac{Nh_j}{u_j}$	Discharge Reynolds Number $Re_j = \frac{Q}{v_s}$	Plume Reynolds Number $Re_v = \frac{(NQ)^{1/2} h_j}{v_s}$
Three spread stages $R(t) \sim t^{2/3}$ t $t^{5/6}$	small	large	large
Two spread stages $R(t) \sim t^{2/3}$ $t^{5/6}$	small	large	large
Two spread stages $R(t) \sim t$ $t^{5/6}$	large	large	large
One spread stages $R(t) \sim t^{5/6}$	large	small	small

These three dimensionless numbers are useful in predicting the four possible different growth histories of the plane intrusion layer. It is easily seen why three kinds of growth rate were observed by Manins (1976a), Maxworthy (1972), Zuluaga-Angel *et al.* (1972) under different combinations of the three parameters. In an analogous way, Imberger *et al.* (1976) showed why two different growth rates occurred with a selective withdrawal theory with no diffusion effects.

As shown in Table 6.2.5 three sets of experiments by Manins, Maxworthy, and Zuluaga-Angel *et al.* have almost the same range of volume flux Q , as does the discharge Reynolds number $Re_j = Q/\nu_s$, since the variation of kinematic viscosity of discharge fluid is rather small. However, the discharge slot thickness $2h_j$ and the Brunt-Väisälä frequency, N , of the ambient stratification, did vary one order of magnitude. Consequently, the discharge Richardson number, $Ri_j = Nh_j/u_j = 2Nh_j^2/Q$, in these three sets of experiments has a wide range of variation and covers three orders of magnitude.

As shown in Figure 6.2.10, Manins (1976a) observed that the length of the intrusion layer increased in proportion with time t in most of his experiments. In some cases, such as in experiments A, B, C, G, and H, the layer decelerated to grow with $t^{5/6}$ at the larger times. As given in Figure 6.2.11, Maxworthy (1972) reported that the length of intrusion layer increased with $t^{5/6}$,

Table 6.2.5 Summary of experimental parameters for submerged plane intrusion layer propagation in a linearly density-stratified environment due to a horizontal slot buoyant jet discharge at its neutral level.

Investigator	Experimental Tank			Water Depth (cm)	Inlet Slot Thickness $2h_j$ (cm)	Brunt-Väisälä Frequency N (sec^{-1})	Volume Flux Q (cm^2/sec)	Kinematic Viscosity ν_s ($10^{-2} \text{ cm}^2/\text{sec}$)	Slot Jet Reynolds Number $Re_j = \frac{Q}{\nu_s}$	Slot Jet Richardson Number $Ri_j = \frac{2Nh_j^2}{Q}$	Prandtl Number Pr	Power-Time Law
	Length (cm)	Width (cm)	Depth (cm)									
Manins (1976a)	183	10.3	20	13 to 16	3	1.76 to 3.94	0.72 to 2.57	?	up to 540	3.39 to 23.6	300	t
Maxworthy (1972)	365.76 (12 ft)	30.48 (1 ft)	45.72 (1.5 ft)	?	0.635 (1/4 in)	1.055 and 1.479	0.055 to 1.479	?	5.5 to 233	0.091 to 3.87	?	$t^{5/6}$
Zuluaga-Angel, Darden and Fischer (1972)	1280.2 (42 ft)	38.10 (1.25 ft)	121.92 (4.00 ft)	100	0.0794 (1/32 in)	0.170 and 0.712	0.277 to 1.93	0.942 to 1.100	27.0 to 175.5	0.00051 to 0.0081	?	$t^{3/4}$

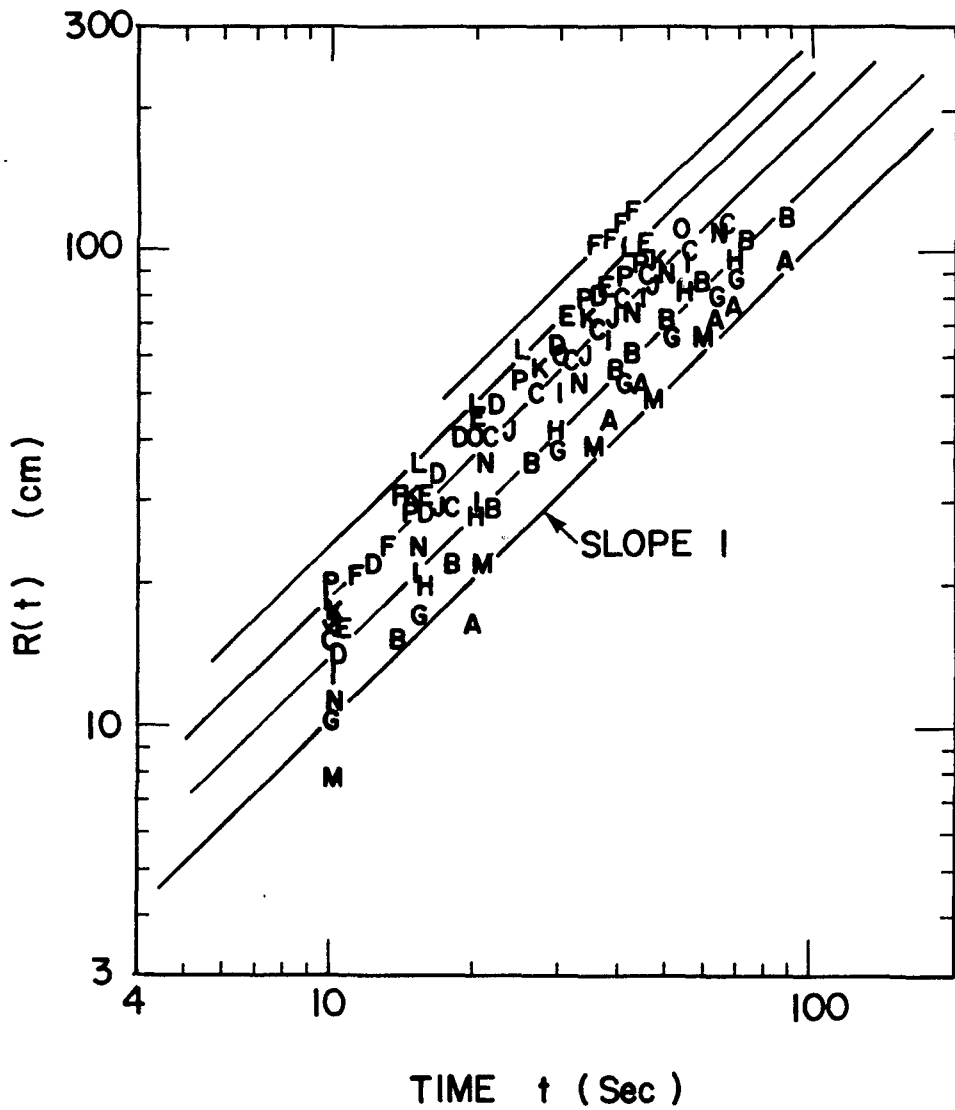


Figure 6.2.10 Growth history of an inertial starting plume observed by Manins (1976a). Details of experimental parameters are given in Table 6.2.6.

Table 6.2.6 Experimental data for plane intrusive layer spreading related to Figures 6.2.10, 6.2.11, 6.2.12, 6.2.15, 6.2.16, and 6.2.17.

Symbol or Run No.	N (sec ⁻¹)	$Re_j = \frac{Q}{v_s}$	$Ri_j = \frac{Nh_j}{u_j}$	Re_V	$\frac{R}{(NQ)^{1/2}}$	Source	
						Place	Author
A	3.78	72	23.6	247.5	0.70	Figure 3	Manins (1976 a)
B	3.51	110	14.4	294.7	0.74		
C	3.81	142	12.1	348.8	0.84		
D	3.39	180	8.48	370.6	0.87		
E	3.94	183	9.68	402.6	0.86		
F	3.59	225	7.18	426.4	0.94		
G	2.58	101	11.5	242.1	0.80		
H	2.58	116	10.0	259.4	0.81		
I	2.65	148	8.04	296.8	0.79		
J	2.57	181	6.39	323.6	0.87		
K	2.55	224	5.13	358.7	0.90		
L	2.70	255	4.76	393.6	0.93		
M	1.95	86	10.2	251.8	0.83		
N	1.76	159	4.98	250.8	1.00		
O	1.87	208	4.05	296.1	1.01		
P	1.94	257	3.39	334.6	1.03		
+	1.48	233	0.128	58.9	1.30	Figure 4	Maxworthy (1972)
□	1.06	233	0.091	49.8	1.27		
×	1.06	161	0.132	41.4	-		
●	1.48	117	0.256	41.7	-		
○	1.06	117	0.183	35.2	-		
▲	1.06	57.3	0.371	24.7	-		
▼	1.06	10.8	1.98	10.7	-		
▼	1.06	5.5	3.87	7.65	-		
▲	1	0.325	175	0.000531	2.86	Tables 1 and 2	Zuluaga-Angel, Darden and Fischer (1972)
▼	2	0.221	136	0.000506	2.16		
▲	3	0.406	132	0.000927	2.85		
◇	4	0.473	129	0.00108	2.99		
▼	5	0.356	82	0.00135	2.13		
D	6	0.170	89	0.000601	1.55		
▲	7	0.284	82	0.00108	1.90		
●	8	0.519	88	0.00197	2.77		
●	9	0.316	83	0.00120	2.04		
●	10	0.219	29	0.00476	0.986		
●	11	0.712	28	0.00810	1.60		
◆	12	0.417	27	0.00475	1.31		

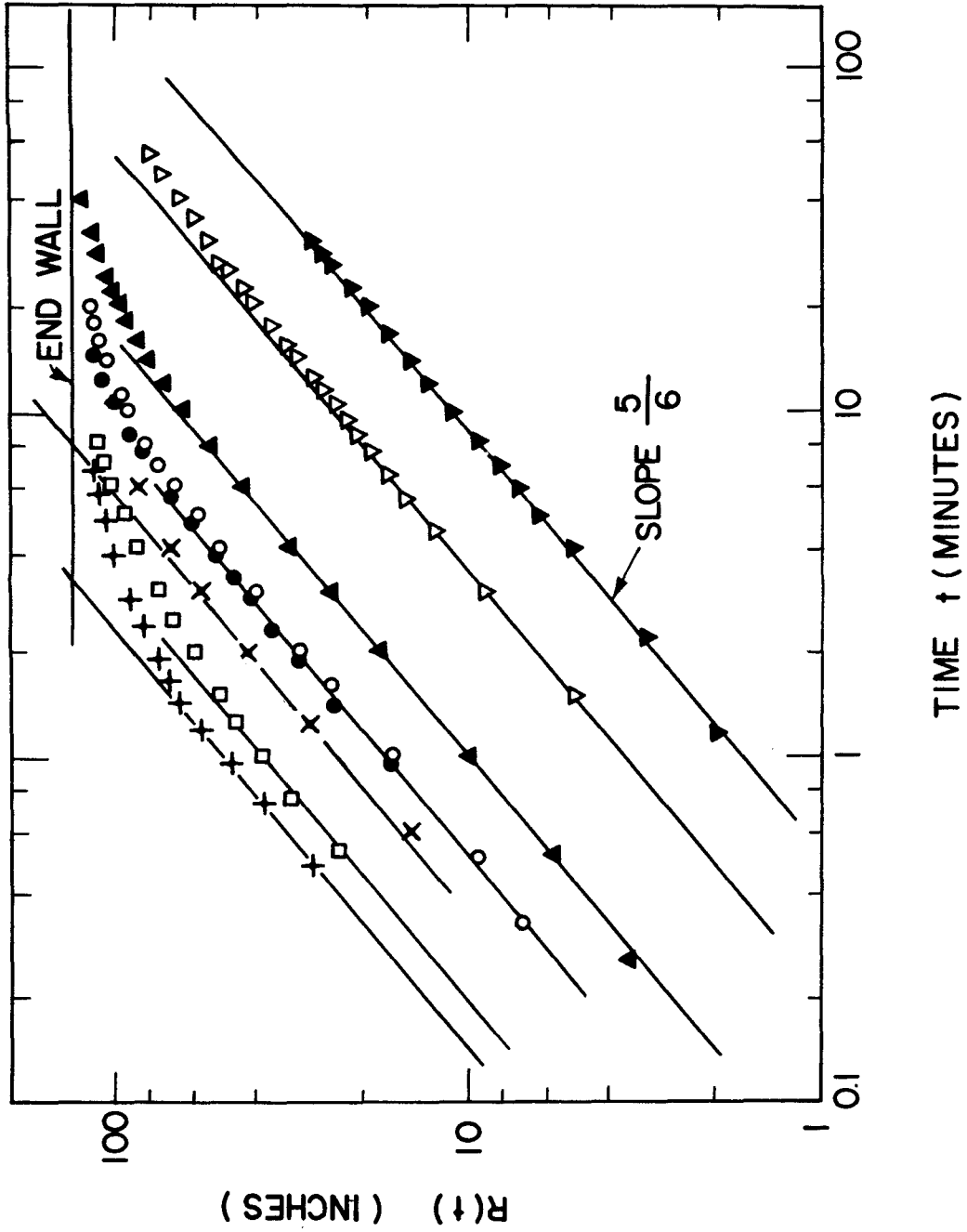


Figure 6.2.11 Growth history of viscous plume observed by Maxworthy (1972). Details of experimental parameters are given in Table 6.2.6.

especially at the lower source flow rate. He found also that it grows proportionally with two-thirds power of discharge rate, i.e. $Q^{2/3}$. The intrusion layer thickness, after an intensive mixing near the source point, increased as $t^{1/6}$, which is predicted by the force scale analysis and also by the viscous long wave theory.

In the experiments by Zuluaga-Angel *et al.* (1972), no discharge Richardson number, Ri_j was above 0.01. It is therefore to be expected that the discharge fluid would undergo intensive jet mixing on entering the stratified tank, just as in the case of the higher flow rate experiments by Maxworthy (1972). The intrusion layer length would then have at least two kinds of spreading history before meeting the end wall of tank. That is to say that the intrusion layer would increase with $t^{2/3}$ at first corresponding to the starting turbulent jet region, and then with t and $t^{5/6}$ for both the inertial and the viscous plume region. The criterion to determine which flow pattern would occur between the two possibilities in the latter stage is the plume Reynolds number Re_v , as defined previously.

As shown in Table 6.2.5 the Reynolds numbers Re_v in the experiments performed by Zuluaga-Angel *et al.* (1972) are rather small, $O(1)$ in magnitude, whereas Maxworthy's are $O(10)$ and Manins' order $O(100)$. Clearly, it is not easy for an inertial starting plume region (i.e. an inertial-buoyancy spreading) to exist behind the starting jet region in those experiments by

Zuluaga-Angel *et al.* As shown in Figure 6.2.12, most of their experiments have two stages of spread, i.e. $t^{2/3}$ and then $t^{5/6}$, except for Run No. R-9. The three-quarters power of time reported by Zuluaga-Angel *et al.* may be due to the fact that the average value of time power between two-thirds and five-sixths was taken in order to cover the two different regions of flow.

According to the three experimental parameters listed in Table 6.2.6, the viscous starting plume region should have appeared after the inertial starting plume in Manins' experiment, however, his experiments were limited by the available length of tank. This is apparently the reason why only one inertial plume was observed by Manins in most of his experiments. Although a slightly longer channel was used by Maxworthy, only the larger time record was presented. It can be surmised that there were also two possible flow patterns which existed before the viscous plume region found by Maxworthy.

A comparison of the experimental results by Manins with the constant propagation velocity inertial intrusion front similarity solution ($n = 0$ and $m = i = 1$) is given in Figure 6.2.13. In Figure 6.2.14 the intrusion layer thickness near the source point is compared with the self-similar solution, i.e.

$$h(r \rightarrow 0, t) = \frac{\dot{R}(t)}{N} H(0) = \left(\frac{Q}{N} \right)^{1/2} H(0) \quad , \quad (6.2.16)$$

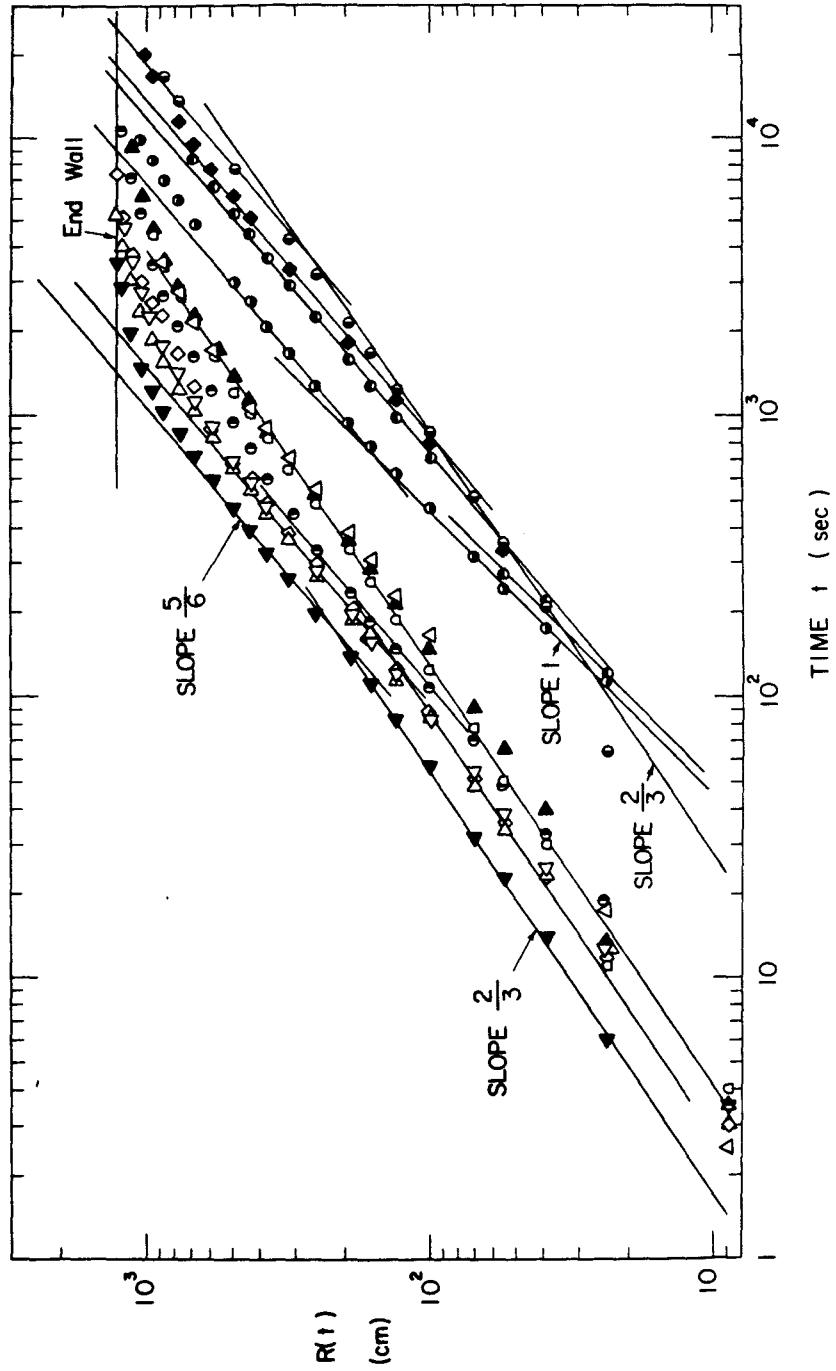


Figure 6.2.12 Growth history for submerged plane horizontal starting buoyant jets observed by Zuluaga-Angel *et al.*, (1972). Details of experimental parameters are given in Table 6.2.6.

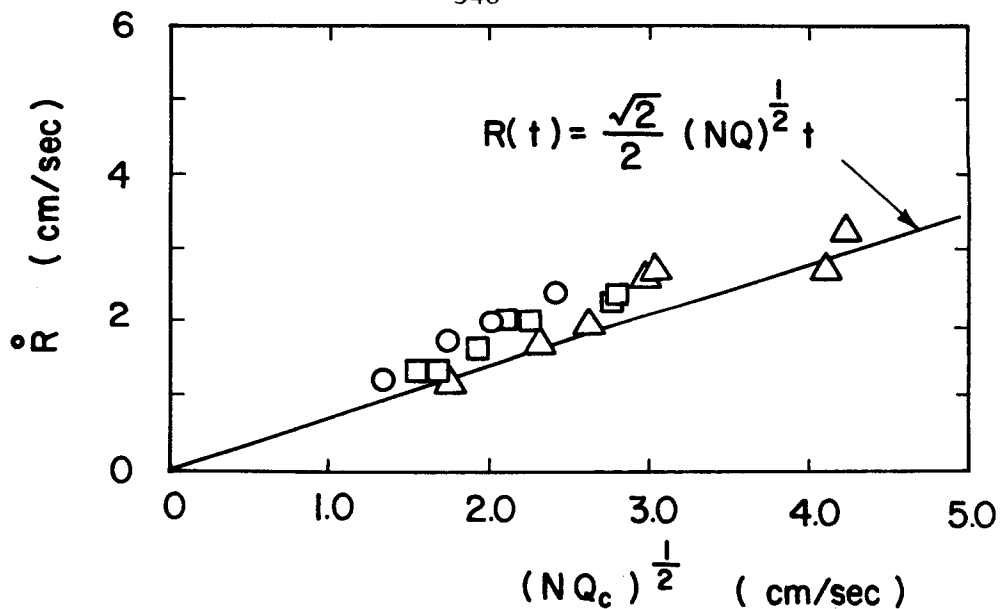


Figure 6.2.13 Intrusion front velocity as a function of buoyancy flux $B_1 = NQ$. Experimental data are taken from Manins (1976a), \circ , $N^2 = 3.5$; \square , $N^2 = 7.0$; Δ , $N^2 = 1.40$.

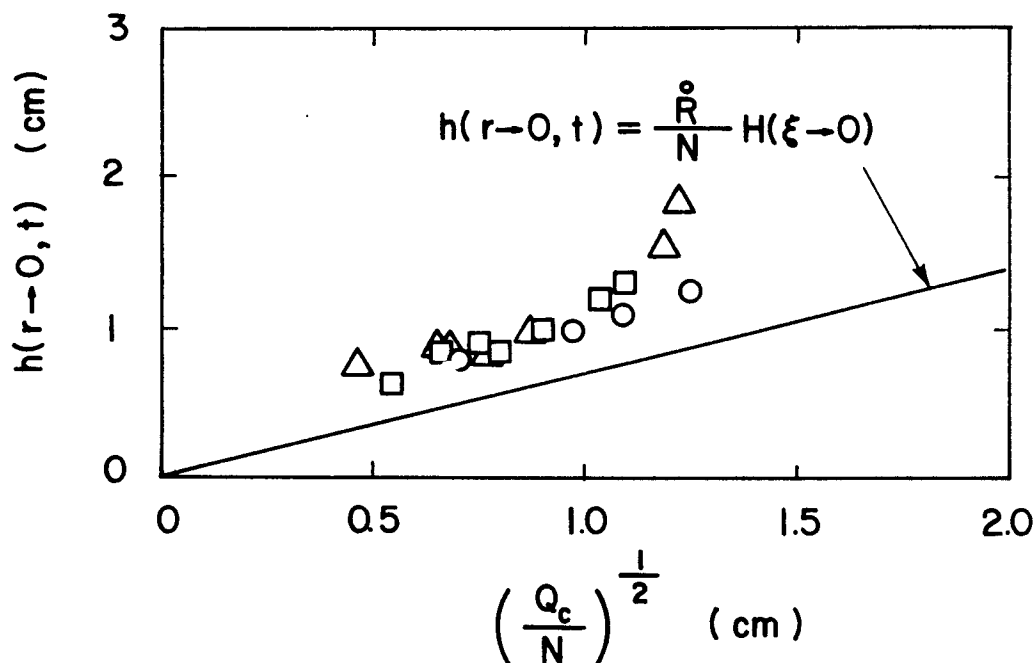


Figure 6.2.14 Self-similar distribution of intrusion layer half-thickness near the source. Experimental data are taken from Manins (1976a), \circ , $N^2 = 3.5$; \square , $N^2 = 7.0$; Δ , $N^2 = 14.0$.

where $H(0)$ is equal to 1. That is to say, the intrusion nose velocity is proportional to the product of the thickness near the source point and the Brunt-Väisälä frequency of the ambient stratification. The values of volume flux Q used in Figures 6.2.13 and 6.2.14 are the Q_c computed by Manins from the actual flow patterns, rather than an initial discharge value Q . The discrepancy shown in the two figures between the experiments and theoretical value may therefore be due to the small amount of jet mixing near the source point. These errors can be seen more clearly from the direct calculation of the coefficients in Eq. (6.2.14).

In Figure 6.2.15 is given the inertial starting plume coefficient, $R(t)/(NQ)^{1/2}t$, which is expressed as a function of discharge Richardson number Ri_j . Twenty data points are asymptotic to the theoretical value $\sqrt{2}/2$ at the higher value of Richardson number. Significant discrepancies occur at the lower Richardson numbers. This is logical because more jet-like flows at lower Richardson numbers will induce more jet mixing near the discharge point so that larger values of coefficients will result.

A similar explanation can be applied to the value of the viscous starting plume coefficient. As shown in Figure 6.2.16, the two groups of data are both asymptotic to a common value around 0.499 at a higher Richardson number. The two groups of data are separated by the dimensionless number Re_v , which is the product of the Reynolds number Re_j and the square root of

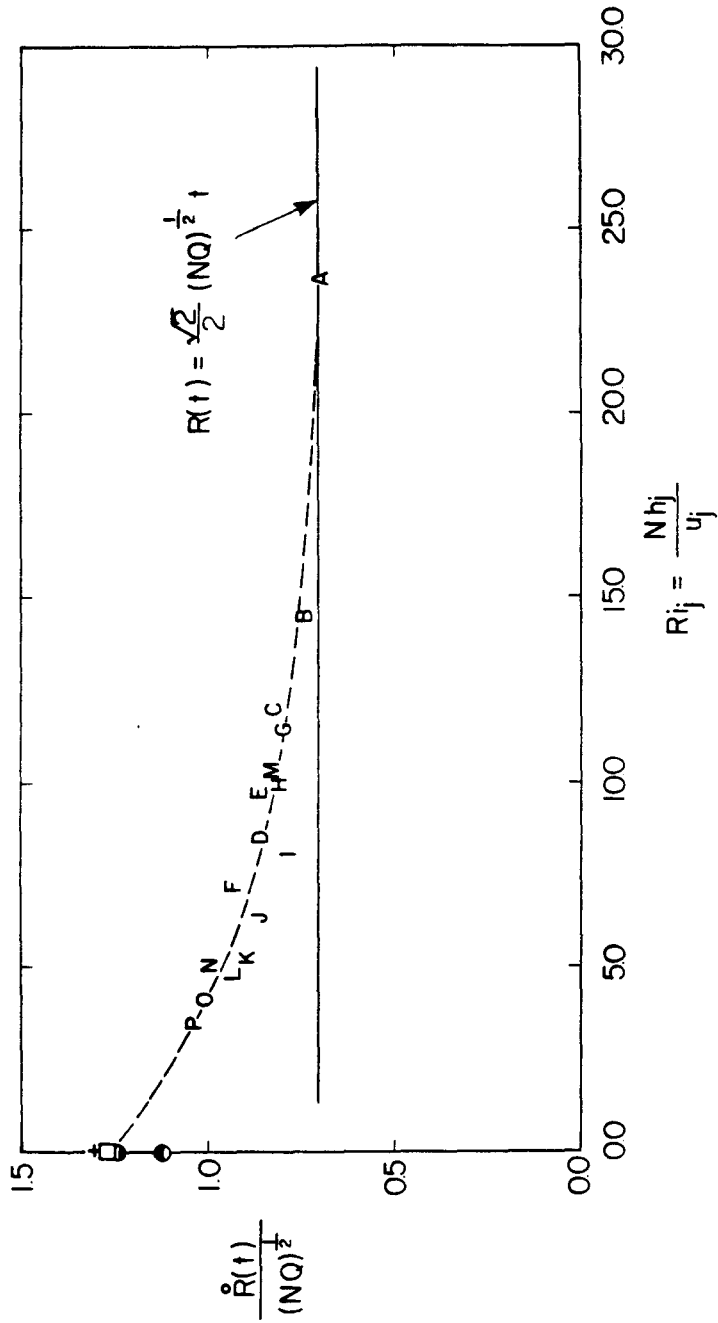


Figure 6.2.15 The plane submerged front velocity due to a starting horizontal slot buoyant jet discharge at its neutral level in a linearly density-stratified environment. The relevant experimental parameters are given in Tables 6.2.5 and 6.2.6.

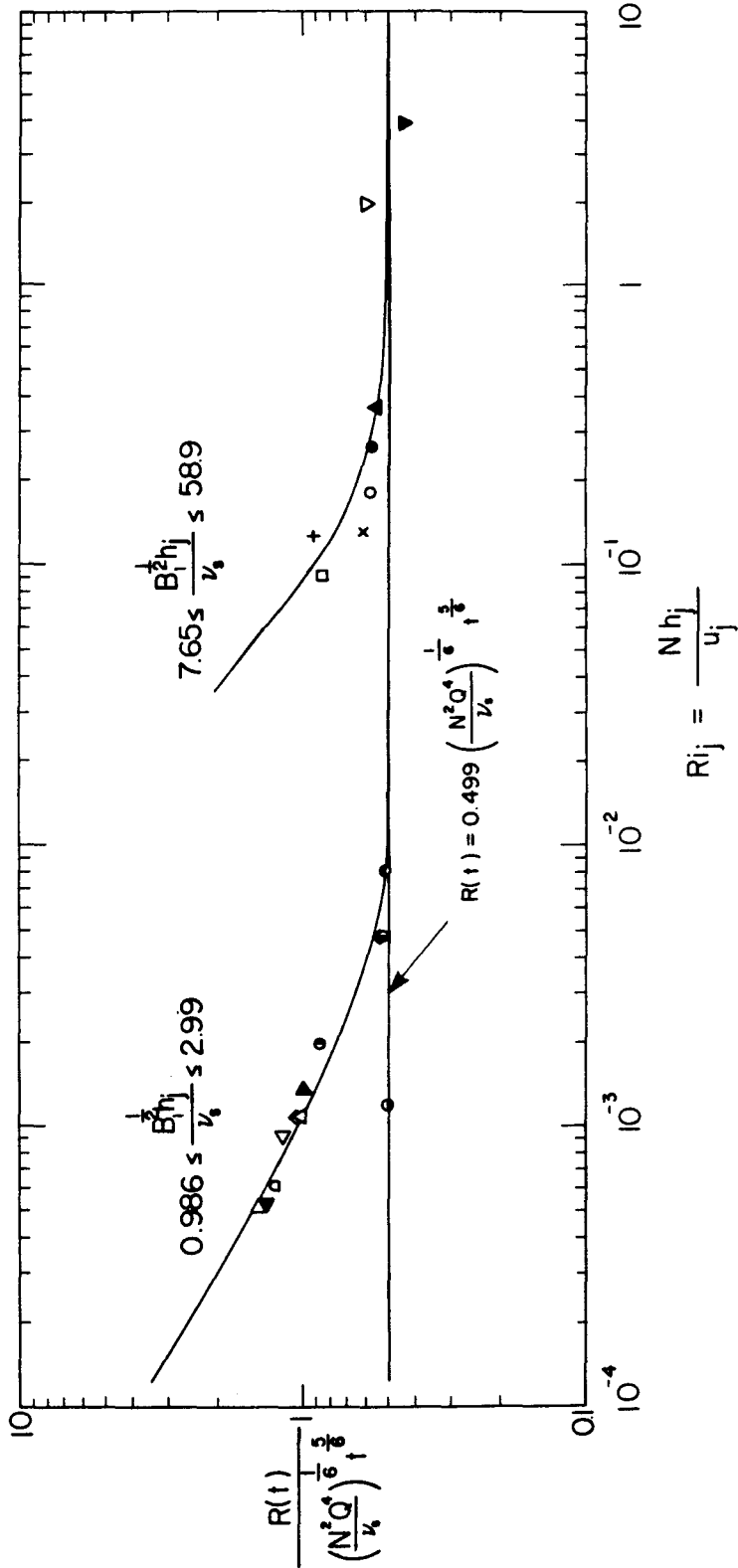


Figure 6.2.16 The coefficient of submerged plane viscous starting plume (or submerged viscous-buoyancy spread) expressed as a function of discharged Richardson number Ri_j and viscous plume Reynolds number Re_v . Experimental parameters given in Table 6.2.6.

Richardson number Ri_j . They are actually separated by the Richardson number, since most of the two sets of experiments cover almost the same range of Reynolds number Re_j . The inertial effects on the viscous intrusion layer spreading can be seen more clearly in Figure 6.2.17.

In Figure 6.2.18 it is seen the starting jet coefficient decreases with increasing Richardson number. The eleven data points, which are taken from Zuluaga-Angel *et al.*, are asymptotic to a constant value of around 1.90 at a lower Richardson number.

Figure 6.3.19(a) presents the typical viscous spreading layer profile at each time of measurement as recorded by Zuluaga-Angel *et al.* The data have a self-similar profile as shown in Figure 6.3.19(b). The normalizing thickness is $(v_s \circ RR/N^2)^{1/4}$, and the horizontal distance is normalized by the frontal length $R(t)$ each time. Since the frontal velocity was not measured by Zuluaga-Angel *et al.*, the value is obtained by differentiating the frontal position function, i.e.

$$R(t) = \frac{5}{6} c \left(\frac{N^2 Q^4}{v_s} \right)^{1/6} t^{-1/6} \quad , \quad (6.2.17)$$

in which c is the coefficient in Eq. (6.2.15). Therefore, the time-varying thickness can be computed directly with time t and the unknown discharge and ambient conditions, i.e.

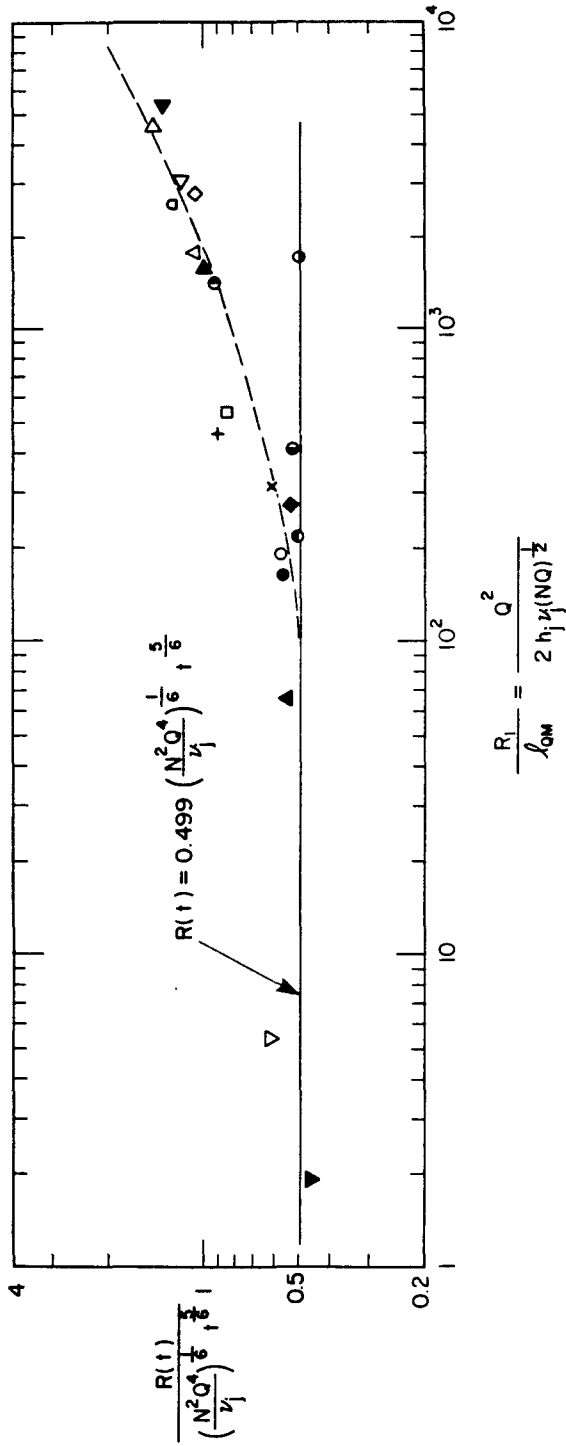


Figure 6.2.17 The coefficient for a submerged plane viscous starting plume expressed as a function of R_1/ρ_{0M} . Symbols are defined in Table 6.2.7.

Table 6.2.7 Calculation of the coefficient of displacement for a submerged plane viscous starting plume as shown in Figure 6.2.17.

SYMBOL and RUN NO.	v_j ($10^{-2}\text{cm}^2/\text{sec}$)	N (1/sec)	Q (cm^2/sec)	$\frac{R(t)}{\left(\frac{N^2 Q^4}{v_j}\right)^{1/6} t^{5/6}}$	$\frac{R_1}{R_{QM}} = \frac{Q^2}{2h_j v_j (NQ)^{1/2}}$	Source
+	1.0	1.48	2.33	0.910	460	Figure 4 of Maxworthy (1972)
□	"	1.06	2.33	0.850	544	
×	"	1.06	1.61	0.615	314	
●	"	1.48	1.17	0.569	163	
○	"	1.06	1.17	0.573	192	
▲	"	1.06	0.573	0.553	66	
▽	"	1.06	0.108	0.620	5.43	
▼	"	1.06	0.055	0.460	1.95	
▲	1	1.100	0.325	1.93	5387	Tables 1 and 2 of Zuluaga- Angel <i>et al.</i> (1972)
▽	2	1.014	0.221	1.38	4284	
△	3	1.043	0.406	1.38	3073	
◇	4	1.072	0.473	1.38	2770	
▶	5	1.014	0.356	0.83	1575	
◻	6	0.995	0.170	0.89	2578	
△	7	1.014	0.284	0.83	1763	
●	8	0.942	0.519	0.83	1404	
●	9	0.995	0.316	0.83	1703	
●	10	1.014	0.219	0.29	414.6	
●	11	0.995	0.712	0.277	218.8	
◆	12	1.028	0.417	0.277	276.7	

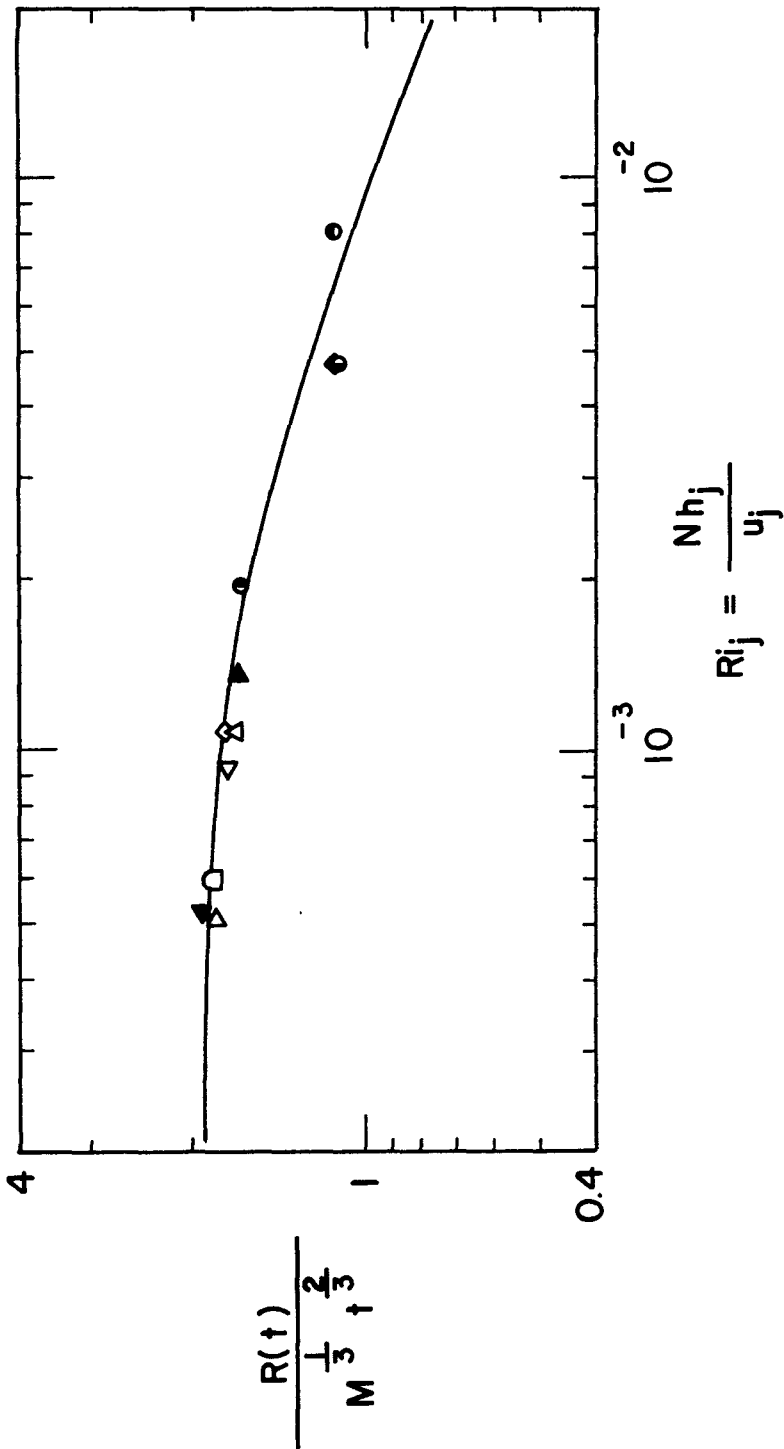


Figure 6.2.18 The coefficient of spreading for a submerged plane starting jet expressed as a function of discharge Richardson number Ri_j , data from Table 6.2.7.

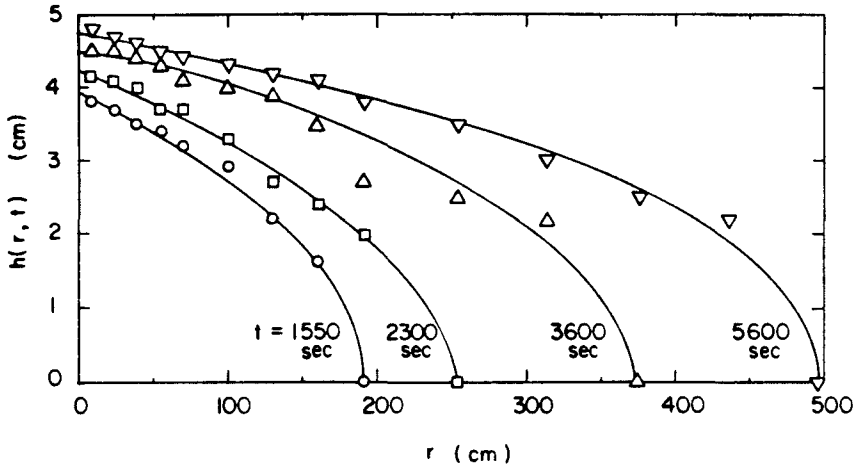


Figure 6.2.19(a) Viscous intrusion layer profiles at each time t . Data are taken from experiment No. R-11 in Table 4 of Zuluaga-Angel *et al.* (1972).

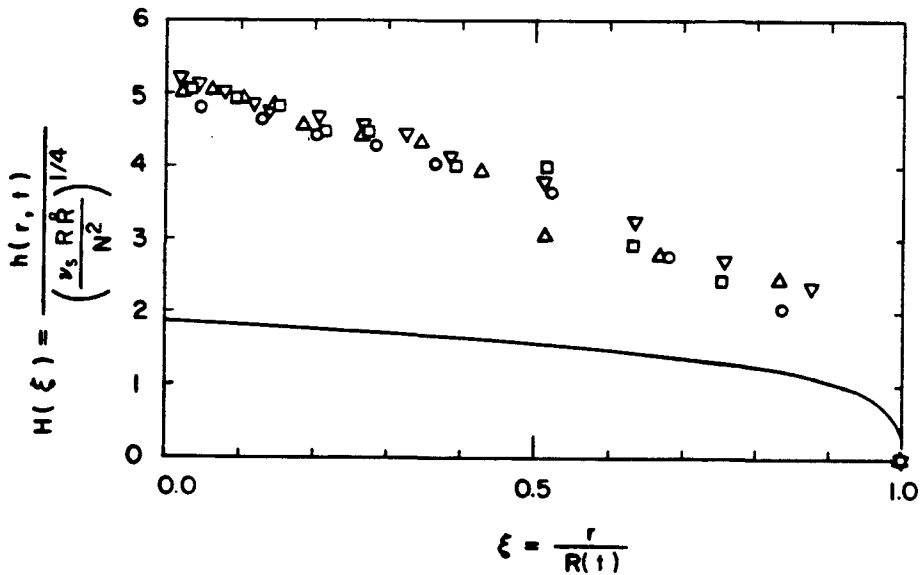


Figure 6.2.19(b) Self-similar thickness distribution of viscous intrusion layer. Solid curve is the viscous long wave solution (3rd order) derived in Subsection 3.3.5.

$$\left(\frac{v_s R R^{\circ}}{N^2}\right)^{1/4} = \left(\frac{5}{6} c^2\right)^{1/4} \left(\frac{v_s t Q^2}{N^2}\right)^{1/6} \quad (6.2.18)$$

Using this scheme the four profiles at each time collapse into a self-similar curve. The theoretical profile $H(\xi)$ calculated from the second-order nonlinear ordinary differential equation in Subsection 3.3.5,

$$(H^5)'' = 3H - 15\xi H' \quad , \quad (6.2.19)$$

with boundary condition $H(1) = 0$ is shown by solid curve. The higher values given by the experimental curve may be due to intensive entrainment due to jet mixing near the discharge point which will give a larger value of Q than used in the normalization.

6.3.3 Radial Submerged Current

Only one field observation result of a horizontal spreading plume in a stably stratified atmosphere is available for comparison with the theoretical prediction. Two aerial photographs of a cooling tower plume were taken by Kramer and Seymour (1976) at the John E. Amos power plant (shown in Figures 2.1.2(a) and (b) of Chapter 2). The submerged radial spreading ring structure at one instantaneous time, as shown

in Figure 2.1.2(b), is reproduced in the line sketch in Figure 6.2.20. If it is assumed that the center of radial spreading plume is located at the point of the maximum height of plume rise, then four subsequent locations of the circular discontinuity can then be scaled from the figure. Three successive ratios for the radii of the discontinuity ring are calculated to be 0.73, 0.72, and 0.71, which are only 6% higher than the theoretical value 0.692 given previously.

Experiments performed recently by Zatsepin *et al.* (reported in Barenblatt and Monin (1979)) show that the radial viscous-buoyancy spreading current advances proportionally to $t^{1/10}$ in a linearly density-stratified environment. Similarity solutions developed independently by Barenblatt and Monin (1979) also show that the plane viscous-buoyancy spreading front increases its length in the linearly density-stratified ambient proportionally to $t^{1/6}$ and the radial front to $t^{1/10}$.

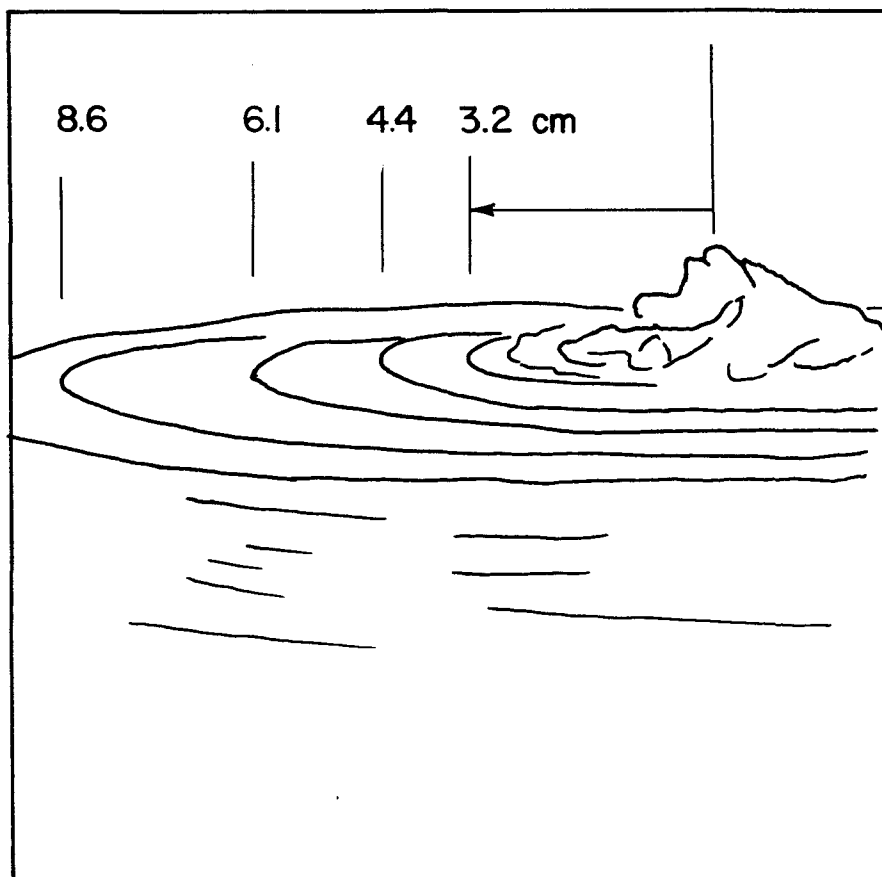


Figure 6.2.20 Line sketch for a series of radial ring discontinuities in a horizontal spreading cooling tower plume in atmosphere.

CHAPTER 7

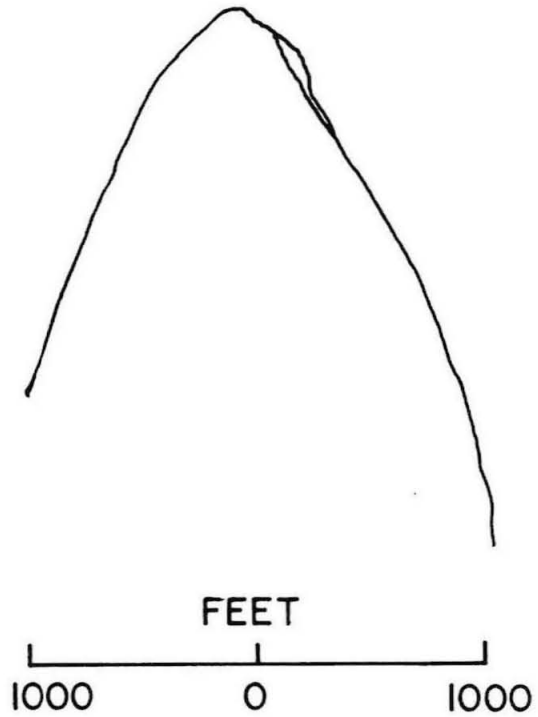
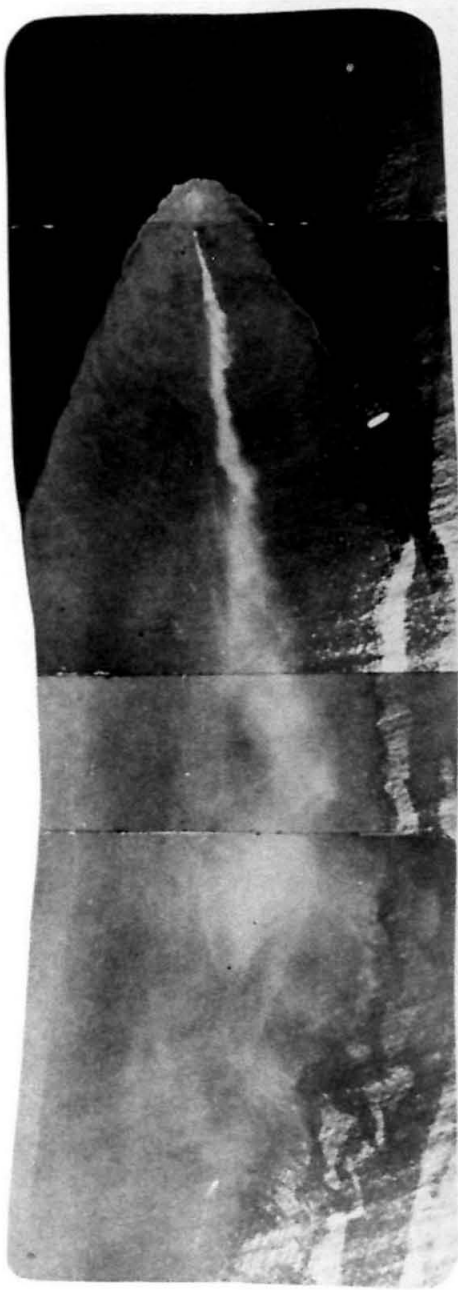
ENGINEERING APPLICATIONS

A primary application of the results of the present investigation is intermediate field problems (buoyancy-driven gravitational spreading) associated with ocean outfall discharge of treated waste waters. Barge disposal of sludge and dredged spoil are also important environmental applications. The results of these investigations can also be applied to the analysis of accidental releases of hazardous fluids, such as the spreading of dense poisonous or explosive gases or liquids. The spreading of cooling water from power plants is a further application.

7.1 Ocean Outfall Discharge

Figures 7.1.1(a), (b), (c), and (d) show four photographs and line sketches of a typical buoyant surface spreading wastewater field under an ambient cross current. The photographs show the situation prevailing before turbulent diffusion becomes dominant and a sharp boundary between the diluted effluent and the ambient sea water can be clearly seen. The width of the sharp boundaries has been plotted in Figure 7.1.2 to determine the lateral growth rate of the plume.

The width of the wastewater field as a function of distance from the source is plotted in Figure 7.1.2 for the four cases shown in Figures 7.1.1(a) - (d). There is no clearly defined growth rate for these field results although a dependence on $x^{1/2}$

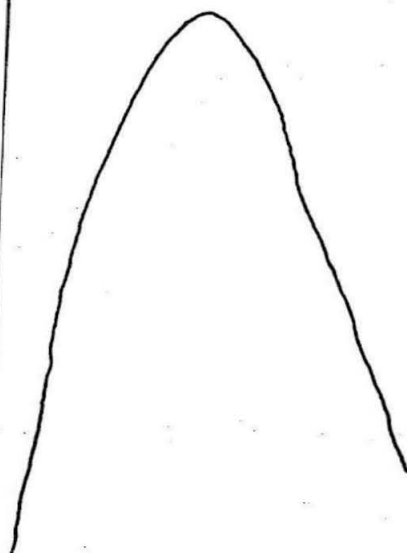


$U = 0.34$ KNOTS

28 JUNE 1963

ORANGE COUNTY
OUTFALL

Figure 7.1.1(a) Buoyant surface spreading wastewater field from submerged single port (diameter 78 inches) discharge, average discharge rate $Q = 120$ mgd (185.6 cfs), submerged depth $H = 55$ ft, $\Delta = 0.025$. Photograph from Figure 21 of Allan Hancock Foundation (1964).



FEET
1000 0 1000

$U = 0.32$ KNOTS

28 JUNE 1963

ORANGE COUNTY
OUTFALL

Figure 7.1.1(b) Photograph from Figure 22 of Allan Hancock Foundation (1964).

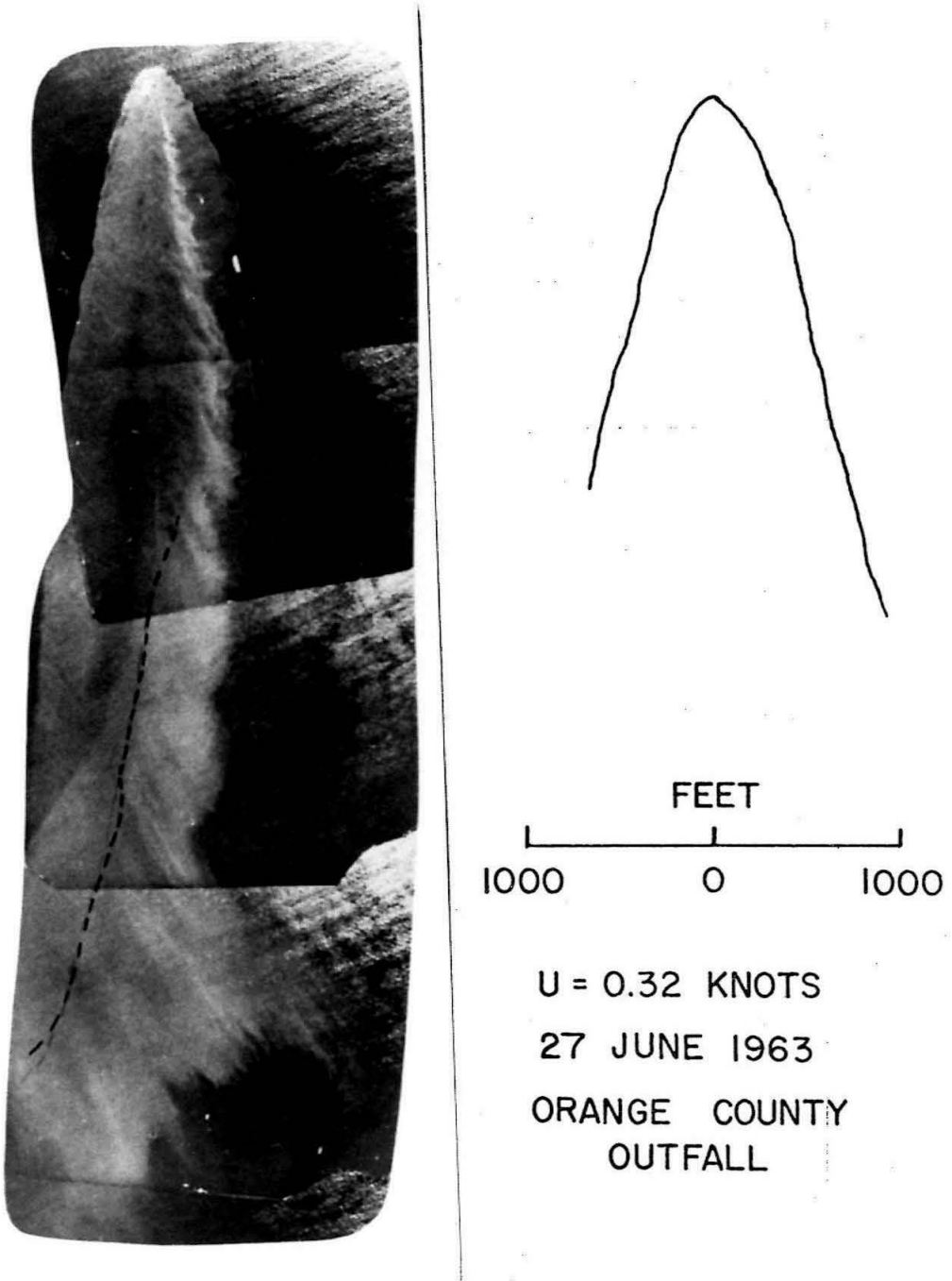


Figure 7.1.1(c) Photograph from Figure 20 of Allan Hancock Foundation (1964).

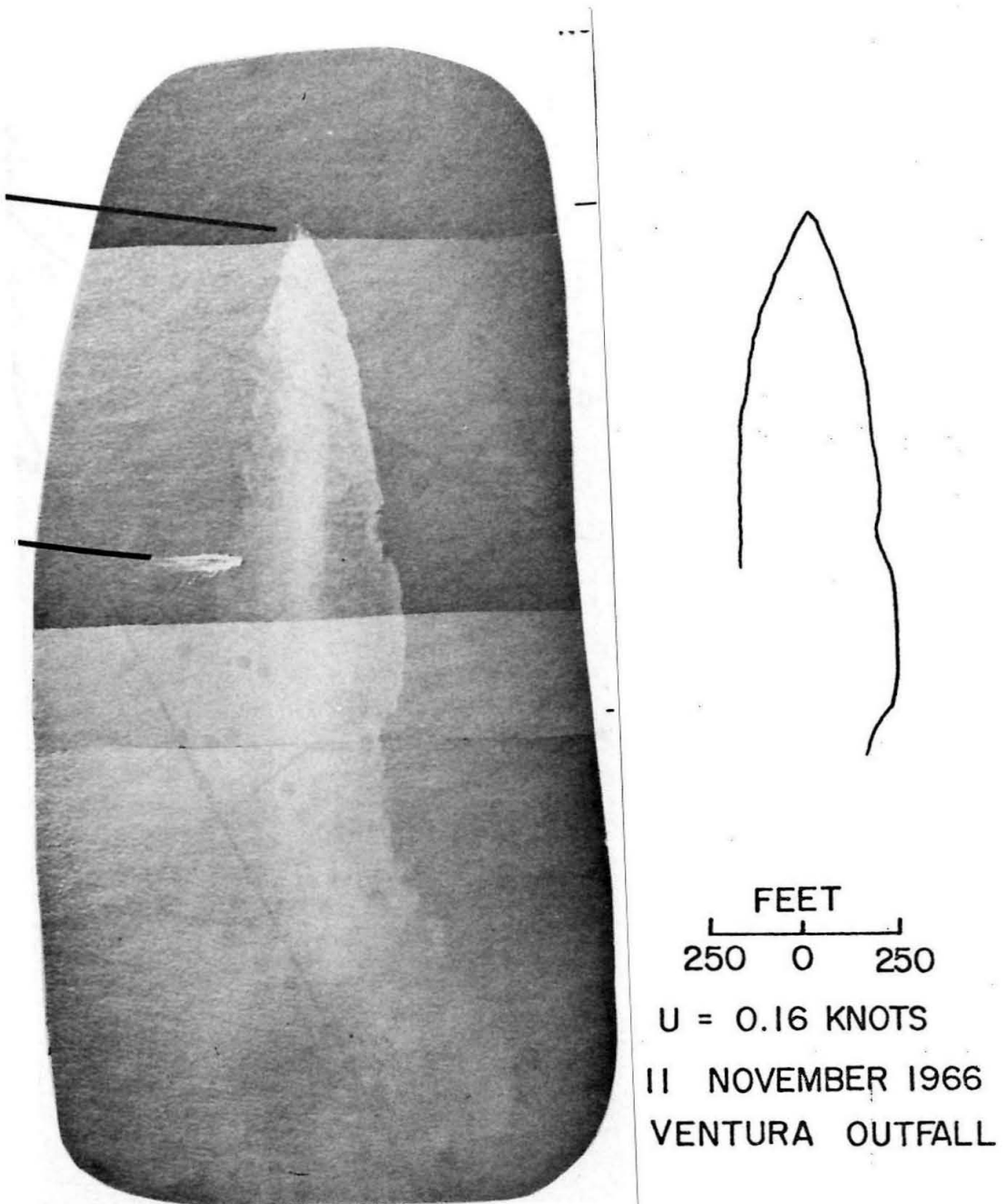


Figure 7.1.1(d) Buoyant surface spreading wastewater field from submerged single port (diameter 36 inches) discharge. Average discharge rate $Q = 2.20$ mgd (3.40 cfs), submerged depth $H = 35$ feet. Photograph from Figure 4 of Foxworthy and Kneeling (1969).

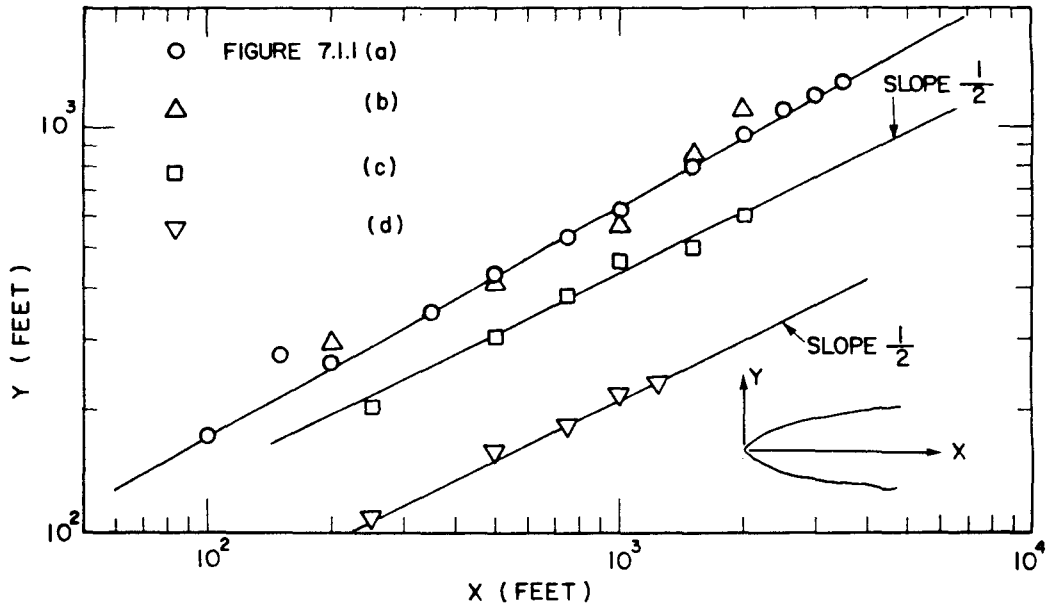


Figure 7.1.2(a) Growth of buoyant surface wastewater field shown in Figures 7.1.1(a), (b), (c), and (d).

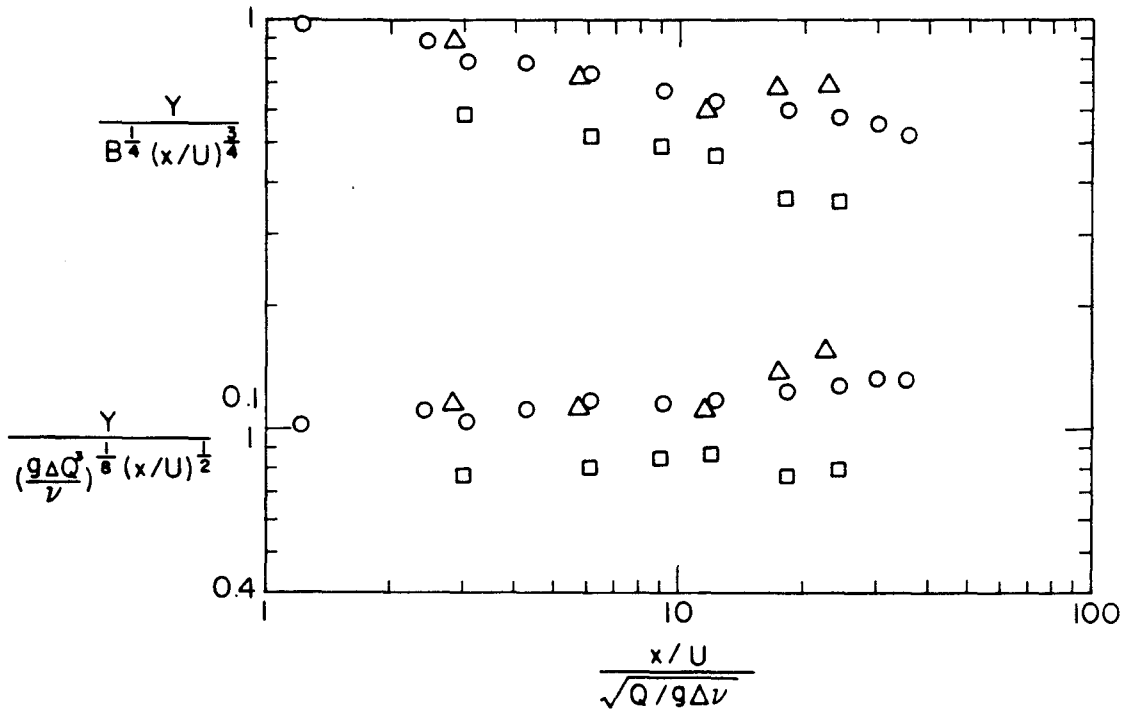


Figure 7.1.2(b) Dimensionless plotting of growth of buoyant surface wastewater field shown in Figure 7.1.2(a).

appears reasonable. A growth rate of $x^{1/2}$ corresponds to buoyancy driven spreading with viscous friction. In Figure 7.1.2(b) one can see the inertial plume coefficient $y/B^{1/4}(x/U)^{3/4}$, is decreasing while the viscous plume coefficient, $y/(g\Delta Q^3/\nu)^{1/8}(x/U)^{1/2}$, remains at a constant value, which is around the experimental value given in Eq. (5.3.10).

Figure 7.1.3 shows a surface thermal field observed by Sonnichsen (1971). The width of the plume grows as $x^{3/4}$ which is consistent with a buoyancy driven inertial plume. There are again unfortunately insufficient data to establish the buoyancy flux.

7.2 Surface Buoyant Discharge

The intermittent surging of a radial discharge as discussed in Section 3.2 has been observed in the field. Figures 7.2.1(a), (b), and (c) show three line sketches of a thermal plume due to cooling water discharged at a low Froude number from the shore-side power plant. The sequential ratio of the position of the radial discontinuities (as noted by circles) is found to vary from 0.79 to 0.63 for Figure 7.2.1(a), from 0.75 to 0.67 for Figure 7.2.1(b), and from 0.79 to 0.72 for Figure 7.2.1(c). The average value of this ratio is around 0.74 which is quite close to theoretical value 0.753 given in Subsection 3.2.5.3. As shown in Figure 7.2.2 the oscillating period experienced by a stationary observer in measuring the temperature and the velocity of the

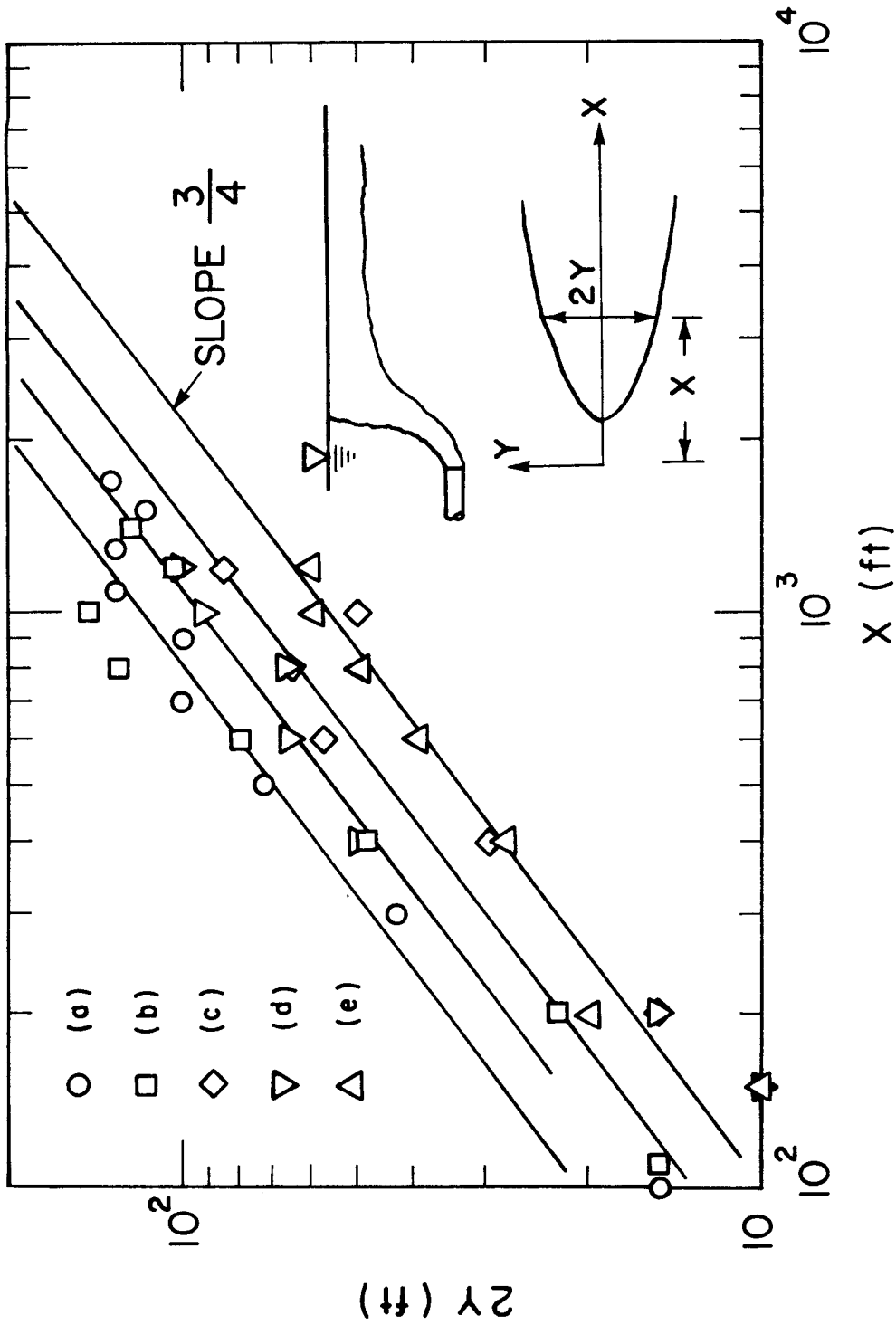


Figure 7.1.3 Growth of heated (a,b,c) and nonheated (d,e) surface plume field due to a submerged outfall discharge. Data from Table 1 of Sonnichsen (1971).
 (a) $Q = 75,000$ cfs, (b) $110,000$ cfs, (c) $145,000$ cfs, (d) $50,000$ cfs, (e) $100,000$ cfs.

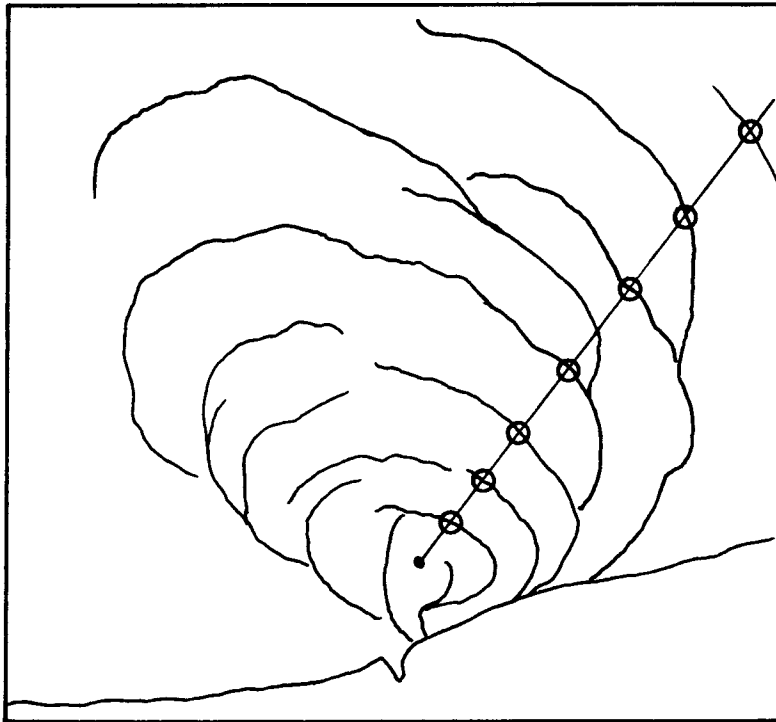


Figure 7.2.1(a) Line sketch of the thermal image of a discontinuous radial thermal plume field at Sheboygan Power Station, Wisconsin, on September 15, 1971; aerial photograph taken at a flying height 5000 feet. Photograph was shown in Figure 19 of Scarpace and Green (1973).

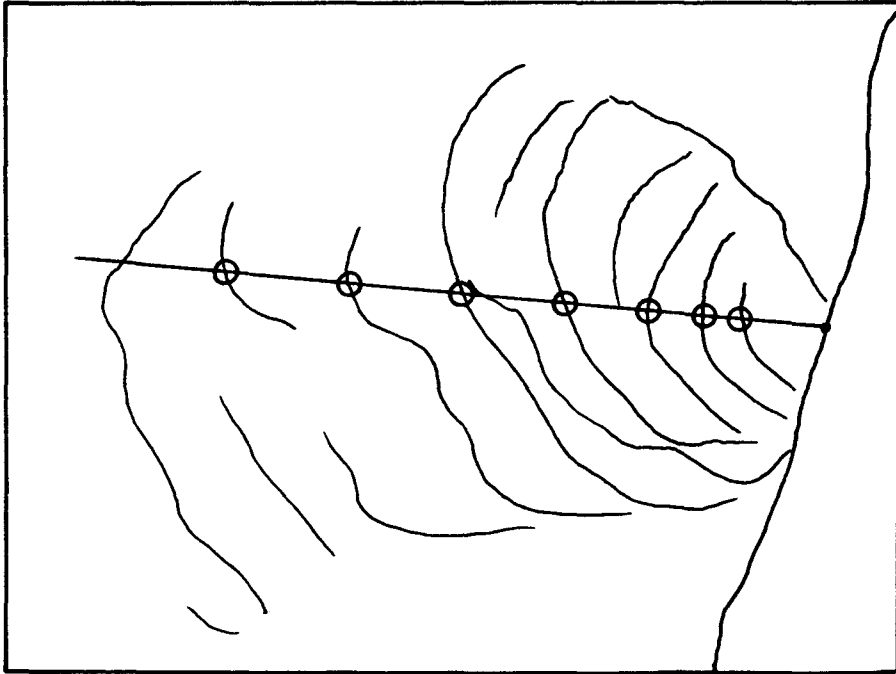


Figure 7.2.1(b) Line sketch of thermal image of a discontinuous radial thermal plume at Sheboygan Edgewater Plant. Photograph was shown in Figure 8a of Green *et al.* (1972).

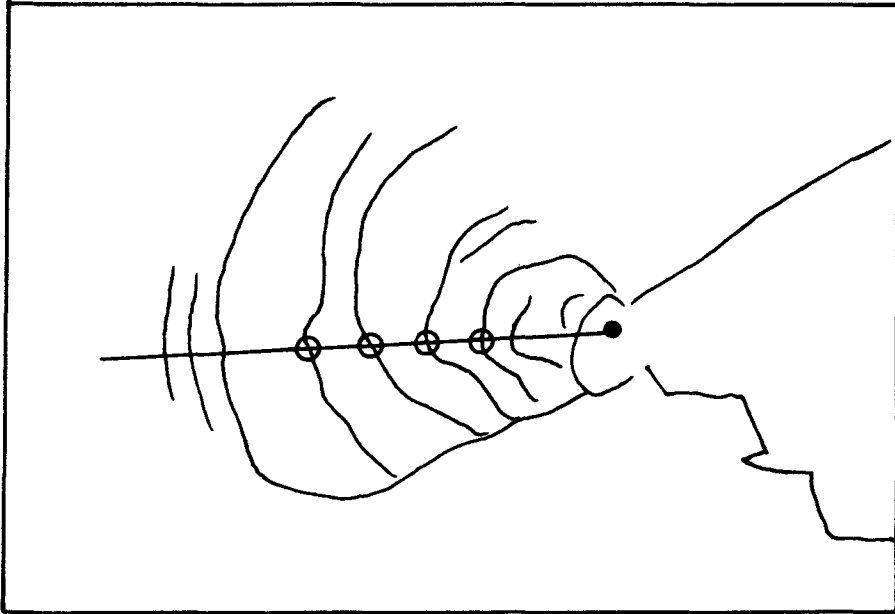


Figure 7.2.1(c) Line sketch of thermal image of a discontinuous radial thermal plume at Port Washington harbor on September 1971. Photograph was shown in Figure 8b of Green *et al.* (1972).

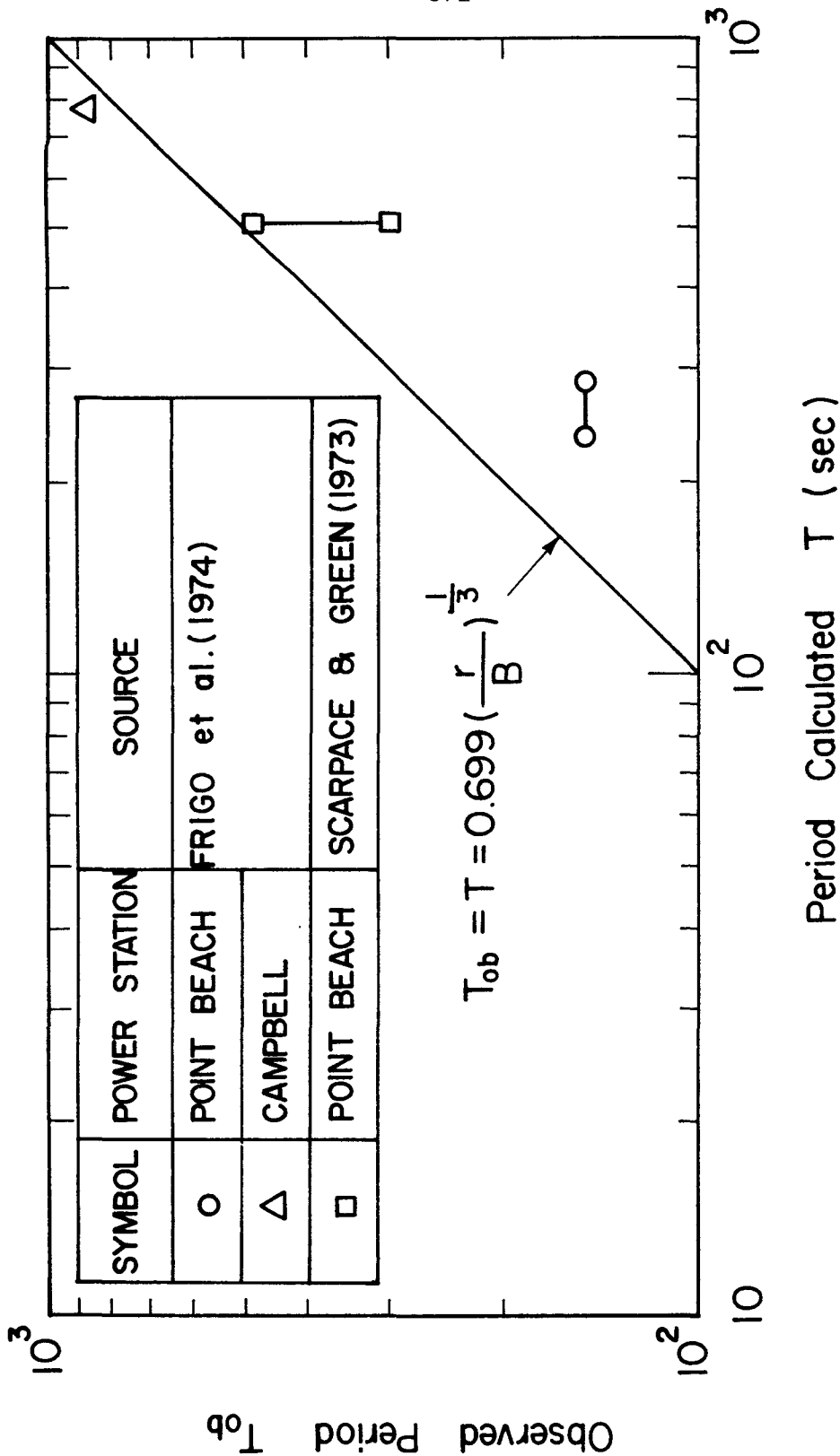


Figure 7.2.2 Comparison of oscillating period of inertial radial surface thermal plume with theoretical value given by Eq. (3.2.87).

thermal plume is also compared fairly well with the predicted value given by Eq. (3.2.87).

The periodic sharp temperature gradients induced by this surging are probably undesirable environmentally. In order to eliminate these oscillations in the plume zone, one would reduce the discharge flow rate Q (simultaneously increasing the relative density difference Δ since the waste heat rate of a power plant is fixed). This would decrease the length scale $R_1 = (Q^5/g\Delta v_s)^{1/8}$ so that a viscous surface thermal plume with an almost uniform thickness of order $(v_s Q/g\Delta)^{1/4}$ would result.

7.3 Barge Disposal of Dredged Spoil and Sludge

Field observations of bottom turbidity clouds produced by the dumping of the noncohesive dredged spoil in the near-shore ocean waters were made by Gordon (1974). After sinking, the negatively buoyant parcel of turbid water impacted the ocean floor, and an outward spreading turbidity current was produced. The turbidity current formed moved as a homogeneous fluid at a speed substantially higher than any ocean current speed. The turbidity current was measured by observing the turbidity and salinity and a sharp distinct interface was observed.

Such a radial turbidity current increases its radius proportionally to $t^{1/2}$, as shown in Figure 7.3.1, and decreases its thickness at a fixed location r_s from the dump site according to

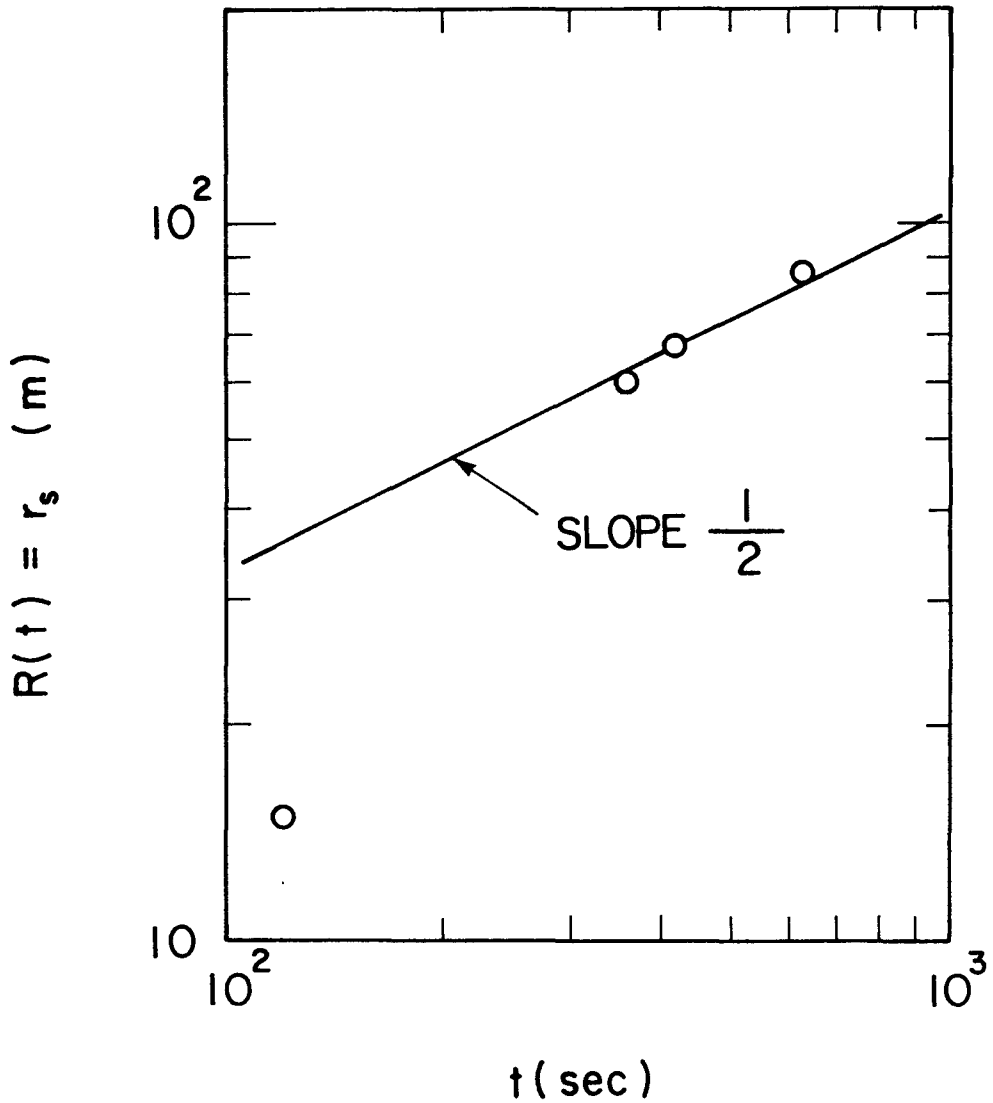


Figure 7.3.1 The time an axially symmetric bottom turbidity current arrived at four fixed locations at a radial distance r_s from the dump site of dredge spoil; data from Figure 2 of Gordon (1974).

$$h(r_s, t) = \frac{r_s^2}{8g\Delta t^2} \quad . \quad (7.3.1)$$

However, there is insufficient information about the relative density difference Δ , to compare those field data measured by Gordon (1974) with Eq. (7.3.1). However, an oblique line with a slope -2 is found to fit the field data, reasonably well, as shown in Figure 7.3.2. This is at least consistent with Eq. (7.3.1).

7.4 Base Surge Flow

According to the report of the U. S. Atomic Energy Commission (1950), at the Bikini shallow ocean atomic bomb test it was observed that as the column of water and spray constituting the plume fell back into the lagoon, there developed a gigantic cloud of radioactive mist on the surface at the base of the column. This mist wave travelled rapidly outward, a short time after the detonation, maintaining an ever-expanding doughnut-shaped form. This dense mist-laden air has the property of flowing almost as if it were a homogeneous fluid. As shown in Figure 7.4.1 its radius increases asymptotically as $t^{1/2}$ at first and then as $t^{1/8}$ as predicted by the long wave theories for bottom current developed in Chapter 3.

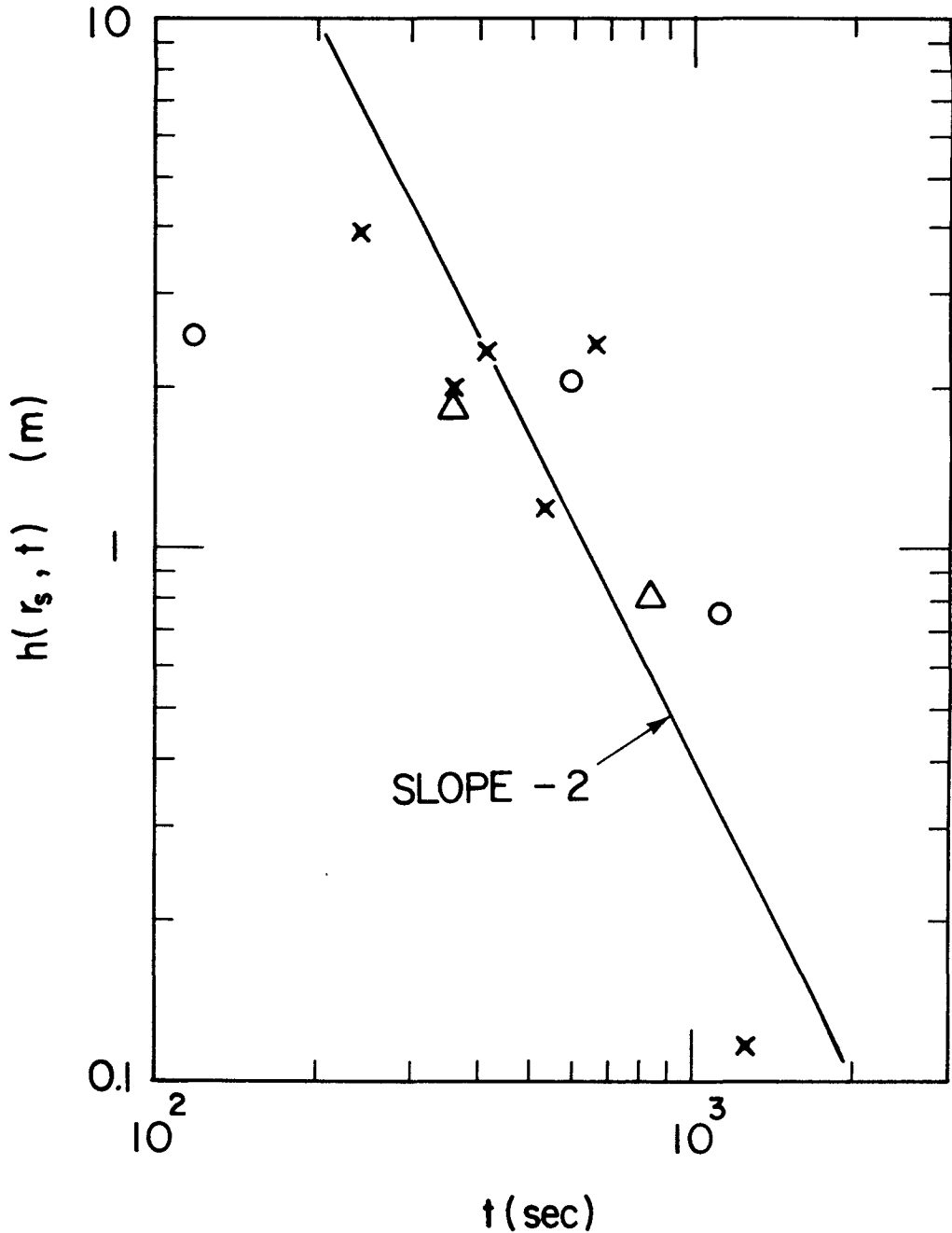


Figure 7.3.2 "Wave-gage type" record of the spreading layer thickness of the bottom turbid cloud from three different dump operations measured at a radial distance $r_s = 30$ meters from the dump site; data from Figure 5 of Gordon (1974).

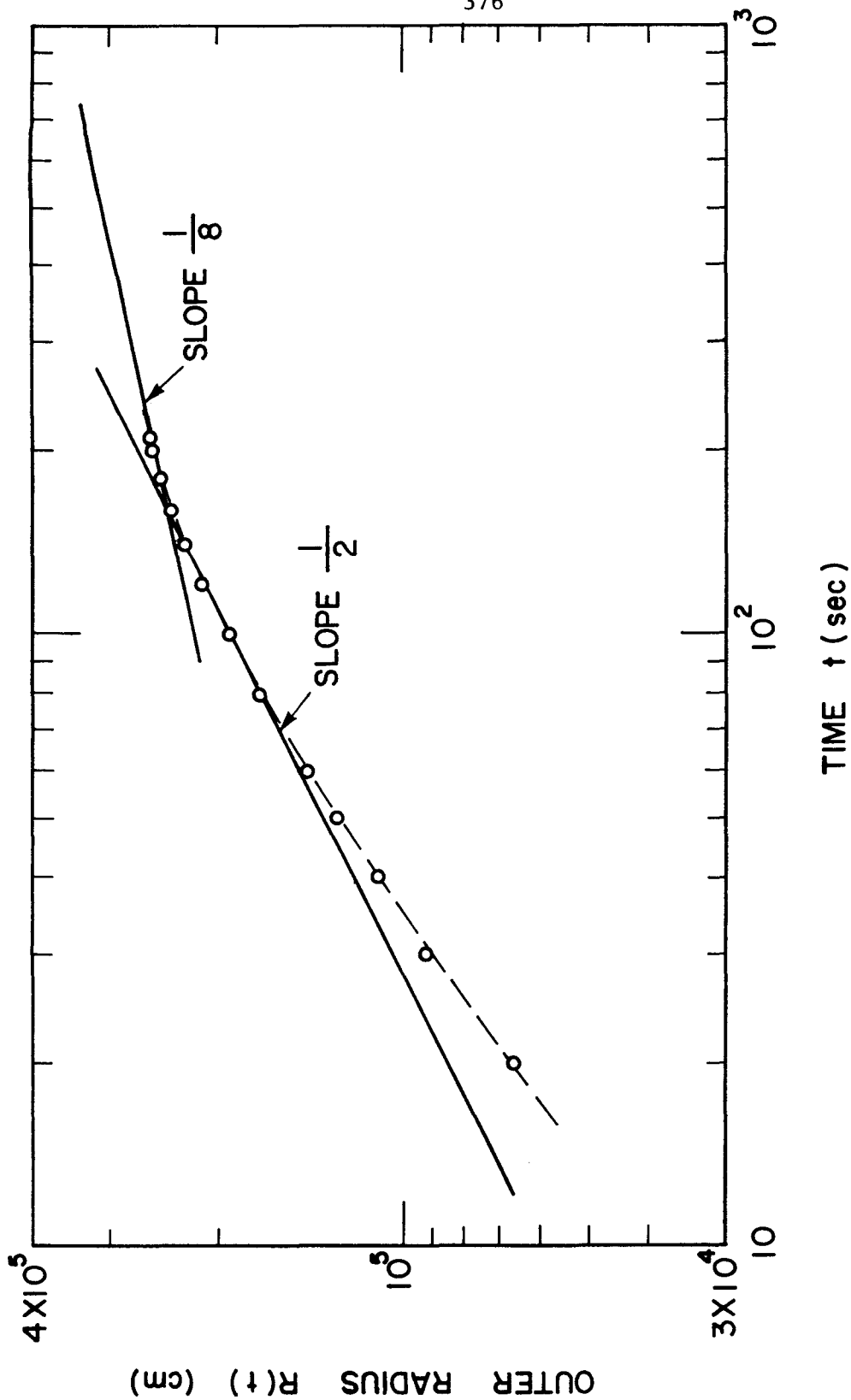


Figure 7.4.1 Propagating mist-laden air forming the base surge following an underwater atomic bomb explosion at Bikini Atoll.

CHAPTER 8

DISCUSSION AND CONCLUSIONS

Gravitational spreading currents are a type of time-dependent, non-linear, non-uniform and unsteady free boundary flow. Given this it is very difficult to have a complete solution which will cover all regimes of flow and include all possible effects from initial and boundary conditions. This investigation is a step forward in this complicated problem which, however, will remain the subject of much further research. The problem has been approached by finding a set of asymptotic solutions appropriate for each region of flow. These were derived by the method of force scale analysis and the development self-similarity solutions for the inertial (shallow-water wave) and viscous long wave equations. Dimensional analysis was used to find the pertinent dimensionless numbers which control the viscous regimes of the spreading currents. The following conclusions may be drawn.

8.1 On the Similarity Solutions for Buoyant Spreading Currents

From the self-similar solutions of inviscid shallow-water waves and the viscous long wave equations, the buoyancy-driven spreading currents grow asymptotically according to

$$R(t) = c_{imn} B_1 \frac{t^{\frac{i+1}{(i+1)(n+1)+2}}}{t^{\frac{m(i+1)+2}{(i+1)(n+1)+2}}} \quad (8.1.1)$$

for the inertial spreading layer with the spreading layer thickness

given by

$$h(r,t) = \left(\frac{R^2}{g\Delta_1} \right)^{\frac{1}{i+1}} H(\xi) \quad (8.1.2)$$

For viscous-buoyancy spreading currents the displacement is given by

$$R(t) = b_{imn} \left(\frac{g\Delta_1 Q^{i+3}}{v_s} \right)^{\frac{1}{(n+1)(i+3)+2}} t^{\frac{m(i+3)+1}{(n+1)(i+3)+2}} \quad (8.1.3)$$

with the thickness given by

$$h(r,t) = \left(\frac{v_s R R^2}{g\Delta_1} \right)^{\frac{1}{i+3}} H(\xi) \quad (8.1.4)$$

in which the kinematic buoyancy flux in general form B_i is equal to $(g\Delta_1)^{\frac{1}{i+3}} Q$.

In the above:

$i = 0$ denotes a uniform density environment

$i = 1$ denotes a linearly density-stratified environment

$\Delta_0 = \Delta$ the density anomaly of the source

$\Delta_1 = \epsilon = -\frac{1}{\rho_s} \frac{d\rho_a(z)}{dz}$, density gradient of stratified environment

$n = 0$ denotes a plane current

$n = 1$ denotes a radial current

m denotes the source condition with

$m = 0$ an finite volume source in which Q is replaced
by V the volume of the source

$m = 1$ a continuous source with flow rate Q

Equations (8.1.1) and (8.1.3) for each case of i , n , and m are listed in Table 8.1.

Table 8.1 Summary of asymptotic formulae of frontal trajectory functions derived by inertial (shallow-water wave) and viscous long wave theories.

Item case		Source Condition	Inertial-Buoyancy Regime	Viscous-Buoyancy Regime
i	n			
Homogeneous Environment i = 0	Plane n = 0	Instantaneous m = 0	$R(t) = 1.890 (g\Delta V)^{1/3} t^{2/3}$	$R(t) = 1.133 \left(\frac{g\Delta V^3}{v}\right)^{1/5} t^{1/5}$
	Radial n = 1	Continuous m = 1	$R(t) = 1.260 (g\Delta Q)^{1/3} t$	$R(t) = 0.804 \left(\frac{g\Delta Q^3}{v}\right)^{1/5} t^{4/5}$
	Plane n = 0	Instantaneous m = 0	$R(t) = 1.502 (g\Delta V)^{1/4} t^{1/2}$	$R(t) = 0.779 \left(\frac{g\Delta V^3}{v}\right)^{1/8} t^{1/8}$
	Radial n = 1	Continuous m = 1	$R(t) = 1.309 (g\Delta Q)^{1/4} t^{3/4}$	$R(t) = 0.63 \left(\frac{g\Delta Q^3}{v}\right)^{1/8} t^{1/2}$
Linearly Density-Stratified Environment i = 1	Plane n = 0	Instantaneous m = 0	$R(t) = 1.414 (NV)^{1/2} t^{1/2}$	$R(t) = 0.689 \left(\frac{N^2 V^4}{v}\right)^{1/6} t^{1/6}$
	Radial n = 1	Continuous m = 1	$R(t) = 0.707 (NQ)^{1/2} t$	$R(t) = 0.499 \left(\frac{N^2 Q^4}{v}\right)^{1/6} t^{5/6}$
	Plane n = 0	Instantaneous m = 0	$R(t) = 1.127 (NV)^{1/3} t^{1/3}$	$R(t) = 0.552 \left(\frac{N^2 V^4}{v}\right)^{1/10} t^{1/10}$
	Radial n = 1	Continuous m = 1	$R(t) = 0.802 (NQ)^{1/3} t^{2/3}$	$R(t) = 0.45 \left(\frac{N^2 Q^4}{v}\right)^{1/10} t^{1/2}$

The spreading layer thickness scale, $\tau(t)$, can be derived from Table 8.1. For the inertial-buoyancy currents,

$$\tau(t) = \left(\frac{\overset{\circ}{R}^2}{g\Delta_i} \right)^{\frac{1}{i+1}} \quad (8.1.5)$$

and for the viscous-buoyancy currents,

$$\tau(t) = \left(\frac{\overset{\circ}{v}_s \overset{\circ}{R} R}{g\Delta_i} \right)^{\frac{1}{i+3}} . \quad (8.1.6)$$

Similarity profiles $H(\xi)$ for each case of i , m and n in Equations (8.1.2) and (8.1.4) can be found in Sections 3.2 and 3.3.

8.2 On the Initial Stage of Flows

Before spreading currents develop fully into the case discussed in the previous section, there is a short initial stage which is governed by the initial conditions.

For a finite volume release an initial spreading current is found to advance with a self-similar mean velocity distribution given by

$$\frac{\overset{\circ}{u}(r,t)}{\overset{\circ}{R}(t)} = \phi(\xi) = \xi \quad , \quad (8.2.1)$$

and a self-similar thickness profile given by

$$\frac{h(r,t)}{h_1} \left(\frac{\overset{\circ}{R}(t)}{R_0} \right)^{n+1} = H(\xi) = (1 - \xi^2)^{\frac{1}{i+1}} \quad , \quad (8.2.2)$$

where the initial thickness scale h_1 is developed from the initial shape

(see Table 3.2.1 for a homogeneous environment ($i=0$) and Table 3.2.2 for currents in a linearly density-stratified environment ($i=1$)).

In this initial stage the trajectory function of frontal displacement is generally described by

$$\tau = \left(\frac{i+1}{2}\right) (n+1)^{1/2} \int_1^n \frac{d\eta}{\left[1 - \eta^{-(i+1)(n+1)}\right]^{1/2}} \quad (8.2.3)$$

in which the dimensionless time $\tau = t \sqrt{g\Delta_i h_1^{i+1}/R_0}$ and $\eta = R(t)/R_0$.

For a continuous buoyant discharge there is initially a starting jet zone followed by a starting plume flow. The starting jet front grows according to

$$R(t) \sim M \frac{1}{n+3} \frac{2}{n+3} t \quad (8.2.4)$$

The coefficient in above equation (8.2.4) is found to depend mainly on the discharge Froude number. For the limiting case where the Froude number is very large, the coefficient appears to be asymptotic to a value of about 1 for a radial surface buoyant jet with small aspect ratio discharging into a homogeneous environment ($i=0$). The coefficient is about 1.50 for a plane slot jet discharging into a linearly density-stratified environment ($i=1$) at a neutrally buoyant level.

8.3 On the Memory of Spreading Currents

The asymptotic similarity solutions are derived on the basis of assuming that the fluid is either perfectly inviscid with no friction or viscous with laminar friction. A transition length scale is established, one limit of which gives the inviscid solution, another

limit gives the viscous solution. However, it is clear that the coefficients in these limiting solutions are, to some degree, dependent on certain initial dimensionless numbers such as the Froude number, Reynolds number, and other geometrical ratios such as the relative depth, and aspect ratio of the discharge. The assumption on the asymptotic solutions is that these parameters only enter in a secondary role in certain regimes of flow in which one effect alone is dominant, as for example, the buoyancy flux in the inertial-buoyancy regime. It is clear that some of the effect of the initial discharge parameters is to drift the time origin, or geometric origin of the flow. It is not always clear whether the variation between experiments and theory is to be accounted for with a time origin shift or through functional dependence of the coefficients on the initial dimensionless parameters of the discharge. In other words, a memory for the initial conditions appears to exist although not at a primary level of flow influence.

8.4 On the Thickness Profile of Spreading Currents

The thickness profile of spreading currents varies significantly from one type of flow situation to another. In general, the transitions in thickness from one regime to another are smooth, but the asymptotic solutions developed in this investigation, of course, do not give such smooth transitions. However, it is clear that it is simply not appropriate to assume an arbitrary distribution for the thickness of a spreading layer, as has been frequently done in previous investigations. The choice of the thickness profile is not free as has been often assumed. The profile thickness appears to be strongly

influenced by initial conditions, especially momentum-induced entrainment, which results in significant increases in spreading layer thickness. Furthermore, the influence of interfacial friction between the spreading layer and the fluid beneath is controlled to a large degree by the momentum flux of the discharge. With a strong relative buoyancy flux and weaker initial momentum flux the friction is clearly viscous as the consequence of a laminar shear layer production. This appears to be given by the transition length scale R_1 (see Tables 3.1 and 3.5).

8.5 On Dimensional Analysis and Spreading Currents

Dimensional analysis is an extremely powerful tool for the development of asymptotic solutions where the major effects of discharge parameters can be reduced to a primary variable such as the kinematic buoyancy flux. The development of characteristic length and time scales based on the relevant parameters appears to give an excellent guide to the appropriateness of given solutions for specific regimes of flow.

APPENDIX A

DERIVATION OF LONGITUDINAL INTERNAL SHALLOW-WATER WAVE EQUATIONS

Two sets of shallow water wave equations are derived here for the inertial regime of surface and subsurface density spreading flows.

A.0 Basic Equations and Assumptions

When surface and interfacial tension forces are neglected, the continuity and the momentum equations for plane or axisymmetric, unsteady, inviscid, and incompressible flow in an infinite depth of fluid are

$$\frac{1}{r^n} \frac{\partial(r^n u)}{\partial r} + \frac{\partial w}{\partial z} = 0 \quad (\text{A.0.1})$$

$$\frac{\partial u}{\partial t} + u \frac{\partial u}{\partial r} + w \frac{\partial u}{\partial z} = - \frac{1}{\rho_s} \frac{\partial p}{\partial r} \quad (\text{A.0.2})$$

$$\frac{\partial w}{\partial t} + u \frac{\partial w}{\partial r} + w \frac{\partial w}{\partial z} = - \frac{1}{\rho_s} \frac{\partial p}{\partial z} \pm g \quad (\text{A.0.3})$$

where u and w are horizontal and vertical velocities in the r and z directions as defined respectively in Figures 3.2.1(a), (b), and (c). The sign before gravitational term g in Eq. (A.0.3) depends on the direction of z chosen; positive when downwards and negative when upwards, ρ_s is the mass density of the spreading

plume and $p = p(r, z, t)$ is the pressure at point (r, z) when time is equal to t . The complete solutions of these three nonlinear equations seem intractable and some assumptions are necessary to simplify the problem. Consider the case when the horizontal scale of a surface spreading layer is very large in comparison with the vertical scale. Then the vertical acceleration is a negligible fraction of the horizontal acceleration so that

$$\frac{Dw}{Dt} = \frac{\partial w}{\partial t} + u \frac{\partial w}{\partial r} + w \frac{\partial w}{\partial z} \approx 0 \quad (\text{A.0.4})$$

and the unsteady pressure distribution is hydrostatic

$$-\frac{1}{\rho_s} \frac{dp}{dz} \pm g = 0 \quad . \quad (\text{A.0.5})$$

Thus the equation of motion is simplified to

$$\frac{\partial u}{\partial t} + u \frac{\partial u}{\partial r} + \frac{1}{\rho_s} \frac{\partial p}{\partial r} = 0 \quad . \quad (\text{A.0.6})$$

Assume that there is no diffusion and no mixing through the interface and no evaporation and no breaking at the free surface, then a particle once on the interfacial surface will remain there, i.e. the density on a particle path is constant.

A.1 Free Surface Density Spreading Flows

In this case the two kinematic boundary conditions on the interface and the free surface of a spreading plume are

$$w(r, h, t) = \frac{\partial h(r, t)}{\partial t} + u(r, h, t) \frac{\partial h(r, t)}{\partial r} \quad (\text{A.1.1})$$

$$w(r, -\delta, t) = -\frac{\partial \delta(r, t)}{\partial t} - u(r, -\delta, t) \frac{\partial \delta(r, t)}{\partial r} \quad (\text{A.1.2})$$

and hydrostatic pressure distribution is

$$p(r, z, t) = \rho_s g \int_{-\delta(r, t)}^z dz = \rho_s g [z + \delta(r, t)] \quad (\text{A.1.3})$$

where the superelevation $\delta(r, t)$ above free surface can be derived as a function of the spreading layer thickness $h(r, t)$ below the free surface from the hydrostatic equilibrium:

$$\rho_a g h = \rho_s g (h + \delta) \quad (\text{A.1.4})$$

i.e.

$$\delta(r, t) = \frac{\rho_a - \rho_s}{\rho_s} h(r, t) = \Delta h(r, t) \quad . \quad (\text{A.1.5})$$

Integrating the continuity Eq. (A.0.1) and the simplified momentum Eq. (A.0.6) from $z = -\delta(r, t)$ to $z = h(r, t)$ one finds

$$\int_{-\delta}^h \frac{1}{r^n} \frac{\partial(r^n u)}{\partial r} dz + \int_{-\delta}^h \frac{\partial w}{\partial z} dz = 0 \quad , \quad (\text{A.1.6})$$

$$\int_{-\delta}^h \frac{\partial u}{\partial t} dz + \int_{-\delta}^h \frac{\partial u}{\partial r} dz + \frac{1}{\rho_s} \int_{-\delta}^h \frac{\partial p}{\partial r} dz = 0 \quad . \quad (\text{A.1.7})$$

This provides the use of the two kinematic boundary conditions (A.1.1) and (A.1.2) and by the aid of Leibniz' rule

$$\int_{-\delta}^h \frac{1}{r^n} \frac{\partial(r^n u)}{\partial r} dz = \frac{1}{r^n} \frac{\partial}{\partial r} \int_{-\delta}^h r^n u dz - u(r, h, t) \frac{\partial h}{\partial r} - u(r, -\delta, t) \frac{\partial \delta}{\partial r} \quad (\text{A.1.8})$$

$$\int_{-\delta}^h \frac{\partial u}{\partial t} dz = \frac{\partial}{\partial t} \int_{-\delta}^h u dz - u(r, h, t) \frac{\partial h}{\partial t} - u(r, -\delta, t) \frac{\partial \delta}{\partial t} \quad (\text{A.1.9})$$

$$\int_{-\delta}^h u \frac{\partial u}{\partial r} dz = \frac{1}{2} \frac{\partial}{\partial r} \int_{-\delta}^h u^2 dz - \frac{1}{2} u^2(r, h, t) \frac{\partial h}{\partial r} - \frac{1}{2} u^2(r, -\delta, t) \frac{\partial \delta}{\partial r} \quad (\text{A.1.10})$$

$$\frac{1}{\rho_s} \int_{-\delta}^h \frac{\partial p}{\partial r} dz = g(h + \delta) \frac{\partial \delta}{\partial r} \quad . \quad (\text{A.1.11})$$

The integral continuity equation becomes

$$\frac{\partial}{\partial t} (h + \delta) + \frac{1}{r^n} \frac{\partial}{\partial r} \int_{-\delta}^h (r^n u) dz = 0 \quad (\text{A.1.12})$$

and the integral momentum equation becomes

$$\begin{aligned} & \frac{\partial}{\partial t} \int_{-\delta}^h u dz + \frac{1}{2} \frac{\partial}{\partial r} \int_{-\delta}^h u^2 dz + g(h + \delta) \frac{\partial \delta}{\partial r} \\ & = u(r, h, t) \frac{\partial h}{\partial t} + u(r, -\delta, t) \frac{\partial \delta}{\partial t} + \frac{1}{2} u^2(r, h, t) \frac{\partial h}{\partial r} + \frac{1}{2} u^2(r, -\delta, t) \frac{\partial \delta}{\partial r} \end{aligned} \quad (\text{A.1.13})$$

Since the spreading layer is very thin, a uniform horizontal velocity distribution is a good approximation, i.e.

$$u(r, z, t) \approx u(r, t) \quad . \quad (\text{A.1.14})$$

Thus, Eqs. (A.1.12) and (A.1.13) are reduced to a set of non-linear shallow water wave equations in explicit form,

$$\frac{\partial h}{\partial t} + \frac{1}{r^n} \frac{\partial}{\partial r} (r^n u h) = 0 \quad (\text{A.1.15})$$

and

$$\frac{\partial u}{\partial t} + u \frac{\partial u}{\partial r} + g \Delta \frac{\partial h}{\partial r} = 0 \quad (\text{A.1.16})$$

which were used earlier by Hoult (1972) to solve the inertial oil slick spreading problem.

A.2 Bottom Surface Density Spreading Flows

For the case of bottom surface spreading layer as shown in Figure 3.3.2 there is only one kinematic boundary condition at the interface, i.e., Eq. (A.1.1). If the bottom floor is perfectly horizontal and impervious, then

$$H_a(r) = H_a \quad , \quad (A.2.1)$$

$$w(r,0,t) \equiv 0 \quad . \quad (A.2.2)$$

The hydrostatic pressure distribution is then

$$\frac{dp}{dz} = -\rho_s g \quad (A.2.3)$$

or

$$p(r,z,t) = \rho_a g [H_a - h(r,t)] + \rho_s g [h(r,t) - z] \quad (A.2.4)$$

Integrate continuity Eq. (A.0.1) and momentum Eq. (A.0.6) from $z = 0$ (rather than from $z = -\delta(r,t)$ in the previous case) to $z = h(r,t)$, i.e.,

$$\int_0^h \frac{1}{r^n} \frac{\partial(r^n u)}{\partial r} dz + \int_0^{h(r,t)} \frac{\partial w}{\partial z} dz = 0 \quad (A.2.5)$$

and

$$\int_0^h \frac{\partial u}{\partial t} dz + \int_0^h u \frac{\partial u}{\partial r} dz + \frac{1}{\rho_s} \int_0^h \frac{\partial p}{\partial r} dz = 0 \quad . \quad (\text{A.2.6})$$

With one kinematic boundary condition (A.1.1) at the interface and the impervious condition (A.2.2), and also by the aid of Leibniz' rule, we have

$$\int_0^h \frac{1}{r^n} \frac{\partial(r^n u)}{\partial r} dz = \frac{1}{r^n} \frac{\partial}{\partial r} \int_0^h r^n u dz - u(r, h, t) \frac{\partial h}{\partial r} \quad (\text{A.2.7})$$

$$\int_0^h \frac{\partial u}{\partial t} dz = \frac{\partial}{\partial t} \int_0^h u dz - u(r, h, t) \frac{\partial h}{\partial t} \quad (\text{A.2.8})$$

$$\int_0^h u \frac{\partial u}{\partial r} dz = \frac{1}{2} \frac{\partial}{\partial r} \int_0^h u^2 dz - \frac{1}{2} u^2(r, h, t) \frac{\partial h}{\partial r} \quad (\text{A.2.9})$$

$$\frac{1}{\rho_s} \int_0^h \frac{\partial p}{\partial r} dz = \left(1 - \frac{\rho_a}{\rho_s}\right) gh \frac{\partial h}{\partial r} \quad . \quad (\text{A.2.10})$$

The integral continuity equation becomes

$$\frac{\partial h}{\partial t} + \frac{1}{r^n} \frac{\partial}{\partial r} \int_0^h (r^n u) dz = 0 \quad (\text{A.2.11})$$

and the integral momentum equation

$$\begin{aligned} \frac{\partial}{\partial t} \int_0^h u dz + \frac{1}{2} \frac{\partial}{\partial r} \int_0^h u^2 dz + g \left(1 - \frac{\rho_a}{\rho_s} \right) h \frac{\partial h}{\partial r} \\ = u(r, h, t) \frac{\partial h}{\partial t} + \frac{1}{2} u^2(r, h, t) \frac{\partial h}{\partial r} \quad \cdot \quad (A.2.12) \end{aligned}$$

If a uniform horizontal velocity (A.1.13) were also assumed, the same set of shallow water wave equations (A.1.14) and (A.1.15) is also derived but with $\frac{\rho_s - \rho_a}{\rho_s}$ instead of $\frac{\rho_a - \rho_s}{\rho_s}$ for Δ . The same equations were also derived by Penney and Thornhill (1952) for the squatting flow of a liquid column with a density comparable to the ambient medium. Freeman (1948) also derived similar plane shallow water wave equations for atmospheric cold front propagation, except $\Delta = \frac{\theta_s - \theta_a}{\theta_s}$, where θ_a and θ_s are the potential temperatures of the ambient warm air and the spreading cold air respectively.

A.3 Submerged Density Spreading Flows

Assume that the submerged spreading interflows are radially symmetric. Let the origin of the chosen coordinate system be at the point of symmetry, as shown in Figure A.3.1. The linear ambient density distribution can be expressed as

$$\rho_a(z) = \rho_s(1 - \epsilon z) \quad (\text{A.3.1})$$

where $\epsilon = \left| \frac{1}{\rho_s} \frac{d\rho_a}{dz} \right|$. Based on the shallow-water wave approximation, the two equations of continuity and of motion become

$$\frac{1}{r^n} \frac{\partial(r^n u)}{\partial r} + \frac{\partial w}{\partial z} = 0 \quad (\text{A.3.2})$$

and

$$\frac{\partial u}{\partial t} + u \frac{\partial u}{\partial r} + \frac{1}{\rho_s} \frac{\partial p}{\partial r} = 0 \quad (\text{A.3.3})$$

The hydrostatic pressure assumption,

$$\frac{\partial p(r, z, t)}{\partial z} = -\rho_s g \quad (\text{A.3.4})$$

gives

$$\begin{aligned} p(r, z, t) &= \int_z^h \rho_s g dz + \int_h^{H_s} \rho_a(z) g dz \\ &= \rho_s g(h - z) + \rho_s g(H_s - \frac{1}{2} \epsilon H_s^2 - h + \frac{1}{2} \epsilon h^2) \quad (\text{A.3.5}) \end{aligned}$$

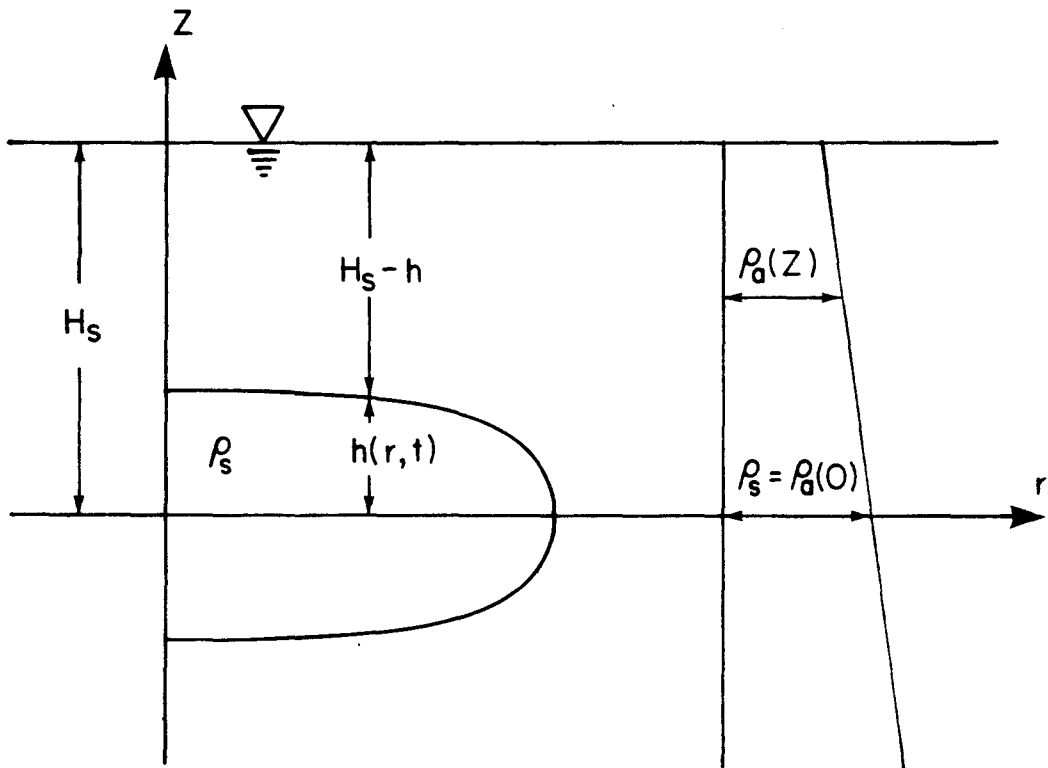


Figure A.3.1 Coordinate system of submerged density spread flows.

The horizontal pressure gradient can be derived directly by the differentiation of Eq. (A.3.5)

$$\frac{\partial p(r, z, t)}{\partial r} = \rho_s g \epsilon h \frac{\partial h}{\partial r} \quad , \quad (\text{A.3.6})$$

in which $h = h(r, t)$ is the half-thickness of the interflowing layer.

Integrating Eqs. (A.3.2) and (A.3.3) from $z = -h(r, t)$ to $z = +h(r, t)$, i.e.

$$\int_{-h}^h \frac{1}{r^n} \frac{(r^n u)}{r} dz + \int_{-h}^h \frac{\partial w}{\partial z} dz = 0 \quad , \quad (\text{A.3.7})$$

$$\int_{-h}^h \frac{\partial u}{\partial t} dz + \int_{-h}^h u \frac{\partial u}{\partial r} dz + \frac{1}{\rho_s} \int_{-h}^h \frac{\partial p}{\partial r} dz = 0 \quad . \quad (\text{A.3.8})$$

Then, with the aid of relationships from Leibniz' rule:

$$\begin{aligned} \int_{-h}^h \frac{1}{r^n} \frac{\partial (r^n u)}{\partial r} dz &= \frac{1}{r^n} \frac{\partial}{\partial r} \int_{-h}^h (r^n u) dz - u(r, h, t) \frac{\partial h}{\partial r} \\ &\quad - u(r, -h, t) \frac{\partial h}{\partial r} \end{aligned} \quad (\text{A.3.9})$$

$$\int_{-h}^h \frac{\partial u}{\partial t} dz = \frac{\partial}{\partial t} \int_{-h}^h u dz - u(r, h, t) \frac{\partial h}{\partial t} - u(r, -h, t) \frac{\partial h}{\partial t} \quad , \quad (\text{A.3.10})$$

$$\int_{-h}^h u \frac{\partial u}{\partial r} dz = \frac{1}{2} \left\{ \frac{\partial}{\partial r} \int_{-h}^h u^2 dz - u^2(r, h, t) \frac{\partial h}{\partial r} - u^2(r, -h, t) \frac{\partial h}{\partial r} \right\} \quad . \quad (\text{A.3.11})$$

The hydrostatic pressure distribution gives

$$\int_{-h}^h \frac{\partial p}{\partial r} dz = 2\rho_s g\epsilon h^2 \frac{\partial h}{\partial r} \quad (\text{A.3.12})$$

and the kinematic boundary conditions at interface, namely,

$$w(r, \pm h, t) = \pm \frac{\partial h}{\partial t} \pm u(r, \pm h, t) \frac{\partial h}{\partial r} \quad (\text{A.3.13})$$

gives

$$2 \frac{\partial h}{\partial t} + \frac{1}{r^n} \frac{\partial}{\partial r} \int_{-h}^h (r^n u) dz = 0 \quad (\text{A.3.14})$$

and

$$\begin{aligned} & \frac{\partial}{\partial t} \int_{-h}^h u dz - u(r, h, t) \frac{\partial h}{\partial t} - u(r, -h, t) \frac{\partial h}{\partial t} \\ & + \frac{1}{2} \frac{\partial}{\partial r} \int_{-h}^h u^2 dz - \frac{1}{2} u^2(r, h, t) \frac{\partial h}{\partial r} - \frac{1}{2} u^2(r, -h, t) \frac{\partial h}{\partial r} \\ & + 2g\epsilon h^2 \frac{\partial h}{\partial r} = 0 \quad . \quad (\text{A.3.15}) \end{aligned}$$

Again, assuming that the horizontal velocity is uniformly distributed,

$$u(r, z, t) = u(r, t) \quad , \quad (\text{A.3.16})$$

gives the continuity equation

$$\frac{\partial h}{\partial t} + \frac{1}{r^n} \frac{\partial (r^n u h)}{\partial r} = 0 \quad (\text{A.3.17})$$

and momentum equation

$$\frac{\partial u}{\partial t} + u \frac{\partial u}{\partial r} + g \epsilon h \frac{\partial h}{\partial r} = 0 \quad . \quad (\text{A.3.18})$$

Both shallow-water wave equations (A.3.17) and (A.3.18) were used earlier by Mei (1969) to solve the initial collapse stage of a mixed region spreading in a linearly density-stratified environment.

APPENDIX B

DERIVATION OF SIMILARITY SOLUTIONS FOR INERTIAL-BUOYANCY SPREAD

Two sets of similarity solutions: (3.2.16) and (3.2.32) and (3.2.16) and (3.2.33), for the inertial-buoyancy regime of both surface density spreading flow and subsurface density spreading flow will be derived here. The derivation technique was initiated by Taylor (1950) to determine the spherical shock wave propagation produced by an intense explosion. A similar technique was also used by Lin (1954), Latter (1955) and Rouse (1959). An overall review of these self-similar processes in gasdynamics was given in Chapter VII of the textbook by Zel'dovich and Raizer (1967). A mathematical discussion on the general type of self-similar solution was presented in a review article by Barenblatt and Zel'dovich (1972). Other application to gas flows were also given by Sakurai (1965) and Korobeinikov (1971).

B.1 Surface Density Spreading Flows

In Appendix A two shallow-water wave equations

$$\frac{\partial h}{\partial t} + \frac{1}{r^n} \frac{\partial (r^n u h)}{\partial r} = 0 \quad (\text{B.1.1})$$

and

$$\frac{\partial u}{\partial t} + u \frac{\partial u}{\partial r} + g \Delta \frac{\partial h}{\partial r} = 0 \quad , \quad (\text{B.1.2})$$

were derived to describe free surface density spreading and an underflowing density spread. We now assume that the two unknowns, u and h , of this unsteady and non-uniform flow have the following form

$$u(r,t) = R^k(t)\phi_1(\xi) \quad (\text{B.1.3})$$

$$h(r,t) = R^\ell(t)H_1(\xi) \quad , \quad (\text{B.1.4})$$

where the dimensionless variable ξ is defined as $r/R(t)$, and $R(t)$ is the frontal position at time t ; k and ℓ are two unknown rational numbers.

Substituting the above two relations into the shallow-water wave equations gives

$$R^{-k} \overset{\circ}{R} (\ell H_1 - \xi H_1') + (\phi_1' H_1 + \phi_1 H_1' + \frac{n\phi_1 H_1}{\xi}) = 0 \quad (\text{B.1.5})$$

and

$$R^{-k} \overset{\circ}{R} (k\phi_1 - \xi\phi_1') + \phi_1\phi_1' + g\Delta R^{\ell-2k} H_1' = 0 \quad (\text{B.1.6})$$

In order to homogenize both Eqs. (B.1.5) and (B.1.6) into a dimensionless form, one has to set

$$R^{-k} \overset{\circ}{R} = A \quad (\text{B.1.7})$$

$$\ell - 2k = 0 \quad (\text{B.1.8})$$

and assume

$$\phi_1(\xi) = A\phi(\xi) \quad , \quad (\text{B.1.9})$$

$$H_1(\xi) = \frac{A^2}{g\Delta} H(\xi) \quad , \quad (\text{B.1.10})$$

in which A is a dimensional constant. Thus, from Eqs. (B.1.3), (B.1.4), (B.1.7), (B.1.8), (B.1.9) and (B.1.10), the similarity solutions are derived as having the following forms

$$u(r,t) = \overset{\circ}{R}(t)\phi(\xi) \quad (\text{B.1.11})$$

and

$$h(r,t) = \frac{\overset{\circ}{R}^2(t)}{g\Delta} H(\xi) \quad , \quad (\text{B.1.12})$$

and the ordinary differential equations (B.1.5) and (B.1.6) are reduced to

$$(\phi - \xi) H' + (\phi' + \ell + \frac{n\phi}{\xi})H = 0 \quad (\text{B.1.13})$$

$$(\phi - \xi) \phi' + k\phi + H' = 0 \quad . \quad (\text{B.1.14})$$

B.2 Submerged Density Spreading Flows

The two shallow-water wave equations in this case are

$$\frac{\partial h}{\partial t} + \frac{1}{r^n} \frac{\partial(r^n u h)}{\partial r} = 0 \quad (\text{B.2.1})$$

and

$$\frac{\partial u}{\partial t} + u \frac{\partial u}{\partial r} + N^2 h \frac{\partial h}{\partial r} = 0 \quad , \quad (\text{B.2.2})$$

in which N is the Brunt-Väisälä frequency for the linearly density-stratified ambient fluid. Assume now that the two unknowns, u and h , of this unsteady and non-uniform flow have the following form

$$u(r, t) = R^k(t) \phi_1(\xi) \quad (\text{B.2.3})$$

$$h(r, t) = R^\ell(t) H_1(\xi) \quad , \quad (\text{B.2.4})$$

where $\xi = r/R(t)$, $R(t)$ is the submerged interflowing front position at time t .

Substituting these assumed forms into two shallow-water wave Eqs. (B.2.1) and (B.2.2), gives

$$R^{-k} \ddot{R} (\ell H_1 - \xi H_1') + (\phi_1' H_1 + \phi_1 H_1' + \frac{n \phi_1 H_1}{\xi}) = 0 \quad (\text{B.2.5})$$

$$R^{-k} \ddot{R} (k \phi_1 - \xi \phi_1') + \phi_1 \phi_1' + R^{2(\ell-k)} N^2 H_1 H_1' = 0 \quad (\text{B.2.6})$$

To homogenize both Eqs. (B.2.5) and (B.2.6) in a dimensionless form, one has to set

$$R^{-k} \ddot{R} = A \quad (\text{B.2.7})$$

$$\ell - k = 0 \quad (\text{B.2.8})$$

and assume that

$$\phi_1(\xi) = A\phi(\xi) \quad (\text{B.2.9})$$

$$H_1(\xi) = \frac{A}{N} H(\xi) \quad , \quad (\text{B.2.10})$$

in which A is a dimensional constant. Thus, from Eqs. (B.2.3), (B.2.4), (B.2.7), (B.2.8), (B.2.9), and (B.2.10) the similarity solutions have the following form

$$u(r,t) = \dot{R}(t) \phi(\xi) \quad (\text{B.2.11})$$

$$h(r,t) = \frac{\dot{R}(t)}{N} H(\xi) \quad , \quad (\text{B.2.12})$$

and the ordinary differential Eqs. (B.2.5) and (B.2.6) are reduced to

$$(\phi - \xi) H' + \left(\phi' + \ell + \frac{n\phi}{\xi}\right) H = 0 \quad (\text{B.2.13})$$

$$(\phi - \xi) \phi' + k\phi + HH' = 0 \quad (\text{B.2.14})$$

APPENDIX C

DERIVATION OF BOUNDARY CONDITIONS AT THE FRONT

C.0 Introduction

To solve the two similarity forms of solution for the shallow-water wave equations, as derived in Appendix B, it is necessary to find appropriate boundary conditions. For surface and bottom spreading we have

$$\phi(\xi) = \frac{u(r,t)}{R(t)} \quad (\text{C.0.1})$$

and

$$H(\xi) = \frac{g\Delta h(r,t)}{R^2(t)} \quad (\text{C.0.2})$$

For an interflowing layer we have

$$\phi(\xi) = \frac{u(r,t)}{R(t)} \quad (\text{C.0.3})$$

$$H(\xi) = \frac{Nh(r,t)}{R(t)} \quad (\text{C.0.4})$$

These functions therefore give the ratio of particle velocity at any location to the frontal propagation velocity, and express the local Richardson number of the spreading layer in terms of the frontal velocity.

Fay (1971) (see Liang, 1971) used von Kármán's solution,

$$H(0) = \frac{g\Delta h(0,t)}{R^2(t)} = \frac{1}{2} \quad (\text{C.0.5})$$

as the boundary conditions. Hoult (1972) and Fannelop and Waldman (1972) used the downstream spreading layer thickness as the boundary condition of their similarity solutions. More generally, a variable λ can be used so that

$$H(0) = \frac{g\Delta h(0,t)}{R^2(t)} = \frac{1}{\lambda^2} \quad . \quad (C.0.6)$$

In this appendix two possible sets of boundary conditions at the front will be derived based essentially on Whitham's rules (1974) for the jumps in conserved properties across the front.

C.1 Surface Density Spread

The spreading flow motion involves discontinuities in three variables: density, velocity and thickness. While we have two equations, continuity (A.1.15) and momentum (A.1.16), which are

$$\frac{\partial(\rho h)}{\partial t} + \frac{1}{r^n} \frac{\partial(\rho r^n u h)}{\partial r} = 0 \quad (C.1.1)$$

and

$$\frac{\partial(\rho u)}{\partial t} + u \frac{\partial(\rho u)}{\partial r} + g\Delta \frac{\partial(\rho h)}{\partial r} = 0 \quad (C.1.2)$$

Equation (C.1.2) can also be rewritten as

$$\frac{\partial(\rho u h)}{\partial t} + \frac{1}{r^n} \frac{\partial(\rho r^n u^2 h)}{\partial r} + \frac{1}{2} g\Delta \frac{\partial(\rho h^2)}{\partial r} = 0 \quad (C.1.3)$$

Now suppose that there is a single discontinuity located at $r = r_d(t)$ between two positions $r = r_2(t)$ and $r = r_1(t)$, i.e., $r_2(t) < r_d(t) < r_1(t)$. Integrating the above three equations from $r = r_2(t)$ to $r = r_1(t)$ gives

$$\int_{r_2}^{r_1} \frac{\partial(\rho h)}{\partial t} r^n dr + \int_{r_2}^{r_1} \frac{1}{r^n} \frac{\partial(\rho u h r^n)}{\partial r} r^n dr = 0 \quad (\text{C.1.4})$$

$$\int_{r_2}^{r_1} \frac{\partial(\rho u)}{\partial t} r^n dr + \int_{r_2}^{r_1} \frac{\partial(\frac{1}{2} \rho u^2 + \rho g \Delta h)}{\partial r} r^n dr = 0, \quad (\text{C.1.5})$$

and

$$\int_{r_2}^{r_1} \frac{\partial(\rho u h)}{\partial t} r^n dr + \int_{r_2}^{r_1} \frac{1}{r^n} \frac{\partial(\rho u^2 h r^n)}{\partial r} r^n dr + \int_{r_2}^{r_1} \frac{1}{2} g \Delta \frac{\partial(\rho h^2)}{\partial r} r^n dr = 0 \quad . \quad (\text{C.1.6})$$

Using Leibniz rule, performing the integrations and then allowing $r_1(t) \rightarrow r_d^+(t)$ and $r_2(t) \rightarrow r_d^-(t)$ gives the conditions

$$- \overset{\circ}{r}_d[\rho h] + [\rho u h] = 0 \quad (\text{C.1.7})$$

$$- \overset{\circ}{r}_d[\rho u] + [\frac{1}{2} \rho u^2 + \rho g \Delta h] = 0 \quad (\text{C.1.8})$$

or
$$- \overset{\circ}{r}_d[\rho u h] + [\rho u^2 h + \frac{1}{2} \rho g \Delta h^2] = 0 \quad (\text{C.1.9})$$

where [] denotes the jump value inside brackets between righthand side and lefthand side of discontinuity at $r_d(t)$ and

$$\frac{dr_1(t)}{dt} = \frac{dr_2(t)}{dt} = \dot{r}_d(t) \quad . \quad (C.1.10)$$

Explicitly, the three boundary conditions at the front for surface density flow are

$$\dot{R}(t) = \frac{[\rho u h]}{[\rho h]} \quad (C.1.11)$$

$$\dot{R}(t) = \frac{[\frac{1}{2} \rho u^2 + \rho g \Delta h]}{[\rho u]} \quad (C.1.12)$$

and

$$\dot{R}(t) = \frac{[\rho u^2 h + \frac{1}{2} \rho g \Delta h^2]}{[\rho u h]} \quad . \quad (C.1.13)$$

It is interesting to note that the radial flow jump conditions are essentially the same as the plane jump conditions. Both can be easily derived from Whitham's (1974, pp. 138) rules, by three partial differential Eqs. (C.1.1), (C.1.2), and (C.1.3).

C.2 Submerged Density Spread

The two equations of continuity and of momentum (A.3.17) and (A.3.18), are

$$\frac{\partial(\rho h)}{\partial t} + \frac{1}{r^n} \frac{\partial(\rho r^n u h)}{\partial r} = 0 \quad (\text{C.2.1})$$

$$\frac{\partial(\rho u)}{\partial t} + u \frac{\partial(\rho u)}{\partial r} + g \epsilon h \frac{\partial(\rho h)}{\partial r} = 0 \quad (\text{C.2.2})$$

and the second equation (C.2.2) can be rewritten as

$$\frac{\partial(\rho u h)}{\partial t} + \frac{1}{r^n} \frac{\partial(\rho r^n u^2 h)}{\partial r} + \frac{1}{3} \frac{\partial(\rho g \epsilon h^2)}{\partial r} = 0 \quad (\text{C.2.3})$$

Suppose that there is a single discontinuity located at $r = r_d(t)$ between two positions, $r = r_2(t)$ and $r = r_1(t)$, i.e. $r_2(t) \leq r_d(t) \leq r_1(t)$. If we integrate the above three equations from $r = r_2(t)$ to $r = r_1(t)$ following the same limiting procedures as previously, we find

$$\dot{R}(t) = \frac{[\rho u h]}{[\rho h]} \quad (\text{C.2.4})$$

$$\dot{R}(t) = \frac{[\frac{1}{2} \rho u^2 + \frac{1}{2} \rho g \epsilon h^2]}{[\rho u]} \quad (\text{C.2.5})$$

or

$$\dot{R}(t) = \frac{[\rho u^2 h + \frac{1}{3} \rho g \epsilon h^3]}{[\rho u h]} \quad (\text{C.2.6})$$

where $[]$ denotes the jump value inside brackets between the righthand side and the lefthand side at a frontal discontinuity. These three jump discontinuity relationships can also be derived easily from Whitham's (1974, pp. 138) rules applied to Eqs. (C.2.1), (C.2.2), and (C.2.3).

APPENDIX D

SEDOV'S (1957) LINEAR SIMILARITY VELOCITY FUNCTION

A linear similarity function for the mean particle velocity was used by Sedov (1959) to solve the problem of spherical expansion of a gas cloud into vacuum. (For details of this gas expansion flow, see Zel'dovich and Raizer (1967), pp. 276-281.) The reason for selection of this linear function was clearly explained independently by Stanyukovich (1960). The concept of his derivation of this linear function is used here to show that the linear function is a good approximate solution to the initial phase of surface and subsurface density spread flows.

The two sets of shallow-water wave equations, which were derived in Appendix A, and used in Chapter 3 to solve the initial stage of density spreading flows, are

$$\frac{\partial h}{\partial t} + u \frac{\partial h}{\partial r} + h \left(\frac{\partial u}{\partial r} + \frac{nu}{r} \right) = 0 \quad , \quad (D.1)$$

$$\frac{\partial u}{\partial t} + u \frac{\partial u}{\partial r} + g\Delta \frac{\partial h}{\partial r} = 0 \quad , \quad (D.2)$$

for the free surface bottom surface spreading and

$$\frac{\partial h}{\partial t} + u \frac{\partial h}{\partial r} + h \left(\frac{\partial u}{\partial r} + \frac{nu}{r} \right) = 0 \quad , \quad (D.3)$$

$$\frac{\partial u}{\partial t} + u \frac{\partial u}{\partial r} + g\epsilon h \frac{\partial h}{\partial r} = 0 \quad , \quad (D.4)$$

for submerged interflows.

Consider the case when the gradient of the spreading thickness, $\frac{\partial h}{\partial r}$, is rather small. Then, two pressure gradient terms in both momentum equations (D.2) and (D.4), $g\Delta \frac{\partial h}{\partial r}$ and $g\epsilon h \frac{\partial h}{\partial r}$, are small in comparison with the inertial term. Therefore, the two momentum equations can be approximated by the equation

$$\frac{\partial u}{\partial t} + u \frac{\partial u}{\partial r} = 0 \quad . \quad (D.5)$$

Equation (D.5) implies that the mean particle velocity must have the form

$$u(r,t) = \frac{r}{t} \quad , \quad (D.6)$$

which means that the mean fluid particle velocity is proportional to the location r . Substituting Eq. (D.6) in Eqs. (D.1) and (D.3), gives

$$\frac{1}{h} \left(\frac{\partial h}{\partial t} + u \frac{\partial h}{\partial r} \right) + \frac{n+1}{t} = 0 \quad , \quad (D.7)$$

or

$$\frac{D \ln h}{Dt} + \frac{n+1}{t} = 0 \quad , \quad (D.8)$$

which implies that

$$h(r,t) \sim \frac{1}{t^{n+1}} \quad . \quad (D.9)$$

For a fixed location $r = r_1$, spreading layer thickness is inversely proportional to t^{n+1} . These two forms were found in Section 3.2.7 for the surface spread layer as

$$h(r,t) = h_1 \left(\frac{R_o}{R(t)} \right)^{(1+n)} (1 - \xi^2) \quad (D.10)$$

and for the submerged spread layer as

$$h(r,t) = h_1 \left(\frac{R_o}{R(t)} \right)^{(1+n)} (1 - \xi^2)^{1/2} \quad , \quad (D.11)$$

in which two thickness scales h_1 are listed respectively in Table 3.2.1 (for surface spreading layer) and Table 3.2.2 (for submerged spreading layer) for each initial shape of released volume. The frontal distance $R = R(t)$ is proportional to time t when t is very large.

APPENDIX E

DERIVATION OF VISCOUS LONG WAVE EQUATION FOR DENSITY SPREADING FLOWS

Two viscous long wave equations describing the viscous-buoyancy region of both surface and submerged density spreading flows will be derived here.

E.0 Basic Equations and Assumptions

The Navier-Stokes equations describing viscous surface and submerged density spreading flows are

$$\frac{\partial u}{\partial t} + u \frac{\partial u}{\partial r} + w \frac{\partial u}{\partial z} = - \frac{1}{\rho_s} \frac{\partial p}{\partial r} + \nu \nabla^2 u \quad (\text{E.0.1})$$

$$\frac{\partial w}{\partial t} + u \frac{\partial w}{\partial r} + w \frac{\partial w}{\partial z} = - \frac{1}{\rho_s} \frac{\partial p}{\partial z} \pm g + \nu \nabla^2 w \quad (\text{E.0.2})$$

and the continuity equation is

$$\frac{1}{r^n} \frac{\partial (r^n u)}{\partial r} + \frac{\partial w}{\partial z} = 0 \quad , \quad (\text{E.0.3})$$

in which u and w are respectively the unsteady horizontal and vertical velocity of the spreading fluid, and ρ_s is its mass density and ν is its kinematic viscosity. ∇^2 is the Laplacian operator. The coordinate system for free surface spreading flow is shown in Figure 3.2.1(a) and that for submerged spreading flow in Figure 3.2.1(c). The positive sign before the gravitational term g is for the surface spreading case and the

negative sign for the submerged spreading case.

In order to simplify the above three equations, the following assumptions are made:

1. A long wave approximation is applicable. The horizontal length scale is much larger than the vertical length scale so that the value of the vertical component of fluid particle velocity is negligible in comparison with that of the horizontal component, i.e. $w \ll u$,
2. The inertial force is negligible in comparison to the viscous force, i.e. $Du/Dt \ll \nu \nabla^2 u$ and $Dw/Dt \ll \nu \nabla^2 w$,
3. A boundary-layer type assumption for the viscous force terms is applicable so that the viscous force terms are dominated by the vertical gradient terms rather than horizontal gradient terms, i.e. $\frac{\partial^2 u}{\partial z^2} \gg \frac{\partial^2 u}{\partial r^2}$ and $\frac{\partial^2 u}{\partial z^2} \gg \frac{1}{r} \frac{\partial u}{\partial r}$.

With these assumptions, the Navier-Stokes equations are simplified to a relationship giving a balance of horizontal pressure force with viscous force,

$$-\frac{1}{\rho_s} \frac{\partial p}{\partial r} + \nu \frac{\partial^2 u}{\partial z^2} = 0 \quad (\text{E.0.4})$$

and a hydrostatic pressure distribution given by

$$-\frac{1}{\rho_s} \frac{\partial p}{\partial z} \pm g = 0 \quad (\text{E.0.5})$$

E.1 Viscous Surface Density Spread

Since the horizontal gradient of the spreading layer thickness is rather small, the super-elevation of a spreading layer above the free surface will be given by

$$\delta(r,t) = \left(\frac{\rho_a - \rho_s}{\rho_s} \right) h(r,t) \quad , \quad (\text{E.1.1})$$

which can be derived from the equilibrium of hydrostatic pressure along the interface.

The pressure force inside the spreading layer is then

$$p(r,z,t) = \int_{-\delta(r,t)}^z \rho_s g \, dz = \rho_s g(z + \Delta h) \quad , \quad (\text{E.1.2})$$

where the dimensionless density difference Δ is defined by

$\Delta = (\rho_a - \rho_s)/\rho_s$. Thus, the horizontal pressure gradient becomes

$$\frac{\partial p(r,z,t)}{\partial r} = \rho_s g \Delta \frac{\partial h}{\partial r} \quad (\text{E.1.3})$$

We assume that the vertical gradient of horizontal fluid velocity at the level of free surface will be vanishing, i.e.

$$\frac{\partial u(r,0,t)}{\partial z} = 0 \quad (\text{E.1.4})$$

and that the value of the horizontal fluid velocity at the interface is negligible, i.e.

$$u(r, h, t) = 0 \quad (\text{E.1.5})$$

Integrating the approximated Navier-Stokes equation,

$$\frac{\partial^2 u}{\partial z^2} = \frac{1}{\nu \rho_s} \frac{\partial p}{\partial r} = \frac{g\Delta}{\nu} \frac{\partial h}{\partial r} \quad , \quad (\text{E.1.6})$$

twice, gives the horizontal component of fluid velocity,

$$u(r, z, t) = - \frac{g\Delta h^2}{2\nu} \frac{\partial h}{\partial r} \left\{ 1 - \left(\frac{z}{h}\right)^2 \right\} \quad (\text{E.1.7})$$

Integrating the continuity equation from $z = -\delta(r, t)$ to $z = h(r, t)$, gives

$$\int_{-\delta(r, t)}^{h(r, t)} \frac{1}{r^n} \frac{\partial(r^n u)}{\partial r} dz + w(r, h, t) - w(r, -\delta, t) = 0 \quad , \quad (\text{E.1.8})$$

so that with the kinematic boundary conditions

$$w(r, h, t) = \frac{\partial h}{\partial t} + u(r, h, t) \frac{\partial h}{\partial r} \quad (\text{E.1.9})$$

$$w(r, -\delta, t) = - \frac{\partial \delta}{\partial t} - u(r, -\delta, t) \frac{\partial \delta}{\partial r} \quad (\text{E.1.10})$$

one has

$$\frac{\partial(h+\delta)}{\partial t} + \frac{1}{r^n} \frac{\partial}{\partial r} \int_{-\delta}^h (r^n u) dz = 0 \quad (\text{E.1.11})$$

From Eqs. (E.1.11) and (E.1.7), the integral term in Eq. (E.1.11) becomes

$$\begin{aligned} \int_{-\delta}^h u dz &= \frac{-g\Delta}{2\nu} \frac{\partial h}{\partial r} (h+\delta) \left(h^2 - \frac{1}{3} h\delta - \frac{1}{3} \delta^2 \right) \\ &\approx - \frac{g\Delta(h+\delta)h^2}{3\nu} \frac{\partial h}{\partial r} \end{aligned} \quad (\text{E.1.12})$$

Thus, the continuity relationship (E.1.11) is reduced to

$$\frac{\partial\{h(1+\Delta)\}}{\partial t} - \frac{1}{r^n} \frac{\partial}{\partial r} \left\{ r^n \frac{g\Delta h^3(1+\Delta)}{3\nu} \frac{\partial h}{\partial r} \right\} = 0 \quad (\text{E.1.13})$$

or

$$\frac{\partial h}{\partial t} - \frac{g\Delta}{12\nu_s} \left\{ \frac{\partial^2 h^4}{\partial r^2} + \frac{n}{r} \frac{\partial h^4}{\partial r} \right\} = 0 \quad (\text{E.1.14})$$

For the case of a plane viscous spreading layer, Eq. (E.1.14) becomes

$$\frac{\partial h}{\partial t} - \frac{g\Delta}{12\nu} \frac{\partial^2 h^4}{\partial r^2} = 0 \quad , \quad (\text{E.1.15})$$

which is in the same form derived by S. H. Smith (1969), P. Smith (1969) and Buckmaster (1977) for a plane viscous sheet advancing over a horizontal dry bed (see Figure 3.2.1(b)) except for the reduced gravitational term $g\Delta$.

We assume that the similarity solution for the thickness of a viscous spreading layer will be

$$h(r,t) = R^\ell(t) H(\xi) \quad . \quad (\text{E.1.16})$$

Substituting this assumption into the viscous long wave Eq. (E.1.14) gives

$$\frac{12\nu\overset{\circ}{RR}}{g\Delta R^{3\ell}} (\ell H - \xi H') = \left\{ \frac{n4H^3H'}{\xi} + (H^4)'' \right\} \quad (\text{E.1.17})$$

In order to homogenize the dimension in both sides of Eq. (E.1.17), one must set

$$R^\ell(t) \sim \left(\frac{\nu\overset{\circ}{RR}}{g\Delta} \right)^{1/3} \quad (\text{E.1.18})$$

so that the similarity assumption (E.1.16) becomes

$$h(r,t) = \left(\frac{\nu\overset{\circ}{RR}}{g\Delta} \right)^{1/3} H(\xi) \quad (\text{E.1.19})$$

where the dimensionless variable ξ is defined as $r/R(t)$, $R(t)$ being the frontal displacement at time t .

E.2 Viscous Submerged Density Spread

The coordinate system for the present case is shown in Figures 3.2.1(c) and A.3.1. Assume that the density of interflowing fluid is uniform and the flow is radially symmetric. The Navier-Stokes equations for this case become

$$0 = \frac{1}{\rho_s} \frac{\partial p}{\partial r} + \nu \frac{\partial^2 u}{\partial z^2} \quad (\text{E.2.1})$$

for the horizontal component and

$$0 = -\frac{1}{\rho_s} \frac{\partial p}{\partial z} - g \quad (\text{E.2.2})$$

for the vertical component. The unsteady pressure distribution at each point (r, z) becomes

$$\begin{aligned} p(r, z, t) &= \int_{H_s}^z \frac{\partial p}{\partial z} dz = -\int_{H_s}^h \rho_a g dz - \int_h^z \rho_s g dz \\ &= g\rho_s \left(-z + \frac{1}{2} \epsilon h^2 + H_s - \frac{1}{2} \epsilon H_s^2\right) \end{aligned} \quad (\text{E.2.3})$$

and the horizontal pressure gradient becomes

$$\frac{1}{\rho_s} \frac{\partial p}{\partial r} = g\epsilon h \frac{\partial h}{\partial r}, \quad (\text{E.2.4})$$

where

$$\epsilon = - \frac{1}{\rho_s} \frac{d\rho_a(z)}{dz} \quad (\text{E.2.5})$$

is considered constant.

The interflowing fluid particle velocity can be found by integrating Eq. (E.2.1) or Eq. (E.2.6):

$$\frac{\partial^2 u}{\partial z^2} = \frac{1}{\nu \rho_s} \frac{\partial p}{\partial r} = \frac{g \epsilon h}{\nu} \frac{\partial h}{\partial r} \quad (\text{E.2.6})$$

from $z = 0$ to z for the first integration

$$\frac{\partial u}{\partial z} = \int_0^z \frac{\partial^2 u}{\partial z^2} dz = \frac{g \epsilon h}{\nu} \frac{\partial h}{\partial r} z \quad (\text{E.2.7})$$

and from $z = h$ to z for the second one

$$u(r, z, t) = \int_h^z \frac{\partial u}{\partial z} dz = \frac{g \epsilon h}{2\nu} \frac{\partial h}{\partial r} (z^2 - h^2) \quad (\text{E.2.8})$$

and using the boundary conditions

$$\frac{\partial u(r, 0, t)}{\partial z} = 0 \quad (\text{E.2.9})$$

and

$$u(r, \pm h, t) = 0 \quad . \quad (\text{E.2.10})$$

Integration of continuity Eq. (E.0.3) from $z = -h(r,t)$ to $z = h(r,t)$, with the boundary conditions

$$w(r, \pm h, t) = \frac{\partial h}{\partial t} + u(r, \pm h, t) \frac{\partial h}{\partial r} \quad (\text{E.2.11})$$

gives

$$2 \frac{\partial h}{\partial t} + \frac{1}{r^n} \frac{\partial}{\partial r} \int_{-h}^h (r^n u) dz = 0 \quad (\text{E.2.12})$$

Substituting Eq. (E.2.8) in Eq. (E.2.12), gives the viscous long wave equation for the interflowing spreading layer as

$$2 \frac{\partial h}{\partial t} - \frac{1}{r^n} \frac{\partial}{\partial r} \left(r^n \frac{2g\epsilon h}{3\nu} \frac{\partial h}{\partial r} \right) = 0 \quad (\text{E.2.13})$$

or more simply

$$\frac{\partial h}{\partial t} = \frac{g\epsilon}{15\nu} \left(\frac{\partial^2 h^5}{\partial r^2} + \frac{n}{r} \frac{\partial h^5}{\partial r} \right) \quad (\text{E.2.14})$$

Assuming a similarity solution of the form (E.1.16) gives the reduced ordinary differential equation as

$$\frac{15\nu \overset{\circ}{R}}{g\epsilon R^{4\lambda-1}} (\lambda H - \xi H') = 20H^3 H'^2 + 5H^4 H'' + \frac{5nH^4 H'}{\xi} \quad (\text{E.2.15})$$

so that for dimensional homogeneity

$$R^{\ell}(t) \sim \left(\frac{\overset{\circ}{\nu} RR}{g\varepsilon} \right)^{1/4} \quad (\text{E.2.16})$$

and the similarity solution must be in the following form

$$h(r, t) = \left(\frac{\overset{\circ}{\nu} RR}{g\varepsilon} \right)^{1/4} H(\xi) . \quad (\text{E.2.17})$$

LIST OF REFERENCES

- Abbott, M. B. (1961) "On the Spreading of One Fluid over Another. Part I. Discharge of Oil into a Canal. Part II. The Wave Front. Part III. Discharge of Oil into Still Water, Radial Flow," La Houille Blanche, Vol. 16, Part I: No. 5, Oct., pp. 622-628; Parts II and III: No. 6, Dec., pp. 827-836 and 837-846.
- Abbott, M. B. (1968) "Unsteady Radial Flow of Oil Being Discharged from a Source on the Ocean," Coastal Engineering in Japan, 11:185-189.
- Abbott, M. B. and Torbe, I. (1963) "On Flows and Fronts in a Stratified Fluid," Proceedings of the Royal Society, London, 273(A):12-40.
- Abraham, G. and Eysink, W. D. (1969) "Jets Issuing into Fluid with a Density Gradient," Journal of Hydraulic Research. 7:(2): 145-175.
- Abramovich, G. N. (1963) "The Theory of Turbulent Jets," The MIT Press, Cambridge.
- Allan Hancock Foundation, University of Southern California (1964), "Final Report on an Investigation on the Fate of Organic and Inorganic Wastes Discharged into the Marine Environment and Their Effects of Biological Productivity," September 15, 77 pp.
- Almquist, C. (1973) "The Two-Dimensional Surface Spreading of a Buoyant Fluid into an Infinite Stagnant Environment," Unpublished student Term Paper for ENV 112 course at the California Institute of Technology, Pasadena, California.
- Amen, R. and Maxworthy, T. (1980) "The Gravitational Collapse of a Mixed Region into a Linearly Stratified Fluid," Journal of Fluid Mechanics, 96(1):65-80.
- Anwar, H. O. (1972) "The Radial Spreading as a Free Surface Layer of a Vertical Buoyant Jet," Journal of Engineering Mathematics, 6(3):257-272.
- Bardey, P. R. (1977) "Height of Rise of a Momentum Jet in a Stagnant Linearly Stratified Fluid," Unpublished student Term Paper in ENV 112 course, Hydrologic Transport Processes, California Institute of Technology, Pasadena, California.

- Barenblatt, G. I. and Monin, A. S. (1979) "The Origin of Oceanic Microstructure," 12th Symposium on Naval Hydrodynamics, National Academy of Science, Washington, D.C., pp. 574-581.
- Barenblatt, G. I. and Zel'dovich, Y.B. (1972) "Self-Similar Solutions as Intermediate Asymptotics," Annual Review of Fluid Mechanics, 4:285-312.
- Barr, D.I.H. (1959) "Some Observations on Small Scale Thermal Density Currents," International Association for Hydraulic Research, 8th Congress, Montreal, August 24-29, 1959, pp. 6-c-1 - 6-c-22.
- Barr, D.I.H. (1967) "Densimetric Exchange Flow in Rectangular Channels, III. Large Scale Experiments," La Houille Blanche, 6:619-632.
- Barr, D.I.H. and Hassan, A.M.M. (1963) "Densimetric Exchange Flow in Rectangular Channels, II. Some Observations of the Structure of Lock Exchange Flow," La Houille Blanche, November, 7:757-766.
- Batchelor, G. (1970) "An Introduction to Fluid Dynamics," Cambridge University Press.
- Bell, H. S. (1942) "Density Currents as Agents for Transporting Sediments," Journal of Geology, 50(5):512-547.
- Bell, T.H., Jr. and Dugan, J. P. (1974) "Model for Mixed Region Collapse in a Stratified Fluid," Journal of Engineering Mathematics, 8(3):241-248.
- Benjamin, T. B. (1968) "Gravity Currents and Related Phenomena," Journal of Fluid Mechanics, 31(2):209-248.
- Berson, F. A. (1958) "Some Measurements on Undercutting Cold Air," Quarterly Journal of the Royal Meteorological Society, 84(359): 1-16.
- Beyer, F. (1955) "The Spreading of Sinking Particles in the Sea," Sewage and Industrial Wastes, 27(9):1073-1078.
- Braucher, E. P. (1950) "Initial Characteristics of Density Current Flow," M.S. Thesis, Massachusetts Institute of Technology, July, 59 pp.
- Britter, R. E. (1979) "The Spread of a Negative Buoyant Plume in a Calm Environment," Atmospheric Environment, 13:1241-1247.

- Britter, R. E. and Simpson, J. E. (1978) "Experiments on the Dynamics of a Gravity Current Head," Journal of Fluid Mechanics, 88(2):223-240.
- Brooks, N. H. (1952) "Some Ocean Outfall Studies," County Sanitation Districts of Los Angeles County, California, September, 55 pp.
- Brooks, N. H. (1960) "Diffusion of Sewage Effluent in an Ocean Current," in "Waste Disposal in the Marine Environment," edited by E. A. Pearson, Pergamon Press, pp. 246-267.
- Buckmaster, J. (1973) "Viscous Gravity Spreading of an Oil Slick," Journal of Fluid Mechanics, 59(3):481-491.
- Buckmaster, J. (1977) "Viscous Sheets Advancing over Dry Beds," Journal of Fluid Mechanics, 81(4):735-756.
- Bühler, J. (1974) "Model Studies of Multiport Outfalls in Unstratified, Stagnant or Flowing Receiving Water," Ph.D. Thesis, University of California, Berkeley, 164 pp.
- Cederwall, K. (1968) "Hydraulics of Marine Waste Water Disposal," Hydraulic Division, Report No. 42, Chalmers Institute of Technology, Göteborg, Sweden, January, pp. 163-165.
- Cerasoli, C. P. (1978) "Experiments on Buoyant-Parcel Motion and the Generation of Internal Gravity Waves," Journal of Fluid Mechanics, 86(2):247-271.
- Chao, J. L. (1975) "Horizontal Spread of Wastewater Field over Calm Ocean Surface," Journal of WPCF, 47(10):2504-2510.
- Chen, J.-C. (1975) "Buoyant Surface Spreading," Taiwan Water Conservancy Quarterly, 23(3):20-28.
- Chen, J.-C. and List, E. J. (1976) "Spreading of Buoyant Discharges," International Centre for Heat and Mass Transfer, Turbulent Buoyant Convection, Dubrovnik, Yugoslavia, August 30-September 4, 1976, pp. 171-182.
- Clarke, R. H. (1961) "Mesostructure of Dry Cold Fronts over Featureless Terrain," Journal of Meteorology, 18(6):715-735.
- Courant, R. and Friedrichs, K. O. (1948) "Supersonic Flow and Shock Waves," Interscience Publishers, Inc., New York, 464 pp.

- Crawford, T. V. and Leonard, A. S. (1962) "Observations of Buoyant Plumes in Calm, Stably Stratified Air," Journal of Applied Meteorology, 1:251-256.
- Dabora, E. K. (1972) "Variable Energy Blast Waves," Technical Notes, AIAA Journal, 10(10):1384-1386.
- Daly, B. J. and Pracht, W. E. (1968) "Numerical Study of Density-Current Surges," The Physics of Fluids, 11(1):15-30.
- Davies, R. W. (1959) "Large-Scale Diffusion from an Oil Fire," Advances in Geophysics, F. N. Frenkiel and P. A. Sheppard, Eds. Academic Press, N.Y., 6:413-415.
- Drake, E. and Reid, R. C. (1977) "The Importation of Liquefied Natural Gas," Scientific American, 236(4):22-29.
- Dugan, J. P., Warn-Varnas, S. C., and Piacsek, S. A. (1976) "Numerical Results for Laminar Mixed Region Collapse in Density Stratified Fluid," Computers and Fluids, Pergamon Press, 4:109-121.
- Ellis, J. and Al-Khairulla, L. M. (1974) "Oscillations in a Surge Tank with Upper and Lower Expansion Galleries," Water Power, 26(11):359-364.
- Ellison, T. H. and Turner, J. S. (1959) "Turbulent Entrainment in Stratified Flows," Journal of Fluid Mechanics, 6:423-448.
- Engelund, F. A. and Christensen, L. (1969) quoted in H. Moshagen (1972).
- Fan, L.-N. (1967) "Turbulent Buoyant Jets into Stratified or Flowing Ambient Fluids," W. M. Keck Laboratory of Hydraulic and Water Resources, Report No. KH-R-15, California Institute of Technology, Pasadena, Calif., 196 pp.
- Fan, L.-N. and Brooks, N. H. (1969) "Numerical Solutions of Turbulent Buoyant Jet Problems," W. M. Keck Laboratory of Hydraulics and Water Resources, Report No. KH-R-18, California Institute of Technology, Pasadena, Calif., 94 pp.
- Fannelop, T. K. and Walman, G. D. (1972) "Dynamics of Oil Slicks," AIAA Journal, 10(4):506-510. Also paper No. 71-14, AIAA 9th Aerospace Meeting, New York, Jan. 1971.
- Fay, J. A. (1969) "The Spread of Oil on a Calm Sea," in "Oil on the Sea," edited by D. P. Hoult, Plenum Press, N.Y., pp. 53-63.
- Fay, J. A. (1971) "Physical Processes in the Spread of Oil on a Water Surface," Conference on Prevention and Control of Oil Spills, Sponsored by API, EPA, and U.S. Coast Guard, Washington, DC, pp. 463-467.

- Fox, D. G. (1970) "Forced Plume in a Stratified Fluid," Journal of Geophysical Research, 75(33):6181-6835. Also NCAR Manuscript 68-197, National Centre for Atmospheric Research, Boulder, Colorado, Sept. 1968, 37 pp.
- Fox, L. and Goodwin, E. T. (1952) In Appendix of W. G. Penney and C. K. Thornhill (1952).
- Foxworthy, J. E. and Kneeling, H. R. (1969) "Eddy Diffusion and Bacterial Reduction in Waste Fields in the Ocean," Allan Hancock Foundation, Report 69-1, University of Southern California, Los Angeles, Calif., 176 pp.
- Foxworthy, J. E., Tibby, R. B., and Barsom, G. M. (1966) "Dispersion of a Surface Waste Field in the Sea," Journal of the Water Pollution Control Federation, 38(7):1170-1193.
- Frankel, R. J. and Cumming, J. D. (1965) "Turbulent Mixing Phenomena of Ocean Outfalls," Journal of Sanitary Engineering Division, Proceedings of the American Society of Civil Engineers, 91(SA2): 39-59. Also Technical Report No. HEL-3-1, Institute of Engineering Research, University of California, Berkeley, 1963.
- Freeman, J. C., Jr. (1948) "An Analogy Between the Equatorial Easterlies and Supersonic Gas Flow," Journal of Meteorology, 5:138-146.
- Freeman, R. A. (1968) "Variable-Energy Blast Waves," British Journal of Applied Physics (Journal of Physics D), Series 2, 1:1697-1710.
- Frenkiel, F. N. (1953) "Turbulent Diffusion: Mean Concentration Distribution in a Flow Field of Homogeneous Turbulence," Advances in Applied Mechanics, Vol. III, Academic Press, Inc., pp. 61-107.
- Frigo, A. A., Zivi, S. M., King, R. M., and Levinson, E. D. (1974), "Field Observations of the Dynamics of Heated Discharge Jets," Proceedings, 17th Conference on Great Lakes Research, International Association for Great Lakes Research, pp. 412-424.
- Gartrell, Gregory, Jr. (1979) "Studies on the Mixing in a Density-Stratified Shear Flow," W. M. Keck Laboratory of Hydraulics and Water Resources, Report No. KH-R-39, California Institute of Technology, Pasadena, Calif., 447 pp.
- Garvine, R. W. (1974) "Physical Features of the Connecticut River Outflow During High Discharge," Journal of Geophysical Research, 79(6):831-846.

- Georgeson, E.H.M. (1942) "The Free Streaming of Gases in Sloping Galleries," Proceedings of the Royal Society of London, 180(A):484-493.
- Gilding, B. H. and Peletier, L. A. (1976) "On a Class of Similarity Solutions of the Porous Media Equation," Journal of Mathematical Analysis and Applications, 55:351-364.
- Glauert, M. B. (1956) "The Wall Jet," Journal of Fluid Mechanics, 1:625-643.
- Gordon, R. B. (1974) "Dispersion of Dredge Spoil Dumped in Near-Shore Waters," Estuarine and Coastal Marine Science, 2:349-358.
- Görtler, H. (1942) "Berechnung von Aufgaben der freien Turbulenz auf Grund eines neuen Näherungsansatzes," ZAMM, 22:5.
- Green, T., Mackenzie, T., Roffler, S., Scarpace, F., Sundby, C., and Keating, T. (1972) "The Point Beach Thermal Plume," Proceedings, 15th Conference on Great Lakes Research, held at the University of Wisconsin-Madison, Madison, WI, April 5-7, 1972, International Association of Great Lakes Research, pp. 588-596.
- Grundy, R. E. (1979), "Similarity Solutions of the Nonlinear Diffusion Equation," Quarterly of Applied Mathematics, 37(3):259-280.
- Harlow, F. H. and Welch, J. E. (1965) "Numerical Calculation of Time-Dependent Viscous Incompressible Flow of Fluid with Free Surface," The Physics of Fluids, 8(12):2182-2189.
- Harremöes, P. (1967) "On the Significance of Density Effects to Marine Disposal," Progress Report, Danish Isotope Center, Fall, 12 pp.
- Hart, W. E. (1961) "Jet Discharge into a Fluid with a Density Gradient," Journal of the Hydraulics Division, Proceedings of the American Society of Civil Engineers, 87(HY6):171-200.
- Hartman, R. J. and Lewis, H. W. (1972) "Wake Collapse in a Stratified Fluid: Linear Treatment," Journal of Fluid Mechanics, 51(3):613-618.
- Hayashi, T. and Ito, M. (1974) "Diffusion of Effluent Discharging Vertically into Stagnant Sea Water," Coastal Engineering in Japan, 17:199-213.
- Hayashi, T. and Shuto, N. (1967) "Diffusion of Warm Water Jets Discharged Horizontally at the Water Surface," Proceedings of the 12th Congress of IAHR, 6:47-59.
- Hoge, E. R. and Brooks, N. H. (1951) "Density Current Experiments," Hydrodynamics Laboratory, Memorandum Report No. EM34, California Institute of Technology, Pasadena, Calif., 12 pp.

- Hoult, D. P. (1972) "Oil Spreading on the Sea," Annual Review of Fluid Mechanics, 4:341-368.
- Hoult, D. P. and Suchon, W. (1970) "The Spread of Oil in a Channel," Stop Oil Pollution Report Two, Fluid Mechanics Laboratory, Department of Mechanical Engineering, Massachusetts Institute of Technology, May, 25 pp.
- Howland, W. E. (1934) Discussion of "Model Law for Motion of Salt Water through Fresh," by M. P. O'Brien and J. Chernoff, Transactions of ASCE, 99:595-597.
- Hydén, H. and Larsen, I. (1975) "Surface Spreading," Proceedings, Sewage from Sea Outfalls, London 1974, Pergamon Press, NY, pp. 277-283.
- Ichiye, T. (1972) "Hydrodynamic Problems Concerning Oil Spillage in the Ocean," Appendix C in "Environmental Aspects of a Supertanker Port on the Texas Gulf Coast," Texas A & M University, Sea Grant Program, Pub. 73-201, pp. 383-421.
- Imberger, J., Thompson, R., and Fandry, C. (1976) "Selective Withdrawal from a Finite Rectangular Tank," Journal of Fluid Mechanics, 78(3):489-512.
- Jeffreys, H. (1952) In W. G. Penney and C. K. Thornhill (1952), p. 38.
- Jirka, G. and Harleman, D.R.F. (1973) "The Mechanics of Submerged Multiport Diffusers for Buoyant Discharges in Shallow Water," Ralph M. Parsons Laboratory for Water Resources and Hydrodynamics, Report No. 169, Massachusetts Institute of Technology, Cambridge, Mass., 313 pp.
- Jirka, G. H., Johnson, R. P., Fry, D. J., and Harleman, D.R.F. (1977) "Ocean Thermal Energy Conversion Plants: Experimental and Analytical Study of Mixing and Recirculation," Ralph M. Parsons Laboratory of Water Resources and Hydrodynamics, Report No. 231, Massachusetts Institute of Technology, 269 pp.
- Kao, T. W. (1974) "Density Current in a Stratified Environment with an Application to Wake Collapse," Proceedings of the 7th Southeastern Conference on Theoretical and Applied Mechanics, The Catholic University of America, Washington, DC, pp. 80-90.
- Kao, T. W. (1976) "Principal Stage of Wake Collapse in a Stratified Fluid: Two-Dimensional Theory," The Physics of Fluids, 19(8): 1071-1074.

- Kao, T. W. (1977) "Density Currents and Their Applications," Journal of the Hydraulics Division, Proceedings of the American Society of Civil Engineers. 103(HY5):543-555.
- Kao, T. W., Park, C., and Pao, H.-P. (1977) "Buoyant Surface Discharge and Small Scale Oceanic Fronts: A Numerical Study," Journal of Geophysical Research, 82(12):1747-1752.
- Kao, T. W., Park, C., and Pao, H.-P. (1978) "Inflows, Density Currents, and Fronts," The Physics of Fluids, 21(11):1912-1922.
- Keulegan, G. H. (1934) Discussion of "Model Law for Motion of Salt Water through Fresh," by M. P. O'Brien and J. Chernoff, Transactions of the American Society for Civil Engineers, 99:602-606.
- Keulegan, G. H. (1946) "First Progress Report on Project 48 Model Laws for Density Currents," for Chief of Engineers, U.S. Army, April 9, 14 pp.
- Keulegan, G. H. (1957) "Thirteenth Progress Report on Model Laws for Density Currents: An Experimental Study of the Motion of Saline Water from Locks into Fresh Water Channels," National Bureau of Standards Report 5168, U. S. Department of Commerce, National Bureau of Standards, March 4, 21 pp.
- Keulegan, G. H. (1958) "Twelfth Progress Report on Model Laws for Density Currents: The Motion of Saline Fronts in Still Water," National Bureau of Standards Report 5831, U. S. Department of Commerce, National Bureau of Standards, April 1, 29 pp.
- Koh, R.C.Y. (1976) "Buoyancy-Driven Gravitational Spreading," Proceedings of the 15th International Conference on Coastal Engineering, Honolulu, Hawaii, July 11-17, 4:2956-2975.
- Koh, R.C.Y., Brooks, N. H., List, E. J., and Wolanski, E. J. (1974) "Hydraulic Modeling of Thermal Outfall Diffusers for the San Onofre Nuclear Power Plant," W. M. Keck Laboratory of Hydraulics and Water Resource, Report No. KH-R-30, California Institute of Technology, Pasadena, Calif., 118 pp.
- Koh, R.C.Y. and Fan, L.-N. (1970) "Mathematical Models for the Prediction of Temperature Distributions Resulting from the Discharge of Heated Water into Large Bodies of Water," Water Quality Office, EPA Program, 16130 DWO, 219 pp.

- Korobeinikow, V. P. (1971) "Gas Dynamics of Explosions," Annual Review of Fluid Mechanics, 3:317-346.
- Koschmieder, H. (1936) "Danziger Seewinduntersuchungen," *Forsch.-Arb. des Observ. Danzig*, Vol. 8.
- Kotsovinos, N. K. (1975) "A Study of the Entrainment and Turbulence in a Plane Buoyant Jet," W. M. Keck Laboratory of Hydraulics and Water Resources, Report No. KH-R-32, California Institute of Technology, Pasadena, Calif., 306 pp.
- Kramer, M. L. and Seymour, D. E. (1976) "John E. Amos Cooling Tower Flight Program Data, December 1975 - March 1976," American Electric Power Service Corporation, Smith-Singer Meteorologists, Inc., 89 pp.
- Langmuir, I. (1933) "Oil Lenses on Water and the Nature of Monomolecular Expanded Films," Journal of Chemical Physics, 1:756-776.
- Larsen, I. and Sörensen, T. (1968) "Buoyancy Spread of Waste Water in Coastal Regions," Chapter 89, Proceedings of the 11th Conference on Coastal Engineering, London, England, September, pp. 1397-1402.
- Latter, R. (1955) "Similarity Solution for a Spherical Shock Wave," Journal of Applied Physics, 26:954-960.
- Lean, G. H. and Willock, A. R. (1965) "The Behaviour of a Warm Water Layer Flowing over Still Water," Paper No. 2.9, International Congress of Hydraulic Research, 11th Congress, Leningrad, Vol. II.
- Lee, J. H., Jirka, G. H., and Harleman, D.R.F. (1974), "Stability and Mixing of a Vertical Round Buoyant Jet in Shallow Water," Ralph M. Parsons Laboratory for Water Resources and Hydrodynamics, Report No. 195, Massachusetts Institute of Technology, Cambridge, Mass., 135 pp.
- Lee, R.A.S. (1971) "A Study of the Surface Tension Controlled Regime of Oil Spread," B.S. and M.S. Thesis, Department of Mechanical Engineering, Massachusetts Institute of Technology, Cambridge, Mass., 57 pp.
- Liang, L.-S. (1971) "Spreading of Oil on Calm Water; Inertial Phase," M.S. Thesis, Department of Mechanical Engineering, Massachusetts Institute of Technology, Cambridge, Mass., 55 pp.

- Lin, S.-C. (1954) "Cylindrical Shock Waves Produced by Instantaneous Energy Release," Journal of Applied Physics, 25(1):554-57.
- Liseth, P. (1970) "Mixing of Merging Buoyant Jets from a Manifold in Stagnant Receiving Water of Uniform Density," Technical Report No. HEL 23-1, Hydraulic Engineering Laboratory, University of California, Berkeley, 181 pp.
- List, E. J. (1977) Private communication.
- List, E. J. and Imberger, J. (1973) "Turbulent Entrainment in Buoyant Jets and Plumes," Journal of the Hydraulics Division. Proceedings of the American Society of Civil Engineers, 99(HY9): 1461-1474.
- Liu, S.-L. (1976) "Mixing of Submerged Two-Dimensional Buoyant Jets in Uniform Bodies of Water in the Absence and Presence of Wind Action," Technical Report HEL 23-5, Hydraulic Engineering Laboratory, University of California, Berkeley, 141 pp.
- Longuet-Higgins, M. S. (1972) "A Class of Exact, Time-Dependent, Free-Surface Flows," Journal of Fluid Mechanics, 55(3):529-543.
- Manins, P. C. (1976a) "Intrusion into a Stratified Fluid," Journal of Fluid Mechanics, 74(3):547-560.
- Manins, P. C. (1976b) "Mixed-Region Collapse in a Stratified Fluid," Journal of Fluid Mechanics, 77(1):177-183.
- Margules, M. (1906) "Zur Sturmtheorie," Meteorologische Zeitschrift Band 23, Heft, 11, pp. 481-497.
- Martin, J. C. and Moyce, W. J. (1952) "Part IV. An Experimental Study of the Collapse of Liquid Columns on a Rigid Horizontal Plane," In "Some Gravity Wave Problems in the Motion of Perfect Liquids," Philosophical Transactions of the Royal Society of London, 244A:312-324.
 "Part V. An Experimental Study of the Collapse of Fluid Columns on a Rigid Horizontal Plane, in a Medium of Lower, but Comparable Density," 244A:325-335.
- Maxworthy, T. (1972) "Experimental and Theoretical Studies of Horizontal Jets in a Stratified Fluid," International Symposium on Stratified Flow, Novosibirsk, pp. 611-618.
- McClimans, T. A. (1978) "Fronts of Fjords," Geophysical and Astrophysical Fluid Dynamics, 11:23-24.

- Mei, C. C. (1966) "Nonlinear Gravity Waves in a Thin Sheet of Viscous Fluid," Journal of Mathematics and Physics, 45:266-288.
- Mei, C. C. (1969) "Collapse of a Homogeneous Fluid Mass in a Stratified Fluid," Proceedings of the 12th International Congress of Applied Mechanics, Stanford University, August 26-31, 1968, Editors: M. Hetényi, W. G. Vincenti, Springer-Verlag, pp. 321-330.
- Meng, J.C.S. (1978) "The Physics of Vortex-Ring Evolution in a Stratified and Shearing Environment," Journal of Fluid Mechanics, 84(3):455-469.
- Meng, J.C.S. and Thomson, J.A.L. (1978) "Numerical Studies of Some Nonlinear Hydrodynamic Problems by Discrete Vortex Element Methods," Journal of Fluid Mechanics, 84(3):433-453.
- Middleton, G. V. (1966) "Experiments on Density and Turbidity Currents. I. Motion of the Head," Canadian Journal of Earth Sciences, 3(4):523-546.
- Milne-Thomson, L. M. (1969) "Theoretical Hydrodynamics," Fifth Edition, second printing, The Macmillan Company.
- Morton, B. R., Taylor, G., and Turner, J. S. (1956) "Turbulent Gravitational Convection from Maintained and Instantaneous Sources," Proceedings of the Royal Society of London, 234(A): 1-23.
- Moshagen, H. (1972) "Density Front between Sliding Layers," International Symposium on Stratified Flows, Novosibirsk, pp. 619-624.
- Murota, A. and Muraoka, K. (1967) "Turbulent Diffusion of the Vertically Upward Jet," Proceedings, 12th IAHR Congress, 4:60-70.
- O'Brien, M. P. and Chernoff, J. (1932) "Model Law for Motion of Salt Water through Fresh," Proceedings of the American Society of Civil Engineers, 58:1769-1788, also Transactions of ASCE, 99:576-609.
- Padmanabhan, H., Ames, W. G., Kennedy, J. F., and Hung, T.-K. (1970), "A Numerical Investigation of Wake Deformation in Density Stratified Fluids," Journal of Engineering Mathematics, 4(3):229-241.

- Penney, W. G. and Thornhill, C. K. (1952) "Part III. The Dispersion, under Gravity, of a Column of Fluid Supported on a Rigid Horizontal Plane," In "Some Gravity Wave Problems in the Motion of Perfect Liquids," Philosophical Transactions of the Royal Society of London, 244A:285-311.
- Pitkin, E. T. (1977) "Perturbation solutions for variable energy blast waves," Acta Astronautica, 4:1137-1158.
- Pohle, F. V. (1952) "Motion of Water Due to Breaking of a Dam, and Related Problems," National Bureau of Standards, Circular 521, pp. 47-53.
- Prandtl, L. (1942) "Bemerkung zur Theories der freien Turbulenz," ZAMM, 22:5.
- Prandtl, L. (1952) "Essentials of Fluid Dynamics," Hafner, New York, pp. 368-370.
- Pryputniewicz, R. J. and Bowley, W. W. (1975) "An Experimental Study of Vertical Buoyant Jets Discharged into Water of Finite Depth." Transactions of the American Society of Mechanical Engineers, Journal of Heat Transfer, May, pp. 274-281.
- Rannie, W. D. (1975) Private communication in Hy 101 class.
- Rawn, A. M. and Palmer, H. K. (1929) "Pre-Determining the Extent of a Sewage Field in Sea Water," Proceedings of the American Society of Civil Engineers, 55(1):1167-1191, also in Transactions of ASCE, 94:1036-1081.
- Rawn, A. M., Bowerman, F. R., and Brooks, N. H. (1960), "Diffusers for Disposal of Sewage in Sea Water," Journal of Sanitary Engineering Division, Proceedings of the American Society of Civil Engineers, 86(SA2):65-105.
- Ritter, A. (1892) "Die Fortpflanzung der Wassewellen," Zeitschrift des Vereines Deutscher Ingenievre, 36(33):947-954.
- Roberts, P.J.W. (1977) "Dispersion of Buoyant Waste Water Discharged from Outfall Diffusers of Finite Length," W, M, Keck Laboratory of Hydraulics and Water Resources, Report No. KH-R-35, California Institute of Technology, Pasadena, Calif., 183 pp.
- Rogers, M. H. (1958) "Similarity Flows Behind Strong Shock Waves," Quarterly Journal of Mechanics and Applied Mathematics, (4): 411-422.
- Rouse, C. A. (1959) "Theoretical Analysis of the Hydrodynamic Flow in Exploding Wire Phenomena," in "Exploding Wire," edited by W. G. Chace and H. K. Moore, Vol. I, Plenum: New York, pp. 227-263.

- Sakurai, A. (1965) "Blast Wave Theory," In "Basic Developments in Fluid Dynamics," edited by M. Holt, New York Academic Press, pp. 309-375.
- Sandstrom, J. W. (1908) "Dynamische Versuche mit Meerwasser," Ann. Hydrogr. Marit. Meteorol., pp. 6-23.
- Scarpace, E. L. and Green III, T. (1973) "Dynamic Surface Temperature of Thermal Plumes," Water Resources Research, 9(1):138-153.
- Schmidt, W. (1910) "Gewitter und Böen, rasche Druckanstiege," Akademik der Wissenschaften, Vienna, Abteilung IIA, 119:1101-1214.
- Schmidt, W. (1911) "Zur Mechanik der Böen," Meteorologische Zeitschrift, 28:355-362.
- Schoklitsch, A. (1917) "Über Dammbbruchwellen," Sitzungsberichte der K. Akademie der Wissenschaften, Vienna, Abteilung IIA, Vienna, Austria, 126:1489-1514.
- Sedov, L. I. (1957) "Similarity and Dimensional Methods in Mechanics," Gostekhizdat, Moscow, 4th Edition, English translation, edited by M. Holt, Academic Press, New York, 1959, 363 pp.
- Seligman, G. (1962) "Snow Structure and Ski Fields," Reprinted in Belgium, Jos. Adam-Brussel-Belgium, 501 pp.
- Sharp, J. J. (1969a) "Spread of Buoyant Jets at the Free Surface," Journal of the Hydraulics Division, Proceedings of the American Society of Civil Engineers, 95(HY3):811-825.
- Sharp, J. J. (1969b) "Spread of Buoyant Jets at the Free Surface--II," Technical Notes, Journal of the Hydraulics Division, Proceedings of the American Society of Civil Engineers, 95(HY5):1771-1773.
- Sharp, J. J. (1971) "Unsteady Spread of Buoyant Surface Discharge," Journal of the Hydraulics Division, Proceedings of the American Society of Civil Engineers, 97(HY9):1471-1492.
- Shwartz, J., van der Watering, W., Landa, I., and Reed, Jr., S. (1973) "Hydrodynamic Study of Density Surges and Turbidity Flows," Technical Report 805-1, Hydronautics, Inc., 45 pp.
- Simpson, J. E. (1972) "Effects of the Lower Boundary on the Head of a Gravity Current," Journal of Fluid Mechanics, 53(4):759-768.

- Simpson, J. E. and Britter, R. E. (1979) "The Dynamics of the Head of a Gravity Current Advancing over a Horizontal Surface," Journal of Fluid Mechanics, 94(3):477-495.
- Smith, A. A. (1965) "The Effect of Gravity Waves on the Spread of an Effluent," Proceedings, 11th IAHR Congress, Paper No. 2.7, Leningrad.
- Smith, J. E. (1968) "Torrey Canyon Pollution and Marine Life," Cambridge University Press, Cambridge.
- Smith, P. (1972) "Long Gravity Waves on a Viscous Fluid Flowing Down an Inclined Plane," Journal of Engineering Mathematics, 6(1):15-21.
- Smith, S. H. (1969a) "A Non-Linear Analysis of Steady Surface Waves on a Thin Sheet of Viscous Liquid Flowing Down an Incline," Journal of Engineering Mathematics, 3(3):173-179.
- Smith S. H. (1969b) "On Initial Value Problems for the Flow in a Thin Sheet of Viscous Liquid," Zeitschrift für Angewandte Mathematik und Physik, 20:556-560.
- Sneck, H. J. and Brown, D. H. (1974) "Plume Rise from Large Thermal Sources Such as Dry Cooling Towers," Journal of Heat Transfer, Transactions of the American Society of Mechanical Engineers, 96:232-238.
- Sokolov, B. I. (1972) "Numerical Methods of Investigations into Stratified Flows," International Symposium of Stratified Flows, Novosibirsk, pp. 657-660.
- Sonnichsen, Jr., J. C. (1971) "Lateral Spreading of Heated Discharge," Journal of the Power Division, Proceedings of the American Society of Civil Engineers, 97(P03):623-630.
- Stanyukovich, K. P. (1960) "Unsteady Motion on Continuous Media," Pergamon Press, New York.
- Stefan, H. (1972) "Dilution of Buoyant Two-Dimensional Surface Discharges," Journal of the Hydraulics Division, Proceedings of the American Society of Civil Engineers, 98(HY1):71-86.
- Stewart, H. J. (1945) "Surfaces of Discontinuity," Section VI of "Kinematics and Dynamics of Fluid Flow," Handbook of Meteorology, edited by R. A. Berry, Jr., E. Bollay, N. R. Beers, McGraw-Hill, New York, pp. 441-446.

- Taylor, Sir G. (1950) "The Formation of a Blast Wave by a Very Intense Explosion. I. Theoretical Discussion. II. The Atomic Explosion of 1945," Proceedings of the Royal Society, London, 201A:159-186.
- Thorpe, S. A. (1973) "Turbulence in Stably Stratified Fluids: A Review of Laboratory Experiments," Boundary Layer Meteorology, 5:95-119.
- Tollmien, W. (1926) "Berechnung turbulenter Ausbreitungsvorgänge," ZAMM, 6:6 and 468.
- U. S. Atomic Energy Commission (1950) "The Effects of Atomic Weapons," Under the direction of the Los Alamos Scientific Laboratory, Los Alamos, New Mexico, McGraw-Hill, New York, 456 pp.
- Vasiliev, O. F. (1975) "Numerical Simulation of the Lock Exchange Flow in a Channel," XVIth Congress of the International Association for Hydraulics Research, São Paulo, Brazil, July 27 to August 1, 1975, 3:46-53.
- Vasiliev, O. F., Kuznetsov, B. G., Lytkin, Y. M., and Chernykh, G. G. (1972) "Development of the Turbulized Fluid Region in Stratified Medium," International Symposium of Stratified Flows, Novosibirsk, 1972, pp. 161-174.
- Vehrencamp, J. E., Ambrosio, A., and Romie, F. E. (1955), "Convection from Heated Sources in an Inversion Layer," First Report of Air Pollution Studies, Report No. 55-27, Department of Engineering, University of California, Los Angeles, 39 pp.
- von Kármán, T. (1940) "The Engineer Grapples with Nonlinear Problems," Bulletin of the American Mathematical Society, 46:615-683.
- Waldman, G. D., Fannelop, T. K., and Johnson, R. A. (1972) "Spreading and Transport of Oil Slicks on the Open Ocean," Paper Number OTC 1548, Preprints 1972 Offshore Technology Conference, May 1-3, Houston, Texas, I:I-353 - I-364.
- van de Watering, W.P.M. (1966) "The Growth of a Turbulent Wake in a Density-Stratified Fluid," Technical Report 231-12, Hydronautics, Inc., 27 pp.
- Wessel, W. R. (1969) "Numerical Study of the Collapse of a Perturbation in an Infinite Density-Stratified Fluid," The Physics of Fluids, Supplement II, 12:171-176.
- Whitham, G. B. (1974) "Linear and Nonlinear Waves," Wiley-Interscience, John Wiley and Sons, 636 pp.

- Wilkinson, D. L. (1970) "Studies in Density-Stratified Flows," Report No. 118, Water Resource Laboratory, The University of New South Wales, Manly Vale, N.S.W. Australia, 167 pp.
- Wilkinson, D. L. and Wood, I. R. (1971) "A Rapidly Varied Flow Phenomenon in a Two-Layer Flow," Journal of Fluid Mechanics, 47(2):241-256.
- Wood, I. R. (1965) "Studies in Unsteady Self-Preserving Turbulent Flows," Report No. 81, Water Research Laboratory, The University of New South Wales, Manly Vale, N.S.W. Australia, 152 pp.
- Wood, I. R. (1967) "Horizontal Two-Dimensional Density Current," Journal of the Hydraulics Division, Proceedings of the American Society of Civil Engineers, 93(HY2):35-42.
- Wu, J. (1965) "Collapse of Turbulent Wakes in Density-Stratified Media," Technical Report 231-4, Hydronautics, Inc., 25 pp.
- Wu, J. (1969) "Mixed Region Collapse with Internal Wave Generation in a Density-Stratified Medium," Journal of Fluid Mechanics, 35(3):531-544.
- Yih, C.-S. (1947) "A Study of the Characteristics of Gravity Waves at a Liquid Interface," M.S. Thesis, State University of Iowa, 18 pp.
- Yih, C.-S. (1965) "Dynamics of Nonhomogeneous Fluids," The Macmillan Company, New York, pp. 134-138.
- Young, J. A. and Hirt, C. W. (1972) "Numerical Calculation of Internal Wave Motions," Journal of Fluid Mechanics, 56(2): 256-276.
- Zel'dovich, Y. B. and Raizer, Y. P. (1967) "Physics of Shock Waves and High-Temperature Hydrodynamic Phenomena, Volumes I and II," edited by W. D. Hayes and R. F. Probstein, Academic Press, 916 pp.
- Zukoski, E. E. (1966) "Influence of Viscosity, Surface Tension, and Inclination Angle on Motion of Long Bubbles in Closed Tubes," Journal of Fluid Mechanics, 25(4):821-837.
- Zuluaga-Angel, A. A., Darden, R. B., and Fischer, H. B. (1972), "Fluid into a Stratified Reservoir," Report EPA-R2-72-037, U. S. Environmental Protection Agency, Washington, DC, 64 pp.